~~The Effect~~ of Fibroblast Growth Factor Signalling ~~on~~ in Choroid Plexus ~~Epithelium Function and Development~~

Adam P. Swetloff

A thesis submitted for the degree of Doctor in Philosophy
University of London

November 2004

Developmental Biology Unit
The Institute of Child Health
30 Guilford Street
London WC1N 1EH

UMI Number: U602442

All rights reserved

INFORMATION TO ALL USERS
The quality of this reproduction is dependent upon the quality of the copy submitted.

In the unlikely event that the author did not send a complete manuscript
and there are missing pages, these will be noted. Also, if material had to be removed,
a note will indicate the deletion.

UMI®
Dissertation Publishing

UMI U602442
Published by ProQuest LLC 2014. Copyright in the Dissertation held by the Author.
Microform Edition © ProQuest LLC.
All rights reserved. This work is protected against
unauthorized copying under Title 17, United States Code.

ProQuest®

ProQuest LLC
789 East Eisenhower Parkway
P.O. Box 1346
Ann Arbor, MI 48106-1346

Abstract

This thesis investigated how fibroblast growth factor (FGF) signalling affects the development and function of the choroid plexus epithelium (CPe) that is normally involved in the secretion and homeostasis of the cerebrospinal fluid. In doing so, it aimed to understand whether the constitutive activation of FGF receptors underlying several cases of syndromic craniosynostosis may affect the development and function of the CPe, and thus be in part responsible for the raised intra-cranial pressure (ICP) and hydrocephalus observed in some of these patients.

I showed that the genes *E2F5*, *FoxJ1* and *p73* involved in the maturation of the CPe and whose knockout cause hydrocephalus were expressed in the developing mouse CPe and the expression was conserved in human embryonic CPe.

I used two cell culture models to test the effect of FGF2 on the function of CPe cells: 1) primary mouse embryonic CPe cells. Dissociated cells were seeded in a tri-dimensional basement membrane matrix (Matrigel) where, following aggregation, they formed fluid-filled hollow vesicles; 2) adult rat CPe cell line (TRCSFB-2) transformed with tsSV40 T-antigen grown as a monolayer. I extended the analysis of the phenotype of the cells in these culture models by showing they expressed E2F5, FoxJ1 and p73, as well as the CPe marker TTR and the tight junction associated protein ZO-1.

I characterized the sequence of events and cellular mechanism leading to CPe vesicle formation in Matrigel using time-lapse microscopy, and showed that the vesicles actively secreted fluid by using secretion inhibitors. I also demonstrated that FGF2 increased the size of the vesicles by increasing cell recruitment but did not affect cell proliferation or fluid secretion. In fact, FGF2 appeared to inhibit secretion. In TRCSFB-2 cells I found that FGF2 decreased the expression of E2F5 and FoxJ1 transcripts, and only a low dose of FGF2 strongly increased cell proliferation.

Finally, I investigated in a mouse model of Apert-Pfeiffer syndromes whether the knockout of the *FgfR2*IIIc isoform affected the ventricular size. I did not observe any abnormalities in the CPe of these animals nor a ventricular enlargement. However, a higher number of neuronal cells seemed to be generated in the cortex of these mutants.

Overall I have provided novel information on the behaviour of CPe cells and the effect of FGF2 on these cells. The future challenge will be to establish whether abnormal FGF-signalling affects fluid secretion and cell proliferation in the context of syndromic craniosynostosis.

Acknowledgements

I am sincerely grateful to my supervisor Dr. Patrizia Ferretti for her intelligent advice and guidance during the course of this project. She has been a wonderful supervisor, and always approachable. I am equally indebted to Sarah Reid for having taught me her laboratory wisdom in my first year and especially how to make those "vesicles"! I would also like to thank my secondary supervisor Dr. Jane Sowden, Professor Andy Copp and Dr Andy Stocker for their appreciated inputs.

I should also like to mention Dr Angie Wade for the help with all the statistical analysis, Dr. Mohammed Hajihosseini (University of East Anglia) for providing the mutant mice in Chapter 9, Dr Terasaki T. (Department of Molecular Biopharmacy and Genetics, Graduate School of Pharmaceutical Sciences and New Industry Creation Hatchery Center, Sendai, Japan) for providing the TRCSFB-2 cells, and Dr Fang Xiang for her help in the laboratory.

Life as a PhD student at the ICH was intellectually stimulating and great fun, and especially on the 7th floor. Special mentions go to Hourinaz Behesti, James Holz, Nathalie Dolmen, David Mowatt, Faisal Idrees, Kathy Whalley, Jean Marie Delalande, Caroline Chilton, Neda Nekbaht, Leonor Santos Ruiz, Esta Adams, Pati, Sofia de Noronha and Diane Vaughan, and all the other members of NDU or MIU I haven't named (there's just too many of you!)

On a more personal note I would like to thank my parents Angela and Denis Swetloff, as well as my brother Alexis Swetloff for their constant support and encouragement over the years. A special thank also goes to Dr[2] Valeria Musi, and Luis Alvarez.

Table of Contents

Title of Thesis: The Effect of Fibroblast Growth Factor Signalling on Choroid Plexus Epithelium Function and Development 1

Abstract 2

Acknowledgements 3

Table of Contents 4

List of Figures 10

List of Tables 14

List of Appendix 15

List of time-lapse microscopy films on CD-ROM 17

Abbreviations 18

Chapter 1 Introduction 20

1.1 The mammalian choroid plexus 20
1.1.1 Anatomical description 20
1.1.2 Ultrastructure of the choroid plexus (CP) 25
1.2 Functions of the choroid plexus 27
1.2.1 Blood-brain barrier 27
1.2.2 Cerebrospinal fluid (CSF) secretion 27
1.2.2.1 CSF production and composition 28
1.2.2.2 Mechanism of CSF secretion 29
1.2.2.3 Main protagonist involved in CSF secretion 30
1.2.2.2 CSF flow and absorption 35
1.2.2.3 Control of CSF secretion 37
1.2.3 Secretion of proteins 38
1.2.3.1 Transthyretin synthesis 38
1.2.4 Other functions 39
1.2.5 Summary- choroid plexus 39
1.3 The embryonic choroid plexus 40
1.3.1 Ontogeny of the embryonic choroid plexus 40
1.3.2 Morphogenesis of the choroid plexuses 41
1.3.2.1 Fourth ventricle development 41
1.3.2.2 Lateral choroid plexus development 42
1.3.2.3 Third ventricle 43
1.3.2.1 Maturation of the choroid plexus epithelium 45
1.3.3 Induction and genes involved in the development of the embryonic choroid plexus 46
1.3.3.1 Induction events 46
1.3.3.2 Genes involved in choroid plexus development 47
1.3.3.3 Recently discovered genes involved in choroid plexus epithelial function and differentiation 48
1.3.4 Summary- the embryonic choroid plexus 54
1.4 Syndromic craniosynostosis 55
1.4.1 Clinical description 55
1.4.2 Aetiology of craniosynostosis 56

1.4.3 Intra-cranial pressure (ICP) and syndromic craniosynostosis 57
1.4.4 Aetiology of intra-cranial pressure in syndromic craniosynostosis 57
1.4.5 Genetic mutations in syndromic craniosynostosis 59
1.5 Fibroblast growth Factors 61
1.5.1 Fibroblast growth factors during the proliferative and neurogenic phases of neural development 62
1.5.2 Fibroblast growth factors and choroid plexus 63
1.6 Fibroblast growth factor receptors 64
1.6.1 FGFR Ig loop III isoforms 66
1.6.2 FGFR and FGF-ligand specificity 66
1.6.3 FGF low affinity receptors: the heparan-sulphate glycoaminoglycans 67
1.6.4 FGF/FGFR complex 68
1.6.5 FGFR signal transduction 68
1.6.6 FGFR expression in the developing central nervous system and the choroid plexus 70
1.6.7 FGFR mutations in syndromic craniosynostosis 72
1.7 In-vivo models for aberrant FGF signalling 73
1.7.1 FGFR mutations in-vivo 73
1.7.2 FGF2 administration to the brain ventricles 77
1.7.2.1 Adult models 77
1.7.2.2 Embryonic models 78
1.7.3 Epithelial fluid secretion affected by FGF 78
1.8 Summary 79
1.9 Hypothesis and experimental strategy 79

Chapter 2 Materials 82

2 .1 General laboratory reagents 82
2.2 Histological reagents and equipment 82
2.3 Immunohistochemical reagents 83
2.3.1 Primary antibodies 83
2.3.2 Blocking peptides and antibody controls 84
2.3.3 Secondary antibodies and signal enhancing reagents 84
2.3.4 Blocking sera 85
2.3.5 Immuhistochemical colorimetric development 85
2.4 Surgical tools and animals 85
2.4.1 Surgical tools 85
2.4.2 Animals 86
2.5 Cells used in tissue culture 86
2.5.1 Embryonic mouse choroid plexus epithelial (CPe) cells 86
2.5.2 Adult T-Antigen transfected rat CPe cells (TRCSFB-2) 86
2.6 Tissue culture reagents and equipment 87
2.6.1 Reagents and equipment for TRCSFB-2 cell line culture 87
2.6.2 Reagents and equipment for CPe primary cell culture 87
2.7 Microscopes 88
2.8 Reagents for RNA expression analysis 88
2.8.1 Reverse transcriptase polymerase chain reaction (RT-PCR) reagents and equipment 88
2.8.2 Oligonucleotides for RT-PCR 89
2.9 Gel electrophoresis and molecular size markers for nucleic acid analysis 92
2.10 Protein Analysis 92

Chapter 3 Methods 94
3.1 Isolation of mouse embryos 94
3.2 Primary culture of choroid plexus epithelial cells 94
3.2.1 Isolation of embryonic choroid plexus epithelial cells 94
3.2.2 Culturing of embryonic CPe primary cells 95
3.2.3 Staining embryonic choroid plexus epithelial cells with diI dye 95
3.2.4 Cytosine Arabinoside treatment 95
3.2.5 Acetazolamide and ouabain treatment 96
3.3 Immunocytochemical staining of embryonic choroid plexus epithelial cell vesicle cultures 96
3.4 CPe vesicle measurement protocols 96
3.4.1 Vesicle and aggregate measurement 96
3.4.2 Assessment of cell proliferation in CPe vesicle cultures 97
3.4.2.1 Quantification of cell proliferation in aggregates 97
3.4.2.2 Quantification of cell proliferation in vesicles 97
3.5 Statistical analysis 99
3.6 ML-wiN modelling 100
3.7 Microscopy of live CPe vesicles 101
3.7.1 Time lapse microscopy of vesicles 101
3.7.2 Deconvolution analysis of vesicles 101
3.8 Protocol for culture of the TRCSFB-2 cell line 101
3.8.1 Thawing of cell stock and culturing 101
3.8.2 Passaging of TRCSFB-2 cells 101
3.8.3 Freezing TRCSFB-2 cells 102
3.8.4 FGF2 treatment 102
3.8.5 Cytosine arabinoside treatment 102
3.9 TRCSFB-2 cell line Transwell secretion assay 102
3.9.1 Growing the cells on Transwell filters 102
3.9.2 Transwell secretion assay 103
3.10 TRCSFB-2 proliferation assays 103
3.10.1 Growing the cells 103
3.10.2 Alamar Blue assay 103
3.10.3 BrdU ELISA assay 104
3.11 Immunocytochemical staining of TRCSFB-2 cells 105
3.12 Paraffin embedding and sectioning of embryos 106
3.12.1 Paraffin embedding 106
3.12.2 Sectioning 106
3.14 Haematoxylin and Eosin staining 107
3.15 Immunohistochemistry on wax sections 108
3.15.1 Re-hydration and pre-treatments 108
3.15.2 Primary antibody application 108
3.15.3 Secondary antibody and visualisation 109
3.16 Immunostaining of vibratome sections 109
3.17 Stereological analysis 109
3.17.1 Neuron number quantification in the cortex 109
3.17.1.1 Systematic random uniform selection (SRUS) of sections for counting neurons 109
3.17.1.2 Counting the neurons 111
3.17.1.3 Estimating the reference volume (Vref) 112
3.17.1.4 Calculating the total number of neurons 113
3.17.1.5 Statistical analysis 113

3.17.2 Ventricle volume determination 114
3.18 RNA isolation 115
3.18.1 Sample preparation 115
3.18.2 RNA extraction 115
3.19 RNA analysis 116
3.19.1 Reverse transcription 116
3.19.2 Primer design 116
3.19.3 Polymerase chain reaction 117
3.19.4 Agarose gel electrophoresis 118
3.19.5 Semi-quantitative analysis 118
3.19.5.1 TRCSFB-2 cell growth and treatment 118
3.19.5.2 Semi-quantification 119
3.20 Protein extraction 119
3.20.1 TRCSFB-2 cells 119
3.20.2 Tissue samples 120
3.21 Protein analysis 120
3.21.1 Quantification 120
3.21.2 SDS-polyacrylamide gel electrophoresis 120
3.21.3 Western blot 121

Chapter 4 Developmental study of the human and murine choroid plexus 123

4.1 Introduction 123
4.2 Results 124
4.2.1 Expression of transthyretin protein in mouse 124
4.2.2 Cell proliferation in the developing choroid plexus 130
4.2.2.1 Cell proliferation in mouse 130
4.2.2.2 Cell proliferation in human 140
4.2.3 Expression of FGF2 protein in the developing choroid plexus 153
4.2.3.1 Expression of FGF2 in mouse 153
4.2.3.2 Expression of FGF2 in human 153
4.3 Discussion 156
4.3.1 Transthyretin expression 156
4.3.2 Cell proliferation in the developing CP 156
4.3.3 FGF2 protein expression in the embryonic CP 158
4.3.4 Summary 158

Chapter 5 Expression of genes associated with cerebrospinal fluid homeostasis and choroid plexus development 159

5.1 Introduction 159
5.2 Results 160
5.2.1 Expression of E2F5 protein 160
5.2.1.1 Expression of E2F5 protein in mouse 160
5.2.1.2 Expression of E2F5 protein in the developing human choroid plexus. 176
5.2.2 E2F5 and PCNA co-localization 185
5.2.2.1 Co-localization in mouse 185
5.2.2.2 Co-localization in human 185
5.2.3 Expression of FoxJ1 protein 191
5.2.3.1 Expression of FoxJ1 protein in mouse 191
5.2.3.2 Expression of FoxJ1 protein in human 191
5.2.4 RNA expression of E2F5, FoxJ1 and p73 195

5.3 Discussion 198
5.3.1 E2F5 expression 198
5.3.2 E2F5 expression and cell proliferation 199
5.3.3 FoxJ1 expression 204
5.3.4 RNA expression of genes whose knockout cause hydrocephalus 204
5.3.5 Summary 205

Chapter 6 Characterization of embryonic murine choroid plexus epithelial cells in culture 206

6.1 Introduction 206
6.1.1 A primary culture of embryonic choroid plexus epithelial cells 206
6.1.2 Characterization of choroid plexus epithelial vesicles 207
6.2 Results 210
6.2.1 Characterization of CPe vesicles 210
6.2.1.1 CPe vesicle cultures 210
6.2.1.2 mRNA expression of CPe vesicles 213
6.2.2 Sequence of events in vesicle formation 215
6.2.3 Time-lapse of vesicle formation and growth 219
6.2.3.1 Vesicle formation 219
6.2.3.2 The dynamic of growth 222
6.2.4 Role of cell proliferation in vesicle formation and growth 225
6.2.4.1 Mitotic events during early vesicle formation 225
6.2.4.2 Mitotic events during vesicle growth 227
6.2.4.3 Effect of Ara-C on early vesicle formation 231
6.2.4.4 Effect of Ara-C on vesicle growth 233
6.2.5 The importance of fluid secretion for vesicle growth 235
6.2.5.1 Effect of fluid secretion inhibitors on vesicle growth 235
6.2.5.2 Recovery of collapsed vesicles 235
6.3 Discussion 238
6.3.1 Vesicle culture characterization 238
6.3.2 Early vesicle formation 238
6.3.3 Late vesicle growth 240
6.3.4 Summary 241

Chapter 7 Effect of fibroblast growth factor signalling on murine embryonic choroid plexus epithelial cells in culture 243

7.1 Introduction 243
7.2 Results 245
7.2.1 Effect of FGF2 on early vesicle formation 245
7.2.1.1 Effect of FGF2 on CPe cell aggregation 245
7.2.1.2 Quantification of the effect of 10 ng/ml on the size of aggregates and vesicles in early vesicle cultures 246
7.2.1.2 Quantification of the effect of 10 ng/ml FGF2 on the number of aggregates and vesicles in early vesicle cultures 247
7.2.1.3 Effects of FGF2 on CPe cell migration and adhesion 250
7.2.1.4 Effect of FGF2 on cell proliferation in early culture 256
7.2.2 Effect of FGF2 on vesicle growth 258
7.2.2.1 Effect of FGF2 on cell proliferation 258
7.2.2.2 Effect of FGF2 on dynamic of growth 260
7.2.2.3 Effect of FGF2 on fluid secretion 262
7.3 Discussion 266
7.3.1 Effect of FGF2 on vesicle formation 266

7.3.2 Effect of FGF2 on vesicle growth 268
7.4.3 Final comments 269

Chapter 8 Effect of FGF2 signalling on the function of rat adult choroid plexus epithelial cells 270

8.1 Introduction 270
8.1.1 TRCSF-B CPe cell line 270
8.1.2 Description of functional assays 271
8.2 Results 273
8.2.1 TRCSFB-2 characterization 273
8.2.1.1 Characterization at the cellular level 273
8.2.1.2 mRNA expression profile 276
8.2.1.3 Protein expression profile 279
8.2.2 Fluid secretion assay 284
8.2.2.1 Method of secretion assay 284
8.2.2.2 Results of secretion assay 286
8.2.3 Effect of FGF2 on hydrocephalic gene markers 288
8.2.3.1 Effect of FGF2 on transcript levels 288
8.2.3.2 Effect of FGF2 on protein expression 294
8.2.4 Effect of FGF2 on TRCSFB-2 cell proliferation 297
8.2.4.1 Alamar blue assay 297
8.2.4.2 BrdU ELISA 298
8.3 Discussion 302
8.3.1 TRCSFB-2 cell characterisation 302
8.3.2 Effect of FGF2 on genes whose knockout cause hydrocephalus 303
8.3.3 Effect of FGF2 on cell proliferation and other TRCSFB-2 function 304
8.3.4 Summary 305

Chapter 9 Mouse model with Apert/Pfeiffer syndrome-like phenotypes 307

9.1 Introduction 307
9.2 Results 308
9.2.1 Histological analysis of Apert/Pfeiffer choroid plexus 308
9.2.2 Ventricle size 311
9.2.3 Apert/Pfeiffer mouse cortex characterisation 314
9.2.3.1 Cortical neuron number and density in post-natal mice 314
9.2.3.2 Cell proliferation in the cortex of post-natal mice 319
9.3 Discussion 321
9.3.1 CP differentiation 321
9.3.2 Neuron number and density 322
9.3.3 Summary 324

Chapter 10 Final discussion 325

10.1 FGF signalling and choroid plexus epithelial cell proliferation 325
10.2 FGF-signalling and choroid plexus epithelial cell fluid secretion 328
10.3 Summary 329

Appendix I 329

Appendix II 334

Appendix III 337

Appendix IV 345

List of References 350

List of Figures

Figure 1. 1 Diagram of the brain ventricles and the location of the choroid plexuses 22

Figure 1. 2 choroid plexus (CP) histology 24

Figure 1. 3 Ultrastructure of the choroid plexus 26

Figure 1. 4 Transport processes involved in CSF secretion by the CP epithelium.34

Figure 1. 5 Flow and absorption of cerebrospinal fluid (CSF) 36

Figure 1. 6 Developmental stages of mouse and human choroid plexus 44

Figure 1. 7 Role of E2F transcription factors in G1-S phase checkpoint control...51

Figure 1. 8 Normal cranial suture development 55

Figure 1. 9 Alternative possible isoforms of the FGFRs 65

Figure 1. 10 Shematic outline of known signal transduction pathways activated by FGFR signalling 70

Figure 1. 11 Description of the strategy for the deletion of the FGFR2 exon 9 (IIIc) 75

Figure 3. 1 Sampling procedure for selecting aggregates based on a systematic random uniform sampling scheme 98

Figure 3. 2 Definition of the focal mid-plane/equatorial plane of an aggregate (or vesicle) 99

Figure 3. 3 Schematic basic of the BrdU ELISA assay 105

Figure 3. 4 Disector stereological probes 111

Figure 3. 6 Point counting grid test system for volume determination of the cortex 112

Figure 4. 1 Immunohistochemical analysis of TTR protein expression in the developing developing mouse IVth ventricle choroid plexus (CP)....126

Figure 4. 2 TTR protein expression in the mouse developing lateral ventricle choroid plexus (CP) and control tissues 128

Figure 4. 3 PCNA protein expression in the embryonic mouse 11.5 dpc-12 dpc choroid plexus 132

Figure 4. 4 PCNA protein expression in the mouse embryonic 12.5 dpc choroid plexus 134

Figure 4. 5 PCNA expression in the 12.5 dpc IVth ventricle CP: higher magnification 136

Figure 4. 6 Sagittal view of the lateral ventricle CP of the 12.5 dpc embryonic mouse stained for PCNA. 137

Figure 4. 7 Sagittal view of the mouse 14.5 dpc IVth and lateral choroid plexus stained for PCNA protein 138

Figure 4. 8 Sagittal view of the mouse 17.5 dpc IVth and lateral choroid plexus stained for PCNA protein 139
Figure 4. 9 PCNA expression in the CS 18 human telencephalic choroid plexus 142
Figure 4. 10 PCNA protein expression in the CS 20 human telencephalic ventricle choroid plexus 144
Figure 4. 11 Higher magnification at the root end of the telencephalic CP of the CS 20 human embryo stained for PCNA protein 146
Figure 4. 12 PCNA protein expression in the CS 23 human embryo telencephalic ventricle CP 147
Figure 4. 13 High magnification of the CS 23 telecencephalic CP stained for PCNA protein. 149
Figure 4. 14 Transverse views of the IVth ventricle CP of the human CS 23 embryo (A-E) and 11 week foetus (F) stained for PCNA protein 151
Figure 4. 15 Expression of FGF2 protein in the mouse and human embryonic choroid plexus 154
Figure 5. 1 E2F5 protein expression in the mouse IVth ventricle CP using the Labvision anti-E2F5 polyclonal antibody 163
Figure 5. 2 E2F5 protein expression in the lateral CP using the Labvision anti-E2F5 polyclonal antibody 165
Figure 5. 3 E2F5 protein expression in the 11.5 dpc mouse embryo using the Santa-Cruz anti-E2F5 polyclonal antibody 167
Figure 5. 4 E2F5 protein in the 13.5 dpc mouse embryo 169
Figure 5. 5 E2F5 protein expression in the 17.5 dpc mouse embryo 171
Figure 5. 6 Staining of mouse embryonic liver (A-B) and dorsal root ganglion (C-D) with St-Cruz anti-E2F5 antibody 173
Figure 5. 7 Western blot analysis of E2F5 protein expression in the developing mouse brain 174
Figure 5. 8 E2F5 protein expression in the CS 18 and CS 20 human embryo lateral choroid plexus (CP) 178
Figure 5. 9 E2F5 protein expression in the CS 23 human embryo lateral CP 180
Figure 5. 10 E2F5 protein expression in the CS 23 human embryo IVth CP 182
Figure 5. 11 E2F5 protein expression in the 11 week fetus IVth CP 184
Figure 5. 12 Co-expression of PCNA and E2F5 in the developing mouse CP 187
Figure 5. 13 Co-expression of PCNA and E2F5 in the CS 23 human lateral CP ... 189
Figure 5. 14 Expression of FoxJ1 protein in the embryonic mouse CP 192
Figure 5. 15 Expression of FoxJ1 protein in the human embryonic CP 194
Figure 5. 16 Expression of E2F5, FoxJ1 and p73 mRNA in the developing mouse choroid plexus 196
Figure 5. 17 Schematic summary of E2F5 protein subcellular expression during choroid plexus epithelium (CPe) development 202

Figure 6. 1 Diagrammatic model of the two main phases of vesicle formation...209
Figure 6. 2 CPe vesicle culture characterization.....211
Figure 6. 3 mRNA expression profile of CPe vesicles. 214
Figure 6. 4 Sequence of events leading to CPe vesicle formation.....216
Figure 6. 5 Linear relationship between the size of aggregates at day 2 and the size of vesicles at day 4. 218
Figure 6. 6 Cell dynamic in early vesicle formation.....220
Figure 6. 7 Dynamic of growth of mature of vesicles. 223
Figure 6. 8 Addition of diI choroid plexus epithelial cells (CPe) to CPe vesicles224
Figure 6. 9 Example of mitotic cells in CPe aggregates after one day in culture. 226
Figure 6. 10 Quantification of mitosis in cultures of CPe grown for one day.....226
Figure 6. 11 Example of mitotic cells in growing vesicles.....228
Figure 6. 12 Quantification of mitosis during the growth of CPe vesicles.....230
Figure 6. 13 Effect of Ara-C on adult choroid plexus epithelial cells transfected with large (SV40) T-antigen (TRCSBF-2).....232
Figure 6. 14 Predicted effect of Ara-C on the initial formation of vesicles.....232
Figure 6. 16 Effect of secretion inhibitors on vesicle growth.....236
Figure 6. 17 Sequence of micrographs illustrating collapsing and recovery of vesicles 237
Figure 6. 18 Recovery of vesicles after washing out secretion inhibitors 237
Figure 6. 19 Diagram of key cellular events involved in vesicle formation and growth.....242
Figure 7. 1 Diagram of cellular events that may be affected by FGF2 during vesicle formation and growth 244
Figure 7. 2 Representative micrographs of the effect of 10ng/ml FGF2 on the formation of vesicles. 248
Figure 7. 3 Multiple linear regression analysis of the size of aggregates and vesicles in ± FGF2-treated early vesicle cultures at different times after seeding.....249
Figure 7. 4 Graph showing the mean number of aggregates and vesicles in ± FGF2-treated and control early vesicle cultures.....250
Figure 7. 5 Graph summarizing the mean area of aggregates in ±100 ng/ml FGF2-treated early vesicle cultures 252
Figure 7. 7 Time-lapse microscopy frames following the effect of 100ng/ml FGF2 on choroid plexus epithelial cell aggregation.....254
Figure 7. 8 Scatter plot showing the number of p-H3 labelled present in control and FGF2-treated early vesicle cultures.....257
Figure 7. 9 Scatter plot showing the number of p-H3 labelled cells present in control and FGF2-treated vesicles.....259

Figure 7. 10 Representative frames from a time-lapse microscopy experiment looking at the effect of 10 ng/ml FGF2 on vesicle growth.....261

Figure 7. 11 Graphical prediction from the multilevel model showing the mean difference in the recovery of FGF2 and control vesicles 265

Figure 8. 1 Activated ts SV40 large T-antigen mechanism of action at 33°C.....271

Figure 8. 3 TRCSFB-2 basic characterisation 274

Figure 8. 4 Expression of the tight junction protein ZO-1 and β-actin by TRCSFB-2 cells.....275

Figure 8. 5 mRNA expression of selected CPe gene markers in TRCSFB-2 cells 278

Figure 8. 6 FGF receptor mRNA expression profile in TRCSFB-2 cells.....278

Figure 8. 7 E2F5 protein expression in TRCSFB-2 cells 280

Figure 8. 8 FoxJ1 protein expression in TRCSFB-2 cells 282

Figure 8. 9 Diagram showing the theoretical basis of the Transwell cell culture assay for measuring fluid secretion 285

Figure 8. 10 TRCSFB-2 secretion curves: absolute concentration of FITC-dextran label 287

Figure 8. 11 RT-PCR products for the choroid plexus epithelial cell gene markers +/- 10ng/ml and 100ng/ml FGF2.....290

Figure 8. 12 Effect of FGF2 on the expression of genes associated with choroid plexus epithelial development predicted by multilevel modelling.....293

Figure 8. 13 Effect of 10ng/ml FGF2 on E2F5 protein expression analysed by Western blot.....295

Figure 8. 14 Effect of FGF2 on TRCSFB-2 cell proliferation assessed by BrdU-ELISA assay 300

Figure 9. 1 Characterization of the FgfR2IIIc$^{+/\Delta}$ mouse choroid plexus at P3 (coronal view).....309

Figure 9. 2 Cell proliferation in the FgfR2IIIc$^{+/\Delta}$ mouse choroid plexus at post-natal day 3 (coronal view) 310

Figure 9. 3 Ventricle volume in wild type (WT) and FgfR2IIIc$^{+/\Delta}$ mice.....312

Figure 9. 4 Example of lateral ventricles from FgfR2IIIc$^{+/\Delta}$ and wild type (WT) 18.5dpc mice stained by haematoxylin and eosin 313

Figure 9. 5 Coronal sections of wild-type (WT) and FgfR2IIIc$^{+/\Delta}$ post-natal day 3 mice cortex stained for the neuronal marker NeuN.....315

Figure 9. 6 Example of the method for sampling neuron counting fields in one selected brain coronal section.....316

Figure 9. 7 Example of an optical disector in a sampled neuron counting field...317

Figure 9. 8 Cell proliferation in the cortex and cerebellum of mutant and wild type (WT) post-natal day 3 mice.....320

List of Tables

Table 1. 1 Concentrations of various solutes in plasma and lumar CSF of human subjects; from (Davson and Segal, 1996) 29

Table 1. 2 Receptors expressed in choroid plexus epithelium (CPe) and their associated cellular response 37

Table 1. 3 Ages at which the choroid plexuses appear in different species 41

Table 1. 4 Stages of differentiation based on the human telencephalic plexus according to (Shuangshoti and Netsky, 1966) 46

Table 1. 5 Putative genes associated with choroid plexus development 52

Table 1. 6 Idiosyncratic table of the principle FGFR mutations associated with the main forms of syndromic craniosynostosis 60

Table 1. 7 Specificity of FGF-FGFR interactions 67

Table 1. 8 Summary of FGFR1 substrates, and their known cellular responses ... 69

Table 1. 9 Mouse models for FGFRs human skeletal dysplasias 74

Table 2. 1 Oligonucleotide primer sequences of reverse transciptase polymerase chain reaction (RT-PCR). 90

Table 3. 1 Concentrations of reagents for one PCR reaction mix with cDNA 118

Table 3. 2 Solutions for preparing Tris-glycine SDS-PAGE 12% resolving gels and 5% stacking gels 121

Table 7. 1 Numerical values of the multiple linear regression model in Fig. 7.1 249

Table 7. 2 Ratio between the number of p-H3 labelled cells and the number of cells present in control and FGF2-treated CPe aggregates 257

Table 7. 3 Ratio between the number of p-H3 labelled cells and the number of cells present in control and FGF2 treated vesicles 259

Table 7. 4 Statistics for ln transformed % recovery of FGF2 and control vesicles 264

Table 7. 5 Independent Student's t-test between ln transformed % recovery of FGF2-treated and control vesicles 264

Table 8. 1 Statistics for the effect of FGF2 on the mRNA of expression of the choroid plexus epithelial cell associated genes 292

Table 8. 2 Descriptive statistics for the effect of FGF2 on BrdU incorporation by TRCSFB-2 cells 299

Table 8. 3 Significance of the effect of FGF2 doses on BrdU incorporation 299

Table 9. 1 Stereological estimates and statistics of the ventricular volume in wild type (WT) and FgfR2IIIc$^{+/\Delta}$ in post-natal day 2 mice 312

Table 9. 2 Neuron cortical numbers and reference volume for wild-type (WT) and FgfR2IIIc$^{+/\Delta}$ mice obtained by stereological counting method 318

List of Appendices

AI. 1 Openlab automation for time lapse-microscopy using three channels: bright field or/and two fluorescent channels 331

AI. 2 Table of incubation times for embedding mouse embryos of different ages in paraffin wax....332

AII. 1 Effect of Ara-C on early CPe vesicle formation 334

AII. 2 Independent Student's t-test of the effect of Ara-C on early vesicle growth....335

AII. 3 Multi-level model for the effect of Ara-C on vesicle growth....335

AII. 4 Effect of Ara-C on mature CPe vesicle growth....336

AII. 5 Independent Student's t-test of effect of Ara-C on mature vesicle growth....336

AIII. 1 Scatter plots of the effect of FGF2 on the size of CPe aggregates....337

AIII. 2 Statistical data for the size of aggregates and vesicles in ± FGF2 treated early vesicle cultures 338

AIII. 3 Independent Student's t-test of the size of aggregates and vesicles between ± FGF2 treated early vesicle cultures....338

AIII. 4 Statistics for the number of aggregates and vesicles in ± FGF2 treated early vesicle cultures 339

AIII. 5 Independent Student's t-test for the number of aggregates and vesicles between ± FGF2 treated early vesicle cultures....339

AIII. 6 Scatter plot of the size of choroid plexus epithelial aggregates cultured with +/- 100ng/ml FGF2....340

AIII. 7 Statistics table of the mean area of aggregates in ±100ng/ml FGF2 treated early vesicle cultures 341

AIII. 8 Statistics table for the mean number of aggregates in ±100ng/ml FGF2 treated early vesicle cultures 341

AIII. 9 Growth curves of recovering vesicles +/- FGF2 after treatment with acetazolamide/ouabain 342

AIII. 10 Correlation between the % of original size after vesicle collapsing and the % recovery in size after eight days....343

AIII. 11 Multi-level modelling vesicle recovery growth curves +/-FGF2....344

AIV. 1 Testing primers for FGFR isoforms on mRNA extract from 11.5dpc whole mouse....345

AIV. 2 Effect of FGF2 on E2F5 mRNA expression 346

AIV. 3 Effect of FGF2 on FoxJ1 mRNA expression 346

AIV. 4 Effect of FGF2 on P73 mRNA expression....347

AIV. 5 Effect of FGF2 on TTR mRNA expression 347

AIV. 6 Multi-level model for the effect of FGF2 on the mRNA expression of selected genes: E2F5, FoxJ1, P73, and TTR.....348

AIV. 7 Effect of FGF2 on TRCSFB-2 cell proliferation assessed by Alamar blue analysis 348

AIV. 8 Graphical prediction from the multi-level model for the effect of FGF2 on TRCSFB-2 cell proliferation assessed by Alamar blue.....349

List of time-lapse microscopy films on CD-ROM

The time-lapse films were saved in a 1024x1022 format in Quicktime version 6 (The CD-ROM is enclosed in the back cover).

Film I.a: Growth of CPe cells on Matrigel over 24 hours starting from the time of seeding. Pictures of the same field of view were taken every 30 minute interval (Chap. 6.3.1).....219

Film I.b: Growth of CPe cells on Matrigel that have been seeded already for one day with 1/4th of the cells stained with diI to help visualization of cell incorporation. Pictures of the same field of view were taken every 30 minute interval over 16 hours (Chap. 6.3.1).....219

Film II.a: Growth of CPe vesicles that have already been eight days in culture. Pictures were taken every one hour interval over 48 hours (Chap.6.3.2).....222

Film II.b: Growth of CPe vesicles stained with 1/4th of CPe cells stained for diI that have been in culture for 5 days. Pictures were taken every one hour interval over 16 hours (Chap.6.3.2).....222

Film III.a: Growth of CPe vesicles over 20 hours starting from the time of seeding. Picture of the same field of view were taken every 30 minute interval. (Chap. 7.2.3.2).....253

Film III.b: Growth of CPe vesicles treated with 100 ng/ml FGF2 over 18 hours from the time of seeding. Pictures of the same field of view were taken every 30 minutes interval (Chap. 7.2.3.2).....253

Film IV.a: Growth of CPe vesicles that have been eight days in culture. Pictures of the same field were taken at 1 hour interval over 48 hours (Chap. 7.3.2.2).....260

Film IV.b: Growth of CPe vesicles that have been eight days in culture, and treated with 10 ng/ml FGF2. Pictures of the same field were taken every 1 hour interval over 48 hours (Chap. 7.3.2.2).....260

Abbreviations

Ara-C:	cytosine arabinoside
Bp:	base pair
BrdU:	bromodeoxyuridine
BSA:	Bovine serum albumin
CAM:	cell adhesion molecule
Cb:	cerebellum
cDNA:	complementary DNA
CI:	confidence interval
CP:	choroid plexus
CPe:	choroid plexus epithelium
CPm:	choroid plexus mesenchyme
dpc:	days post-conception
DEPC:	Diethyl pyrocarbonate
dH_2O:	distilled water
DMEM:	Dulbecco's minimal essential medium
DMSO:	dimethyl sulfoxide
DNA:	deoxynucleic acid
dNTPs:	deoxynucleosides triphosphates
DPBS:	phosphate buffer saline, calcium and magnesium free
ECL:	enhanced chemical luminescence
ECM:	extracellular matrix
EDTA:	ethylene diamine tetra-acetic acid
FCS:	foetal calve serum
FGF:	fibroblast growth factor
FGFR:	fibroblast growth factor receptor
FITC:	fluorescein isothiocyanate
IVth CP:	fourth ventricle choroid plexus
GAG:	glycosaminoglycan
HCl:	hydrochloric acid
HFH-4:	hepatocyte/forkhead-4 (also called FoxJ1)
HRP:	horse radish peroxidase
HRF:	Hypoxia induced factor (HIF) related factor
HSPG:	heparin sulphate proteoglycan
IGF:	insulin growth factor
KDa:	kilo-dalton
MPTP:	1-methyl-4-phenyl-1,2,3,6,-tetrahydropyridine
M-MLV:	Moloney Murine Leukemia Virus Reverse
mRNA:	messenger ribonucleic acid
MW:	molecular weight
NaOH:	sodium hydroxide
pRB:	retinoblastoma tumour suppressor protein
P:	post-natal day
PBS:	phosphate buffer saline
PCNA:	protein cyclin nuclear antigen
PCR:	polymerase chain reaction
PDGF:	platelet derived growth factor

P-H3:	phosho-histone 3
PFA:	paraformaldehyde
PVDF:	polyvinylidene fluoride
RAR:	Retinoic acid receptor
RIPA:	Radioimmunoprecipitation
rpm:	revolutions per minute
RNA:	ribonucleic acid
RT:	room temperature
RT-PCR:	reverse transcription polymerase chain reaction
SRUS:	systematic random nuclear sampling
SDS:	sodium dodecyl sulphate
SDS-PAGE:	SDS-polyacrylamide gel electrophoresis
SD:	standard deviation
SE:	Standard error of the mean
TEMED:	N,N,N',N'-Tetramethylethylenediamine
TGF-β :	transforming growth factor beta
IIIrd CP:	third ventricle choroid plexus
TMD :	transmembrane domain
TTR:	transthyretin
V /SBV :	ventricular zone/subventricular zone
WR :	working reagent

Chapter 1 Introduction

This thesis proposes to study the role of fibroblast growth factor signalling in the function and development of the choroid plexus epithelium in order to understand whether the high incidence of raised intra-cranial pressure in syndromic craniosynostosis can be explained by an increased secretion of cerebrospinal fluid. The introduction will describe these biological concepts by giving an overview of:

- The function and embryonic development of the choroid plexus.
- The craniosynostosis syndromes in man and their genetic aetiology.
- The fibroblast growth factor (FGF) family of ligands and receptors, and downstream signalling pathways.
- The evidence for FGF signalling affecting the function and development of the chororoid plexus epithelium.

Finally, these themes will be synthesised to form the hypothesis of this thesis and the plan of investigation to answer this hypothesis will be presented.

1.1 The mammalian choroid plexus

1.1.1 Anatomical description

The choroid plexuses (CPs) are one of the interfaces that form the blood-brain barrier. They are highly specialised secretory organs situated within the ventricular system of the brain that are primarily involved in secreting cerebrospinal fluid (CSF). The location of the CPs in the human ventricular system is illustrated in Fig.1.1.

The adult choroid plexus is a villous structure that extends from the ependymal surface of the brain into the ventricular lumen. It is made of a single-layered cuboidal epithelium which surrounds a highly vascular connective tissue core (Fig. 1.2). In some textbooks, the vascular fold alone is called the choroid plexus, while this together with the epithelium is called the tela choroidea. However, the term choroid plexus, as used here, which includes both the mesenchymal and epithelial components is more widely used (Peters, 1976). There are four choroid plexuses: the lateral or forebrain CPs are situated in the median wall of each lateral ventricle of the cerebral hemispheres (in the body, the collateral trigone and inferior horn) and in the

roof of the third ventricle. In fact in most mammalian species, the third ventricle CP is continuous with the lateral CPs (Netsky and Shuangshoti, 1975). Hindbrain or fourth ventricle CP is located in the caudal roof of the fourth ventricle. The surface of the choroid plexuses is greatly increased by the presence of villous projections formed by a single layer of epithelial cells surrounding a central core containing capillaries and connective tissue (Figure 1.2). Supplying each choroid plexus are arteries that subdivide into fenestrated capillaries providing blood to each villous, which then join together again to form an efferent vein. Lateral ventricles CPs have a thin, veil-like morphology whereas the fourth ventricle CP is thicker and more lobular in structure. The smaller third ventricle CP has an intermediate morphology (Strazielle and Ghersi-Egea, 2000).

Figure 1. 1 Diagram of the brain ventricles and the location of the choroid plexuses

A: Side view (Left) and frontal view (right) of the ventricular system of the adult human brain (blue). **B**: side view of the adult brain with the location of the choroid plexuses in the floor of the lateral ventricle, the roof of the third ventricle and the roof of the fourth ventricle.

A

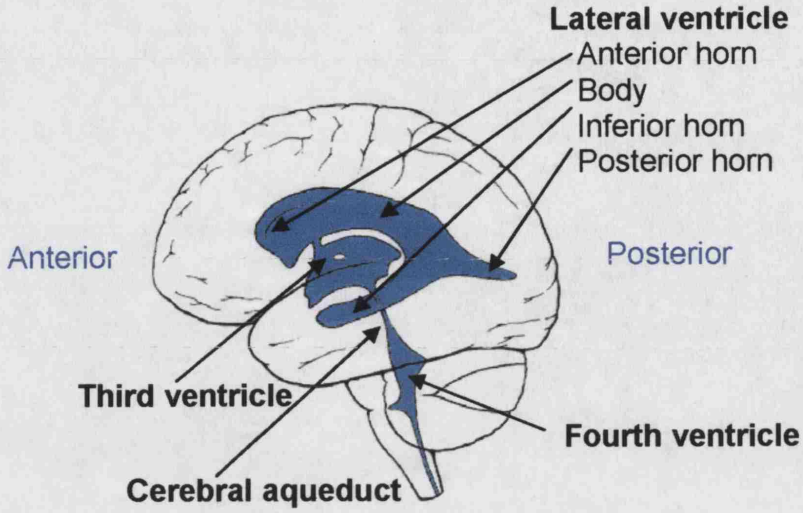
Lateral ventricle
Anterior horn
Body
Inferior horn
Posterior horn
Anterior
Posterior
Third ventricle
Fourth ventricle
Cerebral aqueduct

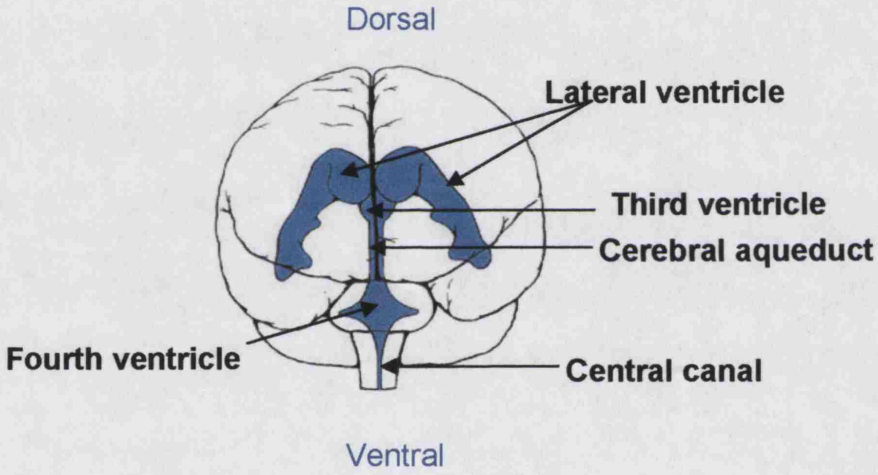
Dorsal
Lateral ventricle
Third ventricle
Cerebral aqueduct
Fourth ventricle
Central canal
Ventral

B

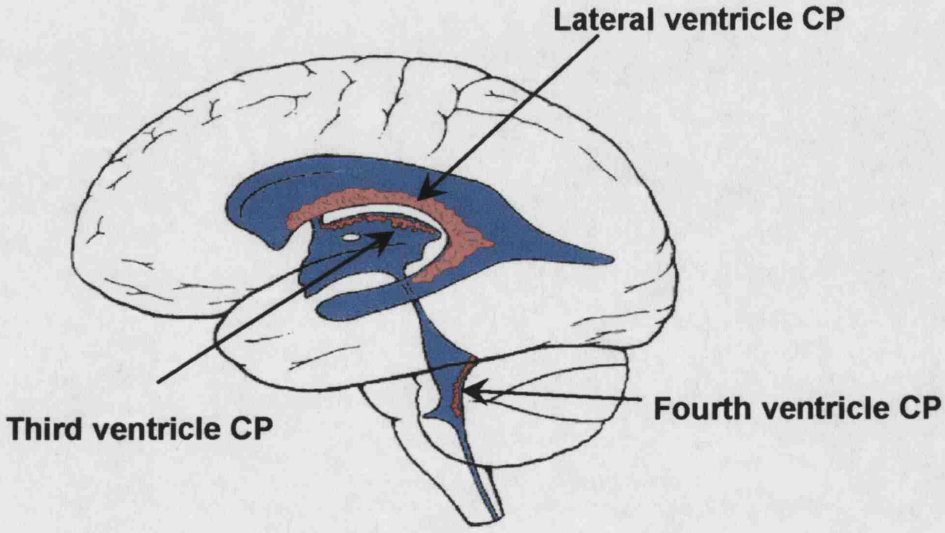
Lateral ventricle CP
Third ventricle CP
Fourth ventricle CP

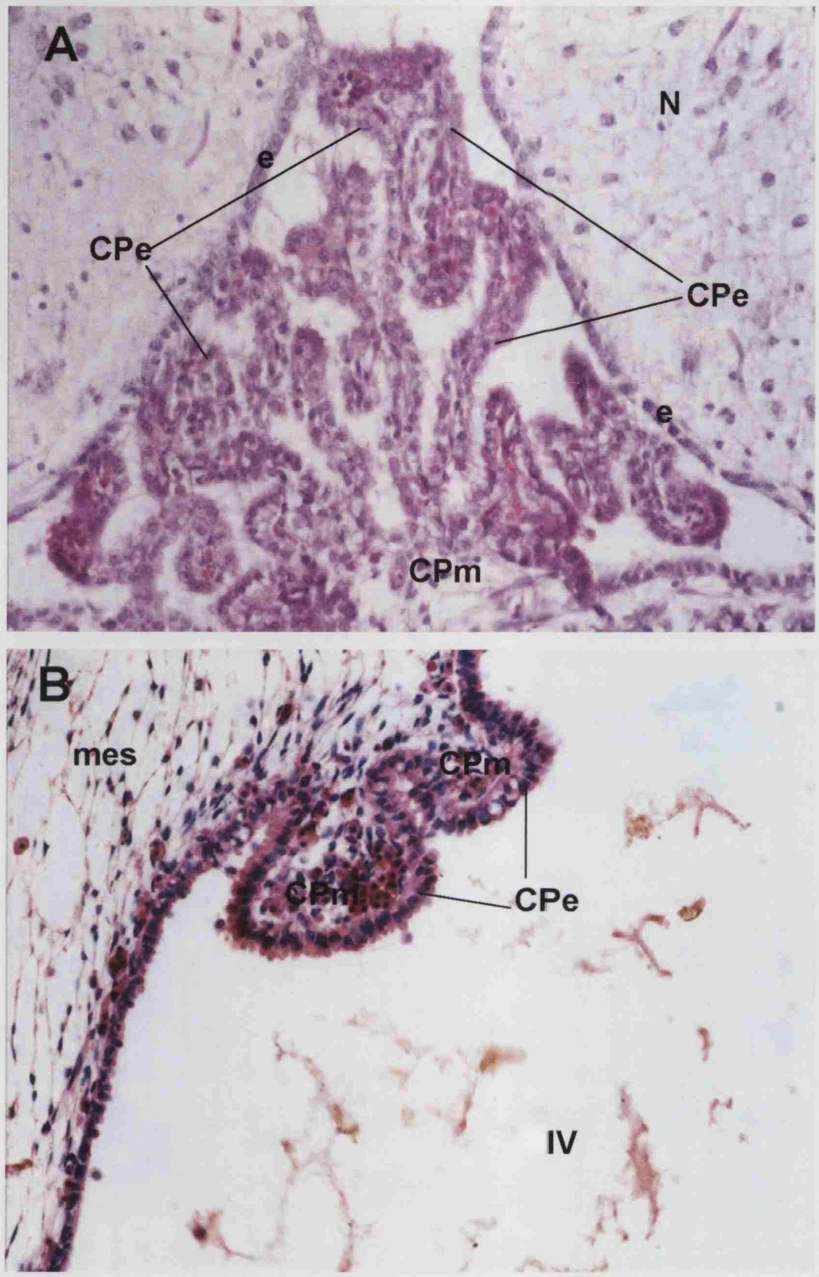

Figure 1. 2 Choroid plexus (CP) histology

A: Adult mouse fourth ventricle choroid plexus and **B**: embryonic mouse fourth ventricle choroid plexus. The CP epithelium (**CPe**) and the CP mesenchyme (**CPm**) are indicated. The CPm in the adult CP is less evident since the villi are thinner and more numerous than in the embryonic CP. **e**: ependyma, **N**: neuroepithelium, **mes:** mesenchyme, **IV**: fourth ventricle.

1.1.2 Ultrastructure of the choroid plexus (CP)

The choroid plexus epithelium (CPe) has a simple cuboidal structure even though foci of pseudostratified stratified epithelium are present (Netsky and Shuangshoti, 1970). The epithelial cells are highly polarized presenting a defined apical and basal pole (Figure 1.3). The apical surfaces, facing the lumen of the ventricles, have multiple irregular and tightly packed microvilli, which form a brush border (Catala, 1998). Cilia may or may not be present at the surface of the epithelial cells; they may occur singly but more often they are present in groups of three. The cilia originate from basal bodies embedded in the apical cytoplasm of the cells. In most studies the CPe cilia are described as having the classic 9 plus 2 configuration: 9 pairs of microtubules surround a central pair of microtubules (Peters, 1976). In the adult animal, the cilia cannot be differentiated from the other projections of the cell surface, since they have similar width and length. In contrast to the apical surface, the basal surfaces are relatively smooth with occasional inpocketings occurring and rest upon a basal lamina. The lateral junctions are responsible for the high intercellular adhesion. At the apical ends, the lateral surfaces of contiguous epithelial cells form zonulae occludens or tight junctions (Brightman, 1968). Just beneath these tight junctions are zonulae adherens and beneath them the plasma membrane of adjacent cells run more or less parallel to each other, apart at their base where complex infoldings occur. These membrane elaborations greatly increase the surface area available for exchange of substances (Tennyson and pappas, 1968). CPe cells are relatively rich in mitochondria, rough endoplasmic reticulum and secretory granules reflecting an important secretory function. In the mouse, by 14 days post conception (dpc) light and dark cells can be identified and the relative proportion of these two cell types remains constant during development and in the adult (Sturrock, 1979). Light and dark choroid epithelial cells were first identified by Wislocki & Ladman (1958) in one of the earliest electron microscopic studies of the choroid plexus. Dark cells appear more electron-dense than lighter cells and have much finer micovilli than the rather spatulate microvilli of the light cells. It has been suggested that the dark cells correspond to relatively dehydrated and shrunken cells, while the light cells are actively secreting, water-laden cells. These light and dark cells may either represent subpopulations of the same basic cell type (Wislocki and Ladman, 1958) or different cell types with distinct functions as suggested by Van Deurs et al. (1978) who found

differences between dark and light cells in the uptake of horseradish peroxidase from the CSF.

Epiplexus, or macrophage like Kolmer cells are also present on the ventricular surface of the CPe. These cells are closely associated with CPs and are regarded as part of the tissue (Ling et al., 1998). Underlying the CPe cells and basement membrane is the CP stroma. This is a fibrovascular matrix, continuous with the leptomeningeal membranes (the pia mater and subarachnoid mater layers) that cover the brain. The CP stroma is highly vascularised with many large capillaries embedded in a loose connective tissue that contains fibroblasts, macrophages and dentritic cells (Fig.1.3).

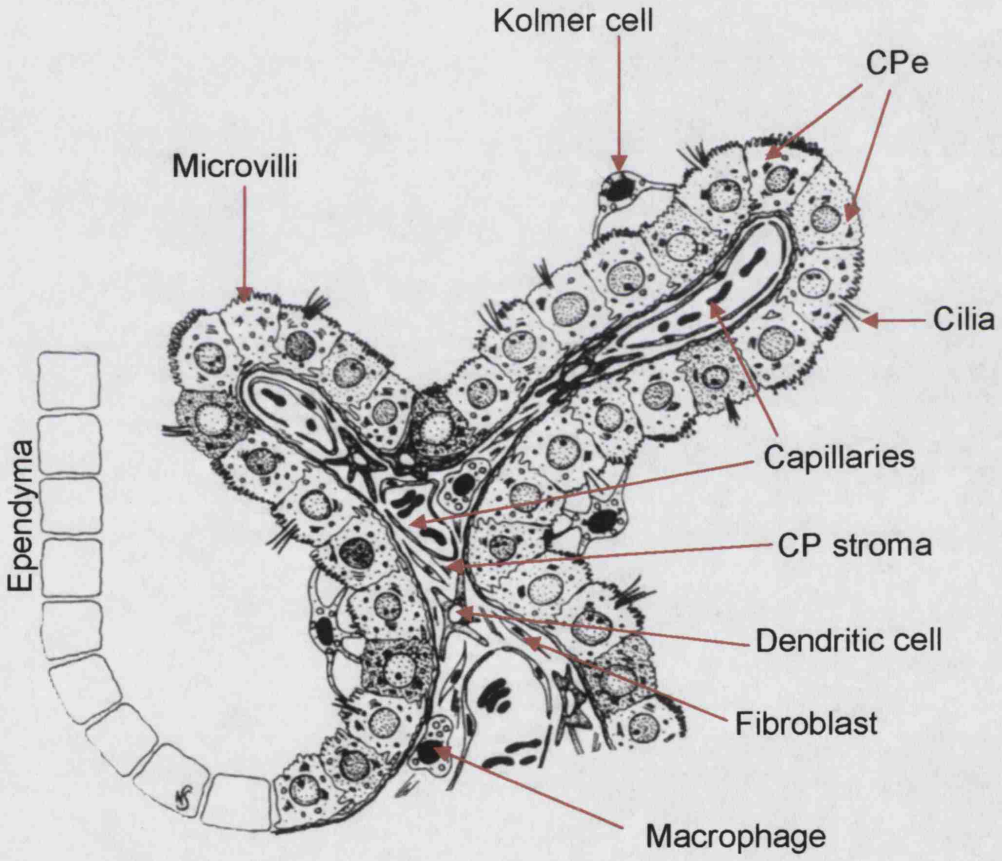

Figure 1. 3 Ultrastructure of the choroid plexus

Diagram representing a high magnification of a choroid plexus villus (see main text for a description). Adapted from Strazielle and Ghersi-Egea (2000).

1.2 Functions of the choroid plexus

1.2.1 Blood-brain barrier

The brain is filled by two fluid compartments: the brain interstitial fluid surrounding the neurons and glia, and the cerebrospinal fluid (CSF) that fills all four ventricles and external surfaces of the central nervous system (CNS) (Segal, 2000). The complex functions of the brain are dependent upon a relatively constant internal chemical environment (Cserr and Bundgaard, 1984). To achieve this, the brain is separated from the blood by two physiological barriers: the blood brain barrier (BBB) and the blood-CSF barrier. In the BBB the endothelial cells separate the blood from the extra-cellular fluid of the brain parenchyma, while in the blood-CSF barrier the choroid plexus epithelium and the arachnoid membrane separate the blood from the CSF (Davson et al., 1987). While the brain capillaries are sealed with tight junctions thus forming the BBB, the capillaries in the choroid plexus do not express tight junction and are "fenestrated", thus allowing the free passage of macromolecules into the surrounding connective tissue (Nilsson et al., 1992). In the CPs, the barrier properties are present at the CPe/CSF interface. CPe cells are interconnected by occlusive tight junctions that severely restrict paracellular movement of fluid and solutes into the CSF. In addition to the choroid plexus epithelium, the arachnoid membrane which has a large contact area with the CSF, serves to impede the passage of solutes from the rather permeable capillaries of the dura mater to the CSF.

1.2.2 Cerebrospinal fluid (CSF) secretion

The choroid plexus epithelial cells produce approximately 80-90% of the total cerebrospinal fluid (CSF). The remaining 10-20% is secreted by the capillary endothelial cells of the blood-brain barrier (Segal, 2001). CSF surrounds the entire brain and spinal cord, filling the ventricular system, the spinal canals, the brain cisternae, and the subarachnoid spaces. The CSF provides hydraulic support that cushions the brain protecting it from trauma. The CSF also provides buoyancy for the brain so that it reduces the weight from some 1500 g to about 50 g (Segal, 2001), and acts as a drainage route for the disposal of waste products from cerebral metabolism (Davson et al., 1987). Moreover, it also appears that CSF holds an important role in neuroendocrine signalling and in maintaining a suitable homeostatic environment for the normal functioning of the central nervous system. Thus it has even been proposed

that the CSF might act as a third circulation system for the transport of peptides and neurotransmitters to the various areas of the brain (Nilsson et al., 1992). It has also been suggested that the CSF secreted into the ventricular system may provide an essential expanding mechanism that determines the shape of the brain during development (Desmond and Jacobson, 1977)

1.2.2.1 CSF production and composition

The bulk of the CSF is continually produced by the choroid plexuses in the four ventricles of the brain so the formation rate of CSF in human adults is approximately 0.35 ml/min, which results in a daily production of roughly 500 ml (Gjerris, 1990).CSF is a clear bright fluid, which has an ionic composition close to that of the plasma. However, differences in ionic composition clearly revealed that CSF is not just a passive ultra-filtrate of plasma but a fluid formed by active secretion (Davson, 1955). The close relation between the capillaries and the choroid plexus epithelium suggests that the fenestrated capillaries produce a plasma filtrate in the interstitium of the choroid plexus. Further transport of solutes and water from the interstitial fluid across the epithelial cells and into the ventricles then depends upon the active transport of ions, particularly sodium. A number of facts support that the existence of specific pathways involved in the process of active secretion of CSF (Speake et al., 2001). Firstly, the hydrostatic pressure in the capillaries of the CP is insufficient for ultrafiltration. Secondly, the osmolarity of the CSF is hypertonic with respect to the plasma (see Table 1.1), whereas if CSF were produced by ultrafiltration it would be slightly hypotonic. Thirdly, the ionic composition of CSF does not match the theoretical concentration as predicted for an ultrafiltrate using the Gibbs-Donnan equilibrium equation (Davson et al., 1987). Finally, the CSF ionic concentrations do not alter in circumstances where plasma ionic concentrations are changed significantly.

Substance	Plasma	CSF	R_{CSF}
Na^+ (mM)	159.00	147.00	0.98
K^+ (mM)	4.63	2.86	0.61
Mg^{2+} (mM)	1.61	2.23	1.39
Ca^{2+} (mM)	4.70	2.28	0.49
Cl^- (mM)	99.00	113.00	1.14
HCO_3^- (mM)	26.80	23.30	0.87
Pi (mg/100ml)	4.70	3.40	0.72
Amino acids (mM)	2.62	0.72	0.27
Osmolality (mosmol/Kg H_20)	289.00	289.00	1.0
pH	7.39	7.30	-
pCO_2 (mmHg)	41.10	50.50	-

Table 1. 1 Concentrations of various solutes in plasma and lumbar CSF of human subjects; from (Davson and Segal, 1996)

The main differences in CSF compared to plasma are that Na^+ and Cl^- are slightly higher, K^+ is lower, and Ca^{2+} and Mg^{2+} have values too large to be accounted for on the basis of simple equilibration. The CSF pH is slightly acid, which reflects the higher pCO_2 and the poor buffering capacity of the CSF (Bradley and Semple, 1962). In addition the concentration of glucose and amino acids is 50 % of the value in plasma. R_{CSF} =CSF/plasma solute concentrations.

1.2.2.2 Mechanism of CSF secretion

A model of the possible mechanism of CSF secretion by the epithelium of the mammalian choroid plexus is shown in Figure 1.4. The basis of CSF secretion relies on the active outward secretion of Na^+ from the choroid plexus epithelial cells into the lumen of the ventricles so that the net movement of Na^+, Cl^- and HCO_3^- produces an osmotic gradient that is sufficient to drive H_2O into the ventricles. The specific processes by which anions, Na^+ and H_2O are transported across the epithelium are given below.

1) Anion transport: about a third of the anions in CSF are made up of bicarbonate (Davson and Segal, 1996). The transport of this ion is not by simple diffusion across the choroidal epithelium but involves a process of CO_2 transport into the epithelial cells from which bicarbonate is derived via the activity of carbonic anhydrase enzymes. These enzymes catalyse the formation of carbonic acid from water and carbon dioxide. The acid then dissociates to form hydrogen and bicarbonate ions. The

HCO_3^- produced helps to drive the Cl^- accumulation on the Cl^-:HCO_3^- exchanger in the basolateral membrane. In addition, the HCO_3^- can directly contribute to CSF secretion by leaving the cell through HCO_3^- permeable channels present in the apical membrane and via the Na^+-HCO_3^- apical co-transporter (Saito and Wright, 1987). Cl^- enters the CSF via Cl^- channels or via the Na^+-K^+-$2Cl^-$ cotransporters, also expressed in the apical membrane.

2) Na^+ transport: Na^+ enters the CPe cells from the blood down a chemical gradient in exchange for the H^+ produced by the action of the carbonic anhydrase, via the Na^+-H^+ exchangers (NHE) on the basolateral membrane. Na^+ is secreted into the ventricles by the electrogenic Na^+-K^+ adenosinetriphosphatase (ATPase) pump located on the apical side of the choroidal epithelium. It is the activity of the Na^+/K^+ ATPase pump that maintains the Na^+ gradient for the activity of the NHE exchanger.

3) H_2O transport: the secretion of Na^+, Cl^- and HCO_3^- across the CPe creates the osmotic gradient that drives H_2O movement into the ventricles of the brain. The route for H_2O is almost certainly transcellular, involving aquaporin 1 in the apical membrane and possibly in the basolateral membrane. Recently, the mRNA for aquaporin 4 was also shown to be expressed in the lateral CP of the rat, which may also be involved in H_2O transport (Venero et al., 2001). In addition, H_2O may also be transported via an ion dependent pathway established by the co-transport of K^+ and Cl^- (Zeuthen, 1994).

4) K^+ transport: there is a small net absorptive flux of K^+ (apical to basolateral) across the CPe (Wright, 1978). However, transporters for K^+ play an important role in the process of CSF formation by making a contribution to the membrane potential of the cell, as well as maintaining the volume of the cell (Speake et al., 2001). The action of the Na^+-K^+ ATPase results in the accumulation of intracellular K^+. The efflux across the apical membrane occurs via the Na^+-K^+-$2Cl^-$ cotransporter or the K^+ channel (Eg. Kir7.1 and Kv1.3), as well as via the channels in the basolateral membrane (Zeuthen and Wright, 1981). This movement of K^+ accounts for the net absorption of K^+ across the epithelium.

1.2.2.3 Main protagonist involved in CSF secretion

1) Carbonic anhydrase: carbonic anhydrase (CA) activity is due to the products of a gene family encoding seven different isozymes (CA I to CA VII). The activity of this enzyme was recognised very early on to be critical for the secretion of CSF.

Acetazolamide or Diamox, a specific inhibitor for certain isozymes of CA, was found to reduce the rate of CSF secretion by 50-60% compared to normal, and is active only from the basolateral side (Maren, 1962; Maren, 1977; Segal, 2000). Several isozymes are expressed by the choroid plexus: the cytosolic carbonic anhydrase type II and type III are present in the epithelial cells (Roussel et al., 1979; Nogradi et al., 1993). The mitochondrial carbonic anhydrase type V is weakly present in the choroidal epithelial cells (Vaananen et al., 1991).

2) The Na^+/K^+ ATPase pump: the Na^+/K^+ ATPase pump transports two K^+ into the epithelial cells for three Na^+ carried into the ventricular lumen. The transport is an active transport and is catalysed by the hydrolysis of one ATP molecule. The cardiac glycoside ouabain inhibits the Na^+/K^+ ATPase pump from the ventricular side of the choroid plexus. This has the effect of decreasing the rate of CSF secretion by roughly 60%, thus confirming the central role of this enzyme in CSF secretion. Immunological techniques confirmed that the enzyme was restricted to the apical side of the epithelium (Masuzawa et al., 1985; Ernst et al., 1986). The enzyme is a ubiquitous plasma membrane-bound enzyme that consists of two proteins subunits in a 1:1 ratio. The α subunit (112 KDa) is the catalytic site for ATP hydrolysis and serves as the receptor site for cardiac glycosides; the β subunit (35 kDa) is a glycoprotein the function of which is still unclear. The two subunits are encoded by multiple gene families: there are at least three different isoforms of the α subunit (α_1, α_2, α_3) and two isoforms of the β subunit (β_1, β_2). It has been suggested that six structurally different $\alpha.\beta$ heterodimers may be expressed by different cells in the brain (Watts et al., 1991). The different isoforms are likely to play distinct physiological roles since they are expressed in a tissue specific manner. The choroid plexus epithelium expresses the α_1, β_1 and β_2 isoforms (Zlokovic et al., 1993). The catalytic α-subunit of Na^+/K^+ ATPase has well characterised phosphorylation sites for adenosine 3', 5'-cyclic adenosine monophosphate (cAMP)-dependent protein kinase (PKA) and protein kinase C (PKC). Activation of PKC was found to inhibit the Na^+/K^+ ATPase activity in the choroid plexus (Fisone et al., 1995).

3) Cl^- and K^+ channels: the patch clamp technique was used to study the ion channel activity in apical membrane of epithelial choroidal cells. The technique revealed the existence of different classes of Cl^- selective channels. A low conductance channel (26 pS), was detected frequently. The occurrence of this channel appeared to increase

in tissue bathed in forskolin; an adenylate cyclase activator. This finding suggests that cAMP is involved in the process (Garner and Brown, 1992). In addition, studies in the dog have shown that cholera toxin increases the rate of CSF secretion, thus confirming the role of cAMP in this process (Epstein et al., 1977). The second class of channel (320pS) was observed infrequently and was similar to the maxi-Cl^- channels described in other cell types. The maxi-Cl^- channels are thought to be involved in volume regulation, whereas the other Cl^- channels are thought to be involved in the mechanism of CSF secretion.

Two potassium currents have bee identified in the rat choroid plexus, both rectifying but in opposite directions and with different time dependence. Only the outward current was shown to be time-dependent. These currents may have a role in the control of the membrane potential and in the activation of ion conductance in response to signalling factors (Kotera and Brown, 1994). These channels are part of the critical control of K^+ concentration in CSF and respond to external K^+ and osmotic stress (Keep and Xiang, 1995; Klarr et al., 1997).

4) The Na^+/H^+ antiporters: the mammalian Na^+/H^+ exchanger (NHE) are a family of integral membrane proteins that translocate Na^+ across the cell surface and mitochondrial membranes. The process is electroneutral and is driven by the combined chemical gradients of Na^+ and H^+. NHEs are involved in the regulation of intracellular pH, cell growth, cell volume and transcellular Na^+ absorption (Yip, 1997). In mammalian cells six NHE isoforms have been identified (Kurashima et al., 1998), which differ in second messenger regulation, sensitivity to the inhibitor amiloride, and in physiological function (Levine et al., 1995). In the choroid plexus NHE activity is found at the basolateral membrane of the epithelial cells (Segal, 2000). NHE1 is expressed in virtually all tissues and cells where it is thought to fulfil house keeping functions. For the moment, only this ubiquitous NHE1 isoform has been identified in the choroid plexus epithelium. NHE1 can be activated by an extreme variety of extracellular stimuli that all result in an increase in affinity of the exchanger for protons (Counillon and Pouyssgur, 2000).

5) The anion coupled transport systems: the coupled anion exchanger Cl^-/HCO_3^- (AE2) is expressed on the basolateral plasma membrane of the choroid plexus epithelium (Lindsey et al., 1990). The activity of AE2 can be demonstrated by the action of DIDS (4,4'-Diisothiocyanostilbene-2,2'-Disulfonic acid), which causes a 30% reduction in the rate of CSF secretion (Segal, 2000). AE2 is an antiporter which

exchanges Cl^- from the interstitial fluid with bicarbonate from the choroidal epithelial cells. Although AE1 (band 3) is known to bind ankyrin and the membrane-cytoskeleton, it is not yet certain whether the AE2 isoform binds to these molecular assemblies (Marrs et al., 1993).

Na^+-K^+-$2Cl^-$: two isoforms of the cotransporter have been identified. NKCC1 appears to be ubiquitously expressed and plays a role in cell volume regulation as well as transepithelial ion transport (Russell, 2000), and NKCC2 is expressed only in the ascending limb of the loop of Henle (Russell, 2000). The CPe expresses the NKCC1 isoform.

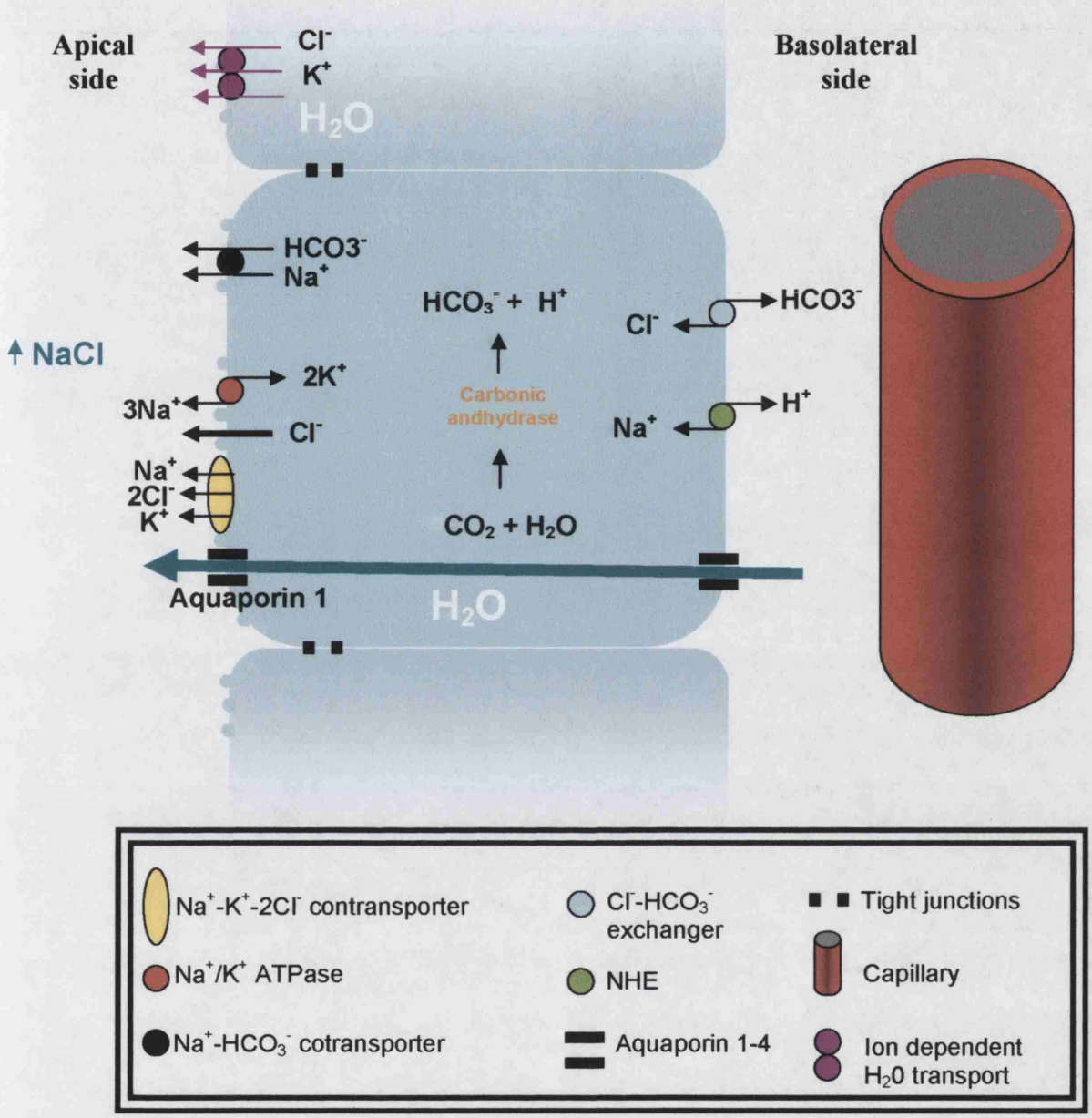

Figure 1. 4 Transport processes involved in CSF secretion by the CP epithelium

The Na^+-K^+ ATPase pump, the channels for Cl^- and K^+, the Na^+-K^+-$2Cl^-$ co-transporter, the Na^+/HCO3$^-$ co-transporter and the aquaporin (1 and 4) channels are located at the ventricular lumen in the apical ciliated side of the CPe. The carbonic anhydrase located in the cytoplasm catalyses the formation of HCO_3^- from H_2O and CO_2. The Na^+/H^+ (NHE) and Cl^-/HCO3$^-$ antiporters and aquaporin channels are located on the blood side of the CPe cells. Water is drawn in into the ventricle lumen by osmosis after a build up of NaCl, and HCO_3^- and via an ion dependent pathway using the Cl^--K^+-H_2O co-transporter. Adapted from (Segal, 2000).

1.2.2.2 CSF flow and absorption

In man, the volume of CSF is about 200ml, of which 25-30ml are contained in the ventricles with the remainder filling the subarachnoid space (the space formed between the middle meningeal layer: the arachnoid mater, that loosely surrounds the brain and the inner most meningeal layer, and the pia mater, that attaches to the surface of the brain), the basal cisterns of the brain (areas of large depressions in the subarachoid space) and the space surrounding the spinal chord and the central canal. The choroid plexuses of the lateral ventricles produce the bulk of the CSF, which drains via the foramina of Munro (also called the interventricular foramen) into the centrally situated third ventricle, and down the narrow aqueduct of Sylvius (also called the cerebral aqueduct) into the fourth ventricle. The CSF then exits from the ventricular system via the foramina of Luschka (the lateral aperture of the fourth ventricle) and Magendie (the median aperture of the fourth ventricle) into the subarachnoid spaces where it fills the basal cisterns of the brain and spinal chord. CSF is drained back into the circulation via three routes: through the valve-like arachnoid villi into the sagittal sinus, via similar structures found around the spinal nerve roots, and finally via the olfactory tracts into the lymphatics of the nasal cavity and cervical region. The time necessary for the replacement of the CSF is about 200 minutes and varies only slightly among mammalian species (Cserr, 1971). The flow of the CSF circulation is shown in Fig.1.5.

Movement of CSF in the ventricles and spinal cord arises as a consequence of asynchronous beating of the cilia on the surface of ependymal cells, the pulsatile blood flow close to the subarachnoid spaces, and the constant production of new CSF by the CPs (Greitz et al., 1997).

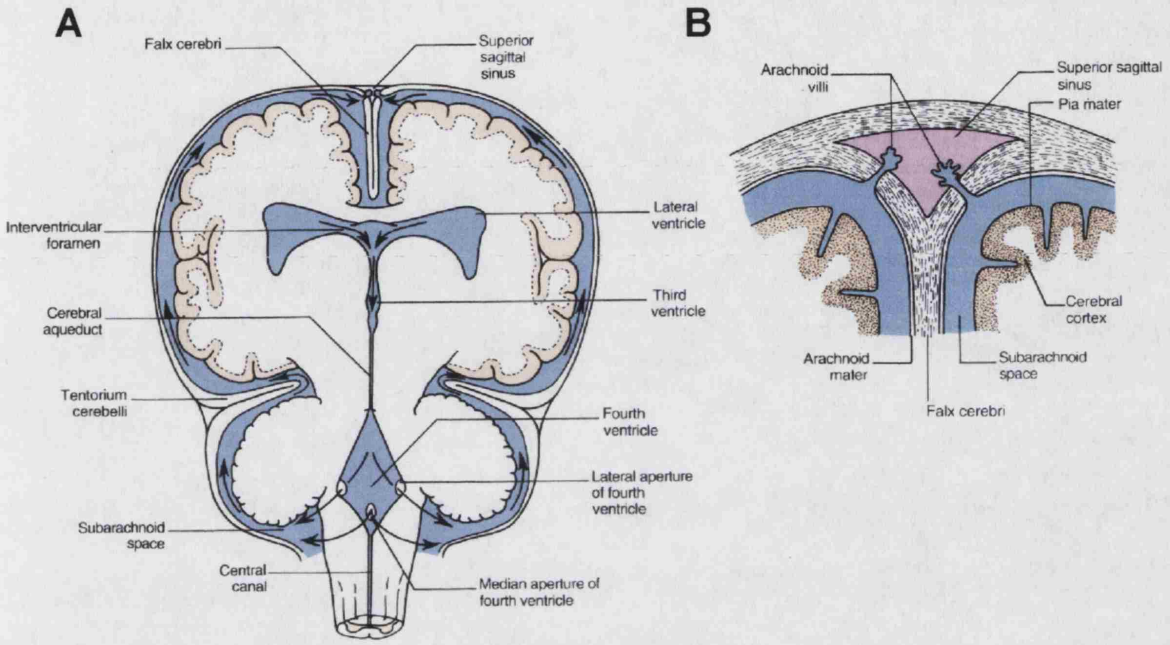

Figure 1. 5 Flow and absorption of cerebrospinal fluid (CSF)

A: the cerebral ventricular system and its relationship with the subarachnoid space; the circulation of CSF is indicated by arrows (see text for details). Cerebrospinal fluid is reabsorbed into the dural venous sinuses, principally through the superior sagittal sinus. **B**: transverse section though the **superior sagittal sinus** showing **arachnoid villi**, which consist of invaginations of **arachnoid mater** through the dural wall and into the lumen of the sinus. The diagram also shows the **pia mater** that adheres to the surface of the brain, the **arachnoid mater** that loosely surrounds the brain and the subarachnoid space between the two. The **dura mater** (or **dura wall**) is represented in dashed-grey. It is the outer-most lepto-meningeal membrane loosely surrounding the brain; it is a tough and fibrous membrane and also forms the **falx cerebri** by extending from the cranial roof into the great longitudinal fissure between the cerebral hemispheres, and the **tentorium cerebelli** by extending inwards from the occipito-temporal region of the skull to lie between the posterior part of the cerebral hemispheres and the cerebellum in the transverse cerebral fissure (as shown in (A)),. Diagrams taken from (Crossman and Neary, 1995).

1.2.2.3 Control of CSF secretion

The mammalian choroid plexus epithelium contains a number of receptors for autonomic neurotransmitters, hormones and growth factors that appear to modulate CSF secretion (Table 1.2, adapted from Nilsson, 1992). Furthermore, the choroid plexus is innervated with noradrenergic sympathetic, cholinergic and peptidergic nerves probably of autonomic origin.

Receptor	Endogenous ligand	2nd messenger	Cellular response
β_1	Noradrenaline	+ cAMP	inhition of CSF via cAMP mediated
β_2	Noradrenaline	+ cAMP	decrease of Na+/K+ ATP
D_1	Dopamine	+ cAMP	DARPP-32
H_2	histamine	+ CAMP	enhances passage of K+ into CSF
$5\text{-}HT_{1C}$	5-hydroxytryptamine	PI-hydrolysis	increased CSF in dog + monkey
Melatonin	melatonin	- cAMP (Gi)	stimula/tion of lateral ventricel CP secretion
Muscarinic	acetylcholine	?	agonist inhibited CSF secretion in rabbit
ANP-A	ANP, BNP	+ cGMP	CSF inhition possibly via inhibtion of NHE
V_1	AVP	PI-hydrolysis	inhibits CSF secretion
AVP_{4-9}	AVP_{4-9}	?	?
Ang-II	Angiotensin II	?	decrease in CSF secretion in rabbits
IGF-I	IGF-I, IGF-II	tyrosine kinase	increased basolateral Na^+ extrusion
Insulin	insulin, IGF-II	tyrosine kinase	"
Man 6-P/IGF-II	IGF-II	?	clearance receptor targeted to lysosomes
Growth hormone	Growth hormone	?	?
VIP	VIP	+ cAMP	decrease CSF production
Endothelin	endothelin	?	?
GABA-A	GABA	?	?
Benzodiazepine	?	?	?
T-2	tryptamine	?	?
Glucocorticoid	cortisol	?	betamethasone decresases CSF secretion + Na+/K+ ATPase activity
Sex steroid	sex steroids	?	?
Thyroid	T_3	?	choline inhibtion, slight stimulation of Na+/K+ ATPase activity
FGFR-1-4	FGF	?	?

Table 1. 2 Receptors expressed in choroid plexus epithelium (CPe) and their associated cellular response

Table showing the receptors or binding site demonstrated in the CPe by either receptor binding, immunohistochemistry, in-situ hybridization, or pharmacological characterization of the second messenger response. The cellular response is defined as the primary effector mechanism after binding of the ligand to the receptor e.g stimulation (+) of cAMP production. (Adapted from Nilsson *et al*, 1992).

1.2.3 Secretion of proteins

The choroid plexus epithelial cells synthesise and secrete numerous plasma proteins into the CSF. Since this fluid is continually produced at a relatively high rate and moves along the ventricular system and subarachnoid spaces, it can distribute CSF-borne polypeptides throughout the brain and spinal cord. This is often referred as "volume transmission" (Chodobski and Szmydynger-Chodobska, 2001). The reason for the high protein synthesis and secretion from the CP may be to provide some supplements that are important in maintaining brain homeostasis, in facilitating normal brain development, and in assisting brain injury repair (Nicholson, 1999). Among these proteins are transferrin, ceruloplasmin, cystatin C, β2-microglobulin, vasopressin, TGFβ (β1, β2, and β3), insulin growth factor II (IGFII), and transthyretin (TTR) (Nilsson et al., 1992; Chodobski and Szmydynger-Chodobska, 2001).

1.2.3.1 Transthyretin synthesis

The expression of transthyretin (TTR) (also called pre-albumin) was of particular interest because it is an important marker for CPe cell differentiation. The three main sources of TTR are the liver, the retina and the choroid plexus epithelium. TTR, which represents about 20% of the total protein synthesized by the choroid plexus, is secreted into the CSF (Dickson et al., 1986). In fact, the CPs produce a hundred times more TTR per gram of tissue than the liver does and at a rate thirteen times faster (Dickson et al., 1986; Zheng et al., 1999). Interestingly, during evolution TTR was first expressed in the choroid plexus and then in the liver (Southwell et al., 1991). TTR is a highly conserved 55kDa tetramer protein, consisting of four identical subunits of 127 amino acids in man (Kanda et al., 1974). TTR binds thyroid hormones derivatives and also participates in the transport of retinol by binding the retinol binding protein (Thomas et al., 1988). The central cleft of the TTR tetramer is the binding site for T3 (triiodothyronine) and T4 (thyroxine) (Sunde et al., 1996). The outer aspects of the TTR molecule bind the retinol-binding protein in association with retinol (Kopelman et al., 1976). Thyroid hormones are known to be essential for the development of the brain, although the precise mode of action of these hormones on the developing brain is less clear. A thyroid deficiency during brain growth leads to multiple abnormalities in the neuronal cells that include decrease in myelin deposition, stunting of dentrite growth, and a reduction in the number of synapses (Thomas et al., 1988). Transthyretin is the only thyroid hormone binding protein

synthesised in the brain, where it acts to buffer the levels of thyroid hormones, particularly thyroxine (T4) since it is the predominant form secreted by the thyroid gland into the blood stream. The T4 present in the blood then enters the CSF either transcellularly via the CPe or into the interstitial fluid via the endothelial cells of the blood brain barrier. Targeted disruption of the TTR gene in stem cells revealed a slight decrease in T4 in the brain from mice as well as decreased residence time (Palha et al., 1997) but the mice were phenotypically normal and fertile, probably due to the multicomponent nature of thyroid hormone homeostasis (Schreiber et al., 2001).

1.2.4 Other functions

The choroid plexus as well as maintaining a blood-brain barrier, secreting CSF, and synthesising and transporting proteins has other key functions, which are the following:

1) Nutritive function for the brain especially in early embryological development (Hakvoort and Johanson, 2000).
2) Intraventricular expanding force for the brain, especially in human (Dziegielewska et al., 2001).
3) Retrograde transport of a variety of endogeneous and exogeneous anionic compounds from the CSF to the blood (Gao and Meier, 2001), amino acids and sugars (Segal, 2001).
4) Metabolism of potentially harmful drugs and modulation of cerebral bioavailability of a drug (Strazielle and Ghersi-Egea, 2000).
5) Accumulations of heavy metal e.g lead (Zheng et al., 2001).
6) Immune system surveillance and allowing communication between the immune system with the CNS (Engelhardt et al., 2001).

1.2.5 Summary- choroid plexus

The CPs are specialized secretory villous structures extending from the ependyma surface of the brain into the ventricular lumen. There are four different choroid plexuses: two of them are situated in each of the lateral ventricles, which extend through the interventricular foramen to form the third ventricle CP; the last choroid plexus is located in the roof of the fourth ventricle. CPs have several important functions: the CPs are the main producers of CSF that provides nutritional,

hydrational and mechanical support for the central nervous system. In addition, CPs act as a barrier to solutes between the blood and the CSF. The CPs are also important in maintaining the homeostasis of the CSF composition, and are sites for immunological and toxicological protection. The embryonic development of the CPs are not very well understood, nor is the function of the embryonic CPs. The next section reviews what is known about CP development.

1.3 The embryonic choroid plexus

This section presents an overview of the development of the embryonic choroid plexus (CP) with a special emphasis on human, mouse and rat CPs. Fisrtly, the general ontogeny of the choroid plexuses will be presented, discussing the timing of the appearance of the different CPs and the embryonic origin of the different cells that form the CP. Secondly, the morphogenetic events underlying the development of the different CPs will be presented along with the different stages of maturation and differentiation of the CPe cells. Finally, the main genetic pathways that are thought to induce formation and differentiation of the CPs will be reviewed, with a specific interest in the newest genes that have been characterised and shown to affect the normal differentiation of CPe cells especially in terms of their normal secretory function.

1.3.1 Ontogeny of the embryonic choroid plexus

Shortly after the anterior neuropore of the neural tube closes, the CPs begin to appear as invaginations of epithelial tissue protruding into the lumen of each of the four cerebral ventricles. In all species so far studied they appear in the sequential order: first IVth, then lateral, and finally IIIrd ventricle. Table 1.3 shows the ages for mouse, rat and human species when the CPs of each ventricle are morphologically first apparent.

Species	Lateral	IIIrd	IVth	Gestation time
Mouse	12.5 dpc	14.5 dpc	10.5-11.5 dpc	21 days
Rat	13 dpc	16 dpc	11 dpc	21 days
Human	Day 44 (CS 18)	Day 57 (CS 23)	Day 41 (CS 17)	38 weeks

Table 1. 3 Ages at which the choroid plexuses appear in different species

The table compares the age, in days post-conception (dpc) or in days gestation (also expressed in Carnagie Stage; CS), at which the different (fourth (IVth), third (IIIrd), and lateral ventricle) choroid plexuses appear in mouse, rat and human species. Adapted from (Catala, 1998).

The choroid plexus has a double embryonic origin. Whilst the CPe is generated from pseudostratified neuroepithelium lining the neural tube, the mesenchymal and vascular cells originate from the paraxial mesenchyme (Wilting and Christ, 1989). In the case of the lateral ventricle CP mesenchyme, the mesodermal cells may be derived from the neural crest cells (Couly et al., 1993; Catala, 1998). Some early histological studies have indicated that the CPe is generated from regions where the neuroepithelium has become nearly effaced or/and in contact with mesenchyme (Birge, 1962).

1.3.2 Morphogenesis of the choroid plexuses

1.3.2.1 Fourth ventricle development

Differentiation of the fourth ventricle (IVth) choroid plexus is thought to occur when the neuroepithelium becomes tightly associated with the underlying mesenchymal tissue via the basement membrane (Thomas et al., 1988). The developing CP primordia in the roof of the fourth ventricle have been identified as a single layer of cells expressing transthyretin (TTR) mRNA, sharply demarcated from adjacent non-TTR expressing neuroepithelium as early as 10dpc in the rat (Cavallaro et al., 1993). In the roof of the fourth ventricle, high level of TTR mRNA synthesis initially appears in two patches of neuroepithelial cells symmetrically arranged on each side of the midline of the neural tube, whilst the morphologically similar epithelium between these two areas synthesises little or no transthyretin (Thomas et al., 1988). These two ridges of TTR expressing neuroepithelium, are also referred as choroidal folds and appear as two thickened areas on either side of the roof of the fourth ventricle, with dense capillary network within the adjacent mesenchymal tissue. By 11.5 dpc in the

mouse and 12dpc in the rat, these choroidal folds protrude into the ventricular space with CP epithelial cells that are polarized and differentiated, both morphologically and functionally. Ultimately, these choroidal folds fuse at the midline junction of the roof of the fourth ventricle as they start forming primitive CP villi at 12.5dpc in the mouse and 13dpc in the rat (see Fig.1.6). Subsequently, the CP becomes more extensively folded, and more vascularized. As development proceeds the CP becomes progressively more convoluted and arborized (Thomas et al., 1988).

1.3.2.2 Lateral choroid plexus development

The CP in the lateral ventricles of the forebrain develops from the inner wall of the telencephalon which separates the lateral ventricles from the third ventricle immediately posterior to the developing foramen of Monro. A part of the medial roof of the telencephalon, referred to as the choroidal plaques is regarded as the CP-forming area. As seen in the fourth ventricle CP development, TTR mRNA is expressed in cells within this area prior to morphological development, between 11 dpc and 11.5 dpc in the rat (Cavallaro et al., 1993). Cell proliferation has been shown to be significantly lower in the dorsal midline and in the medial walls of the telencephalon than in the rest of the telencephalon. The presumptive CP of the lateral ventricles can be recognised at 11 dpc in the mouse as a bilateral ridge in the roof of the interventricular foramen. It has been described as a small region of thinning neuroepithelium at the midline of the dorsal telencephalon, identifiable by the presence of many pyknotic cells that mark the sites of out-folding (Sturrock, 1979). The median wall of the 11 dpc murine telencephalon has four distinct zones at this stage. From dorsal to ventral these are: 1) the neuroepithelial layer of the cerebral cortex, 2) the cortical hem, which is a region of thinning pseudostratified neuroepithelium, 3) a junctional epithelium, which may contain CPe precursors, and 4) the choroid plaque (Grove et al., 1998). As the telencephalic CPs develop further, they extend into the ventricles and become more clearly vascularized. The pseudostratified CP epithelium becomes thinner (i.e more columnar distally). Each epithelial layer possesses at first three, then two, and finally a single layer of cuboidal cells, except at the root of the CP which remains pseudostratified columnar even in post-natal life as observed in human (Shuangshoti and Netsky, 1966). In human, the laterals CPs from week 9 to week 17 of gestation appear extremely large in relation to the lateral ventricles. The lack of such appearance in animal embryos, led some

authors to consider this appearance to be pathological (Voetmann, 1949). However, Netsky and Shuangshoti considered this enlargement as physiological. The loose and bulky stroma is related to the formation of large amounts of mesenchymal mucin (a hygroscopic material consisting of gelatinous polyssacharide-containing and hyaluronic acid material, similar to Wharton's jelly in the umbilical cord), and is thought to be an additional mechanism for expanding the much larger ventricular system of the human foetus during early brain development (Kappers, 1958) (see Figure 1.6).

1.3.2.3 Third ventricle

The third ventricle (IIIrd) CP is the last CP to appear, and its development is the least well documented. It is comparatively smaller in size. It has been suggested that the third ventricle CP develops from the lateral CP via the interventricular foramina. The basic events of IIIrd CP morphogenesis are expected to be the same as for the other CPs, although details of gene expression may show some differences.

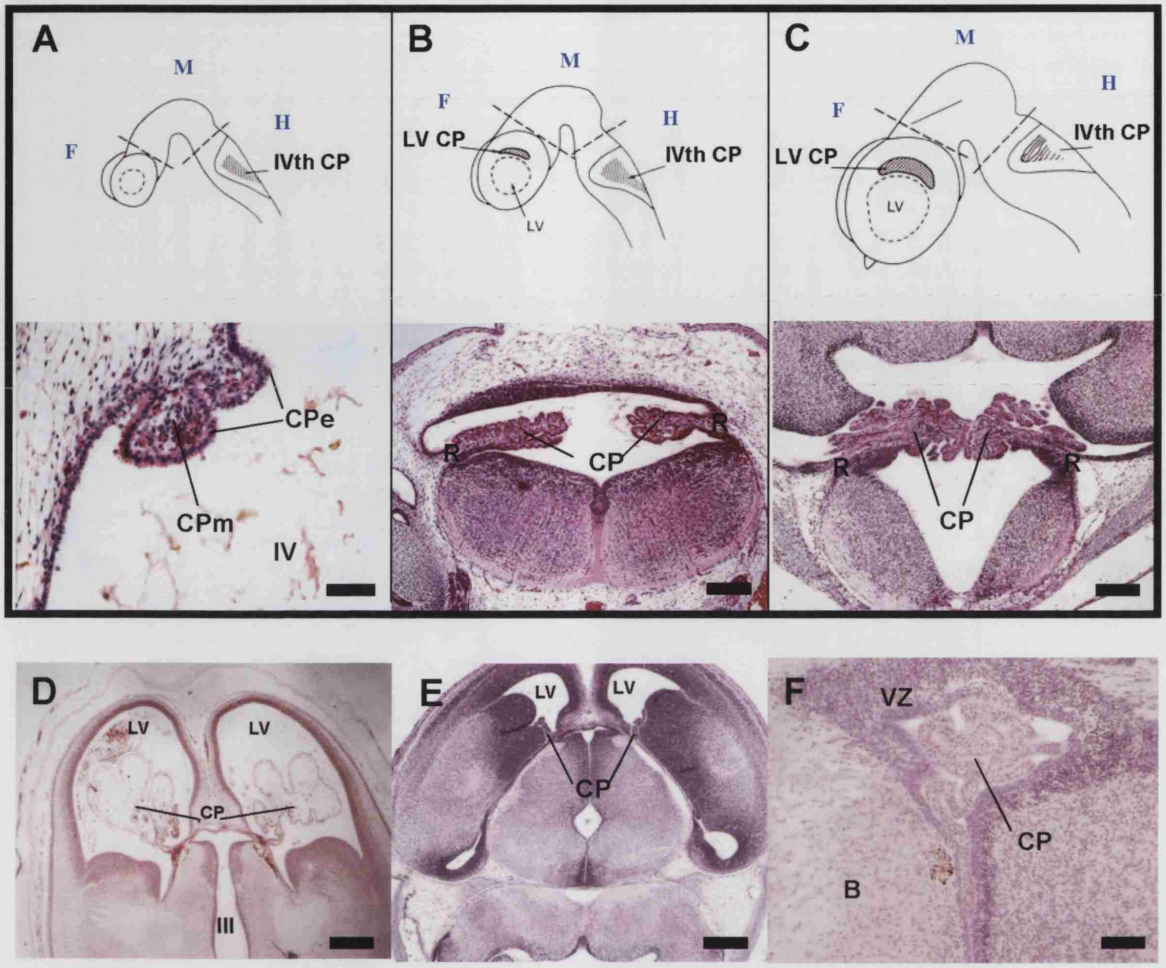

Figure 1. 6 Developmental stages of mouse and human choroid plexus

A-C: sequence showing the development of the mouse IVth ventricle CP (lower pictures) with its corresponding location in the brain (upper pictures, dashed lines separate from left to right the forebrain (F), the mid-brain (M) and the hindbrain (H) regions) at different embryonic ages. **A**: 11.5dpc-12dpc mouse IVth ventricle choroid plexus, only one side of the ventricle is shown where the CP is apparent (transverse view). **B**: 12dpc-12.5dpc mouse IVth ventricle choroid plexus (coronal view), the IVth ventricle CPs from each side of the ventricle are seen. **C**: 14.5dpc mouse IVth ventricle choroid plexus (transverse view), the CPs from each side of the ventricle are fused (already by 12.5dpc). **D**: human lateral Carnagie stage 23 (56 days) CP, is very distinctive by its large size and amorphous material in the CP mesenchyme that gives it a swollen appearance (transverse view). **E**: 14.5dpc mouse lateral CPs (arrows), the CPs are long and thin (transverse view). **F**: post-natal day 3 lateral CP, higher magnification; The CP occupies most of the ventricle. Scale bars are 50μm in A, 200 μm in B-C, 800μm in D, 400 μm in E, and 100 μm in F. **B**: brain tissue, **CP**: choroid plexus, **CPm**: CP mesenchyme, **CPe**: CP epithelium, **III**: third ventrivle, **IV**: fourth ventricle, **LV**: lateral ventricle, **N**: neuroepithelium **R**: CP root. (Diagrams adapted from (Thomas et al., 1988)).

1.3.2.1 Maturation of the choroid plexus epithelium

Shuangshoti and Netsky, (1966) distinguished four stages of development of the CP based on histological studies of the lateral ventricular choroid plexus in the human fetus (Table 1.4). These stages occur in the same order in different species but with different timing and duration (Dziegielewska et al., 2001). Studies at the ultrastructural level of mammalian the CPe show the presence of an effective barrier to protein across the blood-CSF barrier very early in brain development. In fact, it is thought that the epithelial cells are linked by tight junctions probably as early as they differentiate (Mollgard and Saunders, 1986; Dziegielewska et al., 1979). CSF in the immature brain contains high concentration of proteins that are immunologically identical to proteins in plasma, in contrast to the low protein concentration in adult CSF. This finding was stated as evidence for the immaturity of the blood-CSF barrier. However, it was later shown that most if not all of the proteins in CSF could be accounted for by active transfer from the blood (Habgood et al., 1992; Dziegielewska et al., 1979). It has been suggested that the high content of proteins in the embryonic CSF may serve as a trophic or nutritive function during neurogenesis, or may promote the expansion and growth of the brain (Saunders et al., 1999a). Ultrastructurally, the embryonic CPe cells have cilia and microvilli at their apical surfaces as soon as the presumptive CPe cells become evident (Sturrock, 1979). The CPe cells are particularly rich in intracellular Golgi apparatus and endoplasmic reticulum, and there are numerous mitochondria and glycogen stores within the cytoplasm of the CPe between 12dpc and 15dpc in the mouse (Sturrock, 1979; Catala, 1998). This suggests that CPe cells posses the ultrastructural components required for secretory function early in development (Saunders et al., 1999b; Catala, 1998). This view is supported by Catala (1997) who demonstrated expression of the carbonic anhydrase protein in the human lateral CP at 9 weeks of gestation. Similarly, the expression of Na^+/K^+ATPAse in the embryonic rat CPe has been reported at 15dpc (Gonzalez-Martinez et al., 1994). Expression of these secretory enzymes thus lends further support to the idea that the immature CPe cells (stage II in Table 1.4) have secretory capacity.

	Stage I	Stage II	Stage III	Stage IV
Time of development	week 7	Week 9	week 17	week 29
Duration of development	2 weeks	8 weeks	12 weeks	11 weeks
Epithelium	Pseudo stratified, tall, central nuclei	Low columnar, apical nuclei	Cuboidal, apical/central nuclei	Cuboidal/squamous, central/basal nuclei
Glycogen	Absent	Abundant	Moderate	Minimal/absent
Villi	Absent	Sparse	Primary villi	Villi with multiple fronds
Stroma	Loose mesenchyme	Small number of connective fibres	Moderate number of connective fibres	Large number of connective fibres
Blood vessels	Ill defined vascular walls	Defined vascular walls	Well formed vascular walls	Same
Size in relation to ventricles	Tiny	Extremely large	Moderately large	Small

Table 1. 4 Stages of differentiation based on the human telencephalic plexus according to (Shuangshoti and Netsky, 1966).

1.3.3 Induction and genes involved in the development of the embryonic choroid plexus

Very few studies have looked at the signals that induce the development of the choroid plexus, or the signals that govern the maturation and differentiation of the CPe. This section will briefly discuss the major signalling molecules that may be involved in CP ontogeny, and concentrate on the most recent ones that have been implicated in the maturation and differentiation of the epithelium. Table 1.5 summarizes all the genes so far known to be associated with CP development.

1.3.3.1 Induction events

Understanding of the spatial and temporal aspects of CP determination and differentiation has been provided by studies in-vitro. Thomas and Dziadek (1993) cultured regions of mouse embryonic neural ectoderm on Matrigel substrate and assessed the formation of polarised epithelial vesicles and TTR expression, as indicators of CPe phenotype. At 8.5 dpc, all regions of the cranial neural ectoderm had the potential to form CPe, whereas spinal cord neural ectoderm did not. At 9.5 dpc, after closure of the neural tube, only neural ectoderm from forebrain and hindbrain regions had the potential to form CPe. Neural ectodermal cells from these regions that normally do not form CPe, could differentiate to a CPe phenotype when normal cell:cell contact was disrupted prior to plating. These experiments suggest that

the potential for neural ectodermal cells to differentiate into CPe becomes progressively restricted as a consequence of the division of the brain into segments that contain discrete stem cell populations. The study also highlights the importance of cell:cell interaction or/and the cell:matrix interaction. This idea is supported by the work by Birge (1962) who showed that in-vivo the choroid plexus is induced by a subpopulation of mesenchymal cells that produce growth factors or extracellular matrix components that regulate the differentiation of the choroid plexus.

1.3.3.2 Genes involved in choroid plexus development

1) IGF-II: (insulin-like growth factor II) Cavallaro et al. (1993) proposed a model of CP induction implicating IGF-II as the putative mesenchymal signalling molecule in CP induction. In the 10 dpc embryo, IGF-II mRNA is not expressed in the neuropeothelial cells of the primitive neural tube, but is expressed in abundance by the primitive mesenchymal cells. The model proposed by these authors, states that IGF-II signalling occurs when the mesenchyme is in very close proximity to the neuroepithelium. As a consequence, CP morphogenesis is induced by the persistent trophic action of IGF-II, and the CP primordia initiate low level expression of IGF-II themselves. As more CPe cells develop and start expressing IGF-II, mesenchymal expression of IGF-II is downregulated. The maturation of the CPe cells then depends on an autocrine IGF-II regulation.

2) BMPs: (bone morphogenetic proteins) are members of the transforming growth factor β (TGF- β). In the mouse, BMP expression precedes CP differentiation and marks the future site of CP formation. Interestingly, BMP expression domains are very similar to that of the fork head homologue-4 (*Hfh-4*), renamed FoxJ1, at 13.5 dpc in the mouse (Furuta et al., 1997). A study by Furata (1997) showed that exogeneous application of BMP-1 and BMP-2 soaked beads in explants of lateral telencephalon, a region where BMPs are not normally expressed, induced discrete expression of the muscle segment homeobox-1 genes (*Msx1*), as well as changes in proliferation and apoptosis thought to be characteristic of CP morphogenesis.

3) Msx1 and Msx2: (Formally known as *Hox-7* and *Hox-8* respectively) are homologues of the *Drosophila* muscle segment homeobox gene. *Msx* genes in vertebrates encode DNA binding proteins that are involved in several epithelial/mesenchymal interactions. At 12.5 dpc Msx1 and Msx2 are both expressed in the CPe cells themselves and in the cortical hem. Msx1 has been proposed to be

one of the genes involved in the initiation of the CP phenotype as a downstream target of the BMPs (MacKenzie et al., 1991; Furuta et al., 1997; Grove et al., 1998).

4) Wnt: the Wnt family of genes are the vertebrate homologues of Drosophila wingless (wg) genes. Grove et al. (1998) found that Wnt 2b, 3a, 5a and 7a were expressed in the cortical hem just prior to, and as the telencephalic CPs differentiate. This Wnt rich region appeared to form a boundary zone between the developing hippocampus and the telencephalic CPe.

1.3.3.3 Recently discovered genes involved in choroid plexus epithelial function and differentiation

The most recent genes shown to be important for the function of the CPe have in common that when knocked-out, mice suffered from a non-obstructive type of hydrocephalus as a consequence of the abnormal differentiation of the CPe. These genes are:

1) FoxJ1: This gene was previously known as hepatocyte nuclear factor 3/ forkead homolog 4 (*Hfh4*). It is part of the large family of winged helix transcription factors that play important roles in development, cell specific gene expression, and oncogenesis (Hromas and Costa, 1995; Weigel et al., 1989). FoxJ1 mRNA expression is first detected in the roof of the hindbrain, and at a lower level in the dorsal medial telencephalon of the 11 dpc mouse, in the future CP-forming regions (Lim et al., 1997). By 13.5 dpc, FoxJ1 is detected specifically in the CPe of the fourth, lateral and third ventricles. Foxj1 expression is maintained in the adults CPs. In late embryos and adults, it is also expressed in the epithelial cells of the lung, the oviduct and in the testes (Hackett et al., 1995; Lim et al., 1997). Targeted mutations of FoxJ1 in the mouse (*Hfh4*$^{-/-}$ mice, hereon called *FoxJ1*$^{-/-}$ mice) results in absence of (9+2) ciliated cells (Chen et al., 1998). Sensory and other primary type of cilia generally have a (9+0) microtubule ultrastructure, describing the configuration of nine outer pairs of microtubules, whereas most sensory cilia and flagella have a (9+2) microtubule ultrastructure due to an additional inner pair of microtubules and include dynein motors directly linked to the outer pairs that together with other proteins drive movement (Brody et al., 2000). *FoxJ1*$^{-/-}$ mice that survived to postnatal day 7 (P7) developed a characteristic hydrocephalic head shape at P7 to P14, and died between P12 and P40. The brain of these mice had distended hemispheres with markedly dilated lateral ventricles and a thin anterior cortex. The ventricular dilation was not

caused by ventricular obstruction, but was thought to be caused by the absence of cilia that are normally present at the surface of ependymal cells lining the brain ventricles and that drive the flow of cerebrospinal fluid. In addition, FoxJ1 has also been reported to be able to bind DNA sequences upstream of different regulatory elements including the genes encoding for IGF-II and the cystic fibrosis transmembrane conductance regulator (CFTR) (Lim et al., 1997). CFTR is an inward-rectifying anion channel that functions to regulate electrolyte homeostasis and thus modulate CSF secretion. It may therefore be that the hydrocephalus in the FoxJ1$^{-/-}$ mice was also a consequence of an overproduction of CSF.

2) E2F5: this gene belongs to the six member family (E2F1 through to E2F6) of transcriptional regulators (E2F) involved in cell cycle regulation. In heterodimeric complexes with one of the DP proteins (DP 1-3), the E2F proteins regulate the activity of promoters containing E2F binding sites. E2F/DP heterodimers interact with pRb, p107 and p130 members of the pocket protein family. The classical model for the function of E2F/DP transcription factors is presented in Figure 1.7. Complexes of E2F/DP with pocket proteins are active transcriptional repressors with growth suppressing activity. During the progression of cells through the G1 into S phase, pocket proteins are phosphorylated by G1 cyclin-dependent kinases (cdks) (Mittnacht, 1998; Kaelin, Jr., 1999). Pocket protein phosphorylation results in inactivation of it transcriptional repression properties and its E2F binding capacity (Harbour et al., 1999). E2F/DP is then released and able to activate E2F-dependent genes, which in turn lead to G1- to S-phase progression. The E2Fs can be subgrouped, based on certain structural and functional characteristics. E2F1, E2F2 and E2F3 are structurally similar. They all have a nuclear localisation signal (NLS), and all exclusively bind to the pRb retinoblastoma gene. In contrast E2F4 and E2F5 do not have a NLS and interact primarily with pocket proteins p107 and p130. To add to the complexity of the picture, E2F1, E2F2, and E2F3 but not E2F4 and E2F5 contain cyclin binding motifs, which facilitate stable binding of cyclin A/CDK2. Hence, the complexity of E2F activity, generated by the formation of different heterodimeric E2F/DP and pocket protein complexes suggests distinct and diverse functions in cell growth control (Lindeman et al., 1998).

Both the mRNA for E2F4 and E2F5 have been reported to be expressed at high levels in lateral and IVth ventricular CP at 13.5 dpc to 18.5 dpc. In contrast, E2F2 transcripts are barely above background, and E2F1 and E2F3 transcripts are not

detected (Dagnino et al., 1997). Mice with targeted deletion of the E2F5 gene are normal in size and appearance after 2-3weeks. However by 3-4 weeks they begin to suffer from a non-obstructive type of hydrocephalus. The pathogenesis of the hydrocephalus is linked to a dysfunction of the CPe cells, which had a marked electron-lucent "light" appearance characteristic of water-laden cells (Lindeman et al., 1998). The fact that only the CPe is affected by the knockout of the *E2F5* gene suggests that either *E2F5* has no role in other tissues or that in these tissue the absence of E2F5 is compensated by the presence of low levels E2F4 and/or other E2Fs. Interestingly, DP1 transcripts are not detectable in normal embryonic CP, but are abundant throughout the rest of the mouse embryo. This would implicate DP2 or DP3 in heterodimer formation with E2F5 in the CPe.

3) p73: This gene is part of the *p53* family, along with *p53* and *p63*; *p73* is most homologous to *p63,* and unlike *p53* they are not tumour suppressor genes. Furthermore, the complexity of the family is increased by the alternative spliced forms of *p63* and *p73* which give rise to complex networks of proteins involved in the control of cell proliferation, apoptosis and development. The *p73* gene is made up of 14 exons so that the alternative splicing between exons 10 and 14 gives rise to six isoforms ($\alpha,\beta,\gamma,\delta,\varepsilon,\phi$) (Strano et al., 2001). A ΔN variant of these proteins, which lacks the N-terminal activation domain has also been described (Yang and McKeon, 2000). Mice functionally deficient for all p73 isoforms exhibit hydrocephalus as well as other defects such as hyppocampal dysgenesis, chronic infections and inflammation, and abnormalities in pheromone sensory pathways. P73 is highly expressed in the CPe and has been reported to regulate the expression of the water transporter aquoporin 3 (Zheng and Chen, 2001). It was also suggested that p73 might interact with E2F5 in the homeostasis of CSF dynamics (Yang et al., 2000).

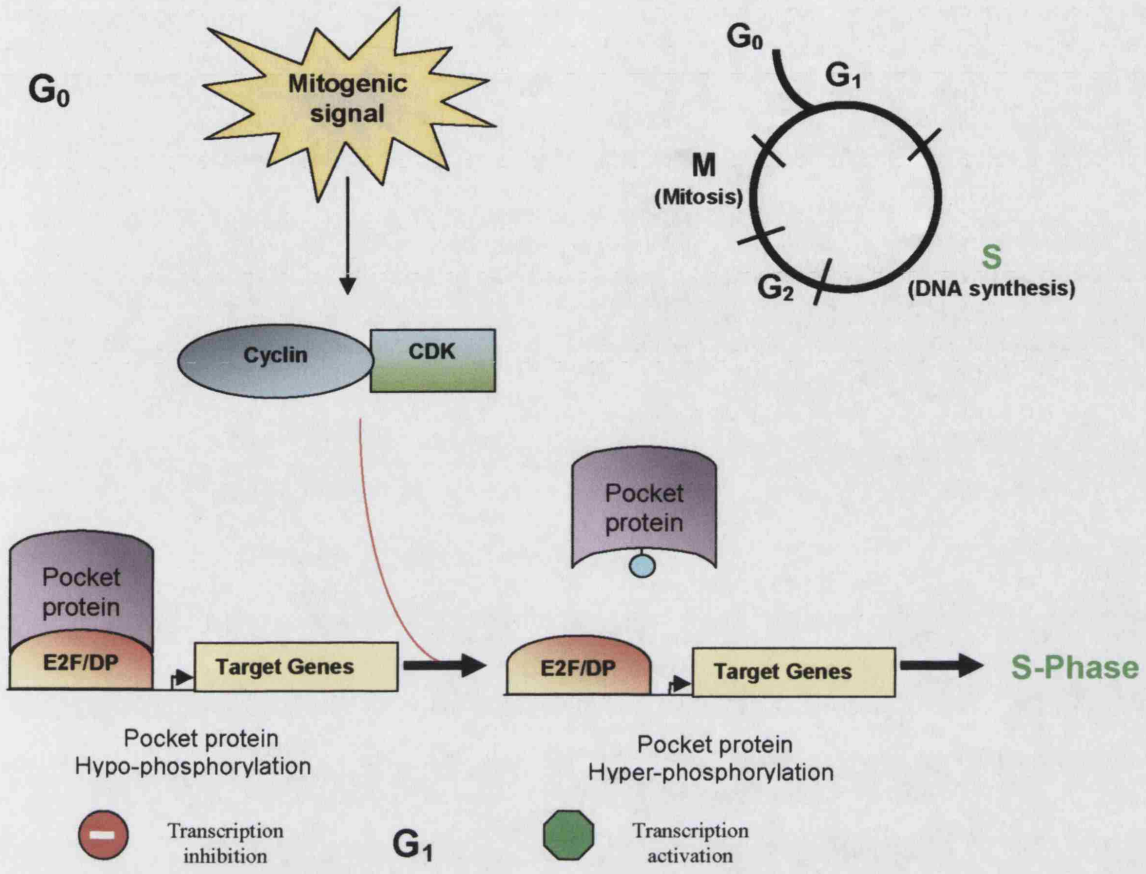

Figure 1. 7 Role of E2F transcription factors in G1-S phase checkpoint control
The exit of mammalian cells from G0-phase (quiescent state), upon stimulation with a mitogenic signal (such as the addition of serum to quiescent cells), triggers the transcription of **cyclin** genes that associate with pre-existing cyclin dependent kinases (**cdk**) molecules. The kinase activity associated with these complexes phosphorylates specific sites of **pocket protein** molecules (eg: pRB, p130 and p107) that are bound to **E2F/DP** dimer molecules. The hypo-phosphorylated form of this complex acts as a repressor for promoters of genes involved in G1 to S-phase transition. The hyper-phosphorylation of the **pocket proteins** after mitogenic stimulation leads to the release of **E2F/DP** which promotes the transcription of **target genes** involved in G1- to S-phase transition. A schematic representation of the different steps in the cell cycle is shown in the right hand corner.

Table 1. 5 Putative genes associated with choroid plexus development

The table summarises the pattern of expression and putative roles of genes that have been detected in the developing CP. Detection was either by immunohistochemistry or in-situ hybridization. The expression pattern and the age of development the genes have been shown to be expressed are given, along with their putative role. Key references are given. The genes which have been studied in this thesis are highlighted in blue. Unless otherwise specified the data are from mouse. **CPe**: choroid plexus epithelium, **CPm**: choroid plexus mesenchyme.

Transcription factors	Expression	Developmental role	Reference:
E2F-5	High level in CPe at 13.5dpc to 18.5dpc	Regulation of CSF secretion, maturation.	(Lindeman et al., 1998e); (Dagnino et al.,)
P73	High level in CPe at 13.5dpc to 18.5dpc	Regulation of CSF secretion, maturation	
FoxJ1	In CPe only from 11.5dpc	Differentiation of cilia, regulation of CSF secretion and IGF-II	(Chen et al., 1998b; Lim et al., 1997d)
BF-1	Specific downregulation in lateral CP primordia at 10.5dpc	Involved in early specification of CP primordial field	(Furuta et al., 1997c)
Lhx5	In pre-primordial lateral ventricle region	Critical for development of the lateral choroid plexus	(Zhao et al., 1999)
TCF-1 and LEF-1	In embryonic CP as early as 10.5dpc	Presumptive role in organogenesis	(Oosterwegel et al., 1993)
Msx-1, -2	In CPe at 12.5dpc and mesenchyme	Possibly induced by BMP, seems to reduce proliferation.	(Furuta et al., 1997b) (Grove et al., 1998b)
Otx2	At 12.5 dpc, specifically expressed in CPe.	Not studied	(Boncinelli et al., 1993)
Emx1 and Emx2	Not expressed in CP, but in overlapping domains in telencephalon	Lateral CP early development	(Yoshida et al., 1997)
Gli3	In early head mesenchyme	Lateral CP early development	(Grove et al., 1998a)
HRF	Highl level in developing CP	Role in vasculogenesis	(Flamme et al., 1997)
Growth factors			
RAR-β	At 14.5dpc in CPm	Not studied	(Ruberte et al., 1993)
Sonic Hedgehog	At 12.5dpc in CPe	Not studied	(Bitgood and McMahon, 1995)
Wnt	In neuroepithelium adjacent to presumptive lateral CP	Lateral CP early development, may lie downstream of Gli3	(Grove et al., 1998e)
BMPs and alk3	In presumptive CPe from 12.5dpc	CP early development	(Dewulf et al., 1995) (Furuta et al., 1997a)
TGF-β1	Mesenchymal component and neural crest cells	Not studied	(Unsicker et al., 1991)
TGF-β2	At 12 dpc and 16dpc in CP	Not studied	(Flanders et al., 1991)
TGF-β3	From 11.5dpc in CPe	Not studied	(Pelton et al., 1990)
PDGFRα	From 9.5 dpc in IVth ventricle roof and in CPe at 16.5dpc	Role in development.	(Schatteman et al., 1992) (Takakura et al., 1997)
IGF-II	First in mesenchyme adjacent to presumptive CP, then in CPe from 14 dpc onwards	Change in transcript type coincident with mature cuboidal cell appearance	(McKelvie et al., 1992)
IGF-IIR & IGFBP-2	In CPe at 12dpc (rat)	Not studied	(Sullivan and Feldman, 1994)
FGF-7&-8	In region of developing CP. Traces of FGF-7 in 14.5dpc and 16.5dpc CP.	Not studied	(Finch et al., 1995b)
FGF2	In mesenchyme of 18 dpc CP rat	Not studied	(Gonzalez et al., 1990b)
FGFR-1, -2,-3,-4	FGFR-1,-4 in 12.5dpcCPe FGFR-2 from 12.5dpc to 18.5dpc FGFR-3 from 12.5dpc to 18.5dpc	Not studied	(Gonzalez et al., 1995) (Yazaki et al., 1994) (Reid and Ferretti, 2003i)
Others			
Transthyretin	In CPe before differentiation at 10.5dpc	Early marker, no demonstrated role	(Murakami et al., 1987)
Tropomyosins	In 10.5dpc CPe precursor cells (rat)	Morphogenetic movements	(Nicholson-Flynn et al., 1996)

1.3.4 Summary- the embryonic choroid plexus

Mammalian CPs develop at four sites in the roof of the neural tube shortly after its closure, and prior to neuronal cell differentiation. The CPs appear first in the IVth ventricle, then in the lateral ventricles, and finally in the third ventricle. Following induction, the embryonic CPs quickly develop many of the characteristic ultrastructural and morphological features of the adult CPs. The embryonic CPe have defined intercellular junctions from the moment they become morphologically distinct, suggestive of an early barrier function. Furthermore, there is growing evidence that the embryonic CPe is capable of CSF secretion, protein synthesis and secretion which are thought to assist the development of the CNS. An early function of the embryonic CPe is also supported by the fact that the embryonic CPs are highly vascular at a time when the blood supply to the developing brain is still very limited. The knowledge of the molecular ontogeny underlying the development of the CPe is very limited, but the major protagonists orchestrating the induction and differentiation of the CPs seem to be the BMPs, IGF-II, Msx and Wnt pathways. Recently, three genes: E2F5, FoxJ1 and p73, have been suggested to play a role in the normal differentiation and function of the CPe as their knockout mice suffer a form of non-obstructive hydrocephalus, thought to be caused by the anomalous maturation of the CPe. The role of these three genes (E2F5, FoxJ1 and p73) in the development and function of the CPe is not well understood.

1.4 Syndromic craniosynostosis

1.4.1 Clinical description

The skull consists of discrete bone plates that form the cranial vault or calvaria. The limits of the adjacent calvarial bones in pre-natal and young vertebrates are defined by mesenchymal borders that form the cranial sutures. This arrangement facilitates some movement and overlap of the calvaria bones during compression in the birth canal, but it also allows appositional growth to occur in parallel with the growth and maturation of the brain (Reardon and Winter, 1995). During cranial growth, the skull bones enlarge by the deposition of mineralised bone matrix along their margins. The sutures are maintained as sites of proliferating undifferentiated preosteogenic mesenchymal tissue. Some sutural cells differentiate into osteoblast cells, and contribute to the formation of new calvarial bone, whereas others are maintained in an undifferentiated proliferative state (Cohen, Jr. and Kreiborg, 1993; Wilkie, 1997). Figure 1.8 illustrates the major cranial sutures in the human skull.

Craniosysnosytosis is a congenital defect characterised by the premature fusion of one or more of the cranial sutures. The craniosynostosis itself may be the consequence of several disease processes. It may be found in isolation (i.e non-syndromic), as a feature of a particular syndrome (syndromic), or occur as a secondary consequence of a primary disease process. The combined incidence of these disorders affects about 1 in 2500 births, with no difference in incidence amongst ethnic groups (Gorlin et al., 1990).

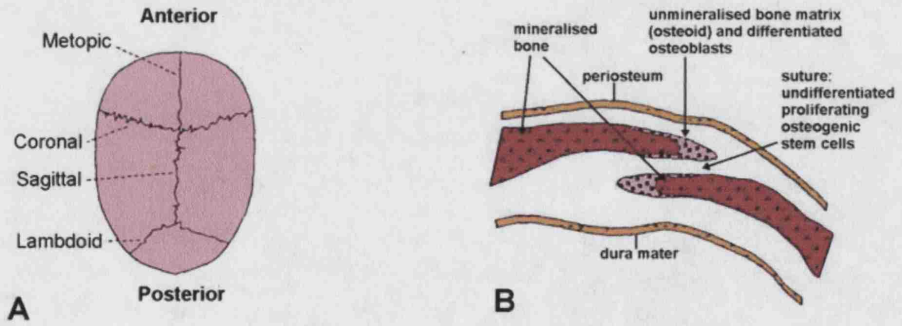

Figure 1. 8 Normal cranial suture development

A: view of a child's head from above, showing position of the major sutures. **B**: Diagrammatic cross-section through a coronal suture. The skull bones overlap slightly, and are separated by a narrow space containing osteogenic stem cells (Wilkie, 1997).

The development of a cranial vault with a compromised growth potential is characteristically associated with a dysmorphology of the skull. The premature fusion of one suture leads to a marked reduction in bone growth perpendicular to the line of fusion. Continued bone growth in regions of the remaining patent sutures results in the development of abnormal skull shape of varying severity. The types of malformations (trigoencephaly, plagiocephaly/brachycephaly, scaphocephaly, and occipital plagiocephaly) can be linked with the fusion of the metopic, coronal, sagittal, and lambdoid sutures respectively (Chan and Thorogood, 1999).

1.4.2 Aetiology of craniosynostosis

The causes of craniosynostosis are diverse. Craniosynostosis can occur in isolation, as a result of a secondary pathogenesis such as metabolic diseases e.g. hyperthyroidism, haematological diseases such as thalassaemia, storage disorders such as Hurler Syndrome, and foetal teratogenesis induced by drugs such as retinoic acid and phenytoin (Gorlin et al., 1990). In 10-20% of the cases of craniosynostosis there is evidence of Mendelian inheritance (Reardon and Winter, 1995; Cohen, Jr. and Kreiborg, 1993).

The most common craniosynostosis syndromes are Crouzon syndrome (1 in 25,000), Jackson-Weiss syndrome (1 in 26,000), Apert syndrome (1 in 55,000), Pfeiffer syndrome (unknown incidence) and Sathre-Chotzen syndrome (unknown incidence), Beare-Stevenson syndrome (Gorlin et al., 1990; El, V et al., 1999). It should be borne in mind that to date more than a 100 causally related syndromic forms of craniosynostosis have been described (Cohen, Jr., 1988). An abnormal skull shape (generally tower-shaped), widely spaced eyes, hooked nose and underdeveloped midface are charactersistic features of these disorders. Hand and foot anomalies are observed in some, but not all craniosysnostosis syndromes. In fact the precise syndromic diagnosis of a patient often rests on these associated malformations (Reardon and Winter, 1995). In addition to these craniofacial anomalies and limb defects, individuals may also present cutaneous, dental, visual, aural and CNS abnormalities (Gorlin et al., 1990). In the CNS, agenesis of the corpus callosum and a generalised hypoplasia of the CNS has been described (Gorlin et al., 1990; Cohen, Jr. and Kreiborg, 1990a; Hayward et al., 1992)

Children with syndromic craniosynostosis suffer from a variety of functional complications. These include difficulty in breathing, due to midface hypoplasia

(Gonzalez et al., 1996), impaired cerebral blood flow, mental retardation, hydrocephalus, ventricuolomegaly and raised intracranial pressure (Lundar and Nornes, 1991; Hayward et al., 1992; Gosain et al., 1995; Thompson et al., 1995).

1.4.3 Intra-cranial pressure (ICP) and syndromic craniosynostosis

Increased intracranial pressure (ICP) is a frequent problem encountered in patients suffering from syndromic craniosynostosis but is difficult to diagnose because of the lack of symptoms in most cases (Lajeunie et al., 2000). It is an insidious process that increases with age and that can lead to blindness, impairment of intellectual development (Renier et al., 1982), seizures, and premature death (Gosain et al., 1995) In one study led by (Thompson et al., 1995), it was found that the incidence of raised ICP was twice as likely in syndromic patients compared to non-syndromic patients. In a study of 53 syndromic children with an age range of 1 month to 15 years, normal ICP levels were detected in just four of the cases analysed. Individuals with Crouzon syndrome appeared to be more at risk of raised ICP, with no cases recording normal out of twenty individuals (Thompson et al., 1995). Renier et al. (1982) suggested that the incidence of raised ICP in syndromic craniosysnostosis could be as high as 83%. In addition to raised intracranial pressure, high pressure hydrocephalus is prevalent amongst individuals with syndromic craniosysnostosis. Collmann et al. (1988) described ventricular dilation in 41% of syndromic cases as opposed to an incidence of 1.5% in non-syndromic patients (Collmann et al., 1988).(Murovic et al., 1993a) reported hydrocephalus in 66% of patients with Apert syndrome, and (Cinalli et al., 1998a) reported that patients with Crouzons were far more likely to have hydrocephalus than those with other syndromes. Although raised ICP and hydrocephalus is a significant feature of syndromic craniosynostosis, the actual causes of raised ICP in these individuals are still a very contentious area.

1.4.4 Aetiology of intra-cranial pressure in syndromic craniosynostosis

Traditionally, raised ICP in craniosynostosis was attributed to the biomechanical constraint imposed upon the growing brain by the cranial vault, which has lost its capacity to expand in the regions of the affected sutures (David and Simpson, 1982). In fact, it was rationalized that since the resulting intracranial volume was insufficient

to accommodate brain growth, surgical remodelling of the cranial vault would alleviate the ICP. However, surgery often does not solve the problem of raised ICP (Thompson et al., 1997). In spite of surgical intervention some individual continue to suffer recurrent raised ICP, which can persist into adulthood (Gosain et al., 1995c; McCarthy et al., 1995). Interestingly, the cranial volume in craniosynostosis is often larger than normal (Posnick et al., 1994), and there is no correlation between cranial volume and intracranial pressure (Gault et al., 1992; Fok et al., 1992). Whilst the fused suture(s) cannot facilitate further bone expansion, unaffected sutures are frequently widely patent (Cohen, Jr. and Kreiborg, 1993a). This suggests that the brain is able to expand in spite of the cranial malformation.

Various other mechanisms have been proposed as causative factors of raised ICP in syndromic craniosynostosis based on clinical observations.

Using magnetic resonance imaging, Hayward et al. (1992) discovered hindbrain abnormalities in 16 out of 30 children with syndromic craniosynostosis. Common findings included the descent of the cerebellar tonsils below the foramen magnum, hindbrain herniation to the level of the second cervical vertebra, brainstem kinking and a downward shift in pontomedullary junction. These anatomical displacements of brain tissue were thought to partially obstruct the normal flow of cerebrospinal fluid (CSF), and result in the reduced drainage of CSF leading to raised ICP (Hayward et al., 1992).

Another explanation brought forward is that children with syndromic craniosynostosis may have abnormal cranial venous sinus architecture. There is evidence of severe stenosis or non-visualisation of major venous sinuses in some patients, in particular the sigmoid sinus-jugular complex, when they are examined using angiography (Taylor et al., 2001a). In a study of cerebral blood flow, 12 out of 16 syndromic craniosynostosis exhibited signs of moderately, or severely narrowed venous sinuse (Taylor et al., 2001b). The authors hypothesised that in syndromic cases where hydrocephalus is absent, the anomalous venous anatomy may result in venous hypertension, which in turn increases intracranial pressure. However, the authors found no direct correlation between the severity of venous stenosis, and the degree of raised ICP (Taylor et al., 2001c).

Finally, Lundar and Normes (1991) found high CSF outflow resistance in 7 out of 17 children with syndromic craniosynostosis. The authors found that there was significant impedance to CSF absorption in these individuals, which they

hypothesised, might be caused by a depression of the subarachnoid spaces (Lundar and Nornes, 1991).

All these observations indicate that raised ICP in syndromic craniosynostosis does not arise merely as a secondary effect of cranial vault constraint, but the aetiology must be more directly affecting CSF dynamic at various levels. Intracranial pressure is directly affected by the production and secretion rates of CSF, as well as flow and absorption of CSF (Davson et al., 1987). An alternative hypothesis proposed by Chan and Thorogood (1999) and in this thesis is that the raised ICP in syndromic craniosynostosis occurs as a result of over production and secretion of CSF. This would imply that alterations in the development and/or function of the choroid plexuses are responsible for the disease process. Interestingly, Hayward et al. (1992) commented that one four year old individual with Pfeiffer syndrome drained over 700ml of CSF via an external tap over a 24hours period. This output rate is elevated above the normal value for adult CSF production, which is approximately 600ml in 24hours (Wright, 1978).

1.4.5 Genetic mutations in syndromic craniosynostosis

The first genetic mutation identified in syndromic craniosynostosis was in the homeodomain of the transcription factor *MSX2* (Jabs et al., 1993). However, *MSX2* mutations are confined to the 'Boston-type' craniosynostosis syndrome which is described in a single extended family. Single point mutations in members of the fibroblast growth factor receptor (FGFR) family in patients with syndromic craniosynostosis were discovered during the mid-1990s. There is now clear evidence of a direct correlation between the normal developmental expression pattern of these genes, and the structures that are affected in syndromic craniosynostosis (Chan and Thorogood, 1999). In 1994, a breakthrough discovery revealed that the FGFR2 gene was mutated at various locations in children with Crouzon syndrome (Muenke et al., 1994). Since then Crouzon, Pfeiffer, Jackon Weiss and Beare Stevenson cutis gyrate syndromes have all been shown to arise as a result of mutations in FGFR2 (Muenke et al., 1994; Wilkie et al., 1995). Mutations in *FGFR1* can also occur in Pfeiffer syndrome and mutations in *FGFR3* in Crouzon patients with acanthosis nigricans and patients with Muenke syndrome (Muenke et al., 1994; Schell et al., 1995; Przylepa et al., 1996). Mutations in *FGFR3* have also been discovered in skeletal dysplasias with no craniosynostosis for e.g. achondroplasia, a disorder characterised by short-limb

dwarfism, macrocephaly, and other skeletal abnormalities (Shiang et al., 1994; Rousseau et al., 1994). To date no mutations have been identified in the other FGFR members, either *FGFR4* (Gaudenz et al., 1998), or the newly identified *FGFR5* (Kim et al., 2001d). Table 1.6 summarizes the *FGFR* genes affected by mutations underlying the major craniosynostosis syndrome, and shows that mutations in the *FGFR2* genes are associated with most syndromes.

	FGFR-1	FGFR-2	FGFR-3
Apert	×	✓	×
Crouzon	×	✓	✓
Pfeiffer	✓	✓	×
Jackson-Weiss	×	✓	×
Beare Stevenson	×	✓	×

Table 1. 6 Idiosyncratic table of the principle FGFR mutations associated with the main forms of syndromic craniosynostosis

The table shows which of the three FGFRs (FGFR1-3) is affected by point mutations in the main forms of syndromic craniosynostosis. A cross (×) means that no mutations have been observed in the FGFR for a given syndrome, a tick (✓) means that mutations have been associated with the FGFR for a given syndrome. The table shows quite clearly that most syndromes have been linked to FGFR2 mutations.

More recently, mutations in TWIST, a basic helix loop helix transcription factor, were identified in individuals with Saethre-chotzens syndrome (Howard et al., 1997; El Ghouzzi et al., 1997). The mechanism of action of mutated TWIST is not well understood, although most of the mutations result in a non-functional protein and are likely to result in haploinsufficiency (Wilkie, 1997). Wild type TWIST is thought to inhibit osteogenesis, and so a reduction in functional TWIST protein would provide an explanation for the premature fusion of the cranial sutures in craniosynostosis (Rose et al., 1997).

Since most of the mutations responsible for the major forms of syndromic craniosynostosis have been linked to the FGFR gene family, and more specifically to the *FGFR2* gene, it is quite pertinent to point out that FGFR2 as well FGR1, 3 and 4 are all expressed in the choroid plexus (Reid and Ferretti, 2003h). This is consistent

with the hypothesis that abnormal CPe function may be in part responsible for the raised ICP in syndromic craniosynostosis. Aberrant FGF signalling would affect the normal function and/or differentiation process of the CPe, which would lead to an over secretion of CSF. The following section will present an overview of the different members of the FGF family ligands and receptors expressed in the CNS and implicated in syndromic craniosynostosis.

1.5 Fibroblast growth factors

Fibroblast growth factors (FGFs) are a family of structurally related growth factors that play an important role in normal development and wound healing, but also in tumour development and progression (Powers et al., 2000). The effect of FGFs on cellular function is contextual and depends on the biochemical state and environment of their target cells. In addition to their initially observed effects on cell replication and angiogenesis, FGFs have been implicated in the regulation of cell survival and apotosis, adhesion, motility, and differentiation (Szebenyi and Fallon, 1999). There are 23 FGF genes in the human and mouse that are scattered throughout the genome (Ornitz and Itoh, 2001). The defining features of the FGF family are a strong affinity for heparin and heparin-like glycoaminoglycan (HLGAGs) (Burgess and Maciag, 1989), as well as a central core of 140 amino acids that is highly homologous between different family members that share a 30-60% amino acid identity across the family (Ornitz and Itoh, 2001). This central core folds into twelve anti-parallel β-strands that together form a cylindrical barrel closed by the more variable amino- and carboxy-terminal stretches (Ago et al., 1991). The typical *FGF* gene contains three exons, but several *FGF* genes have additional 5' transcribed sequence that initiates from CUG codons (Kiefer et al., 1994; Arnaud et al., 1999). In several FGF subfamilies, exon 1 is subdivided into two to four alternatively spliced sub-exons. Consequently, FGFs and their isoforms range in molecular weights between 17 to 34 kDa in vertebrates (Reuss and Bohlen und, 2003). Most FGFs (FGF 3-8, 10, 15, 17-19, and 21-23) have amino-terminal signal peptides and are readily secreted from cells. FGFs 9, 16 and 20 lack an obvious N-terminal signal but are nevertheless secreted. FGF1 and FGF2 also lack signal sequences, and are not secreted through canonical pathways. They are however found on the cell surface and within the extracellular matrix. It is thought that they may be released via an exocytotic mechanism that is independent of the endoplasmic reticulum-Golgi pathway (Mignatti et al., 1992; Florkiewicz et al.,

1995). Interestingly, it was suggested that the α subunit of the Na^+/K^+ ATPase may be an integral component of this alternate exocytotic pathway mediating translocation of FGF2 to the cell surface (Florkiewicz et al., 1998). In addition, FGF1 and FGF2 both possess a nuclear localization signal. Nuclear localization of FGF1 has been shown to be required for FGF1 induced mitosis (Imamura et al., 1990). The larger isoforms of FGF2 that have the NLS have been detected in the nucleus. Nuclear FGF2 can bind chromatin, and is postulated to control gene expression directly (Delrieu, 2000), although the role of nuclear FGF2 is not yet clearly defined (Powers et al., 2000).
Several FGFs hold an important role in the development of the central nervous system (CNS) development and are expressed at various sites in the developing CNS. These FGFs are reviewed in the following section.

1.5.1 Fibroblast growth factors during the proliferative and neurogenic phases of neural development

Expression studies demonstrate that FGF1, FGF2, and FGF15 are more generally expressed throughout the developing neural tube. These FGFs are present in both the embryonic and adult CNS, while FGF8 and FGF17 are tightly localised to specific regions in the developing brain and only expressed in the embryo during the early phases of proliferation and neurogenesis (Ford-Perriss et al., 2001).
This section will concentrate on FGF1 and FGF2 that have been most extensively studied. They have been found to have mitogenic and neurotrophic effects on the developing CNS (Ford-Perriss et al., 2002; Murphy et al., 1990). Studies in the rat and mouse show that FGF2 is more widely expressed in the developing CNS than FGF1. FGF2 is localized to both neuronal and non-neuronal cell types, whereas FGF1 is mostly confined to neuronal cells with little or no glia expression. FGF1 levels are in fact low in the developing nervous system until 12 dpc, with high levels detectable from 16 dpc (Nurcombe et al., 1993). Although it has been thought that FGF1 has a role in the maturation of neurons of the CNS, *Fgf1* null mutant mice appear normal, and do not display any behavioural abnormalities. This suggests that FGF1 is either not essential for neuronal development or maturation, and/or that other FGFs compensate for its absence (Miller et al., 2000).

FGF2 is localised in the basement membranes around the neural tube, and within the neuroepithelium during early development (Murphy et al., 1994; Nurcombe et al., 1993). FGF2 has been identified specifically in the ventricular zone from 9-10

dpc onwards (Nurcombe et al., 1993; Ford-Perriss et al., 2001). Recent studies have shown that FGF2 is expressed in the ventricular region of the developing cortex in a dorsoventral gradient, with levels increasing between 14 dpc and 18 dpc (Raballo et al., 2000). However, from 18 dpc expression of FGF2 diminishes in neuronal cell types and in the post-natal to adult brain, highest levels are present in the astrocytes (Gomez-Pinilla et al., 1994; Gonzalez et al., 1990b). In-vivo demonstration that FGF2 plays a role in the development of the brain came through studies on FGF2-deficient mice (Dono et al., 1998; Ortega et al., 1998), which are viable but display defects in the cerebral cortex. There is a reduction in pavalbumin-positive neurons in cortical layers, most pronounced in the frontal motor sensory area. Further studies have shown that both cortical neurons and glia are also reduced in *Fgf2*-deficient mice. Interestingly, the degree of apoptosis within the ventricular zone was not changed in the knockouts, which suggests that FGF2 does not act as a survival molecule in-vivo (Vaccarino et al., 1999b), as reported for neuroepithelial cells grown in-vitro (Murphy et al., 1990). In-vivo, FGF2 also increases the proportion of dividing cells without affecting the cell cycle (Vaccarino et al., 1999a). Since the *Fgf2*-null mice exhibit disruption of the large neurons of the deep cortical layers, it is thought that FGF2 is important for the expansion and subsequent differentiation for this subset of neuronal progenitor cells (Vaccarino et al., 1999a). As with FGF1, it is possible that other FGFs compensate for the absence of FGF2 in these mice knockouts.

1.5.2 Fibroblast growth factors and choroid plexus

In spite of numerous reports of FGF expression in the developing CNS, there is little mention of their expression in the choroid plexus. It is likely that that the expression of FGFs in the CPs has been under-reported, except for one notable exception; FGF2.

FGF2 transcripts and protein have been detected in the ventricular zone and the 15.5 dpc CPs of the early developing murine brain (Vaccarino et al., 1999a; Raballo et al., 2000). Raballo et al. (2000) even suggested that FGF2 may be secreted into the CSF to assist neuronal development. FGF2-immunoreactivity is lost from the ependymal cells by 17 dpc, but remains high in the CPs, meninges and superficial tissues. FGF2 immunoreactivity in the CPs persist during adulthood, but expression seems to be confined to the epithelial cells of the CPe (Cuevas et al., 1994; Fuxe et al., 1996), although Gonzalez (1990) reported that immunoreactive FGF2 was associated with the mesenchymal component rather than the epithelial cells.

1.6 Fibroblast growth factor receptors

FGF signalling is mediated by the complex interaction between FGFs and their receptors. Two classes of cell surface receptors have been identified for FGFs: high affinity and low affinity receptors. The FGF polypeptides bind in an overlapping pattern to four high affinity tyrosine kinase receptors (a fifth FGFR protein (FGFR5) has also been reported (Kim et al., 2001) encoded by four separate genes *FGFR1-4*. The low affinity receptors are heparin sulphate proteoglycans (HSPGs) (Plotnikov et al., 2001).

FGFRs are single transmembrane proteins that belong to the immunoglobulin (Ig) superfamily of receptors (Muenke, 1995) and have similar structural features (Figure 1.9). The extracellular domain consists of three cysteine-flanked immunoglobulin-like motifs (Ig loops): IgI, IgII and IgIII. Situated between the Ig loops I and II is a region of 4-8 amino acid residues, called the "acid box". In this same region there is also the "cell adhesion molecule (CAM) homology domain" which is a stretch of 20 amino acids that shares sequence homology with N-CAM, N-cadherin and L1. IgII and IgIII share a high degree of sequence homology and are more conserved between species than the IgI region. FGFRs have a single transmembrane domain (TMD), and with the exception of FGFR5, a split intracellular tyrosine kinase domain separated in two parts by a 14 amino acid insert. The FGFR5 terminates in the region of the TMD and has no intracellular domain (Kim et al., 2001).

The use of splice variants for a given FGFR gene and the expression of different FGFR genes give rise to a diverse array of FGFRs protein products. Thanks to the modular nature of the FGFR genes, FGFR genes can generate many different isoforms. These are schematically presented in Figure 1.9. The most commonly described FGFR isoforms in vivo include those lacking the Ig-like loop, those which transcribe alternative exons of the Ig-loop II, and those lacking the transmembrane domain and intracellular regions (Ferguson and Johnson, Jr., 1991). The most important mechanisms by which FGFRs determine binding specificity for different FGFs is by the alternate usage of the IgIIIb-c forms. These are reviewed in the following section.

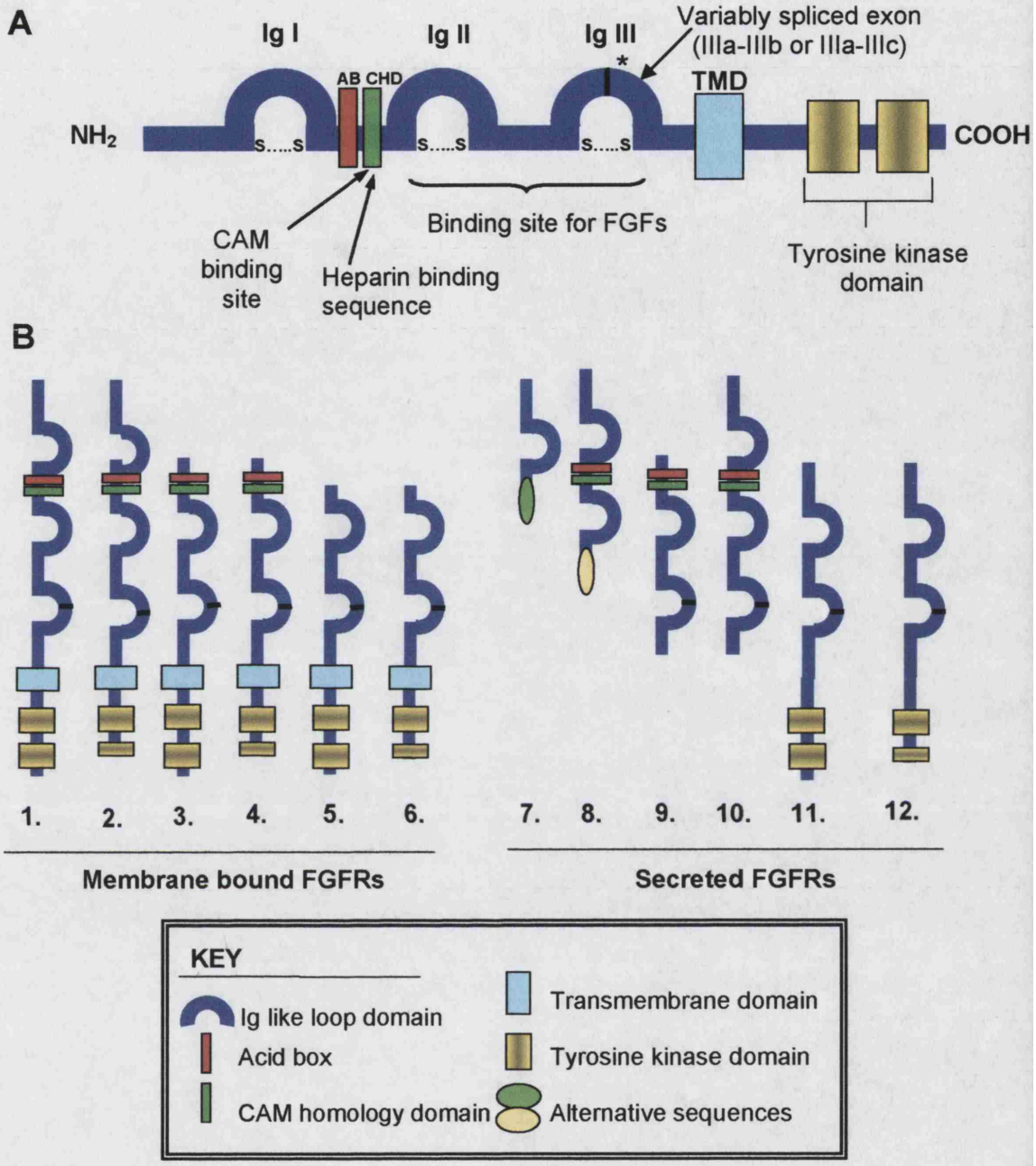

Figure 1. 9 Alternative possible isoforms of the FGFRs

A: schematic diagram of a typical FGFR protein. **B**: possible splice-forms of the FGFR protein. Variants include those that lack one or more Ig domains (3-9; 11-12), the acid box (5-6, 11, 12), or the transmembrane domain (11, 12). Some isoforms have a truncated carboxy terminus (2, 4, 6, 12), whilst others contain regions of alternative sequence (7-10). Some receptors may contain one or more of these variations. Alternatively spliced Ig III isoforms are not taken into account. Adapted from (Green et al., 1996).

1.6.1 FGFR Ig loop III isoforms

For FGFRs 1, 2 and 3, the IgIII extracellular loop domain is encoded by the three contiguous exons 7- 9, which code respectively for the three alternate domains IgIIIa, IgIIIb, IgIIIc (Powers et al., 2000e). Exon 7 (IgIIIa) encodes for the N-terminal half that is common to all FGFR IgIII isoforms. The use of either exons 8 (IgIIIb) or exon 9 (IgIIIc) to encode the C-terminal half of the IgIII loop generates FGFR molecules with very different ligand-binding specificity. For instance, exon IIIb generates the FGFR2 IIIb isoform (or KGFR) that binds to FGF1, 3, 7 and 10 specifically and is expressed mainly in epithelial cell types. The use of exon IIIc generates the FGFR2 IIIc isoform (Bek) that binds a different set of FGF ligands, with the exeption of FGF1, and is mainly found in mesenchymal cell types (Orr-Urtreger et al., 1993b; Ornitz et al., 1996b). In contrast, FGFR4 is unique in that it only has one form of the IgIII domain (Vainikka et al., 1992). Isoforms for FGFR5 have not yet been characterised.

1.6.2 FGFR and FGF-ligand specificity

Using *in-vitro* assays, it has been shown that the interactions between the various FGFR isoforms and FGF ligands are highly specific. Ornitz et al (1996) measured the differences in ligand/receptor interaction by overexpressing different FGFR isoforms in BaF3 cells, which do not normally express FGFRs. [H^3]-thymidine incorporation was measured in transfected cell following treatment with various FGFs. The results proved that mitogenic responses to FGF signalling were highly specific, and dependent upon the combination of ligand and an FGFR isoform. In this assay, FGF1 stimulated all receptor isoforms, and this was used as an internal standard to determine the relative activity of other FGFs. Table 1.7 shows the relative specificities of some FGFRs and FGFs based on this study. *In-vivo*, the endogeneous HSPGs to which FGFs are initially bound to are also likely to affect FGFR binding. Therefore, the relative affinities in Table 1.7 may not truly reflect the binding of FGFs to their receptors *in-vivo* (Ford-Perriss et al., 2001c).

FGFR	isoform	FGF1	FGF2	FGF3	FGF4	FGF5	FGF6	FGF7	FGF8	FGF9
FGFR1	IIIb	+++	++	+	+	-	-	-	-	-
	IIIc	+++	+++	-	+++	++	++	-	-	+
FGFR2	IIIb	+++	-	++	+	-	-	+++	-	-
	IIIc	+++	++	-	+++	+	++	-	+	+++
FGFR3	IIIb	+++	-	-	-	-	-	-	-	++
	IIIc	+++	+++	-	+++	+	-	-	++	+++
FGFR4	IIIc	+++	+++	-	+++	-	+++	-	+++	+++

Table 1. 7 Specificity of FGF-FGFR interactions

Table showing the specificity of different FGFs for different FGFR isoforms as determined by mitogenic stimulation. Mitogenic activities of FGF paralogs were measured in BaF3 cells expressing various FGFR variants. FGF1 showed maximal response in these assay and the activities of other FGFs were expressed as a percentage of FGF1 activity (-:<10%; 10-40%; ++: 40-75%; +++: 75-100%) adapted from (Ornitz et al., 1996a).

1.6.3 FGF low affinity receptors: the heparan-sulphate glycosaminoglycans

Heparan sulphate proteoglycan molecule (HSPGs) are sulphated glycosaminoglycans (GAGs) covalently bound to a core protein (Aviezer et al., 1994). The conserved central core of FGFs facilitates low affinity binding to heparin and heparan sulphate proteoglycans such as syndecan, perlecan and glypican. HSPGs are located on the cell surface and/or within the extracellular matrix (ECM). Binding of FGFs to HSPGs has been proposed to restrict the dispersion of FGFs in the ECM, providing a reservoir of FGF and maintaining a local source of growth factors. The release of the FGFs from this reservoir either requires specific proteases or heparanases that cleave ECM components to free the FGFs. Alternatively, a carrier protein like the FGF binding protein can deliver FGFs to their receptor. In addition, binding to HSPGs in the ECM may protect the growth factor from degradation by proteases (Powers et al., 2000f).

HSPG molecules facilitate FGF binding to FGFR, but also facilitate FGF signalling. In fact, FGF induced mitogenic activity can be shown to be heparin dependent and that heparin is required for FGF2 binding to FGFR1 in a cell free assay (Ornitz, 2000). HSPGs are thought to favourably stabilise the interaction between FGF and their receptor (Spivak-Kroizman et al., 1994; Klagsbrun and Baird, 1991), and even dictate ligand-receptor specificity (Guimond et al., 1993; Guimond and Turnbull, 1999).

1.6.4 FGF/FGFR complex

FGFRs, like other tyrosine kinase receptors, transmit extracellular signals to various cytoplasmic signal transduction pathways through tyrosine phosphorylation. This is induced by ligand binding, and dimerization of the receptors, which then become capable of auto-phosphorylating specific tyrosine residues (Lemmon and Schlessinger, 1994). Indeed, the recent crystal structure of the FGFR1 ectodomain containing IgII and IgIII bound to FGF2 showed that FGF/FGFR/HSPG interaction involves two FGF molecules bound to two FGFR molecules in the region of IgII and IgIII, and the interlinker between them. The binding conformation of two FGF molecules and two FGFRs produces a large anionic central canyon which is hypothesised to be the site spanned by long chain HSPGs that serve to stabilise the complex (Plotnikov et al., 1999). The formation of this complex drives the dimerisation of the receptors and the subsequent autophosphorylation of tyrosine residues that leads to biological signalling.

1.6.5 FGFR signal transduction

It is supposed that the signalling pathways from different FGFRs are quite similar given their high degree of homology at the amino-acid level (Powers et al., 2000). There are seven tyrosine residues in the cytoplasmic tail of FGFR-1 which are important for the catalytic activity of the activated receptor and essential for signalling. Tyr^{766} has been shown to bind the SH2 domain of phospholipase C-gamma (PLCγ) and is necessary for FGFR activation of PLC-γ. Activated PLCγ can then catalyse the formation of diacylglycerol (DAG) and inositol-1-4-5-triphosphate (IP-3). DAG can then activate protein kinase C (PKC), whereas IP3 can stimulate release of Ca^{2+}. Furthermore, PLCγ was also shown to inhibit the activity of Src (Powers et al., 2000). Src is a small non-receptor tyrosine kinase bearing an SH2 and SH3 domain adjacent to its kinase domain, which has been suggested to link FGFR signalling to cortactin, a focal adhesion-associated protein that binds filamentous protein, which is important for cell migration (Zhan et al., 1994). Src activation would depend upon its SH2 domain binding with an FGFR phosphotyrosine.

Crk-mediated signalling- Crk is an SH2/SH3 containing adaptor protein, which may link FGFR to the downstream signalling molecules Shc, C3G, and Cas (Powers et al., 2000), and in turn may propagate a mitogenic signal via the Ras-Map

kinase pathway (Pawson, 1995), or other none determined pathways (for e.g. via the RAP1 mediated pathways (Caron, 2003; Feller, 2001)). In endothelial cells it has been shown that Crk binds via its SH2 domain to Tyr463 of the activated FGFR, and that this residue is critical for activation of both Erk2 and Jun kinase (Powers et al., 2000).

Recent evidence suggests the existence of an alternative pathway for the recruitment of SH2-containing proteins. It has been shown that both wild type and a mutant receptor lacking all non-catalytic tyrosine residues could phosphorylate a novel 90 kDa protein, which was identified as SNT-1/FRS2. The activation of SNT-1/FRS2 was shown to link the FGFR activation to the Ras-MAP kinase signalling pathway according to the following scheme: activation of SNT-1/FRS2 recruits the adaptor complex Grb-2/SOS that in turn catalyses the formation of the GTP-activated form of Ras responsible for triggering the activation of the MAP kinase signalling cascade. SNT-1/FRS2 has also been reported to bind the protein tyrosine phosphatase Shp2 in a complex with the docker protein Gab-1 (Ong et al., 1997). In addition, SNT-1/FRS2 can link the FGFR activation to atypical PKC istotypes (Lim et al., 1999).

Table 1.8 summarises the observed biological role of the main FGFR substrates based on FGFR1 and Figure 1.10 summarises the signal transduction pathways activated by the FGFRs.

FGFR1 substrate	Cellular response	FGFR1 binding sites
CrK	Proliferation	Y463Pi
PLCγ	Proliferation and migration	Y766Pi
FRS2	Proliferation and differentiation	Juxta-membrane domain
Shc	Proliferation, and differentiation	Multiple
Src	Proliferation, differentiation and migration	?
Shb	Apoptosis	?
SHP-2	?	Via FRS-2
?	Migration	Amino acid 759-774

Table 1. 8 Summary of FGFR1 substrates, and their known cellular responses

The table shows the cellular response induced by FGFR1 substrates, and their binding sites on the FGFR1 or the use of adaptor molecules (i.e. FRS-2). **YxPi**: phosphorylated tyrosine residue number. Adapted from (Klint and Claesson-Welsh, 1999).

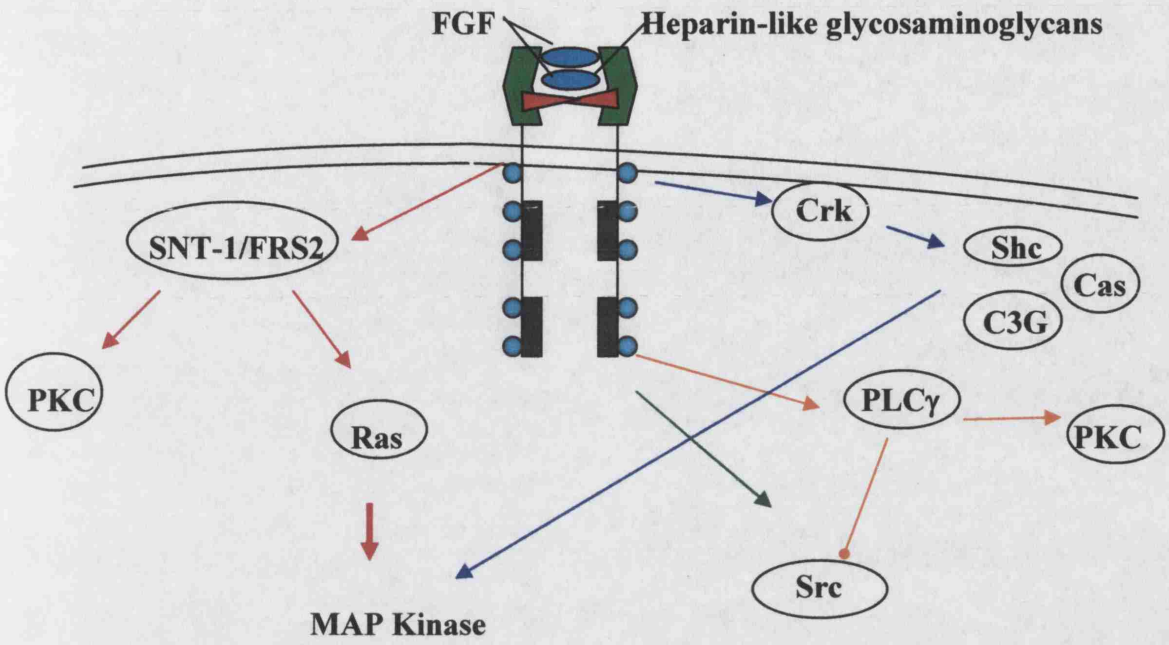

Figure 1. 10 Shematic outline of known signal transduction pathways activated by FGFR signalling

The different signal transduction pathways activated by dimerization of FGFRs are shown, as described in the main text. The pathways are colour coded to help their visualization. Pointed arrows show the downstream target second messenger molecules that are activated for a given signalling pathway (intermediate steps are not shown for clarity), whilst a rounded arrow shows the inhibition of a downstream target molecule. Note that in FGFR1 PLCγ and MAP kinase (Ras) activation is strong, whilst in FGFR2 PLCγ is strong but MAP kinase weak. Adapted from (Klint and Claesson-Welsh, 1999b; Szebenyi and Fallon, 1999).

1.6.6 FGFR expression in the developing central nervous system and the choroid plexus

The activity of FGFs in the developing neural tube is ultimately controlled by their receptors. The FGFRs like the FGFs are expressed in distinct and overlapping spatiotemporal patterns.

FGFR1 mRNA is expressed in the ventricular zone of the mouse and chick neural tube during early to mid-phases of neurogenesis. FGFR1 protein expression has been described in the dorsal and basal parts of the neuroepithelium, and in the

of development there is a downregulation of expression. Interestingly, this expression pattern corresponds to that of FGF2, which binds to FGFR-1. The choroid plexus is strongly FGFR1 immunoreactive at 12.5 dpc, but the immunoreactivity declines from 15.5 dpc onwards, which was confirmed at the transcript level by RT-PCR (Reid and Ferretti, 2003). At 12.5 dpc, FGFR1 is most strongly localized to the CPe, and slightly less strongly expressed in the mesenchyme. RT-PCR analysis has shown that the IIIc isoform is the most predominant in the CP.

In the embryonic mouse FGFR2 mRNA is expressed throughout the brain and strongly in the developing midbrain and hindbrain from 9.5 dpc to 16.5 dpc (Peters et al., 1992); a similar pattern of expression has been reported in the chick (Walshe and Mason, 2000). By 16.5 dpc, the levels of FGFR2 mRNA expression fall markedly in the developing CNS with the exception of the neuroepithelium closest to the ventricles, and the CPe, which maintains a high level of FGFR2 mRNA expression (Ford-Perriss et al., 2001). Expression of two distinct isoform of the FGFR2 gene, FGFR2IIIb (KGFR) and IIIc (bek) in the CPe of the embryonic human between 10 and 18 weeks gestation has been reported (Chan and Thorogood, 1999). The expression of these two isoforms was recently confirmed in the mouse CP by RT-PCR (Reid and Ferretti, 2003). FGFR2 protein appears to be strongly expressed in the CPe and CPm at 12.5 dpc, however by the second half of gestation FGFR2 protein immnuorecativity became restricted to the CPe.

FGFR3 is generally largely confined to the CNS and developing bone (Peters et al., 1993). FGFR3 is strongly expressed in the ventricular zone of the neural tube from 9 dpc to 16 dpc in the mouse. After 16 dpc, the expression seems to be confined to the gial cell population, and the cochlea in the inner ear (Peters et al., 1993). The mouse embryonic CP is also immunoreactive for FGFR3 from 12.5 dpc onwards, both mesenchymal and epithial cell appear positive. Interestingly, the staining is nuclear. RT-PCR analysis showed that FGFR3IIIc is the predominant isoform expressed in the whole CP (Reid and Ferretti, 2003)

FGFR4 expression in the developing CNS has not been studied in detail in the mouse or chick. FGFR4 has been identified in the ventricular zone of the cortex at 11 dpc (Ozawa et al., 1996). The mouse embryonic CP is immunoreactive for FGFR4 at 12.5 dpc, but the immunoreactivity appears to decline by 15.5 dpc. Immunoreactivity is generally stronger in the CPe than the CPm. (Reid and Ferretti, 2003)

FGFR5 localises predominantly to the pancreatic tissue, but the expression pattern for this new gene has not yet been well characterised (Kim et al., 2001)

1.6.7 FGFR mutations in syndromic craniosynostosis

This section describes the point mutations associated with the *FGFR-1*, *-2* and *-3* genes that have been described in several of the most common forms of syndromic craniosynostosis.

Over the last few years, activating point mutations in the *FGFR1-3* have been linked to five of the major types of syndromic craniosynostosis: Crouzon, Jackson-Weiss, Pfeiffer, Apert, Beare-Stevenson cutis gyrata (Lajeunie et al., 1999; De Moerlooze and Dickson, 1997). In fact to date, most of the mutations have been mapped to the *FGFR2 gene* (Yamaguchi and Rossant, 1995).

There is a distinct clustering in terms of type of mutation and position within FGFR molecules. One of the most striking features is the extent of similar or homologous mutations that have been mapped to equivalent positions in more than one of the FGFRs. Not only is the position of the amino acid conserved, but also the nature of the replacement (Burke et al., 1998). It is quite surprising that similar craniosynostosis syndromes have been mapped to point mutations in all three receptors and yet FGFR-1, -2 and -3 are all expressed in the bone primordia with distinct spatial and temporal expression patterns (Webster and Donoghue, 1997). Even more perplexing is that the same point mutations on different FGFRs can give rise to different cases of syndromic craniosynostosis.

Point mutations have been found in the extracellular domain in the IgIII loop and the region between the second and third Ig-like domain, the transmembrane domain, and the kinase domain of FGFR molecules. It is quite revealing to classify the mutations in terms of their effect on the FGFR protein. The overall picture is that the mutations cause the FGFRs to become partially or constitutively activated, typically but not always with ligand independent dimerization and autophosphorylation (Burke et al., 1998)

1) **Alteration in the number of cysteine residues,** either by addition or removal of cysteine at the point of the Ig loop disulphide bridges (particularly the IgIII loop). Unpaired cysteine residues at these sites are able to covalently bind another mutant receptor, thus causing receptor dimerization in the absence of ligand (Kannan and Givol, 2000).

2) **Destabilisation of the disulphide bridge**. Mutations within the IgIII that do not lead to the formation of unpaired cysteines are thought to affect the conformation of the protein, with potential disrupting disulphide bridge formation. Altered structure may result in the formation of alternative intermolecular bonds leading to receptor dimerization.
3) **Formation of hydrogen bonds** in the transmembrane domain (TMD). The mutations that introduce charged residues in the otherwise hydrophobic protein domain of the FGFR leads to conformational changes and the stabilization of the receptor in a dimeric form due to the formation of hydrogen bonds, leading to elevated receptor tyrosine kinase activity (Burke et al., 1998; Webster and Donoghue, 1997)
4) **Increased affinity or change in specifity for ligand**. Mutations in the IgII and IgIII interlinker region can reduce the dissociation kinetics of FGF ligand leading to prolonged FGFR signalling (Anderson et al., 1998). It has also been demonstrated that these mutations can alter the specificity of the FGFR for its ligand (Yu et al., 2000).
5) **Conformational change of the kinase domain**. Mutations in the activation loop of the kinase domain are thought to relieve the auto-inhibitory configuration of the kinase active site, and therefore abrogate the need for receptor dimerization for activity (Webster and Donoghue, 1997)

1.7 In-vivo models for aberrant FGF signalling

1.7.1 FGFR mutations in-vivo

The disruption of either FGFR1 and FGFR2 in mice both results in homozygous mutant embryos that die immediately prior to gastrulation (Deng et al., 1994; Yamaguchi et al., 1994; Arman et al., 1998). Nonetheless, several mouse strains and transgenic mice have been generated in recent years to study the effect of FGFR mutation in syndromic craniosynostosis (Table 1.9). The characterisation of these mice has essentially focused on the development of skeletal elements, particularly the cranial and facial bones, rather than on the choroid plexuses (Table 1.9).

Hajihosseini (2001) generated a mouse with an Apert/Pfeiffer like phenotype. This mouse was generated by the heterozygotic abrogation of fibroblast growth factor receptor 2 (*FgfR2*) exon 9 (IIIc) using a Cre/loxP recombination strategy. Deletion of

exon 9 caused a splicing switch to include exon 8 (IIIb), and results in a gain of function phenotype reminiscent of Apert and Pfeiffer Syndromes (Fig.1.11). This phenotype was thought to occur because the ectopic expression of the FGFR2 IIIb isoform in cells that normally only express the FGFR2 IIIc isoform would make these cells responsive to a broader set of FGF ligands. The mice had skeletal defects that included coronal fusion (craniosynostosis), zygomatic arch bones fusion, and sternal bones fusion, as well as visceral defects that included lobulation defects of the lung and the liver, fewer nephron units in the kidney, the absence of exorbital lacrimal glands, and a distension of the hindgut.

Gene	Syndrome	Mutation in gene	Reference:
FGFR1	Pfeiffer	P250R	(Zhou et al., 2000)
FGFR2	Apert	S250W	(Chen et al., 2003)
		S251R	(Coumoul and Deng, 2003)
	Apert/Pfeiffer	Exon 9 knock- out	(Hajihosseini et al., 2001)
FGFR3	Achondroplasia	G374R	(Wang et al., 1999)
		G374R	(Coumoul and Deng, 2003)
		G374R	(Naski et al., 1996)
	Thanatophoris dysplasia	G374R	(Monsonego-Ornan et al., 2000)
	Thanatphoris dysplasia II	G369C	(Chen et al., 1999)
		S365C	(Chen et al., 2001)
		K644E	(Li et al., 1999)
	Severe achondroplasia with developmental delay	K644M	(Iwata et al., 2001)

Table 1. 9 Mouse models for FGFRs human skeletal dysplasias

The table shows the FGFR genes mutated, the location in the protein sequence of the amino acid substitution, and the phenotype. Adapted from (Coumoul and Deng, 2003).

Figure 1. 11 Description of the strategy for the deletion of the *FgfR2* exon 9 (IIIc)

The scheme is taken from Hajihosseini MK *et al.* (2000). **A**: Schematic structure of the FGFR2 highlighting the third Ig loop; the alternative usage of exon 8 or 9 leads to the generation of the IIIb or IIIc isoforms respectively. TM: transmembrane domain. **B**: The main ligands activating each isoforms. **C**: Schematic representation, drawn to scale, of mouse *FgfR2* genomic DNA exons (boxes) 7, 8, 9 and 10 are indicated, and the main restriction enzyme sites shown (Av: AvaI; RV: EcoRV; B: BamHI; K: KpnI). **D**: Targeting construct showing loxP sequences placed downstream of exon 9, and flanking the selectable marker gene neo driven by HSV-TK promoter located upstream of exon 9. Thick lines indicate the extent of the targeting construct. **E**: Homologous recombinant embryonic stem cells were identified by Southern blotting of BamHI-digested DNA by using a 450bp genomic probe located 3' of the target vector sequence (gray bar in D). Homologous recombinant cells (*FgfR2*IIIc$^{+/neo\text{-}flox}$) yielded a 6.5kb fragment and wild type yielded a 5.0 kb fragment. Both 5' and 3' joins were checked by PCR analysis. **F**: Hemizygous (*FgfR2*IIIc$^{+/\Delta}$) mutant mice were generated by crossing FgfR2IIIc$^{neo\text{-}flox/neo\text{-}flox}$ with ZP3-Cre females, and then crossing F1 females carrying one copy of the targeting construct as well as the Cre transgene with wild type males. Approximately 50% of such females gave Cre-mediated excision. **G**: 90% of these excisions were complete (*FgfR2*IIIc$^{+/\Delta}$); the remainder excised only the selectable marker (*FgfR2*IIIc$^{+/\Delta neo\text{-}flox}$), as determined by PCR using the pair of primers shown in (C). The potential excision product, FgfR2IIIc$^{+/neo\text{-}\Delta flox}$, was not observed. **H**: Growth retardation in *FgfR2*IIIc$^{+/\Delta}$ mice; hemizygotes were identifiable at birth by the smaller sizes, characteristic dome-shaped heads, and truncated faces. The genotype was confirmed by PCR using tail genomic DNA.

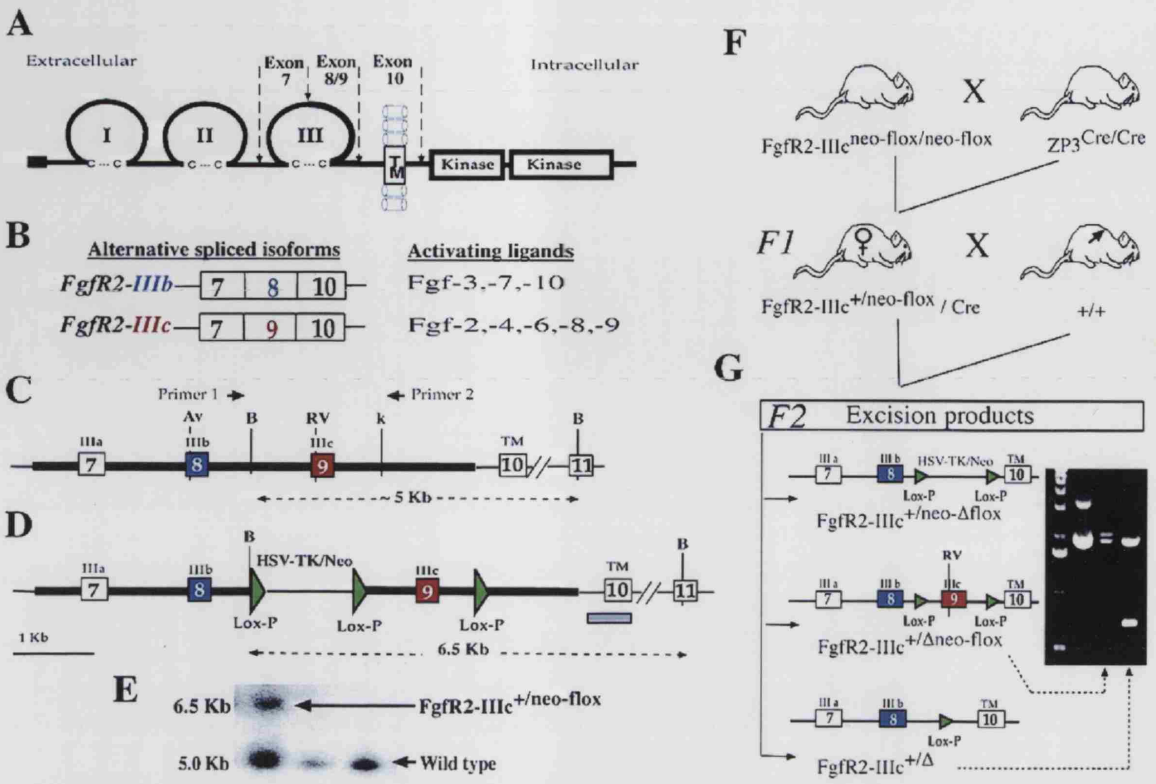
A
Extracellular
Exon 7
Exon 8/9
Exon 10
Intracellular
I
II
III
TM
Kinase
Kinase
B
Alternative spliced isoforms
Activating ligands
FgfR2-IIIb
7
8
10
Fgf-3,-7,-10
FgfR2-IIIc
7
9
10
Fgf-2,-4,-6,-8,-9
C
Primer 1
Primer 2
Av
B
RV
k
B
IIIa
IIIb
IIIc
TM
7
8
9
10
11
~5 Kb
D
B
HSV-TK/Neo
B
IIIa
IIIb
IIIc
TM
7
8
9
10
11
Lox-P
Lox-P
Lox-P
1 Kb
6.5 Kb
E
6.5 Kb
FgfR2-IIIc+/neo-flox
5.0 Kb
Wild type
F
X
FgfR2-IIIcneo-flox/neo-flox
ZP3Cre/Cre
F1
X
FgfR2-IIIc+/neo-flox / Cre
+/+
G
F2
Excision products
IIIa
IIIb
HSV-TK/Neo
TM
7
8
10
Lox-P
Lox-P
FgfR2-IIIc+/neo-Δflox
RV
IIIc
9
FgfR2-IIIc+/Δneo-flox
FgfR2-IIIc+/Δ

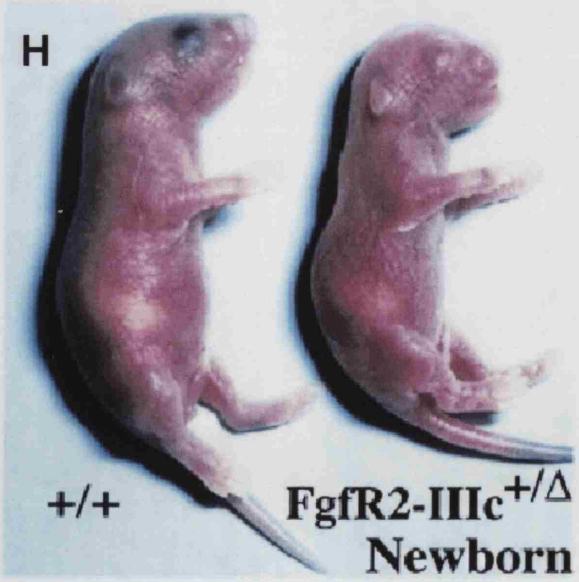
H
+/+
FgfR2-IIIc+/Δ
Newborn

1.7.2 FGF2 administration to the brain ventricles

Several groups have investigated the effects of exogeneous administration of FGF2 to the ventricles of the brain in both adult and embryonic models. Effectively, this leads to artificially high FGF signalling as encountered in syndromic craniosynostosis due to the constitutively activated FGFRs.

1.7.2.1 Adult models

In a study to determine the effect of FGF2 treatment on the symptoms of Parkinson's disease, Pearce et al (1996) administered FGF2 continuously via a ventricular infusion pump for 7 weeks to adult Marmosets, pre-treated with the Parkinson syndrome-inducing drug, 1-methyl-4-phenyl-1,2,3,6,-tetrahydropyridine (MPTP). Animals treated with a continuous ventricular infusion of 1 ng of FGF2 per day, over seven weeks, developed hydrocephalus, whereas control animals did not. On histological examination, the authors described a 'gross enlargement' of the choroid plexus and ependyma. These results indicated that FGF2 administration might have caused choroid plexus hypertrophy and over-secretion of CSF in these primates.

Johanson et al., (1999) induced hydrocephalus in wild-type adult rats by continuous ventricular infusion of 250–1000 ng of FGF2 per day over 10-12 days. Hydrocephalus was evident in all treatment groups within 2 days. After 12 days, the ventricles had doubled in size, although the rate of secretion of CSF by the choroid plexuses was reduced in these animals. The authors measured an increase in resistance to CSF absorption in these animals. On histological examination, collagen deposits were identified in the arachnoid villi, the sites of CSF absorption. Based on these findings, it was hypothesised that the rapid onset of hydrocephalus resulted from an FGF2-induced reduction in CSF absorption.

From these two experimental series, intraventricular infusion of FGF2 has been shown to alter CSF dynamics, inducing hydrocephalus and ventriculomegaly. The aetiology however, appears to be different. FGF2 stimulated over production of CSF by the CP in the marmoset, yet FGF2 reduced CSF absorption in the rat. These differences, although seemingly contradictory, may have occurred as a consequence of the 250-fold difference in FGF2 concentration infused, the length of treatment, species differences, and the fact that the marmoset model was pre-treated with MPTP.

1.7.2.2 Embryonic models

Intraventricular administration of FGF2 has also been attempted in embryonic systems. Vaccarino et al., (1999) demonstrated that a single ventricular injection of 75 ng FGF2 at 15.5 dpc in the embryonic rat results in an increase in brain volume, and in the number of neurons in the adult cortex. By contrast, a ventricular injection of 75 ng FGF2 at the end of neurogenesis, at 20.5 dpc selectively increases the number of glial cells in the adult cortex. In this study, however, the ventricular morphology was not described, suggesting that there was no evidence of ventriculomegaly, or enlargement of the CP.

Ohmiya et al., (2001) injected a single bolus dose of FGF2 to embryonic mouse cerebral ventricles *in utero* at 14 dpc. Enlarged cerebral ventricles, deformation of the calvarium, and thinning of the cerebral cortex were evident within 2-3 days after birth in embryos treated with 200 ng or 300 ng FGF2. Interestingly, lower doses of FGF2 (100 ng) did not cause hydrocephalus or ventriculomegaly (Ohmiya et al., 2001). This finding indicates that hydrocephalic symptoms are initiated above a 'threshold' level of FGF concentration. Ohmiya et al., (2001) did not investigate nor speculate upon the causes of ventriculomegaly in these experiments.

1.7.3 Epithelial fluid secretion affected by FGF

The work by Reid S (PhD thesis, 2002) showed that choroid plexus epithelial (CPe) cells grown on reconstituted basement membrane substratum (Matrigel) formed vesicle structures that were hollow and thought to be filled with fluid. FGF2 increased these vesicles in a dose-dependent fashion suggesting that FGF signalling may be increasing fluid secretion. However, using porcine CPe cells grown as a monolayer on a filter in bi-chamber cultures, Hackvoort (2000) found that FGF2 in fact decreased the secretion of fluid by the cells. Interestingly, in other fluid secreting epithelial tissues such as the lung and lacrimal gland FGF signalling has been implicated in controlling fluid secretion. In the murine and human foetal lung, FGF7 and FGF10 have both been shown to stimulate liquid secretion by the pulmonary epithelium, that was CFTR-independent and that involved the Na/K ATPase and the Na-K-Cl cotransporter (Zhou et al., 1996; Graeff et al., 1999). In addition, an absence of FGF2 expression has been associated with reduced levels of lacrimal gland fluid secretion in human patients (Nguyen et al., 1997).

1.8 Summary

The choroid plexuses are specialized secretory organs located in the four ventricles of the brain. The main function of these organs is to secrete and maintain the composition of the cerebro-spinal fluid. Although very little is known about the development and function of the CPs during embryogenesis, there is growing evidence that the CSF is secreted early on by mid-gestation as soon as the CPs are morphologically distinct, and that this secretory activity may be important for the normal development of the brain. Recently, three genes: E2F5, p73 and FoxJ1 have been shown to be important for the normal maturation of the CP and their knockout lead to hydrocephalus.

Syndromic craniosynostosis is a term describing a family of congenital conditions that have in common craniofacial malformations due to premature fusion of one or more cranial sutures. Several of the most important syndromic cases have been linked to point mutations in members of the fibroblast growth factor receptor (FGFR) gene family, which cause these receptors to become constitutively activated. Raised intra-cranial pressure (ICP) is frequently observed in these patients, although the aetiology is not well understood.

Since FGFR1-4 are dynamically expressed in the choroid plexus during development, it has been suggested that FGFR signalling may alter the secretory function of the CPe cells. In a culture model based on embryonic CPe cells that form fluid-filled vesicles, Reid S (PhD thesis, 2001) finds that FGF2 increases the size of these vesicles in a dose-dependent fashion. In addition, the FGF signalling pathway has also been shown to stimulate fluid secretion by the foetal lung epithelium and may modulate lacrimal gland function.

Hence, there is evidence that the high incidence of raised ICP in syndromic craniosynostosis may be in part due to the aberrant secretory function of the choroid plexus epithelium caused by the constitutive activation of the FGF signalling pathway.

1.9 Hypothesis and experimental strategy

The aim of this thesis was to investigate how fibroblast growth factor signalling affects the development and function of the choroid plexus epithelium, and in doing

so to test the hypothesis that fibroblast growth factor signalling can modulate cerebrospinal fluid secretion by the choroid plexus epithelium.

The specific research questions were the following:

- What are the cellular effects of FGF signalling on the CPe cells, and more specifically can it affect CSF secretion?
- Is the expression of the hydrocephalic gene markers i.e. E2F5, P73 and FoxJ1 affected by FGF signalling?

The effect of FGF signalling on the development and function of the CPe cells was mainly studied using in-vitro cell culture models based on the CPe vesicle model, and a rat adult cell line (TRCSFB-2). The phenotype of the cells in these culture models needed to be characterised. Hence, a better understanding of CP development was required and the expression of the genes used to characterise these cell cultures farther extended.

Thus, in the first part of my study, the development of the embryonic murine and human CPs was investigated. The importance of cell proliferation for CP growth, and expression of transthyretin (TTR) and FGF2 proteins was assessed, since surprisingly very little or no data had been published on the expression of these genes in the developing mouse CPs (Chap. 4). Expression of E2F5, FoxJ1 and p73 proteins whose absence causes hydrocephalus was studied in the developing CPs. In addition, since E2F5 is intrinsically linked with the cell cycle, its expression pattern was also compared with that of cell proliferation in the developing brain (Chap. 5).

In the second part of the study, the effect of FGF2 on the function and development of embryonic CPe cells was investigated. The characterization of the phenotype of the embryonic CPe cells in the vesicle model used by Reid (2002) was extended by looking at the expression of genes E2F5, FoxJ1 and P73, that are normally expressed in the CPe and whose knockout cause hydrocephalus, and the tight junction associated protein ZO-1. In addition, the sequence of events leading to the formation of vesicles was characterized, and most importantly whether the cells were capable of secreting fluid (Chap. 6). The effect of FGF2 on embryonic CPe cell function was assessed using this vesicle model in order to specifically understand the mechanism by which FGF2 increases the size of vesicles as reported by Reid S (2001), and whether fluid secretion was affected (Chap. 7).

In the third part, a rat adult CPe cell line (TRCSFB-2) was used to carry out experiments, which could not be done using primary cells due to the limited number of cells obtained for each dissection. The phenotype of the TRCSFB-2 cell line was farther characterised by studying the expression of selected genes such as FGFR isoforms, genes associated with hydrocephalus when knocked-out, TTR and the tight junction associated protein ZO-1, and by establishing whether the cells were able to secrete fluid. The effect of FGF2 on fluid secretion and on the expression of the hydrocephalic markers was then assessed. In addition, the effect of FGF2 on TRCSFB-2 cell proliferation was also investigated to compare it with proliferation in the vesicle model and with the expression of E2F5 (Chap. 8).

Finally, the brain of mice mutants lacking FGFR2-exon 9 (IIIc) that had Apert/Pfeiffer syndrome-like phenotypes was studied in order to see whether the CPs, ventricular spaces and brain tissue exhibited any abnormalities (Chap. 9).

Chapter 2 Materials

2 .1 General laboratory reagents

All general reagents were purchased from BDH (Dorset, UK) except where mentioned otherwise. Sigma-Aldrich (Dorset, UK) supplied bovine serum albumin (BSA), diethylpyrocarbonate (DEPC), ethidium bromide, orange G, paraformaldehyde (PFA), Tween-20, citric acid and hydrogen peroxide. Phosphate buffered saline (PBS) tablets were purchased from Oxoid (Hampshire, UK).

2.2 Histological reagents and equipment

Glass staining troughs and racks, storage containers, glass microscope slides, coverslips, and all histological stains with the exception of Hoechst nuclear stain were obtained from BDH (Leicestershire, UK). Hoechst nuclear stain was from Sigma Aldrich (Dorset, UK). Mounting media were dextropropoxyphene (BDH, UK) or Citifluor aqueous mount (Citifluor Scientific, Cambridge, UK). The wax pen was purchased from DAKO (Buckinghamshire, UK) and clear nail varnish from Boots.

Paraffin wax sections: Sections were cut on a Microm HM330 rotary microtome using disposable blades (both from Raymond Lamb, East Sussex, UK). Heraeus Instruments (Essex, UK) supplied the T6030 wax oven. Paraffin wax (Lambwax - melting point 57-58°C) and plastic troughs were obtained from Raymond Lamb (UK). HistoClear was purchased from National Diagnostics (Atlanta, GA, USA). Poly–l-lysine was purchased from Sigma Aldrich (UK).

Vibratome sections: The vibratome machine (Series 1000) and blades were from Agar Scientific Ltd. (Stanstead, UK). The grade II albumin, the gelatine (300 Bloom) and sucrose powder were all supplied by Sigma-Aldrich (Dorset, UK). 24 well plates were purchased from Philip Harris (Stone, Staffordshire, UK).

The ***vibratome embedding solution*** (400 ml volume) was made by adding 1.8 g gelatine to 40 ml PBS and heated to dissolve with continuous stirring. Once dissolved a farther 360 ml of PBS were added and the mixture cooled to room temperature. A 112 g of albumin grade II was then added and stirred into the mixture overnight.

2.3 Immunohistochemical reagents

2.3.1 Primary antibodies

E2F-5 rabbit polyclonal antibody *(Neomarkers, Californa, USA)* recognises a protein of 58kDa identified as E2F-5. Total IgG purified from rabbit anti-serum by protein-A chromatography. Immunogen: a synthetic peptide corresponding to the N-terminus of E2F-5 protein. The antibody was used at a dilution of 1 in 50.

E2F5 rabbit polyclonal antibody (clone E19) *(Santa Cruz Biotechnology, Inc., California, USA)* is an affinity purified rabbit polyclonal IgG antibody raised against a peptide mapping at the amino terminus of human E2F-5. The antibody is used at a dilution of 1 in 50.

Anti-Hepatocyte Nuclear Factor 3/forkhead homologue 4 (HFH-4) antibody *(Neomarkers, California, USA,)* is a mouse monoclonal $IgG_{1/\kappa}$ antibody recognises a 46kDa protein identified as HFH-4. The antibody was raised against recombinant HFH-4 protein. The antibody was used at a dilution of 1 in 200.

Anti human pre-albumin/transthyretin (TTR) goat anti-serum *(Sigma-Aldrich, UK)* developed in goat using human pre-albumin isolated from normal human adult plasma as the immunogen. The antiserum was treated to remove lipoproteins and is supplied as a liquid containing 2.8-4.2 mg of specific antibody with 0.1% sodium azide. The antibody was used at a 1 in 20 dilution.

Anti-Proliferating Cell Nuclear Antigen (PCNA- clone PC10) *(Santa Cruz Biotechnology, Inc., California, USA)* is a mouse monoclonal IgG2a antibody derived by fusion of spleen cells form a BALB/c mouse immunised with recombinant PCNA with Sp2/0-Ag14 myeloma cells. It reacts against the PCNA p36 protein expressed at high levels in proliferating human and murine cells. It was used at a 1 in 100 dilution

Anti-phospho histone H3 *(Upstate Biotechnology, Buckingham, UK)* is a rabbit polyclonal IgG that recognizes specifically the phosphorylated form of histone H3 (17kDa) in mitotic cells. It was raised against a peptide corresponding to amino acids 7-20 of human histone H3. The antibody was used at a 1 in 100 dilution.

Anti-NeuN *(Chemicon International, Inc., California, USA.)* is a mouse monoclonal antibody raised against purified nuclei from mouse brain. It reacts with most neuronal cell types throughout the nervous system of mice including cerebellum, cerebral cortex, hippocampus, thalamus, spinal cord and neurons in the peripheral

nervous system. NeuN was used at a 1 in 100 dilution on paraffin wax section, and at 1 in 1000 dilution for vibratome section staining.

Anti-ZO-1 (clone R26.4C) *(Hybridoma Bank, Iowa, USA)* is a mouse monoclonal IgG antibody raised against a Z0-1 peptide (Stevenson et al., 1986). The Antibody was used at a dilution of 1 in 50.

Anti-Pan-Cadherin *(Sigma-Aldrich, UK)* is a mouse monoclonal IgG1 antibody, supplied as ascitic fluid, raised against a synthetic peptide conjugated to KLH, corresponding to the amino acids 889-912 of chicken N-cadherin. The antibody was used at a dilution of 1 in 50.

Anti-Beta-actin *(Sigma-Aldrich, UK)* is a mouse monoclonal IgG2a antibody raised against a slightly modified synthetic β-cytoplasmic actin N-terminal peptide conjugated to KLH. The antibody was used at a dilution of 1 in 1000.

2.3.2 Blocking peptides and antibody controls

E2F5- anti-peptide *(Neomarkers, USA)* is a peptide corresponding to the amino-terminus of human E2F5 protein. The peptide was used at dilution of 1 in 10.

E2F5- anti-peptide *(Santa-Cruz, USA)* is a peptide corresponding to the amino-terminus of E2F5 of human origin. The peptide was used at dilution of 1in 10.

Mouse IgG2b negative control *(Dako, UK)* is a mouse monoclonal IgG2b antibody supplied as tissue culture supernatant. The antibody specificity is directed towards *Aspergillus niger* glucose oxidase, an enzyme which is neither present nor inducible in mammalian tissues. The antibody was used at dilution of 1 in a 100.

2.3.3 Secondary antibodies and signal enhancing reagents

Biotin conjugated anti-mouse and anti-rabbit goat immunoglobulins were purchased from DAKO (UK). The immunogens were immunoglobulins (predominantly IgG) from goat serum. The antibody was used at a dilution of 1 in 100.

Peroxidase conjugated anti-mouse rabbit immunoglobulins were purchased from DAKO (UK). The immunogens were immunoglobulins (predominantly IgG) from rabbit serum. The antibody was used at a dilution of 1 in 100.

Peroxidase conjugated anti-rabbit immunoglobulins were purchased from DAKO (UK). The immunogens were IgG from goat serum. Dilution was 1 in 100 for immunohistochemistry and 1 in 400 for Western blot.

FITC-conjugated F (ab')$_2$ fragment of goat anti-mouse immunoglobulins was purchased from Jakson Immunoresearch Laboratories, Inc, (West Grove, USA). The immunogens used for raising this antibody were IgGs isolated from mouse serum. In all experiments, the antibody was used at a dilution of 1 in 40.

FITC-conjugated AffiniPure goat anti-rabbit immunoglobulins IgG (H+L) was purchased from Jakson Immunoresearch Laboratories, Inc, (West Grove, USA). The antibodies were raised against IgGs isolated from goat serum. The antibody was used at a dilution of 1 in 50.

Cy3-conjugated AffiniPure Goat Anti-mouse immunoglobulins IgG (H+L) was purchased from Jakson Immunoresearch Laboratories, Inc, (West Grove, USA). The immunogens used for raising this antibody were IgGs isolated from goat serum. The antibody was used at a dilution of 1 in 50.

Cy3 AffiniPure Goat Anti-Rat IgG was purchased from Jakson Immunoresearch Laboratories, Inc, (West Grove, USA). The immunogens used for raising this antibody were IgGs F(ab')2 isolated from goat serum. The antibody was used at a dilution of 1 in 50.

StreptABComplex/HRP (ABC duet kit), used for the labelling and signal amplification of secondary antibodies used in immunohistochemistry was purchased from DAKO Ltd (UK), and used at a dilution of 1 in 100.

2.3.4 Blocking sera

Goat serum was obtained from DAKO Ltd (UK). Foetal Calve serum (FCS) and bovine serum albumin were obtained from Sigma-Aldrich (UK).

2.3.5 Immuhistochemical colorimetric development

Diaminobenzidine tetrahydrochlorodihydrate (DAB) and o-Phenylenediamine (OPD) tablets were obtained from Sigma-Aldrich (UK).

2.4 Surgical tools and animals

2.4.1 Surgical tools

All dissecting instruments were purchased from John Weiss and Son Ltd (Milton Keynes, UK). 4.5 mm straight bladed iris scissors were used for fine dissection of choroid plexus tissue. 0.25 mm bore tungsten wire (Agar, Cambridge, UK) was used

to make sharp tungsten needles. Tungsten needles were made by inserting a 3 cm tungsten wire into a glass Pasteur pipette and secured it into place using Araldite glue (Jana, Saudi Arabia). The glue was left to set overnight. Needles were sharpened by repeatedly dipping and rotating the secured tungsten wire into boiling sodium nitrite (Sigma Aldrich, UK) until the tip had been reduced to a very fine point.

2.4.2 Animals

Out-bred CD-1 albino mice were supplied by Charles River Mouse Farms (Kent, UK), and housed under Home Office regulations. The morning of detection of a vaginal plug was designated as embryonic day 0.5 (0.5 dpc). Pregnant time-mated mice were killed by cervical dislocation. In each case, the uterus containing between 9 and 21 embryos was removed whole and placed in ice-cold phosphate-buffered saline (PBS). The embryos were dissected free of uterine and amniotic tissues and decapitated immediately.

2.5 Cells used in tissue culture

2.5.1 Embryonic mouse choroid plexus epithelial (CPe) cells

As described in Chapter 3, the primary choroid plexus epithelial cells were derived from 12.5 dpc CD-1 mouse fourth ventricular choroid plexus.

2.5.2 Adult T-Antigen transfected rat CPe cells (TRCSFB-2)

TRCSFB-2 cells were obtained from Tetsuya Terasaki et al (Department of Molecular Biopharmacy and Genetics, Graduate School of Pharmaceutical Sciences and New Industry Creation Hatchery Center, Tokohu University, Japan). The conditionally immortalised choroid plexus epithelial cells (TRCSFB-2) were established from a transgenic rat (Tg rat) harboring the temperature sensitive simian virus 40 (ts SV 40) large T-antigen. This TRCSF cell line exhibits a temperature sensitive cell growth due to the stable expression of the T-antigen. The T-antigen is in its activated form in cultured cells at 33°C and inactive at 37°C. The active form is thought to induce cell proliferation by interacting with the retinoblastoma gene products (Rb) and p53, and thus inactivating the growth suppressive function of these two proteins.

2.6 Tissue culture reagents and equipment

Trypsin-EDTA (5 g/L trypsin and 2 g/L EDTA), calcium -, magnesium- and sodium bicarbonate-free phosphate buffered saline (DPBS) were all provided by Gibco-BRL (Parsley, UK). Arabinoside cytosine was purchased from Sigma (UK), haemocytometer was purchased from Biowhittaker (Walkersville, MD, USA).

2.6.1 Reagents and equipment for TRCSFB-2 cell line culture

DMEM medium (4.5 g/l glucose, 110 mg/ml sodium pyruvate 3700 mg/L sodium bicarbonate), Penicillin-streptomycin (10,000 units/ml penicillin and 10,000 μg/ml streptomycin) were all provided by Gibco-BRL (Parsley, UK). DMEM#2 medium was made using DMEM supplemented with 10% FCS (Sigma, UK). Bromo deoxyuridine (BrdU) was purchased from Sigma (UK). 25 cm^2, 75 cm^2, and 145 cm^2 sterile plastic tissue culture flasks were provided by Nunc Inc (Naperville, IL, USA), other tissue culture plastic was provided by Philip Harris (Stone, Staffordshire, UK). Cell culture flasks were coated with Collagen-1 (Vitrogen), purchased from Cohesion Technologies, Inc. (California, USA). Transwell plate inserts were purchased from Corning Life Sciences (London, UK). The 33°C incubator (model MCO-17AIC) was purchased from Sanyo (Gunma, Japan). The EVOM Epithelial Voltohmmeter was purchased from World Precision Instruments (Stevenage, UK) the Alamar blue was purchased from Serotec Inc (Raleigh, NC, USA).

2.6.2 Reagents and equipment for CPe primary cell culture

HEPES buffered Dulbecco's modified essential medium (H-DMEM) was supplied by Gibco BRL (Paisley, UK). Foetal calf serum (FCS), ouabain and acetazolamide were purchased from Sigma-Aldrich (UK). The same batch of FCS was used in all cultures. Glass cloning cylinders were provided by Sigma-Aldrich (UK), and Petri-dishes (35 mm, and 150 mm) were provided by Philip Harris (Stone, Staffordshire, UK). Matrigel is an extract of the Elgelbroth Swarm mouse sarcoma cell line, manufactured by Becton Dickinson (Massachusetts, USA) and supplied by Stratech Scientific Ltd, (Dudley, UK). DiI, or 1,1'-dioctadecyl-3,3,3',3'-teramethylindocabocyanine ($C_{59}H_{97}ClN_2O_4$) (stock solution in DMSO: 1mg/ml) was purchased from Molecular Probes (Eugene, OR, USA).

2.7 Microscopes

Cell culture microscopy: Microdissection was carried out under a Zeiss SV6 stereomicroscope (Carl Zeiss, Oberkochen, Germany). Photography of large specimens was performed using a Zeiss SV11 stereomicroscope (Carl Zeiss, Germany). Cultured cells were imaged with an inverted Axiovert 135 microscope (Zeiss, Germany), equipped with a Hamamatsu digital camera (C4742-95 Hamamatsu Photonics, Japan). Hoffman optic was used to image vesicles under a 10x objective. To analyse fluorescently stained samples, 20x and 40x objectives were used. The images were captured as Openlab files that were converted into TIFF files using the OpenLab software version 3.05 (Improvision, Coventry, UK) on a Macintosh G4 computer. For time-lapse microscopy additional units were connected to the Axiovert 135 microscope, namely a temperature controller 37.2 unit and a CTI-controller 3700 unit (Zeiss, germany), which controlled the ambient temperature and the percentage of CO_2 in the incubation chamber.

Glass-slide microscopy: Brightfield microscopy was performed with a Zeiss Axioplan 2 microscope, using objective lenses of 2.5x, 10x, 20x, 40x, and 63x. Digital images were captured electronically using a Zeiss Kontron ProgRes 3012 digital camera (Imaging Associates LtD, Thame, Oxon, UK), version 2.0 of the associated software and processed with Adobe Photoshop v6.0 (Adobe Systems Europe, Edinburgh, UK). Fluorescent microscopy was performed with a Zeiss Axiophot microscope using fluorescent illumination and images were digitally scanned using a Hamamatsu digital camera (C4742-95, Hammatsu photonics KK, Japan) into Openlab software. Stereological estimation of neuron number was done using the Axiovert 135 microscope under control of the Orbit unit and software (Improvision, UK) using 5x and 63x objectives.

2.8 Reagents for RNA expression analysis

2.8.1 Reverse transcriptase polymerase chain reaction (RT-PCR) reagents and equipment

For the RNA extraction step, TRI-Reagent was purchased from Sigma (UK) and Dispase enzyme from Gibco BRL (Paysley, UK). The RNA-DNA Gene quant spectrophotometer was purchased from Amersham Biosciences (Amersham, UK). All the following reagents were purchased from Promega (Madison, USA): M-MLV

Reverse transcriptase (200 units/ml), Random hexamers (500 μg/ml), Rnasin ribonuclease inhibitor (400 units/μl), Reverse transcriptase buffer (x5 solution), Taq polymerase (5 units/μl), PCR buffer (x10 solution), MgCl (25 mM), deoxynucleoside triphosphates (dNTPs) (10 mM). Thermostable PCR tubes were purchased from Elkay Laboratory Supplies Ltd. (Hampshire, UK). PTC-1000 thermal cycler machine was from MJ Research Inc. (Boston MA, USA).

2.8.2 Oligonucleotides for RT-PCR

Oligonucleotide primers were designed using the Whitehead MIT software available on the Web (http://frodo.wi.mit.edu/cgi-bin/primer3/primer3.cgi/results_from_primer3) and ordered from Genosys (Cambridge, UK). The oligonucleotides were designed using published cDNA sequences obtained from the Pubmed nucleotide database on: www.ncbi.nim.nih.gov/entrez/query.fgci?db=Nucleotide. The sequences, annealing temperatures, and product size for all the oligonucleotide primers that were used in this thesis are shown in Table 2.1.

Table 2. 1 Oligonucleotide primer sequences of reverse transciptase polymerase chain reaction (RT-PCR).

The first column gives the name of the gene. The second column gives the oligonucleotide sequence information: the accession number of the cDNA sequence is underlined and in parentheses the animal species it was isolated from is indicated; **bold** characters indicate the expected product size in base pairs; *italics* indicate the position of the primer sequence relative to the position of the corresponding base pairs in the cDNA sequence. Primer annealing temperatures used are shown to the right of the product size. The two columns on the right specify whether the oligonucleotides primers recognise rat or mouse cDNA.

Gene	Sequence	Rat	Mouse
GAPDH Forward Reverse	M32599 (mouse) **491 bp** 57°C *179-201* 5' TTCCAGTATGACTCCACTCACG 3' *670-651* 5' GGATGCAGGGATGATGTTCT 3'	Yes	Yes
E2F5 Forward Reverse	NM_007892 (mouse) **227 bp** 57°C *440-469* 5' TGTGGCTACAGCAAAGCATC 3' *654-634* 5' GGCCCTGAGTGACTCTTCAG 3'	Yes	Yes
FOXJ1 Forward Reverse	L13204 (mouse) **205 bp** 57°C *1027-1047* 5' TACTGCTGACCCAGGAGGAG 3' *1227-1207* 5' GGTAGCAGGGCAGTTGATGT 3'	Yes	Yes
TTR Forward Reverse	NM_013697 (mouse) **505 bp** 57°C *4-24* 5' CAGATCCACAAGCTCCTGAC 3' *509-490* 5' CTGCTTTGGCAAGATCCTGC 3'	Yes	No
TTR*rat* Forward Reverse	K03252 (rat) **225 bp** 57°C *366-386* 5' CTCTGGTCATCGCCACTACA 3' *571-551* 5' AGAACGTTTCACGGCATCTT 3'	No	Yes
P73 exon 6 to 9 Forward Reverse	AF138873 (mouse) **253 bp** 55°C *2100-2125* 5' AGAGTGTGGTTGTGCCGTATG 3' *3587-3568* 5' TCCCGGTAATGGTCTTCATC 3'	Yes	Yes
P73 exon10 Forward Reverse	AF138873 (mouse) **99 bp** 57°C *5-23* 5' GAGCCGGGAGAACTTTGA 3' *103-83* 5' GCTGCTGTCGATAGCAGTCA 3'	Yes	Yes
FGFR1 IIIb *mouse* Forward Reverse	AF176552 (mouse) **466 bp** 56°C *415-434* 5' GCCACCTGGAGCATCATAAT 3' *865-846* 5' CCACAGGTCTGGTGACAGTG 3'	No	Yes
FGFR1 IIIb *rat* Forward Reverse	AF000144 (rat) **466 bp** 56°C *211-230* 5' GCCACTTGGAGCATCATAGT 3' *1179-1160* 5' GCACAGGTCTGGTGACAGTG 3'	Yes	No
FGFR1 IIIc Forward Reverse	M28998 (mouse) **453 bp** 56°C *688-707* 5' GCCACCTGGAGCATCATAAT 3' *1138-1129* 5' CTTCCAGAACGGTCAACC 3'	Yes	Yes
FGFR2 IIIb Forward Reverse	XM_215079 (mouse) **422 bp** 56°C *821-841* 5' AAACCAGCACTGGAGCCTTA 3' *1244-1224* 5' TGGTTGGCCTGCCCTATATA 3'	Yes	Yes
FGFR2 IIIc Forward Reverse	XM_215079 (mouse) **310 bp** 56°C *957-980* 5' CCCATCCTCCAAGCTGGACTGCCT3' *1419-1396* 5' CAGAACTGTCAACAATGCAGAGTG 3'	Yes	Yes
FGFR3 IIIb Forward Reverse	L26492 (mouse) **471 bp** 56°C *823-842* 5' AGTGGAGCTTGGTCATGGAA 3' *1294-1277* 5' TGAACACGAAGCCAAAAG 3'	Yes	Yes
FGFR3 IIIc Forward Reverse	AF277717 (mouse) **428 bp** 56°C *823-842* 5' AGTGGAGCTTGGTCATGGAA 3' *1251-1232* 5' ACGCAGAGTGATGGGAAAAC 3'	Yes	yes
FGFR4 Forward Reverse	NM_008011 (mouse) **397 bp** 56°C *1273-1292* 5' AAGTCATCCGTGGCCACTAC 3' *1670-1651* 5' GTCTGCCAAATCCTTGTCGGG 3'	yes	Yes

2.9 Gel electrophoresis and molecular size markers for nucleic acid analysis

Agarose powder was supplied by Gibco BRL (UK). Agarose gels were run in the Horizon horizontal gel electrophoresis system (Gibco BRL, UK). The hyperladder IV 100 bp ladder from Bioline (London, UK) was used for DNA analysis. The reagents to make tris- boric- EDTA electrophoresis buffer (TBE: 108 g tris-base, 55 g boric acid, 6.85 g EDTA in 1L of DEPC-treated water) were purchased from Sigma Aldrich (UK). Gel images were captured using the AlphaImage 1200, and Alphaease 3.3 software (Alpha Innotech Corporation, USA).

2.10 Protein analysis

2.10.1 protein extraction reagents

Protease inhibitor cocktail: a mixture of protease inhibitors with broad specificity for the inhibition of serine, cysteine, aspartic proteases and aminopeptidases. Contains 4-2(2-aminoethyl) benzenesulfonyl fluoride, pepstatin A, E-64, bestatin, leupeptin, and aprotinin (Sigma, UK). RIPA buffer was made of 150 mM NaCl, 1.0 % IGE-PAL CA630 NP-40, 0.5 % deoxycholate, 0.1 % sodium dodecyl sulphate (SDS), and 50 mM Tris. Loading buffer was made as a two times concentrate (25 % (v/v) glycerol, 10 % β-mercaptoethanol, 6 % SDS, 0.25 M Tris-HCl pH6.8, and 0.2 % (w/v) bromophenol blue).

2.10.2 Separation and blotting

BCA Protein Assay Kit was purchased from Pierce (Rockford, IL, USA). The 30 % polyacrylamide/ bis solution, with 29:1 crosslinker ratio (3.3 %C) was purchased from Biorad (Hercules, CA, USA), TEMED, ammonium persulphate (Sigma), Mini Protean Electrophoresis System and the Transblot SD, Semi-Dry Transfer Blotter was purchased from Biorad (Hertfordshire, UK). Rainbow Markers was purchased from Amersham Biosciences (Amersham, UK). Gel running buffer was made as a solution of 0.025 mM Tris base, 0.192 mM glycine, 0.1 % SDS in water. HyBond-PVDF (Polyvinylidene Difluoride) membrane was purchased from Amersham Biosciences (UK). Coomasie blue (Brilliant Blue G solution- Sigma): after dilution with dionized water to a final volume of one litre, the solution contained 0.1% (w/v) Brilliant Blue G, 25% (v/v) methanol and 5% (v/v) acetic acid (Sigma, UK). Ponceau S solution (sigma, UK) was used neat. Transfer buffer for Western blot was made as a solution

of 25 mM Tris base, 192 mM glycine, 0.037 % SDS, and 20% (v/v) methanol in water. The enhanced chemiluminescence reagent kit was purchased from Amersham Pharmacia Biotech (Buckinghamshire, UK). Autoradiography film, MXB film (100 NIF/ 18 x 24 cm), was purchased from Genetic Research (Rayne, UK).

Chapter 3 Methods

3.1 Isolation of mouse embryos

A naturally mated 8 to 12 week female CD-1 mouse was killed by cervical dislocation at different days of post-conception (dpc); between 11 and 17.5 dpc. The animal was swabbed with 70% ethanol and a midline incision was made to expose the reproductive tract. The foetuses were dissected out from the uterine tract and placed in DPBS. Fine scissors and forceps were used to open the uterine horn and release the foetuses. The foetuses were freed from the placenta and extra embryonic membranes and placed in fresh DPBS.

3.2 Primary culture of choroid plexus epithelial cells

3.2.1 Isolation of embryonic choroid plexus epithelial cells

Isolation of fourth ventricle choroid plexus: Under a dissecting microscope the fourth ventricle choroid plexus of 12.5 dpc embryos was exposed, using iris scissors, by a midline incision at the midbrain, hindbrain boundary. The choroid plexus was dissected from the surrounding neuronal tissue, and then transferred in H-DMEM medium kept at 37°C; choroid plexuses from one litter (10-15 embryos) were pooled together.

Isolation of choroid plexus epithelial (CPe) cells: The pooled choroid plexuses were transferred to a 35 mm dish containing 2.5% pancreatin and 0.5% trypsin in DPBS and incubated for 30 minutes at 4°C. Then they were transferred in 10% FCS/ H-DMEM to inhibit the activity. The epithelial layer was then separated from the underlying vascularised mesenchyme using sharp tungsten needles. Once the epithelia sheets were isolated, they were transferred with the smallest possible volume to a 15 ml Falcon tube and incubated at 37°C with 1 ml of 0.5% trypsin-EDTA for 3 minutes. The reaction was then neutralised with 0.5ml of 10% FCS/ H-DMEM, and the epithelial sheets gently pipetted several times through a 1ml Gilson pipette tip to obtain a single cell suspension. After centrifugation at 1000 rpm for 5 minutes, the supernatant was decanted and the cells were resuspended in 0.5 ml 10% FCS/ H-DMEM.

3.2.2 Culturing of embryonic CPe primary cells

Plating: A 250 µl aliquot of the cell suspension, containing 1-2 x 10^5 CPe cells as determined by using a haemocytometer, was plated on Matrigel in a cloning cylinder of 8 mm of diameter in tissue culture medium with or without FGF2 growth factor. Depending on the experimental design, FGF2 was added either immediately after plating or after one day in culture at final concentrations ranging from 10 ng/ml to a 100 ng/ml (1 µl of 2500 ng/ml FGF2 was added to 250 µl medium to obtain a final concentration of 10 g/ml, and 1 µl of 25000 ng/ml FGF2 was added to 250 µl medium to a final concentration of 100 ng/ml). The cells were grown in a humidified environment at 37°C in the presence 5% CO_2.

Feeding: For each experiment stock media of 5 to 10 ml 10% FCS/H-DMEM were prepared and FGF2 was added at the required concentration (0 ng/ml, 10 ng/ml or 100 ng/ml). Vesicle cultures were fed every 2-3 days by removing half of the culture medium (i.e. 125 µl), and replacing it with fresh 10% FCS/H-DMEM with or without FGF2.

3.2.3 Staining embryonic choroid plexus epithelial cells with dil dye

Freshly isolated CPe cells were incubated with 5 µM diI in DMSO for 30 minutes in a humidified incubator at 37°C and with 5% CO_2. The cells were centrifuged at a 1000 rpm for 5 minutes, the supernatant decanted and replaced with twice the volume of fresh medium. The centrifugation step was repeated another two times and the cells were then re-suspended in a final volume of medium to obtain the required cell density. Fifty micro-litres of labelled CPe cells at a concentration of 20-40x10^5 CPe cells/ml were then added to 200 µl of unlabelled cells at a concentration of 20-40x10^5 CPe cells/ml.

3.2.4 Cytosine Arabinoside treatment

50 µM of cytosine arabinoside (Ara-C) (in 10% FCS/H-DMEM with or without FGF2) was added one day or five days after plating on Matrigel. Stock media of 5 ml 10% FCS/H-DMEM treated and non-treated with Ara-C were made up. On the day of treatment, all the culture medium was removed and replaced with fresh culture medium treated with 50µM Ara-C. Subsequently, half the culture medium was

replaced with fresh Ara-C treated medium every two days, for the duration of the assay. Control cultures without Ara-C were included in each experiment.

3.2.5 Acetazolamide and ouabain treatment

Vesicle cultures were treated with a combination of 100 μM acetazolamide and 5 mM ouabain over 48 hours. In order to remove and replace the culture medium (250 μl) fresh medium containing 5 mM ouabain and 1 μl of a 25 mM stock solution of acetazolamide in DMSO was added. Control cultures were ran in parallel in medium containing only DMSO.

3.3 Immunocytochemical staining of embryonic choroid plexus epithelial cell vesicle cultures

CPe vesicle cultures grown in Matrigel inside an 8 mm cloning cylinder placed on top of a 13 mm glass coverslip were washed four times with PBS for 5 minutes each, and fixed either in 4% PFA for 10 minutes (for p-H3 staining) or ice cold methanol (-20°C) (for ZO-1 staining). After rinsing four times with PBS, non-specific binding sites were blocked with 1% goat serum in PBS for 40 minutes. The CPe vesicles were incubated overnight at 4°C with primary antibody (or 2 hours at room temperature (RT)) at the dilutions specified in Chap.2.3. The CPe vesicles were washed six times with PBS and incubated with secondary antibody (FITC goat anti-rabbit for the p-H3 staining, and Cy3 goat anti-rat for the ZO-1 staining) for 30 minutes at room temperature in the dark. After washing off the secondary antibodies, the CPe vesicles were incubated 15 minutes with Hoescht nuclear stain. The Matrigel was cut at the edges with a sharp epidermal needle and the cloning cylinder removed. The coverslip with the Matrigel was mounted with Citifluor and sealed with nail varnish.

3.4 CPe vesicle measurement protocols

3.4.1 Vesicle and aggregate measurement

The number and size of aggregates and vesicles was measured using the Openlab 3.1.5 software. The size of aggregate and vesicles was estimated by measuring the surface area in μm^2 of their focal equatorial plane (see Fig. 3.2) (the arbitrary units given by the Openlab had to be calibrated with a millimetre graticule calculated the area in μm^2). The measurements were automatically recorded by the Openlab 3.1.5

programme, stored in Microsoft Excel and later transferred to SPSS 11.5 for statistical analysis. Aggregates and vesicles were measured in the same fields at different days, although given the daily changes it was not possible to identify individual aggregates. The same field could be easily identified by using the co-ordinates on a finely graduated x-y stage, fitted to the Zeiss inverted microscope. Four fields of view were taken on each measurement day.

3.4.2 Assessment of cell proliferation in CPe vesicle cultures

3.4.2.1 Quantification of cell proliferation in aggregates

Ten to fifteen aggregates from cultures stained with the mitotic marker p-H3 were selected using a systematic random uniform sampling scheme (Fig. 3.1). The first aggregate was chosen at random in the field that was first focused on, and then aggregates were selected with a fixed frequency (usually one out of every 5-10 aggregates) following a set of rules: 1) the closest adjacent aggregate was chosen; 2) if different aggregates had similar distances, the aggregates were selected following a clockwise orientation; 3) aggregates that had been counted once were not counted again.

This method allowed an unbiased statistical "snapshot" of the population of aggregates rather than having to go through all the aggregates or choosing them at random (and thus biasing the selection). Each selected aggregate was then optically sliced manually by increments of roughly 5 μm to count the total number of positive cells for p-H3. A picture of the mid-plane/equatorial-plane section of each selected aggregate (see Fig. 3.2) was also taken to estimate its area using the Openlab 3.1.5 software. By establishing the average number of cells present in a fixed area from four aggregates, it was then possible to estimate from the unknown area of the equatorial plane of selected aggregates, the corresponding number of cells. The total number of p-H3 labelled cells contained within the three dimensional structure of an aggregate was then plotted against the total number of cells within the equatorial plane of that aggregate. All pictures were captured and analysed using Openlab 3.1.5.

3.4.2.2 Quantification of cell proliferation in vesicles

The sampling scheme was the same as for the CPe aggregates previously described. Because vesicles were flattened out by the coverslip, they appeared two dimensional.

The area of a selected vesicle was measured, and the total cell number in that area estimated by statistically establishing the number of cells associated with a given area of a vesicle (four vesicles were used). It was then possible to obtain the number of p-H3 labelled cells against the estimated total number of cells for each sampled vesicle. The pictures were captured and analysed using Openlab 3.1.5.

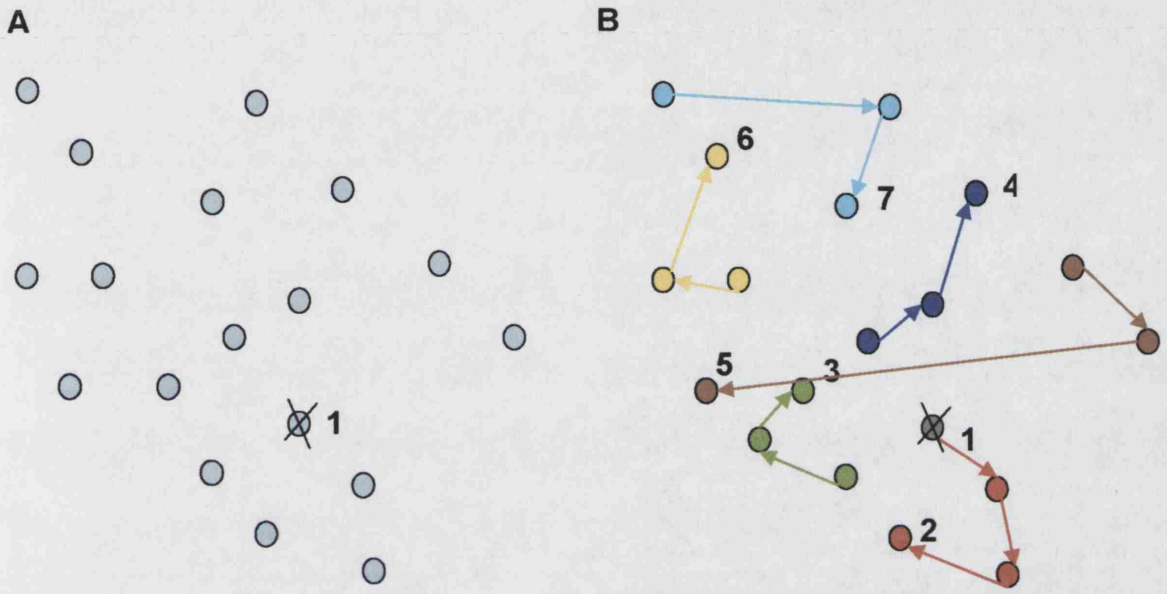

Figure 3. 1 Sampling procedure for selecting aggregates based on a systematic random uniform sampling scheme

The sampling rule for selecting aggregates with a fixed frequency are described in the main text (3.2.2.1), and is illustrated in the above diagram. **A**: the diagram shows 19 aggregates randomly distributed. The first aggregate is chosen randomly and is indicated by a cross in **(1)**. **B**: In this example, one out of every three aggregates is selected so that a total of seven aggregates (labelled as **1-7**) are sampled. Arrows show the direction of counting for each selection; the arrows have different colours for each group of three aggregates. For example, starting from **(1)**, the red arrows show which aggregates are counted in order to get to **(2)**. The closest adjacent aggregate to **(1)** is counted in a clockwise direction (between aggregates that have roughly the same distance, the one that first appears in the clockwise direction is selected). Each aggregate that has been already counted once cannot be counted or selected again.

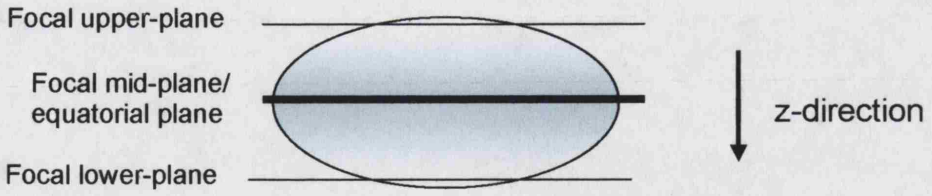

Figure 3. 2 Definition of the focal mid-plane/equatorial plane of an aggregate (or vesicle)

Focusing down (optical sectioning) an object it is the plane of focus situated at an equal distance from the top and bottom of an object (focal upper- and lower-plane).

3.5 Statistical analysis

Statistical tables, providing information on count, mean, minimum/maximum, 95% confidence interval, standard deviation and standard error were computed using SPSS 11.5. All graphs were constructed using SPSS 11.5.

For each set of experiments, the normality of the data was assessed by plotting a frequency histogram of the data. Usually, a scatter plot was sufficient to show that the data were compatible with a normal distribution. The standard deviation and standard error of the mean for each set of data was systematically estimated, and Independent Student's t-test were performed to compare the means from two conditions (normally distributed).

The minimum number of samples required to detect a significant difference between two conditions (FGF2-treated and control cultures) was assessed by using a power calculation (provided the data was normally distributed). The significance value of the difference between two means was taken as $p < 0.05$, with a power ranging from 80% to 95%. This gave F values of 7.85 or 12.99 respectively. Typically, d was taken as $\sigma > d > 2\sigma$.

F: power values

$$n \geq 2F(\frac{\sigma}{d})^2 = 2F(\frac{\sigma}{d})^2$$

d: difference between two means

σ: standard deviation of each sample

The use of more specific statistical tests is described in the relevant result chapters, such as non parametric significance tests, regression analysis, correlation analysis, and ML-wiN modelling (see Chap. 3.5).

3.6 ML-wiN modelling

Hierarchically structured or multilevel data was analysed by multilevel modelling using the computer package ML-wiN, (Institute of Education, London), with the assistance of Dr A. Wade, Senior Lecturer in Statistics, Institute of Child Health.

Multilevel data referred to data that had different levels of variation and which could not simply be summarised by fitting a regression line to it (least mean square method). Multilevel data were separated into different groups that were assigned a specific level of hierarchy, so that the ML-wiN programme analysed the contribution of each group to the overall variation of the data. For example if three groups contributed to the variation of the data, a level 3 analysis would be used where:

- Level 1 variation: looked at the degree of scatter about a regression line summarising all the data points. This was the overall variation of the data.
- Level 2 variation: each unit was modelled jointly to obtain the variation between the intercept and slopes that were normally distributed by fitting regression lines for each level 2 unit of the data.
- Level 3 variation: the variation between the slopes and intercept was analysed by fitting regression lines for each level 3 units.

The basic algebraic notation of a multilevel model follows the same principles as an ordinary regression analysis ($y_i = a + bx_i + e_i$ or $y_i = \beta_0 x_0 + \beta_n x_{ni} + e_i$) (where e_i is a random quantity), except that it is refined to include any additional factor that may influence the outcome of the model. A multi-level model therefore has:

- A fixed part that encompassed a fixed parameter associated with the intercept ($\beta_0.x_0$) and the explanatory variables with their respective coefficient ($\beta_n.x_n$)

- A random part that expressed the variation at the different levels of the data

Effectively, the ML-wiN model assesses the data by using a series of steps whereby potential influencing factors are added to the model, one following another. A $^{-}2$ log likelihood value is initially calculated, as a measure for determining how well the model fitted the data. When used as it was here, in a stepwise fashion, the $^{-}2$ log likelihood tested the null hypothesis that the coefficients of the terms added to the model were zero. Any large changes in $^{-}2$ log likelihood suggested a highly significant effect.

3.7 Microscopy of live CPe vesicles

3.7.1 Time lapse microscopy of vesicles

Using an inverted microscope equipped with an incubation chamber with temperature and CO_2 percentage control, and the Openlab 3.1.5 automation, it was possible to take pictures of the same field of view at fixed time intervals. Since CPe cells were grown on a three dimensional Matrigel, the Openlab automation programme controlling the microscope parameters was set to take pictures at different focal planes under Hoffman or/and under fluorescence optics (see Appendix I for details of the automation programme). Pictures taken of the same focal distance were collected together to make time-lapse films (1024 x 1022 pixels). The films presented in this thesis can be viewed using the Quicktime version 6 software.

3.7.2 Deconvolution analysis of vesicles

The deconvolution analysis of vesicles used a specific "δz- deonvolution" automation of the Openlab 3.1.5 software that allowed acquiring optical sections through an object under a normal inverted microscope. The focal boundaries (top and bottom of a vesicle) were first chosen. The thickness ($\delta z = 5$ μm) of the optical slices was then specified, so that Openlab computed how many slices were needed to cover the specified focal boundaries.

3.8 Protocol for culture of the TRCSFB-2 cell line

3.8.1 Thawing of cell stock and culturing

The TRCSFB-2 stock cryotube was thawed at 37°C and the cells washed three times by centrifugation at 1000 rpm and resuspending them in medium#2. To eliminate any traces of DMSO contained in the stock, the cells were suspended in 5 ml medium#2 and seeded in a 25 cm^2 flask; the cells were cultured at 33°C in a humidified atmosphere of 5% CO2. Once the cell attached to the flask the medium was replaced every two days until the cells reached 70% confluency.

3.8.2 Passaging of TRCSFB-2 cells

Passage of the cells was performed once the cells reached 70% confluency. Cells grown in a 25 cm^2 flask were washed with DPBS and incubated with 2.5 ml of 0.25 %

trypsin-EDTA, (5 ml was used for 75 cm^2 flasks). The trypsin was inactivated with twice the volume of medium#2 and the cell suspension transferred to a 15 ml Falcon tube after repeated pipetting through a 10 ml pipette. The cells were then centrifuged at 1000 rpm for 5 minutes, the supernatant discarded and the pellet resuspended in 2 ml medium#2. Any remaining aggregates were mechanically dissociated by repeated pipetting through a 5ml pipette. This step was repeated one more time, and the cells were then resuspended in the appropriate volume of medium in order to plate $5\text{-}6 \times 10^5$ cells per 75 cm^2 flask.

3.8.3 Freezing TRCSFB-2 cells

The TRCSFB-2 cells were passaged as described above. The final pellet was suspended in 1-2 ml of medium#2 to which 10% DMSO was added. Over 1×10^6 cells per cryotube were stocked. The cells were frozen overnight at -80°C in isopropanol, and the next day transferred in liquid Nitrogen for permanent cryo-storage.

3.8.4 FGF2 treatment

TRCSFB-2 cells were treated for 14-16 hours with 1 ng/ml, 10 ng/ml, or 100 ng/ml FGF2 before the start of an assay. FGF2 was made up to the required concentration in DMEM using a 25 μg/ml stock solution of FGF2.

3.8.5 Cytosine arabinoside treatment

TRCSFB-2 cells were treated overnight with 50 μM cytosine arabinoside (Ara-C) made in DMEM before the start of a proliferation assay.

3.9 TRCSFB-2 cell line Transwell secretion assay

3.9.1 Growing the cells on Transwell filters

TRCSFB-2 cell were seeded on a 12 mm COL-1 Transwell filters at a density of 5×10^5 cells/ml in 200 μl medium, and 1 ml medium was dispensed in the bottom chamber. The cells were grown to confluency over two to four days at 33°C in 1% FCS/DMEM. Confluency of the cells was tested using different means: by visual inspection of the cells under the microscope, by looking at the level of the meniscus in the upper chamber compared to the lower chamber, and by testing the transepithelial electrical resistance using an EVOM ohmmeter (predicted values were ~140 $\Omega.cm^2$). TRCSFB-2 cells were grown at 33°C but the assay was performed at 37°C. Before the

start of an assay cells intended to be treated were grown for 14-16 hours with the appropriate compound (FGF2, Ara-C or acetazolamide/ouabain) or its vehicle.

3.9.2 Transwell secretion assay

All dilutions were done in 1% FCS/DMEM. A primary solution of 1 mg/ml 500 kDa FITC-dextran was filter sterilized through a 0.22 μm filter and diluted to make a stock solution of 0.1 mg/ml FITC-dextran (1/10 dilution). This was diluted to different concentrations to make a calibration curve for determining the absolute concentration of FITC-dextran present in the samples. The different concentrations of FITC-dextran used were: 0.032 mg/ml, 0.016 mg/ml, 0.008 mg/ml, 0.004 mg/ml, 0.002 mg/ml, 0.001 mg/ml, and 0.0005 mg/ml. The working FITC-dextran solution used in the assay was 0.008 mg/ml. 1.5 ml of this solution was dispensed in the lower chamber of the COL-I transwell and 0.5 ml TRCSFB medium was added to the upper chamber. 200 μl aliquots were taken from the lower chamber at every time point and diluted in 600 μl medium inside plastic cuvettes for spectrophotometry. The fluorescence was determined using a fluorimeter set at an excitation wavelength of 490 nm, and an emission wavelength of 520 nm. For each experiment control Transwells with no cells on their filter were run in parallel. In some experiments, cells were grown in the presence of the secretion inhibitors 100 μM acetazolamide and 5 mM ouabain.

3.10 TRCSFB-2 proliferation assays

3.10.1 Growing the cells

For all cell growth assays, TRCSFB-2 cells grown at 33°C were plated in 96-well plate at a density of $5x10^3$ cells/well in a 100 μl of 1% FCS/DMEM using a multi-channel pipette. The cells were grown for 24 hours time at 37°C until they reached 40-50% confluence. The medium was then replaced with 0.1% FCS/DMEM with or without treatment (FGF2 or Ara-C) and cells grown for a further 16 hours before the start of a growth assay.

3.10.2 Alamar Blue assay

The Alamar Blue assay incorporates a fluoremetric/colourimetric growth indicator that is sensitive to the redox (chemical oxidation-reduction) state of the culture medium due to the inherent metabolic activity of the cells. As the cells grow in

culture, the innate metabolic activity of the cells results in the chemical reduction of the medium, whilst an inhibition of growth maintains an oxidized environment. The reduction is related to growth and thus causes the redox indicator to change from an oxidized (non-fluorescent, blue) to a reduced (fluorescent, red) form. The absorbance of the colourimetric reaction can then be measured spectrophotometrically using a wavelength of 570 nm. The assay was started once the cells had reached 40-50% confluency. The medium from each well was then replaced with 200 µl of DMEM containing 0.1% FCS and 10% Alamar Blue solution, and the cells were returned to the 37°C incubator for 2 to 24 hours. For each chosen time point, the Alamar Blue reaction medium was transferred to a new 96-well containing no cells, which was used to measure the A_{570} nm absorbance of the reaction medium using a 96-well plate reader. The background absorbance was measured by subtracting the absorbance value from wells with no cells.

3.10.3 BrdU ELISA assay

The assay relies on the fact that the cells undergoing proliferation require nucleotides to carry out DNA replication. By providing a thymidine analogue (BrdU) in the culture medium, it is possible to follow the incorporation of this base into the proliferating cells by immunocytochemistry. BrdU was added to the micro-cultures with or without FGF at a final concentration of 1 µM. After 2 hours, BrdU incorporation was terminated by aspirating the medium and washing with 200 µl/well of Hank's balanced salt solution- three times. The cells were then fixed with 200 µl/well of 70% ethanol for 20 minutes at RT. The wells were washed with water and the DNA denatured by incubation with 100 µl per well of 2M HCl for 10 minutes at 37°C. Following aspiration, the wells were filled with borate buffer (0.1M, pH 9.0) to neutralise the residual acid. After washing with PBS, the cells were treated with 50 µl of blocking buffer (0.1% Triton X-100 + 2% normal goat serum in PBS) for 15 minutes at 37°C. Monoclonal mouse raised against BrdU diluted in blocking buffer at a concentration of 1 µg/ml was added for 60 minutes at 37°C (50µl/well). Unbound antibody was removed by three washes with 0.1 % Triton X-100/PBS. Bound antibody was detected by peroxidase- conjugated goat anti-mouse (2 µg/ml) diluted in block solution and incubated for 30 minutes at 37°C. After three washes with 0.1% Triton X-100/PBS and a final rinse with PBS, a 100 µl/well of OPD substrate was added. Two negative controls were run in parallel for each time point: 1) cells were

grown without BrdU; 2) cells were grown with BrdU but the primary anti-BrdU antibody was omitted from the staining protocol. Absorbance was measured at 490 nm wavelength using a micro-plate reader (Fig. 3.3).

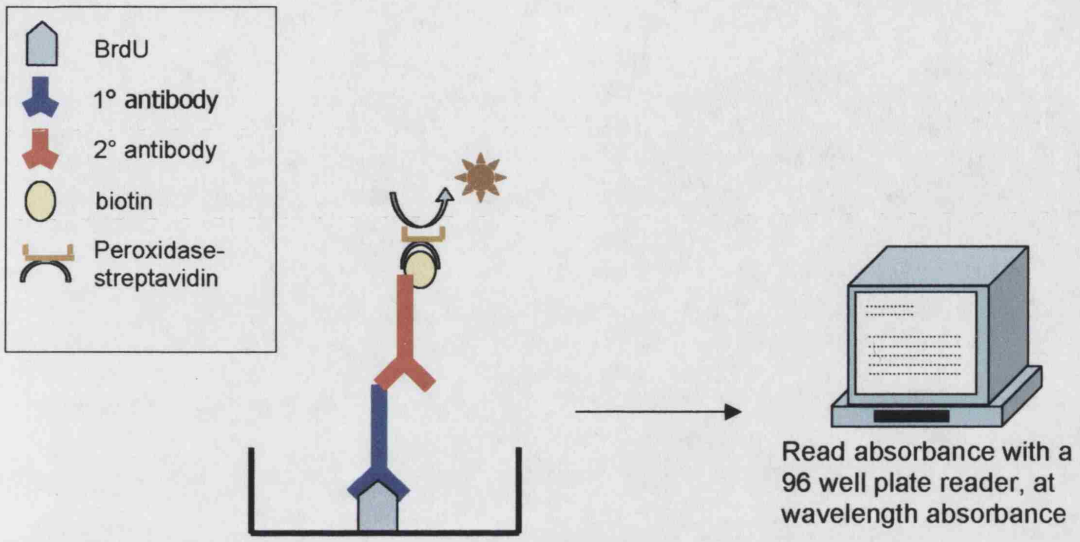

Figure 3. 3 Schematic basic of the BrdU ELISA assay

A mouse primary antibody raised against BrdU is applied to cells that have been incubated with BrdU. A goat anti-mouse IgG secondary antibody conjugated to the horse-radish peroxidase (HRP) enzyme is then used specifically to label primary antibodies bound to BrdU. It is then possible to assess the relative number of bound primary antibodies based on the catalysis by the HRP enzyme of an OPD substrate that produces a coloured product that can be monitored spectrophotometrically at a wavelength of 490 nm using a computer-assisted plate reader.

3.11 Immunocytochemical staining of TRCSFB-2 cells

Cells grown on 13 mm coverslips were first rinsed three times in L15 medium, the excess fluid was blotted off and the cells fixed with either 4% PFA (E2F5, FoxJ1 antibodies) or acid alcohol (TTR, ZO-1 antibodies). If using an HRP conjugated secondary antibody, the coverslips were incubated 5 minutes with 3% hydrogen peroxide and rinsed with PBS. Non specific binding sites were blocked with 10% FCS and 1% bovine serum albumin (BSA) in PBS for 20 minutes, before adding the primary antibody at the appropriate dilution for 1 hour. All washes were performed by rinsing the coverslips three times with 0.1% Tween/PBS followed by a PBS rinse. The secondary antibody was then added, and after 30 minutes at room temperature coverslips were rinsed as above.

HRP based visualisation: the coverslips were incubated with secondary antibody conjugated either with HRP or with biotin (If using a biotin conjugated secondary antibody, the coverslips were incubated 30 minutes at RT with a streptavidin-peroxidase conjugate, ABC kit). Peroxidase activity was detected using the DAB substrate in the presence of H_2O_2 that gave rise to a brown reaction product after 5-10 minutes incubation, and the reaction was quenched by dipping the coverlips in dH_2O. Nuclei were counterstained with methyl green.

Fluorescence based visualisation: visualisation of the signal when using FITC- or TRITC-conjugated secondary antibodies was direct and only required an additional wash.

Coverlips (stained by HRP or fluorescence) were mounted unto histological glass slides with Citifluor and the edges of the coverslip sealed with nail varnish. HRP based staining was visualised with a bright-field microscope, whereas fluorescent based staining was viewed under fluorescent microscope. Nuclei were stained with Hoechst dye.

3.12 Paraffin embedding and sectioning of embryos

3.12.1 Paraffin embedding

Embryos of different ages require different fixation, dehydration and embedding protocols, which are detailed in Appendix I.2. In brief, embryos were fixed in 4% paraformaldehyde (PFA) at 4°C, typically for 16-24 hours, then washed with PBS and dehydrated through increasing grades of ethanol from 50% to 100%. Once dehydrated each embryo was placed in a glass vial and washed twice in Histoclear and then three times with paraffin wax. After the last wax change, each embryo was placed in a plastic or glass embedding mould and oriented as needed before the wax solidified. The wax block was left to set overnight and then placed at -20°C for 5-10 minutes in order to facilitate removal of the wax block from its mould.

3.12.2 Sectioning

The wax block was trimmed around the area containing the embryo. It was cooled on ice before cutting 6-10 μm thick sections with the microtome. Sections were placed onto a 0.5 ml distilled water droplet on top of a Poly-L-lysine coated glass slide. Poly-L-lysine is highly cationic, and hence interacts with the anionic sites of the

tissue, resulting in good adhesion between the slide and the sample. The water served to flatten the samples. Excess water was removed using a Pasteur pipette, and the slides were put to dry vertically in a rack at 37 °C overnight. Slides were stored un-mounted at 4 °C until used.

3.13 Vibratome embedding and sectioning of brains

Dissecting out the mouse brain: embryos were fixed in 4% PFA overnight at 4°C, and rinsed with PBS. The fixed brain was freed from the calvarium by cutting through the sagittal suture with flat scissors making sure the scissors were facing upwards. The sutures on each side of the skull were freed in the same way. Using hooked forceps the plates of the calvarium were lifted up gently and removed. The plates could be additionally teased away by removing any meningeal membrane between the brain and the calvarium, using a pair of fine forceps. Once the calvarial plates were removed, the fine forceps were used to remove any remaining connective tissue that was attached to the brain, namely at the base of the brain and near the olfactory bulb. The brain was then lifted from the base of the skull and rinsed in PBS before processing for vibratome embedding.

Embedding of the brains: the brain was incubated in vibratome embedding solution (see Chap. 2.2) overnight at 4°C. The smallest possible plastic mould that could accommodate the brain was used for the embedding step. The embedding solution was placed into the plastic mould, and a volume of 3% grade I glutaraldehyde solution that represented 10% (v/v) of the volume of the embedding solution was quickly stirred in. The brain tissue was then dropped in before the embedding solution solidified after a few seconds.

Vibratome sections of the brain: 50 μm sections were cut with the vibratome. Each section was placed in 60% glycerol/PBS in a separate well of a 24-well plate, each labelled with a number according to the order of the cut. Approximately 150-200 sections were produced for post-natal mouse brains, which required 6-8x24-well plates. The sections were stored at 4°C, or frozen at -20°C for future use.

3.14 Haematoxylin and Eosin staining

The wax was removed from the sections by complete immersion in Histoclear twice, for 10 minutes each. The sections were then rehydrated by sequentially passing them through a graded ethanol series of 100% (x2), 95%, 85%, 70%, 50% and 30% each

for 5 minutes. The slides were then washed in MilliRO water for 5 minutes. Nuclei were stained by immersing the slides in Erhlich's or Mayer's haematoxylin for 2-5 minutes, followed by a 30 second dip in acid alcohol (1% HCl in 70% ethanol). Slides were then placed into a trough of running tap water for a further 5 minutes to develop a blue colouration. The sections were dehydrated in graded ethanol from 30% to 95% (5 minutes in each grade), before being immersed in 1% eosin in 95% ethanol for 5 minutes to stain the cytoplasm of the cells. The eosin treatment was followed by a wash in 95% and 100% ethanol. Finally, the slides were immersed in Histoclear twice for 10 minutes each before mounting in DPX. They were left to dry overnight in a fume hood.

3.15 Immunohistochemistry on wax sections

3.15.1 Re-hydration and pre-treatments

Six micrometer thick paraffin wax sections were deparafinized in histoclear for 10 minutes and re-hydrated through graded concentrations of ethanol as follows: 3 minutes in 100% ethanol, 1 minute each in 90%, 70%, 50%, 30% ethanol and 5 minutes in dH_20. The slides were then heated in a microwave at 540W in 0.01 M citric acid (pH6.0) for 5 to 10 minutes to unmask the epitopes, and cooled 10 minutes under running tap water before rinsing with dH_20. Alternatively, for epitope unmasking the slides were incubated for 2 minutes at 37°C with a non-specific type XIV protease from *Streptomyces griseus*, and rinsed in dH_20 for 5 minutes. If using an HRP based detection method, endogenous peroxidase activity was quenched with 3% hydrogen peroxide/ PBS 15 minutes and washed with dH_20 twice for 5 minutes. Non-specific binding sites were blocked by applying a protein-rich solution, containing 10% FCS and 1% bovine serum albumin (BSA) in PBS for 30 minutes. If the seconday antibody was raised in goat, 10% goat serum was used.

3.15.2 Primary antibody application

The slides were then incubated with primary antibody at the appropriate dilution (as given in chap. 2.3.1) for 2 hours at room temperature or 16 hours at 4°C. Negative controls were run in all experiments. If the specific peptide or the antigen the antibody was raised against was available, the antibody was pre-adsorbed with the specific

blocking peptide for 1 hour at 37°C. If no blocking peptide was available, the primary antibody was simply omitted.

3.15.3 Secondary antibody and visualisation

The antibody incubation times and visualisation techniques were the same as for immunocytochemistry (described in section 3.10). However for histochemistry, all washes were performed with 0.1% Triton/PBS and rinsing with PBS.

3.16 Immunostaining of vibratome sections

All incubations were carried out in a 24-well tissue culture plate placed on a horizontal rotatory shaker. 50 μm vibratome sections were rinsed in PBS for four times for 30minutes periods at RT. In order to permeabilize the tissue sections, they were dehydrated and then re-hydrated through an alcohol gradient of 10%, 25%, and 40% ethanol. The sections were incubated for 5 minutes in each alcohol solution. After re-hydration, the sections were incubated in 1% Triton in 2% goat serum/PBS for 30 minutes. The sections were then incubated with the primary antibody anti-NeuN in 500 μl of 0.5% goat serum and 0.5%Triton x-100/PBS for 48 hours at 4°C. The sections were washed three times with 0.1% Triton X-100/PBS for 10 minutes periods. The sections were then incubated with secondary anti-mouse–cy3 conjugated antibody in 500 μl of 0.1% Triton and 0.2% goat serum/PBS for 24 hours at 4°C. The sections were washed three times with 0.1% Triton/PBS for 10 minutes periods. The sections were then mounted with Citifluor on glass slides and the slides sealed with nail varnish.

3.17 Stereological analysis

3.17.1 Neuron number quantification in the cortex

3.17.1.1 Systematic random uniform selection (SRUS) of sections for counting neurons

The method was adapted from (Gundersen et al., 1988). Neurons were counted using an optical disector probe (Fig. 3.4), which samples isolated objects with a uniform probability in 3-D space, irrespective of size and shape. The areas where neurons were counted were selected according to a fractionator sampling scheme (Gundersen, 1986). The brains were cut with a vibratome into 50 μm sections; about 7-10 evenly

spaced sections were chosen by systematic random uniform selection (SRUS) (i.e sampling with a predetermined periodicity form a random start position): the first section was randomly chosen using a dice or a randomisation table, and was within the first 10-15 sections; then one section out every 10-15 sections was taken. Sections were immunostained for NeuN and imaged under a Zeiss axiovert microscope equipped with a motorised z-step focus drive interfaced with the Openlab software. An image of each brain section was taken at x2.5 magnification and imported in PowerPoint where a grid was apposed to the image so that each line intersection that hit the cortex was marked with a little square, which represented an area or field where neurons were to be counted (as no grid system was available in Openlab). The line periodicity of the grid, was fixed for all brains and sections, and allowed at least 2-3 hits located in the cortex of one hemisphere. The same grid used in the PowerPoint application was printed on an overhead that was apposed onto the computer screen. This grid helped locating the neuron counting fields once back in the Openlab imaging application, which showed in real time what was being seen under the microscope. The focusing target cross of the microscope was brought to the SRUS areas chosen for neuron counting (to conserve the original intersection with the cortex, the grid on the transparency was apposed onto the screen image in exactly the same position as in the PowerPoint image and the targeting cross was put on one of the line intersections, as the image was moved around in the x-y space following the grid spacing). In each area where neurons were to be counted, the x2.5 magnification was switched to the x63 immersion oil magnification. The section was optically sliced with a fixed periodicity. Roughly, 3-4 μm sections were made which represented 16 to 20 optical sections. The first two sections and the last two sections were not counted since they represented the safety guard areas, to prevent under- and over-projections in the neuron number estimate. Fields of count on the two sides of the brain were taken. The spacing of the grid allowed counting two to three fields per hemisphere. This procedure provided neuron numbers in a total of about 20-30 fields of neuron count across the whole brain. In each field roughly 10-15 neurons were present. Therefore, approximately 200-450 neurons were counted for each whole brain; this was well within the range of the 100-200 minimum number of neurons that need to be theoretically counted to obtain an adequate precision count.

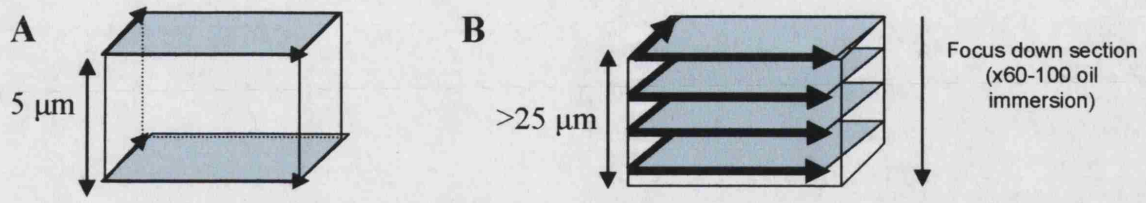

Figure 3. 4 Disector stereological probes

The dissector is a 3-D stereological probe that samples objects with a probability that is proportional to their number not their size. **A:** the physical dissector involves the use of two sections typically 5 µm apart (one counts the objects on the second section of a pair that are absent in the first). **B:** in the optical dissector, the focal plane (optical sectioning) is moved a known distance through the thickness (>25 µm) of a section producing a series of superimposed sections within which objects can be counted with dissector counting rules.

3.17.1.2 Counting the neurons

The stacks of optical sections for each field were analysed using the Openlab software. A sterological grid defining a known area, which had been printed on a transparency, was apposed onto the computer screen. The size of the grid was designed so that only a maximum of two neurons were counted per optical sections. The standard rules for a sterological grid were applied, namely that neurons crossing the left and bottom sides were not counted, whereas any neuron crossing the right and top side were counted (Fig. 3.5)

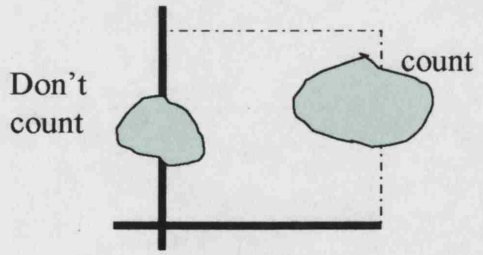

Figure 3. 5 Example of a stereological grid and counting rule

Using the Openlab software point counting option, each neuron appearing in focus (Q-) was marked and counted. The total number of neurons counted in each field was registered and the same procedure repeated for each optical stack of sections.

3.17.1.3 Estimating the reference volume (Vref)

In order to calculate the total number of neurons, the reference volume (Vref) of the cortex was estimated using the Cavalieri principle (equation **(1)**): This required a "point grid system" with each point homogeneously spaced with a fixed periodicity (Fig. 3.6). The volume of the cortex was estimated by counting the points that fell into the cortex of each slide. Since each point had a defined area (a/p) associated with it, and knowing the average distance (t) separating each slide, it was possible to estimate the volume of the cortex. The programme "Stereology Toolbox" (NIH, Davis, USA) was used for this method. The pictures were taken at x1.5 magnification in Openlab and copied directly into Stereology Toolbox. The Vref was estimated using the test system with a set of regularly spaced points (also called a point counting grid, see Fig.3.4) and the Cavalieri principle formula:

$$Vref = {}^{a}\!/_{p} \times \sum P_i \times t \qquad \textbf{(1)}$$

a/p: area per point

Pi: grid points inside the reference volume

t: distance between two adjacent sections used for the estimation

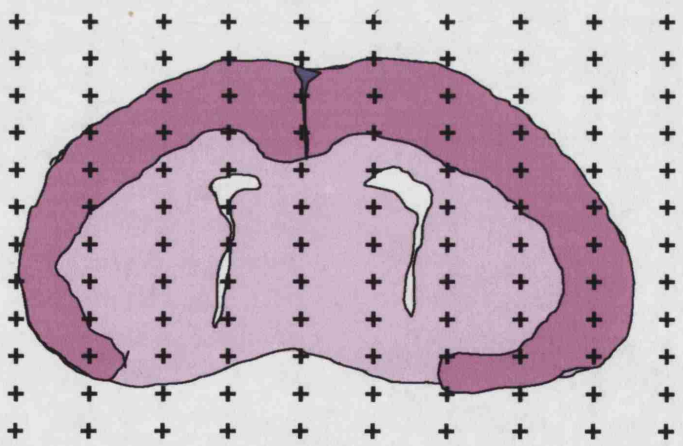

Figure 3. 6 Point counting grid test system for volume determination of the cortex

The diagram represents a section of brain superposed with a point counting grid. The points (shown as crosses) of the point counting grid are regularly distributed. An area can therefore be associated with each point i.e. an area per point value (a/p). By counting the total number of points that hit the cortex (shown in deep purple), in all SRUS sampled brain sections, its volume can be calculated using the Cavalieri principle (equation (1)).

3.17.1.4 Calculating the total number of neurons

The total number of neurons present in the cortex (N) was calculated based on the average number of neurons counted per mm^3 (Nv) based on the neurons counted in each optical disector (Q^-) and the total volume of the cortex (Vref), using the following equation **(2)**:

$$N = Nv \times Vref = \frac{\sum Q-}{n \times Vdis} \times Vref \qquad \textbf{(2)}$$

***Vdis**: volume of dissector (area of disector multiplied by total thickness of optical stacks)*
***n**: number of optical stacks or fields of view*

3.17.1.5 Statistical analysis

The number of neurons that had to be counted and how much sampling was required followed the stereological method described by Gundersen (1986). In summary, a study is typically divided into different sampling levels from individuals, to sections, to dissectors. The variances of the estimates taken at each sampling step all contribute to the overall variance of the study. Thus, the total coefficient of variance (CV^2) is the sum of the biological coefficient of variance (BCV^2) that is inherent to different animal samples, and the coefficient of the coefficient of variance of the estimator counting probe (expressed by the mean CE^2), which reflects the precision of the estimates in individual samples. This relationship is formulated in the following manner:

$$CV^2 = BCV^2 + CE^2 \qquad \textbf{(3)}$$

As a rule the CE^2 should be 50% smaller than the CV^2. However, if the BCV^2 is the major contributor to the overall variance, then more animals are required. This relationship was the guiding principle used to determine how much sampling was required.

Estimating the CE^2:

The precision of an individual estimate (in this case neuron number) is expressed by the coefficient of error, CE. This value expresses the intra-individual variation due to the stereological estimating procedure i.e the sampling of sections and counting locations.

Generally, the CE should be under 0.1 and is defined as:

$$CE(\sum Q-) = \frac{\sqrt{total\ \mathrm{var}\,iance}}{\sum Q-} \qquad \textbf{(4)}$$

the total variance of the estimate is the sum of the Noise effect of the counting process that indicates how much the estimate would have changed had the field selecting grid been placed differently, and the variance of the sum of the areas, which takes into account the variance due to the orientation of sectioning.

Total variance: Total variance of $\sum Q$- = Noise + Var_{SURS} ($\sum Q$-) **(5)**

Noise effect: $Noise = \sum Q_i^-$ **(6)**

Variance of $\sum$area: Var_{SURS} ($\sum Q$-) = (3(A-Noise) - 4B+C)/240 **(7)**

With $A = \sum Q_i^- \cdot \sum Q_i^-$; $B = \sum Q_i^- \cdot Q_{i+1}^i$; $C = \sum Q_i^- \cdot Q_{i+2}^-$

Q_i: number of neurons counts in one sampled section;

Q_{i+1}: number of neuron counts in the next sampled section

Q_{i+2}: number of neuron counts in the section after next

Estimating the inter animal variation CV^2 and BCV^2

The CEs of the inter-individual estimates for each animal are averaged to obtain the mean CE, the square of the CE gives the coefficient of variance for the estimate (CE^2).

$$\text{Mean CE} = \sqrt{mean \sum (CE^2)} \quad \textbf{(8)}$$

The inter-individual variation is estimated using the following relationship

$$CV^2 = (S.D / \bar{x})^2 \quad \textbf{(9)}$$

S.D: standard deviation of the mean neuron count; $\bar{x}$: *mean number of neuron number of all individuals in the study.*

The biological variation is derived using equation (3): $BCV^2 = CV^2 - CE^2$

3.17.2 Ventricle volume determination

The volume of the ventricles was estimated using 50 μm thick vibratome sections of the brain. A fractionator approach and the Cavalieri principle described in 3.17.1.3 were used, sampling 1 out of every 4 sections. The Cavalieri principle was used to evaluate the volume of the ventricles of the sampled sections using a point counting grid (the points are evenly spaced with a fixed periodicity); the area associated with each point (a/p) was 139 μm^2. Pictures were taken at x2.5 magnification.

The same principle as for the neuron estimation method was used to estimate the CE, BCV and CV of the point counting method (Pi) for the Cavalieri method of

volume determination. Except that in counting the CE, the noise effect due to the grid position was:

$$Noise = 0.0724 \times 9 \times \sqrt{(n \times \sum Pi)}$$

Where, ***n:*** *number of sections sampled*

ΣPi: *number of grid points inside the ventricles*

3.18 RNA isolation

3.18.1 Sample preparation

Tissue: Dissected tissue was rapidly frozen at -20°C in TRI-Reagent (50-100 mg per ml TRI-Reagent). Upon thawing, the tissue was homogenised either by using the piston of a syringe as a plunger in a 1 ml RNAse free Eppendorf or using an electric homogeniser. The resulting homogenate was then passed through a 22G syringe to ensure lysis of the cells.

Monolayer cells: The cells were trypsinised (see section 3.7.2), and after the first centrifugation step, the pellet was resuspended in TRI-Reagent. 1 ml of TRI-Reagent was sufficient to isolate RNA from 5-10x 10^6 cells. The cells were lysed by pipetting though a 1ml pipette tip and then frozen at -20°C.

CPe cells in Matrigel: The medium was removed from the Matrigel and replaced by 250 µl (0.6 U/ml) of dispase enzyme. After two hours of incubation at 37°C, the liquidified Matrigel was pipetted repeatedly though a 1 ml pipette tip to disaggregate the cells, transferred to a 1 ml Eppendorf tube and centrifuged at 1000 rpm for 5 minutes. The supernatant was discarded, the pellet rinsed with PBS, and centrifuged again. The supernatant was discarded and the pellet resuspended in 1 ml TRI-Reagent. The cells were passed through a 22G syringe several times to ensure lysis. The resulting lysate was stored at -20°C.

3.18.2 RNA extraction

The cell lysate stored at -20°C in TRI-Reagent was thawed and 0.2 ml of chloroform were added for every 1ml of TRI-Reagent used. The sample was mixed vigorously for 30 seconds with the Vortex, left to stand on ice for 15 minutes, and centrifuged at 12,000 rpm for 15 minutes at 4°C. The centrifugation step separates the mixture into three phases: a red organic phase containing proteins, an interphase containing the DNA, and a colourless upper phase containing the RNA. This aqueous phase was

transferred to a fresh tube and 0.5 ml of isopropanol added per ml of TRI-Reagent used during the sample preparation. The sample was kept on ice for 10 minutes and centrifuged at 12,000 rpm for 10 minutes to precipitate the RNA. The supernatant was removed and the pellet was washed with 1 ml of 75% ethanol per ml of TRI-Reagent. The sample was briefly mixed with a Vortex and centrifuged at 12,000g for 5 minutes at 4°C. The RNA pellet was then air dried and resuspended in 20 µl to 100 µl of DEPC H_20. The RNA concentration of the extracts was evaluated by measuring the absorbance at 260 nm wavelength using a Genequant spectrophotometer. The RNA samples were diluted to 200 µg/ml.

3.19 RNA analysis

3.19.1 Reverse transcription

This technique relies on the fact that reverse transcriptase allows to reverse transcribe mRNA to produce complementary DNA (cDNA). In a 0.5 ml PCR tube, 5 µl of RNA and 1 µl of 500 µg/ml random hexamers were added to 4 µl of DEPC H_2O. The mixture was heated for 10 minutes at 70°C in the thermocyler to linearise the RNA and then immediately put on ice for 5 mins in order prevent the reformation of secondary structures. After this step, 4µl of 5x reverse transcriptase buffer was added to the tube, 2 µl of 10 mM dNTPs, 1 µl of 40 units/µl RNAse inhibitor (RNAsin), and 1 µl of 200 units/ µl reverse transcriptase enzyme. The whole mixture (20 µl volume) was heated at 42°C for 60 minutes to allow reverse transcription followed by 10 minutes at 95°C to inactivate the reverse transcriptase.

3.19.2 Primer design

Primers to detect expression of genes of interest were designed from cDNA sequences published in original papers, or from 'Pubmed Nucleotide Enquiry' and imported into the Primer 3 (NIH) oligonucleotide primer design software. Primers consisted of 20 to 26 bases, and flanked specific regions of the cDNA of interest, usually spanning a region of 200 to 600 bases. cDNA sites were chosen to match specific isoforms (in the case of FGFRs and p73), and to cross intron/exon boundaries in all cases, in order to detect potential contamination by genomic DNA. The expected product sizes for genomic DNA and cDNA would be very different. Primers were selected to contain approximately 55% guanidine or cytosine residues. Complementarity between primers

was avoided to prevent the formation of primer dimers, which could disrupt the efficiency of the polymerase chain reaction. Care was taken to avoid sequences that could potentially produce internal secondary structures. Generally, the primer concentration was 25 pM in a 50 µl reaction.

3.19.3 Polymerase chain reaction

In order to eliminate any variability between different batches of buffer, aliquots of a x2 PCR reaction mix (x2 PCR buffer, 3 mM $MgCl_2$, 0.4 mM dNTPs, DEPC H_2O) were made and frozen in aliquots at -20°C. In a 0.5 ml PCR tube, one PCR reaction mix was made up to a final volume of 25 µl with a final concentration of x1 PCR buffer (20 mM Tris-HCl pH 8.4, 50 mM KCl), 1.5 mM $MgCl_2$, 0.2 mM dNTPs, 1 pmol/ reverse and forward primers, 1 unit/µl Taq polymerase and 1-2 µl of cDNA template (Table 3.1). If running the same set of primers for more than one sample, then the volume of the PCR reaction mix was adjusted according to the number of samples to be tested (master mix).

The 0.5ml PCR tubes were placed in the thermal-cycler and ran with the following programme in order to amplify the gene products:

Stage 1:	3 minutes	95°C	(DNA melting)
Stage 2:	30 seconds	95°C	(DNA melting)
Stage 3:	30 seconds	55-57°C	(DNA primer annealing)
Stage 4:	40 seconds	72°C	(DNA primer elongation)
Stage 5:	GO TO **Stage 2** as many times as required		(amplification)
Stage 6:	10 minutes	72°C	(neutralization of Taq polymerase)

One PCR cycle corresponded to one run from stage 1 to stage 5. Typically 25-30 cycles were used to amplify a cDNA product.

Reagents	Stock concentration	Final concentration	x1 reaction
x2 PCR buffer	x2 PCR buffer, 3 mM $MgCl_2$, 0.4 mM dNTPs	½ dilution	12.500 µl
DEPC H_2O	-	-	9.375 µl
primer Reverse	25 pmol/ µl	0.5 pmol/µl	0.500 µl
primer Forward	25 pmol/ µl	0.5 pmol/µl	0.500 µl
Taq polymerase	1 U/µl	0.05 U/µl	0.125 µl
cDNA	-	-	2.000 µl

Table 3. 1 Concentrations of reagents for one PCR reaction mix with cDNA

The Table shows the concentrations of the reagents required for a 25µl PCR reaction master mix, along with the appropriate dilutions of the stock concentrations of reagents.

3.19.4 Agarose gel electrophoresis

Agarose gels for electrophoresis of amplified cDNA were made by heating 1.5% pure agarose in 100 ml tris acetate EDTA electrophoresis buffer (TAE) with 0.0025% ethidium bromide (1 µl /ml) for 1 minute at full power in a 700W microwave oven. The liquid gel was allowed to cool slightly, and poured into a gel mould. Appropriate size combs were fitted, and the gel was left to set at room temperature for at least 30 minutes. The polymerized gel was placed into an electrophoresis tank containing 800 ml TAE and 0.0025% ethidium bromide. 5 µl of orange G running buffer (10 g sucrose, 50 mg orange G, 5 mg sodium azide in 20 ml H_2O) was added to each 25 µl PCR product, and 15 µl were loaded into each well. A 100 bp DNA ladder was loaded into the first well of each lane, so that the size of cDNA products could be determined. The voltage was set at approximately 100 mV, and the current applied. The cDNA was left to migrate towards the anode through the agarose gel for approximately 1 hour. Ethidium bromide intercalates between molecules of DNA and is fluorescent under long wave ultra violet (UV) light. This permitted visualisation of the DNA bands. Gels were exposed to UV and captured digitally using the Alpha-imager and Alphaease software imaging system.

3.19.5 Semi-quantitative analysis

3.19.5.1 TRCSFB-2 cell growth and treatment

TRCSFB-2 cells were grown at 33°C until 50-60% confluent, and then grown at 37°C for 48 hours. The last 16 hours the cells were grown with or without different

concentrations of FGF2. The cells were roughly 70% subconfluent when harvested for extraction following the method described in 3.17.2. Each of the TRCSFB-2 mRNA extracts was diluted to 200 μg/ml before analysis by RT-PCR.

3.19.5.2 Semi-quantification

For consistency, a standard concentration of RNA was used at all times (200 μg/ml for the TRCSFB-2 cell line). The linear range for each gene to be tested was established by using cycle numbers typically ranging from 20 to 40 cycles: GAPDH (x20 cycles), E2F5 (x25 cycles), FoxJ1 (x25 cycles), TTR (x30 cycles) and p73 (x 30 cycles). The samples were then run on an agarose gel and the intensity of the bands was measured using the spot densitometry programme in the Alphaease 3.3 software. The intensity of each DNA band was plotted against their respective cycle time so that a sigmoidal relationship was produced. Such a plot allowed to determine the linear range (or log phase) of DNA amplification of a set of primers. Each set of primers was then used to amplify the cDNA using a number of cycles within their linear range. After running the reaction products on a 1.5% agarose gel, the intensity of each band was measured by spot densitometry. In order to get a semi-quantitative value for the expression of RNA and to compare gene products, the intensity values for each gene product was normalised against the house-keeping gene GAPDH, which has a relatively constant expression. For each gene a minimum of eight cultures was analysed (according to the variability in the results) as estimated by a "Power test" calculation (see section 3.3).

3.20 Protein extraction

3.20.1 TRCSFB-2 cells

The cells were grown, treated and trypsinized as in section 3.18.5.1, except that the cell were grown in 125 cm^2 flasks. The cells were centrifuged at 1000 rpm and resuspended in typically 1ml of RIPA buffer (4°C) supplemented with 60 μl/ml of protease cocktail inhibitor. The sample was immediately frozen at -20°C and upon thawing was passed through an epidermal needle to lyse the cells on ice. The lysate was then centrifuged at 4°C at 13,000 rpm for 10 minutes, the supernatant transferred to a fresh microtube and centrifuged again for 10 minutes. The final supernatant contained the extracted protein.

3.20.2 Tissue samples

One ml of RIPA buffer supplemented with 60 µl/ml of protease cocktail inhibitor was used for every 0.1 g of tissue to be extracted. The tissue was frozen in RIPA at -20°C and upon thawing was homogenized with a dounce homogenizer or polytron device, maintaining 4°C throughout the procedure. The lysate was then processed as in section 3.19.1 in order to extract the protein.

3.21 Protein analysis

3.21.1 Quantification

Protein quantification was carried out using the bicinchroninic acid (BCA) Protein Assay kit. The method combines the well-known reduction of Cu^{2+} to Cu^{1+} by protein in an alkaline medium with the colorimetric detection of the cuprous cation (Cu^{1+}) using a unique reagent containing bicinchoninic acid. The chelation of two molecules of BCA with one cuprous ion forms a purple-coloured reaction product which exhibits a strong absorbance at 562 nm that is linear with increasing protein concentrations (20 µg/ml-2000 µg/ml).

Bovine serum albumin (BSA) standards ranging between 20 µg/ml and 2000 µg/ml were prepared. Twenty five µl of each standard or unknown protein sample was pipetted into a microwell plate. Twenty five µl of RIPA alone was used as negative control. Each sample was repeated in triplicate. Two hundred µl of working reagent (WR) was added to each well, mixed on a plate shaker for 30 seconds and incubated at 37°C for 30 minutes. After incubation the plate was cooled at room temperature and the absorbance measured with a micro-plate reader at 562 nm wavelength. By plotting the absorbance read at 562 nm for each protein standard against their respective protein concentrations in µg/ml, a calibration curve was obtained from which it was possible to estimate the concentration of the unknown protein samples.

3.21.2 SDS-polyacrylamide gel electrophoresis

Protein extracts were separated by sodium dodecyl sulphate polyacrylamide gel electrophoresis (SDS-PAGE) with a 12% polyacrylamide content (Table 3.2). The concentration of the protein samples after quantification was corrected in order to load 60 µg total protein in a 40 µl volume (3 mg/ml protein). The protein samples were diluted 1:2 with loading buffer and heated at 100°C for 3 minutes to farther denature

the proteins before loading 40 µl on the gel placed inside a tank containing running buffer. For each SDS-PAGE gel 7 µl of Rainbow markers were loaded. The gel was run at 60V until the protein front reached the resolving gel and then at a 100V. Once the 30 kDa molecular weight marker reached the bottom of the gel, the gel was taken out and either stained with Coomasie blue for 15 minutes and then washed until clear with 10% acetic acid washes and a final water wash, or processed for Western blotting.

12% Resolving Gel	Volume (ml)	5% Stacking gel	Volume (ml)
H_2O	4.9	H_2O	5.5
30% acrylamide mix	6.0	30% acrylamide mix	1.3
1.5 mM Tris (pH8.8)	3.8	1.0 mM Tris (pH6.8)	1.0
10% SDS	0.15	10% SDS	0.08
10% ammonium persulphate	0.15	10% ammonium persulphate	0.08
TEMED	0.006	TEMED	0.008

Table 3. 2 Solutions for preparing Tris-glycine SDS-PAGE 12% resolving gels and 5% stacking gels

3.21.3 Western blot

A Hybond-PVDF membrane and six pieces of filter paper roughly the same size of the polyacrylamide gel were cut out. The PVDF membrane was first incubated in methanol for 15 seconds to activate the binding sites and then rinsed in water for 2 minutes, and incubated in transfer buffer. The six pieces of filter paper were soaked in transfer buffer for 5 minutes, and then three layers of filter paper were placed on the surface of a semi-dry blotter. A sandwich was made with three layers of filter paper, the PVDF membrane, the SDS-polyacrylamide gel with the separated proteins and another three layers of filter papers placed on top. The gel was transferred with the semi-dry blotter for 30-40 minutes at 15V. The PVDF membrane was placed in Ponceau red for 5 minutes and washed with water in order to confirm the transfer of protein.

Immunodetection: after protein transfer, the membrane was blocked with blocking solution (5% casein protein or low fat dried milk (Marvel) diluted in PBS supplement with 0.3% Tween-20 (PBT)) overnight at 4°C. The membrane was then incubated with primary antibody (E2F5 (Santa-Cruz) was diluted 1 in 400) in blocking solution for 2 hours at room temperature (RT). The membrane was washed with blocking

solution and incubated with secondary antibody (for E2F5 (Santa-Cruz): goat anti-rabbit-HRP) diluted 1 in 500 in blocking solution for 30 minutes at RT. The membrane was washed with blocking solution and a final wash in PBS before developing it by enhanced chemical luminescence (ECL). The ECL detection reagent was added to the protein side of the immunoprobed membrane for 1 minute at RT. The excess reagent was then drained off, the membrane wrapped in SaranWrap, and placed in a film cassette (protein side up). In a dark room, an autoradiography film was placed on top of the membrane, the cassette closed for 30 seconds to 5 minutes, and the film removed and developed with an automatic autoradiography film processor.

Chapter 4 Developmental study of the human and murine choroid plexus

4.1 Introduction

Exogenous administration of FGF2 in the ventricles of the mouse and rat brain caused hydrocephalus (Chap. 1.7.2), and in the marmoset, this was accompanied by an increase in the surface area of the choroid plexus epithelium (CPe) (Pearce et al., 1996). FGF2 was also found to affect the proliferation of CPe cells when applied to cultured primary embryonic cells in culture (Reid S, 2001). However, the normal extent of proliferation in the developing CPe has been scantly studied and the expression pattern of FGF2 has only been studied in the adult CP and in the late gestation embryonic CP. Therefore the aim of this chapter was to assess the pattern of cell proliferation to gain insight into the growth and development of the CP, and characterize the expression pattern of the FGF2 protein in the developing embryonic human and mouse CP to establish whether there was any relationship between areas of cell proliferation and FGF2 protein expression. In addition, the CPe cell differentiation marker transthyretin (TTR) was used to characterise the maturity of CPe cells since quite surprisingly TTR expression had never been studied in the developing mouse CP.

As explained in Chapter 1.2.3.1, TTR is a retinol binding protein that has a fairly restricted pattern of expression and is strongly expressed by the CPe. In the rat, expression of TTR mRNA and protein was shown to be confined to the epithelial layers of the CP primordium even though the position of these cells could not be predicted by identifiable morphological changes within the neuroepithelium (Thomas et al., 1988) (Kato et al., 1986). Intracellular TTR protein was also detected by immunocytochemistry in the epithelial cells of the foetal, neonatal, and adult human CP (Mollgard et al., 1979; Jacobsen et al., 1982; Aleshire et al., 1983). In human, the intracellular staining for TTR was described as dispersed throughout the cytoplasm with occasional perinuclear rarefactions (Aleshire et al., 1983), or distributed evenly in the whole apical region of the cytoplasm (Mollgard et al., 1979; Jacobsen et al.,

1982). The aim of this study was to farther characterise the intracellular immunocytochemical staining of TTR in the developing lateral and fourth mouse CPs, as well as the spatial distribution of the staining throughout the CP. This study was also aimed at confirming the specificity of the anti-TTR antibody in order to be able to use it to characterise cultured CPe cells in my in-vitro studies.

Little is known about CP development and there is a paradox between the reported very low number of proliferating cells and the rapid growth in surface area of the CPe. Hence, in order to better understand the role of cell proliferation for the development of the CP, cell proliferation in the developing mouse and human CP was studied by immunocytochemistry staining for the proliferating cell nuclear antigen (PCNA). This labels cells in S-phase with much greater intensity than cells in the other phases of the cell cycle, thus representing a sensitive marker for detecting cell proliferation (Woods et al., 1991; Hyde-Dunn and Jones, 1997). Since most studies on cell proliferation have concentrated on the lateral CPs (Shuangshoti and Netsky, 1966; Sturrock, 1979), this study compares the extent of cell proliferation in the IVth and lateral ventricle CPs, as well as in between mouse and human CPs.

Although there is a strong emphasis in the literature on the role of FGF2 in CNS development (Vaccarino et al., 1999a; Raballo et al., 2000), there are few studies that have looked at the expression of FGF2 during embryonic CP development (Chap. 1.5.2), including the developing human CP. Thus, in order to assess whether the FGF2 protein was localized in areas of cell proliferation during CP development, it was essential to first study its expression pattern in the CPe at the early stages of development of the mouse and human CPe.

4.2 Results

4.2.1 Expression of transthyretin protein in mouse

The expression of TTR protein in the developing IVth and lateral CPs was studied by DAB based immunohistochemistry in mouse embryos at different stages of development from 11.5 dpc to 17.5 dpc. At least two embryos were examined for each stage.

IVth ventricle choroid plexus: Cytoplasmic staining for the TTR protein was first seen in the roof of the fourth (IVth) ventricle at 11.5 dpc (Fig. 4.1A). At this stage, the CP still consisted of a thin layer of columnar cells continuous with the

pseudostratified neuro-epithelium that is associated with the underlying head mesenchyme. By embryonic age 12.5-14.5 dpc, the TTR protein was expressed strongly in the CPe (Fig. 4.1B). The IVth ventricle CP developed farther into a villous structure extending into the ventricular lumen. At 14.5dpc, the TTR protein was detected in the already columnar and polarised CPe, but not in the pseudostratified layers of the CP forming the root of the CP (Fig. 4.1B). By embryonic stage 16.5 dpc, the CP filled the ventricular space and had well developed villi, and the epithelial cells had become cuboidal. By that stage, it had more or less reached its mature form, which is maintained throughout adulthood. Staining for TTR remained strong in the CPe (Fig. 4.1C). At all ages, diffuse background staining could be seen in the adjacent brain tissue (Fig. 4.1). Intracellular staining for TTR was cytoplasmic. However, the staining was not diffused throughout the cytoplasm but localized above the nucleus at the apical end of the cells facing the lumen. (Fig. 4.1B, C). No staining was observed when the primary antibody was omitted (Fig. 4.1D)

Lateral ventricle choroid plexus: TTR expression was also observed in the lateral CP. In the 14.5 dpc lateral CP, TTR staining was in the two to three layer cell thick CPe (Fig. 4.2A). Stronger staining, however, was observed in the distal end of the CP that extends into the lumen, mostly as a single columnar epithelium (Fig. 4.2B), whereas only a faint staining was apparent at the root end of CP which had a more pseudostratified epithelium organisation (Fig. 4.2C). At the intracellular level, staining for TTR, like in the IVth ventricle CP, was cytoplasmically located at the apical end of the CPe cells that faced the lumen of the ventricle (Fig. 4.2B-C).

To confirm the specificity of the antibody, TTR staining was assessed in the adult liver and in the developing lung of a 14.5 dpc mouse. No staining was observed in the epithelium of the developing lung (Fig. 4.2D), which confirmed the specificity of the antibody for TTR since neither the RNA nor the protein has been shown to be expressed in this organ. In contrast, TTR was expressed, as expected, in the adult liver; the staining was diffused throughout the cytoplasm (Fig. 4.2E), and no staining was observed when the primary antibody was omitted (Fig. 4.2F).

Figure 4. 1 Immunohistochemical analysis of TTR protein expression in the developing developing mouse IVth ventricle choroid plexus (CP)

Sagittal views of mouse IVth ventricle CP at different developmental stages stained for TTR (brown). All nuclei are counterstained with methyl green.

A: 11.5 dpc, TTR staining is present in the columnar epithelial layer budding from the IVth ventricle dorsal wall (positive staining shown by red arrowheads) **B:** 14.5 dpc, only epithelial cells of the CP with a low columnar organisation are stained for TTR protein (red arrowhead). Staining in the columnar pseudostratified cell layers at the root of the CP is low or absent (black arrowheads). **C:** 17.5 dpc; staining is in most of the epithelium, which is simple cuboidal in organisation (red arrowheads). Negative staining persists in the columnar pseudostratified layers forming the root of the CP (black arrowheads). Low background staining is also present in the CP mesenchyme of the CP and in the neuroepithelium. **D:** 17.5 dpc, negative staining for TTR in absence of primary antibody. Scale bars in A and B are 100 μm, in C and D are 50 μm. **cb** = cerebellum, **CP** = choroid plexus, **CPe** = choroid plexus epithelia, **CPm** = choroid plexus mesenchyme, **N** = neuronal cells, **IV** = fourth ventricle, **R** = CP root.

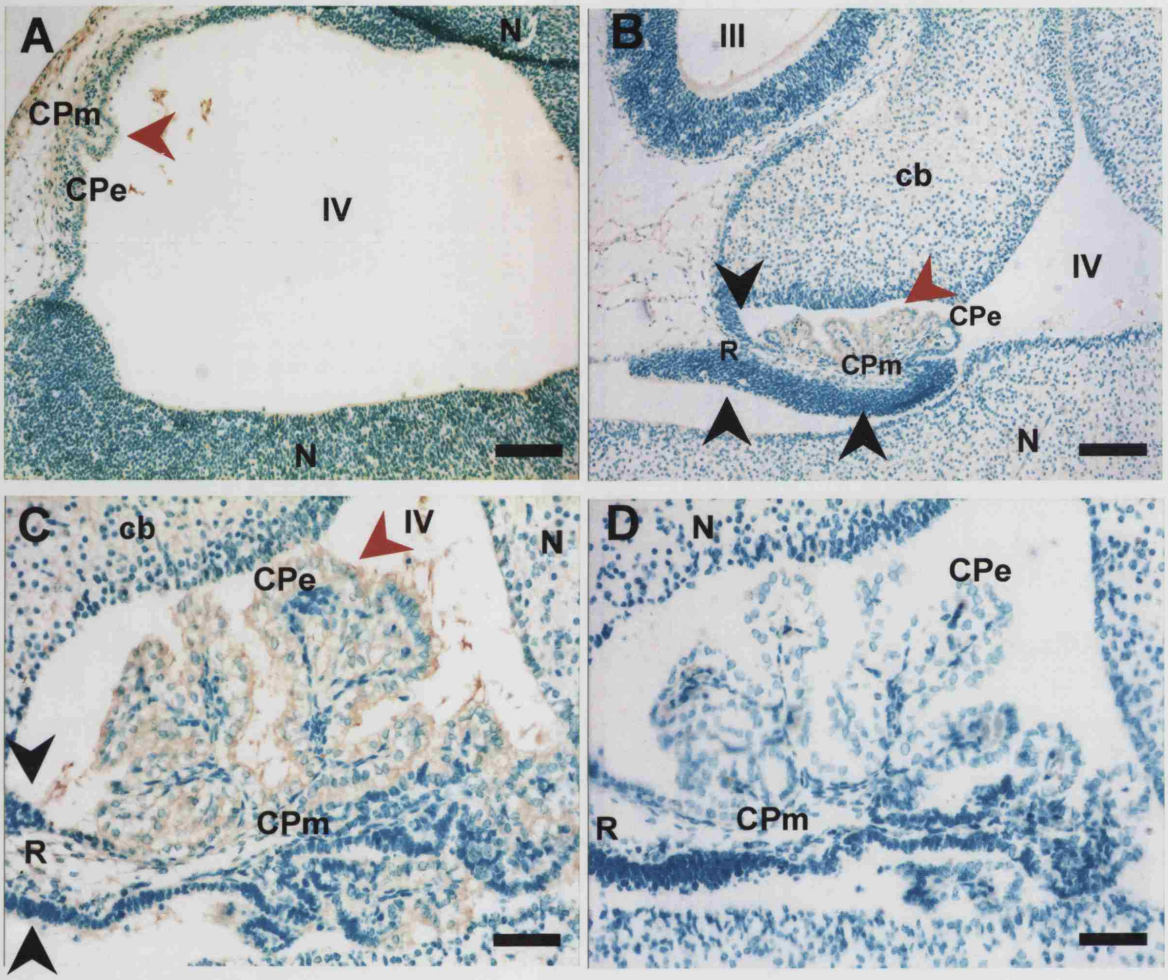
A
N
CPm
CPe
IV
N
B
III
cb
IV
CPe
R
CPm
N
C
cb
IV
N
CPe
CPm
R
D
N
CPe
R
CPm

Figure 4. 2 TTR protein expression in the mouse developing lateral ventricle choroid plexus (CP) and control tissues

Sagittal views of mouse lateral ventricle CP at different developmental stages, the embryonic lung and adult liver stained for TTR protein (brown). All nuclei are counterstained with methyl green.

A: 14.5 dpc CP, staining for TTR is localized in the CPe that has a columnar organization (red arrowhead in A and B), whereas cells at the root of the CP have a less intense staining for TTR (black arrowhead in A and C). **B:** High power magnification of the distal end of the lateral CP extending in the telencephalic lumen shown in (A). **C:** High power magnification of the root of the lateral CP shown in (A). **D:** 14.5 dpc lung, negative for TTR protein; epithelial cells of the lung are indicated by black arrowheads. **E:** Adult mouse liver stained for TTR protein. **F:** Adult mouse liver stained for TTR in the absence of primary antibody. Scale bar in A is 50 μm, scale bars in B, C, E-F are 15 μm, scale bar in D is 25 μm. **CP** = choroid plexus, **CPe** = choroid plexus epithelia, **CPm** = choroid plexus, mesenchyme, **Pt** = putamen, **N** = neuronal cells, **L** = lateral ventricle, **R** = CP root.

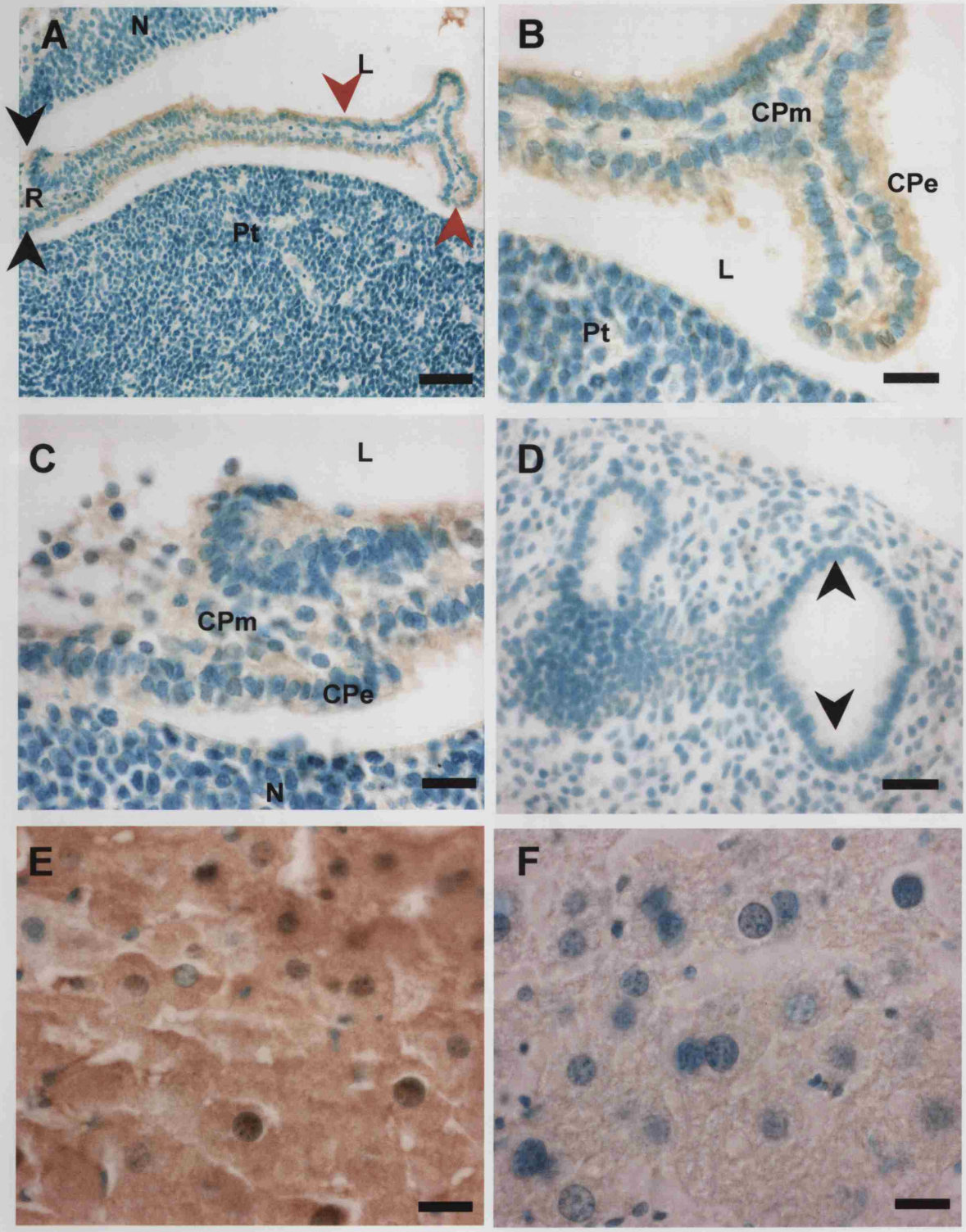
A
N
L
R
Pt
B
CPm
CPe
L
Pt
C
L
CPm
CPe
N
D
E
F

4.2.2 Cell proliferation in the developing choroid plexus

4.2.2.1 Cell proliferation in mouse

Cell proliferation was assessed by Cy3-red fluorescence immunohistochemistry for the proliferating cell nuclear antigen (PCNA), using a monoclonal antibody raised against the recombinant PCNA (PC-10 clone). At least two embryos were examined for each stages.

At 11 dpc, nuclear staining for PCNA was observed in the neuroepithelium lining the ventricular system but not in the roof of the fourth ventricle where the choroid plexus primordium develops (Fig. 4.3A, C, E). At 11.5 dpc, when the first morphological signs of choroid plexus cell differentiation occur, no cell proliferation was observed in the CPe (Fig. 4.3B, D, F). However positive staining was observed in what seemed like developing blood vessels in the mesenchyme (Fig. 4.3D).

At 12.5 dpc, most of the IVth ventricle CPe was negative for PCNA, except at the root of the CP desribed as the junction between the ependyma and the epithelium (Fig. 4.4A-B). The neuroepithelium at the periphery of the ventricle was in contrast highly positive for PCNA (Fig. 4.4A-D). At high magnification, the PCNA positive cells were observed in the root of the IVth ventricle CPe, but confirmed most of the other cells in the CPe were negative (Fig. 4.5A-B). A fluorescent signal was also observed in the stroma, but viewing the CP under phase contrast (Fig. 4.5C) or under a FITC filter (Fig. 4.5D) showed that it was due to the presence of red blood cells that auto-fluoresced. The lateral choroid plexuses were apparent as neuroepithelial folds protruding into the ventricles at 12.5 dpc. In contrast to the IVth ventricle CP, they were highly positive for PCNA (Fig. 4.6A-D). PCNA protein was also highly expressed throughout the telencephalic neuroepithelium, its expression being stronger in some regions than others (Fig. 4.6A, B). In fact the areas that expressed the highest levels of PCNA were just adjacent to the budding lateral choroid plexus in the hem region and the putamen (Fig. 4.6A-B).

At 14.5 dpc, staining for PCNA protein was strong in the neuroepithelium of the IVth and telencepehalic ventricles (Fig. 4.7A-D) but no expression was observed in the largely monostratified columnar epithelium of the IVth ventricle choroid plexus (Fig. 4.7A-B). However, strong staining was observed in the columnar pseudostratified layer in the root of the choroid plexus (Fig. 4.7A-B). The lateral CPe was mainly negative for PCNA especially in the most distal part that was

monostratified columnar epithelium (Fig. 4.7C-D). In contrast, PCNA positive cells were often observed at the root of the lateral CP where epithelial cells have a more pseudostratified organization (Fig. 4.7C-D).

At 17.5 dpc, expression of PCNA was still observed in the ependyma of the IVth and IIIrd ventricles (Fig. 4.8A-B). PCNA positive cells were lining the developing cerebellum that extended from the IIIrd ventricle down to the base of the IVth ventricle CP (Fig. 4.8A-B). However, the epithelium of the CP was negative for PCNA, except in the the root of the CP and some PCNA-positive cells were oberved in the mesenchyme (Fig. 4.8A-B). The lateral ventricle CPe was also negative for PCNA, although staining was strongly positive in the neuroepithelium lining the ventricle (Fig. 4.8C-D).

The specificity of PCNA staining was confirmed by its localization in the ependyma as previously reported (Ino and Chiba, 2000), and the absence of staining when only the secondary antibody was used (not shown).

Figure 4. 3 PCNA protein expression in the embryonic mouse 11.5 dpc-12 dpc choroid plexus

Sagittal view of the 11.5 dpc and 12 dpc hind-brain stained for PCNA protein (bright red). **A, C, E:** 11.5 dpc IVth ventricle and CP primordium. **A:** Overview of the 11.5 dpc embryo under dark field. The location of the presumptive CP is shown with white arrowheads. **C:** IVth ventricle stained for PCNA; the CP primordium is negative for PCNA stain (shown by white arrowheads). Green arrowheads show positive staining in the neuroepithelium. **E:** Hoechst staining of the 11.5 dpc IVth ventricle. **B, D, F:** Sagittal view of the 12 dpc ventricle and budding CP. **B:** Overview of the 12 dpc embryo under darkfield. The location of the budding CP is shown with a white arrowhead. **D:** PCNA staining of the 12 dpc IVth ventricle CP, negative for PCNA (shown by white arrowhead). The green arrowhead shows a group of PCNA positive cells from a blood vessel. **F:** Hoechst stain (blue) of the same field of view as in D. Scale bars in A and B are 500 μm, in C and E are 250 μm, in D and F are 50 μm. **CP** = choroid plexus, **CPe** = choroid plexus epithelium, **CPm** = choroid plexus mesenchyme, **N** = neuroepithelium, **IV** = fourth ventricle, **III** = third ventricle.

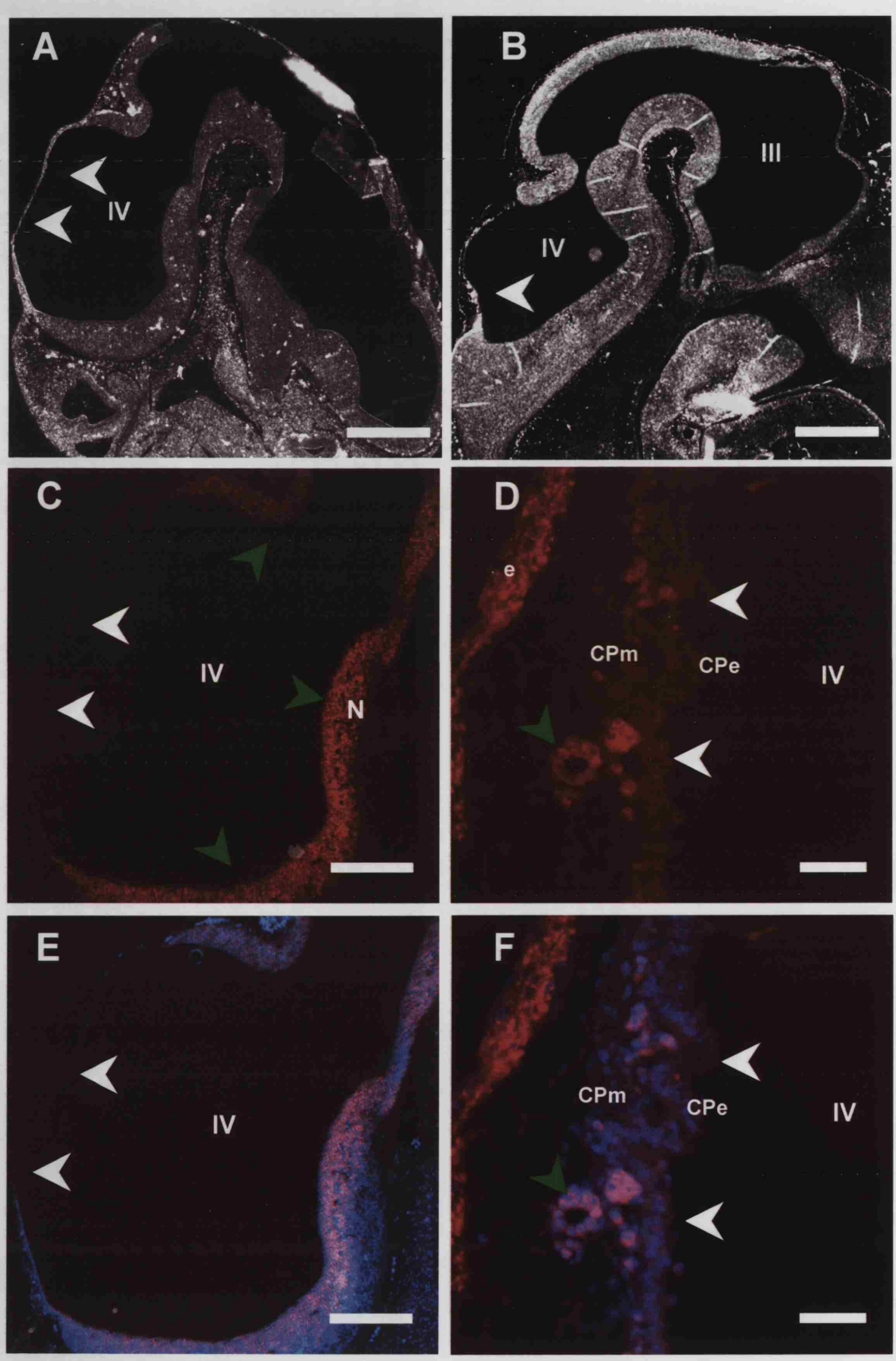
A
IV
B
III
IV
C
IV
N
D
e
CPm
CPe
IV
E
IV
F
CPm
CPe
IV

Figure 4. 4 PCNA protein expression in the mouse embryonic 12.5 dpc choroid plexus

Sagittal view of the mouse embryonic 12.5 dpc brain stained for PCNA protein (bright red). **A:** Low magnification, PCNA staining is mainly restricted to the neuroepithelium surrounding the ventricles. **B:** Phase contrast view of the 12.5 dpc head. In **A** and **B**, the IVth and lateral CPs are shown with white arrowheads. **C:** IVth ventricle stained with PCNA. Neuroepithelial cells lining the ventricles label positive for PCNA, while the CPe is negative, except at its root. **D:** Hoechst nuclear staining (blue) of the same field of view shown in C. Scale bars in A and B are 500 μm, in C and D are 250 μm. **CP** = choroid plexus, **CPe** = choroid plexus epithelium, **CPm** = choroid plexus mesenchyme, **N** = neuroepithelium, **IV** = fourth ventricle, **III** = third ventricle, **L** = lateral ventricle, **VZ/SVZ** = ventricular zone/sub-ventricular zone.

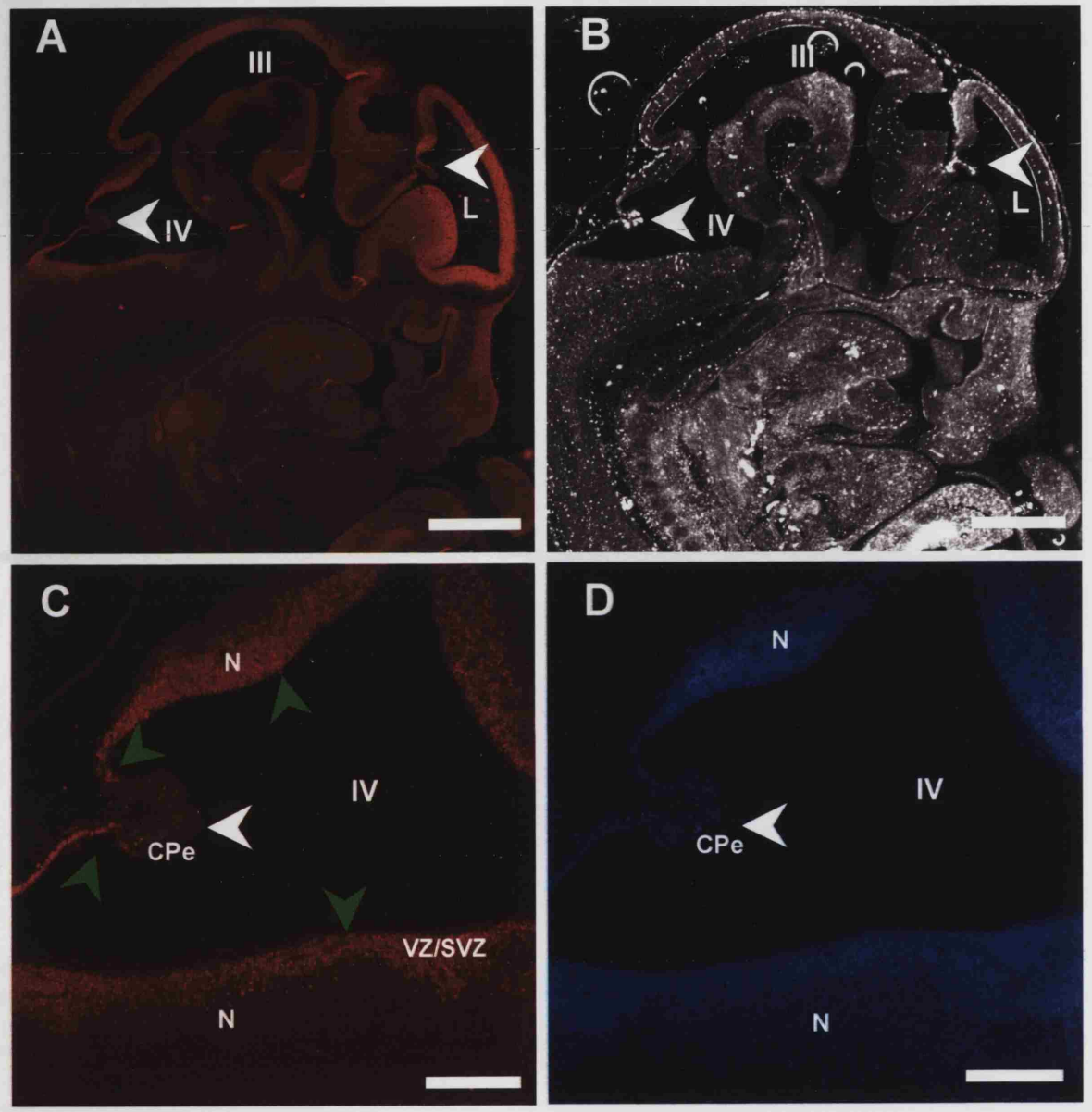
A
III
IV
L
B
III
IV
L
C
N
IV
CPe
VZ/SVZ
N
D
N
IV
CPe
N

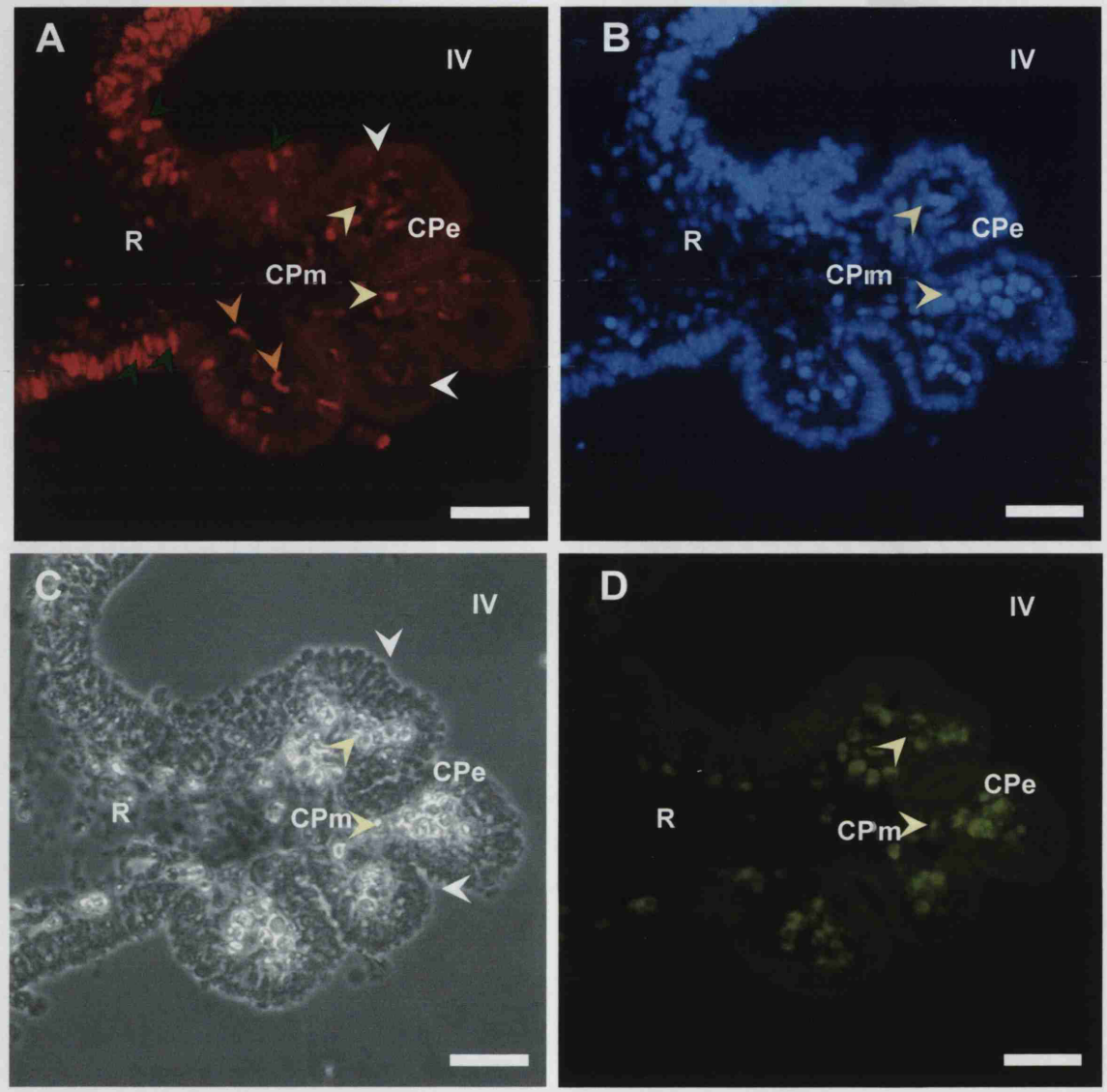

Figure 4. 5 PCNA expression in the 12.5 dpc IVth ventricle CP: higher magnification

A: Sagittal view of the IVth ventricle CP stained for PCNA at high magnification. Green arrowheads point at PCNA labelled cells (bright red) in the root of the CP. White arrowheads point at the negatively labelled cells of the CPe; some PCNA positive cells are also present in the CP mesenchyme (orange arrowhead); yellow arrowheads point to autofluorescent signal thought to due to the presence of red blood cells. **B:** Hoechst stain of the same field of view (blue). **C:** Phase contrast of the same field of view **D:** FITC specific wavelength to reveal autofluorescence due to the presence of red blood cells in the CP mesenchyme (yellow arrowheads). Scale bars are all 50 μm. **CP** = choroid plexus, **CPe** = choroid plexus epithelium, **CPm** = choroid plexus mesenchyme, **IV** = fourth ventricle, **R** = CP root.

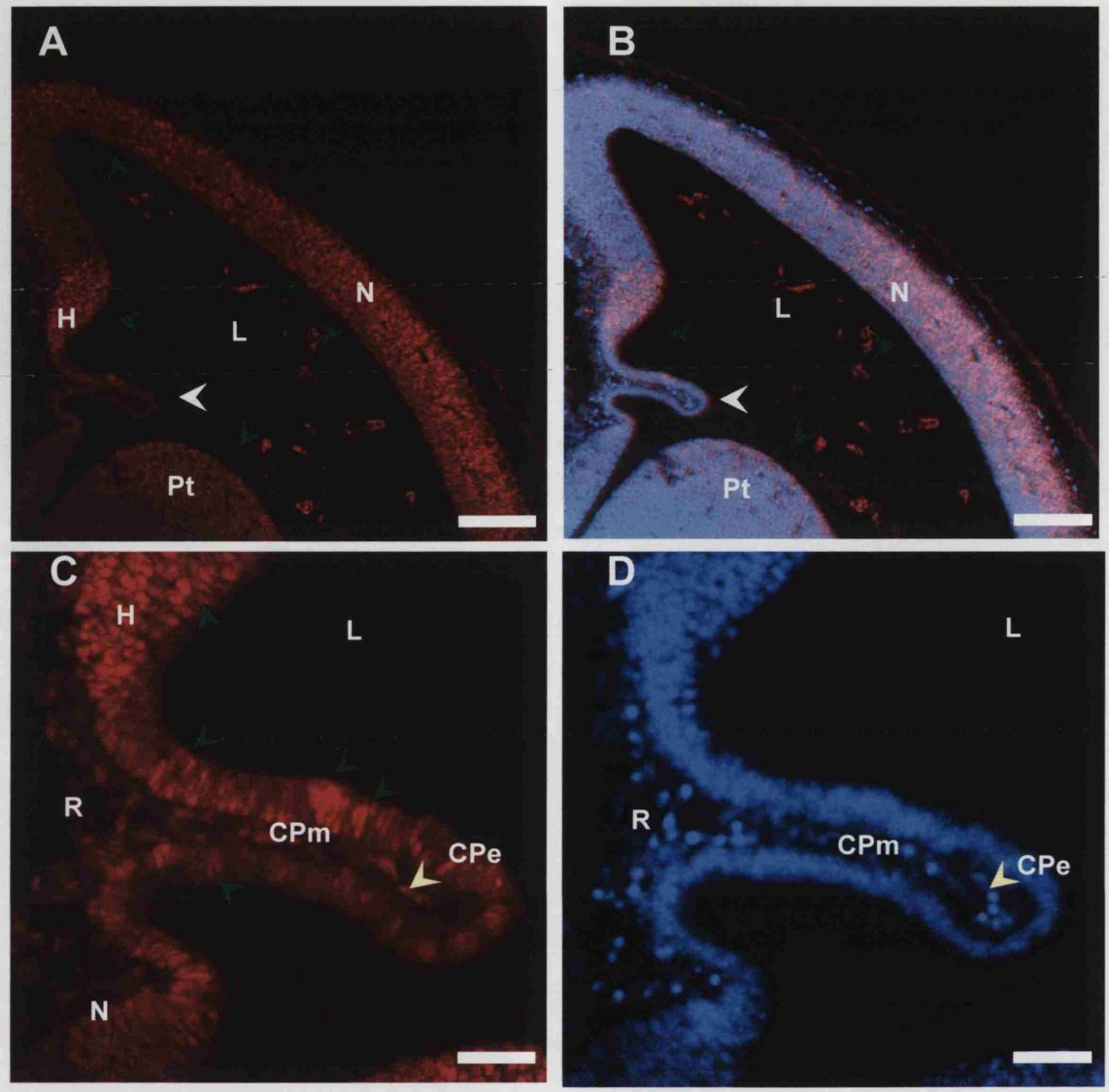

Figure 4. 6 Sagittal view of the lateral ventricle CP of the 12.5 dpc embryonic mouse stained for PCNA.

A: Micrograph of the telencephalic vesicle; the neuroepithelium is highly positive for PCNA (green arrowheads), a white arrowhead points to the CP. **B:** Hoechst stain and overlay of PCNA staining, strongest PCNA labelling is in the hem region, the putamen and ventral side of the ventricle as indicated by the green arrowheads. **C:** Higher magnification of the lateral CP; PCNA labelled cells are scattered throughout the CPe (green arrowheads); auto-fluorescing red blood cells are present in the CPm (yellow arrowhead). **D:** Hoechst stain of the same field of view. Scale bars in A and B are 200 μm, and C and D are 50 μm. **CP** = choroid plexus, **CPe** = choroid plexus epithelium, **CPm** = choroid plexus mesenchyme, **H** =Hem, **L** = lateral ventricle, **N** = neuroepithelium, **Pt** = putamen, **R**= CP root.

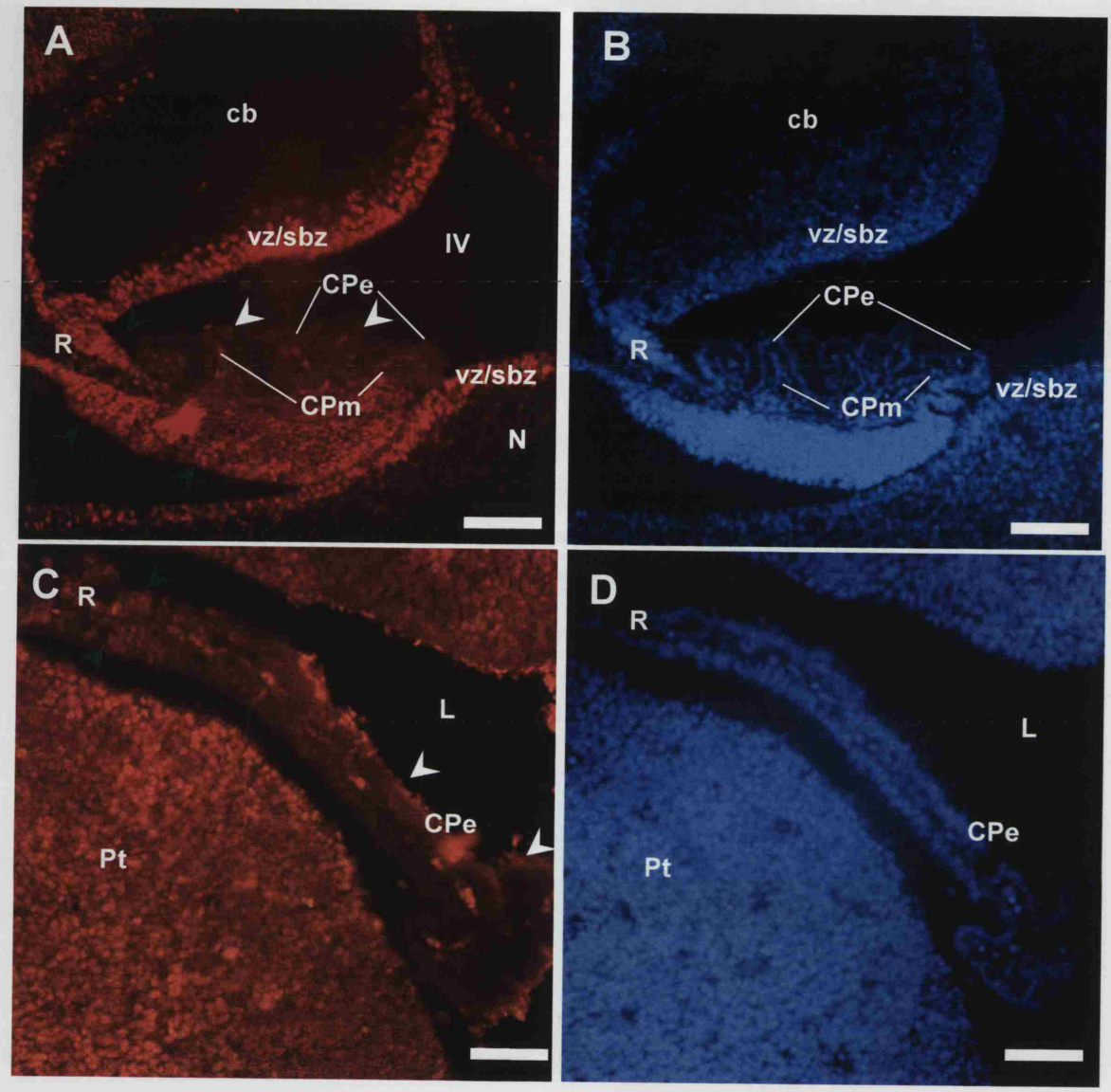

Figure 4. 7 Sagittal view of the mouse 14.5 dpc IVth and lateral choroid plexus stained for PCNA protein

A: IVth ventricle CP stained for PCNA (red), PCNA positive cells are observed in the root region of the CP (green arrowheads), while most of the simple columnar CPe is negative (white arrowheads). **B:** IVth ventricle counterstained with Hoechst nuclear stain. **C:** Lateral CP stained for PCNA; green arrowheads show PCNA positive CPe cells in the root of the CP, white arrowheads point to the distant end of the CPe that is PCNA-negative. **D:** Lateral CP stained with Hoechst nuclear dye (blue). Scale bars are 50 μm. **CP** =choroid plexus, **CPe** = choroid plexus epithelium, **CPm** = choroid plexus mesenchyme, **Cb**= primodial cerebellum, **N** = neuronal cells, **pt**= putamen, **IV** = fourth ventricle, **L** = lateral ventricle, **R** = CP root, **VZ/SVZ** = ventricular zone/sub-ventricular zone.

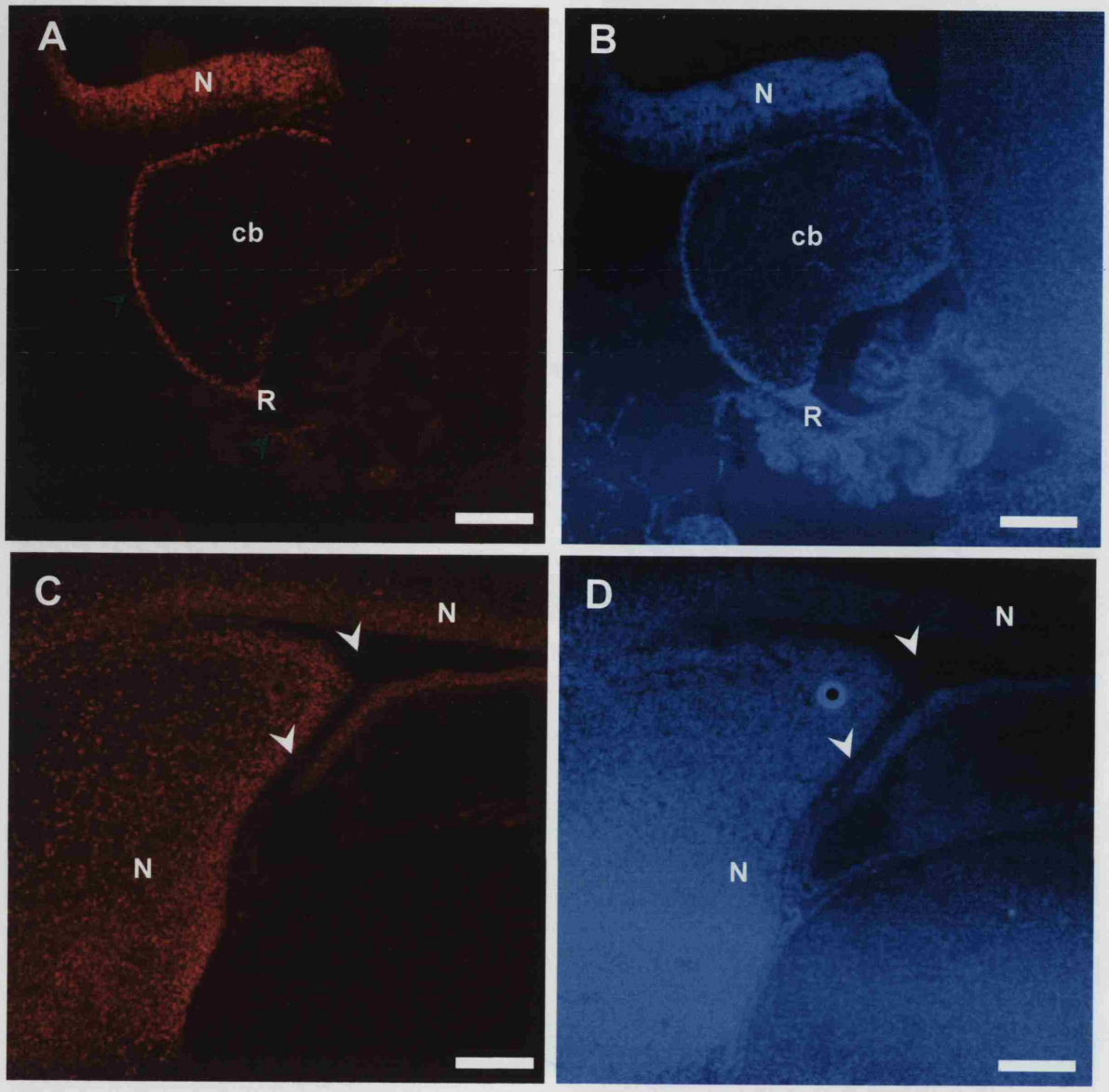

Figure 4. 8 Sagittal view of the mouse 17.5 dpc IVth and lateral choroid plexus stained for PCNA protein

A: IVth ventricle CP stained for PCNA. Green arrowheads point to positive cells in the root of the CP and lining the developing cerebellum, white arrowheads point to the CPe that is PCNA-negative. **B:** Hoechst staining of the same field of view. **C:** Lateral ventricle CP stained for PCNA. PCNA positive cells are observed in the ependyma (green arrowheads), while the CPe is negative (white arrowheads). **D:** Hoechst stain of the same field of view. Scale bars are all 200 μm. **CP** = choroid plexus, **CPe** = choroid plexus epithelium, **CPm** = choroid plexus mesenchyme, **IV** = fourth ventricle, **L** = lateral ventricle, **N** = neuroepithelium, **R** = CP root.

4.2.2.2 Cell proliferation in human

Cell proliferation in the developing human CP was studied by DAB based immunohistochemistry for the PCNA antigen, using a monoclonal antibody raised against human PCNA. Human embryos ranging from Carnagie stage (CS) 16 to 23, and of a foetus of 11 weeks were used. The ages examined in this study were largely restricted by the embryos and sections available. They were kindly provided by the Institute of Child Health/University of Newcastle, Wellcome/MRC-funded, Human Developmental Biology Resource.

At CS 16, cell proliferation as revealed by PCNA nuclear staining was extensive in the whole head. At this early stage the CP was not detected (not shown). By CS 18, proliferation was restricted to the ependyma of the ventricles (Fig. 4.9A). In the telencephalic vesicles, cell proliferation was also observed in what appeared to be the choroid plexus primordia budding in each of the telencephalic ventricular cavity (Fig. 4.9B). Staining was absent when the primary antibody was omitted (Fig. 4.9C). At CS 20, PCNA staining was important in the neuroepithelium (Fig. 4.10A-B), while only sporadic labelling was observed in the lateral choroid plexus epithelium, which had a pseudostratified columnar cell organisation (Fig. 4.10B). The PCNA staining was absent when the primary antibody was omitted (Fig. 4.10C). A higher magnification of the CPe confirmed the presence of PCNA-positive epithelial cells, which was more important at the root end of the CP (Fig. 4.11A-B). No staining was observed when the primary antibody was omitted (Fig. 4.11C-D). At CS 23, the lateral choroid plexus had undergone a huge growth in surface. The CPe had stretched out and acquired a monostratified columnar organization and was negative for PCNA (Fig. 4.12A, B); in contrast, the neuroepithelium was positive for PCNA in the periphery of the ventricles (Fig. 4.12A-B), which was absent on omission of the primary antibody (Fig. 4.12C). At high magnification, it was observed that mesenchymal cells of the lateral CP sporadically stained positive for PCNA, while monostratified CPe was negative (Fig. 4.13A-D). In contrast, strong nuclear staining for PCNA was present in the root of the CPe, which was pseudostratified (Fig. 4.13E-F).

Due to the lack of sections containing early developing IVth ventricle choroid plexus, it was possible to study its development only in a CS 23 embryo and in an 11 week foetus. The CS 23 embryonic IVth ventricle CPe was completely negative for

PCNA (Fig. 4.14A-E); in contrast, strong nuclear staining was present in the neuroepithelium lining the ventricle (Fig. 4.14E). Also, the 11 week foetal IVth ventricle CP was negative for PCNA (Fig. 4.14F). Immunoreactivity of the antibody was confirmed by the fact that nuclear staining was observed in the neuroepithelium (not shown).

Figure 4. 9 PCNA expression in the CS 18 human telencephalic choroid plexus

Transverse sections of the telencephalic ventricles stained for PCNA protein (brown); the orientation of the section is shown in the insert in (A). Nuclei are revealed by methyl green counter-staining. **A:** Telencephalic vesicles stained for PCNA. The budding appendages protruding into the ventricular cavity are the presumptive CP primordia. Neuroepithelial cells are positive for PCNA. Black arrowheads point to the presumptive CP primordia. **B:** Higher magnification of the CP primordia. Black arrowheads show examples of PCNA labelled cells. **C:** CP primordia negatively stained in the absence of primary antibody. Scale bar in A is 800 μm, and in B and C is 50 μm. **CP** = choroid plexus, **prCP** = presumptive CP, **CPe** = choroid plexus epithelia, **CPm** = choroid plexus mesenchyme, **N** = neuroepithelium, **L** = lateral ventricle.

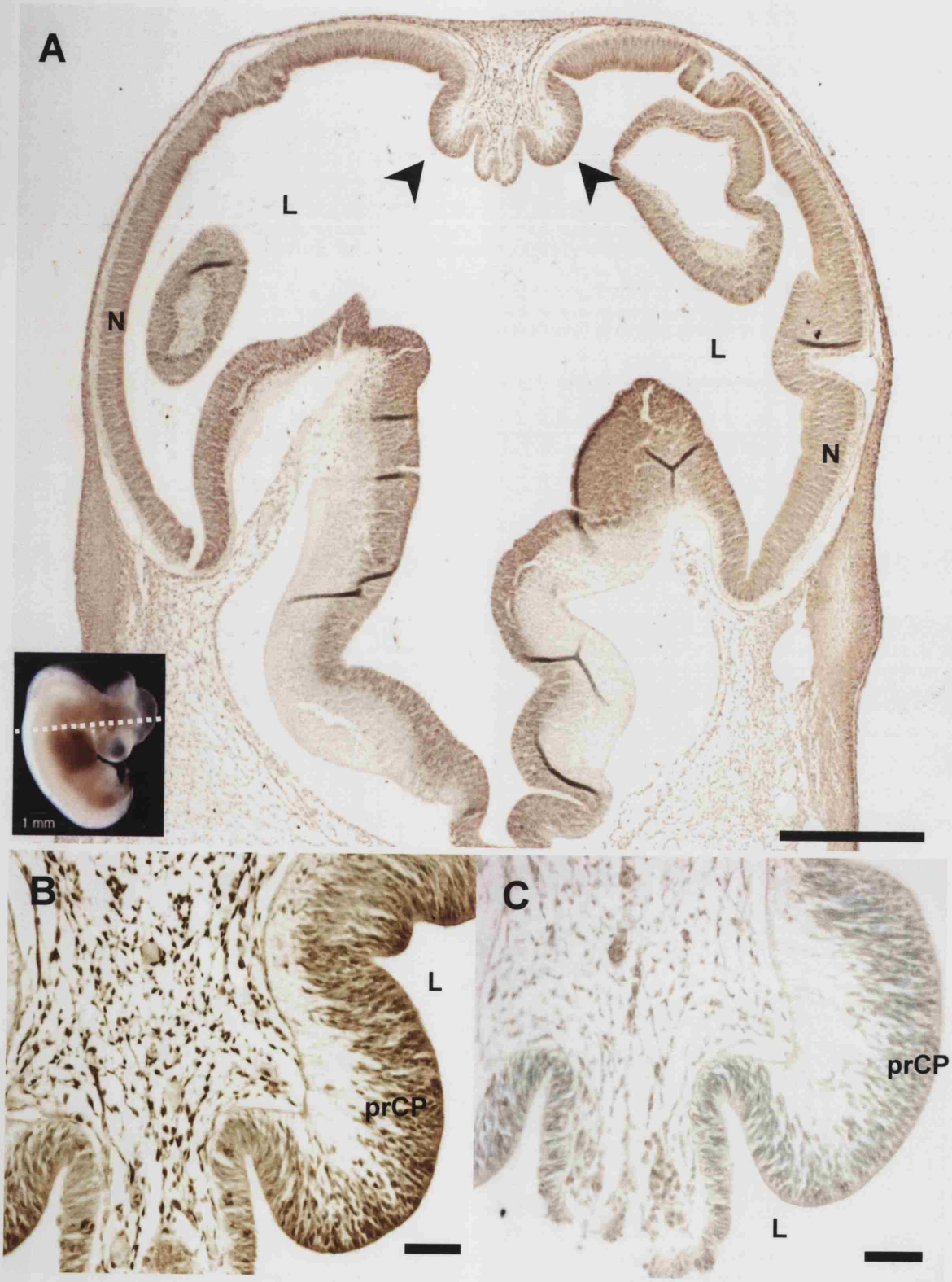
A
L
N
L
N
1 mm
B
L
prCP
C
prCP
L

Figure 4. 10 **PCNA protein expression in the CS 20 human telencephalic ventricle choroid plexus**

Transverse section of the human embryonic CS 20 telencephalic ventricles stained with PCNA (brown), the orientation of the sections is shown in the insert in (A). All nuclei are lightly counterstained with methyl green. **A:** Transverse view of the telencephalic vesicles. Scattered PCNA-labelling is observed in the neuroepithelium and the neural tissue. **B:** Higher magnification of the frame in (A) at the level of the CP and the neuroepithelium. Black arrowheads point to some of the PCNA-positive cells in the neuroepithelium. **C:** Negative staining in the absence of primary antibody. Scale bar in A is 500 μm, scale bars in B and C are 50 μm. **CP** = choroid plexus, **CPe** = choroid plexus epithelium, **CPm** = choroid plexus mesenchyme, **L** = lateral ventricle, **N** = neuroepithelium.

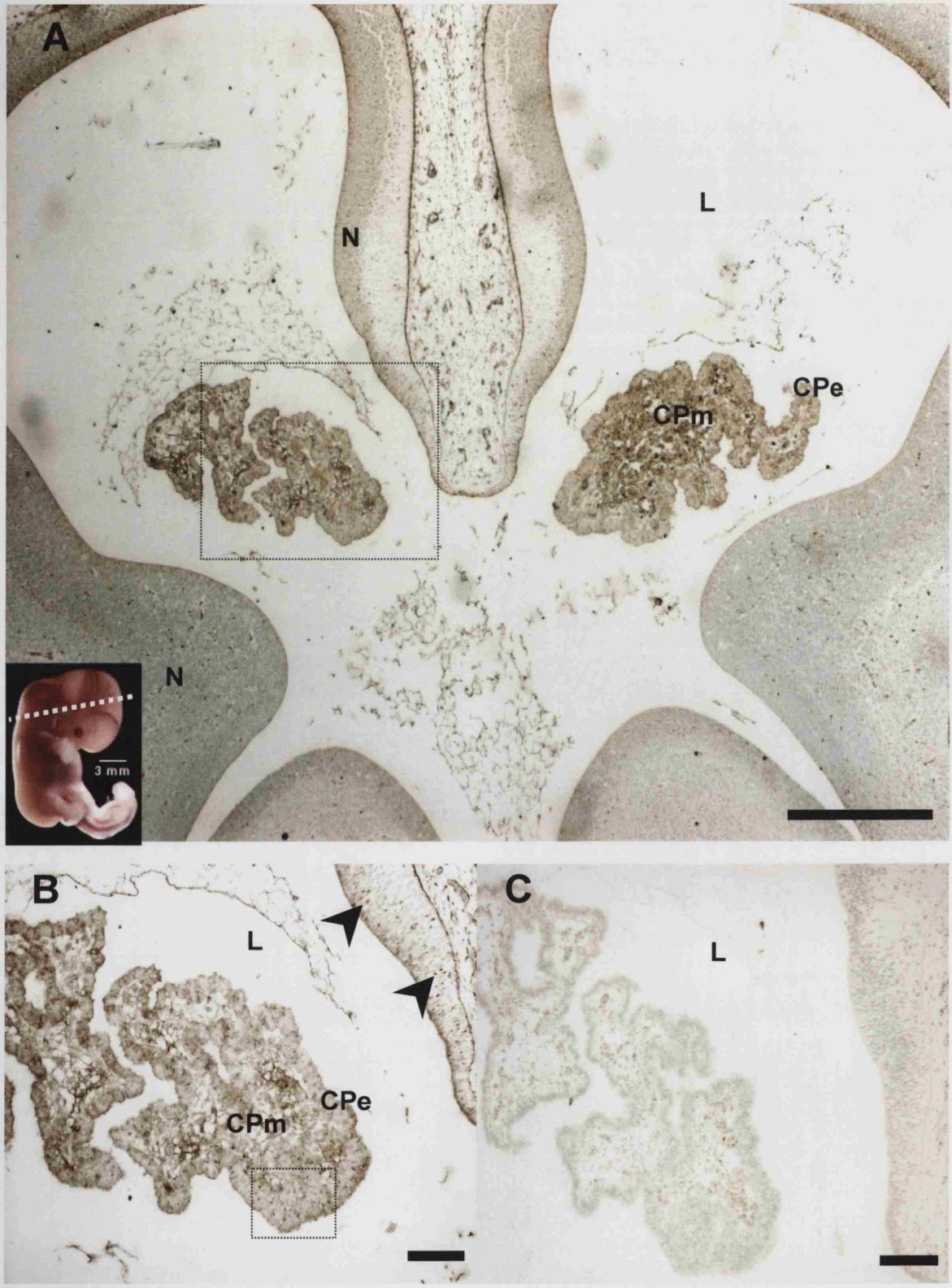
A
N
L
CPe
CPm
N
3 mm
B
L
CPe
CPm
C
L

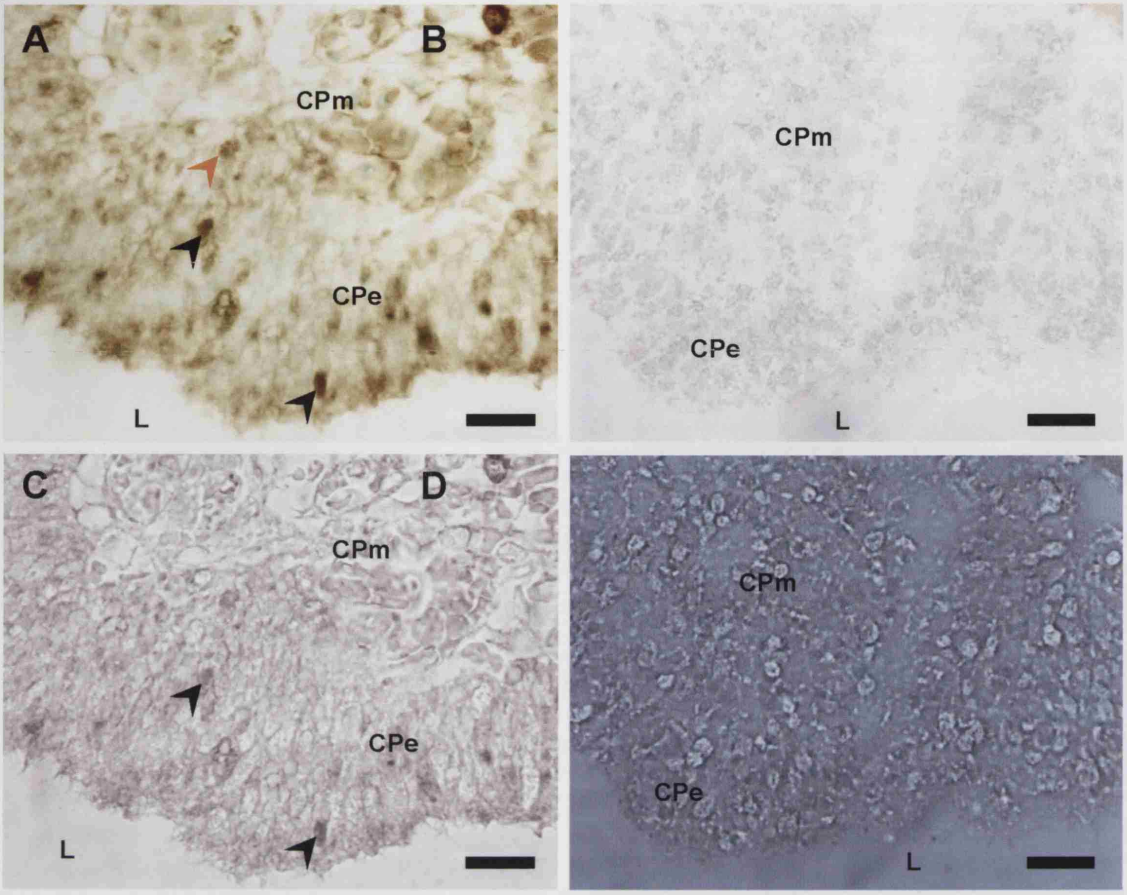

Figure 4. 11 Higher magnification at the root end of the telencephalic CP of the CS 20 human embryo stained for PCNA protein

A: High magnification of Fig. 4.10B. Black arrowheads point to cells in the CPe positive for PCNA, sporadic labelling is also observed in the mesenchyme (orange arrowhead). **B:** High magnification of Fig. 4.10C, negative staining. **C:** Phase contrast of the same field of view as in (A). **D:** Phase contrast of the same field of view as in (B). Scale bars are 15 μm. **CP** = choroid plexus, **CPe** = choroid plexus epithelium, **CPm** = choroid plexus mesenchyme, **L** = lateral ventricle.

Figure 4. 12 **PCNA protein expression in the CS 23 human embryo telencephalic ventricle CP**

Transverse section of the human embryonic CS23 telencephalic vesicles stained for PCNA protein (brown); the orientation of the sections is shown in the insert in (A). Nuclei were counter-stained with methyl green. **A**: Tranverse view of the ventricles; strong PCNA labelling is seen in the neuroepithelium. **B**: Higher magnification of (A) showing the CPe and neuroepithelium. Only the neuroepithelium is positively stained for PCNA. **C**: Equivalent field of view as in (B) in absence of primary antibody. Scale bar in A is 500 μm, scale bars in B and C are 50 μm. **CP** = choroid plexus, **CPe** = choroid plexus epithelium, **CPm** = choroid plexus mesenchyme, **L** = lateral ventricle, **III** = third ventricle, **N** = neuroepithelium.

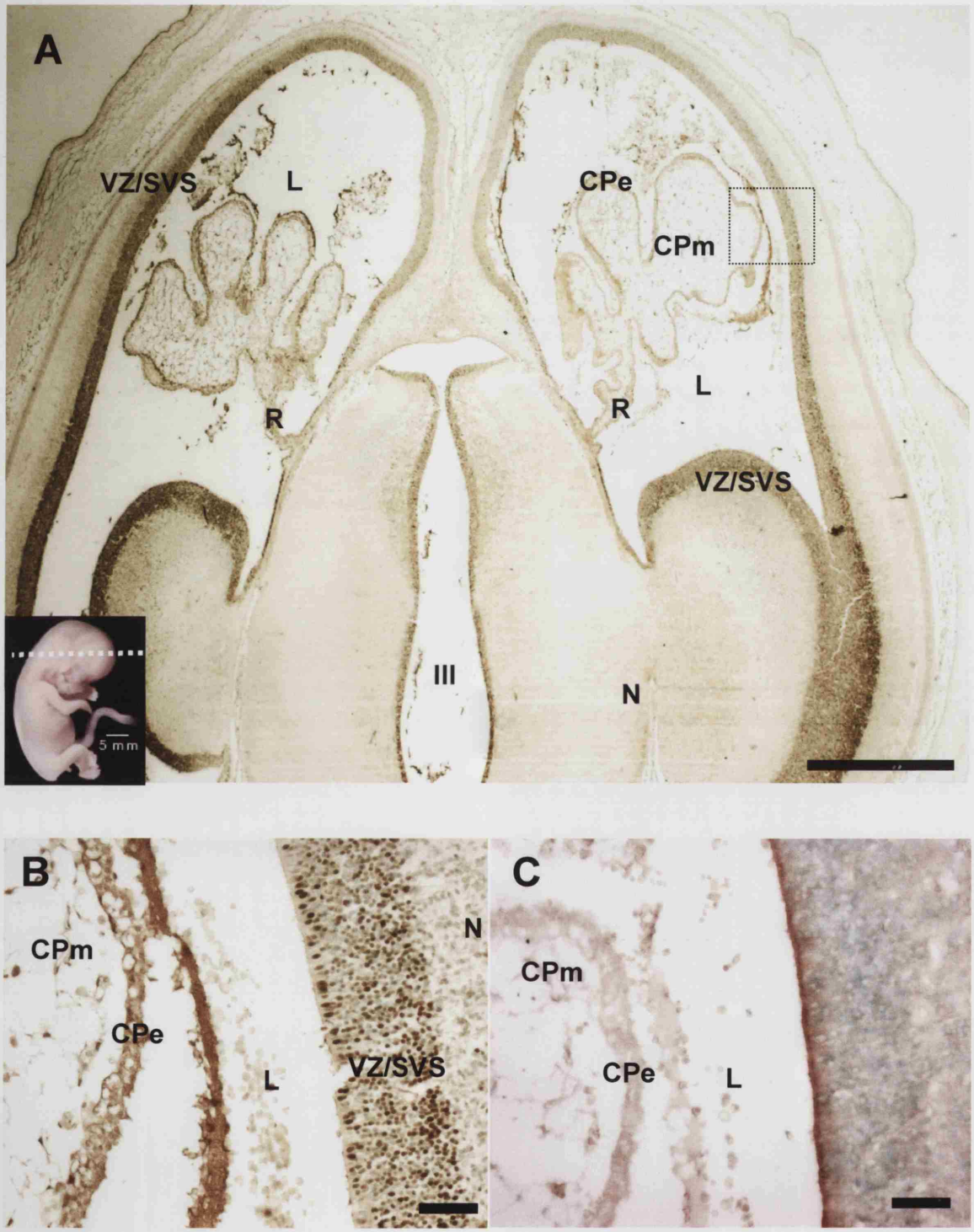
A
VZ/SVS
L
CPe
CPm
L
R
R
VZ/SVS
III
N
5 mm
B
CPm
CPe
L
VZ/SVS
N
C
CPm
CPe
L

Figure 4. 13 High magnification of the CS 23 telecencephalic CP stained for PCNA protein.

A: Apex (most ventral side) of the telecenphalic CP stained for PCNA (brown) shown in Fig. 4.12A. The CPe (CPe) is negative for PCNA staining. Black arrowheads point to examples of nuclei in the CPe. Orange arrowheads point to examples mesenchymal cells positive for PCNA **B:** Phase contrast of the same field of view as in (A). **C:** Higher power magnification of the CPe confirming negativity for PCNA labelling. **D:** Equivalent phase contrast as in (C). **E:** High power magnification of the root of the CP stained for PCNA (brown). Green arrowheads point to PCNA labelled nuclei in the CPe, orange arrowheads points to PCNA-positive cells in the CP mesenchyme. **F:** Phase contrast of the same field of view as in (E). Scale bars in A and B are 25 μm, and in C, D, E and F are 15 μm. **CP** = choroid plexus, **CPe** = choroid plexus epithelium, **CPm** = choroid plexus mesenchyme, **L** = lateral ventricle.

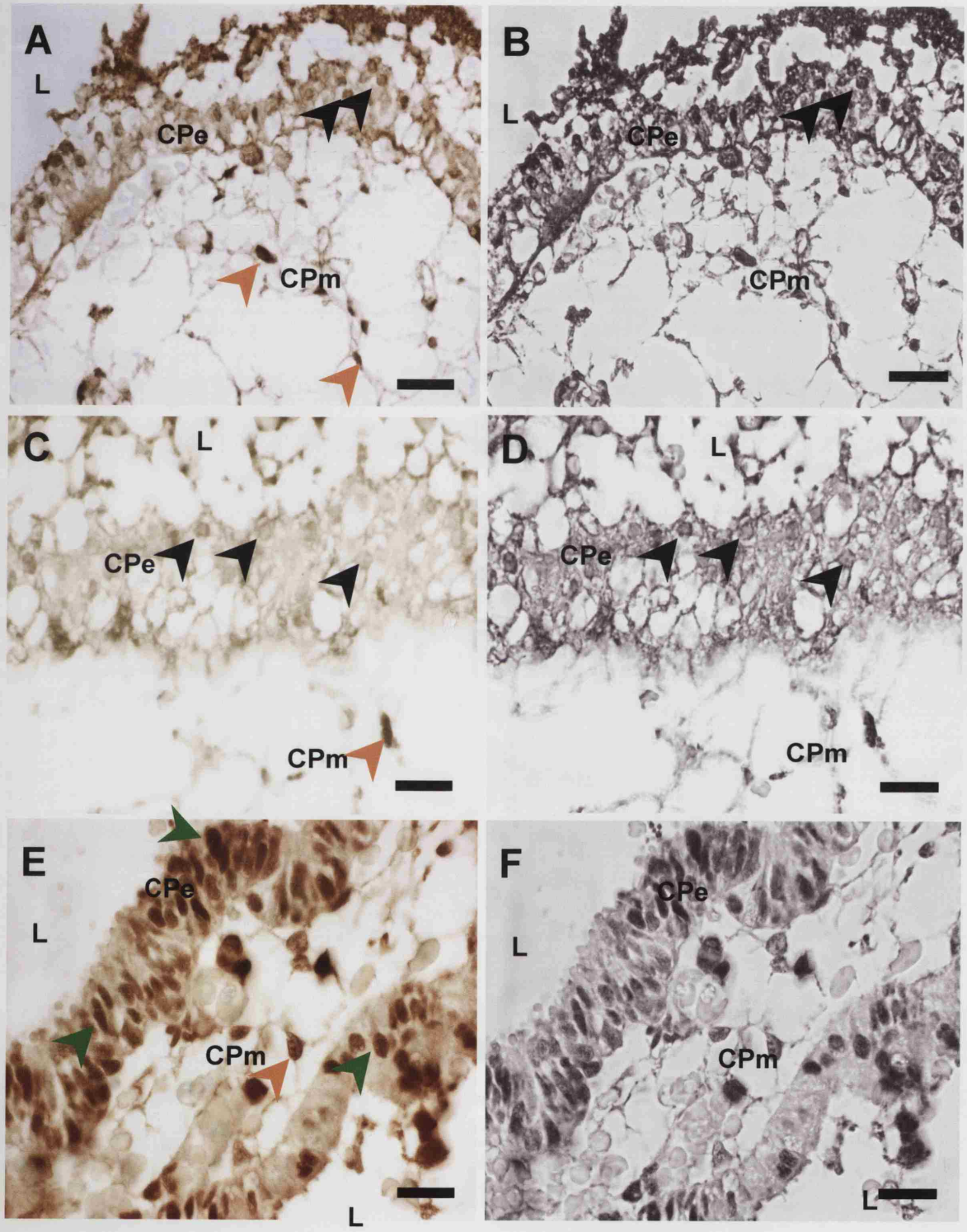
A
L
CPe
CPm
B
L
CPe
CPm
C
L
CPe
CPm
D
L
CPe
CPm
E
CPe
L
CPm
L
F
CPe
L
CPm
L

Figure 4. 14 Transverse views of the IVth ventricle CP of the human CS 23 embryo (A-E) and 11 week foetus (F) stained for PCNA protein

A: Low magnification of the IVth ventricle of a CS 23 embryo stained for PCNA (brown). Black arrowheads point at the location of the CP. **B:** High magnification of the IVth ventricle CP bridging the ventricle, no PCNA positive cells are seen. **C**: High power magnification of the root of the IVth ventricle; no PCNA positive cells are seen. **D:** Same field of view as in (C) viewed under phase contrast optics. **E:** High power magnification of the CP and the neuroepithelium that is positive for PCNA at the level of the ventricular zone/subventricular zone (green arrowheads). **F:** IVth ventricle CP of an 11 week foetus; no PCNA positive cells are present. Scale bar in A is 800 μm, scale bar in B is 400 μm, scale bars in C, D, E and F are 50 μm. **CP** = choroid plexus, **CPe** = choroid plexus epithelium, **CPm** = choroid plexus mesenchyme, **IV** = fourth ventricle, **N** = neuroepithelium.

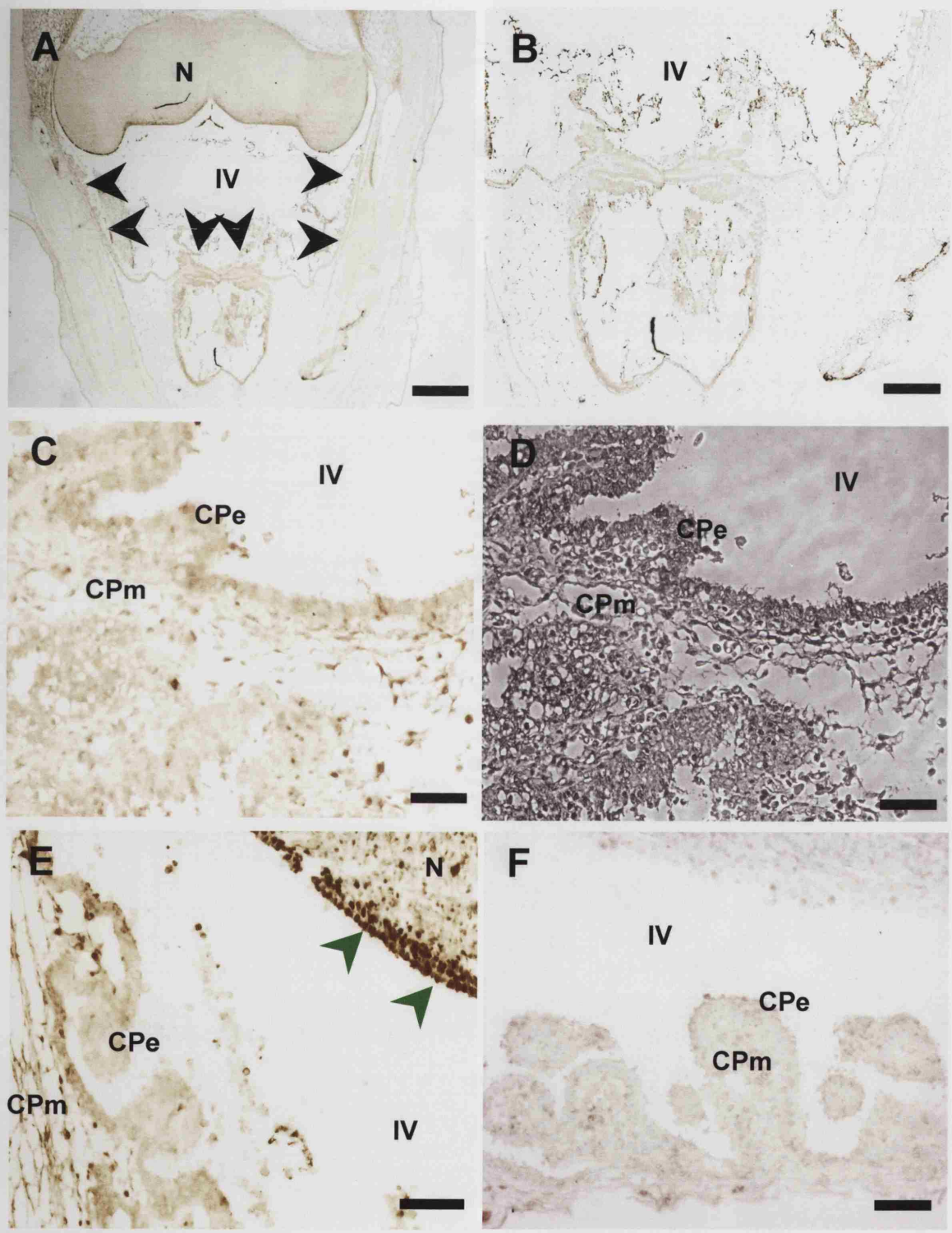
A
N
IV
B
IV
C
IV
CPe
CPm
D
IV
CPe
CPm
E
N
CPe
CPm
IV
F
IV
CPe
CPm

4.2.3 Expression of FGF2 protein in the developing CP

Peroxidase based immunohistochemical analysis of FGF2 protein was carried out using a monoclonal antibody raised against the amino terminal of FGF2. The antibody recognized all high molecular weight and low molecular weight isoforms of the protein. All nuclei were counterstained with methyl green.

4.2.3.1 Expression of FGF2 in mouse

Expression of FGF2 was observed in the 12.5dpc mouse IVth ventricle (Fig. 4.15A). Immunohistochemical labelling for FGF2 in the CP seemed stronger in the epithelium than in the mesenchyme. Staining in the CP mesenchymal and epithelial cells was uniformly spread in the cytoplasm with no apparent labelling in the nuclei. Staining was observed throughout the CPe with no specific localization. Positive staining was also apparent in the cytoplasm of the cells in the neuroepithelium. Staining was also observed in the nucleus of some neuroepithelial cells (not shown). No staining was present when the primary antibody was omitted (Fig. 4.15B)

4.2.3.2 Expression of FGF2 in human

High levels of expression of FGF2 protein was also observed in the cytoplasm of human embryonic CS23 lateral (Fig. 4.15C) and IVth ventricle CPs (Fig. 4.15E), and in the neuroepithelium and the cortical plate (Fig. 4.15D). The labelling was homogenously distributed throughout the CPe, with no indication of areas expressing FGF2 more strongly. The mesenchyme also labelled positive for FGF2, albeit less strongly (Fig. 4.15C, E). No staining was present when the primary antibody was omitted (Fig. 4.15F).

Figure 4. 15 Expression of FGF2 protein in the mouse and human embryonic choroid plexus

Sagittal section of the mouse 12.5dpc IVth CP and the transverse section of the human CS23 IVth ventricle CP stained for FGF2 (brown). Nuclei are counterstained with methyl green. **A:** 12.5 dpc mouse embryonic IVth ventricle CP; strong cytoplasmic staining for FGF2 is seen in the CPe, a less intense staining is present in the CPm. **B:** 12.5 dpc mouse IVth CP, negative staining in the absence of primary antibody. **C:** High magnification of human CS23 lateral CP; strong cytoplasmic labelling for FGF2 is seen in the CPe. **D:** High magnification of the neuroepithelium; positive cytoplasmic FGF2 labelling is seen in the neuroepithelial cells. **E**: Human CS 23 IVth ventricle, strong cytoplasmic staining for FGF2 is seen in the CPe. **F:** Human CS 23 IVth ventricle; negative staining in the absence of primary body. Scale bars for A, B, E, F are 50 μm, and for C-D are 15 μm. **CP** = choroid plexus, **CPe** = choroid plexus epithelium, **CPm** = choroid plexus mesenchyme, **IV** = fourth ventricle, **L** = lateral ventricle, **N** = neuroepithelium.

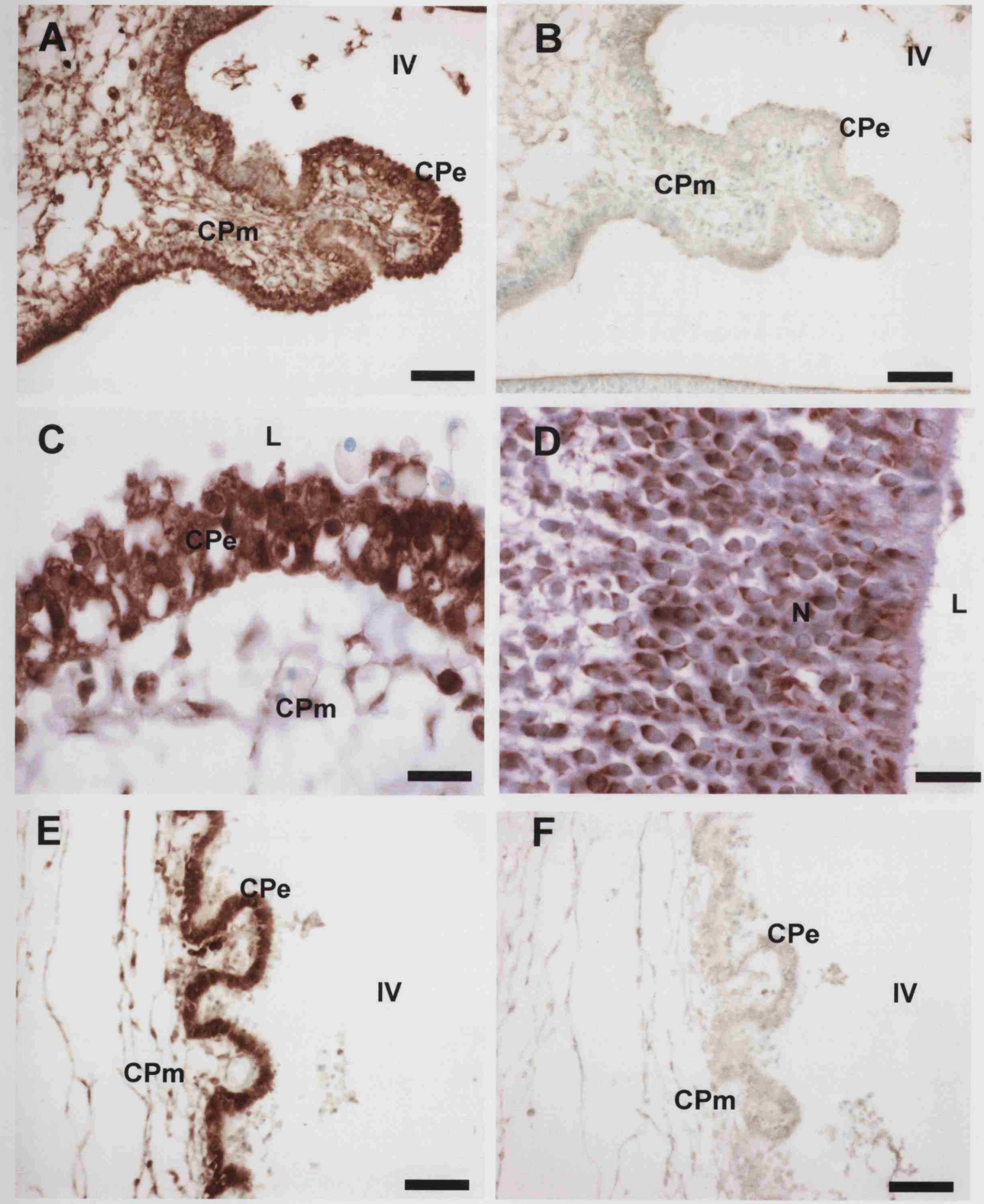
A
IV
CPe
CPm
B
IV
CPe
CPm
C
L
CPe
CPm
D
N
L
E
CPe
IV
CPm
F
CPe
IV
CPm

4.3 Discussion

4.3.1 Transthyretin expression

In the present study, I confirmed that TTR was expressed in the developing mouse CPe and validated the specifity of staining of the TTR antibody. Transthyretin protein was expressed in the mouse embryonic CPe as early as 11.5 dpc when the CP is not yet morphologically distinct, as reported in the rat (Cavallaro et al., 1993). The TTR protein in CPe cells was concentrated in the apical side of the cytoplasm above the nucleus, which is consistent with previous descriptions of TTR protein expression in the human and rat CPe (Mollgard et al., 1979; Jacobsen et al., 1982) (Kato et al., 1986). In contrast, the spatial differences in TTR expression observed in the developing CPe had not been reported. It appeared that the level of expression of TTR was related to the state of maturity (and possibly differentiation) of CPe cells: stronger TTR immunoreactivity was observed in the CPe that had a columnar to cuboidal single cell organisation, whilst TTR staining was faint or absent in the epithelium of the root of the CP that had a pseudostratified columnar organisation where cell proliferation was present. This finding is supported by the observation that TTR expression is intimately related to the differentiation of CPe cells (Xiao et al., 1998; Makover et al., 1989), and thus it is not surprising that TTR is more strongly expressed in CPe cells that have reached a more advance state of maturity also in the mouse (see Chap. 1.3.2.1). In order to better understand this relationship, it will be important in future studies to see whether TTR mRNA follows the same spatial pattern of expression.

4.3.2 Cell proliferation in the developing CP

Cell proliferation was studied in the mouse and human embryonic IVth and lateral CP by looking at the expression of PCNA, that allows detection of cells entering the S-phase of the cell cycle, rather than mitotic events as in previous studies (Sturrock, 1979; Kappers, 1958), which represent a very narrow windowof the cell cycle. In both species, cell proliferation was absent throughout development in the CPe with a monostratified columnar to cuboidal organisation as reported by (Shuangshoti and Netsky, 1966) and (Sturrock, 1979). I also confirmed, as observed by Knudsen (1964) and Sturrock (1979), that in general cell proliferation was restricted to the pseudostratified epithelium at the root of the CPe, which then supposedly thinned out

into a columnar epithelium allowing the CPe to grow. However in the mouse, the actual timing of this event differed between the IVth and lateral ventricle CP. In the IVth ventricle CP, no proliferation was apparent in the monostratified CP primordium and at early stages of its formation. Only from 12.5 dpc onwards cell proliferation was present in the root of the IVth ventricle CPe. In contrast, the lateral choroid plexus primordium contained proliferating cells, and many PCNA labelled cells were present in the budding lateral CP at 12.5 dpc. Only later in development, from 13.5dpc-14dpc onwards when the CP elongates into the telencephalic ventricle, did proliferation become restricted to the root of the CPe as in the IVth ventricle CPe.

In the developing human CPs, the amount of cell proliferation was very different in the telencephalic and myelencephalic (IVth) ventricle CPes. This reflected the differences in the dynamic of growth between the telencephalic and myelencephalic CPs. PCNA labelling was consistently observed in telencephalic pseudostratified CPe, especially at the root level of the CP. This showed that cell proliferation was important in this region of the CP as observed by Netsky and Shuangshoty (1966). It is interesting to note that these cells have been found to contain very little glycogen compared to the abundant amount found in the epithelial cells in the rest of the CPe (Shuangshoti and Netsky, 1966). This is consistent with the observation that such high amount of glycogen in the epithelial cells would be incompatible with mitosis (Kappers, 1958). In contrast, in the myelencephalic CPe of the CS 23 and 11 week foetus, no PCNA protein labelling was observed, not even in the roots of the CP; the lack of cell proliferation in the IVth ventricle was rather surprising, although a more comprehensive study would probably show some areas of cell proliferation like in the root of the telencephalic CP. It is also possible that at these stages of development cell proliferation has ceased and may only be happening locally during the early stages of CP development.

Hence, lateral ventricle CPe in both human and mouse was more positive than IVth ventricle CPe, where cell proliferation was observed in pseudostratified CPe principally at the root of the CPs. The human IVth ventricle CPe, however, was negative for cell proliferation at the ages studied, but it is possible that cell proliferation is present at ealier stages of development.

4.3.3 FGF2 protein expression in the embryonic CP

I found that FGF2 protein was expressed in the cytoplasm of both human and mouse embryonic CPe as well as in the stromal mesenchyme. This expression study contradicted the finding by Gonzalez (1994) that found that FGF2 immunoreactivity was only present in the CP mesenchyme. It was consistent, however, with other studies that showed similar staining of FGF2 in the epithelium and mesenchyme of the late rat embryo and adult rat CP (Cuevas et al., 1994; Fuxe et al., 1996; Raballo et al., 2000). The expression of FGF2 protein that was observed in the embryonic human lateral and IVth CP was comparable to that in the mouse. It was found in both species that FGF2 protein was more strongly expressed in the CPe, and that there was no obvious compartmentalisation of FGF2 protein within the CPs that correlate to the areas of cell proliferation.

4.3.4 Summary

The expression of TTR protein was confirmed in the mouse embryonic CPe by immunohistochemical analysis. Labelling for TTR was not uniform throughout the CPe. In fact, the immunoreactivity was stronger in the monostratified CPe and nearly absent in the pseudostratified epithelium where most of the cell proliferation took place especially at the early stages of development. The specificity of this antibody raised against TTR used was established, and validated its use for the characterisation of CPe cells in culture.

This study confirmed that cell proliferation was absent in the human and mouse monostratified CPe. In contrast, cell proliferation was observed in pseudostratified CPe, especially at the root of the CP in both IVth (except in human at the ages studied) and lateral ventricle CPs, where presumably the CPe cells are in a less advanced state of differentiation as suggested by the low level of TTR protein labelling that was found in these cells.

Finally, the expression of FGF2 protein was studied in the mouse and human embryonic CPe and mesenchyme. It was found that FGF2 protein was expressed throughout the CP structure with no discrete localization that may have explained the distinct regions of cell proliferation within the CPs. This result was important for interpreting the studied on the effect of FGF2 in the cell culture models I will discuss in the next Chapters.

Chapter 5 Expression of genes associated with cerebrospinal fluid homeostasis and choroid plexus development

5.1 Introduction

The transcription factors E2F5, FoxJ1 and p73 have been shown to be strongly expressed in the embryonic choroid plexus epithelium (CPe) at the mRNA level, and surmised to be important in determining the proper differentiation of the CPe as well as having a role in the homeostasis of CSF secretion. This is supported by the fact that the knockout of *E2F5*, *FoxJ1* or *p73* in the mouse cause a non-obstructive type of hydrocephalus with concomitant enlargement of the brain ventricles and subtle developmental defects in the CPe. Since expression of these genes has mainly been studied at the mRNA level in the embryonic CP, the aim of this chapter was to characterize the expression pattern of these genes at the protein level by immunohistochemistry in order to better understand their role in the development of the CP.

E2F5 mRNA was shown to be expressed in the developing and post-natal choroid plexus by in-situ hybridisation (Dagnino et al., 1997; Lindeman et al., 1998). Dagnino et al. (1997) showed that E2F5 mRNA was highly expressed in the posterior (IVth ventricle CP) and the anterior (IIIrd and lateral CPs) choroid plexuses in 13.5 dpc to 18.5 dpc embryos, while Lindeman et al. (1998) showed that E2F5 RNA was also expressed in the IVth ventricle CP in the one day old mouse. To date no study has been carried out to study the expression of the E2F5 protein, either in the mouse or human developing central nervous system or CPs. The first part of this chapter thus aimed to study the expression of E2F5 protein by immunohistochemistry in the developing mouse and human CP and peri-ventricular regions of the CNS. E2F5 is a member of the E2F family of transcription factors that have an important role in determining the progression of a cell through the cell cycle. Therefore, the expression of E2F5 protein was examined in parallel with that of PCNA that is present in the

nucleus of cells entering the G1 to S phase of the cell cycle, in the CP and neuroepithelium.

FoxJ1 has been studied both at the mRNA level and protein level in the developing choroid plexus. Expression of FoxJ1 mRNA by in-situ hybridization was detected at 11dpc in certain areas of the ependyma lining the ventricles that constituted the presumptive CPe. This expression was shown to persist in the mature and differentiated CPe and to extend into the ependyma lining the ventricles at E14.5. Expression in the adult rat choroid plexus was also confirmed by RNase protection assays (Lim et al., 1997). The FoxJ1 protein was detected by immunohistochemistry in the developing CP at E13.5 and E15.5 (Tichelaar et al., 1999; Blatt et al., 1999). However, expression of the FoxJ1 protein was not studied at earlier stages of mouse CP development, 11.5 dpc and 12.5 dpc. Therefore I studied the expression of FoxJ1 protein by immunohistochemistry in the developing mouse choroid plexus at 11.5 dpc and at 17.5dpc, which marks the end of gestation, using a commercially available antibody. FoxJ1 protein expression was also studied using this antibody in the developing human choroid plexus.

The presence of p73 mRNA has been reported in the choroid plexus of the developing mouse (Yang et al., 2000), but no published study has yet shown the cellular localization of P73 protein in the developing choroid plexus. Unfortunately, only recently anti-p73 antibodies have become commercially available, so in this study the expression of p73 in the developing whole CP was only examined at the mRNA level by RT-PCR.

5.2 Results

5.2.1 Expression of E2F5 protein

5.2.1.1 Expression of E2F5 protein in mouse

Expression of the E2F5 protein was studied by peroxidase based immuno-histochemistry in the developing mouse CP using two commercially available polyclonal antibodies raised against the N-terminal of the E2F5 protein.

The first antibody used was provided by Labvision (California, USA). Staining for E2F5 was found to be strong in the 11.5 dpc IVth ventricle presumptive CP, and to be both in the nucleus and the cytoplasm (Fig. 5.1A). From 12.5 dpc to

14.5 dpc, staining in the IVth ventricle CP was found to be stronger in the CPe than in the mesenchyme, but was mostly cytoplasmic like in the rest of the CNS (Fig. 5.1B, C). By 15.5 dpc staining in the IVth ventricle CPe was found to be markedly reduced (Fig. 5.1D). By 17.5 dpc of development, staining in the IVth ventricle CPe was hardly visible (Fig. 5.1E), and remained so until the end of embryonic development and post-natal development (not shown). Staining for E2F5 had generally decreased in the whole of the CNS, although staining could still be observed in the retina (not shown) and the mouth epithelium at 17.5 dpc (Fig. 5.1F). Staining in the lateral CP followed a similar pattern of expression as in the IVth ventricle CP, in that its expression was thought E2F5 was strongly expressed in CPe at 12.5 dpc and 15.5 dpc (Fig. 5.2A, B). By 17.5 dpc staining of the lateral CP was reduced in intensity (Fig. 5.2C). The antibody stained the embryonic 13.5dpc liver as predicted by the mRNA expression of E2F5; interestingly, staining had a more nuclear localization than that observed in the CPe (Fig. 5.2E). However, strong staining for E2F5 was also found in the dorsal ganglia of the 13.5 dpc mouse (Fig. 5.2F), where the mRNA for E2F5 was only barely detected (Dagnino et al., 1997).

A second study was carried out using another commercially available polyclonal antibody raised against human E2F5 (Santa-Cruz, USA). At 11.5 dpc, staining was found to be intensely nuclear in the neuroepithelium as well as in the CP primordia while the CP mesenchyme was largely negative (Fig. 5.3A, C, E). The signal could be abolished by pre-incubating the primary antibody with E2F5 peptide, confirming the specificity of this antibody (Fig. 5.3B, D, F). By 13.5 dpc, staining was observed throughout the brain but was stronger in the peri-ventricular regions (Fig. 5.4A). The IVth and lateral ventricle CP were intensely positive (Fig. 5.4B, C). A predominantly nuclear staining was observed in the CPe cells while a rather low cytoplasmic staining was present in the mesenchyme. By 17.5 dpc, the levels of staining in the neural tissue and CP were markedly reduced. Only a few areas, mainly around the ventricles of the CNS were still positive (Fig. 5.5A, E). Staining in the CPe was not only markedly reduced but had become predominantly cytoplasmic (Fig. 5.5C). In contrast, staining of the whisker barrels at 17.5dpc was intensely positive and predominantly nuclear (Fig. 5.5B). The liver of the 13.5 dpc mouse presented a nuclear pattern of staining comparable to that observed with the Labvision antibody (Fig. 5.6A), but the dorsal ganglia were negative (Fig. 5.6B).

The specificity of the Santa-Cruz antibody was also confirmed by Western blot analysis of protein extracts from mouse brain at different stages of development (Fig. 5.7A). A single ~54 kDa band was detected in the embryonic brain at all stages examined and its molecular weight is consistent with that published by other authors (Vaishnav et al., 1998), although the predicted, non-phosphorylated form of the protein is 36 kDa. Decrease in E2F5 expression was observed at 17.5 dpc and the protein was hardly detectable in adult brain. The Ponceau red stain of the blotted membrane showed that the loading of the protein was similar or equal between samples (Fig. 5.7B), although there was variation in the protein band patterning profile.

Figure 5. 1 E2F5 protein expression in the mouse IVth ventricle CP using the Labvision anti-E2F5 polyclonal antibody

Sagittal views of IVth ventricle CP at different stages of embryonic development stained by DAB based immunohistochemistry using the Labvision anti-E2F5 antibody (brown). Nuclei are revealed by methyl green counterstain.

Strong positive staining for E2F5 is found in **A:** 11.5dpc CP, **B:** 12.5dpc CP, **C:** 14.5 dpc CP. Although the staining is in both the mesenchyme and CPe, its intensity is stronger in the latter. **D:** 15.5 dpc CP, weaker E2F5 staining than in (C) is observed in the CPe and mesenchyme. **E:** 17.5 dpc CP; very low cytoplasmic labelling for E2F5 is observed in the CPe. **F:** 17.5 dpc oral epithelium; strong cytoplasmic staining observed in the oral epithelial cells. **G** and **H:** 12.5 dpc CP; E2F5 staining without and with prior pre-adsorption with E2F5 peptide respectively. All scale bars are 50 μm except F which is 15 μm. **CP** = choroid plexus, **CPe** = choroid plexus epithelium, **CPm** = choroid plexus mesenchyme, **IV** = fourth ventricle.

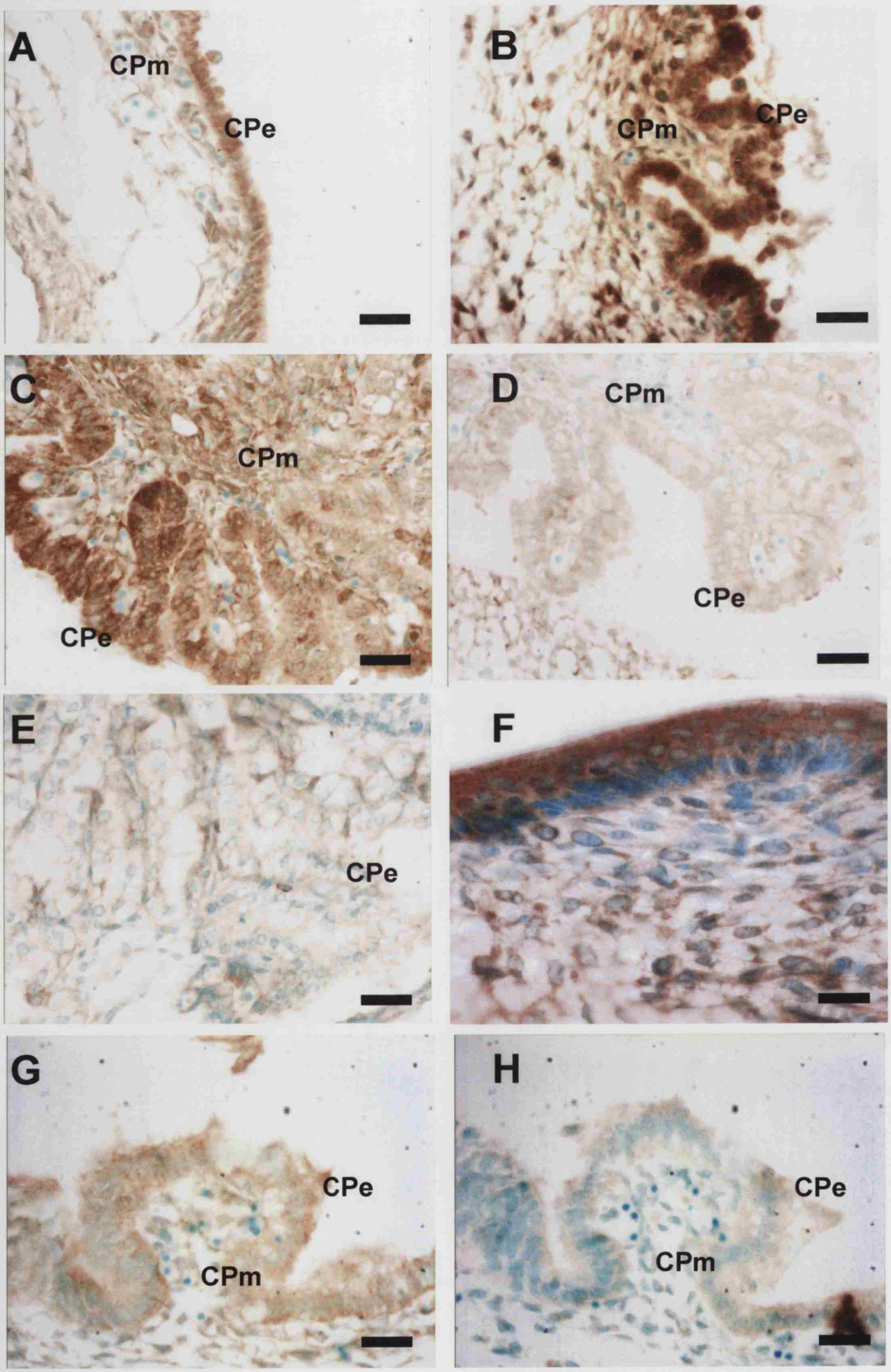
A
CPm
CPe
B
CPm
CPe
C
CPm
CPe
D
CPm
CPe
E
CPe
F
G
CPe
CPm
H
CPe
CPm

Figure 5. 2 E2F5 protein expression in the lateral CP using the Labvision anti-E2F5 polyclonal antibody

Sagittal views of lateral ventricle CP at different stages of embryonic development stained by DAB based immunohistochemistry using the Labvision anti-E2F5 antibody (Brown). Nuclei are revealed by methyl green counter-stain.

A: 12.5 dpc lateral CP; strong staining is observed in the CPe and ependyma. **B:** 15.5 dpc lateral CP; strong staining is maintained in the CPe and ependyma. **C:** 17.5 dpc lateral CP; staining is weaker in the CPe (black arrows) but the same as at 15.5dpc in the neuroepithelium. **D:** 17.5 dpc lateral CP; negative staining in absence of primary antibody. **E:** 13.5 dpc liver; nuclear staining for E2F5 is observed in most liver cells. **F:** 14.5 dpc dorsal ganglia; staining is observed, although E2F5 mRNA is reported to be barely detectable (see text). Scale bars in A and E are 25 μm, in B is 50 μm, in C, D and F are 100 μm. **CP** = choroid plexus, **CPe** = choroid plexus epithelium, **CPm** = choroid plexus mesenchyme, **L** = lateral ventricle, **N** = neuroepithelium.

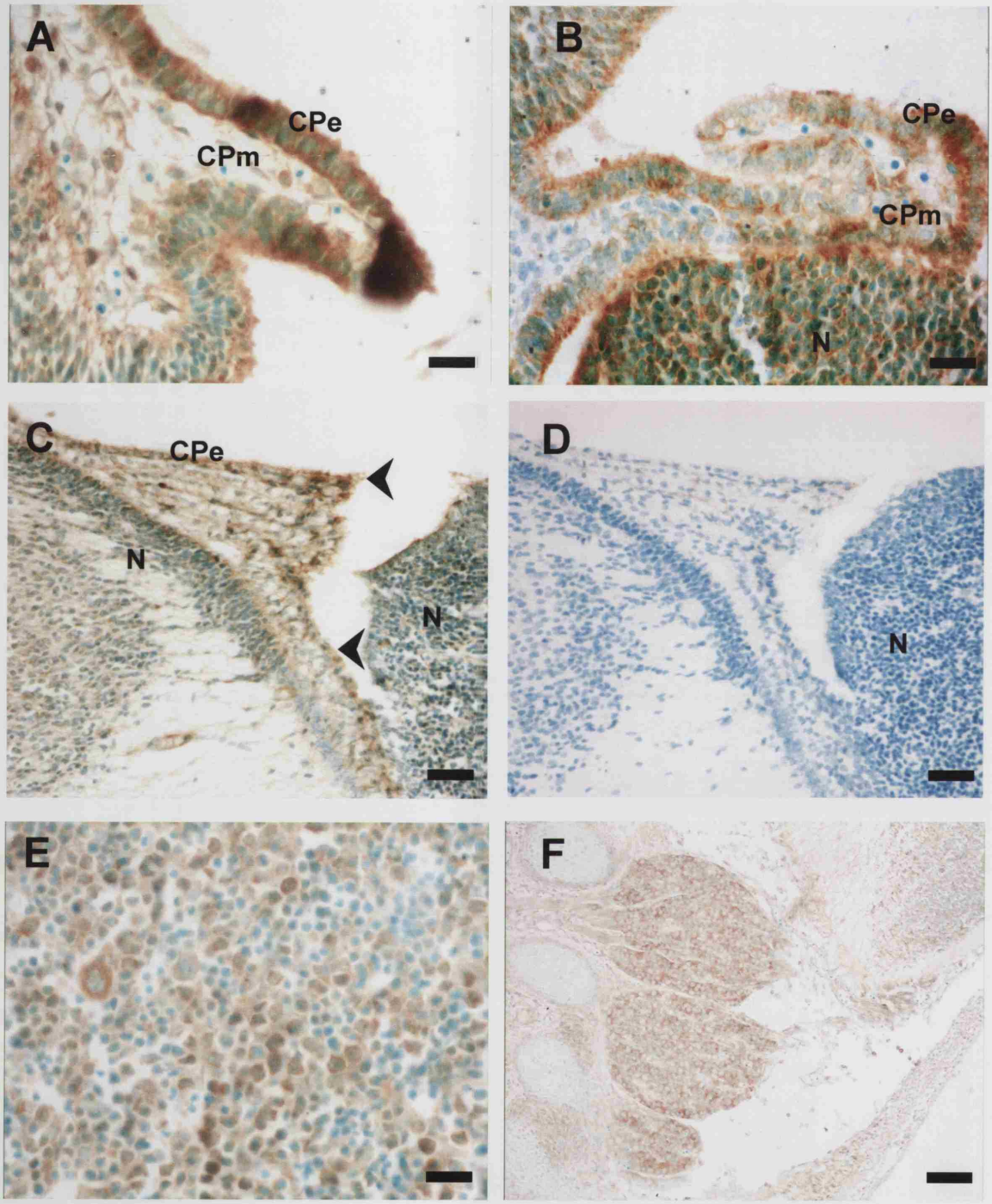
A
CPe
CPm
B
CPe
CPm
N
C
CPe
N
N
D
N
E
F

Figure 5. 3 E2F5 protein expression in the 11.5 dpc mouse embryo using the Santa-Cruz anti-E2F5 polyclonal antibody

Representative sagittal views of an 11.5 dpc mouse embryo stained by DAB based immunohistochemitry using the Santa-Cruz anti-E2F5 polyclonal antibody (brown). **A, C and E:** E2F5 staining of the same 11.5 dpc embryo; **A:** sagittal overview of the 11.5 dpc embryo labelled for E2F5; strong staining is observed in the neuroepithelium. **C:** Higher magnification of the cerebellum primordium (black arrowhead in A); strong nuclear staining for E2F5 is observed in the neuroepithelium only. **E:** Higher magnification of the IVth ventricle CP primordium (red arrowhead in A), strong nuclear staining is observed in the cells of the CP primordium but not in the mesenchyme. **B, D and F**: Staining with primary antibody pre-adsorbed with the recombinant E2F5 peptide. **B:** Sagittal overview showing little residual staining. **D:** Higher magnification of the cerebellum primordium (black arrowhead in B); no staining is seen. **F:** Higher magnification of the IVth ventricle CP primordium (red arrowhead in B); a slight residual staining is visible. Scale bars in A-B are 400 μm, and in C-F are 25 μm. **CPe** = choroid plexus epithelium, **Cb** = cerebellum, **IV** = fourth ventricle, **III** = third ventricle, **I** =lateral ventricle, **m** = mesenchyme, **N** = neuroepithelium.

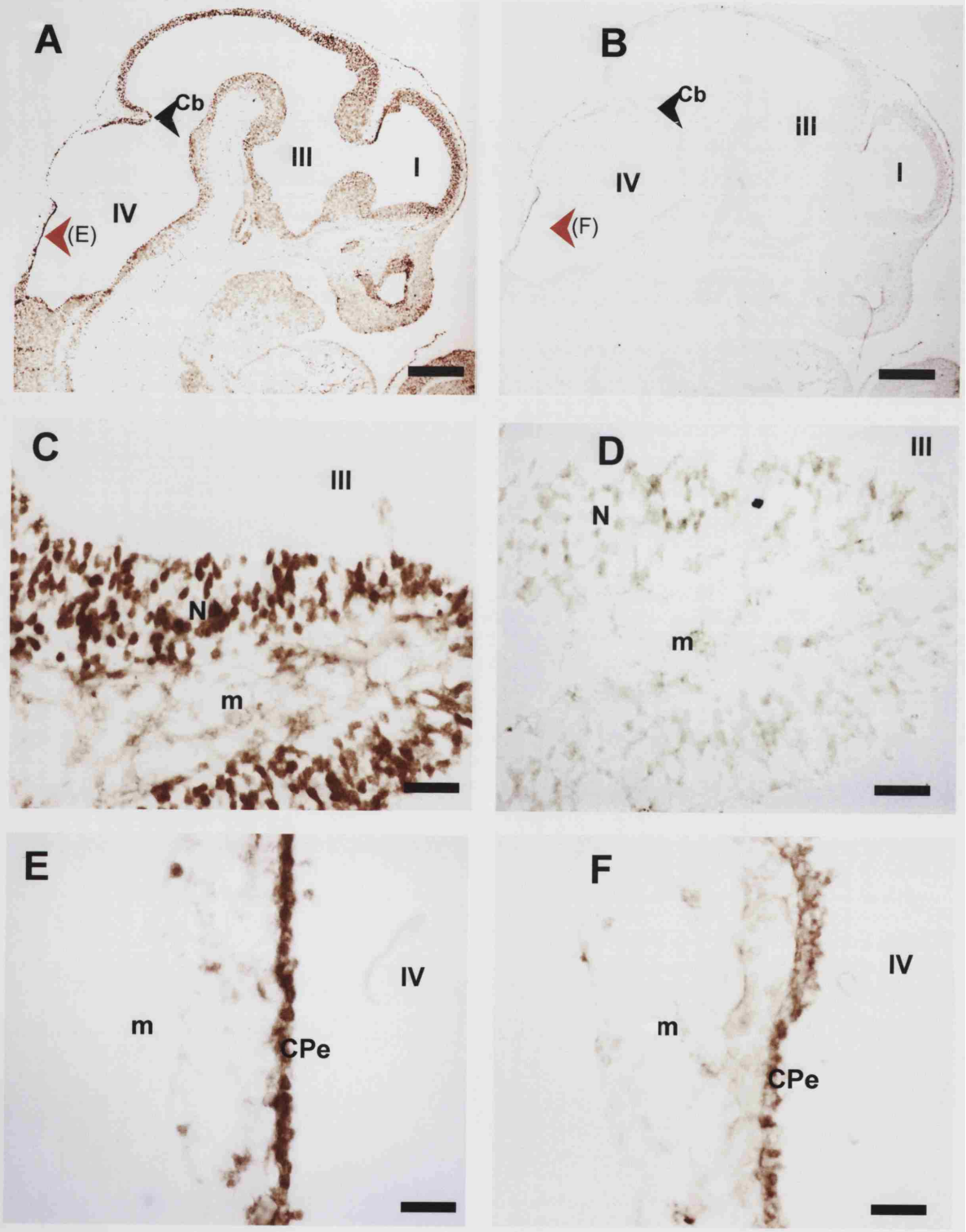
A
Cb
III
I
IV
(E)
B
Cb
III
IV
I
(F)
C
III
N
m
D
III
N
m
E
IV
m
CPe
F
IV
m
CPe

Figure 5. 4 E2F5 protein in the 13.5 dpc mouse embryo

Sagittal view of a 13.5 dpc mouse embryo stained by DAB based immunohistochemitry using the Santa-Cruz anti-E2F5 polyclonal antibody (brown). **A:** View of the 13.5 dpc mouse embryo; staining for E2F5 is strong in the neuroepithelium. **B:** sagittal view of the IVth ventricle CP; strong nuclear staining for E2F5 is observed in the CPe, with low level cytoplasmic staining in the mesenchyme. **C:** Sagittal view of the lateral CP stained for E2F5 protein; strong nuclear staining for E2F5 is observed in the CPe, with cytoplasmic staining in the mesenchyme just above background. **D:** High magnification of the IVth ventricle; positive nuclear labelling for E2F5 is observed in the CPe. **E:** High magnification of the IVth ventricle with prior pre-adsorption of the primary antibody with E2F5 recombinant peptide; no labelling is observed. **F:** Phase contrast image of the same field of view as in E. Scale bars in A is 800 μm, in B is 50 μm, and in C-F are 25 μm. **CP** = choroid plexus, **CPe** = choroid plexus epithelium, **CPm** = choroid plexus mesenchyme, **IV** = fourth ventricle, **N** = neuroepithelium.

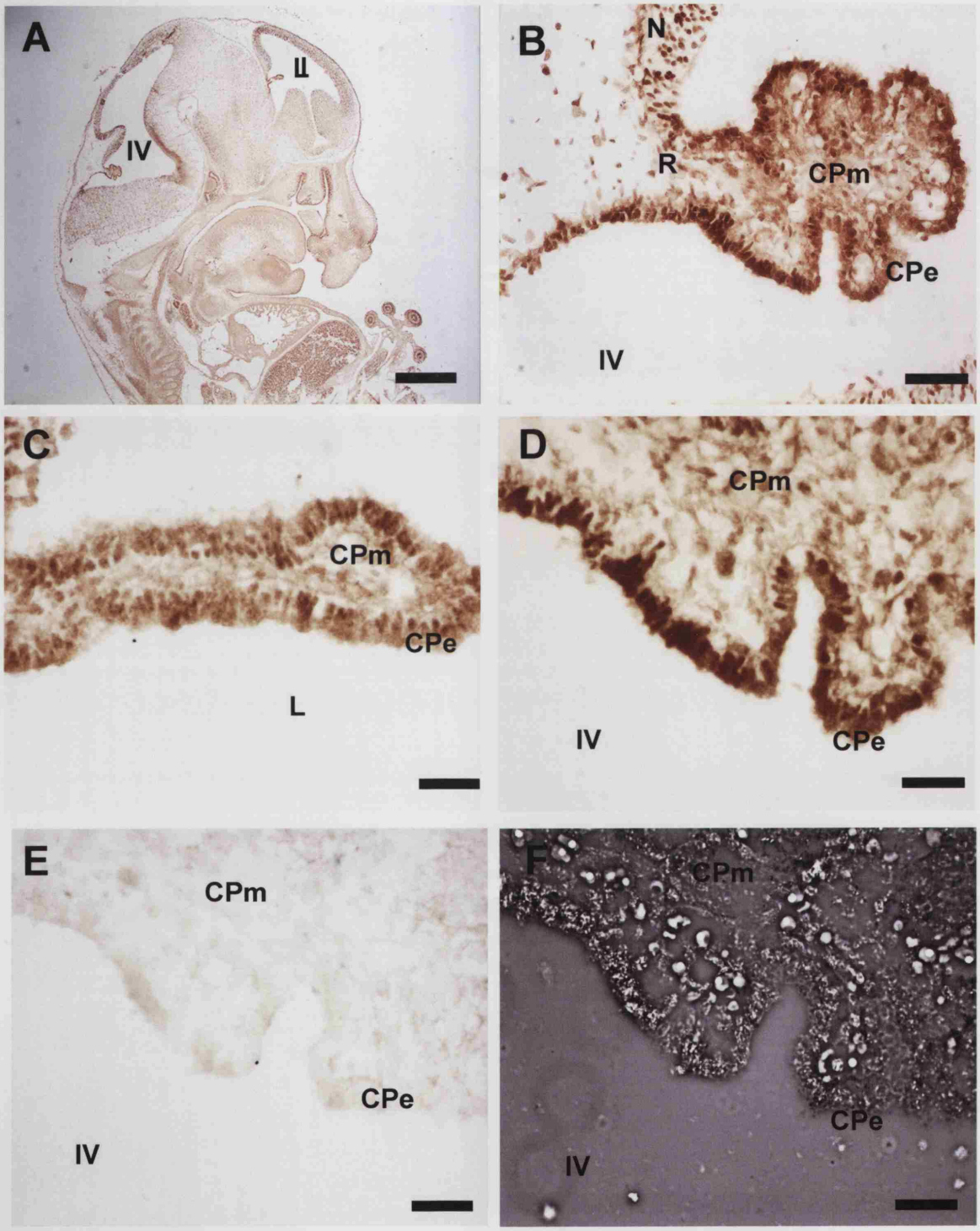
A
II
IV
B
N
R
CPm
CPe
IV
C
CPm
CPe
L
D
CPm
IV
CPe
E
CPm
CPe
IV
F
CPm
CPe
IV

Figure 5. 5 E2F5 protein expression in the 17.5 dpc mouse embryo

Sagittal view of a 17.5 dpc mouse embryo stained by DAB based immunohistochemitry using the Santa-Cruz anti-E2F5 polyclonal antibody (brown). **A:** Low magnification of the IVth ventricle and developing cerebellum; positive labelling is present in some areas of the neuroepithelium and in cells lining the cerebellum (Black arrowheads), but most of the brain is negative. **B:** strong nuclear and cytoplasmic staining is observed in the whisker barrels. **C:** IVth ventricle CP; staining is low and cytoplasmic in the CPe; the insert on the top right shows a high magnification of the CPe. The cells lining the developing cerebellum are strongly positive (black arrowhead) as well as the root of the CP (green arrowheads). **D:** IVth ventricle CP staining with prior pre-adsorption of the primary antibody with E2F5 peptide; the insert on the top right shows a high magnification of the CPe. Very little residual labelling is observed (dark patch to the right is artifactual). **E:** Lateral CP; staining of the CPe appears low and cytoplasmic (green arrowheads), whereas staining is stronger in the neuroepithelium in the ventricular zone/subventricular zone. **F:** Lateral CP, staining with prior pre-adsorption of primary antibody with E2F5 peptide. Scale bar in A is 200 μm, in B is 25 μm, in C-F are 100 μm. **CP** = choroid plexus, **CPe** = choroid plexus epithelium, **CPm** = choroid plexus mesenchyme, **IV** = fourth ventricle, **N** = neuroepithelium, **VZ/SVZ** = ventricular zone/subventricular zone.

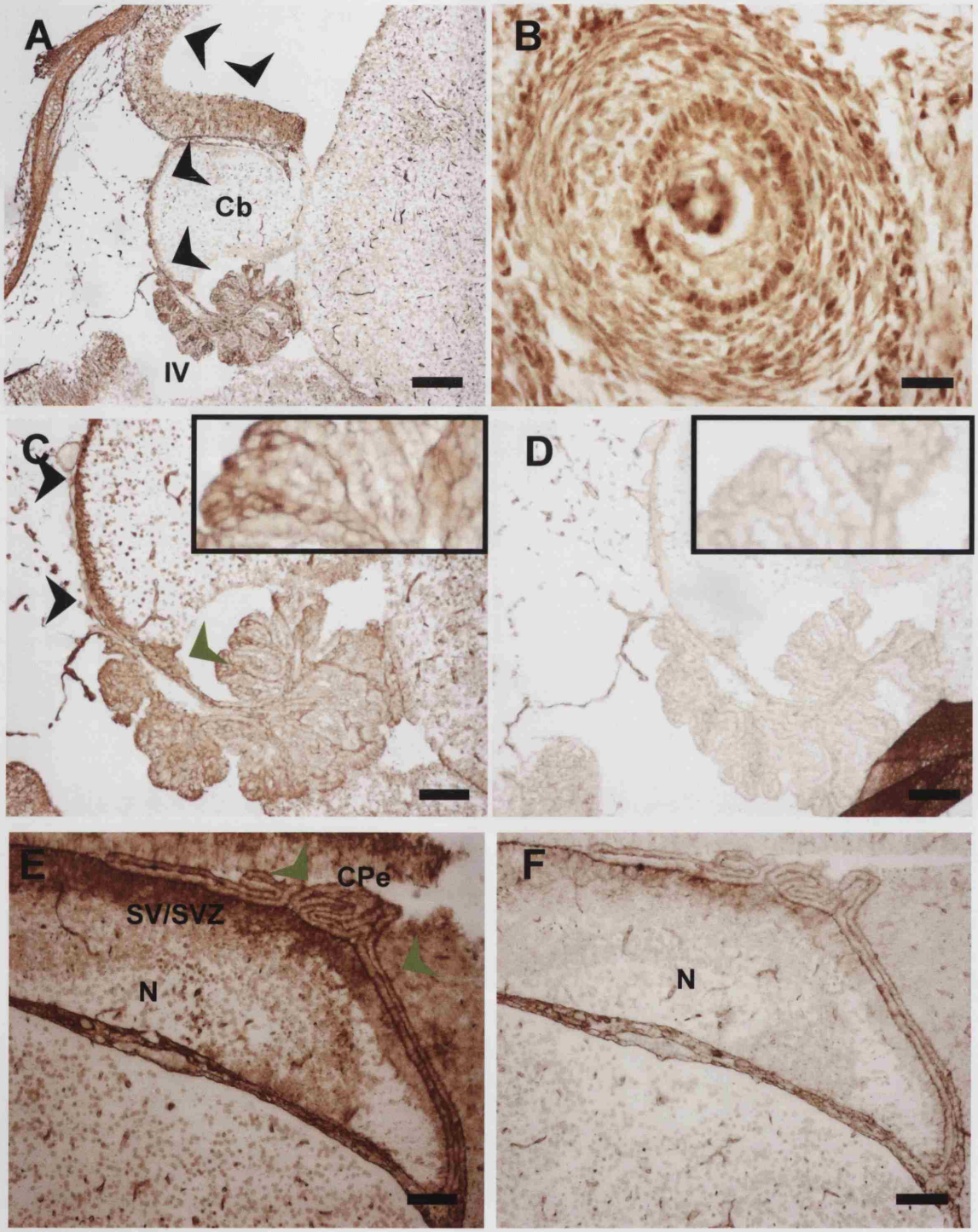
A
Cb
IV
B
C
D
E
CPe
SV/SVZ
N
F
N

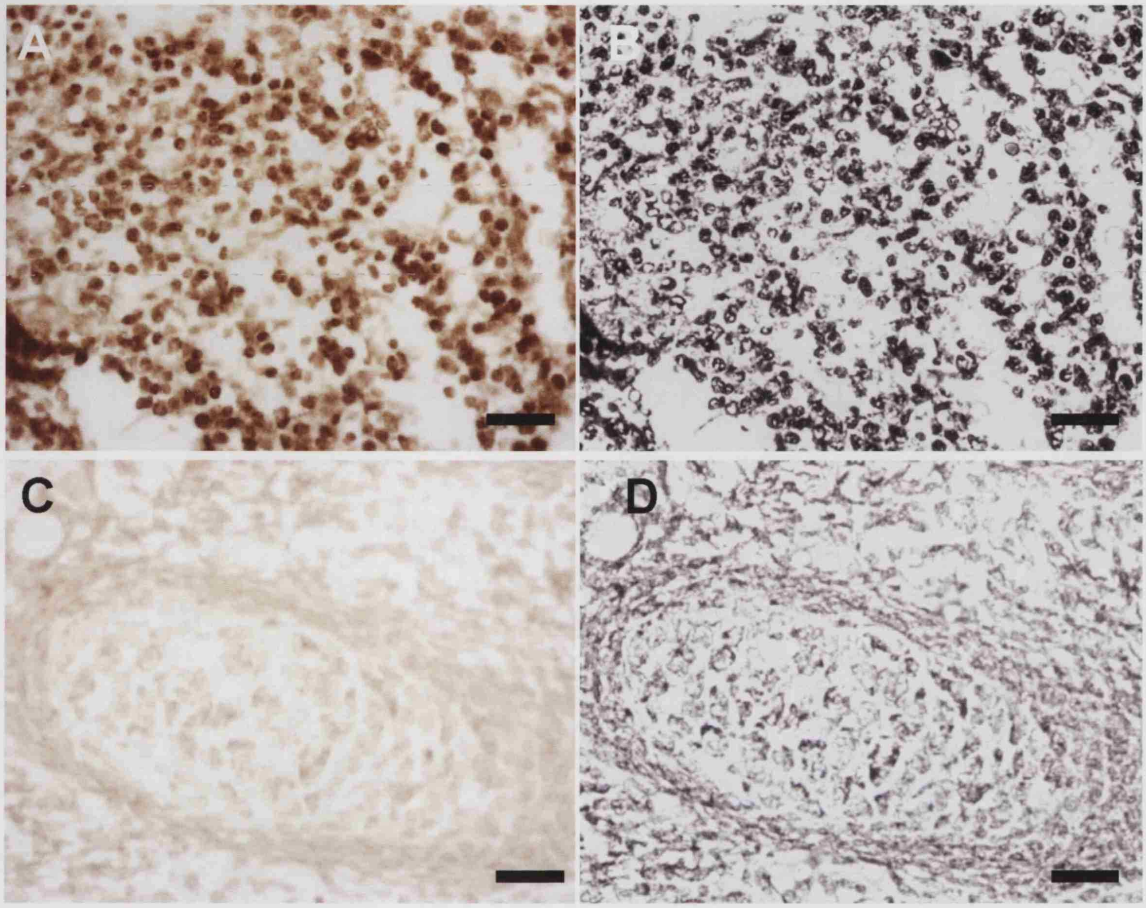

Figure 5. 6 Staining of mouse embryonic liver (A-B) and dorsal root ganglion (C-D) with St-Cruz anti-E2F5 antibody

A: 13.5 dpc embryonic liver; strong E2F5 expression observed in most nuclei. **B:** corresponding phase contrast. **C:** Dorsal root ganglion; no positive stain is detected. **D:** Corresponding phase contrast. Scale bars are all 25 μm.

Figure 5. 7 Western blot analysis of E2F5 protein expression in the developing mouse brain

A: Western blot for E2F5 of whole brain protein extracts from different developmental stages (11.5-17.5 dpc and adult). Immunoblot using the Santa-Cruz anti-E2F5 antibody; the molecular weight of the E2F5 protein is ~54 kDa. **B:** Corresponding Western blot membrane straight after transfer stained with Ponceau red. **C:** Densitometric analysis of E2F5 protein expression from the Western blot bands in (A). For (A) and (B) the molecular weight ladder is on the left (values are in kDa).

A

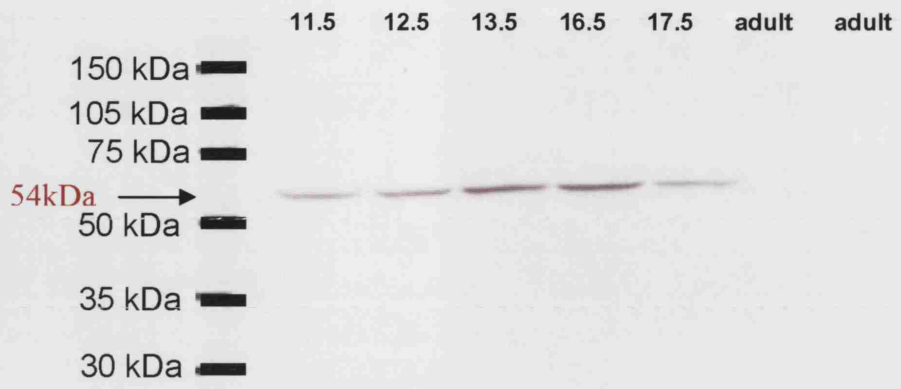
11.5
12.5
13.5
16.5
17.5
adult
adult
150 kDa
105 kDa
75 kDa
54kDa
50 kDa
35 kDa
30 kDa

B

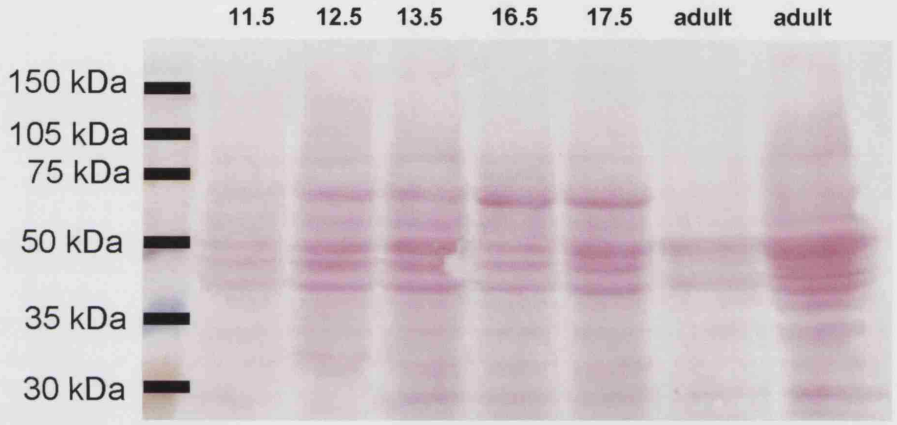
11.5
12.5
13.5
16.5
17.5
adult
adult
150 kDa
105 kDa
75 kDa
50 kDa
35 kDa
30 kDa

C

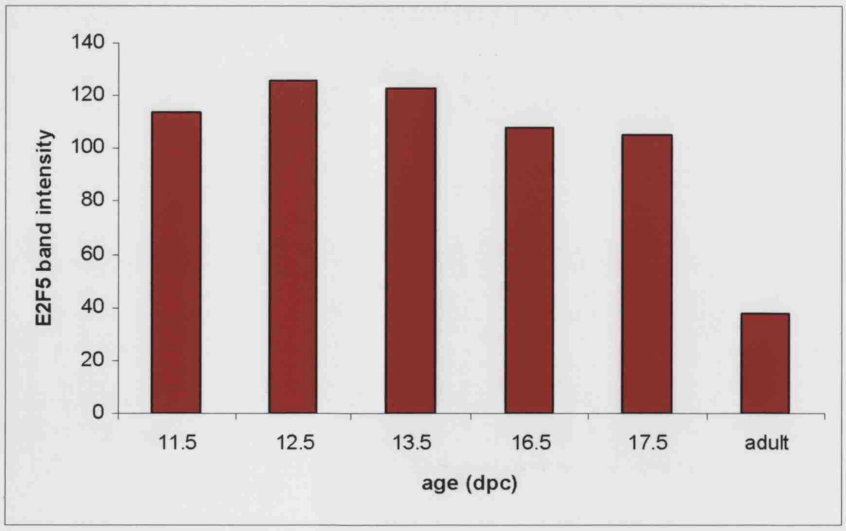
E2F5 band intensity
140
120
100
80
60
40
20
0
11.5
12.5
13.5
16.5
17.5
adult
age (dpc)

5.2.1.2 Expression of E2F5 protein in the developing human choroid plexus

Expression of E2F5 protein in the developing human embryonic and foetal CP was studied by peroxidase based immunohistochemical analysis using the Santa-Cruz (USA) polyclonal antibody raised against the N-terminal of human E2F5 protein. The expression of E2F5 protein was studied in the telencephalic CP and IVth ventricle CP.

In the Carnagie stage (CS) 18 embryo, predominant nuclear staining for E2F5 protein was found in the neuroepithelium surrounding the telencephalic ventricle as well as in the CP primordia budding out into the ventricular cavity (Fig. 5.8A, C). Pre-adsorption of the primary antibody with E2F5 recombinant peptide abolished the staining (Fig. 5.8B, D). At CS 20, strong staining for E2F5 was found in the neuroepithelium as well as in the CP of the telencephalic ventricle (Fig. 5.8E). The cells in the neuroepithelium had intense nuclear labelling for E2F5 (Fig. 5.8F), whilst the CPe exhibited a mixture of cytoplasmic and nuclear staining; the mesenchyme of the CP was only lightly stained with occasional nuclear staining (Fig. 5.8G). No staining was present in the CP when the primary antibody was pre-adsorbed with recombinant E2F5 peptide (Fig. 5.8H). At CS 23, both the CP and neuroepithelium expressed E2F5 protein (Fig. 5.9A). The neuroepithelium was positive for E2F5, but nuclear labelling was not observed as frequently as at earlier stages (Fig. 5.9A, B). In fact, some cells in the neuroepithelium were negative for E2F5 labelling. The cortical plate had strong nuclear stain for E2F5 (Fig. 5.9B). Sharply defined nuclear staining for E2F5 was found in the columnar cells of the telencephalic CPe (Fig. 5.9A, C), whilst the staining in the pseudostratified cells at the root of the CP was both cytoplasmic and nuclear (Fig. 5.9A, E). The staining was absent when the primary antibody was pre-adsorbed with recombinant E2F5 peptide (Fig. 5.9.D, F).

The expression of E2F5 protein was studied in the IVth ventricle CP of the CS 23 embryo and the 11 week foetus (Fig. 5.10 and 5.11). At CS23, mainly nuclear labelling for E2F5 was detected in the CPe cells (Fig. 5.10A-D). However, regional differences were also observed. For instance, in areas where the epithelium was single columnar, staining was both cytoplasmic and nuclear (Fig. 5.10C), and in the pseudostratified columnar epithelium in the CPs bridging the IVth ventricle diverticulum, stronger nuclear labelling was mostly found in the cells that were closest to the lumen rather than in the more basal cells close to the stromal

mesenchyme (Fig. 5.10D, E). The staining was specific and was abolished by pre-adsorption of the primary antibody with the recombinant E2F5 peptide (compare Fig. 5.10A and B, Fig. 5.10E and F). By 11 weeks, foetal IVth ventricle CP E2F5 immunoreactivity was much lower and cytoplasmic (Fig. 5.11A), whereas nuclear staining was obvious in the retina (Fig. 5.11C). The staining was abolished by pre-adsorption of the primary antibody with the E2F5 recombinant peptide (Fig. 5.11B, D).

Figure 5. 8 E2F5 protein expression in the CS 18 and CS 20 human embryo lateral choroid plexus (CP)

Transverse sections of human CS 18 and 20 telencephalic CP stained by DAB based immunohistochemitry using the Santa-Cruz anti-E2F5 polyclonal antibody (brown). **A:** CS 18 telencephalic ventricles. Black arrowheads show the presumptive CP primordia budding out into the ventricles and which are labelled intensely for E2F5. **B:** Corresponding control with pre-adsorbed primary antibody. **C:** High magnification of the presumptive CP primordium (black arrowhead) and neuroepithelium stained for E2F5. **D:** Corresponding control with pre-adsorbed primary antibody. **E:** CS 20 telencephalic CP and ventricles stained for E2F5. **F:** High magnification of the neuroepithelium with cells showing nuclear staining for E2F5 protein. **G:** High magnification of the CP. Staining is both nuclear (black arrowhead) and cytoplasmic (blue arrowhead). **H:** Corresponding control with pre-adsorbed primary antibody. Scale bars in A-B are 100 μm, in C, D, F, H and G are 25 μm, and in E is 400 μm. **L** = lateral ventricle, **CP** = choroid plexus, **CPe** = choroid plexus epithelium, **CPm** = choroid plexus mesenchyme, **N** = neuroepithelium.

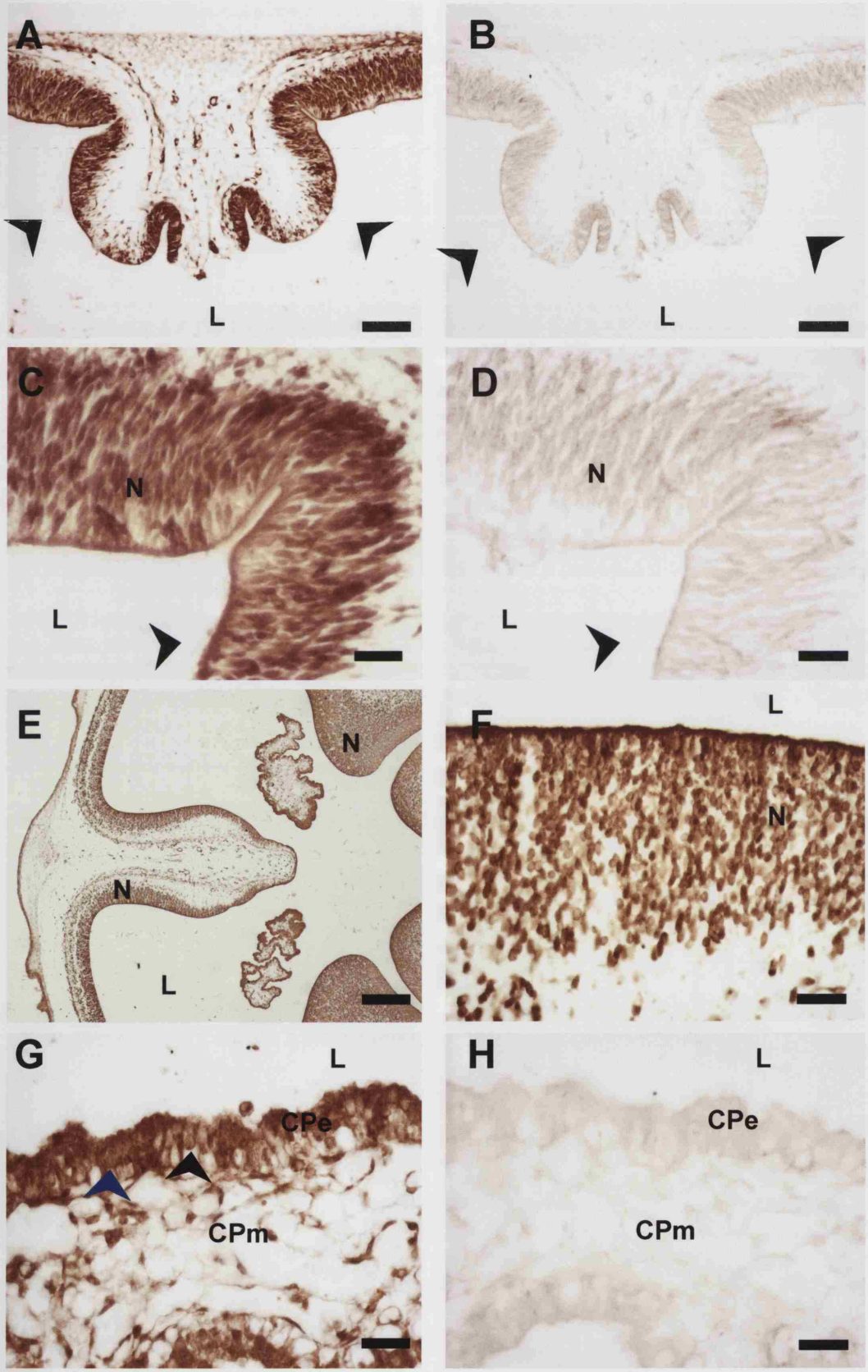
A
L
B
L
C
N
L
D
N
L
E
N
N
L
F
L
N
G
L
CPe
CPm
H
L
CPe
CPm

Figure 5. 9 E2F5 protein expression in the CS 23 human embryo lateral CP

Tranverse section of human CS 23 telencephalic region stained by DAB based immunohistochemitry using the Santa-Cruz anti-E2F5 polyclonal antibody (brown). Nuclei are counterstained by methyl green.

A: View of one of the telencephalic ventricle CP stained for E2F5. **B:** the ventricular surface stained for E2F5, and so does the cortical plate. **C:** High power magnification of the CPe (black box in A). Black arrowheads point to CPe cells with specific nuclear labelling for E2F5. **D:** Corresponding control stained with pre-adsorbed primary antibody. **E:** High power magnification of the CPe at the root of the CP (Red box in A). Staining is largely cytoplasmic, although there are also a number of positive nuclei. **F:** Corresponding control with pre-adsorbed primary antibody. Scale bar in A is 200μm, in B is 100μm, in C-F are 15μm. **L** = lateral ventricle, **CP** = choroid plexus, **CPe** = choroid plexus epithelium, **CPm** = choroid plexus mesenchyme, **R** = CP root, **Ctp** =cortical plate, **N** = neuroepithelium

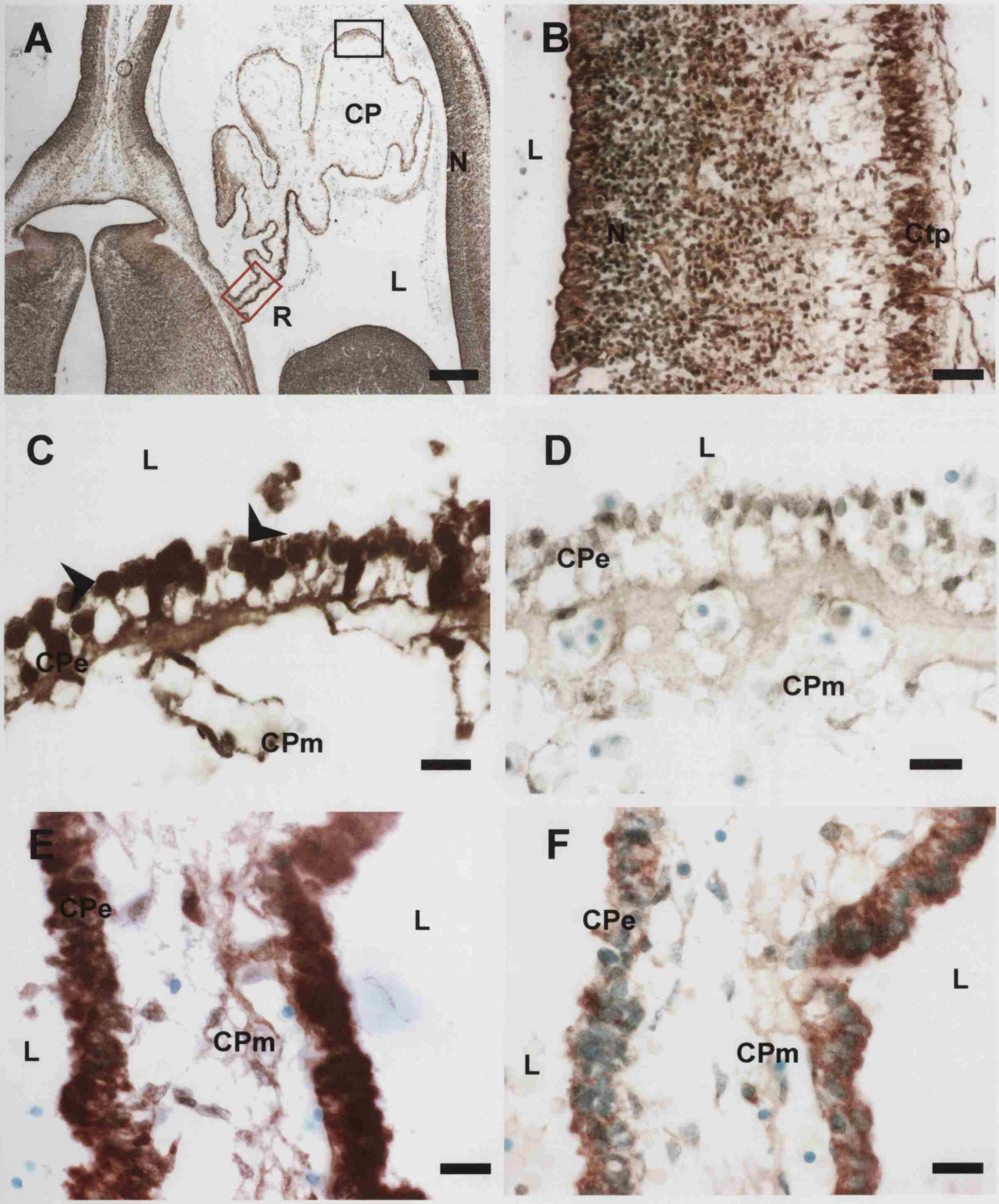
A
CP
N
L
R
B
L
N
Ctp
C
L
CPe
CPm
D
L
CPe
CPm
E
CPe
L
L
CPm
F
CPe
L
L
CPm

Figure 5. 10 E2F5 protein expression in the CS 23 human embryo IVth CP

Transverse view of human CS 23 IVth ventricle stained by DAB based immunohistochemitry using the Santa-Cruz anti-E2F5 polyclonal antibody (brown). Nuclei are counterstained with methyl green.

A: Low magnification of the IVth ventricle stained for E2F5. **B:** Corresponding control stained with pre-adsorbed primary antibody. In (A) and (B) the arrowheads show the location of IVth ventricle CP in the lateral roof (black) and the roof of the ventricle (red). **C:** High power magnification of the CP from the lateral roof of the ventricle (C-labelled black arrowheads in A); staining is both cytoplasmic and nuclear. **D:** High magnification of the CP in the roof of the ventricle (D-labelled red arrowhead in A). **E:** High power magnification with a 180° turn of the frame in (D). The more apical cells of the pseudostratified CPe have strong nuclear staining (green arrowheads), whereas the more basal cells display a weaker staining (black arrowheads). **F:** Corresponding control stained with pre-adsorbed primary antibody. Scale bars in A-B are 800 μm, in C, E and F are 15 μm, and in D is 100 μm. **CP** = choroid plexus, **CPe** = choroid plexus epithelium, **CPm** = choroid plexus mesenchyme, **N** = neuroepithelium, **IV** = fourth ventricle.

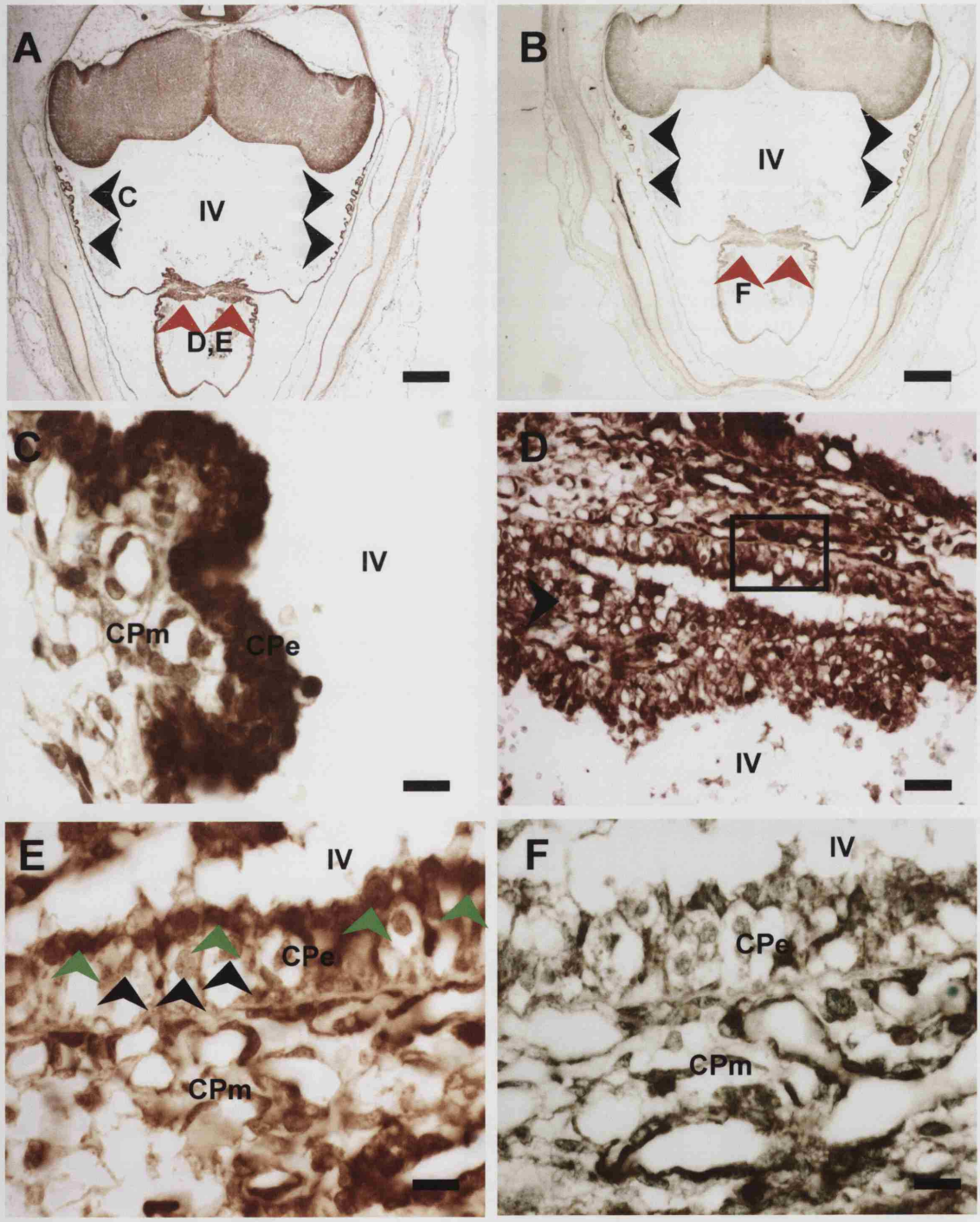
A
C
IV
D,E
B
IV
F
C
IV
CPm
CPe
D
IV
E
IV
CPe
CPm
F
IV
CPe
CPm

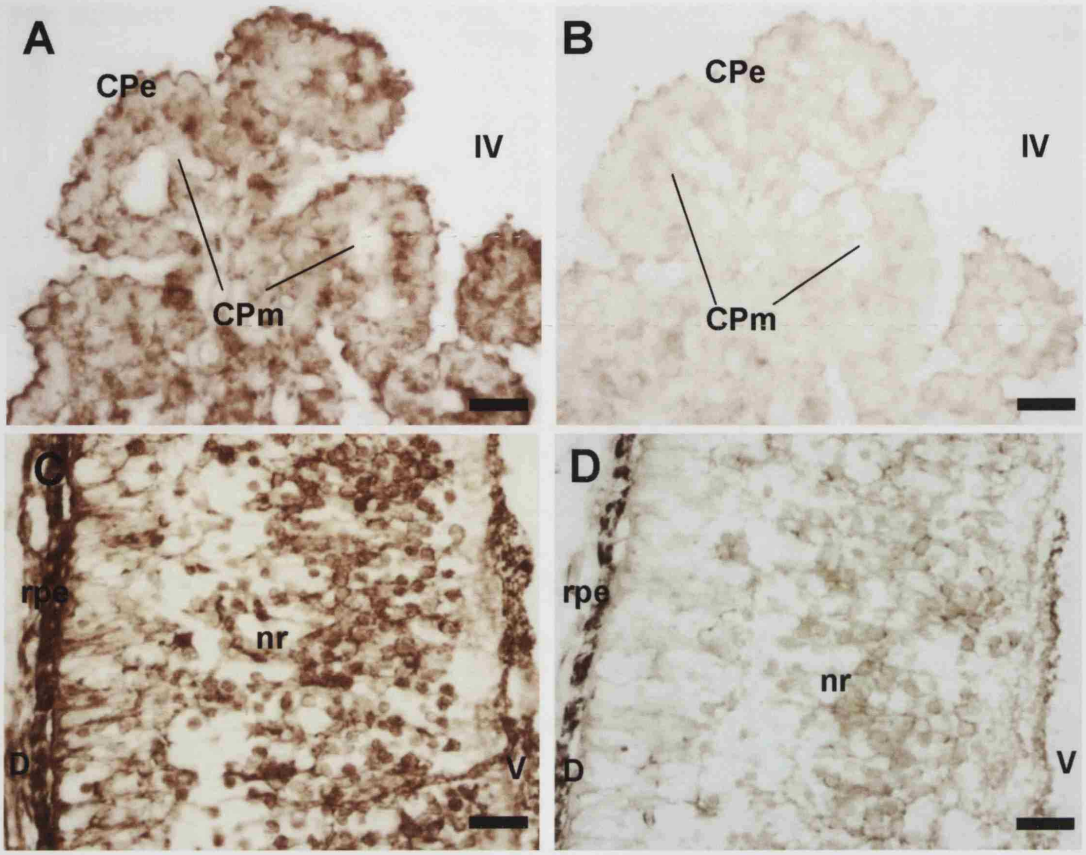

Figure 5. 11 E2F5 protein expression in the 11 week fetus IVth CP

Transverse view of 11 week foetal IVth ventricle CP stained by DAB based immunohistochemitry using the Santa-Cruz anti-E2F5 polyclonal antibody (brown). **A:** IVth ventricle CP labelled for E2F5 protein. Staining is cytoplasmic. **B:** corresponding control with pre-adsorbed primary antibody. **C:** Positive nuclear labelling for E2F5 protein in the retina of the eye. **D:** Corresponding control with pre-adsorbed primary antibody. Scale bars are all 25 µm.**CP** = choroid plexus, **CPe** = choroid plexus epithelium, **CPm** = choroid plexus mesenchyme, **D** = dorsal part of retina, **N** = neuroepithelium, **IV** = fourth ventricle, **nr** = neural layer of retina, **rpe** = retinal pigmented epithelium, **V** = ventral part of retina.

5.2.2 E2F5 and PCNA co-localization

Double labelling for PCNA and E2F5 was not possible due to incompatible epitope unmasking procedures; adjacent sections were therefore independently stained with PCNA and E2F5 for all the developmental stages in human and mouse studied here.

5.2.2.1 Co-localization in mouse

In the 11.5 dpc CP primordium (not shown), and the CPe of the IVth ventricle CP at 12.5 dpc (Fig. 5.12A, A' and B, B'), staining for E2F5 and PCNA protein did not coincide except at the level of the root (yellow arrowheads). Staining for PCNA was negative in the CPe, while E2F5 reactivity was both nuclear and cytoplasmic. In the 17.5 dpc IVth ventricle CPe labelling for E2F5 was predominantly cytoplasmic and much reduced in intensity, but did not coincide with PCNA expression with the exception of the root of the CP (yellow arrowhead) (Fig. 5.12C, C'). In contrast, E2F5 and PCNA labelling overlapped in the neuroepithelium, and in the streak of cells lining the cerebellum (green arrowheads) (Fig. 5.12C, C'). In the primitive 12.5 dpc lateral CP, E2F5 and PCNA were both expressed in the CPe cells (Fig. 5.12D, D'). In the 17.5 dpc lateral CPe E2F5 was expressed, albeit less strongly, but no PCNA staining was detected (Fig. 5.12E, E'). In the neuroepithelium nuclear localization of E2F5 was found to be associated with areas of cell proliferation like in the neuroepithelium (Fig. 5.12B, B'; C, C'; D, D' and E, E'). In other tissues, like the embryonic gut (Fig. 5.12F, F'), whisker barrels, umbilical chord epithelium, embryonic lung, and the retina (not shown) a strong coincidence was also found between E2F5 and PCNA expression in the nucleus.

5.2.2.2 Co-localization in human

At CS 18, both E2F5 and PCNA were detected in the neuroepithelium and the presumptive CP primordia (not shown). In the CS 20 lateral CPe, staining for E2F5 was a mixture of cytoplasmic and nuclear staining (cf. Fig 5.8G). Interestingly, PCNA was sporadically expressed in the CPe at this stage (not shown- cf. Chap. 4.10B). At CS 23, staining in the lateral CPe was localized to the nucleus, and no PCNA was detected (Fig. 5.13A-B). However, at the root of the CP where E2F5 labelling was both cytoplasmic and nuclear, PCNA labelling was strong (Fig. 5.13C-D). Surprisingly, the nuclei of the cells in the cortical plate labelled positive for E2F5, but were clearly negative for any PCNA labelling (Fig. 5.13E-F). In the IVth ventricle

CPe of the CS 23 embryo and 11 week foetus, E2F5 and PCNA labelling did not co-localize (not shown)

Figure 5. 12 Co-expression of PCNA and E2F5 in the developing mouse CP

PCNA protein was stained by fluorescence immunohistochemistry (bright red), and E2F5 by peroxidase based immunohistochemistry using the Santa-Cruz antibody (brown). PCNA and E2F5 were stained independently on adjacent sections.

A: 12.5 dpc IVth ventricle CP labelled for E2F5. **A'**: equivalent CP section stained for PCNA; yellow arrowheads point to the root of the CPe that is PCNA-positive. **B**: Low power magnification of the 12.5 dpc IVth ventricle. **B'**: adjacent section stained for PCNA. **C**: 17.5 dpc IVth ventricle CP stained for E2F5. **C'**: adjacent section stained for PCNA; yellow arrowheads point to the root of the CP that is PCNA-positive, green arrowheads point to the streak of PCNA-positive cells lining the cerebellum. **D**: 12.5 dpc lateral CP stained for E2F5. **D'**: adjacent section stained for PCNA. **E**: 17.5 dpc lateral CP stained for E2F5. **E'**: adjacent section stained for PCNA. **F**: Embryonic gut stained for E2F5. **F'**: Equivalent embryonic gut section stained for PCNA. Scale bars in A, A' are 50 μm, scale bars in B, B', C, C', E, E' are 100 μm, in D, D', F, F' are 25 μm. **Cb** =cerebellum, **CP** = choroid plexus, **CPe** = choroid plexus epithelium, **CPm** = choroid plexus mesenchyme, **IV** = fourth ventricle, **L** = lateral ventricle, **N** = neuroepithelium, **R** = CP root, **VZ/SVZ** = ventricular zone/subventricular zone.

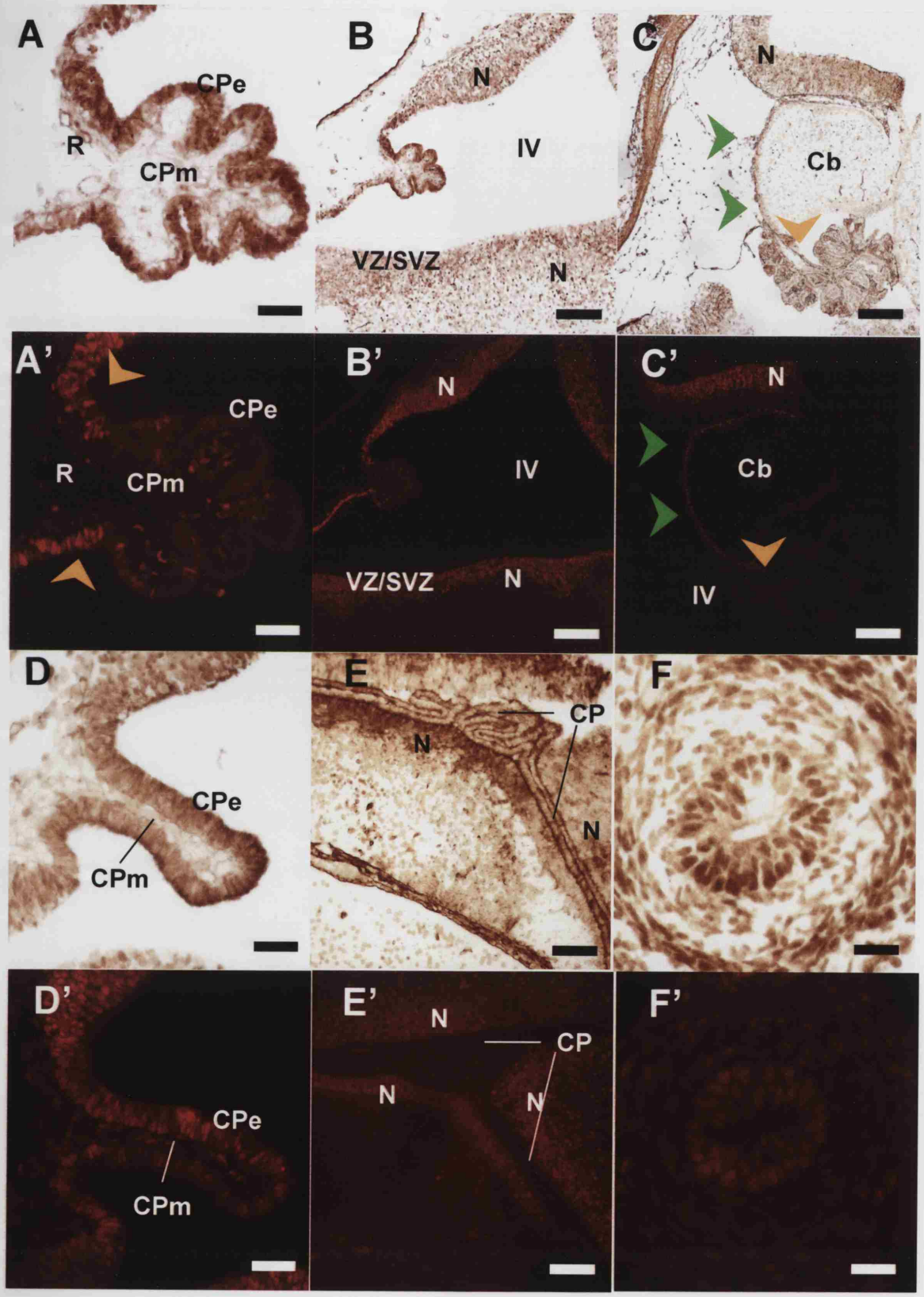
A
CPe
R
CPm
B
N
IV
VZ/SVZ
N
C
N
Cb
A'
CPe
R
CPm
B'
N
IV
VZ/SVZ
N
C'
N
Cb
IV
D
CPe
CPm
E
CP
N
N
F
D'
CPe
CPm
E'
N
CP
N
N
F'

Figure 5. 13 Co-expression of PCNA and E2F5 in the CS 23 human lateral CP

PCNA and E2F5 protein were stained by peroxidase based immunohistochemistry (brown) independently on adjacent sections.

A: Telencephalic CPe; staining for E2F5 is nuclear. **B**: Adjacent section, negatively stained for PCNA. **C**: Root of the telencephalic CPe, staining for E2F5 is both cytoplasmic and nuclear. **D**: Adjacent section; the root of the CP and the neuroepithelium are positively stained for PCNA. **E**: Telencephalic ventricular surface; E2F5 staining is expressed in the cortical plate and less strongly in the ventricular/subventricular zone of the neuroepithelium. **F**: Adjacent section; PCNA staining is only located in the neuroepithelium and not in the cortical plate. Scale bars in A and B are 25 μm, in C, D, E and F are 50 μm. **CP** = choroid plexus, **CPe** = choroid plexus epithelium, **CPm** = choroid plexus mesenchyme, **Ctp** = cortical plate, **L** = lateral ventricle, **N** = neuroepithelium, **R** = CP root, **VZ/SVZ** = ventricular zone/subventricular zone.

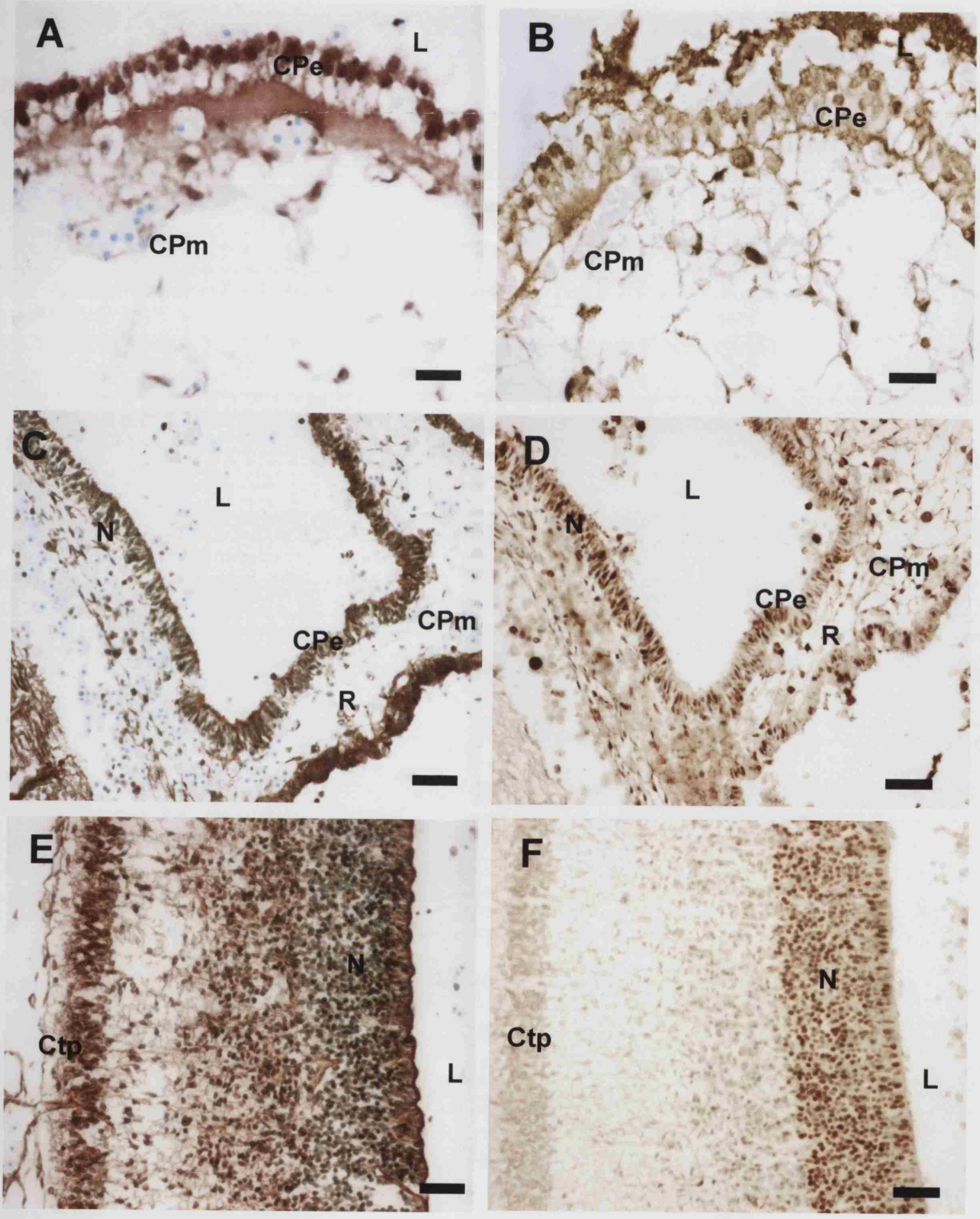
A
L
CPe
CPm
B
L
CPe
CPm
C
L
N
CPm
CPe
R
D
L
N
CPm
CPe
R
E
N
Ctp
L
F
N
Ctp
L

5.2.3 Expression of FoxJ1 protein

FoxJ1 protein was studied in the developing mouse and human embryonic CP by peroxidase based immunohistochemistry. Nuclei were revealed by methyl green counter-staining

5.2.3.1 Expression of FoxJ1 protein in mouse

FoxJ1 protein was strongly expressed in the epithelium of the IVth and lateral CP (Fig. 5.14). At 12.5 dpc, FoxJ1 was present in the cytoplasm of CPe cells in the IVth ventricle CP (Fig. 5.14A), and continued to be expressed in late development at 17.5 dpc (Fig. 5.14B). FoxJ1 was also expressed in the cytoplasm of the 14.5 dpc lateral ventricle CPe (Fig. 5.14C). No staining was observed when the primary antibody was omitted (Fig. 5.14D). As expected the ciliated epithelium of the trachea stained positive for FoxJ1, but a lot of aspecific staining was present in the cartilage (Fig. 5.14E), which was absent if the primary antibody was omitted (Fig. 5.14F).

5.2.3.2 Expression of FOXJ1 protein in human

Staining for FOXJ1 was observed in the whole brain tissue at CS16 of embryonic development (Fig. 5.15A). By CS 17, staining was restricted to the neuroepithelium surrounding the ventricles and the IVth ventricle primordium (Fig. 5.15B). By CS 20, staining was totally restricted to the CPe, and was cytoplasmic (Fig. 5.15C-D).

Figure 5. 14 Expression of FoxJ1 protein in the embryonic mouse CP

Sagittal sections of IVth and lateral CPs at different developmental stages stained for FoxJ1 (brown). Nuclei are counter-stained with methyl green.

A: 12.5 dpc IVth ventricle CP; positive labelling is present exclusively in the CPe cytoplasm. **B**: 17.5 dpc IVth ventricle CP; positive labelling is present in the CPe cytoplasm. **C**: 14.5 dpc lateral CP; positive labelling is present in the CPe cytoplasm. **D**: Negative control in absence of primary body application. **E**: High magnification of the mouse adult trachea; Black arrowheads point to cilia in the tracheal epithelium. Labelling appears mainly cytoplasmic and is not restricted to the epithelium. **F**: Negative control, staining in absence of primary antibody application. Scale bars in A and B are 25 μm, in C and D are 50 μm, in E and F are 15 μm. **CP** = choroid plexus, **CPe** = choroid plexus epithelium, **CPm** = choroid plexus mesenchyme, **Crt** = cartilage, **IV** = fourth ventricle, **L** = lateral ventricle, **Pt** = putamen, **R** = CP root, **Tre** = tracheal epithelium.

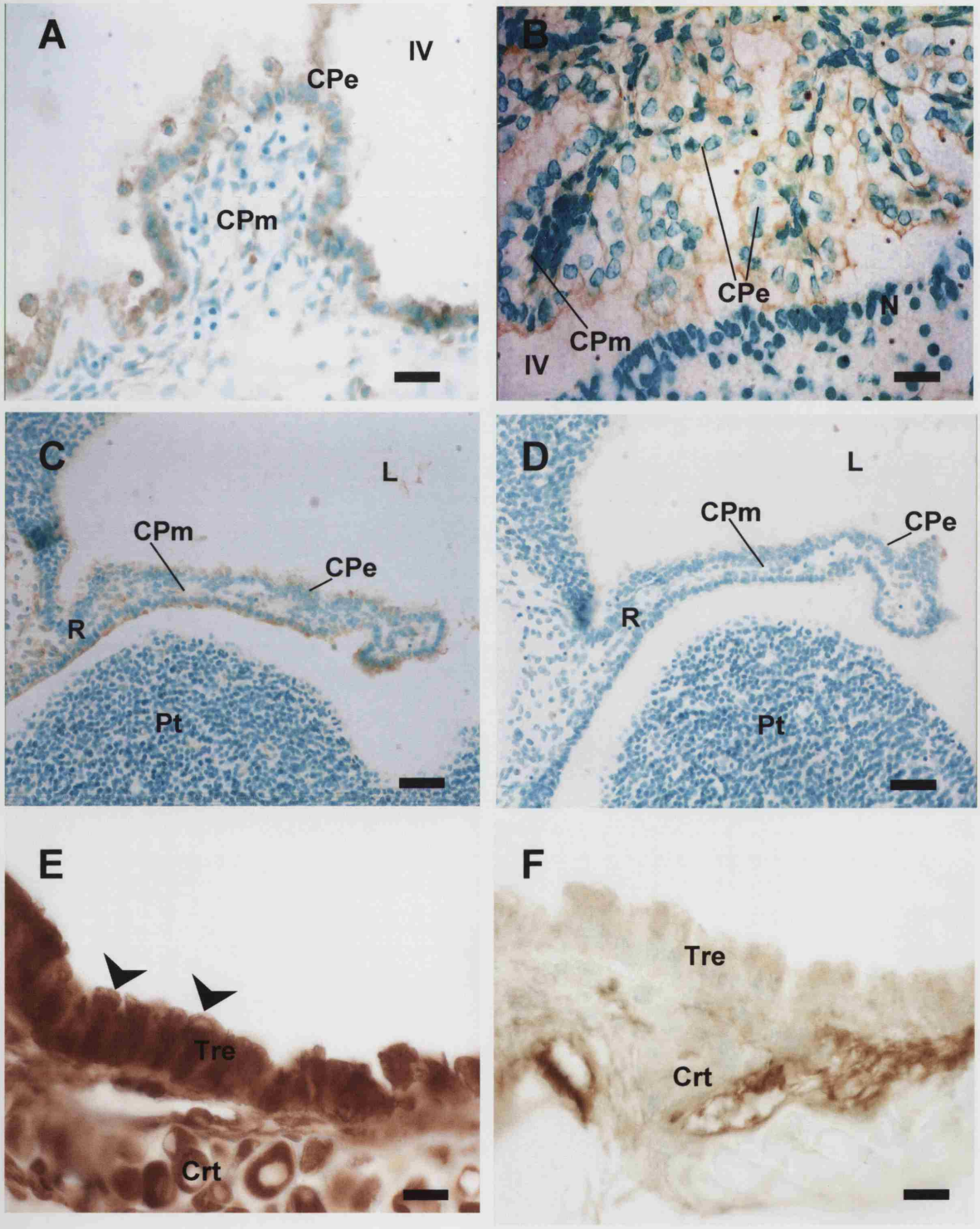
A
IV
CPe
CPm
B
CPe
N
CPm
IV
C
L
CPm
CPe
R
Pt
D
L
CPm
CPe
R
Pt
E
Tre
Crt
F
Tre
Crt

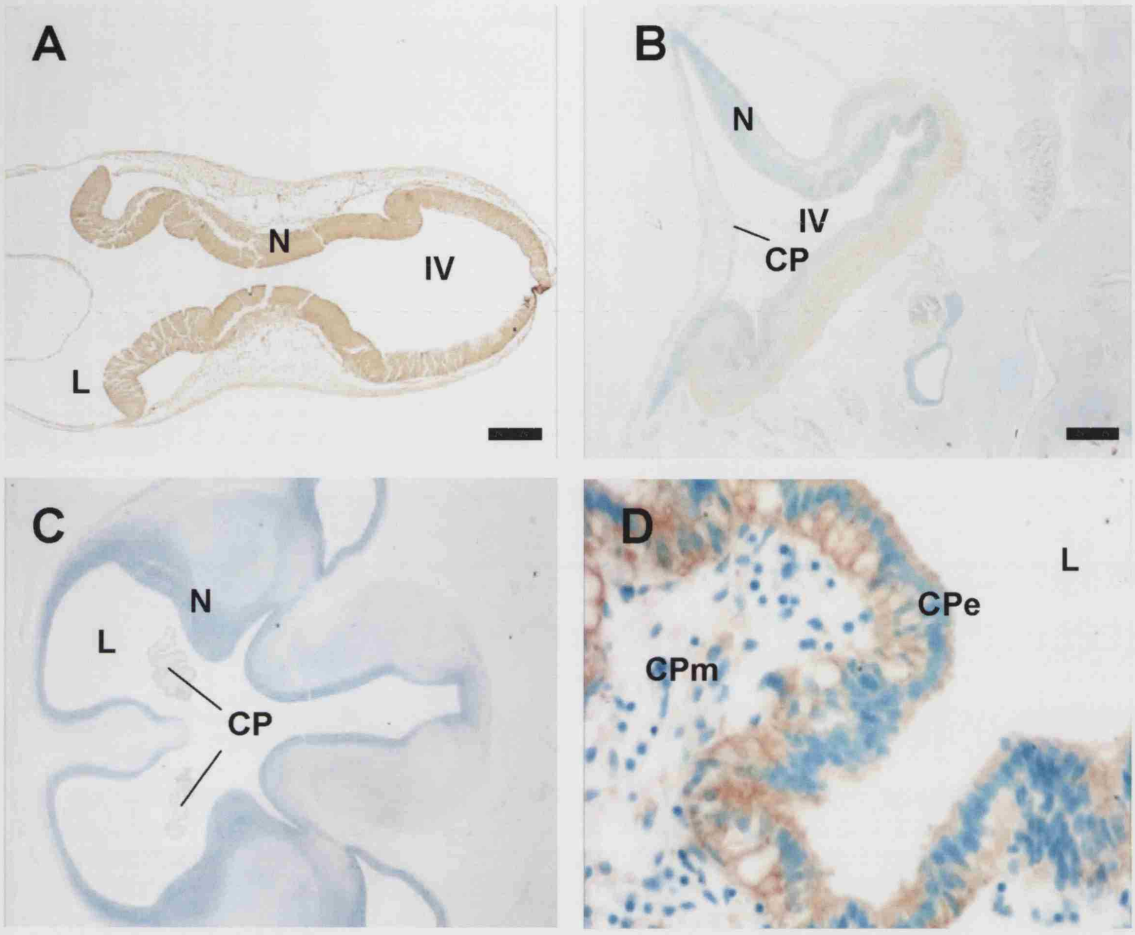

Figure 5. 15 Expression of FOXJ1 protein in the human embryonic CP

Nuclei are counterstained with methyl green. **A:** Transverse view of a CS 16 brain, positive cytoplasmic staining is observed in the neuroepithelium. **B:** Sagittal view of the CS 17 IVth ventricle CP; staining is restricted to the area around the ventricles and there is a low level of expression in the CPe primordium. **C:** Transverse view of a CS 20 IVth ventricle; staining has disappeared from the areas around the ventricles, and is restricted to the CPe. **D:** Higher magnification of the CS 20 CP; staining in the CPe is cytoplasmic. Scale bars in A, B and C are 400 μm, and scale bar in D is 25 μm. **CP** = choroid plexus, **CPe** = choroid plexus epithelium, **CPm** = choroid plexus mesenchyme, **IV** = fourth ventricle, **L** = lateral ventricle, **N** = neuroepithelium.

5.2.4 RNA expression of E2F5, FoxJ1 and p73

The expression of E2F5, FoxJ1 and p73 mRNA was studied by RT-PCR in the developing IVth ventricle CP of the 12.5 dpc, 16.5 dpc, 17.5 dpc and adult mouse (Fig. 5.16A). The study was only performed once. All three genes were expressed at all stages of the CP development. The housekeeping gene GAPDH was used as a positive control to normalize the levels of expression and TTR to confirm the CP nature of the mRNA extracted.

E2F5 appeared to be expressed at higher levels at 12.5dpc and slightly decreased with development. FoxJ1, appeared more strongly expressed at 12.5 dpc and then to be stably expressed at a lower level throughout development. P73 and TTR were stably expressed from 12.5 dpc onwards (Fig. 5.16B).

Figure 5. 16 Expression of E2F5, FoxJ1 and p73 mRNA in the developing mouse choroid plexus

A: 1.5% agarose gel showing RT-PCR products amplified using primer sequences specific for GAPDH, E2F5, FoxJ1, p73 and TTR. Whole CP RNA was prepared from (1) 12.5 dpc, (2) 16.5 dpc, (3) 17.5 dpc embryos, and from (4) adult. Water was used as negative control (5). Expected product sizes are: GAPDH (491 bp), E2F5 (227 bp), FoxJ1 (205 bp), p73 (253 bp), TTR (505 bp). A 100 bp molecular weight ladder is shown to the left. **B**: Bar chart showing levels of expression relative to GAPDH mRNA of FoxJ1, E2F5, p73 and TTR mRNA at the different developmental stages of the CP.

A

GAPDH
E2F5
FOXJ1
1 2 3 4 5 1 2 3 4 5 1 2 3 4 5
600 bp
500 bp
400 bp
300 bp
200 bp
100 bp
P73
TTR
1 2 3 4 5 1 2 3 4 5
500 bp
400 bp
300 bp
200 bp
100 bp

B

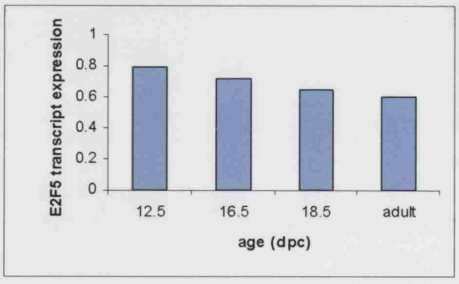
E2F5 transcript expression
1
0.8
0.6
0.4
0.2
0
12.5
16.5
18.5
adult
age (dpc)

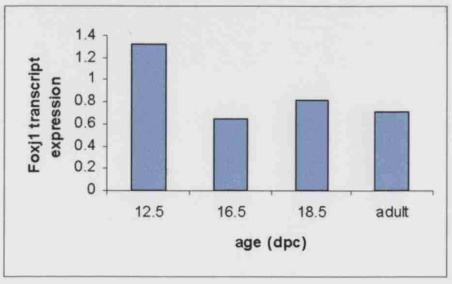
Foxj1 transcript expression
1.4
1.2
1
0.8
0.6
0.4
0.2
0
12.5
16.5
18.5
adult
age (dpc)

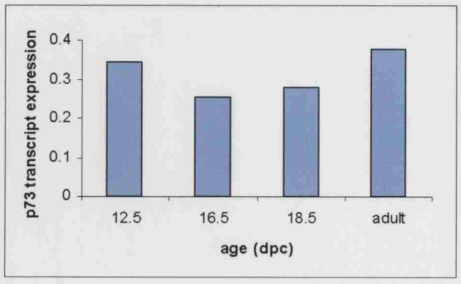
p73 transcript expression
0.4
0.3
0.2
0.1
0
12.5
16.5
18.5
adult
age (dpc)

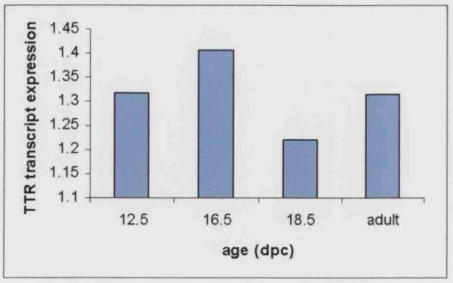
TTR transcript expression
1.45
1.4
1.35
1.3
1.25
1.2
1.15
1.1
12.5
16.5
18.5
adult
age (dpc)

5.3 Discussion

5.3.1 E2F5 expression

Expression of the E2F5 protein in the developing murine and human IVth and lateral CP was studied by immunohistochemistry using two commercially available antibodies both raised against the N-terminal of the E2F5 protein. The two antibodies gave two distinct expression patterns and subcellular types of labelling. Labelling with the first antibody (Labvision) was found to be mainly cytoplasmic, except in the mouse 11.5 dpc CPe and in the embryonic liver where the nuclear staining was however ambiguous. Furthermore, staining was found in the dorsal root ganglia that had previously been reported not to express E2F5 mRNA (Dagnino et al., 1997), though they expressed E2F4 mRNA. Therefore, it is conceivable that this antibody was cross-reacting with the E2F4 protein in tissue sections, even though by Western blot analysis only one single band was detected (not shown). Since the specificity of this antibody was not fully convincing, I tested another commercial antibody to carry out the immunohistochemical analysis. Ideally, one should have used an antibody against a different region of the E2F5 protein (e.g. the C-terminus rather than the N-terminus region) to eliminate the remote possibility that the antibody was only detecting the fraction of E2F5 that remained cytoplasmic. E2F5 does not have a nuclear localisation signal (NLS) and therefore requires either a pocket protein or a DP protein in order to translocate into the nucleus (Mollgard et al., 1979). Thus, it is possible that the fraction of E2F5 that is nuclear is therefore not recognised by the antibody since the epitope it binds to is shielded by the auxiliary proteins. However, no adequate antibodies raised against the C-terminus of the E2F5 protein were commercially available to test this hypothesis.

The immunohistochemical labelling obtained with the second antibody (Santa-Cruz, USA) was more convincing, in that nuclear as well as cytoplasmic staining was observed, as one would expect from a transcription factor like E2F5. At early stages of CP development, the E2F5 protein labelled more strongly the nuclei than the cytoplasm. Interestingly, the intensity of the E2F5 staining appeared to decrease in the mouse CPe around 15.5-16.5 dpc and became largely cytoplasmic. This downregulation of E2F5 protein was also observed with the Labvision antibody, but no shift in intracellular distribution was observed, probably because only the cytoplasmic fraction of E2F5 protein was being detected. The same trend in

downregulation of E2F5 expression and translocation of E2F5 protein was observed in the human CPe. Interestingly, in the early human lateral and IVth ventricle CPs, when the CPe was still columnar pseudostratified, the cells closest to the lumen were most strongly labelled, generally in their nuclei, while cells closest to the mesenchyme had a fainter staining. Regional differences in the CPe were even more marked in the stage II lateral human CP (CS 23) where labelling in the pseudostratified CPe of the lateral CP root was both nuclear and cytoplasmic, whilst a distinct nuclear localization was found in single cell columnar epithelium. Although the downregulation and cytoplasmic translocation of E2F5 protein was only observed at later stages of development in the IVth ventricle CPe, it is conceivable that this would be the case also for the lateral CPe. However, a more complete study may reveal some differences in the pattern of gene expression in the two CPs given that the two CPs are morphologically so distinct, and their development different (Franz, 1994; Thomas et al., 1988; O'Rahilly and Muller, 1990; Netsky and Shuangshoti, 1975).

5.3.2 E2F5 expression and cell proliferation

The expression pattern of the E2F5 protein in the developing mouse and human CPe is summarized in Fig. 5.17. E2F5 appeared to be slightly downregulated with development as supported also by a decrease in mRNA and protein dected by RT-PCR and Western blotting respectively. The most striking finding however, was the apparent translocation of the E2F5 protein from nucleus to cytoplasm during the course of CPe cell differentiation, which was observed in both human and mouse CPe. E2F5 has been reported by some authors to be primarily cytoplasmic in-vivo and in cycling cells especially, due apparently to its lack of nuclear localization signal (NLS) (Humbert et al., 2000; Lindeman et al., 1997). In contrast, this work on the CPe supports the idea that E2F5 protein is capable of more dynamic changes in subcellular compartmentalization. This idea is corroborated by other published studies. Indeed, in exponentially growing myoblasts, E2F5 was reported to be primarily nuclear, whereas in differentiated myotubes, both in-culture and in-vivo, E2F5 was found exclusively in the cytoplasm (Gill and Hamel, 2000). Keratinocyte differentiation induced by Ca^{2+} or BMP-6 signalling was shown to be accompanied by the up-regulation of E2F5 and a change in its subcellular localization from the cytoplasm to the nucleus (D'Souza et al., 2001; Apostolova et al., 2002). Finally, It was shown that the pathway that signals

repression of the growth promoting c-myc gene in the HaCat keratinocyte cell line was mediated by a pre-assembled complex of smad-E2F4 and E2F5-p107 proteins that translocate from the cytoplasm to the nucleus to bind to the c-myc DNA promoter region (Chen et al., 2002).

In general, expression of E2F5 in-vivo is thought to be restricted to terminally differentiated cells (Dagnino et al., 1997; Gaubatz et al., 2000). However, this observation also does not always hold true. For instance, E2F5 mRNA expression has been reported in the proliferating undifferentiated ventricular regions of the developing mouse brain and in the embryonic retinoblastic cell layer (Dagnino et al., 1997). The same authors also showed that by late gestation, at 17.5-19.5 dpc, the transcript levels for E2F5 become very low. Indeed, I confirmed this observation by immunohistochemistry and showed a correlation between the expression of E2F5 and PCNA in the mouse neuroepithelium. Western blot of whole protein extracts of brains taken at different developmental stages confirmed this decrease in E2F5 expression, which was most striking in the adult brain. In the human, however, this relationship between PCNA and E2F5 was not so evident. It seemed to be quite strong at the early stages of development CS 18-20, but by CS 23 expression of E2F5 did not seem to be restricted to the proliferating PCNA positive neural progenitor cells, but appeared also to be expressed in the non-proliferating cells of the cortical plate.

In the mouse CPe and the human IVth ventricle CPe, the expression and sub-localization of E2F5 was clearly not related to the proliferative state of the cells. Nonetheless, in the mouse it was found that at later stages, from 15.5 dpc to 17.5 dpc, the nuclear expression of E2F5 persisted in the root of the CP, which was also positive for PCNA. In the human lateral CPe, it was less clear whether or not E2F5 expression and its compartmentalisation related to CPe cell proliferation. In proliferating pseudostratified columnar epithelium, E2F5 labelling was both cytoplasmic and nuclear, whereas in the monostratified columnar differentiated epithelium the labelling was restricted to the nuclear compartment of the cells. This observation will need to be confirmed using a double-labelling method, which was not possible in this study, due to the incompatibility in unmasking method for the two antibodies I used. If indeed confirmed, this would suggest that the mechanism of development of the human lateral CP somehow differs from that of the IVth ventricle CP and even the mouse lateral CP.

The downregulation and translocation of E2F5 from a predominantly nuclear to a cytoplasmic compartment as CPe differentiation progresses (as observed in mouse CPe and human IVth CPe) would indicate that E2F5 has some sort of role in the differentiation process of the CPe between the initial formation of the CPe at stage I and maturation at stage II (see Table 1.4). By the time the CP reaches stage III maturation, E2F5 is downregulated and predominantly cytoplasmic in most of the CPe, and may have a different function. The biological significance of these events still remains to be understood, especially as they do not seem to coincide with changes in the cell cycle. Nonetheless, these results suggest that E2F5 must have an important developmental role in determining the normal differentiation of the CPe cells, similar to what has been described in other cell types (Gill and Hamel, 2000; D'Souza et al., 2001; Apostolova et al., 2002; Chen et al., 2002), and as supported by the abnormal CP development in the *E2F5* knockout mouse (Lindeman et al., 1998).

This study also refutes the idea that E2F5 is uniquely involved in maintaining cells in a differentiated state, but argues for different roles of the E2F5 protein depending on the cell type. It is possible that in neural progenitor cells or in the epithelial cells of the embryonic gut, E2F5 is associated with proliferation, whereas in other cell types, like the CPe cells, it is mainly involved in directing cell differentiation.

Figure 5. 17 Schematic summary of E2F5 protein subcellular expression during choroid plexus epithelium (CPe) development

The stages of development (I, II, III, and IV) of the CPe (CPe) in mouse and human are based on those defined for the human lateral CPe by (Shuangshoti and Netsky, 1966). For each stage of development the corresponding embryonic age (human: Carnagie stage (CS) and mouse: days post-conception, dpc) is given and corresponds to the beginning of the developmental stages. **A**: E2F5 protein expression in the mouse CPe at different developmental stages (I, II, III, IV). The developmental stages for the lateral (Lat.) and IVth ventricle (IVth) CPs are given. (Note that for the IVth ventricle CP, at 12.5 dpc the CPe is mostly single cell columnar with pseudostratified columnar epithelium at its root). **B**: E2F5 protein expression in the developing human lateral CP; labelling is both nuclear and cytoplasmic in pseudostratified epithelium (stage I) and nuclear in single columnar epithelium (stage II); labelling in cuboidal epithelium (Stage III/IV) was not studied. **C**: E2F5 protein expression in the developing human IVth ventricle CP; in pseudostratified epithelium (Stage I) labelling was mainly nuclear, with nuclear labelling being stronger in cells closest to the lumen. The model is not based on CS 18 CPe but rather on the expression of E2F5 in the CS 23 IVth ventricle CPe, where some regions were columnar pseudostratified (a Stage I type of organisation) and single columnar (a Stage II organisation). Expression of E2F5 was both cytoplasmic and nuclear in single columnar epithelium (stage II), and in cuboidal epithelium (stage III/IV) expression was much lower and cytoplasmic.

A. Mouse lateral and IVth ventricle CPe

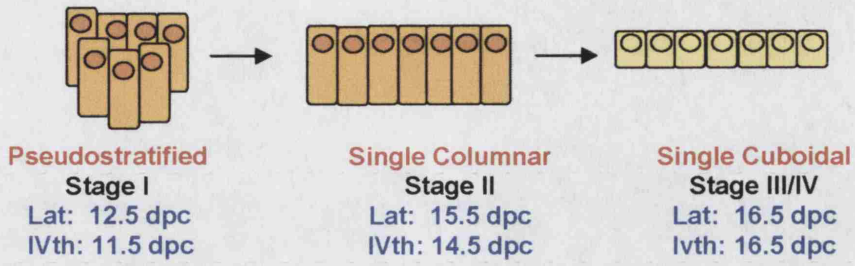

B. Human lateral CPe

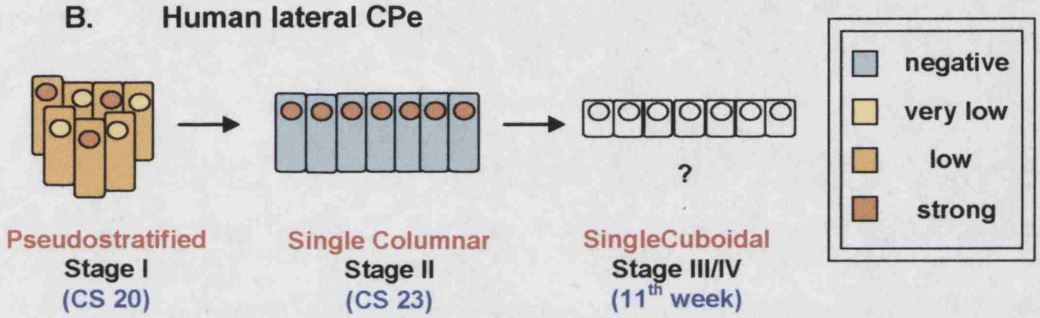

C. Human IVth ventricle CPe

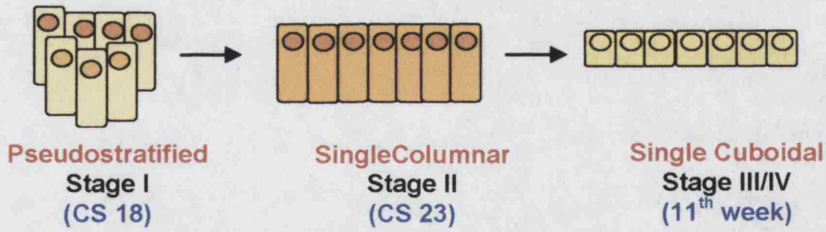

5.3.3 FoxJ1 expression

The expression of FoxJ1 was studied in the developing embryonic CP, and was shown to be expressed in the cytoplasm of the CPe cells. However, this is not in agreement with the predominant nuclear localization for FoxJ1 reported in the literature (Tichelaar et al., 1999; Blatt et al., 1999). FoxJ1 is a member of the forkhead transcription factor family that translocate from the cytoplasm to the nucleus. As a transcription factor, it makes sense that it should be located to the nucleus, it is nevertheless possible that the antibody used in this study recognized the portion of forkhead protein that was cytoplasmic; this would explain why the signal was so low. Unfortunately, the company providing the antibody did not disclose against which part of the FoxJ1 protein the antibody was raised. No FoxJ1 peptide was available to confirm the specificity of the labelling, and the antibody did not work in Western blot. As a positive control, I stained the ciliated epithelial cells of the trachea. They were indeed positive (Blatt et al., 1999), although a lot of background staining was also present. Since this antibody was not very satisfying, the pattern of expression obtained in human was taken with caution. It should nevertheless be interesting to study the expression pattern of FOXJ1 transcripts in order to see whether it mirrors that of FOXJ1 protein, which I found expressed all over the early embryonic brain and to become increasingly restricted to the ventricular zone and then uniquely to the CPe, by the time this one became morphologically apparent.

5.3.4 RNA expression of genes whose knockout cause hydrocephalus

The expression of E2F5, FoxJ1 and p73 mRNA in the whole CP was studied at different developmental stages by RT-PCR. The major pitfall of this study was that it assayed gene expression in both the CP epithelium and mesenchyme. For FoxJ1, this problem was less serious since their expression is specific to the CPe. Nonetheless, it was evident that transcripts for all four genes (*E2F5*, *FoxJ1*, *p73* were expressed at all stages of CP development that were studied. Interestingly, it appeared that E2F5 was expressed most strongly in the 12.5 dpc CP, and then steadily fell to lower levels by the end of gestation and adulthood. The decrease was not as dramatic as that observed at the protein level by immunohistochemitry, but this may have been due to the mesenchymal mRNA contribution clouding the real decrease in E2F5 transcript levels

in the epithelium. FoxJ1 mRNA also appeared most stongly expressed at 12.5dpc and then stably expressed throughout the rest of development. However, the high expression at 12.5dpc may have been artifactual since by immunohistochemistry FoxJ1 protein was expressed at the same level at all ages studied. p73 mRNA was found expressed at the same level at all ages studied; future studies will however show whether the protein is also stably expressed and whether it is follows a similar distribution to that of E2F5.

5.3.5 Summary

In this chapter, the expression of genes involved in the development of the CPe and associated with the homeostasis of CSF secretion, namely *E2F5*, *FoxJ1* and *p73*, was confirmed at the protein level by immunohistochemistry or/and at the RNA level by semi-quantitative RT-PCR of the whole CP. E2F5 protein expression was shown to be downregulated in the CPe at late gestation; this was confirmed by RT-PCR of the whole CP. The subcellular location of the expression of E2F5 was also found to vary during the course of development and between species. The meaning for these changes and differences between species remained speculative.

The presence of FoxJ1 protein was confirmed in the embryonic CPe, and shown to be located in the cytoplasm. This subcellular distribution conflicted with that published in the literature, raising questions about the actual specificity of the antibody. Presence of transcripts for FoxJ1 was observed throughout development, in agreement with previous published work.

Expression of *p73* was studied only at the mRNA level by RT-PCR, and no significant variation was observed during CP development. A study of P73 protein expression would be important to assess whether the protein is actually expressed at the same levels throughout development.

Chapter 6 Characterization of embryonic murine choroid plexus epithelial cells in culture

6.1 Introduction

The previous chapters were concerned with characterizing the in-vivo development of the choroid plexuses (CPs). They confirmed and extended the analysis of genes found both important for the normal maturation and CSF secretory function of the CPe. The purpose of this chapter was to farther characterize a culture system for growing CPe cells, which had been previously used by S.Reid (PhD thesis, 2002) to study these cells in-vitro. This cell culture model was first described by Thomas et al. (1992) who showed that mid-gestational embryonic CPe cells cultured on Matrigel, a laminin rich basement membrane matrix, formed spherical, fluid filled hollow structures that were called vesicles. However, this cell culture model was insufficiently characterised to be useful for functional studies. There was no knowledge of how the vesicles formed and increased in size over time. The aim of this chapter was therefore to focus on the characterization of this CPe vesicle culture in order to shed light on the dynamics of vesicle formation and growth, at the cellular level. I will briefly summarize the advantages of this culture system/model over others, and then discuss what is known of this vesicle model and highlight the aspects of this model that needed to be characterized.

6.1.1 A primary culture of embryonic choroid plexus epithelial cells

Thomas et al. (1992) found that dissociated embryonic CPe cells responded dramatically to the Matrigel substratum, clustering into small aggregates within two days. By four days in culture, the CPe cells had formed small fluid filled spherical structures, had apical and basal polarity, displayed ultrastructural characteristics of CPe cells *in vivo*, and transcribed transthyretin, (TTR). The vesicles were hollow and

fluid filled, suggestive of a functional secretory capacity, despite the absence of a blood supply. In contrast, CPe cells cultured on collagen alone did not exhibit the ultrastructural characteristics nor secretory capacity of CPe cells *in vivo*, although gene expression for TTR was maintained (Thomas et al., 1992). Laminin, which is the main component of Matrigel was not sufficient by itself to rescue the CPe phenotype of the cells. Thomas et al. (1996) thus hypothesised that the CPe cells must be interacting with components of the Matrigel other than laminin to form a functional polarized epithelium. Southwell et al. (1993) showed that embryonic CPe cells formed monolayers on Transwell inserts coated with type I and III collagen gels and laminin. Plating the CPe cells on Matrigel, however, was best suited for studying CPe cell function because the cells not only retained their epithelial phenotype and their in-vivo secretory functions, but also formed vesicular structures, with correct polarization (villi in the lumen), that allowed to create an artificial environment similar to the natural environment in the brain.

6.1.2 Characterization of choroid plexus epithelial vesicles

Both Thomas et al (1992) and Reid S. (PhD thesis 2002) characterized the cells forming the vesicles at the ultra-structural level. They both showed that the CPe cells plated in Matrigel retained their in-vivo cuboidal epithelial phenotype with a distinct apical and basal polarity: the apical surfaces of the CPe cells were rich in microvilli, which protruded into the central lumen of the vesicle. The basal surfaces of the CPe cells were surrounded by Matrigel. Tight junctions and zonula adherens junctions were evident between adjacent CPe cells. Furthermore, the cells expressed and secreted TTR. However, apart from the knowledge that the CPe cells initially formed aggregates and after four days in culture formed fluid filled vesicles that grew in time (Fig. 6.1), scant information was available about the cellular mechanisms underlying vesicle formation and growth. It was not established whether vesicle growth ever reached a plateau, whether the vesicles were still structures or quite dynamic, or how much cell migration, cell-cell adhesion, and cell proliferation are involved in vesicle formation and growth. Perhaps most importantly, the active secretion of fluid by the CPe was assumed but never shown experimentally, nor was its role in vesicle growth investigated.

Therefore I set to address these issues and characterize in detail the events leading to vesicle formation and growth. The first step in this study was to

characterize the phenotype of the CPe vesicles in culture at the cellular and at the molecular level, to confirm that I was able to reproduce the same type of cultures described by Reid S. and Thomas et al (1992), and confirm the CPe phenotype of the cells. The second part of this study concentrated on the characterization of the role of cell migration and cell:cell adhesion during the early formation of vesicles and later during the growth of vesicles using time-lapse microscopy. In the third part of this study, I assessed the role of cell proliferation during the early formation and growth of vesicles. Cell proliferation was studied by green fluorescence immunocytochemistry using a primary antibody raised against human phosphorylated histone 3 protein (p-H3). In addition, the importance of cell proliferation for the early formation of vesicles was also studied by looking at the sensitivity of this process to treatment with cytosine arabinoside (Ara-C), which is a cytotoxic structural analog of 2'-deoxycytidine; Ara-C is a nucleoside with an arabinose sugar component, and acts as an inhibitor of DNA synthesis (Brewer and Scott, 1983). It therefore targets primarily mitotic cells rather than quiescent cells. Finally, this study also investigated whether active fluid secretion into the lumen of the vesicles did occur and whether it was important for the growth of the vesicles. To this purpose, a combination of drugs that specifically inhibit the enzymatic pathways involved in the secretion of fluid, and that have been shown to inhibit CSF secretion by the CPe in-vivo, was used. They were acetazolamide, which is an inhibitor of the carbonic anhydrase enzyme, and ouabain, that specifically inhibits the Na^+/K^+ ATPase enzymatic pump (Davson and Segal, 1970) (see Chap.1.2.2.2).

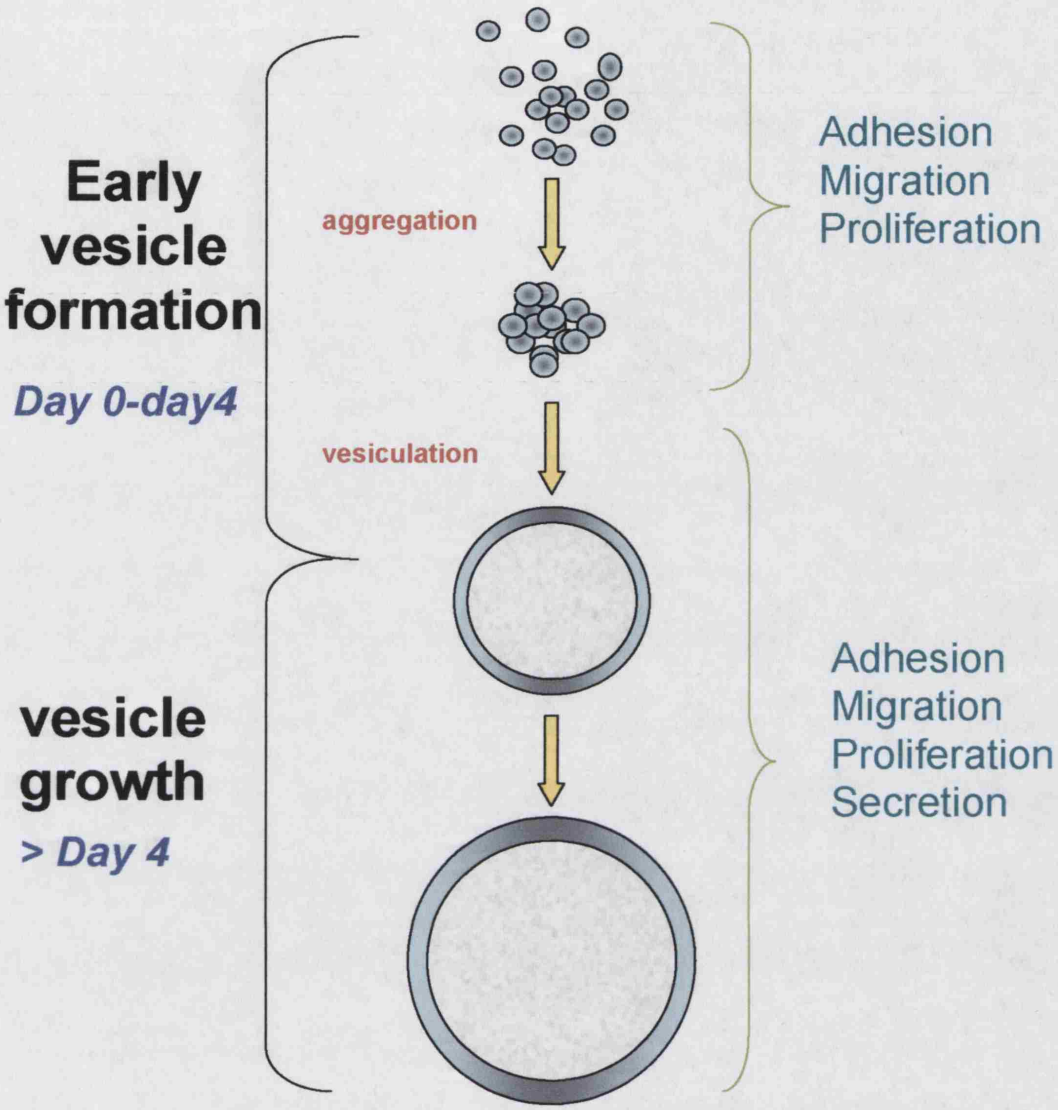

Figure 6. 1 Diagrammatic model of the two main phases of vesicle formation

Initial vesicle formation: this first phase is separated into the aggregation of the single CPe cells into aggregates, and the hollowing out of aggregates into vesicles (vesiculation). **Vesicle growth:** this second phase refers to the steady increase in size of the vesicles with time. At each step, the possible cellular events that could be underlying vesicle formation and growth are given.

6.2 Results

6.2.1 Characterization of CPe vesicles

6.2.1.1 CPe vesicle cultures

CPe cells isolated from 12.5dpc mice embryos were seeded on Matrigel where they invaded the matrix and formed fluid filled vesicles within 72 hours, as previously reported (Thomas et al., 1992, Stadler et al., 1994). The cells obtained from one litter were plated at a density of $20x10^{\wedge 4}$ cells/ml. Only two to three cultures could be produced per dissection. The cultures were in general free of any contaminating cells; infrequently some neuronal cells were identified that could easily be distinguished because of their axonal radial projections; mesenchymal cells were also sometimes seen, which formed clumps that did not grow in size as noted before (Stadler and Dziadek, 1996; Thomas et al., 1992). Mesenchymal and neuronal cells did not mix with CPe cells. On the whole, these cultures provided a very pure population of CPe cells (Fig 6.2A-B), which was comparable to that obtained by other authors (Thomas et al., 1992; Reid S, 2001).

When vesicles grown for at least four days in culture were stained with Hoechst dye and optically dissected by deconvolution analysis, the vesicles obtained were confirmed to be hollow (see sequence Fig. 6.2C-D). This could also be observed under Hoffman optics (Fig. 6.2A-B). Furthermore, this analysis showed that the walls of young vesicles were one to two cells thick (Fig 6.2C), and in older vesicles were usually one cell thick (not shown). The CPe cells forming the wall of the vesicles labelled positively for ZO-1 protein, a member of the membrane associated guanylate cyclase kinase (MAGUK) family of proteins that has been found in tight junction structures. Immunofluorescent labelling was apparent at the point of contacts between CPe cells (Fig. 6.2E-F).

Figure 6. 2 CPe vesicle culture characterization.

A: Low magnification of vesicles in culture viewed under Hoffman optics. **B**: Higher magnification of a vesicle viewed under Hoffman optics. **C**: Top view of a vesicle stained with nuclear Hoechst dye (blue). **D**: Equatorial view of the same vesicle. **E**: High power magnification of a vesicle surface labelled for ZO-1 protein (bright red). **F**: Same field of view with nuclei revealed by Hoechst dye. Scale bars in A, C, D are 200 μm; scale bar in B is 50 μm; scale bars in E-F are 20 μm.

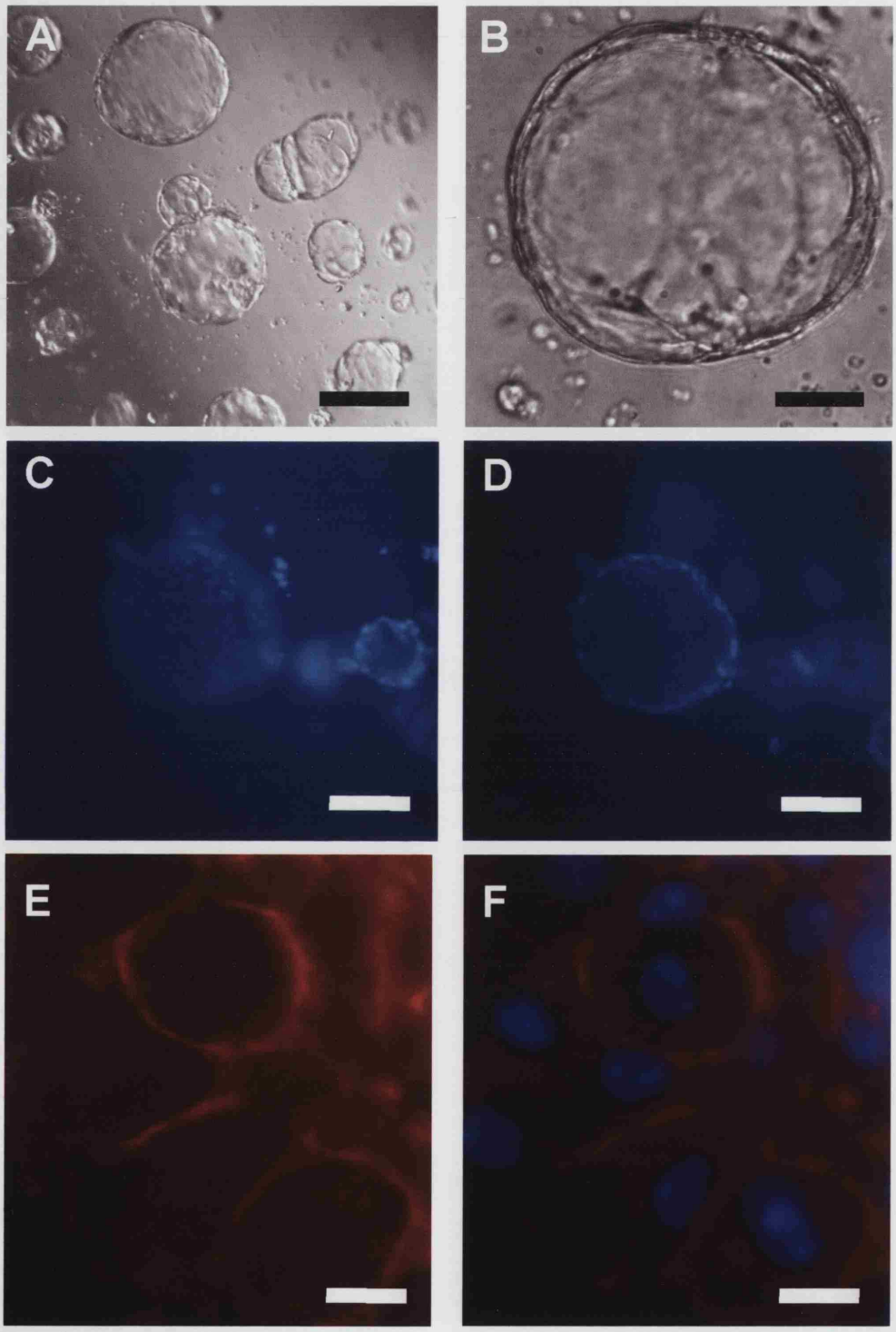
A
B
C
D
E
F

6.2.1.2 mRNA expression of CPe vesicles

E2F5, FoxJ1, p73 and TTR are four genes important for the normal development of the CPe in-vivo. In the CNS, TTR mRNA is exclusively expressed in the CPe (see Chapter 4 and (Thomas et al., 1989), (Kuchler-Bopp et al., 1998). TTR is the most specific marker for identifying the CPe, but, in order to establish whether expression of other genes important for CPe development and function was maintained in the CPe vesicles, expression of FoxJ1, E2F5 and p73 in the CPe culture was studied. Their expression analysed by RT-PCR in eight day cultures. As a positive control, the mRNA from freshly dissected IVth ventricle CP from 12.5 dpc embryos was used. GAPDH was used as an internal control since it is expressed abundantly in all cells and should reflect mRNA content. The amount of total mRNA extracted from vesicle cultures was low, precluding accurate semi-quantitative analysis.

Expression of E2F5, FoxJ1, p73 and TTR mRNA was analysed in day 8 vesicles (Fig. 6.3). Their relative levels of expression in the vesicles were similar to those found in the whole CP after the same number of cell cycles. TTR and FoxJ1 bands were the strongest, whilst the intensity of the E2F5 band was lower and that of p73 was very weak. Since FoxJ1 is only expressed in the ciliated ependymal cells of the ventricles but not in the mesenchyme, it is along with TTR the most specific CPe marker. This gene expression profile thus confirmed that CPe cells grown on Matrigel conserved their *in-vivo* CPe phenotype.

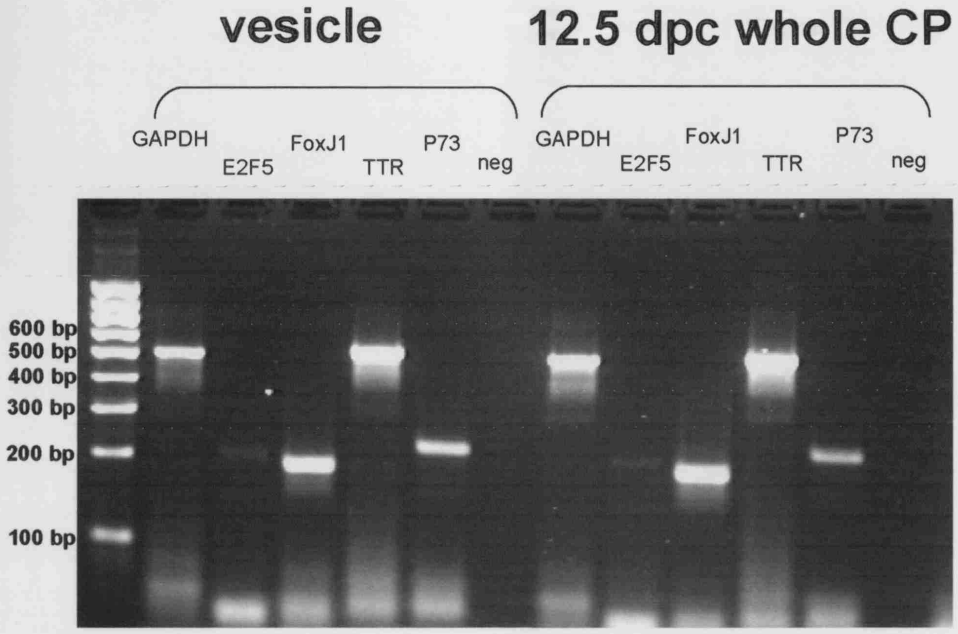

Figure 6. 3 mRNA expression profile of CPe vesicles.

RT-PCR products for GAPDH (491 bp), E2F5 (227 bp), FoxJ1 (205 bp), p73 (253 bp) and TTR (505 bp) ran on 1.5% agarose gel electrophoresis loaded with ethidium bromide. The molecular weight ladder is on the left and band size are indicated. The RT-PCR products of mRNA extracted from an eight day old vesicle and freshly dissected 12.5 dpc mouse whole IVth ventricle CPs are shown. RT-PCR products for GAPDH and "no CDNA" (replaced with water) controls (neg) were run for each tissue.

6.2.2 Sequence of events in vesicle formation

Dissociated single CPe cells seeded on Matrigel formed vesicles after about three to four days as described by Thomas et al. (1992). In this study, unless mentioned otherwise, days in culture are defined as the days in culture since first seeding the CPe cells. The initial stages of vesicle formation were monitored daily over four days of growth (Fig. 6.4). It was found that the formation of vesicles always followed the same sequence of events. The first stage started with the dissociated single CPe cells infiltrating the matrix. After 24 hours in culture, the cells formed distinct aggregates of various sizes, although many single cells were still present. After two days in culture, the aggregates usually appeared tighter and some aggregates had fused with each other. After three days, the aggregates appeared compact and some were starting to become hollow. By the fourth day in culture, most aggregates had become hollow vesicles.

This study indicated that most of the cell movements happened within the first 48 hours after seeding the CPe cells, when the cells formed aggregates. After two days in culture most of the cells had been incorporated into cell aggregates of various sizes, thereafter the aggregates did not show any obvious changes in number, location and even size until they formed vesicles after about three to four days in culture. Thus after two days in culture, the vesicle culture was relatively inert in terms of cell migration or aggregates fusing together. This was analysed by plotting the areas of the aggregates formed after two days in culture against the area of the vesicle they formed after four days. The scatter plot showed a positive correlation coefficient of R: 0.8, indicating a high degree of linear association between the two variables (Fig. 6.5). Thus the size of a given vesicle was directly proportional to the size of the aggregate it originated from, although the relationship was not absolute due to some residual cell/aggregate recruitment.

Figure 6. 4 Sequence of events leading to CPe vesicle formation

The growth of dissociated single CPe cells seeded onto Matrigel is followed over four days and pictures taken every 24 hours. **Day 0:** shows the cells immediately after seeding, as a single cell suspension. **Day 1:** same field of view 24 hours later; the CPe cells have formed loose aggregates and few isolated cells are observed. **Day 2**: same field of view; the aggregates appear more compact and have started to become hollow. **Day 4**: all aggregates have formed vesicles, but have hardly changed in number or location compared to day 2; some aggregates are numbered (1-5) to help visualization. Scale bar is 200 μm (shown in bottom picture).

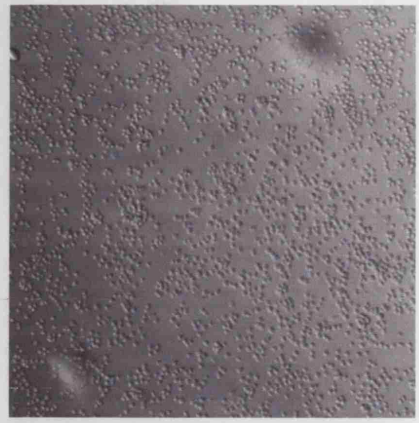

Day 0

(single CPe cells)

Day 1

(aggregation of CPe cells)

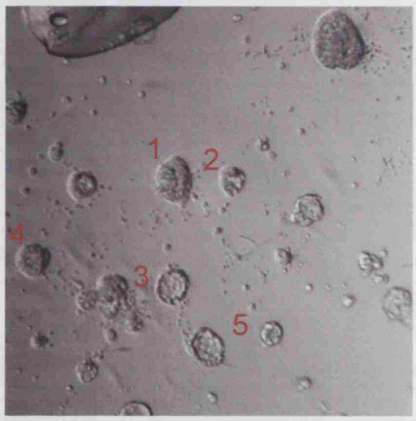

Day 2

(compaction of aggregates and first vesiculation events)

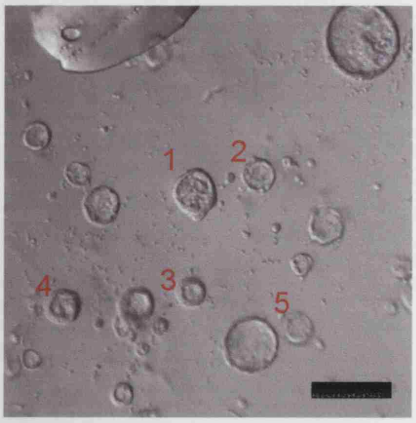

Day 4

(vesiculation of most aggregates)

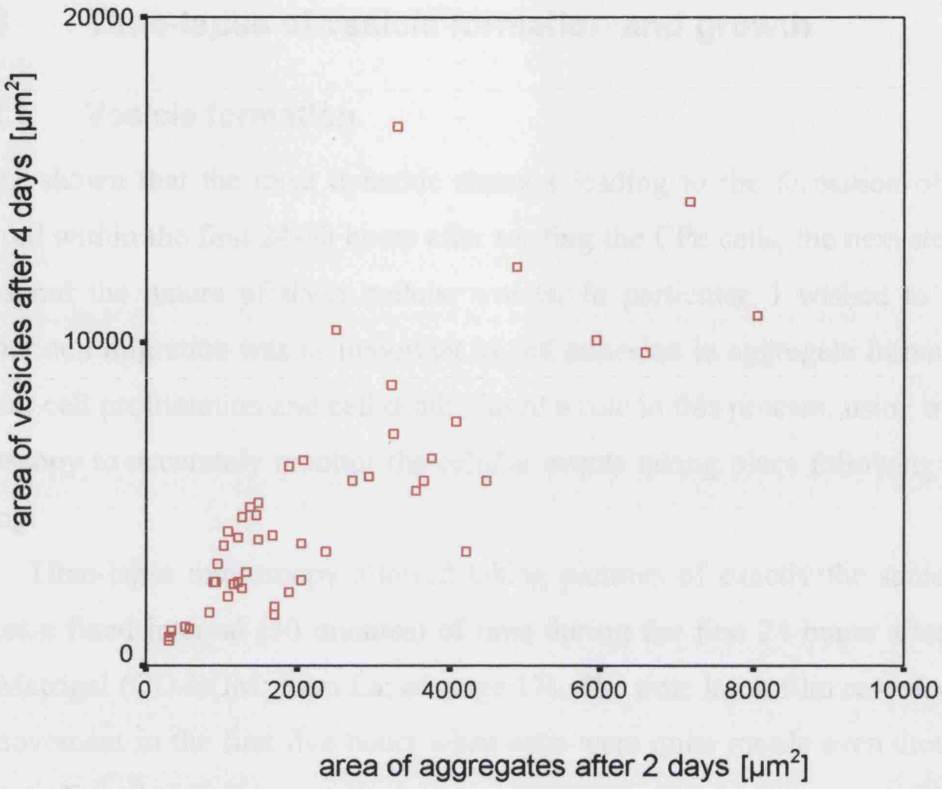

Figure 6. 5 Linear relationship between the size of aggregates at day 2 and the size of vesicles at day 4.

The area of the equatorial plane (see Chap. 3.3.2.1 for definition) of 50 CPe aggregates formed after two days in culture is plotted against the area of the equatorial plane of the same entities as they form vesicles. The correlation coefficient between the points (using a Pearson's correlation test) is R: 0.815, (p: 1.0×10^{-6}).

6.2.3 Time-lapse of vesicle formation and growth

6.2.3.1 Vesicle formation

Having shown that the most dynamic changes leading to the formation of vesicles occurred within the first 24-30 hours after seeding the CPe cells, the next step was to understand the nature of these cellular events. In particular, I wished to establish whether cell migration was as important as cell adhesion in aggregate formation, and whether cell proliferation and cell death played a role in this process, using time-lapse microscopy to accurately monitor the cellular events taking place following CPe cell seeding.

Time-lapse microscopy allowed taking pictures of exactly the same field of view at a fixed interval (30 minutes) of time during the first 24 hours after seeding unto Matrigel (CD-ROM: Film I.a; cf. page 17). The time lapse film revealed a lot of cell movement in the first five hours when cells were quite motile even though most of them adhered to their nearest neighbour. The formation of aggregates then tended to attract isolated cells so that cell migration was not stochastic. After five hours, loose aggregates had already formed. By ten hours, these aggregates became more defined and by 20 hours it had usually reached their final size and very few single cells were present (Fig. 6.6A). At high power magnification after 5 hours in culture, no visible signs of proliferation or cell death were observed (Fig. 6.6B).

A similar time lapse study was carried out over 16 hours to follow how much cell migration and cell incorporation into aggregates took place after one day (~ 30 hours) in culture (CD-ROM: Film I.b; cf. page 17); (Fig. 6.6B-D). In order to facilitate the monitoring of cells becoming aggregates, cells loaded with the red fluorescent vital dye diI were mixed 1:4 with the non-labelled cells before seeding onto Matrigel. This gave rise to mosaic vesicles composed of fluorescently labelled CPe cells and unlabelled cells. Thus, it was easier to monitor the incorporation of single cells in the aggregates, which typically would only have a few red labelled cells. The result of this study showed that in general single CPe cells and CPe aggregates were rather non-motile after one day in culture compared to the early stages (the first 20 hours) in culture. Nonetheless, some single CPe cells and aggregates could display a relatively dynamic behaviour and were capable of migrating short distances to incorporate other CPe cells or aggregates.

Figure 6. 6 Cell dynamic in early vesicle formation

A: Representative frames from a time-lapse microscopy experiment monitoring dissociated CPe cells seeded on Matrigel over 20 hours (Film I.b). **B**: Representative frames of a time lapse microscopy experiment where a one day culture of diI labelled CPe cells plated with non labelled CPe cells was followed over 16 hours (one frame every 20 minutes); the CPe cells and aggregates are generally less motile than in the first 20 hours in culture after seeding the cells. **C:** Higher magnification of the field in (B) following the recruitment of a CPe cell into an aggregate over 200 minutes time. **D:** Higher magnification of the field in (B) following the recruitment of a cell into an aggregate over 120 minutes. In C-D, the arrowhead shows a particular aggregate migrating towards a cell, and the star the cell that is being recruited into the aggregate. Scale bar in A is 200 μm, and in B is 100 μm, scale bars in C-D are 20 μm.

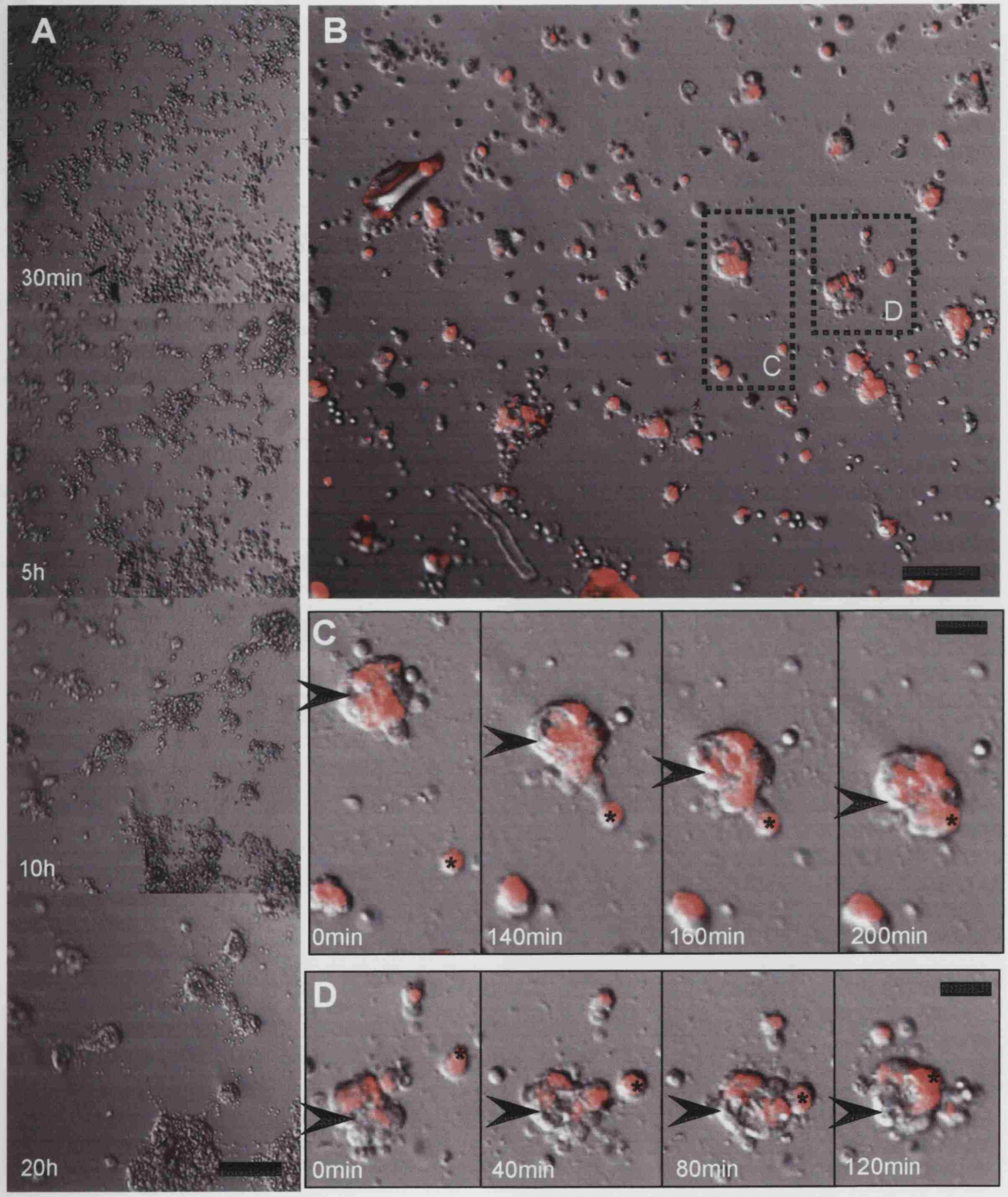
A
30min
5h
10h
20h
B
C
D
C
0min
140min
160min
200min
D
0min
40min
80min
120min

6.2.3.2 The dynamic of growth

Time-lapse microscopy was used to understand how vesicles grew in size over time, whether it was a linear process and whether CPe cells were recruited into the vesicle walls. The growth of vesicles that had already been eight days in culture was followed over 48 hours taking pictures at one hour intervals. Vesicles were observed to be very dynamic structures. They were quite pulsatile and they contracted to different degrees and re-expanded. However, the overall mean size of the vesicle population increased more or less linearly (Fig. 6.7A, and Film II.a; cf. page 17).

A fraction of CPe cells were labelled with fluorescent red vital dye diI in order to help visualize cell incorporation events monitored by time-lapse microscopy over 16 hours. After 5 days in culture, not many single CPe cells were left in the culture, and most aggregates were most likely mesenchymal cells, which did not mix with CPe cells. Hence, at this stage, single CPe cell recruitment into the vesicles was too infrequent to account for the growth of the vesicles (Fig. 6.7B, and Film II.b; cf. page 17).

After 15-20 days in culture the vesicles reached a growth plateau; individual vesicles did not grow unless they fused and recombined with other neighbouring vesicles. Interestingly, when diI labelled dissociated CPe cells were added to vesicles that had reached their growth plateau after 15 days in culture, these vesicles resumed growth and their size was much increased four days after seeding the labelled cells (Fig. 6.8). This resuming of growth coincided with the incorporation of diI labelled cells into the vesicles. This experiment showed that the limiting factor in the final size of the vesicles is the amount of CPe cells available in the culture.

The other important observation from the time-lapse experiments with diI was that the diI signal did not spread around nor became diluted in time, as one would have expected if the cells were proliferating. Of course this method was not in itself an adequate or sufficiently sensitive assessment of cell proliferation. Hence, in order to identify cells undergoing mitosis cultures were stained with a polyclonal antibody raised against human phosphorylated histone H3 (p-H3).

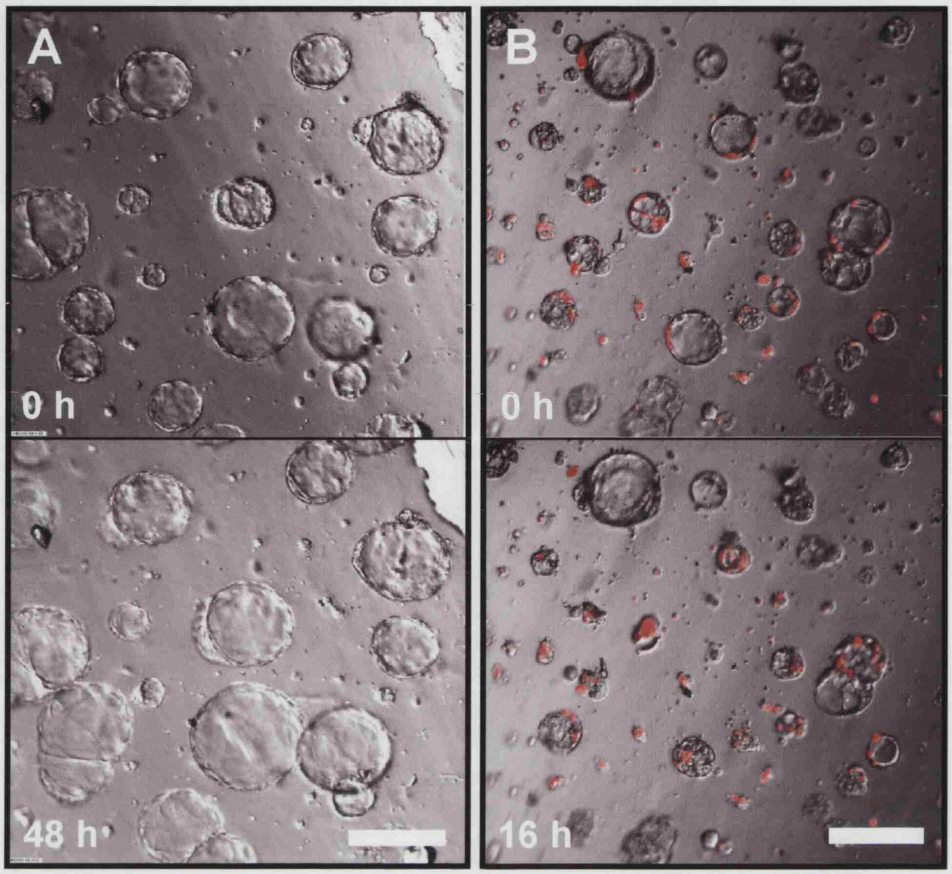

Figure 6. 7 Dynamic of growth of mature of vesicles.

A: Representative frames from a 48 hour long time-lapse microscopy experiment following the growth of vesicles formed 8 days after seeding CPe cells on Matrigel. The time at which the pictures were taken (h, hours) is indicated on each frame. The vesicles are very dynamic, and contract and expand to different degrees in a pulsating fashion. No CPe cell migration and recruitment into vesicles is observed.

B: Representative frames from a 16 hour long time-lapse microscopy experiment following the growth of vesicles formed 5 days after seeding a fraction of diI labelled cells with non-labelled CPe cells on Matrigel. The time at which each picture was taken is indicated on each frame. DiI label is intended to help visualise the recruitment of cells into vesicles. During the course of the time-lapse no CPe cells are successfully recruited into a vesicle and no CPe cell migration is observed. Scale bars in A and B are 200 μm.

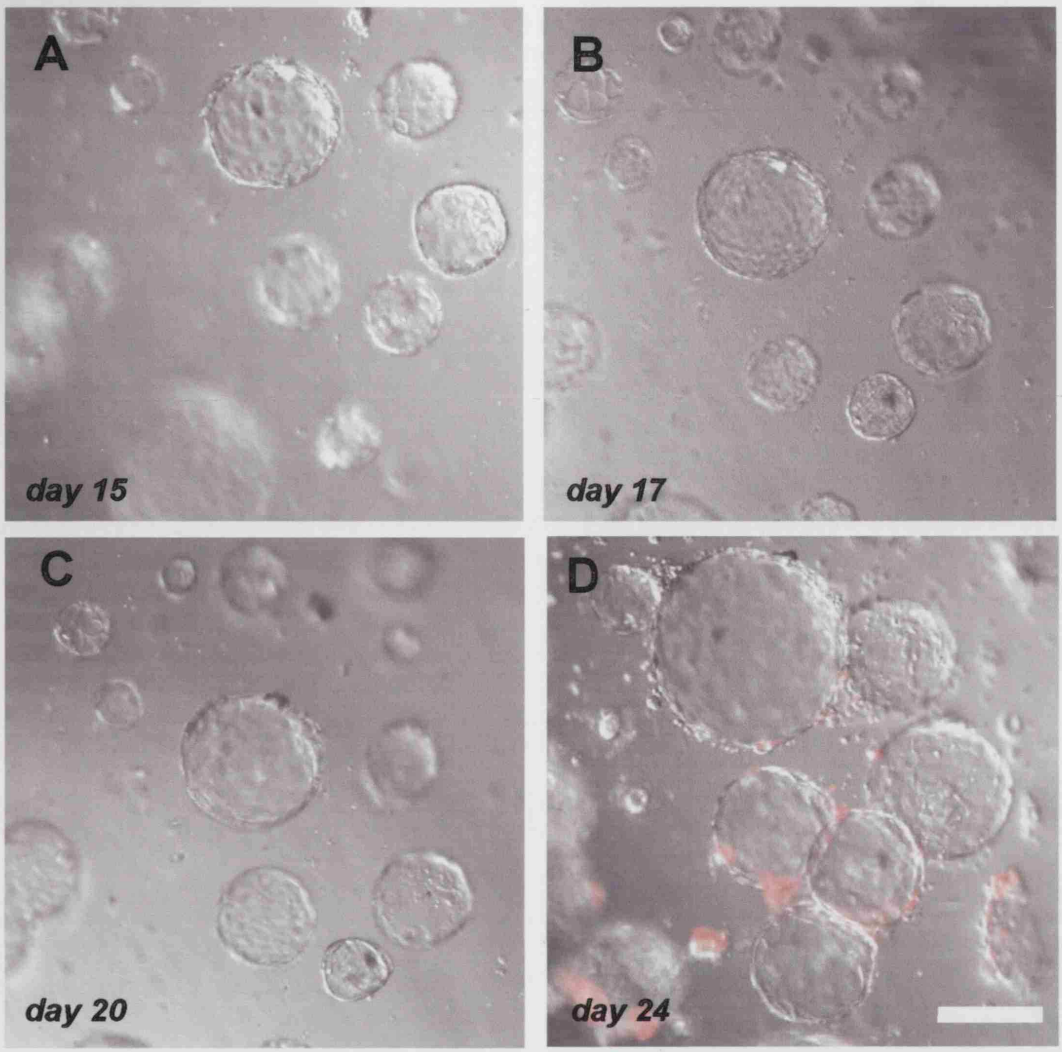

Figure 6. 8 Addition of diI choroid plexus epithelial cells (CPe) to CPe vesicles

A: CPe vesicles grown for 15 days in culture that have reached a growth plateau; **B**: the same vesicles after 17 days and **C**: after 20 days. DiI labelled cells were added after taking this picture. **D**: Vesicles at 24 days, showing incorporation of the added diI labelled cells and increase in size. Scale bar shown in **D** is 200 μm.

6.2.4 Role of cell proliferation in vesicle formation and growth

6.2.4.1 Mitotic events during early vesicle formation

Two cultures produced on different days and grown for one day after initial CPe cell seeding were stained for phosphoryalted histone-3 (p-H3). Very few positive cells were observed (Fig. 6.9). The number of p-H3 positive cells was counted in 10 to 15 aggregates selected by systematic randon uniform (SRU) selection as explained in Chap. 3.4.2.1.

Aggregates are three dimensional entities but for simplicity aggregates were analysed as 2D objects. An optical section cutting through the equatorial plane (see definition in Chap. 3.4.2.1) of SRU selected aggregates was taken and its area measured in order to estimate the number of cells present in it. By measuring the area of the optical section taken at the equatorial plane of a selected aggregate, it was possible to estimate the number of cells present in that section by defining how many Hoechst stained nuclei were on average counted in a given area. Each aggregate was then optically sectioned from top to bottom in order to count the number of p-H3 positive cells. The pie chart in Fig. 6.10A shows that the percentage of p-H3 positive cells obtained was very low compared to the total number of cells, estimated in the equatorial plane of the selected aggregates. To assess the correlation (using the non-parametric Spearman's Rho test) between the number of positive p-H3 cells and the estimated number of cells present in the equatorial plane of 10 SRU selected aggregates, these two variables were plotted as a function of each other (Fig. 6.10B). This analysis showed that there was no relationship (R: 0.458, p: 0.158) between the size (in terms of cell number) of an aggregate and the number of proliferating cells it contained. Cell proliferation therefore did not seem important for the formation of vesicles and occurred sporadically throughout the culture.

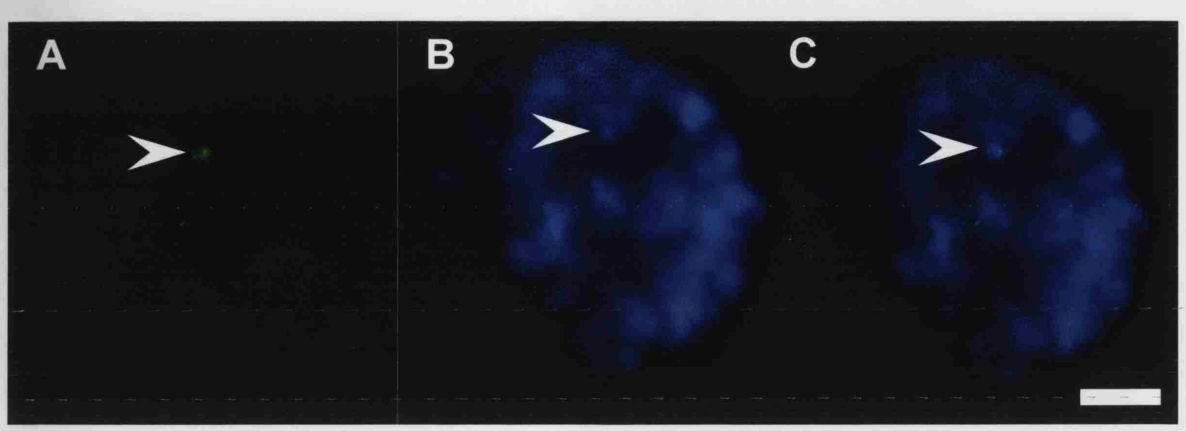

Figure 6. 9 Example of mitotic cells in CPe aggregates after one day in culture.

CPe cells grown on Matrigel for one day are stained for p-H3 (bright green). **A:** CPe aggregate labeled for p-H3; the white arrowhead points to the only positively labeled cell. **B:** Hoechst nuclear staining alone. **C:** Overlay of Hoechst nuclear labeling and p-H3 staining. Scale bar shown in **C** is 50 μm.

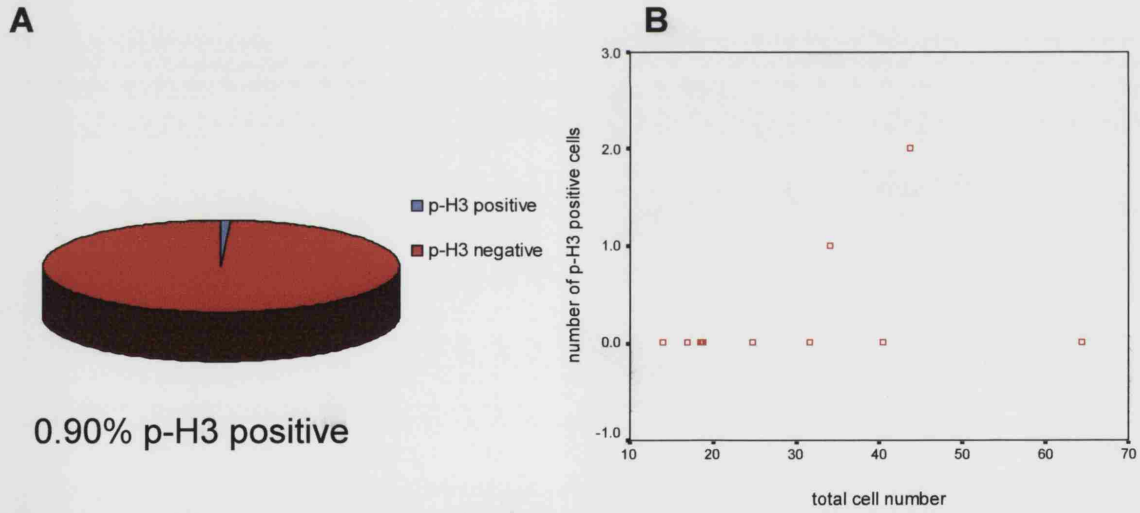

Figure 6. 10 Quantification of mitosis in cultures of CPe grown for one day.

A: Pie chart showing the number of p-H3 labelled cells as a percentage of the estimated total number of cells present in the equatorial plane of SRU selected aggregates. **B**: Scatter plot of the total number of CPe nuclei in the equatorial plane of SRU sampled aggregates against the total number of p-H3 labelled cells in the aggregates. The Spearman's rho correlation coefficient between the two variables is R: 0.458 (p: 0.158), n = 10 aggregates.

6.2.4.2 Mitotic events during vesicle growth

Vesicles that had formed four days after seeding CPe cells were immunocytochemically stained for p-H3 (Fig. 6.11). Three cultures generated on different days were stained and the number of p-H3 positive cells quantified as described in Chap.3.4.2.2. Ten to fifteen vesicles per culture were selected (systematically randomly uniformly (SRU)). Since the vesicles were mounted under a glass coverslip, they were flattened out and became two dimensional. The vesicles appeared like a circle full of cells (Fig 6.11C). By defining the number of cells associated with a fixed area based on at least three flattened vesicles, it was possible to measure the area of SRU selected vesicles and estimate the total number of cells present in that area. The cells that labelled positive for p-H3 were then counted in each SRU selected vesicle (n = 33). The pie chart in Fig. 6.12A shows that the number of p-H3 positive cells represented a very small percentage (0.88%) of the total cell number estimated for the SRU selected vesicles. When the data was plotted as the number of p-H3 positive cells for a given vesicle against the total number of cells present (Fig. 6.12B), a Spearman's (non-parametric) correlation coefficient (R: 0.195) was obtained that was not significant (p: 0.285). These results indicate that mitotic events are not dependent on vesicle size and occur randomly within the vesicles at a low frequency.

Figure 6. 11 Example of mitotic cells in growing vesicles

Vesicle formed four days after seeding CPe cells are stained for p-H3 (bright green). **A, C, E**: Low magnification of the same vesicle; all dividing cells are indicated with white arrowheads. **B, D, F**: Corresponding high magnification of the highlighted areas in (A, C, E). **A-B**: p-H3 labelled cells (green). **C-D**: Overlay of p-H3 labelled cells (green) and Hoechst nuclear stain (blue). **E-F**: Cells labelled with Hoechst nuclear stain alone. Scale bar shown in **E** is 200 μm, and scale bar shown in **F** is 25 μm.

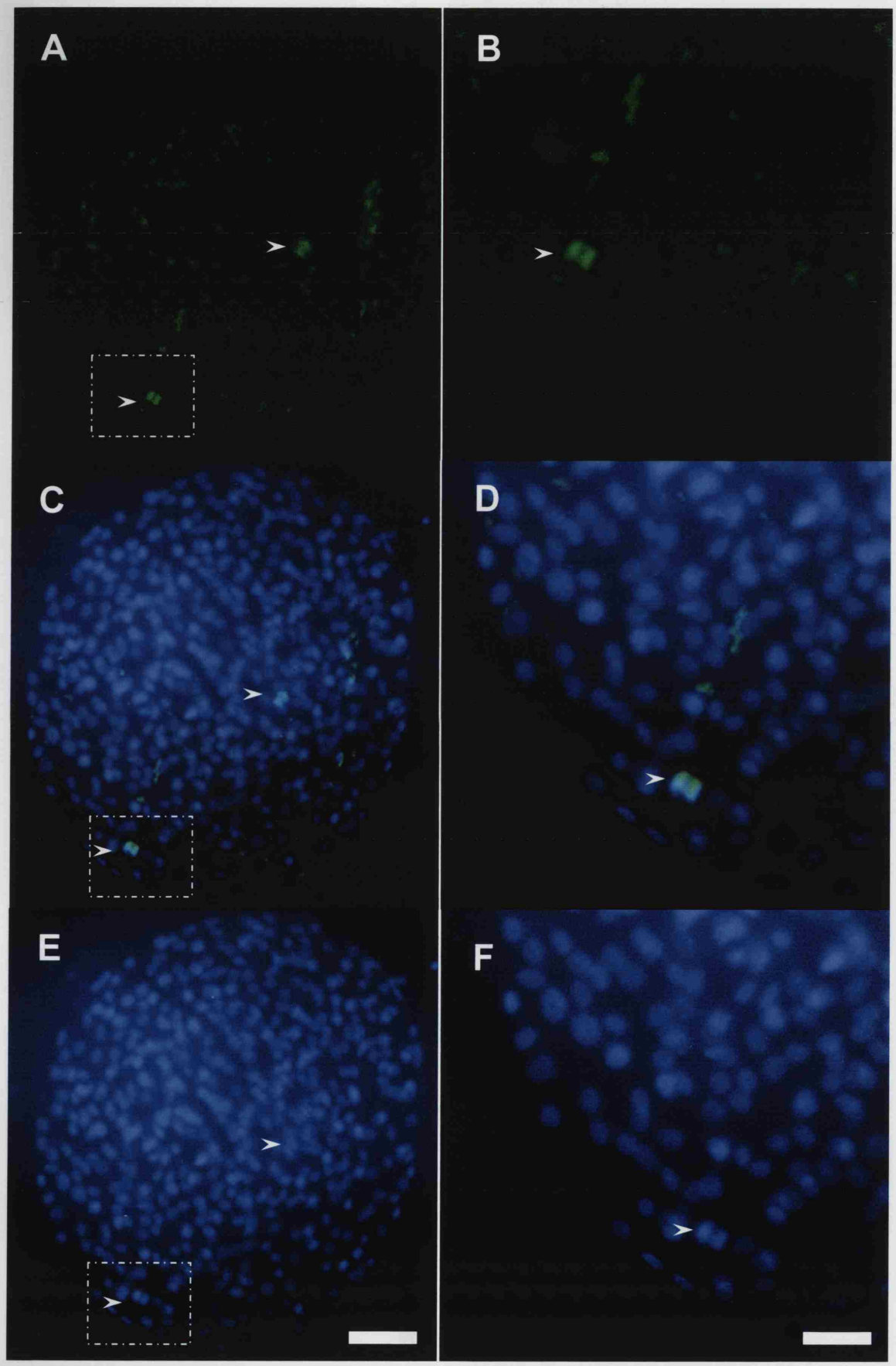
A
B
C
D
E
F

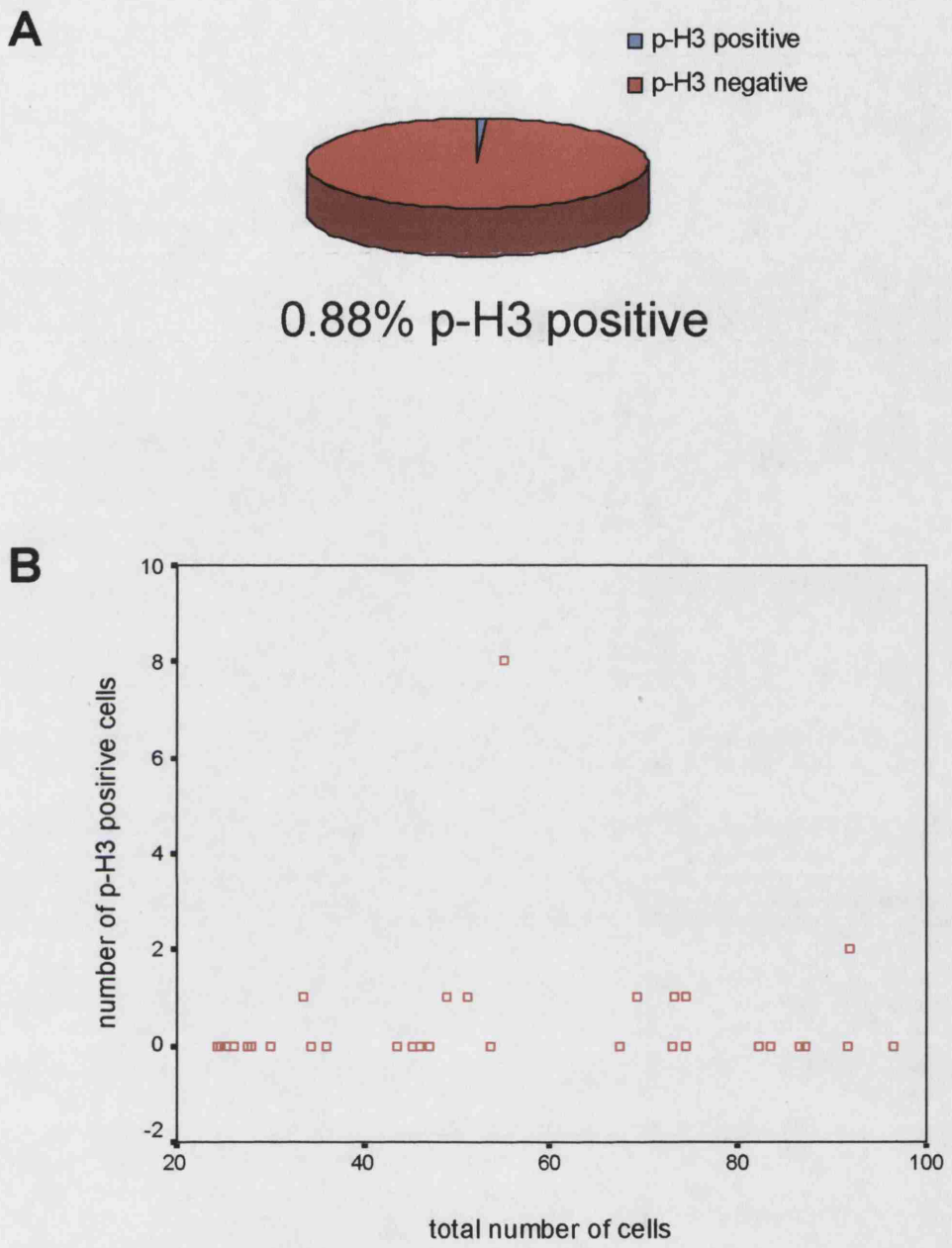

Figure 6. 12 Quantification of mitosis during the growth of CPe vesicles

A: Pie chart showing the number of p-H3 labelled cells as a percentage of the estimated total number of cells present in SRU selected vesicles. **B**: Scatter plot of the estimated total number of CPe nuclei in SRU selected vesicles against the number of p-H3 labelled cells. The Spearman's rho correlation coefficient between the two variables is R: 0.195 (p: 0.285), n= 33 vesicles.

6.2.4.3 Effect of Ara-C on early vesicle formation

The formation of vesicles was studied in the presence of 50 μM cytosine arabinoside (Ara-C) to further investigate the importance of cell proliferation for the formation of vesicles. As a previous study claimed that CPe cells are not affected by AraC (Hakvoort et al., 1998b), I initially tested the effect of Ara-C on a monolayer of immortalised adult choroid plexus epithelial cell line using a metabolically based assay system-Alamar Blue, which showed that Ara-C significantly (p: 1.47×10^{-4}) reduced cell proliferation (see Fig. 6.13).

Independent Student's t-test were performed comparing the mean size of aggregates and vesicles in control and Ara-C treated cultures measured every day over four days of growth after initial seeding of the CPe cells (see Appendix II.1-.2). One day after treatment (day 2), the mean size of early vesicles treated with Ara-C was significantly reduced (p: 0.036). However, the p-values at all other days were non-significant ($p > 0.05$).

Using the ML-wiN software package (see Chap. 3.5), a 2-level model (see Appendix II.3) showed that Ara-C did not have any significant effect on early vesicle formation and growth. The multi-level model showed that individual early vesicles treated with Ara-C were on average 1959μm^2 smaller ($\beta 1$) (SE: 1879 μm^2), but that this effect was not significant (p: 0.4). In addition the mean departure of the growth curves for individual Ara-C treated early vesicles relative to control vesicles was 96 μm^2 ($\beta 3$) (SE: 754 μm^2), which was highly non-significant ($p > 0.8$). The model shows that the area of vesicles increased by 1445 μm^2 for each day of growth ($p < 0.01$), but that the individual slopes for each vesicle growth curve varied about this mean with a variance estimated at 3321 μm^2 (SE: 1422 μm^2), the level 2 residuals. The variation in the area of individual vesicles around the mean vesicle growth curve was 5530 μm^2 (SE: 1177 μm^2), the level 1 residuals. The graphical predictions for this model are shown in Fig. 6.14. This analysis thus suggested that overall Ara-C did not affect the growth and formation of early vesicles and therefore that cell proliferation was not important for early vesicle formation.

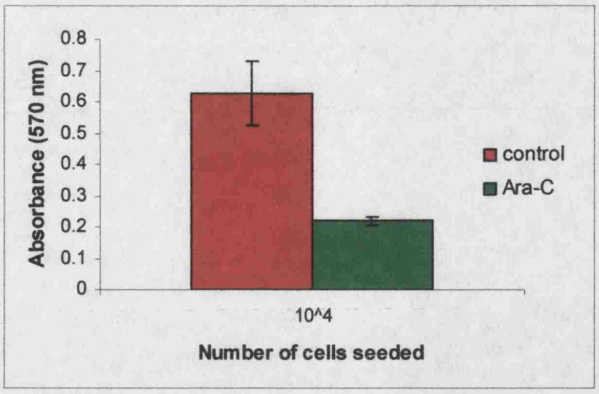

Figure 6. 13 Effect of Ara-C on adult choroid plexus epithelial cells transfected with large (SV40) T-antigen (TRCSBF-2)

The bar chart shows the average Alamar Blue absorbance readings from three separate experiments (5 samples for each experiment) looking at the effect of 50μM Ara-C on the growth/proliferation of TRCSFB-2 plated at **1x10^4** cells/ml. The red bar shows the average value for control cultures, whilst the green bar summarizes the average value for Ara-C treated cultures (along with standard deviation bars). Independent Student's t-test showed that the effect of Ara-C was significant (p: 1.47x10^-4).

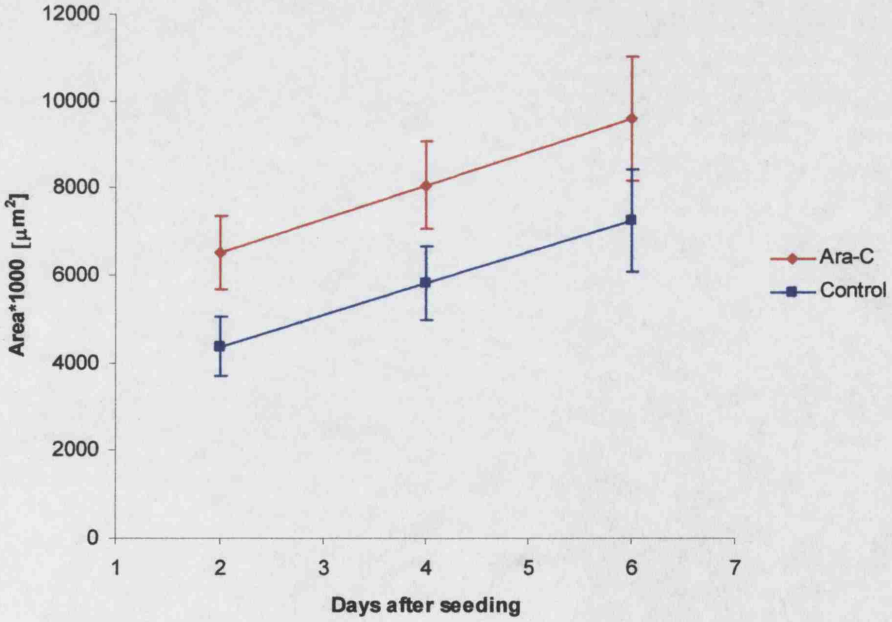

Figure 6. 14 Predicted effect of Ara-C on the initial formation of vesicles

Graph showing the average predicted growth of Ara-C treated (red line) and non-treated vesicles (blue), over four days in culture. The lines are derived from the fixed part intercept and slope coefficients (β0, β1, β2, β3) of the multilevel model. (Area*1000 is in μm^2). Standard error bars are shown for each predicted mean.

6.2.4.4 Effect of Ara-C on vesicle growth

In order to confirm that proliferation was not an important cellular mechanism by which the vesicle increased in size, cultures of vesicles were treated with 50μM of the DNA synthesis inhibitor cytosine arabinoside (Ara-C), five days after seeding the CPe cells unto the Matrigel. The growth of individual vesicles was followed over 6 days in control and Ara-C treated cultures. Roughly 20 to 30 vesicles per group were followed in two independent experiments and the area of these vesicles was measured every 24 hour (see Appendix II.4). Independent Student's t-tests were performed to compare the mean area of control and treated vesicles at each day. As summarized in Appendix II.5, Ara-C did not have any significant effect on the growth of vesicles.

A 2-level model of the data (c.f Appendix II.3), using the ML-wiN software package (see Chap. 3.5), confirmed that the effect on vesicle growth was insignificant (Fig. 6.15). Multi-level modelling showed that CPe vesicles treated with Ara-C were on average ($\beta 1$) 3849μm^2 bigger (SE: 2755 μm^2) than non-treated vesicles, but the difference was not significant (p: 0.2). For each day of growth, Ara-C treated vesicles grew by 1148 μm^2 ($\beta 3$) less than control vesicles (SE: 1172 μm^2), but this difference was not significant ($p > 0.8$). The model showed that the area of vesicles increased by 3258 μm^2 for each day of growth ($p < 0.01$), but that the individual slopes for each vesicle growth curve varied about this mean with a variance estimated at 4986 μm^2 (SE: 2984 μm^2), the level 2 residuals. The variation in the area of individual vesicles around the mean vesicle growth line was 45787 μm^2 (SE: 10847 μm^2), the level 1 residuals. The graphical predictions for this model are shown in Fig. 6.15.

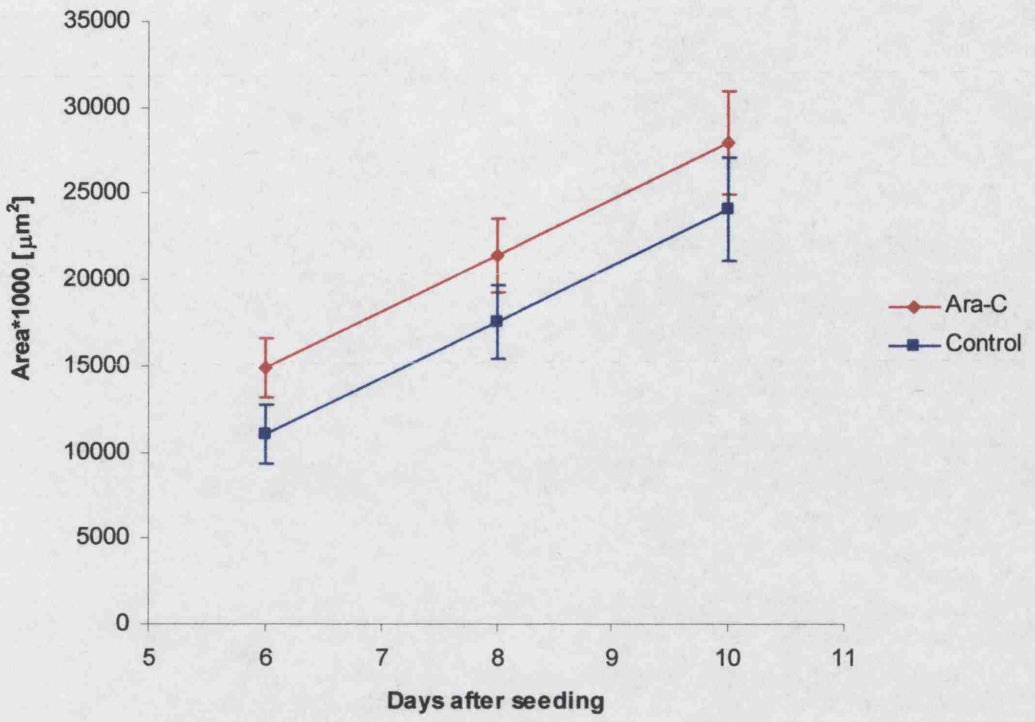

Figure 6. 15 Predicted effect of Ara-C on vesicle growth

Graph showing the average growth of Ara-C treated (red line) and non-treated vesicles (blue), over four days in culture. The lines are derived from the fixed part intercept and slope coefficients (β0, β1, β2, β3) of the multilevel model. Standard error bars are shown for each predicted mean.

6.2.5 The importance of fluid secretion for vesicle growth

6.2.5.1 Effect of fluid secretion inhibitors on vesicle growth

In order to show that the CPe cells were actively secreting fluid into the lumen of the vesicles, mature vesicles grown for eight days in culture were collapsed with a combination of acetazolamide (carbonic anhydrase inhibitor), and ouabain (a Na^+/K^+ ATPase inhibitor). The vesicle cultures were treated with this combination of drugs over two days, which induced the collapsing of all the vesicles. Smaller vesicles collapsed entirely so that vesicles appeared like aggregates again, while bigger vesicles retained some vesicle-like appearance. The effect of these fluid secretion inhibitors on vesicle growth was highly significant (p: 1.38×10^{-59}) as analysed by a paired Student's t-test comparing their size before and after treatment.

If each collapsed vesicle was plotted as the percentage of its original size against its original size (in μm^2), a scatter plot was produced from which a correlation coefficient between the two variables was calculated (Fig. 6.16). Pearson's correlation coefficient was R: -0.362 and was highly significant (p: 2.32×10^{-5}). This suggested that bigger vesicles collapsed more extensively than smaller vesicles. On closer inspection of the data, it appeared that there was a cut-off point where vesicles under about 4000 μm^2 collapsed very little (because they had less fluid to loose before they reached an aggregate state), while vesicles over this size more or less collapsed by the same magnitude, so that they were on average 25-30% of their original size.

When acetazolamide and ouabain were added one day after seeding the CPe cells on the Matrigel, the cells formed aggregates but never formed vesicles and, after a few days, died off (not shown). This showed that fluid secretion was crucial for the growth of vesicles.

6.2.5.2 Recovery of collapsed vesicles

Once acetazolamide and ouabain were removed and washed out from the cultures, the recovery of collapsed vesicles was followed over eight days as shown by the sequence of micrographs shown in Fig. 6.17. The vesicles recovered their original size on average after four days and continued their normal growth pattern. The recovery of vesicles was followed by expressing the size of a collapsed or recovering vesicle as the percentage of its original size. By plotting the average percentage recovery of fifty vesicles over eight days, a linear growth was observed (Fig. 6.18)

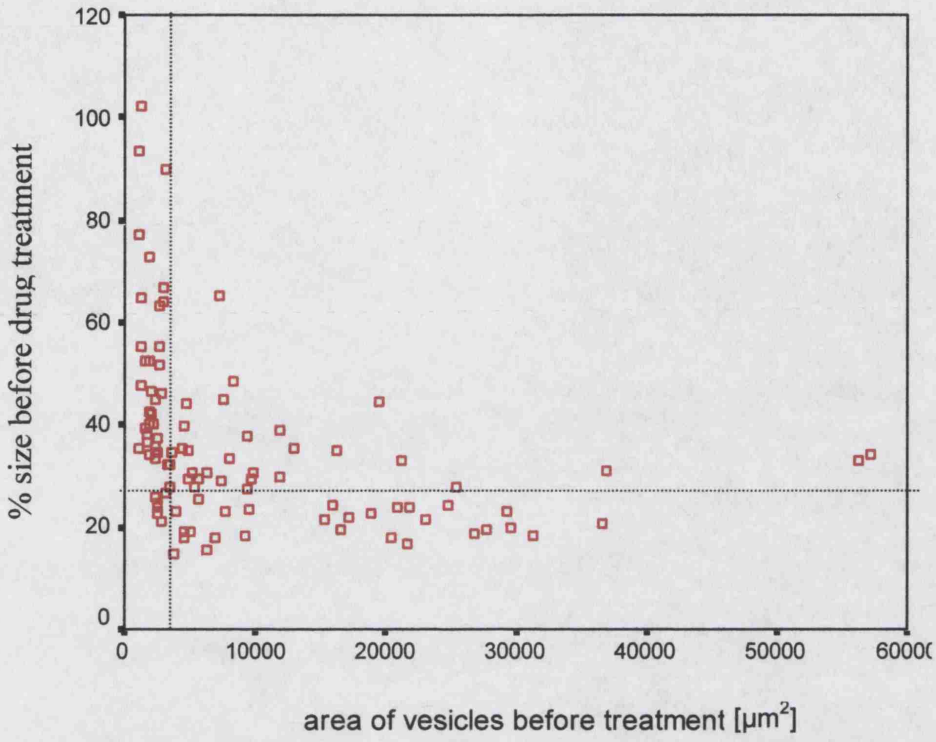

Figure 6. 16 Effect of secretion inhibitors on vesicle growth

Graph showing the effect of acetazolamide and ouabain treatment on vesicles in relation to their size. The size of vesicles after treatment is expressed as a percentage of their size before treatment (in μm^2). The Pearson's correlation coefficient (R: -0.362) for this data is highly significant (p: 2.31×10^{-5}). Closer inspection of the data shows that vesicles under 4000 μm^2 (vertical dotted line) collapse very little, whereas vesicles above this size tend to collapse relatively homogeneously and on average are reduced to 25-30% of their original size (horizontal dotted line). Since there are many vesicles under 4000 μm^2 in this data set, they strongly bias the correlation coefficient. In fact, if the analysis is repeated with only vesicles above a cut-off point of 4000 μm^2, the Pearson's correlation coefficient R: -0.165 is not significant (p: 0.234).

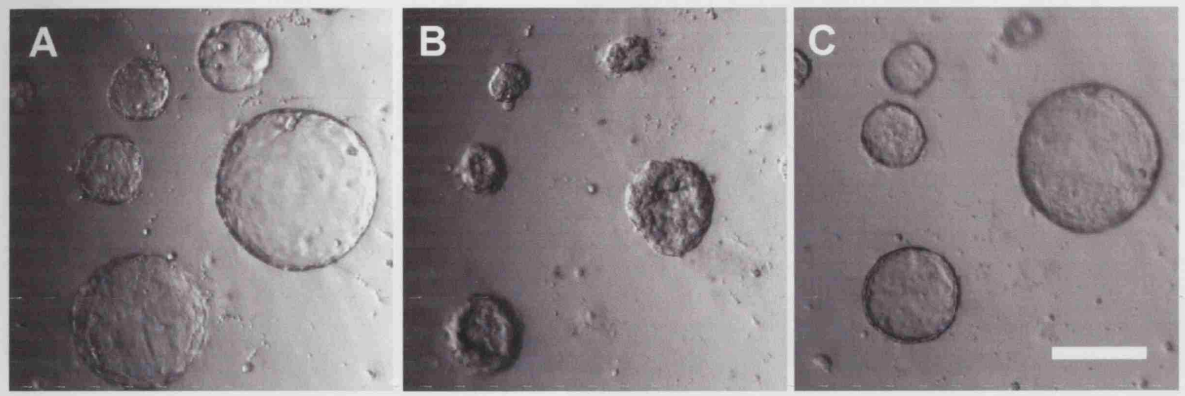

Figure 6. 17 Sequence of micrographs illustrating collapsing and recovery of vesicles

The same group of vesicles grown for eight days after CPe cell plating are shown. **A**: before treatment, **B**: collapsed with ouabain and acetazolamide, **C**: recovery at two days after washing out the drugs. Scale bar for all pictures is 100 μm as shown in **C**.

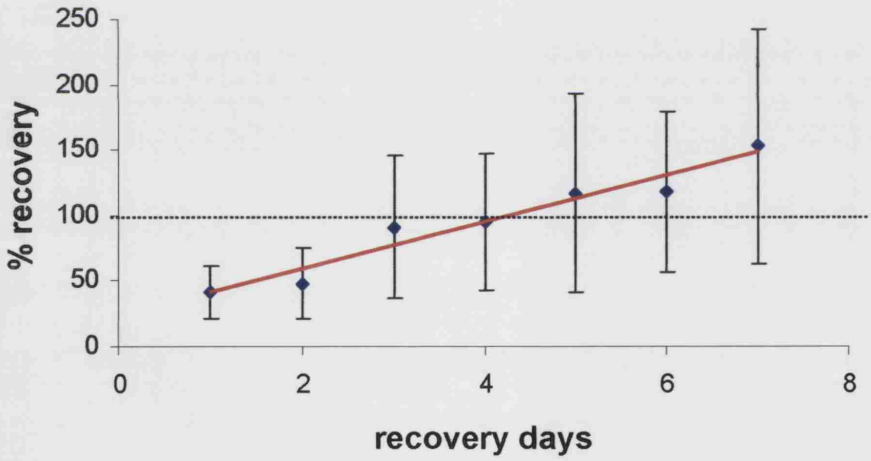

Figure 6. 18 Recovery of vesicles after washing out secretion inhibitors

The average size of vesicles (n = 48) expressed as a percentage of their original size (**% recovery**) are plotted against the number of days after the secretion inhibitors have been washed out (**recovery days**). The recovery of the vesicles is linear over 8 days, as shown by the least square trend line fitted through the data points (red line). The standard deviation error bars are shown for each day of recovery, and the dotted line highlights the 100% recovery mark when the vesicles have recovered their original size (on average by recovery day 4).

6.3 Discussion

6.3.1 Vesicle culture characterization

In this study, a relatively pure population of CPe cells was successfully isolated from 12.5 dpc mouse IVth ventricular CP. When these cells were plated on Matrigel they formed hollow, fluid filled vesicles as reported by Thomas et al (1992). The vesicles were confirmed to be hollow by optical deconvolution analysis. They were shown to express at least at the mRNA level several of the markers associated with normal CPe differentiation. In addition, the CPe cells forming the vesicles were shown to express the tight junction associated protein ZO-1. This observation confirmed the previous finding by Reid S. (PhD thesis, 2002) that showed the presence of tight junction complexes by electron microscopy analysis. It also farther supported the idea that the vesicles formed a sealed environment where fluid was secreted into, thus mimicking the environment found in the ventricular system of the brain. With this study I was not only confident that I could reproduce the vesicle culture described by Thomas et al. (1992) and Reid S. (PhD thesis, 2002), but I also extended the characterization of the CPe phenotype of the cells forming the vesicles.

6.3.2 Early vesicle formation

It was found that CPe cells plated at a density of roughly 20-40x10^4 cells/ml followed a stereotypical sequence of events that led to the formation of vesicles over three to four days (see Fig. 6.19). Four key stages were distinguished: 1) after plating on Matrigel, the CPe cells were very dynamic and formed loose aggregates (day 0-day 1); 2) these aggregates became more defined and compact in appearance (day 2); 3) these aggregates started vesiculating (day 3); 4) they formed fluid filled vesicles (day 4). However, if the number of cells plated was under the 20x10^4 cell/ml threshold, the cells either remained mono-dispersed, or formed small aggregates that did not vesiculate (data not shown). The general behaviour of the CPe cells was reminiscent of that described for other epithelial cell types grown in culture. For instance, also dissociated immature rat testicular cells grown on plastic or Madin-Darby canine kidney cells form aggregates (Davis, 1978; Tanner et al., 1992) that then form fluid-filled vesicle-like structures. It is worth noting that not all epithelial cells grown in culture form fluid filled vesicles for e.g. dissociated epithelial cells of the lactating bovine mammary gland grown on Matrigel form a aggregates after a few days but

then form cell filled "mammospheres" or "duct-like network structures" (German and Barash, 2002).

Time lapse microscopy analysis of the first 24 hours in culture showed that the single CPe cells were quite motile with many cells migrating short distances and adhering to one another to form aggregates. This observation was in agreement with the model for the kinetics of homotypic cellular aggregation proposed by (Neelamegham et al., 1997). This model predicted that aggregation rates were dependent on the motility of the cells and aggregates, the frequency of cell-cell collisions and the strength of intercellular bonds. In the vesicle cultures, the aggregation rates were dependent on the number of CPe cells plated; low aggregation rates were oberved in sparsely plated cultures which minimised the frequency of collisions between cells. The cells often remained mono-dispersed, and formed small aggregates only after four or five days (not shown). It thus showed that the motility of the cells as well as cell:cell adhesion was an important component in the aggregation process.

The culture was shown to be most dynamic during the first 48 hours after plating the CPe cells. The aggregates formed after this period of time behaved as separate entities that rarely fused with one another and that hardly changed in size until they formed hollow vesicles. In fact, it was possible to correlate the size of aggregates formed after 48 hours and the size of vesicles formed after four days. This showed that after the first 48 hours very little movement of single cells took place, mainly because most single cells had already been recruited into aggregates.

The role of cell proliferation for vesicle formation was studied using two different approaches. The first approach was based on the immunocytochemical detection of the mitotic marker p-H3, and the second on looking at the effect of the cell proliferation inhibitor Ara-C on the formation of vesicles. It was found that very few mitotic cells were present in the cultures plated after one day. The amount of mitotic cells was insignificant and there was no correlation between the size of aggregates and the number of mitotic cells they harboured. It should be noted that it was not obvious at this stage whether all the cells positive for p-H3 were actually CPe cells. It could be assumed however that cells in the aggregates would all be CPe cells, contaminating cells would not be incorporated into these aggregates. The addition of the cell proliferation inhibitor Ara-C confirmed this observation as it did not significantly affect vesicle formation. Hence, from this study it could be concluded

that very few mitotic cells were present in the aggregates, and that cell proliferation was not an important cellular mechanism for the early formation of vesicles.

Therefore the key cellular mechanisms governing early formation of vesicles were likely to be cell migration and cell-cell adhesion.

6.3.3 Late vesicle growth

Time lapse microscopy analysis showed for the first time that CPe vesicles grew over time in a pulsating fashion, by collapsing and re-growing again. No cell recruitment was observed over 48 hours recording. Most vesicles did not contain any proliferating cells and vesicle growth was not affected by the proliferation inhibitor Ara-C, consitent with the presence of only very few mitotic cells. These results refute the previous finding by Stadler and Dziadek, (1998) who reported that vesicles grown for 5 days and BrdU treated for 12 hours, roughly 20% of the CPe cells incorporated the base thus suggesting that cell proliferation was important for vesicle growth. In this study, BrdU-positive cells were counted in vesicle cultures embedded in wax and sectioned. The histological resolution of the sections, however, did not allow to distinguish contaminating mesenchymal cells from CPe cells.

From my study, it appeared that fluid secretion in the lumen was the main mechanism underlying vesicle growth, as indicated by experiments where the vesicles were induced to collapse using acetazolamide and ouabain. These drugs had been previously shown to inhibit fluid secretion (Chap. 1.2.2.3): percentage inhibition of CSF secretion in the rabbit due to ouabain was 55%, and due to acetazolamide was 64%. The combination of both drugs induced a 69% inhibition of CSF (Davson and Segal, 1970). In addition ouabain was also shown to inhibit fluid secretion of porcine CPe cells grown as a monolayer on a filter of a Transwell bi-chamber (Hakvoort et al., 1998a). It is interesting that acetazolamide alone did not efficiently collapse the vesicles (not shown); this suggests that the drug may act synergistically with ouabain when combined together. However, the effect of ouabain alone on vesicle growth was not tested.

This artificial collapsing of the vesicles also strenghtened the observation that the vesicles were dynamic, pulsating structures. Possibly, they had to allow for fluid release from the lumen to alleviate the hydrostatic tension building up inside the vesicle due to constant secretion of fluid as observed in the growth of fluid filled blastocysts (Massip et al., 1982). Vesicles under a certain size threshold, about 4000

μm^2 did not collapse homogeneously and tended to collapse less extensively upon acetazolamide/ouabain treatment. This was because smaller vesicles, containing less fluid, reached their aggregate state more quickly (effectively reaching a limit at which they could not collapse more); this translated in a lower percentage decrease (relative to their original size) to reach their final collapsed state.

It was found that after 15 to 20 days in culture the growth of the vesicles stopped but could resume following the addition of CPe cells, as they became incorporated into the vesicle epithelium. This was an important observation, as it supported the view that it was the total number of cells initially plated that determined the final size of the vesicles. It also showed that single cells were indeed capable of becoming incorporated into the vesicle epithelium. Indeed, the result suggested that the size of a vesicle was directly proportional to the size of the cellular aggregates they derived from. Presumably, as the vesicles stretched out under the hydrostatic force built by the secretion of fluid, the walls of the vesicles became thinner as the CPe cells rearranged into a single CPe cell monolayer. The cellular mechanisms underlying vesicle growth are summarised in Fig. 6.19.

6.3.4 Summary

This chapter focused on the analysis of the cellular mechanisms underlying CPe vesicle formation and growth, after further characterizating the phenotype of the CPe cells in the vesicles. Cell-cell adhesion and cell migration were the primary cellular mechanisms responsible for the formation of aggregates. The size of the vesicles was directly proportional to the initial size of aggregates and therefore the number of cells plated. Cell proliferation was not important for vesicle formation or/and growth. In contrast, the secretory activity of the CPe cells was found to be the key process underlying vesicle growth.

This study showed that the early phases of vesicle formation (mainly the first 48 hours) provide a good assay system to study the effect of growth factors and drugs on migration and adhesion of CPe cells, as the cells behaved according to the mathematical model for the kinetics of homotypic aggregation (Neelamegham et al., 1997). Furthermore, vesicles could be used as a model of "blood-brain barrier" to test the effect of drugs and growth factors on fluid secretion and substance transport by the CPe cells, in a similar fashion to kidney epithelial cyst model (Tanner et al., 1992).

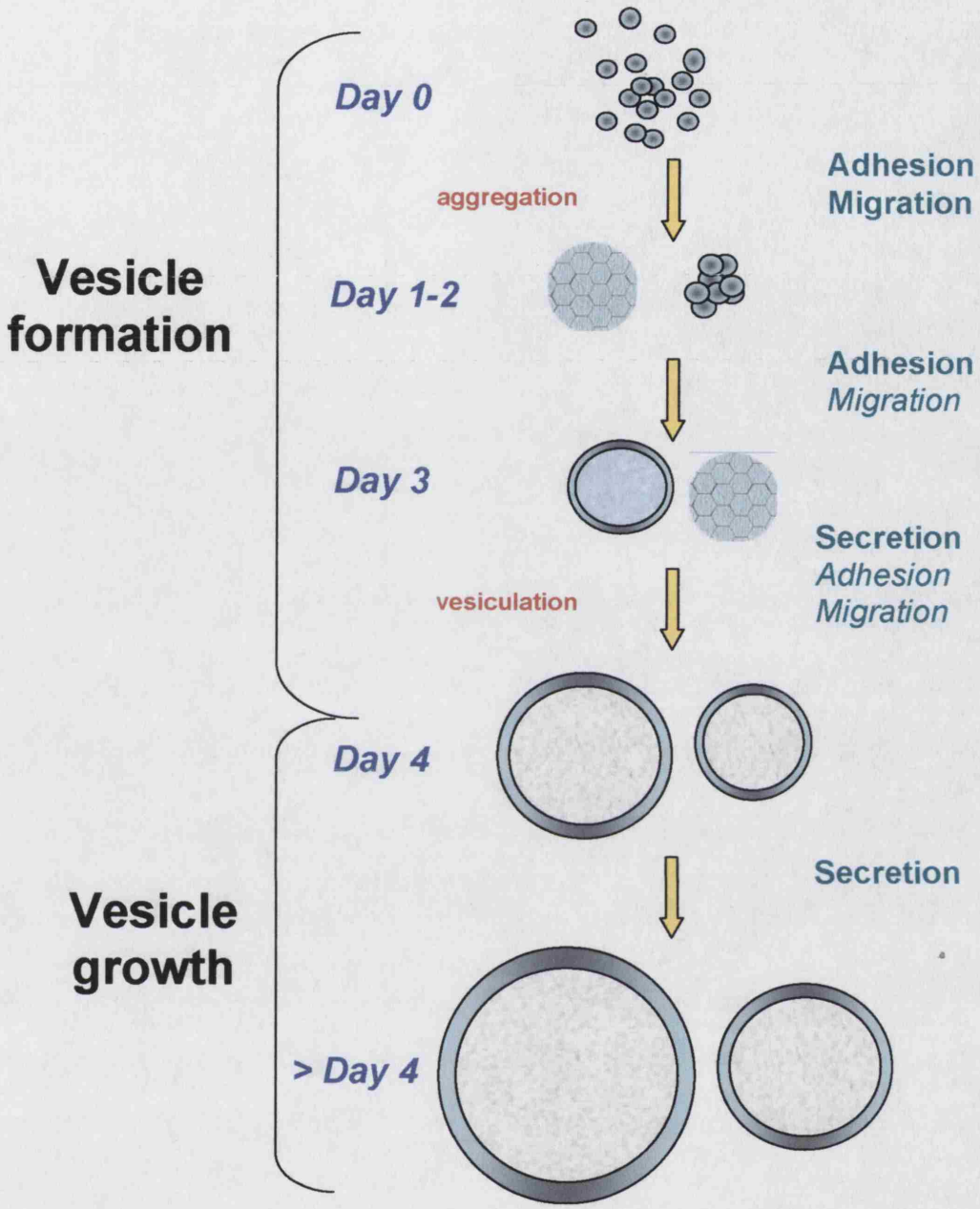

Figure 6. 19 Diagram of key cellular events involved in vesicle formation and growth

Vesicle formation: cell:cell adhesion primarily drives the aggregation, and the tightening of the CPe into aggregates, and fluid secretion drives the vesiculation of the aggregates into vesicles. **Vesicle growth:** Fluid secretion is the main process driving vesicle growth. For each stage the number of days since first plating the CPe cells is given.

Chapter 7 Effect of fibroblast growth factor signalling on murine embryonic choroid plexus epithelial cells in culture

7.1 Introduction

As described in chapter 6, murine embryonic CPe cells seeded on Matrigel form hollow, fluid-filled vesicles that grow in size over time. S.Reid (PhD thesis, 2002) observed that FGF2 could increase the size of these vesicles in a dose dependent manner, but did not investigate which specific cellular functions are affected by FGF2 that would lead to the formation of bigger vesicles.

Interestingly, although FGF2-treated vesicles are larger than controls, their rate of growth is comparable. Furthermore, if FGF2 is added once vesicles have formed, it does not appear to increase their size, but in contrast, transiently decreases vesicle growth (Reid S, 2001). This suggested that FGF2 affects the behaviour of CPe cells before the vesicles have formed, in a way that causes them to form bigger vesicles. FGF2 has been show to support cell proliferation, protect from cell death, increase cell motility and/or cell:cell adhesion, and also increase secretory activity of cells (Szebenyi and Fallon, 1999; Burgess and Maciag, 1989; Hakvoort and Johanson, 2000). Since FGF2 has been shown to increase cell proliferation in cultures of embryonic CPe cells grown as a monolayer on laminin coated coverlips (Reid S, 2001), as it does in other cells (reviewed by (Burgess and Maciag, 1989)), it was conceivable that the increase in size of the CPe vesicles may have been at least in part due to increased cell proliferation. The transient inhibition of vesicle growth after FGF2 treatment may have been due to an inhibition in fluid secretion as supported by the observation that FGF2 inhibits fluid secretion in cultures of porcine CPe cell monolayer (Hakvoort and Johanson, 2000).

The aim of this chapter was to understand how FGF2 influences the cellular responses of the CPe cells that cause them to form bigger vesicles. The first part of this study focused on how FGF2 affected the early cellular events leading to vesicle formation, which occurs in the first few days after seeding the CPe cells on Matrigel.

Specifically, the effect of FGF2 on cell:cell adhesion, cell migration, and cell proliferation was investigated. The second part of this study examined cellular responses induced by FGF2 during vesicle growth, particularly changes in secretory activity. The different cellular events potentially affected by FGF2 that were investigated in this study are summarized in Fig. 7.1.

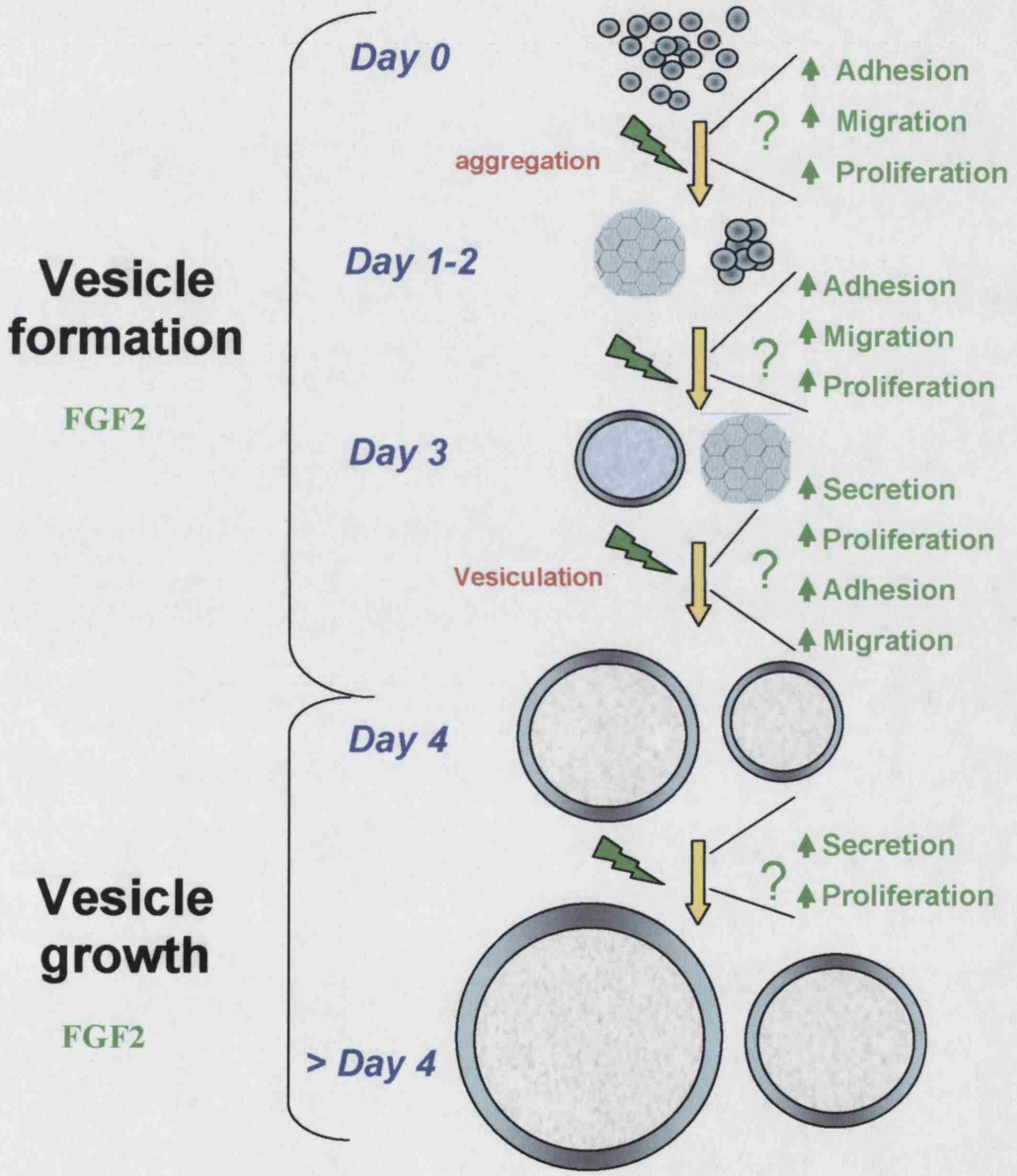

Figure 7. 1 Diagram of cellular events that may be affected by FGF2 during vesicle formation and growth

The possible effects of FGF2 (green) at different steps of vesicle formation and growth (red) are given. For each stage of vesicle formation the number of days since first plating the CPe cells is indicated.

7.2 Results

7.2.1 Effect of FGF2 on early vesicle formation

7.2.1.1 Effect of FGF2 on CPe cell aggregation

The effect of 10 ng/ml FGF2 on the early formation of vesicles was followed over the first four days after seeding the CPe cells, and pictures taken at 24 hour intervals (Fig. 7.2). FGF2 was added to the CPe cells after one day in culture. Control cultures, where FGF2 was absent, were always done in parallel. FGF2 was added one day after plating to be able to quantify the initial sizes of the aggregates in control cultures and cultures to be treated, in order to ensure they were comparable. This way it was possible to follow more accurately the cellular responses triggered by growth factor treatment (and rule out plating artefact). Moreover, it also allowed checking for variability due to seeding between experiments run on different days.

After one day of FGF2-treatment, an increase in the size of the aggregates as compared to controls was already apparent. In addition, the number of aggregates appeared to have dramatically decreased in FGF2-treated cultures. In FGF2-treated cultures, aggregates changed position and fused with each other much more frequently, and after three/four days in culture the aggregates became hollow and formed vesicles that were larger than those in control cultures (see Fig. 7.2).

In order to quantify this effect of FGF2 on the CPe cells, the area of aggregates and vesicles was measured over four days in the same fields of view. Four cultures per treatment were analysed. The number of aggregates and vesicles were counted in the same four representative fields of each culture. Since the culture was highly dynamic, the most precise way to consistently monitor aggregate/vesicle growth was, in addition to visual cues, to use the x-y co-ordinates of the inverted microscope stage (see Chap. 3.3.1).

The area of the equatorial plane of aggregates and vesicles was measured using the Openlab software in four independent experiments (see Chap. 3.3.1). Aggregates representing only two to four cells were not measured (under 30 μm^2), and the distinction between aggregates and vesicles was not made. It was assumed, as was visually observed, that the proportion of vesicles and aggregates present a given time point was the same in control cultures and FGF2-treated cultures. The areas and

number of each aggregate and vesicle at each time point and each condition (control and FGF2-treated) were plotted on a scatter-plot graph (Appendix III.1).

7.2.1.2 Quantification of the effect of 10 ng/ml on the size of aggregates and vesicles in early vesicle cultures

The statistics tables for this quantification are shown in Appendix III.2-III.3. Independent Student's t-test showed that FGF2 significantly increased the size of aggregates which then formed bigger vesicles.

One day after seeding the CPe cells (day 1), only single cells and small aggregates were present. The size of the CPe aggregates was equivalent in all culture studied in both control and cultures to be treated with 10 ng/ml FGF2. The size of aggregates in cultures that were not treated was 573 μm^2 (SE: 22.9 μm^2), whilst the average size in cultures to be exposed to FGF2 was 580 μm^2 (SE: 22.71 μm^2). Independent Student's t-test showed that the mean of the aggregates in control and pre-FGF2-treated cultures was not significant (p: 0.822). On addition of 10 ng/ml FGF2 after one day in culture, the mean size of aggregates in FGF2-treated cultures increased significantly compared to control cultures. The mean size of aggregates in FGF2-treated cultures was 1234 μm^2, whilst in control cultures the mean size of the aggregates was 725.7 μm^2. The difference between the means was highly significant (p: 2.22×10^{-20}). After four days in culture (day 4), most of the aggregates had formed vesicles, so that the measurement reflected the size of vesicles. The mean size of FGF2-treated vesicles was 2850 μm^2 and that of control vesicles 1312 μm^2. Independent Student's t-test showed that this difference was significant (p: 1.51×10^{-25}).

The size of aggregates and vesicles in control and FGF2-treated cultures over time was also fitted to a multiple regression model the outcome of which is summarized in Figure 7.3 and in Table 7.1. The regression model incorporated the effect of time (**day**), the effect of FGF2 treatment (**treatment**) and an interaction term between days and treatment. This interaction term (**interaction**) assessed the average increase in size of aggregates and vesicles for every day in culture due to FGF2-treatment. The parameter coefficients (B_n) for **day**, **treatment** and **interaction** are given by B_1, B_2 and B_3 respectively. The B_0 constant is the fixed term of the equation and gives the intercept of the fitted line.

The regression model is given below:

Area = $\mathbf{B_0}$ constant + $\mathbf{B_1}$ day + $\mathbf{B_2}$ treatment + $\mathbf{B_3}$ interaction

(B_0) + (B_1) + (B_2) + (B_3)

Area = **262.40** (SE: 56.7) + **250.31** (SE: 21.5) +

Control → 0 + 0

FGF2 → **462.47** (SE: 87.2) + **492.03** (SE: 35.7)

The regression analysis showed that for every day of growth the vesicles increased in size on average by (B_1) 250.31 μm^2 (SE: 21.5) and the FGF2-treated aggregates and vesicles increased by an additional 492.03 μm^2 (SE: 35.72) per day.

7.2.1.2 Quantification of the effect of 10 ng/ml FGF2 on the number of aggregates and vesicles in early vesicle cultures

The presence of 10 ng/ml FGF2 reduced the number of aggregates and vesicles present in culture as observed in Fig. 7.2 and summarized in Fig. 7.4. The statistics tables for this result are shown in Appendix III.4-III.5. After one day in culture the mean number of aggregates in control cultures and cultures to be treated with FGF2 was comparable. On average there were 310 aggregates in control cultures, whereas cultures not yet exposed to FGF2 contained on average 289 aggregates. A Mann Whitney U test analysis showed that the difference was not significant (p: 0.513). Upon addition of 10 ng/ml FGF2, 24 hours later the number was significantly reduced in FGF2-treated cultures (mean number: 103.5) compared to control cultures (mean number: 188.5). The difference was statistically significant (p: 0.021). After four days in culture, most of the aggregates had formed vesicles. The mean number of vesicles in control cultures was 164, whereas in FGF2-treated cultures it was 72. This difference in number was statistically significant. (p: 0.021).

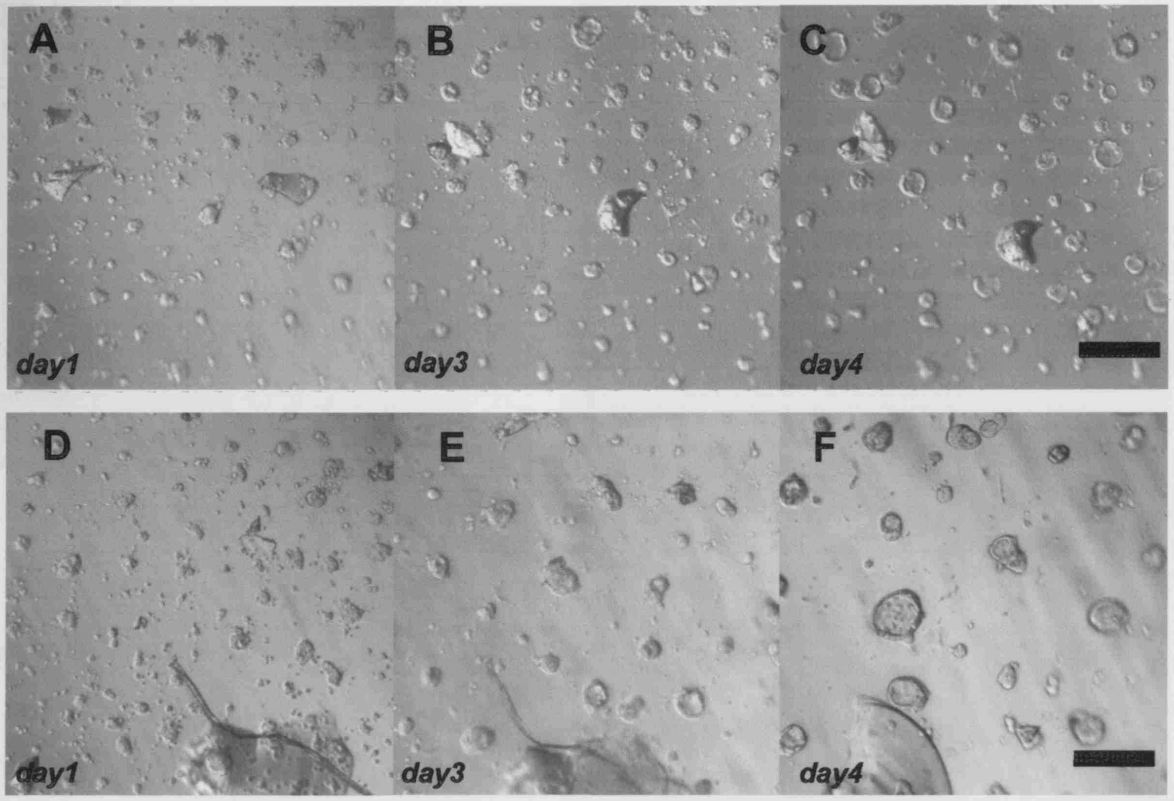

Figure 7. 2 Representative micrographs of the effect of 10ng/ml FGF2 on the formation of vesicles.

A, B, C: same field of view following the early formation of vesicles one, three, and four days after plating (italic). **D, E, F**: Same field of view following the formation of 10 ng/ml FGF2-treated vesicles after one (not treated), three, and four days (italic). **D:** CPe cells before adding 10 ng/ml FGF2 form aggregates that are the same size as in **(A)**. **E:** CPe cells treated with FGF2 for two days have formed bigger aggregates than untreated cells **(B)**. **F:** The same culture treated with FGF2 for three days contain bigger vesicles than the control culture in **(C)**. Scale bars for all pictures are 200μm as shown in **(C)** and **(F)**.

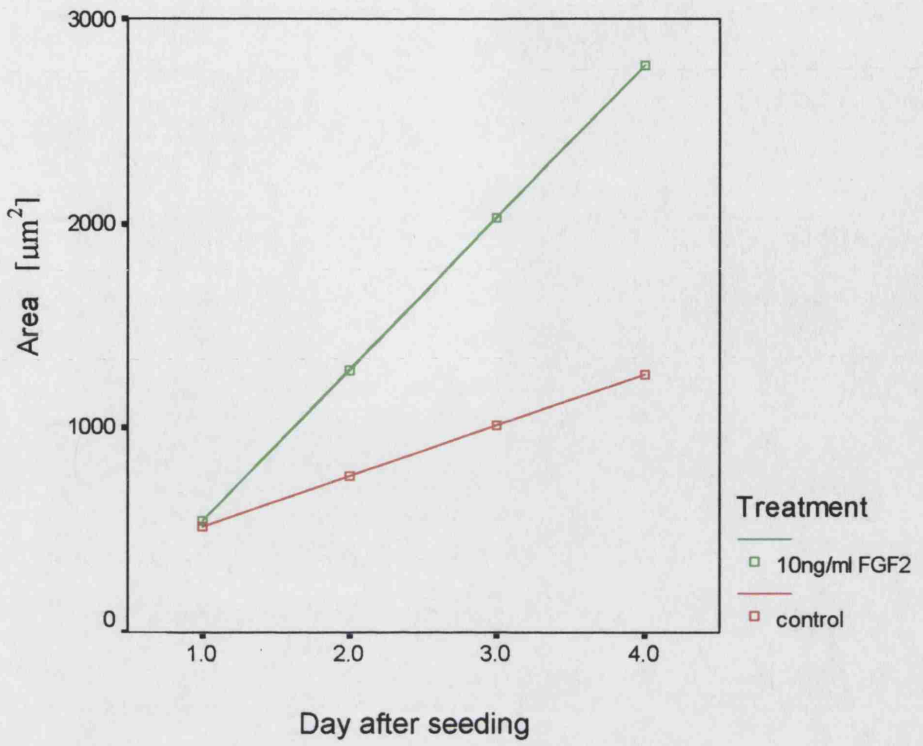

Figure 7. 3 Multiple linear regression analysis of the size of aggregates and vesicles in ± FGF2-treated early vesicle cultures at different times after seeding

The details of the model are given below in table 7.1. The fitted lines show that FGF2-treated aggregates and vesicles become bigger in size over time, the average size difference between control and FGF2 cultures is 462.5 μm^2 (SE: 87.25 μm^2), and the mean difference between the size of aggregate and vesicles between FGF2 and control culture increases every day by 492.03 μm^2.

Model	B_n coefficients	SE	significance	95% CI for B	
				Lower bound	Upper bound
constant	262.240 (B0)	56.70	3.85 e-006	151.085	373.395
Day	250.314 (B1)	21.51	7.70 e-031	208.141	292.488
Treatment	-462.470 (B2)	87.25	1.21 e-007	-633.517	-291.420
Interaction term	492.026 (B3)	35.733	3.04 e-042	421.971	562.081

Table 7. 1 Numerical values of the multiple linear regression model in Fig. 7.1

The table shows the numerical values of the regression model described in the text (Chap.7.2.1.1), for the effect of 10 ng/ml FGF2 on the size of aggregates and vesicles over four days since plating the CPe cells. **SE**: standard error, **95% CI**: 95% confidence interval.

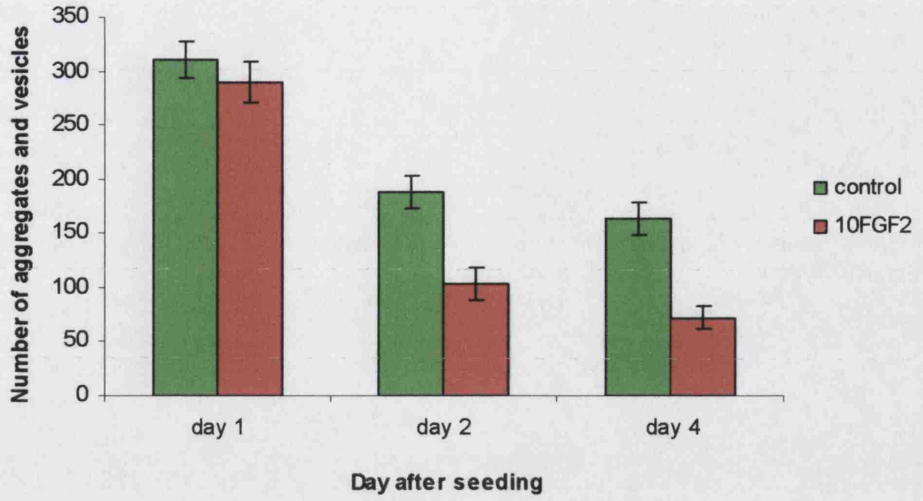

Figure 7. 4 Graph showing the mean number of aggregates and vesicles in ± FGF2-treated and control early vesicle cultures

At least three cultures were used for each treatment, and aggregates/vesicles measured in four fields of view. The standard error bars are shown for each measurement. At 2 and 4 days, the number of aggregates and vesicles is significantly lower in FGF2-treated cultures ($p<0.05$).

7.2.1.3 Effects of FGF2 on CPe cell migration and adhesion

Time-lapse microscopy was used to assess changes in cell behaviour triggered by FGF2. More specifically how cell:cell adhesion and cell migration were affected. In order to do so, a ten-fold higher dose of 100 ng/ml FGF2 was used, which was added on the day of plating the cells in order monitor early cellular responses. A high dose of FGF2 was used to easily visualize cellular responses to this factor as Reid S. (PhD thesis, 2002) showed that FGF2 increased the size of vesicles in a dose dependent manner. The effect of adding a 100 ng/ml FGF2 on the day of seeding the cells (day 0) was first investigated by following the progression of non-treated and FGF2-treated cultures over three to four days.

7.2.1.3.1 Effects of a 100 ng/ml FGF2 on CPe aggregate formation

Pictures of the same fields of view for each culture were taken every 24 hours. The effect of adding a 100 ng/ml FGF2 to CPe cells was dramatic; after the first 24 hours in culture, the aggregates in FGF2-treated cultures were strikingly bigger than in control cultures, and very few in number. To quantify this result, three cultures for

each treatment groups (FGF2 and control) were produced on different days, the areas and the number of aggregates for each treatment groups were measured in four fields of view per culture and plotted against each time point of measurement. Bar charts show the mean size of aggregates (Fig. 7.5) and the mean number of aggregates after one and three days after plating (Fig. 7.6). The scatter plots and the details of the statistical analysis for these results are shown in Appendix III.6-8. The mean size of aggregates after one day in culture (day 1) was 1137.9 μm^2 (SE: 80.8) for control, and 10749 μm^2 (SE: 2119.8) for FGF2-treated cultures. Independent Student's t-test analysis showed that the mean difference between treatments was 7928.6 μm^2 (SE: 532.3), and was strongly significant (p: $1.11x10^{-38}$). After three days in culture the area of aggregates in control cultures was 2922 μm^2 (SE: 335) and in FGF2-treated cultures 15724 μm^2 (SE: 2378). Independent Student's t-test analysis showed that the mean difference between treatments increased to 12801 μm^2 (SE: 1267), and was significant (p: $2.55x10^{-17}$).

The number of aggregates was also quantified. After one day in culture, the mean number of aggregates in non-treated cultures was 143.5 aggregates (SE: 13.6) and in FGF2-treated cultures the mean number was 18 aggregates (SE: 4.0). The mean difference was 125 aggregates (SE: 16.43), and a Mann Whitney U test showed that it was significant (p: 0.032). After three days in culture the mean number of aggregates in control cultures dropped to 92 aggregates but in FGF2-treated cultures the mean number of aggregates remained unchanged, with 18.6 aggregates (SE: 4.37). The mean difference between the treatments was 73 (SE: 11.86) and was significant (p: 0.05).

A 100 ng/ml FGF2 added at the time of plating increased the size of aggregates more dramatically compared to 10ng/ml FGF2 added 24 hours later. Furthermore, cultures treated with a 100ng/ml FGF2 aggregates most of the time failed to form vesicles either because they were too large or/and too compact.

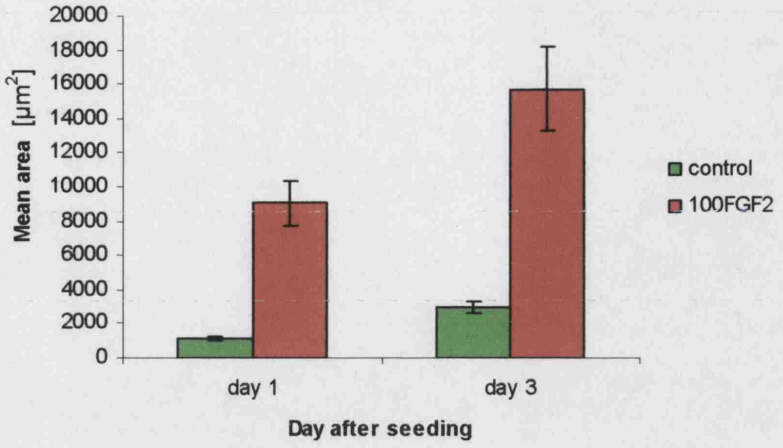

Figure 7. 5 Graph summarizing the mean area of aggregates in ±100 ng/ml FGF2-treated early vesicle cultures

Graph showing the mean areas (in μm^2) of control and 100 ng/ml FGF2-treated CPe aggregates (100FGF2) at one day and three days after seeding the CPe cells along with the standard error of the mean (SE). At least three cultures per condition are used.

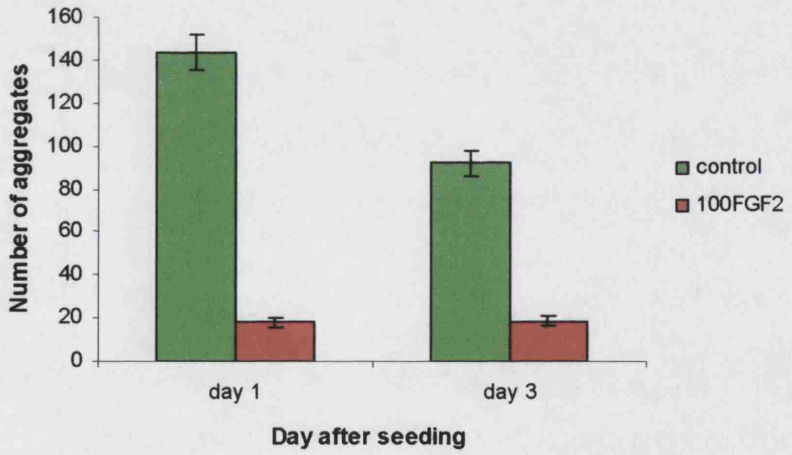

Figure 7. 6 Graph summarizing the mean number of aggregates in ±100ng/ml FGF2-treated early vesicle cultures.

Graph showing the mean number of aggregates in control and 100 ng/ml FGF2-treated cultures (100FGF2) along with the standard error of the mean (SE) at one and three day after seeding the CP cells. At least three cultures per condition are used.

7.2.1.3.2 Effect of a 100ng/ml FGF2 on the rate of aggregate formation

The behaviour of CPe cells seeded on Matrigel with and without 100 ng/ml FGF2 was studied by time-lapse microscopy. Cells were monitored over 20 hours starting at the time of seeding and pictures taken every 30 minutes (CD-ROM: film III.a-b; cf. page 17). The time-lapse experiments were repeated twice for each treatment group. Since only one culture at the time could be followed by time-lapse microscopy, this meant that the time-lapse for different treatments had to be run on two independent experiments. However, each time-lapse had its own control, so that if an untreated culture was analysed, then an FGF2-treated culture was run in parallel and vice versa. Representative frames from the time lapse microscopy experiments for control and FGF2-treated cultured are shown in Fig. 7.7.

The time-lapse study showed that in FGF2-treated cultures, distinct aggregates had formed with very few single cells left by 10 hours after seeding, (Fig. 7.7A-B). After 18 hours, in comparison with control cultures FGF2-treated CPe cells had formed much bigger aggregates that appeared tight, with very little single cells present in the surrounding matrix (compare Fig. 7.7B and C). In contrast, aggregates in non-treated cultures appeared less tight even after 20 hours in culture and many single CPe cells were still present (Fig. 7.7A). Hence, CPe cells formed aggregates much faster in FGF2-treated cultures supporting the idea that FGF2 may be increasing migration or/and cell:cell adhesion. The time-lapse analysis did not allow to clearly distinguish between these two possibilities that are not mutually exclusive.

Figure 7. 7 Time-lapse microscopy frames following the effect of 100ng/ml FGF2 on choroid plexus epithelial cell aggregation

A-B: Time-lapse microscopy picture frames of CPe cells forming aggregates over 20 hours from the time of seeding the cells. Frames are taken after 30 minutes, 5 hours, 10 hours, and 20 hours of growth. **A:** Untreated CPe cells; **B:** CPe cells treated with 100 ng/ml FGF2. **C:** Untreated cells from the same dissection as (B), photographed 18 hours after seeding. Cells in (A) and (B) originate from two separate dissections. Scale bars are 200 μm as shown in the bottom pictures of **(A-C).**

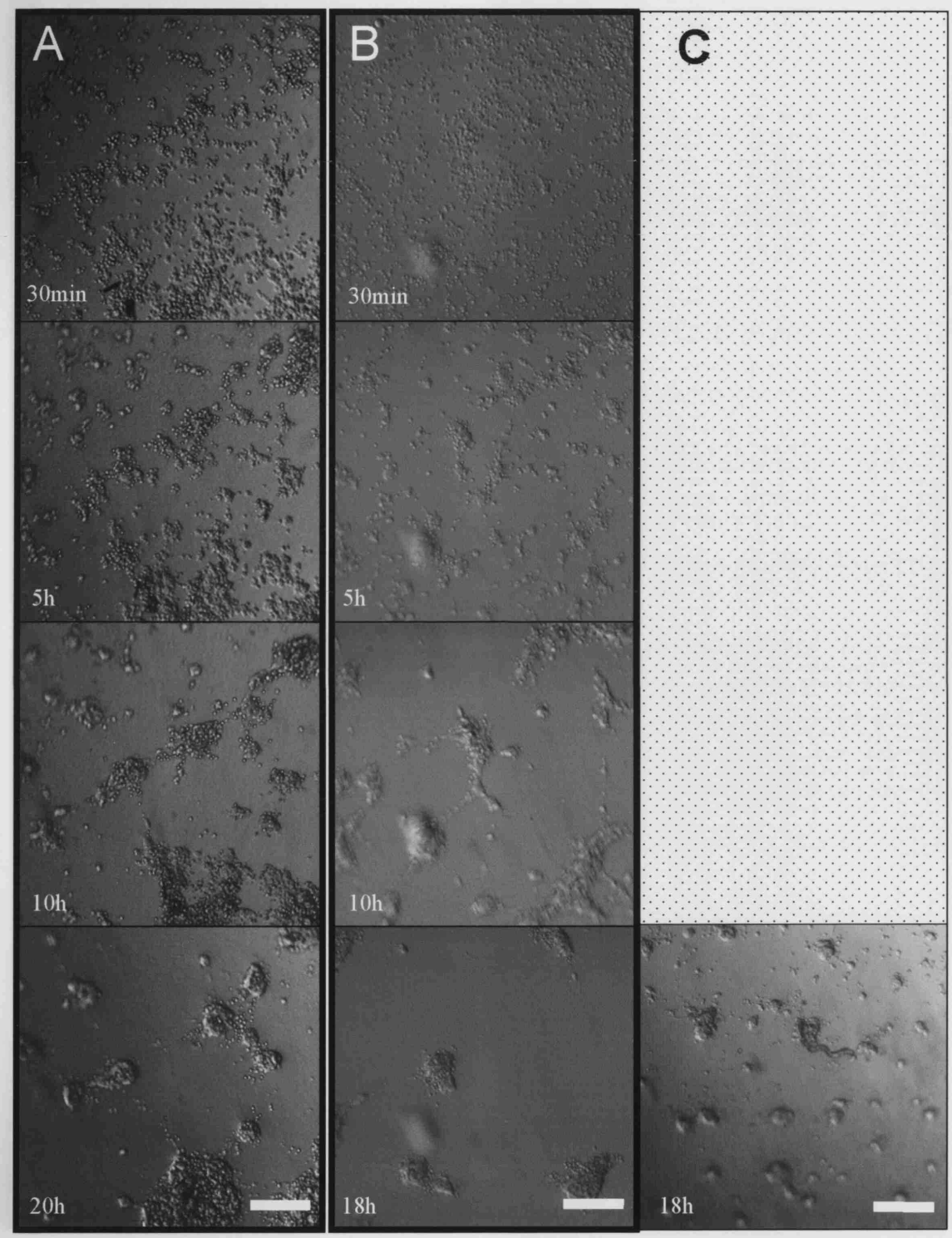
A
B
C
30min
30min
5h
5h
10h
10h
20h
18h
18h

7.2.1.4 Effect of FGF2 on cell proliferation in early culture

The effect of FGF2 on CPe cell proliferation was studied at the early stages of vesicle formation. Cell proliferation was studied by FITC-fluorescence immunocytochemistry using a primary antibody raised against the mitotic marker phosphorylated histone-3 (p-H3). Hence, the effect of 10 ng/ml and 100 ng/ml FGF2 on CPe cell mitosis was studied as the CPe cells first formed aggregates. The growth factor was added on the day of plating and the cells were grown for 24 hours then fixed and processed for p-H3 immunocytochemistry. Only two cultures treated with 100 ng/ml FGF2 were stained but no positively labelled p-H3 cells were detected. Three cultures treated with 10 ng/ml FGF2 and their corresponding controls were stained and the number of p-H3 quantified, using the method described previously in Chapter 6.4.1. There were very few p-H3-positive cells in the aggregates in FGF2-treated and control cultures (Fig. 7.8). Consequently, the mean percentage of p-H3 labelled cells was close to zero for both control and FGF2-treated aggregates (0.62% and 0.47% respectively, the statistics are shown in Table 7.2). Because the distribution of the number of p-H3 cells was non-normal, a Mann-Whitney U test was used. No significant difference was observed in the number of p-H3-labelled cells (p: 0.865) and no correlation was found between the number of p-H3 cells and the number of cells in an aggregate (R: 0.454, p: 0.089).

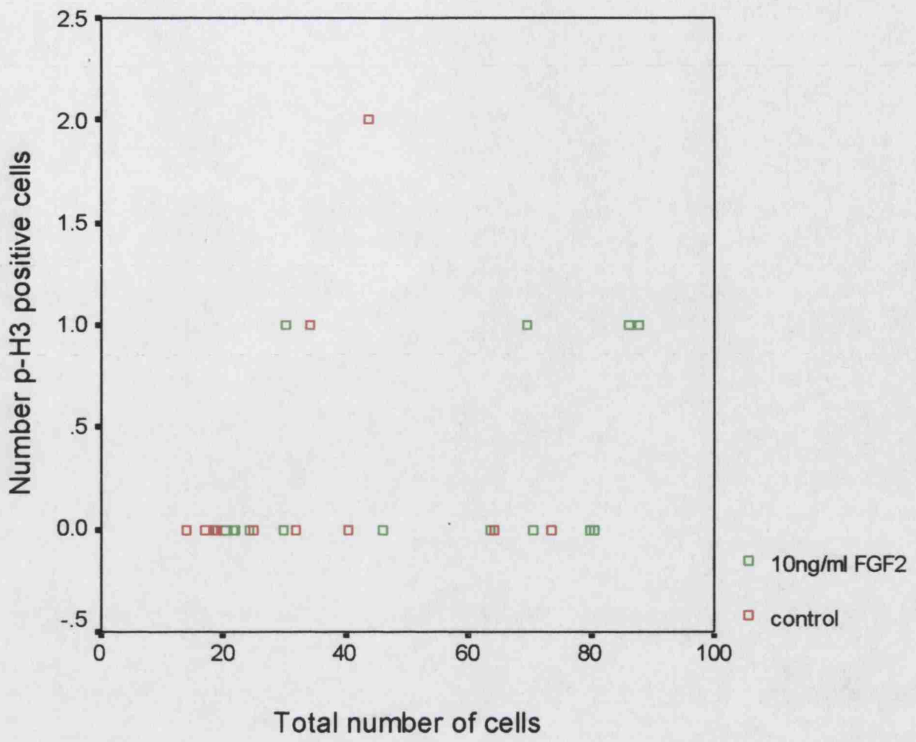

Figure 7. 8 Scatter plot showing the number of p-H3 labelled present in control and FGF2-treated early vesicle cultures

The relationship between the two continuous variables was investigated using Spearman's Rho correlation analysis. No significant relationship was found between the number of cells in the equatorial plane of an aggregate and the number of positive p-H3 labelled cells either in control (R: 0.333, p: 0.190) or FGF2-treated (R: 0.454, p:0.089) cultures.

condition	Mean	N	SD	SE	Minimum	Maximum	Median
control	.0062	12	.01501	.00433	.00	.05	.0000
10FGF2	.0047	15	.00940	.00243	.00	.03	.0000

Table 7. 2 Ratio between the number of p-H3 labelled cells and the number of cells present in control and FGF2-treated CPe aggregates

FGF2 (10 ng/ml) was added to the cultures at the time of plating. The **Mean**, the number of aggregates (**N**), the standard deviation of the mean (**SD**), the standard error (**SE**), the **maximum, minimum**, and **median** values are shown.

7.2.2 Effect of FGF2 on vesicle growth

The effect of FGF2 was also investigated during growth of the vesicles once they had formed. More specifically the effect of FGF2 on cell proliferation, vesicle pulsations, cell recruitment, and on the fluid secretory activity of the CPe cells was studied.

7.2.2.1 Effect of FGF2 on cell proliferation

Vesicles treated with and without 10 ng/ml FGF2 were cultured for four days after plating the CPe cells, fixed in 4% PFA and stained for p-H3 by FITC immuno-fluorescence. Three cultures for each condition were used and 8-15 vesicles were sampled in each culture. The number of p-H3 cells was quantified as described in Chapter 6.4.2. The number of p-H3 cells in each sampled vesicle was plotted against the corresponding total cell number. The scatter plot is shown in Fig. 7.10. Spearman's Rho correlation analysis showed that in control culture there was no relationship between the size of vesicles and their number of p-H3 positive cells (R: 0.198, p: 0.277). In contrast, in FGF2-treated cultures there was a significantly higher correlation between the two variables (R: 0.451, p: 0.012). The mean ratio of p-H3 labelled cells to total number of cells for control cultures was 0.85% (SE: 0.46%), and for FGF2-treated cultures was 1.28% (SE: 0.47%). The statistics for the mean ratio are given in Table 7.3. A non-parametric Mann-Whitney U test showed that the difference between the means for each condition was not significant (p: 0.125).Therefore this suggested that FGF2 did not increase the size of the vesicles by significantly increasing cell proliferation. Since the statistics showed that bigger vesicles had a higher number of mitotic cells in FGF2 treated vesicles, it may be that FGF2 had a slight mitogenic effect on the CPe cells that was more apparent in bigger vesicles which bore more cells.

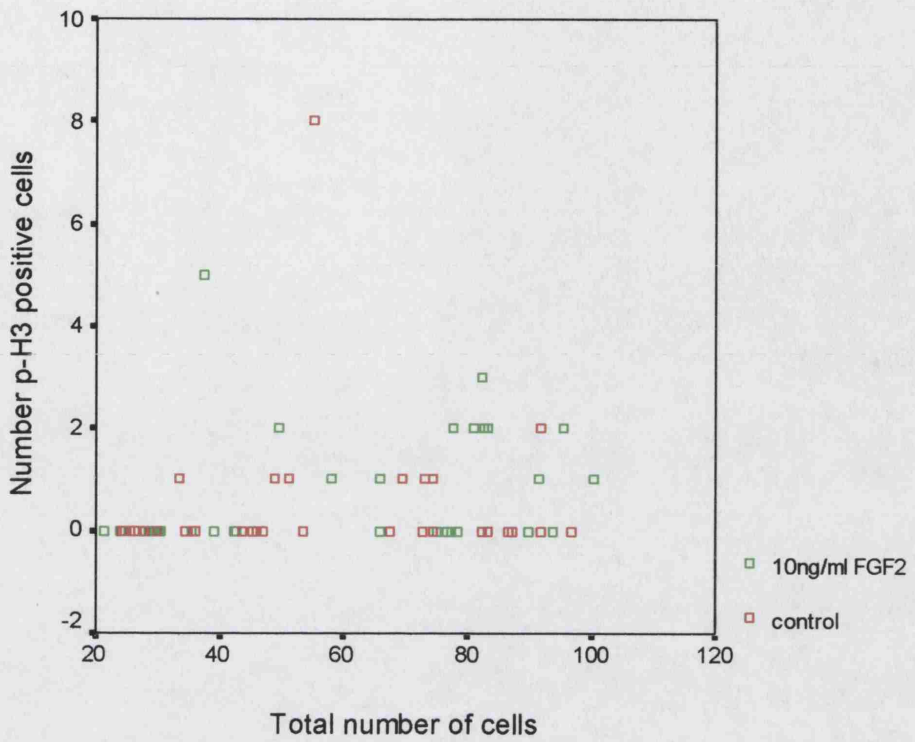

Figure 7. 9 Scatter plot showing the number of p-H3 labelled cells present in control and FGF2-treated vesicles

The relationship between the two continuous variables was summarized by Spearman's Rho correlation analysis. In control cultures the relationship was not significant (R: 0.198, p: 0.277), but in FGF2-treated cultures the positive relationship was significant (R: 0.451, p: 0.012).

condition	Mean	N	SD	SE	Minimum	Maximum	Median
control	.0087	32	.02630	.00465	.00	.15	.0000
10FGF2	.0128	30	.02604	.00475	.00	.13	.0000

Table 7. 3 Ratio between the number of p-H3 labelled cells and the number of cells present in control and FGF2 treated vesicles

FGF2 (10 ng/ml) was added at the time of plating and cell proliferation analysed in vesicles formed four days after plating. The **mean**, the number of vesicles sampled (**N**), the standard deviation of the mean (**SD**), the standard error (**SE**), the **maximum minimum**, and **median** values, are shown.

7.2.2.2 Effect of FGF2 on dynamic of growth

FGF2 (10 ng/ml) was added at day 1 after plating the cells, and its effect on vesicle behaviour monitored on 8 day cultures by time-lapse microscopy over 48 hours (CD-ROM: Film IV.a-b; cf. page 17) and Fig. 7.11. This study was purely qualitative, and the experiments were repeated at least twice for each condition.

As in control cultures, no cell migration and cell recruitment of CPe cells into the vesicles was observed in FGF2-treated cultures during the course of the time-lapse recording. Only a very few single cells were present in the cultures by 8 days. The single cells and the small aggregates present at that stage were more likely to be contaminating mesenchymal cells or neuronal cells than CPe cells. Hence, FGF2 didn't affect CPe cell recruitment simply because all CPe cells had already incorporated into vesicle structures and no single CPe cells were left in the cultures.

The contraction and expansion of the vesicles observed in control cultures was also observed in FGF2-treated cultures, and no obvious differences were apparent between FGF2-treated and control vesicles. The pulsations, however, were not systematically quantified to assess any subtle change due to FGF2-treatment. Since it was surmised that the pulsation of the vesicles was a consequence of the secretory activity of the cells, rather than measuring the frequencies of pulsations of the vesicles, the secretory activity of the CP cells was evaluated using the approach described in the next section.

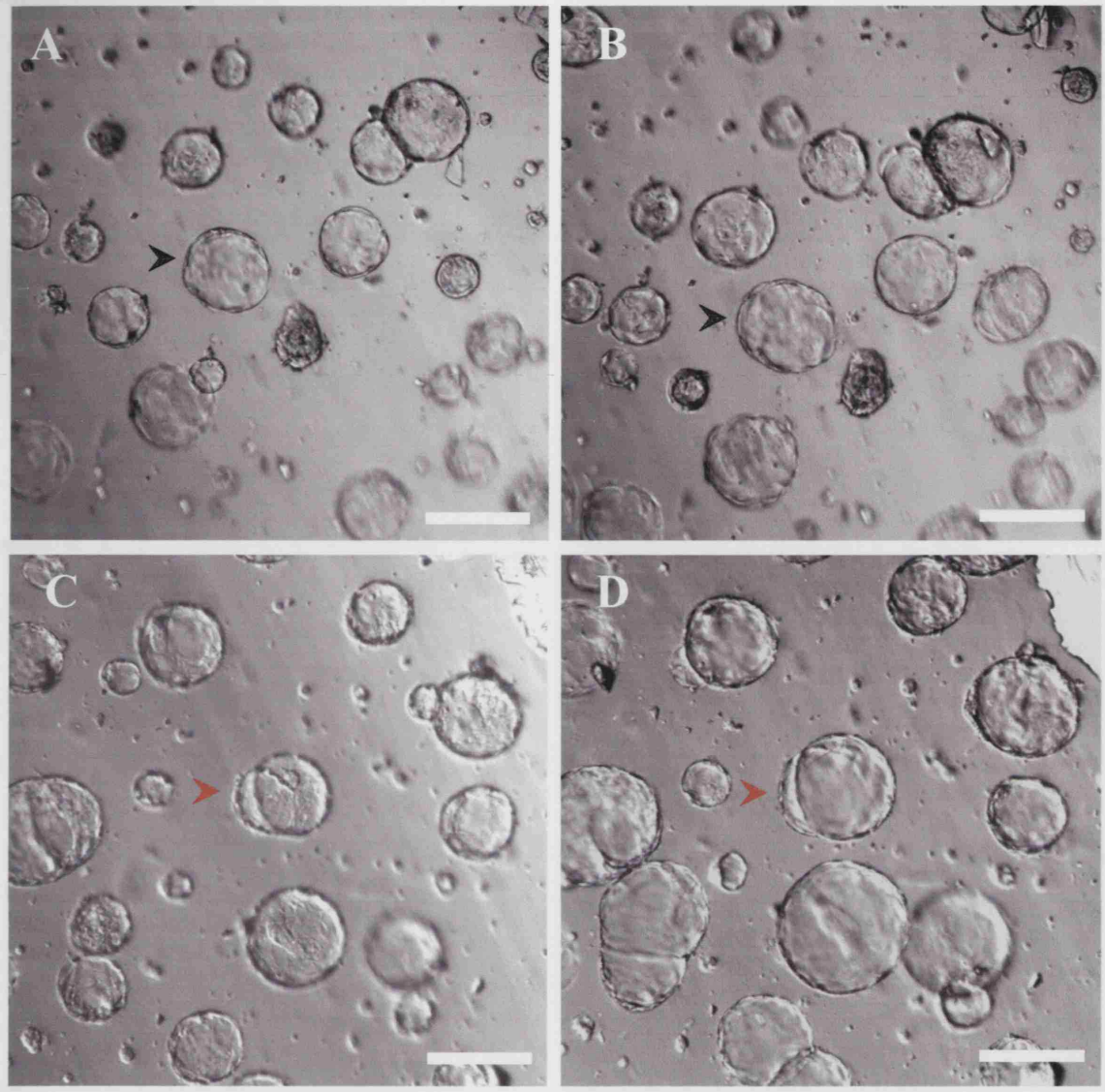

Figure 7. 10 Representative frames from a time-lapse microscopy experiment looking at the effect of 10 ng/ml FGF2 on vesicle growth

Beginning (A-C) and end time points (B-D) of time lapse microscopy experiments following the effect of 10 ng/ml FGF2 on vesicle growth over 48 hours (CD-ROM: Film IV. a-b). The vesicles have been in culture for eight days either with or without FGF2, which was added one day after plating. **A-B:** Control vesicles; **A:** time-lapsed 1 hour, **B:** time lapsed 48 hours; in A and B a black arrowhead points to the centre of the culture to help orientation. **C-D:** FGF2-treated vesicles; **C:** time-lapsed 1 hour, **D:** time-lapsed 48 hours. In **C-D** a red arrowhead points to the centre of the culture to help orientation. Scale bars are all 200 μm.

7.2.2.3 Effect of FGF2 on fluid secretion

Vesicles cultured for eight days after plating the CPe cells, with and without 10 ng/ml FGF2, were collapsed with a combination of 5 mM ouabain and 100 μM acetazolamide for two days. The recovery of individual vesicles, with and without FGF2, was then monitored daily over eight days, taking pictures of the cultures every 24 hours. Since vesicles had different sizes, the recovery of each vesicle was expressed as a percentage of its original *area* measured on the day before the addition of ouabain and acetazolamide (% recovery). In order to ensure a narrower margin of variation of the data, the natural logarithm (ln) of the % recovery was taken. The individual recovery curves for each vesicle are summarized in Appendix III.9. The statistics for this data are shown in Table 7.4, and the significance between the mean percentage of recovery in FGF2 and control vesicles at each time point was assessed by independent Student's t-test analysis (Table 7.5).

Control vesicles collapsed significantly less than FGF2-treated vesicles (day 0, p: 0.034). However, since vesicles below a certain *area* (< 4000μm^2) collapsed non-homogeneously (see Chap. 6), when only vesicles over 4000 μm^2 were considered, then the difference in collapse between control and FGF2-treated vesicles was non-significant (p: 0.132; [N_{FGF2}: 105 vesicles, $N_{control}$: 102 vesicles]). By plotting the % recovery values after collapsing the vesicles and the % recovery values after eight days of recovery period (Appendix III.10), it was possible to show that there was no correlation between the amount a vesicle was collapsed and the amplitude of its recovery after eight days (R: 0.077, p: 0.510), but that there was a lot of variability in the % recovery of the vesicles. By day 8, control vesicles had recovered on average 37% more than FGF2 vesicles (day 8, p: 2.56×10^{-4}). However, it was the slope of the recovery lines for each vesicle that reflected the rate of fluid secretion expanding the vesicles. It was therefore more informative to reason in term of the slopes of the recovery lines using a multilevel modelling approach.

The results were analysed by multilevel modelling using the MLwiN 1.10 software (*Centre for Multilevel Modelling, Institute of Education, University of London*). A 3-level model of the data was used that looked at the variation of the data at each day (Level 1), for each vesicle (Level 2), and for each experiment (Level 3). It incorporated as influencing factors (or explanatory variable), the effect of days in cultures (**day**), the effect of treatment (**treatment**), and a quadratic term

int(day*treatment), that assessed the average daily increase or decrease in recovery due to the presence of FGF2 . The β_0 **.constant** term is the fixed parameter associated with the intercept of the lines i.e it gives the smallest possible % recovery value for FGF2-treated and control vesicles. The numerical values for the coefficients (β_n) of each explanatory variable are given along with their standard error. The fixed part of the model was the following:

% recovery = β_0**.constant** + β_1**.day** + β_2**.treatment** + $\beta 3$ **. int(day*treatment)**

% recovery = β_0: -0.922 (SE: 0.084) + β_1: 0.174 (SE: 0.008) +

Control ⟶

10ng/ml FGF2 ⟶ β_2: **-0.009** (SE: 0.121) + β_3: **-0.013** (SE: 0.012)

The random variation associated with each level of the model was:

Level 1- variation between all vesicles at each day: 0.145 (SE: 0.006)

Level 2-variation between each vesicle line: slope: 0.003 (SE: 0.001), intercept: 0.103 (SE: 0.016)

Level 3- variation between experiments: 0.017 (SE: 0.012)

The variance is given for each level of analysis of the model, and the units for all the values are (ln % recovery). The graphical details of the model are shown in Appendix III.11.

The ln % recovery of a vesicle over time was a linear relationship. The slope of this line reflected the rate of recovery of the vesicle. Thus, the multi-level model allowed comparing the mean rate of recovery for FGF2-treated and non-treated vesicles. It was assumed following S.Reid's results (PhD thesis) that the rate of recovery of vesicles was independent of their size. The model showed that for each additional day of recovery, % recovery of vesicles was 1.19 (95% confidence interval [1.17, 1.21]) times higher than the previous day (since anti-log of (0.174) = 1.19 and anti-log (1.19 ± 1.96 (0.008)), $p<0.05$). However, there was no significant difference in recovery patterns between control and FGF2 treatment groups (p: 0.1), even though there was a trend for FGF2-treated vesicles to recover less fast than non-treated ones (Fig. 7.11). This result therefore cast some reservations on the inhibitory effect of FGF2 on vesicle recovery as supported by Student's Independent t-test analysis in Table 7.5.

Day	Treat	Mean	N	SD	SE	Min.	Max.	Med.
0	Control	0.35	115	1.55	1.04	0.11	1.02	0.35
	FGF2	0.31	110	1.44	1.04	0.15	1.00	0.32
1	Control	0.42	84	1.53	1.05	0.14	1.70	0.41
	FGF2	0.37	96	1.56	1.05	0.11	1.19	0.36
2	Control	0.66	115	1.84	1.06	0.11	3.19	0.63
	FGF2	0.56	110	1.62	1.05	0.16	2.12	0.56
3	Control	0.80	84	1.60	1.05	0.30	3.03	0.77
	FGF2	0.89	96	1.77	1.06	0.21	4.10	0.87
4	Control	0.93	115	1.70	1.05	0.23	4.66	0.94
	FGF2	0.97	110	1.75	1.05	0.24	2.86	0.90
6	Control	1.03	84	1.64	1.06	0.39	3.39	1.00
	FGF2	0.82	96	1.64	1.05	0.14	2.41	0.83
8	Control	1.26	83	1.71	1.06	0.36	4.90	1.12
	FGF2	0.89	94	1.70	1.06	0.23	3.82	0.83

Table 7. 4 Statistics for ln transformed % recovery of FGF2 and control vesicles

Day: number of days (1-8) the vesicles have been recovering after having been collapsed by acetazolamide/ouabain treatment; **treat**: refers to whether the vesicles are **FGF2-treated** or **control** vesicles; The results table shows the **mean** (inversed ln[% recovery]), the number of vesicles per condition (**N**), the standard deviation of the mean (**SD**), the standard error of the mean (**SE**), the **minimum**, **maximum**, and **median** values.

Day	Significance	Mean	SE	95% Confidence Interval	
				Lower	Upper
0	0.034	0.116	0.0542	0.00907	0.222
1	0.023	0.148	0.0645	0.0202	0.275
2	0.019	0.175	0.0734	0.0289	0.320
3	0.166	-0.113	0.0816	-0.275	0.0476
4	0.594	-0.0416	0.780	-0.195	0.112
6	0.009	0.232	0.0877	0.0586	0.405
8	2.56E-4	0.363	0.0969	0.172	0.555

Table 7. 5 Independent Student's t-test between ln transformed % recovery of FGF2-treated and control vesicles

Day: number of days (1-8) the vesicles have been recovering after having been collapsed by acetazolamide/ouabain treatment. The table shows the **significance** of the t-test, the mean difference (**mean**) between control and FGF2-treated vesicles, the standard error of the mean difference (**SE**), the **95% confidence interval** of the mean difference (**lower** and **upper** bounds).

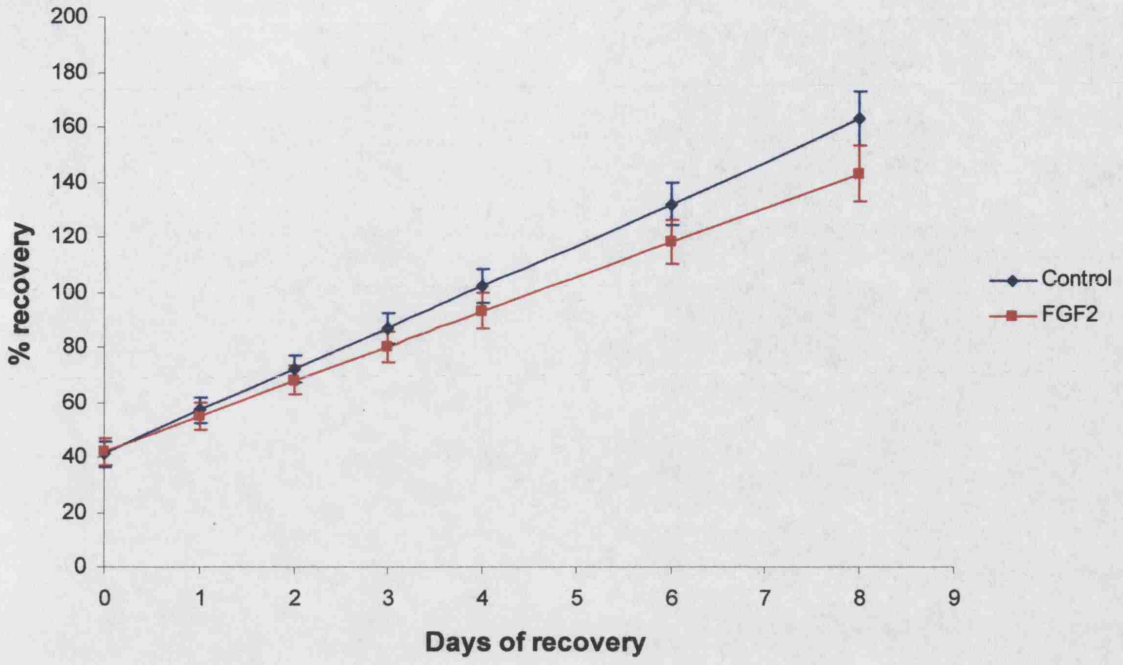

Figure 7. 11 Graphical prediction from the multilevel model showing the mean difference in the recovery of FGF2 and control vesicles

The recovery of the vesicles is expressed as the ln of the percentage of the vesicle area before collapsing. The multilevel model predicted that on average FGF2-treated vesicles had a recovery rates (the slope of the line) that was -0.013 (ln %recovery) per day (SE: 0.012) lower than control vesicles. The error bars show the standard error of the mean for the recovery of FGF2 and control vesicles.

7.3 Discussion

7.3.1 Effect of FGF2 on vesicle formation

In order to understand how FGF2 causes the growth of bigger vesicles, the effect of FGF2 on the early stages of vesicles formation was investigated. It was found using two doses of FGF2 (10 ng/ml and 100 ng/ml) that the basic effect of FGF2 on the CPe cells was to cause them to form bigger aggregates, which then translated in the formation of bigger vesicles. The higher dose of FGF2 (100 ng/ml) induced formation of bigger aggregates than the lower dose (10 ng/ml) confirming the dose dependent effect of FGF2 (Reid S, 2001). This finding is also consistent with the observation in chapter 6 that the size of vesicles was a function of the size of the aggregates formed 48 hours after plating the CPe cells. It also explained why when FGF2 was added on the day of plating the vesicles treated with FGF2 were already bigger after four days in culture but then did not grow faster than control vesicles.

The bigger aggregates in FGF2-treated cultures were not caused by an increase in proliferating cells. This was not surprising since in-vivo the CPe expresses high level of FGF2 (Chap. 4 and (Sturrock, 1979)) but is devoid of mitotic cells except in the localised region of its root. Interestingly, FGF2 was found by Reid S. (PhD thesis, 2002) to act as a mitogen on embryonic CPe cells grown as a monolayer on laminin substrate. This differential effect of FGF2 showed that CPe cells were sensitive to the environment and substrate they were in and that the Matrigel substrate mimicked best their in-vivo environment. Having ruled out cell proliferation, it was then clear that the effect of FGF2 was to increase cell recruitment into aggregates. In fact, time-lapse microscopy revealed non-quantitatively that the rate of aggregation of FGF2-treated CPe cells was faster than in contol. However, it was not clear whether FGF2 was affecting cell migration or cell:cell adhesion or both.

The actual cell:cell adhesion molecules that mediated the aggregation of CPe cells still remain to be elucidated. The best candidates are the members of the cadherin family of cell adhesion molecules. The CPe cells have been shown to express the cell adhesion molecules cadherin B-, N-, and R- (Napolitano et al., 1991; Marrs et al., 1993; Lagunowich et al., 1992) (Redies et al., 1993). Therefore it is possible that FGF2 signalling as reported by other authors in the literature may modulate the expression and post-translational state of the cadherins. For instance, FGF2 has been shown to increase the expression of N-cadherin in human calvaria

osteoblasts (El Hariry et al., 2001), and in pancreatic adenocarcinoma cells FGF2 upregulated E-cadherin and β-catenin proteins (Debiais et al., 2001). It is interesting that in the presence of 100 ng/ml FGF2, although much bigger CPe aggregates formed than with 10 ng/ml FGF2, vesicles often did not form as if the aggregates were too compact to hollow out, suggesting stronger cell:cell adhesion contacts.

Of course FGF2 may also have been increasing CPe cell migration. After all, the effect of FGF2 on cell migration is well established. In wound healing FGF2 has been found to increase and facilitate the migration of endothelial and fibroblastic cells (Gualandris and Presta, 1995; Besser et al., 1995; Sepp et al., 1994). In human lens epithelial cells FGF2 was found to induce actin cytoskeleton reorganization and the formation of focal adhesions that was mediated, at least in part, through the Rho/Rho kinase-mediated signalling pathway (Maddala et al., 2003), and FGF2 was also found to significantly increase the cell migration of retinal pigment epithelial cells (Spraul et al., 2004)

Further studies are needed to dissect out whether FGF2 is affecting CPe cell migration and/or cell:cell adhesion. Time lapse microscopy experiments based on the mathematical model proposed by Neelameghan S et al. (1997) to study the kinetics of homotypic cellular aggregation should enable evaluating the migration and adhesivity of the cells. A molecular approach would complement this method and help to understand the role of FGF2. For example, specific cell:cell adhesion molecules like the cadherins could be modulated (such as B- or N-cadherin) to study how they inhibit the formation of CPe cell aggregates in the presence and absence of FGF2 at different doses. Quantitative analysis of protein and RNA expression by Western blotting and semi-quantitative are unfortunately not compatible with the low cell yield associated with this model, but the use of real time RT-PCR should allow to determine changes in RNA expression. The use of a stable cell line would be much advantageous for these types of studies.

At present, the role of FGF2 in CP development is still unclear as in-vivo FGF2 doesn't seem to be expressed in any specific pattern within the CPe or ependyma. It may be that FGF2 is important for maintaining cell adhesion and normal function of the CPe as its expression is maintained in the adult CPe. It is also possible that FGF2 is required along with other growth factors or extracellular matrix components present within the Matrigel to induce cell migration and/or cell:cell adhesion.

7.3.2 Effect of FGF2 on vesicle growth

FGF2 did not increase proliferation, or recruitment of CPe cells into vesicle epithelial walls. This was consistent with the finding that vesicles formed from a finite number of cells within the aggregate they originated from, and that the main effect of FGF2 was to induce formation of bigger aggregates. The effect of FGF2 on fluid secretion was studied using an assay based on the knowledge acquired in chapter 6 that it was possible to collapse the vesicles with pharmacological inhibitors of fluid secretion. The vesicles were collapsed all at once and the effect of FGF2 was observed as the vesicles recovered from the drug treatment over eight days. The rate of recovery for each vesicle was independent of its original size and reflected the rate of fluid secretion that drove its growth.

A multi-level analysis showed showed that on average FGF2-treated vesicles recovered slightly slower than non-treated vesicles, although the significance of this result was shaded by the high variability in recovery rates of individual vesicles. It may be possible that by increasing the number of vesicles and experimental runs the significance of this result could be confirmed. This result, however, was consistent with the previous finding by Reid S. who showed that a 100 ng/ml FGF2 transiently inhibited (albeit over two days) the growth of vesicles grown six days after seeding the CPe cells. It also confirmed the finding by (Hakvoort and Johanson, 2000), that FGF2 rather than increasing fluid secretion actually inhibited it. In fact, experimental evidence from other studies corroborates the idea that FGF signalling may actually have an inhibitory role on fluid secretion by the CPe cells in contrast to the lung where FGF7 was shown to activate fluid secretion. Indeed, activation of PKC, one of the main second messengers stimulated by FGFR signalling, was found to inhibit the Na/K ATPase pump (Cheng et al., 1997), as well as the inward rectifying Cl^- conductance (similar to CIC-2) in the rat choroid plexus (Kajita et al., 2000). Furthermore, in astrocytes PKC was also found to inhibit the aquaporin 4 water channel (Nakahama et al., 1999). It is interesting that Reid S (Phd thesis 2002) showed that a high dose of FGF2 appeared to transiently inhibit vesicle growth over two days, whereas the relatively low dose of FGF2 tested here appeared to induce a more sustained response. It is possible that a high dose of FGF2 caused only a transient inhibitory effect due to a downregulation of a subset of the FGFR receptors involved in mediating this particular response, as part of a negative feedback

mechanism. For instance, exposure of mouse fibroblasts to FGF2 results in the dramatic downregulation of the mRNA levels for FGFR2, while expression for FGFR1 appears unaffected (Ali et al., 1995). It would thus be interesting to study the effect of FGF1 that stimulates a broader set of FGF receptors and see whether the inhibitory effect can be maintained or amplified.

7.4.3 Final comments

During the early events leading to the formation of vesicles, FGF2 increased cell:cell adhesion and/or cell motility between CPe cells which led to the formation of bigger aggregates that eventually hollowed out into vesicles. FGF2 did not seem to affect other cellular mechanisms such as cell proliferation.

FGF2 did not increase cell proliferation in mature vesicles growth. FGF2 did not increase cell recruitment into vesicles, nor did it noticeably alter the dynamic pulsations of the vesicles in the vesicle model. An assay was developed in order to investigate whether FGF2 affected fluid secretion. The assay showed that FGF2 may have a slight inhibitory effect on fluid secretion as reported in the literature; however the model was not fully satisfactory due to the inherent variability of vesicle structures. A more direct and sensitive approach to investigate whether FGF2 affected fluid secretion by the CPe was needed, such as the bi-chamber Transwell system used by Hackvoort et al (1998). Since the number of embryonic mouse CPe cells obtained from each time-consuming dissection was prohibitively too low for this type of assay, a rat adult cell line was used to attempt to resolve this question as described in the next chapter.

Chapter 8 Effect of FGF2 signalling on the function of rat adult choroid plexus epithelial cells

8.1 Introduction

The drawback with the mouse primary cell cultures was that very small numbers of CPe cells were obtained from each time-consuming dissection and this prevented the design of experiments that necessitated a high number of cells. For this reason, an immortalized CPe cell line was used, which was called TRCSFB-2. This is one of the five cell lines isolated by Kitazawa T et al. (2001) from a transgenic adult rat harbouring a temperature-sensitive simian virus (ts SV40) large T-antigen gene (Tg rat). The aim of this chapter was to extend the characterization of this cell line and to test the effect of FGF2 on the function of these cells, namely their fluid secretory activity and cell proliferation. Therefore, I studied the expression of genes associated with hydrocephalus (see Chaps.4-5), the expression profile of FGF receptors (FGFR), and established whether these cells were able to secrete fluid. I then investigated whether FGF2 affects fluid secretory activity. Two approaches were used to this purpose: (1) set up a functional assay to measure the effect of FGF2 on fluid secretion, and (2) study the effect of FGF2 on the transcription and translation of genes (E2F5, FoxJ1, p73) associated with a hydrocephalic phenotype and hence possibly involved in the control of secretion (see Chap.1). In the final part of the study I examined the effect of FGF2 on the cell proliferation of the TRCSFB-2 cells using different assays to compare their response to that of the primary embryonic cells.

8.1.1 TRCSF-B CPe cell line

The TRCSFB-2 cell line can be immortalized by growing them at 33°C. At this temperature, the T-antigen becomes active and induces cell proliferation by interacting with the retinoblastoma family (Rb) of tumour suppressors (pRb, p107, and p130) and p53, which normally regulate cell proliferation and mediate cellular growth-arrest (see Fig. 8.1) (Terasaki and Hosoya, 2001). At 37°C the Ts T-antigen is inactivated and the TRCSB-2 cells grown under more normal conditions and have a

more limited life span. In this study the characterisation of the cells and the functional assays were carried out on TRCSFB-2 cells grown for at least two days at 37°C.

The large T-antigen was reported to be unlikely to disrupt any other critical genes in the TRCSFB cells since the Tg rat was homozygous (Terasaki and Hosoya, 2001). The TRCSFB cells were shown to have a polygonal shape typical of CPe cells. Furthermore, they stained strongly for TTR and Na^+/K^+ ATPase, which are two genes expressed specifically by CPe cells. The author's were also able to use the cells in collagen coated Transwell (bi-chamber) devices where they were able to study Na^+ dependent amino-acid transport activity. Therefore, the TRCSFB-2 cells seem to bear properties of normal CPe cells.

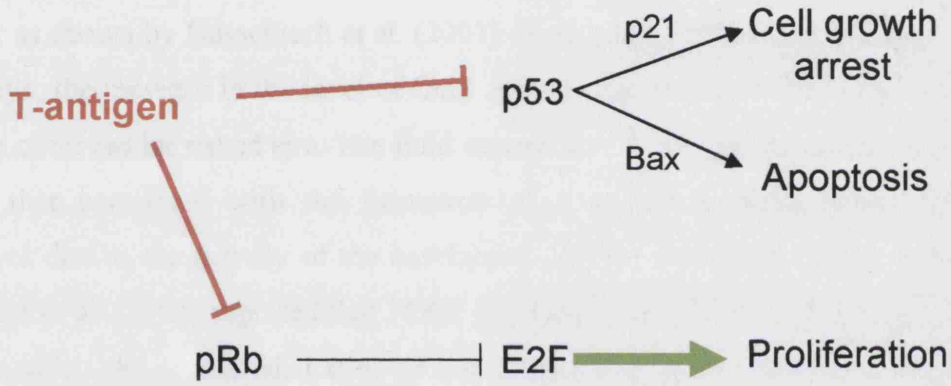

Figure 8. 1 Activated ts SV40 large T-antigen mechanism of action at 33°C

The T-antigen binds to the pRb allowing release of E2F transcription factors that induce cell proliferation, while also inhibiting the p53 protein which mediates cell growth arrest and/or apoptosis in response to abnormal mitogenic signals (such as high levels of free E2F)

8.1.2 Description of functional assays

8.1.2.1 Secretion assay

Haselbach et al. (2001) and Southwell et al. (1993) showed that CPe cells grown as a monolayer over a permeable Transwell filter separating two chambers have tight junctions, and when confluent form a water tight, polarised barrier that is able to maintain a hydrostatic pressure difference between the upper (apical) and lower (basal). CPe cells including TRCSFB-2 have been shown to become polarized when cultured as monolayers with the apical ciliated side facing upwards. Thus, the basal

side of the cells faces the basal/bottom chamber, whilst the apical, ciliated side of the cells faces the apical/top chamber.

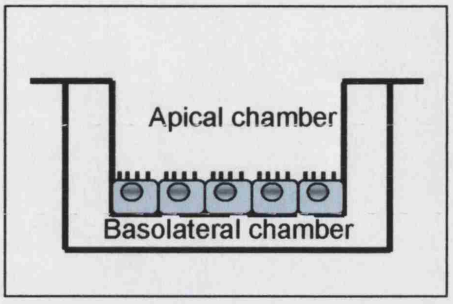

Figure 8. 2 diagram of the in-vitro cellular barrier model

CPe cells were grown on a permeable Transwell filter insert. The apical compartment corresponds to the CSF-side in-vivo, whereas the basolateral compartment corresponds to the blood side (adapted from (Haselbach et al., 2001))

This means that the cells secrete fluid from the basal chamber into the apical chamber as shown by Hasselbach et al. (2001) using adult porcine primary cells. Over a few days, the increase in the level of fluid actively secreted into the apical chamber could be observed by naked eye. The fluid secretion was also shown to be a saturable process that correlated with the formation of a proton gradient across the cell monolayer due to the activity of the basolateral Na^+/H^+ exchanger. Using this assay Hackvoort et al. (2001) reported that FGF2 decreased the amount of fluid secreted by the CPe cells. As discussed, I tried to use a modified version of this assay to see whether the TRCSFB-2 cells were capable of active fluid secretion, and how it was affected by FGF2.

8.1.2.2 Proliferation assay

It had been previously shown that FGF2 could increase the amount of cell proliferation in embryonic CPe cell cultures grown as monolayers on laminin (Reid S, 2001). Therefore, it was important to establish whether TRCSFB-2 cells would respond to FGF2 in the same way. Two types of assays were used to assess the effect of FGF2 on TRCSFB-2 proliferation: 1) an assay based on the metabolic activity of the TRCSFB-2 cells (Alamar Blue assay), and 2) an enzyme linked immuno assay (ELISA) measuring bromodeoxyuridine (BrdU) incorporation into the DNA of the cells adapted from (Muir et al., 1990; Profit and Unteregger, 2001).

8.2 Results

8.2.1 TRCSFB-2 characterization

8.2.1.1 Characterization at the cellular level

The TRCSFB-2 cells were grown on collagen type I substrate as described by Kitazawa et al. (2001). When they reached confluency, the cells exhibited a cuboidal shaped morphology typical of CPe cells (Fig. 8.3A). In contrast, non confluent cells had a fibroblastic like appearance (Fig. 8.3B). It was shown by immunocytochemistry that the cells expressed TTR cytoplasmically (Fig. 8.3), as reported by Kitazawa et al. (2001). The tight junction protein ZO-1 was specifically expressed at the point of cell:cell contact in confluent TRCSFB-2 cells (Fig. 8.4); the actin cytoskeleton of the cells was revealed by immunocytochemical staining of the cytoskeletal protein β-actin. This immunocytochemical analysis thus confirmed that those cells have a CPe phenotype and were capable of forming a water tight barrier. It was also observed, however, that some cells tended to grow one unto another rather than in apposition.

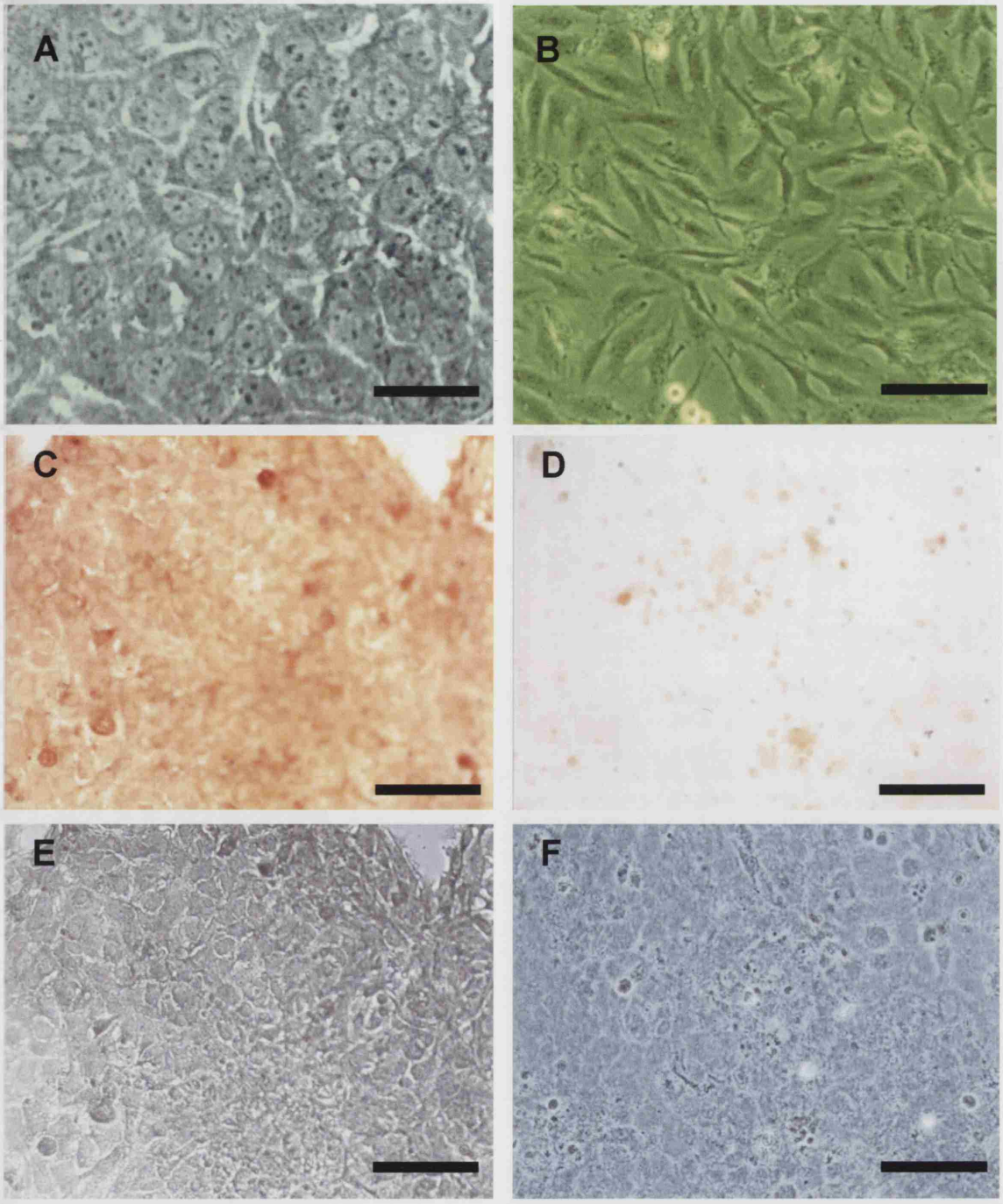

Figure 8. 3 TRCSFB-2 basic characterisation

A: Phase contrast picture of confluent cells; **B:** phase contrast of sub-confluent cells. **C:** TTR staining. **D:** Control TTR staining, no primary antibody was added. **E:** Phase contrast of (**C**). **F:** Phase contrast of (**D**). Scale bars in A is 20 μm and in B is 40 μm, scale bars in **C-F** are 50 μm.

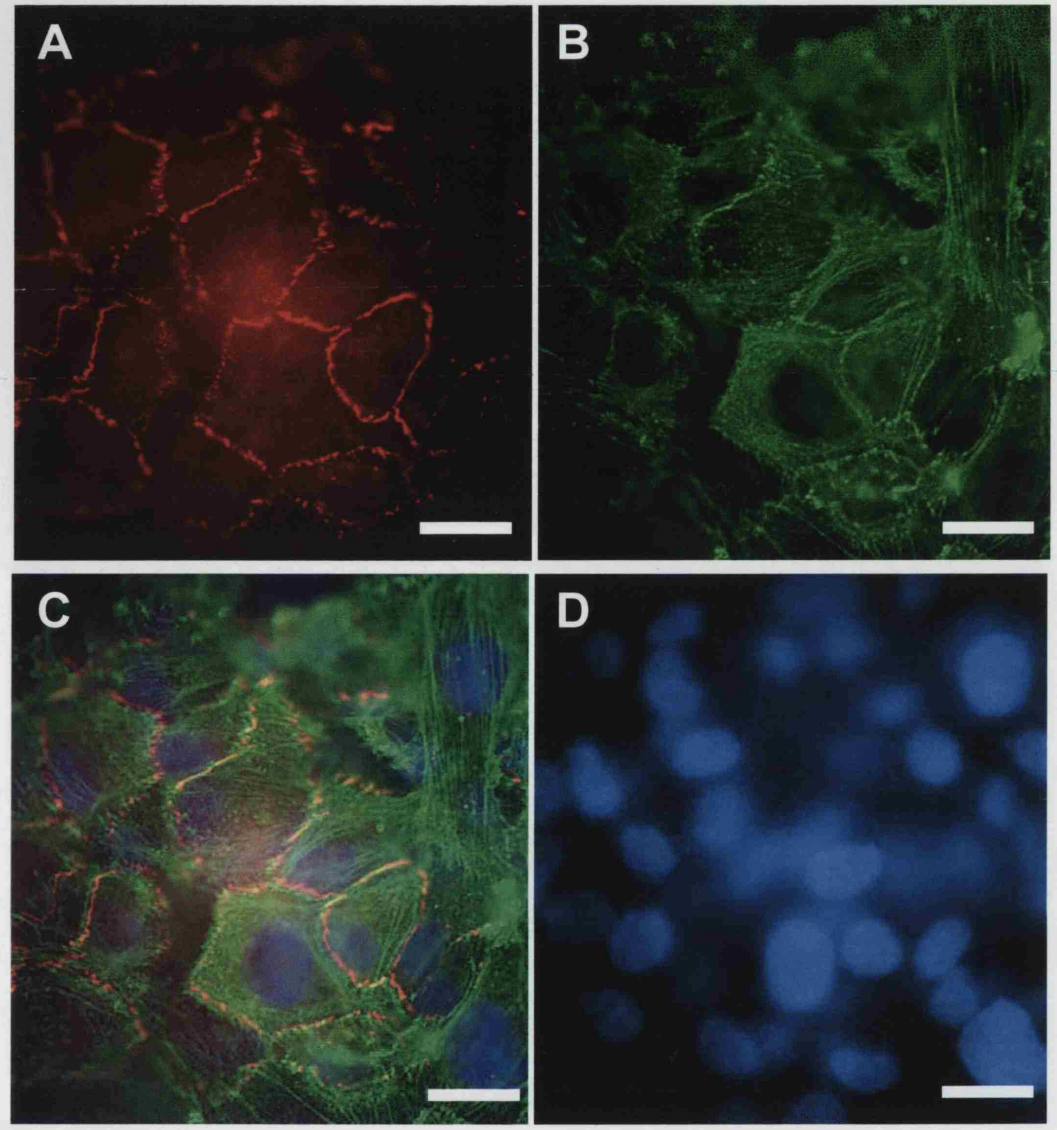

Figure 8. 4 Expression of the tight junction protein ZO-1 and β-actin by TRCSFB-2 cells

A-D: View of the same field under different fluorescent filters. **A**: ZO-1 protein; labelling is localized to the edges of the cells. **B**: β-actin protein staining reveals the actin-cytoskeleton of the cells. **C**: Overlay of A and B. **D**: Hoechst nuclear staining. Scale bars are all 20 μm.

8.2.1.2 mRNA expression profile

8.2.1.2.1 CPe gene markers

Transcription of genes whose knockout lead to hydrocephalus, E2F5, FoxJ1, and p73 was analysed by reverse transcription polymerase chain reaction (RT-PCR) using mRNA extracts from 70% confluent TRCSFB-2 cultures grown at 37°C for 2 days. It is important to point out that no difference in the expression of these genes was observed between mRNA extracts from TRCSFB-2 cells grown at 33°C and 37°C (not shown). The housekeeping gene GAPDH showed that mRNA was successfully extracted, and allowed comparing the relative level of expression for each gene. In addition, TTR expression was also examined. Amplification of the cDNA fragments for each gene marker was checked using mRNA extracts from a 14.5 dpc mouse brain (Fig. 8.5). Products of the predicted size were amplified from each set of primers.

As shown by RT-PCR, E2F5 mRNA was strongly expressed in TRCSFB-2 cells grown at 37°C, whereas FoxJ1 mRNA was more weakly expressed. Two sets of primers were used to amplify two different fragments of p73 cDNA. One set of primers span exon 10 and yielded a 100 bp product, whereas the second set of primers span exon 6 to exon 9 and yielded a 268 bp product. However, both PCR products had low band intensity (Fig. 8.5)

The amplification of TTR and FoxJ1 cDNA fragments was specific to CPe cells, since no amplification was observed using cDNA from the MC3T3 osteoblastic cell line (not shown). In contrast, GAPDH, E2F5 and p73 cDNA fragments were amplified in both MC3T3 and TRCSFB-2 cells (not shown). If no mRNA was added to the RT-PCR reactions bands were observed (lane 6, Fig. 8.5).

8.2.1.2.2 FGF receptor mRNA expression profile

The mRNA profile of the FGF receptors expressed by the TRCSFB-2 cells grown at 37°C for two days was analysed by RT-PCR. Oligonucleotide primers were designed to amplify the different isoforms of the receptors: FGFR 1 IIIb and IIIc, FGFR2 IIIb and IIIc, FGFR3 IIIb and IIIc, and FGFR4. The specificity of each set of primers was assessed using cDNA from a 14.5 dpc mouse brain (Appendix IV.1) and products of the predicted size were amplified by all sets of primers. If no mRNA was added to the RT-PCR reaction no amplification resulted thus confirming the specifity of the amplification reaction (Appendix IV.1).

The FGFR1 IIIc isoform band was very intense, whereas the IIIb isoform band was hardly visible (Fig. 8.6). Both FGFR2 IIIb and IIIc isoforms were present, the IIIb isoform band being slightly more intense. The FGFR3 IIIb and IIIc isoforms were also both present, although the IIIc isoform seemed to be expressed at higher levels. Finally, FGFR4 was clearly detectable but expressed at lower levels than the other FGFRs.

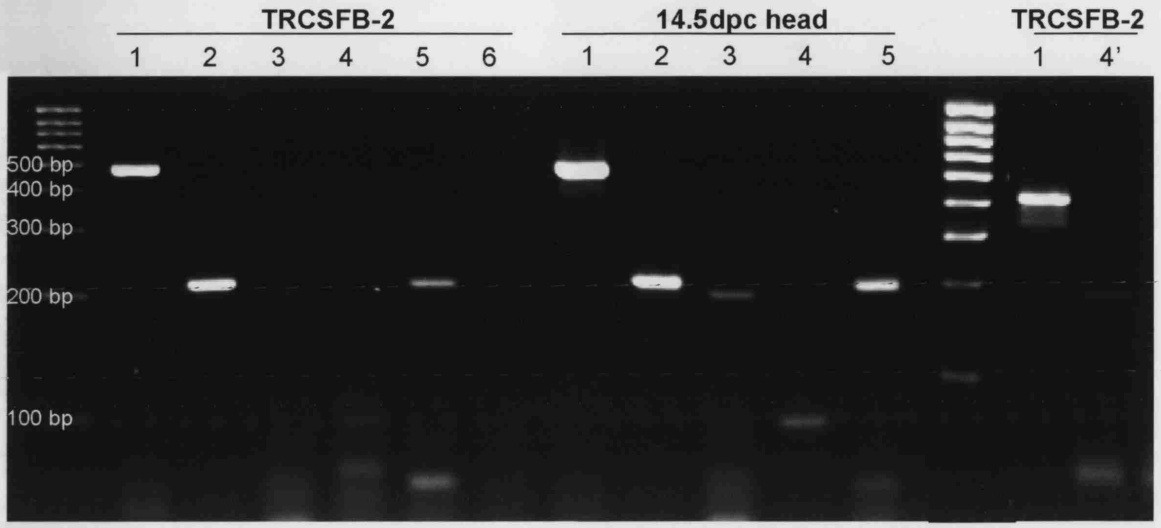

Figure 8. 5 mRNA expression of selected CPe gene markers in TRCSFB-2 cells

RT-PCR amplification of **1:** GAPDH (491 bp), **2:** E2F5 (227 bp), **3:** FoxJ1 (205 bp), **4:** p73 exon 10 (99 bp), **4':** p73 exon 6 to exon 9 (253 bp), and **5:** TTR (225 bp) from mRNA extracts of TRCSFB-2 cells grown at 37°C, and from the head of 14.5 dpc mouse embryo. RT-PCR for GAPDH with no mRNA is shown in (**6**). The molecular weight ladder (100 bp interval) is given to the left. The same number of cycles (x30) was used for all RT-PCR products.

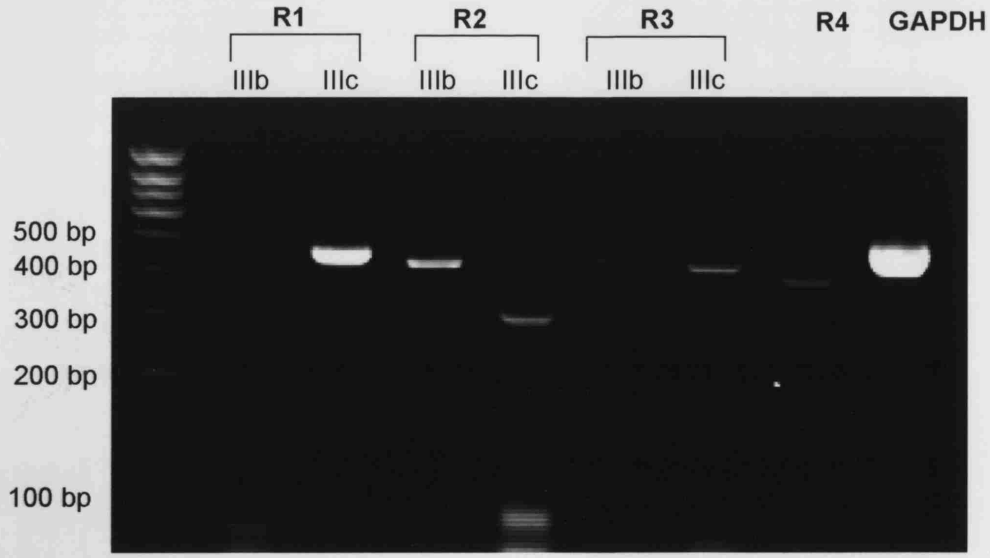

Figure 8. 6 FGF receptor mRNA expression profile in TRCSFB-2 cells

RT-PCR amplification of FGFR1 (**R1**) IIIb (466 bp) and IIIc (453 bp), FGFR2 (**R2**) IIIb (422 bp) and IIIc (310 bp), FGFR3 (**R3**) IIIb (471 bp) and IIIc (428 bp), FGFR4 (**R4**) (397 bp), and **GAPDH** (491 bp). The molecular weight ladder is shown to the left and band size indicated.

8.2.1.3 Protein expression profile

The expression of E2F5 and FoxJ1 proteins was studied by fluorescent immunocytochemistry using the polyclonal anti-E2F5 antibody (Santa-Cruz) and monoclonal anti-HFH-4 antibody (Neomarkers) respectively.

TRCSFB-2 cells expressed E2F5. The labelling was either nuclear or cytoplasmic. It was observed that in low density cultures E2F5 labelling was often mainly nuclear (Fig. 8.7A, C, E), whereas in subconfluent to confluent cells the labelling was mainly cytoplasmic (Fig. 8.7B, D, F). No labelling was present when the primary antibody was omitted (not shown).

The TRCSFB-2 cells also labelled positive for the FoxJ1 protein. The staining for FoxJ1 was punctate and cytoplasmic (Fig. 8.8A, C, E). When the primary antibody was omitted no staining above background was detected (Fig. 8.8B, D, F).

Figure 8. 7 E2F5 protein expression in TRCSFB-2 cells

A, C, E: Micrographs of the same group of cells in a low density culture. **A:** positive nuclear labelling for E2F5 protein; **C:** E2F5 labelling with Hoechst nuclear stain; **E:** Phase contrast view under bright field. **B, D, F:** Micrographs of the same group of cells in a dense culture. **B:** Positive cytoplasmic labelling for E2F5 protein; **D:** E2F5 labelling with Hoechst nuclear stain; **F:** phase contrast image. All scale bars are 50 μm.

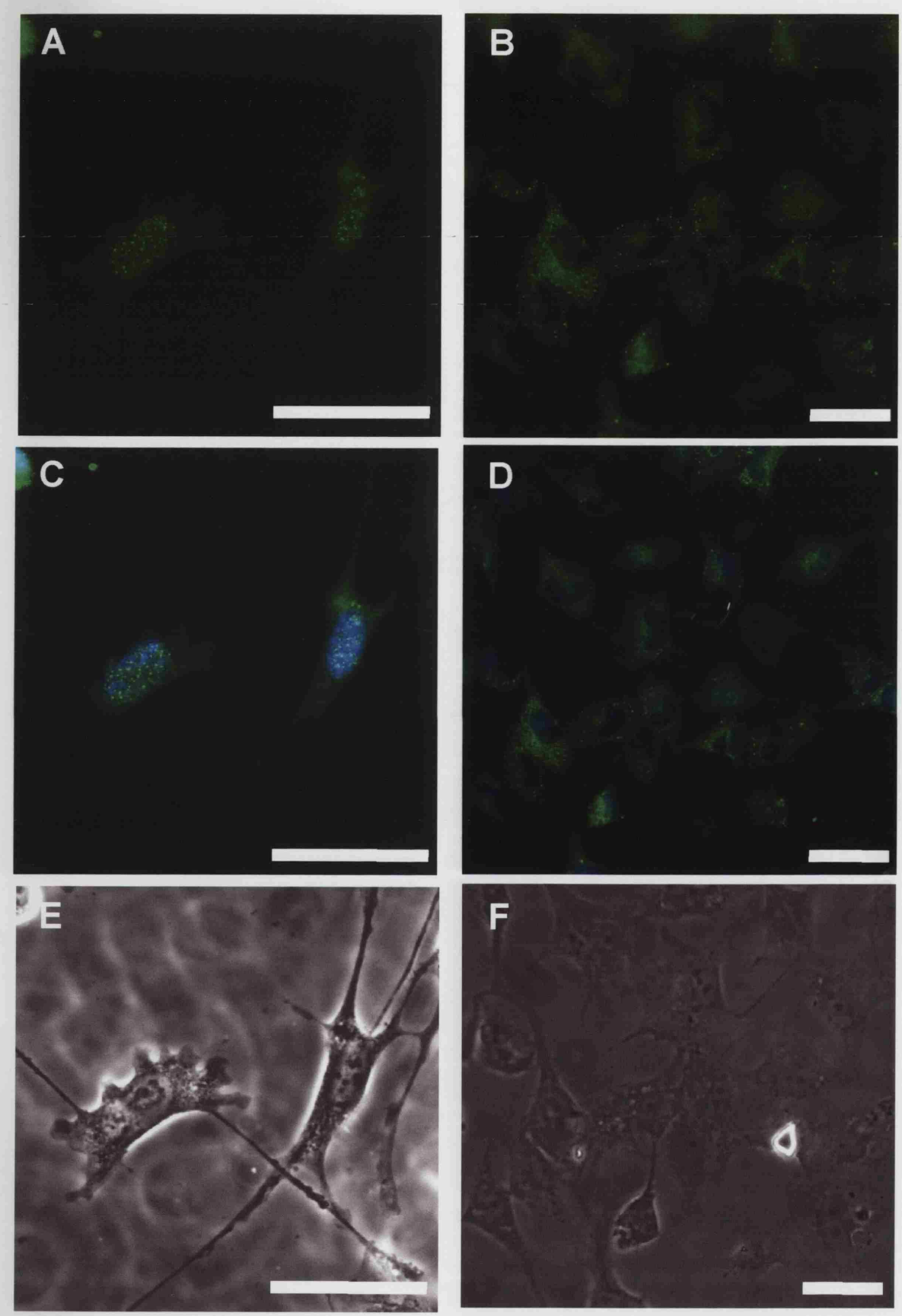
A
B
C
D
E
F

Figure 8. 8 FoxJ1 protein expression in TRCSFB-2 cells

A, C, E: Micrographs of the same group of cells stained for FoxJ1. **A**: Positive labelling for FoxJ1 protein; the staining is cytoplasmic and punctate. **C:** Same field shown in (A) with superimposed Hoechst nuclear staining. **E:** Corresponding phase contrast image. **B, D F:** Micrographs of the same group of cells stained in absence of primary antibody. **B:** Negative labelling for FoxJ1 protein in the absence of primary antibody. **D:** Same field shown in (B) with superimposed Hoechst nuclear staining. **F:** Corresponding phase contrast image. Scale bars are all 30 μm

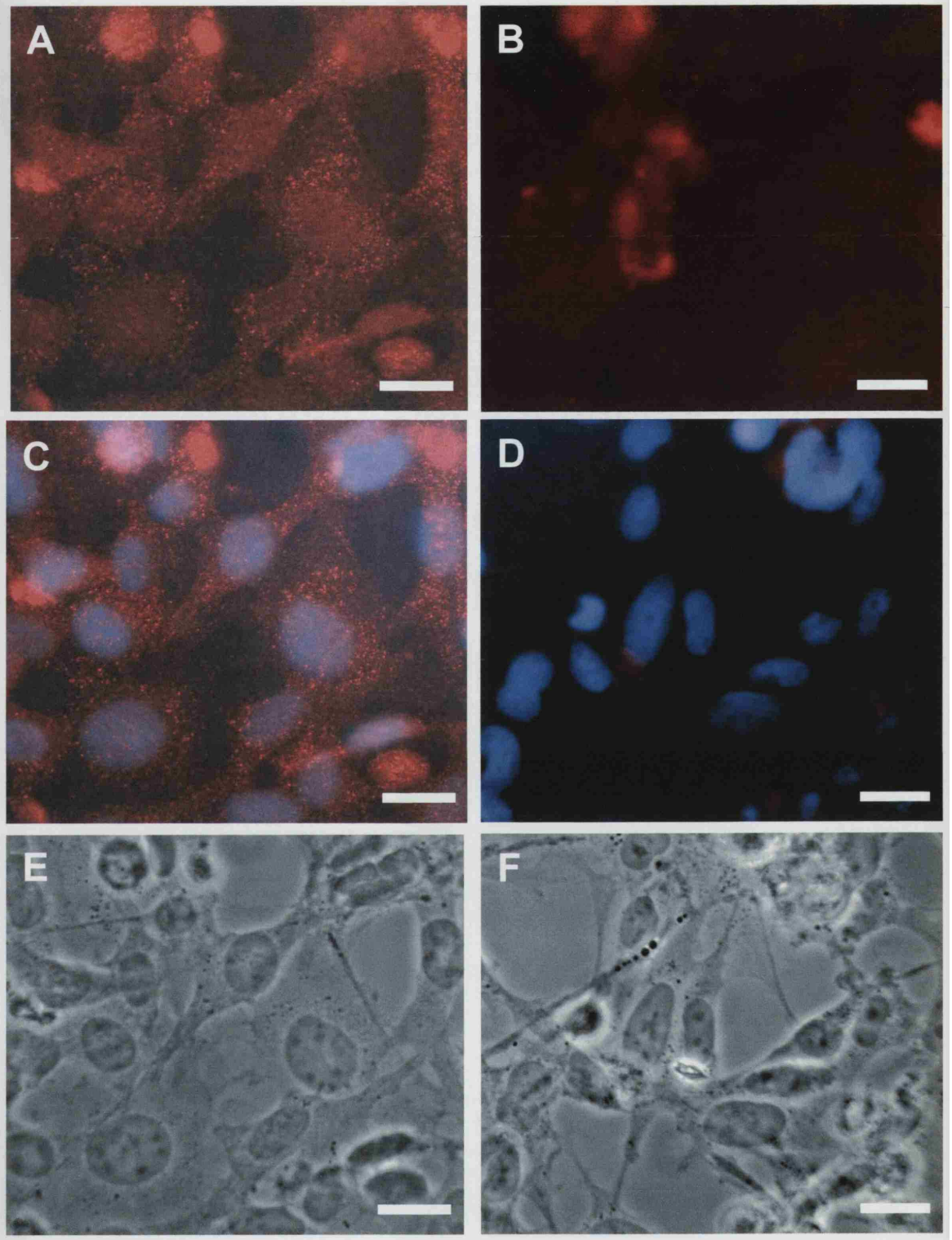
A
B
C
D
E
F

8.2.2 Fluid secretion assay

8.2.2.1 Method of secretion assay

The assay relied on the observation by Hakvoort et al. (1998) that confluent monolayers of CPe cells grown on a Transwell insert were impermeable to FITC-labelled dextrans over 150 kDa. In this study a 500 kDa FITC-labelled dextran was used. Since the polarity of a CPe cell monolayer is such that the apical side faces the upper chamber, water is transported from the basolateral to upper chamber. This means that when impermeable 500 kDa FITC-dextran is added to the medium in the basolateral chamber, the concentration of the fluorescent dextran in this chamber should increase with time as fluid is secreted to the upper chamber (see Fig. 8.9).

In order to assess when that the TRCSFB-2 cells grown on the Transwell had reached confluency and formed a water tight barrier, in addition to visual cues, an ohm-meter was used to measure the trans-epithelial electrical resistance (TEER) or membrane resistance of the cells. The published TEER for confluent TRCSFB cells was 139-143 ohm.cm^2 (Kitazawa et al., 2001). Similar readings between 150-180 ohm.cm^2 were obtained for confluent cells in this study which were generally, while the TEER for Transwell filters without cells was 130 ohm.cm^2.

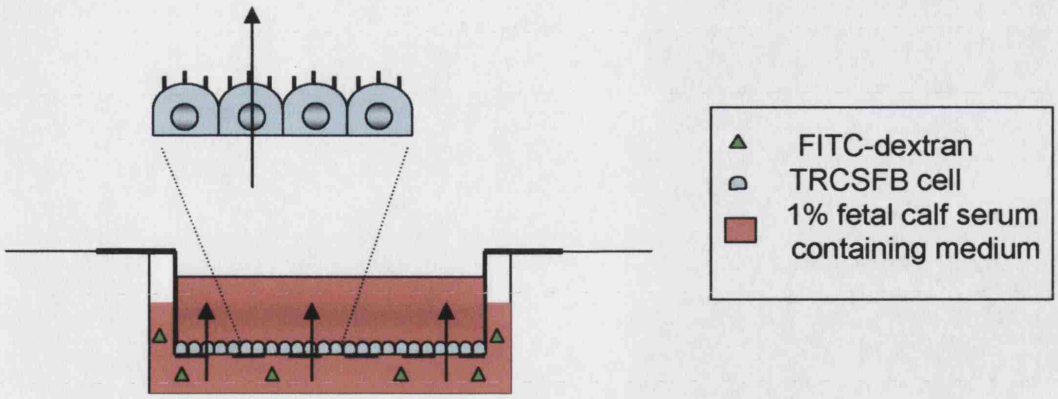

Figure 8. 9 Diagram showing the theoretical basis of the Transwell cell culture assay for measuring fluid secretion

The TRCSFB-2 cells are cultured to confluency on the 0.2 μm porous Transwell filter so that they form an impermeable seal. The polarised nature of the cell monolayer means that the apical brush border faces the upper chamber, whereas the basolateral cell membrane faces the bottom chamber. A 500 kDa FITC-dextran solution is added in the basolateral chamber, so that as the cells transport water trans-epithelially through to the apical chamber, the concentration of the fluorescent marker is increased. By measuring this increase in fluorescence it is possible to assess the amount of fluid secreted by the cells.

8.2.2.2 Results of secretion assay

The TRCSFB-2 cells were incubated 24 hours at 37°C prior to carrying out the secretion assay at 37°C. For each time point a calibration curve, relating known concentrations of FITC-dextran standards to a fluorescence signal, was generated (see Chap. 3.9). This method allowed to estimate an absolute value for the concentration of FITC-dextran based on the fluorescence measured at each time point rather than a relative value based on the ratio of the value obtained at a given time point against the value of the negative control (a Transwell without any cells). During the first hour after the start of the assay, the fluorescence signal increased in test-transwells compared to control (filters with no cells). However, after that time the fluorescence signal strongly decreased (Fig. 8.10). By 6 hours, the dilution of the fluorescence marker stagnated in test Transwells, while it continued for control cultures, suggesting that the cell monolayer may have become water tight again, and by 22 hours, the concentration of FITC-dextran was slightly higher in test-Transwells compared to control. For each experiment, at least three filters with TRCSFB-2 cells were treated with the fluid secretion inhibitors ouabain and acetazolamide. Not surprisingly, the effect of the inhibitors was not significant (p: 0.418) as the assay was not detecting a secretory activity. Interestingly, after 22 hours in culture, a small pH difference between the apical and basolateral chambers that was about 0.5 pH units was sometimes detected, which supposed that the cells were able to secrete fluid but did not survive long enough for it to be detectable (Hakvoort et al., 1998b). Longer periods of incubation at 37°C were not possible because the cells tended to die after 72 hours in culture. Therefore, it was unfortunately not possible to use this assay to show that the TRCSFB-2 cells secreted fluid and therefore to test the effect of FGF2 on fluid secretion using this cell line.

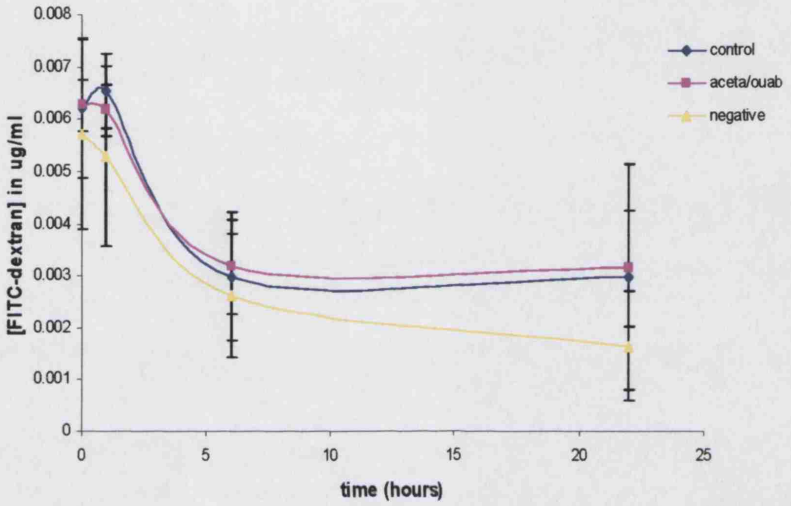

Figure 8. 10 TRCSFB-2 secretion curves: absolute concentration of FITC-dextran label

Graph showing the absolute concentration of FITC-dextran over time in the basolateral chamber of Transwell cultures culture with confluent cells (N: 13) (**control**), with acetazolamide and ouabain treatment (N: 5) (**aceta/ouab**), with no cells on the filter (N: 6) (**negative**). For each time point standard deviation bars are shown. (N: number of repeats).

8.2.3 Effect of FGF2 on hydrocephalic gene markers

8.2.3.1 Effect of FGF2 on transcript levels

The effect of 10 ng/ml and 100 ng/ml FGF2 on the mRNA expression of E2F5, FoxJ1, and p73 was investigated in the CPe cell line by semi-quantitative RT-PCR. In addition, the effect of FGF2 on TTR transcription was investigated to follow up the observation that the expression of this gene may be downregulated by FGF2 in primary embryonic CPe cells (Reid S, 2001). For each experiment three independent cultures were analysed as shown in Fig. 8.11.

The semi-quantification was carried out with respect to the house-keeping gene GAPDH that is expressed ubiquitously by all cells. GAPDH was used since its expression levels under each experimental conditions was relatively constant (Fig. 8.11). One experimental run was defined as three 25 cm^2 culture flasks (originating from the same flask split into three), of which one was the untreated control, one was treated with with 10 ng/ml, and one with 100 ng/ml FGF2 for 24 hours. Since the same number of cells were plated, and grown in the same conditions, it was possible to consider the three samples from each experimental run as linked variables.

The descriptive statistics for the effect of FGF2 on each set of gene are shown in Table 8.1. The graphical representations of these results are shown in Appendix IV.2-5. The significance of the effect of FGF2 on each transcript was assessed by one way-ANOVA analysis, as well as by ML-wiN modelling. This incorporated the effect of increasing doses of FGF2 (**FGF2 dose**) on the mRNA levels (**Gene expression**), the details of the model are specified in Appendix IV.6), for which the graphical output are shown in Fig. 8.12.

FGF2 significantly decreased E2F5 transcription in a dose dependent manner (p_{ANOVA}: 0.001). The ML-wiN model showed that for every ten-fold increase in FGF2 the mRNA expression for E2F5 decreased by 13.4% of its original non-treated value or by 0.109 normalised band intensity value (β_1) (SE: 0.025), this was a highly significant effect ($p < 0.01$) (Fig. 8.12A and appendix IV.2).

FoxJ1 transcription was also significantly decreased in a dose dependent fashion by FGF2 (p_{ANOVA}: 0.037). Although the decrease was less significant than for E2F5, ML-wiN modelling showed that for each ten-fold increase in FGF2, FoxJ1 expression decreased by 17.6% or by 0.091 normalised band intensity value (β_1) (SE: 0.032), and was significant (p: 0.01); (Fig. 8.12B and appendix IV.3).

FGF2 did not to significantly affect p73 (p_{ANOVA}: 0.24) and TTR (p_{ANOVA}: 0.816). ML-wiN modelling for p73 revealed that for each ten-fold increase in FGF2, p73 expression decreased by 10.8% or 0.064 normalised band intensity value (SE: 0.078), but was not significant (p: 0.4). ML-wiN modelling for TTR in contract revealed that FGF2 tended to increase TTR transcription. For each ten-fold increase in FGF2, TTR mRNA expression increased by 10.6% or by 0.049 normalised band intensity value (SE: 0.074), but was not significant (p: 0.6); (Fig. 8.12C-D and appendix IV.4-5).

Figure 8. 11 RT-PCR products for the choroid plexus epithelial cell gene markers +/- 10ng/ml and 100ng/ml FGF2

The RT-PCR amplified cDNA products for **E2F5** (227 bp), **FoxJ1** (205 bp), **p73** (253 bp) and **TTR** (225 bp) are run on a 1.5% agarose gel with ethidium bromide. For each sample and each gene, **GAPDH** (491 bp) is run alongside. Each treatment is indicated in the top frame; **Control**: cDNA derived from non-treated TRCSFB-2 cells, **10FGF2**: cDNA derived from TRCSFB-2 cells treated with 10 ng/ml FGF2 (10FGF2), **100FGF2**: cDNA from cells treated with 100 ng/ml FGF2 (100FGF2). Every treatment group shows three independent experimental runs (**1, 2, 3**). **A**: GAPDH and E2F5, **B**: GAPDH and FoxJ1, **C**: GAPDH and P73, **D**: GAPDH and TTR. A 100 bp molecular weight ladder is shown to the left of each gel (A-D).

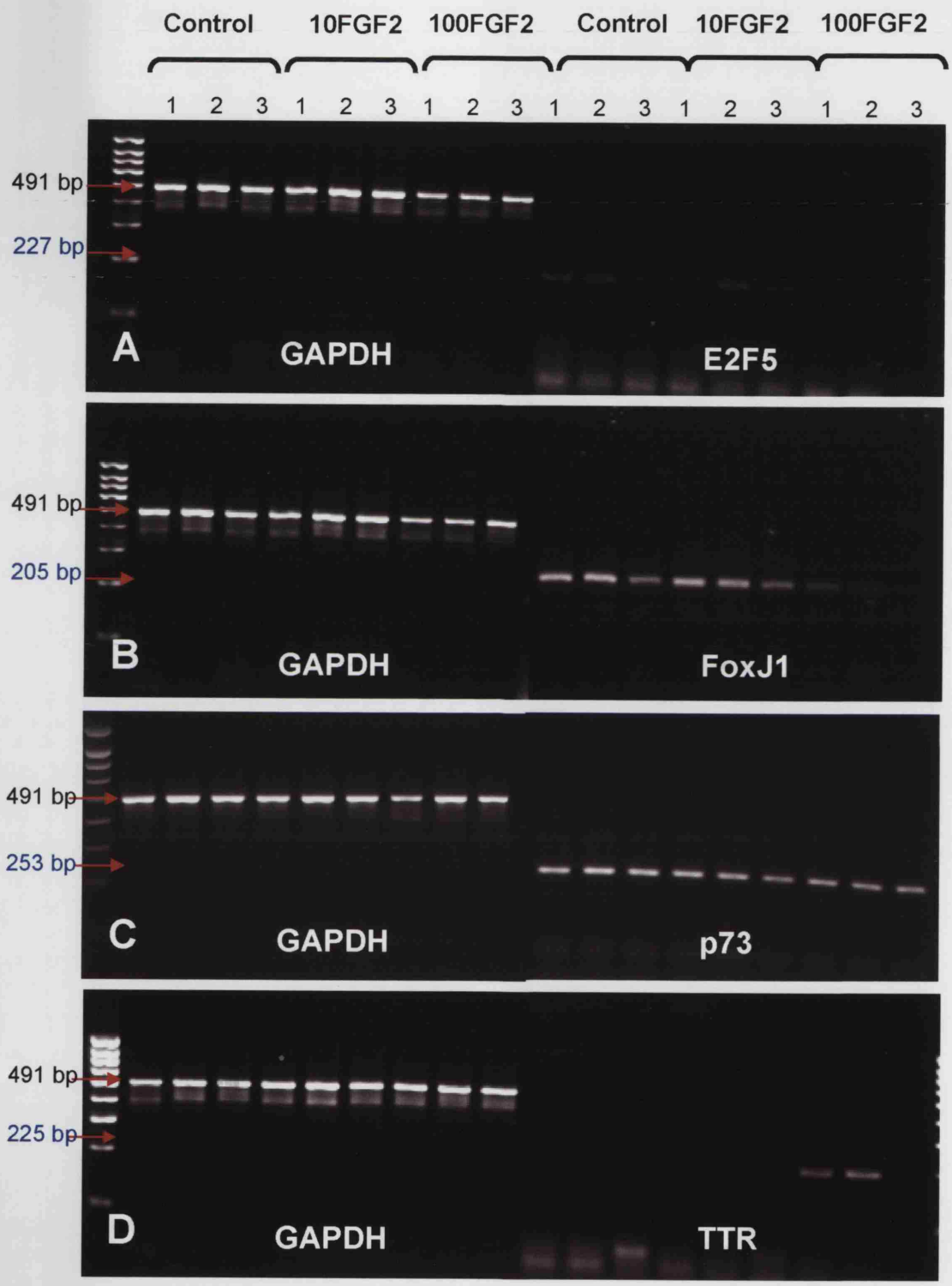
Control
10FGF2
100FGF2
Control
10FGF2
100FGF2
1 2 3 1 2 3 1 2 3 1 2 3 1 2 3 1 2 3
491 bp
227 bp
A
GAPDH
E2F5
491 bp
205 bp
B
GAPDH
FoxJ1
491 bp
253 bp
C
GAPDH
p73
491 bp
225 bp
D
GAPDH
TTR

Treat (E2F5)	Mean	N	SD	SE	Min	Max	Median	p_{ANOVA}
Control	0.830	10	0.124	0.040	0.660	1.00	0.812	
10FGF2	0.672	10	0.111	0.035	0.470	0.86	0.680	0.001
100FGF2	0.611	9	0.098	0.033	0.440	0.75	0.620	
Treat (FoxJ1)	**Mean**	**N**	**SD**	**SE**	**Min**	**Max**	**Median**	p_{ANOVA}
Control	0.536	13	0.196	0.054	0.310	0.960	0.550	
10FGF2	0.379	13	0.156	0.044	0.140	0.630	0.370	0.037
100FGF2	0.356	12	0.115	0.033	0.130	0.510	0.370	
Treat (p73)	**Mean**	**N**	**SD**	**SE**	**Min**	**Max**	**Median**	p_{ANOVA}
Control	0.615	12	0.518	0.150	0.240	2.10	0.454	
10FGF2	0.475	12	0.301	0.087	0.170	1.06	0.374	0.24
100FGF2	0.472	11	0.250	0.075	0.180	0.90	0.484	
Treat (TTR)	**Mean**	**N**	**SD**	**SE**	**Min**	**Max**	**Median**	p_{ANOVA}
Control	0.452	8	0.259	0.091	0.250	1.030	0.351	
10FGF2	0.508	8	0.384	0.135	0.210	1.160	0.316	0.816
100FGF2	0.554	7	0.254	0.096	0.270	0.970	0.524	

Table 8. 1 Statistics for the effect of FGF2 on the mRNA of expression of the choroid plexus epithelial cell associated genes

The table shows the mean band intensity of E2F5, FoxJ1, p73, and TTR amplified cDNA products normalised to that of the housekeeping gene GAPDH (**Mean**), from mRNA extracted from TRCSFB-2 cells grown without (**control**) and with 10 ng/ml FGF2 (**10FGF2**) or 100 ng/ml FGF2 (**100FGF2**), the total number of experiments (**N**), the standard deviation of the mean (**SD**), the standard error of the mean (**SE**), the minimum (**Min**), the maximum (**Max**), and the median (**Median**), as well as the statistical significance for the effect of FGF2 was assessed by One way ANOVA analysis (p_{ANOVA}).

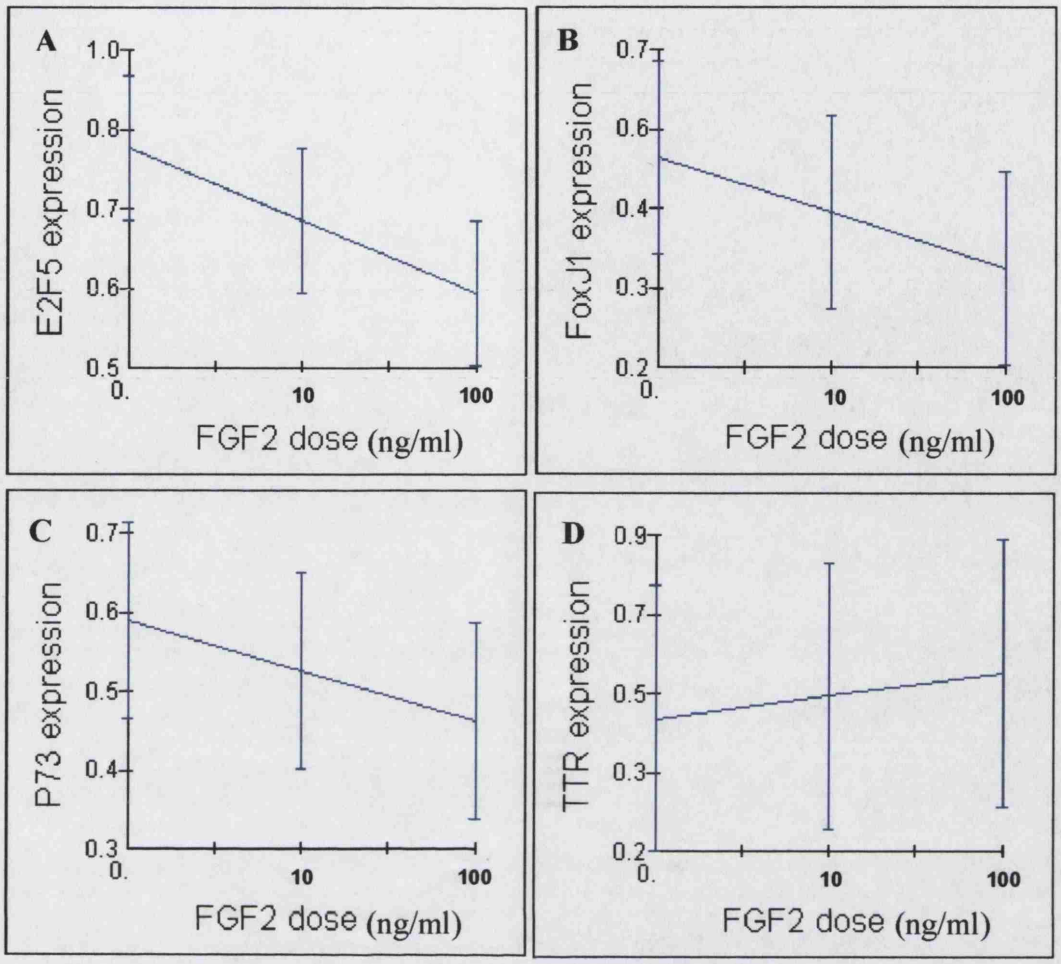

Figure 8. 12 Effect of FGF2 on the expression of genes associated with choroid plexus epithelial development predicted by multilevel modelling

Graphs show the average fitted lines from different experimental runs (see Appendix IV) along with the standard deviation error bars for the effect of increasing concentrations of FGF2 (0 ng/ml, 10 ng/ml, 100 ng/ml) on the mRNA expression of selected genes expressed as the ratio of the RT-PCR band intensity of a given gene with that of the housekeeping gene GAPDH. For every ten-fold increase in FGF2 **A**: E2F5 mRNA expression decreases by 13.4% compared to its non-treated level (or by 0.109 normalised intensity value, SE: 0.025). **B**: FoxJ1 mRNA expression decreases by 17.8% (or by 0.091 normalised intensity value, SE: 0.032). **C**: p73 mRNA expression decreases by 10.8% (or by 0.064 normalised intensity value, SE: 0.078). **D**: TTR mRNA increases by 10.6% (or by 0.049 normalised intensity value, SE: 0.074).

8.2.3.2 Effect of FGF2 on protein expression

Total protein extracts from TRCSFB-2 subconfluent cultures grown 48 hours at 37°C, were ran on a denaturing 12% SDS-PAGE and then processed for Western blotting. However, only the E2F5 protein could be detected by this method. The antibodies for FoxJ1 and TTR did not work on Western blot even on positive controls such as adult lung and liver protein extracts. Hence, only the effect of 10 ng/ml FGF2 on the translation of E2F5 by TRCSFB-2 cells was investigated (Fig. 8.13). The same amount of protein (60 μg) was loaded in each condition and the SDS-PAGE gel was stained with Coomasie blue (after transfer of the proteins on membranes) in order to inspect that the amount of protein loaded were equivalent. Staining the Western membrane directly with Ponceau red tended to upset the anti-E2F5 immunostaining procedure. Spot densitometric analysis of the intensity of each band from three independent cultures showed that on average a tenfold increase in FGF2 decreased protein expression by 15.2% (p: 0.053).

Figure 8. 13 Effect of 10ng/ml FGF2 on E2F5 protein expression analysed by Western blot

A: Western blot of protein extracts of three independent cultures of TRCSFB-2 cells either untreated (**1, 2, 3**) or treated with 10 ng/ml FGF2 (**1', 2', 3'**) separated by 12% SDS-PAGE and probed for E2F5 protein. **B**: Coomasie blue staining of the 12% SDS-PAGE gel after transfer used for the Western blot in (**A**), showing an equivalent amount of protein in each sample. **C**: Graph showing the average spot densitometric intensity values of the bands on Western blot from three independent culture experiments. 10 ng/ml FGF2 decreases E2F5 by 15% relative to its expression level in non-treated cultures (p: 0.051); the standard deviation bars are shown for each condition.

A

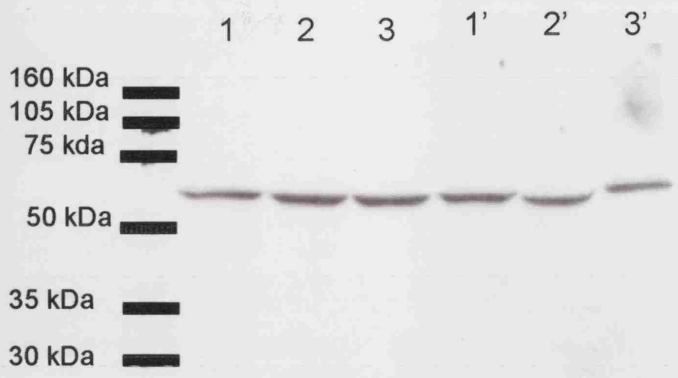
1
2
3
1'
2'
3'
160 kDa
105 kDa
75 kda
50 kDa
35 kDa
30 kDa

B

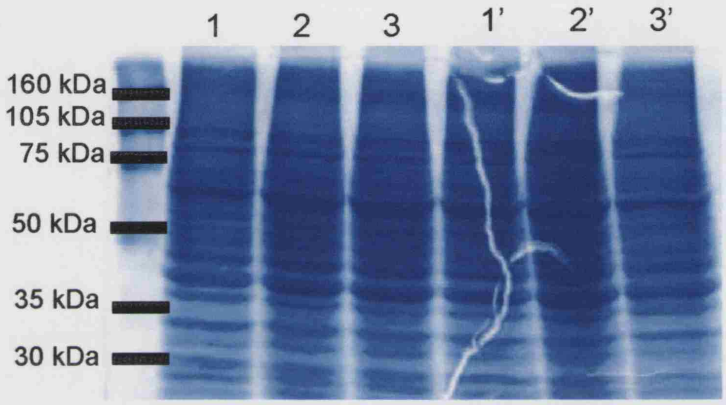
1
2
3
1'
2'
3'
160 kDa
105 kDa
75 kDa
50 kDa
35 kDa
30 kDa

C

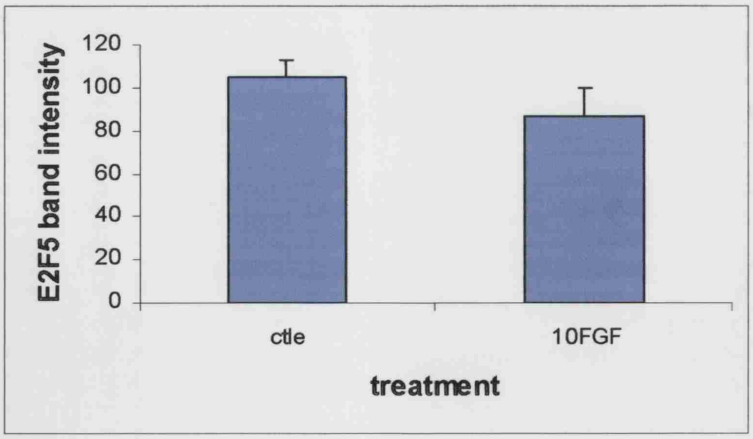
E2F5 band intensity
120
100
80
60
40
20
0
ctle
10FGF
treatment

8.2.4 Effect of FGF2 on TRCSFB-2 cell proliferation

8.2.4.1 Alamar blue assay

The effect of 50 ng/ml FGF2 on TRCSFB-2 cell proliferation was investigated using the Alamar Blue assay. Subconfluent TRCSFB-2 cells were grown for two days at 37°C and treated with 50 ng/ml FGF2 for 24 hours before carrying out the assay. The growth of TRCSB-2 cells in microtiter cultures was followed over 22 or 30 hours. Six micro-wells were plated with TRCSB-2 cells simultaneously to have one well per time point at which the Alamar blue reaction was terminated, 0h, 2h, 4h, 8h, 16h, 22h, or 30h. Effectively, each set of wells generated a time-response curve. For all time points, negative controls (wells without cells) were run in parallel in absence of any cells, each time point was replicated 16-22 times over 4 separate experiments (see Appendix IV.7)

ML-wiN modelling showed that there were no significant differences between FGF2 and control curves. The fixed part of the model took into account the effect of **time** (hours), and of the treatment with FGF2 **(treatment)**, and an interaction term **(treatment * time)**, that allowed to assess the average daily difference in cell proliferation in FGF2-treated compared to control cultures as assessed by Alamar blue **(Alamar value)**; the β_0 **.constant** gives the smallest possible Alamar blue value. The β_n coefficients are given for each explanatory variables. The fixed part of the model is thus:

$$\textbf{Alamar value} = \beta_0 . \textbf{constant} + \beta_1 . (\textbf{time}) + \beta_2 . (\textbf{treatment}) + \beta_3 . (\textbf{treatment*time})$$

The random part of the model is given by the:

- Level 1: variation between time points
- Level 2: variation between curves
- Level 3: variation between experimental runs

There was only a slight effect due to the treatment so that the average difference between FGF2-treated and control curves was about 0.026 units $absorbance_{570nm}$ (SE: 0.079), which was not significant (p: 0.7). The model showed that FGF2-treated growth curves on average increased daily by 0.001 units $absorbance_{570nm}$ (SE: 0.004) compared to control curves, which was highly non-significant (p: 0.8) (see Appendix IV.8 for graph).

8.2.4.2 BrdU ELISA

The effect of 1 ng/ml, 10 ng/ml and 100 ng/ml FGF2 was investigated by BrdU ELISA. TRCSFB-2 cells were grown 48 hours at 37°C, with or without FGF2 in the last 24 hours before the start of the assay. The cells were then incubated with BrdU for 2 hours, which was shown by fluorescence immunocytochemistry to be an optimal time for the cells to incorporate the nucleotide analogue (Muir et al., 1990); in addition, the concentration of anti-BrdU antibody used did not give any significant background (not shown). For each set of experiments two levels of negative controls were used to confirm the specificity of the assay. The first control consisted in leaving the BrdU out of some cell cultures. The second control was to omit the mouse primary anti-BrdU antibody from the BrdU staining protocol.

The readings obtained in the ELISA assay for each FGF2 dose (0 ng/ml, 1 ng/ml, 10 ng/ml, 100 ng/ml) are summarised in Table 8.2. The values were plotted against their respective FGF2 dose; a bar chart (standard error of the mean) is shown in Fig. 8.14A. Independent Student's t-tests were performed to assess the significance of the difference of the means between control and individual FGF2-treated cultures (Table 8.3). It was found that 1 ng/ml FGF2 increased BrdU incorporation most significantly compared to control (p: 0.002); the effect of 10 ng/ml FGF2 was less lower but still highly significant (p: 0.018), whereas the effect of a 100 ng/ml FGF2 was not significant (p: 0.985). Therefore, cell proliferation decreased with increasing doses of FGF2 (pANOVA: 0.002). A regression analysis for the values of the FGF2-treated cultures (1 ng/ml, 10 ng/ml, 100 ng/ml) was performed to validate this trend, and the regression plot is shown in Fig. 8.14B. The coefficient for the regression line was -0.007 (SE: 0.002), which was a highly significant (p: 0.002); it corresponded roughly to a 13% decrease in BrdU incorporation for each ten-fold increase in FGF2 relative to that at 1 ng/ml FGF2.

Treatment	Mean	N	SD	SE	Minimum	Maximum	Median
Control	0.036	33	0.014	0.0024	0.0060	0.0740	0.032
1FGF2	0.055	18	0.029	0.0069	0.025	0.16	0.048
10FGF2	0.046	17	0.015	0.0035	0.024	0.077	0.045
100FGF2	0.036	18	0.010	0.0034	0.016	0.052	0.038

Table 8. 2 Descriptive statistics for the effect of FGF2 on BrdU incorporation by TRCSFB-2 cells

The table gives the mean value for BrdU-incorporation (**Mean**), number of experimental repeats (**N**), standard deviation of the mean (**SD**), standard error of the mean (**SE**), **minimum**, **maximum**, and **median** values in TRCSFB-2 cells grown either without FGF2 (control), or with 1 ng/ml (1FGF2), 10 ng/ml (10FGF2), and 100 ng/ml (100FGF2) of FGF2.

Treatments	Significance	SE	95% confidence interval	
			Lower	Upper
1FGF2-Control	0.0020	0.006	0.0074	0.032
10FGF2-Control	0.018	0.005	0.0018	0.019
100FGF2-Control	0.985	0.004	0.0076	0.0075

Table 8. 3 Significance of the effect of FGF2 doses on BrdU incorporation

Independent Student's t-tests were performed to assess the significance of the difference between the mean values for each FGF2-treated and control cultures. (SE is standard error of the mean)

Figure 8. 14 Effect of FGF2 on TRCSFB-2 cell proliferation assessed by BrdU-ELISA assay

A: Graph showing mean values and standard error bar (SE) for the incorporation of BrdU by TRCSFB-2 cells at the different doses of FGF2 tested: 0 ng/ml, 1 ng/ml, 10 ng/ml, 100 ng/ml FGF2. **B**: Scatter plot of the values for the BrdU incorporation by the TRCSFB-2 cells at 1 ng/ml, 10 ng/ml, 100 ng/ml FGF2. A least squares line is fitted to the data showing a clear decrease in incorporation over the 100-fold increase in FGF2 concentration; the slope of the line is -0.007, which means that for every ten-fold increase in FGF2, BrdU incorporation decreases by 12.3% compared to TRCSFB-2 cells treated with 1 ng/ml FGF2 (p: 0.002).

A

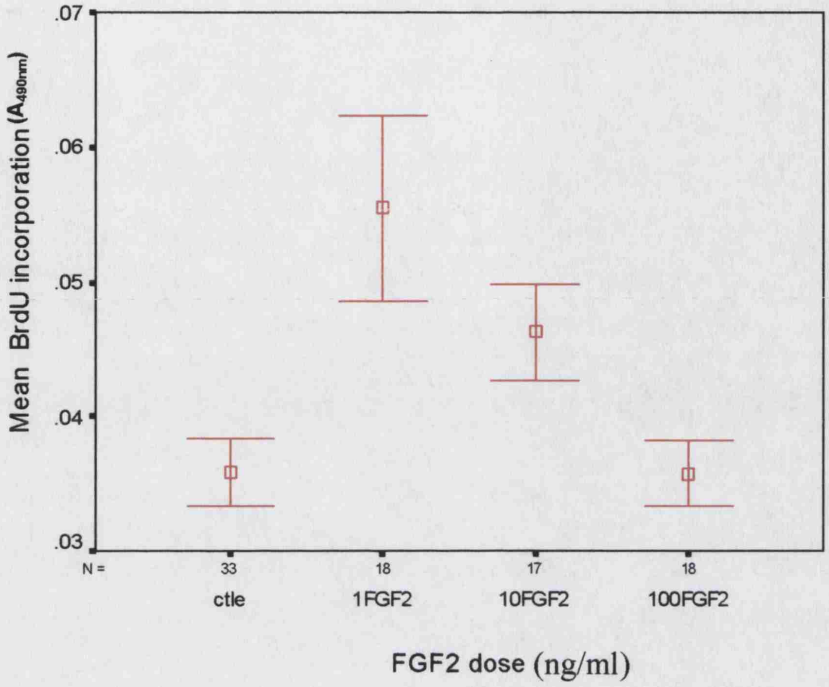
Mean BrdU incorporation (A_{490nm})
.07
.06
.05
.04
.03
N =
33
18
17
18
ctle
1FGF2
10FGF2
100FGF2
FGF2 dose (ng/ml)

B

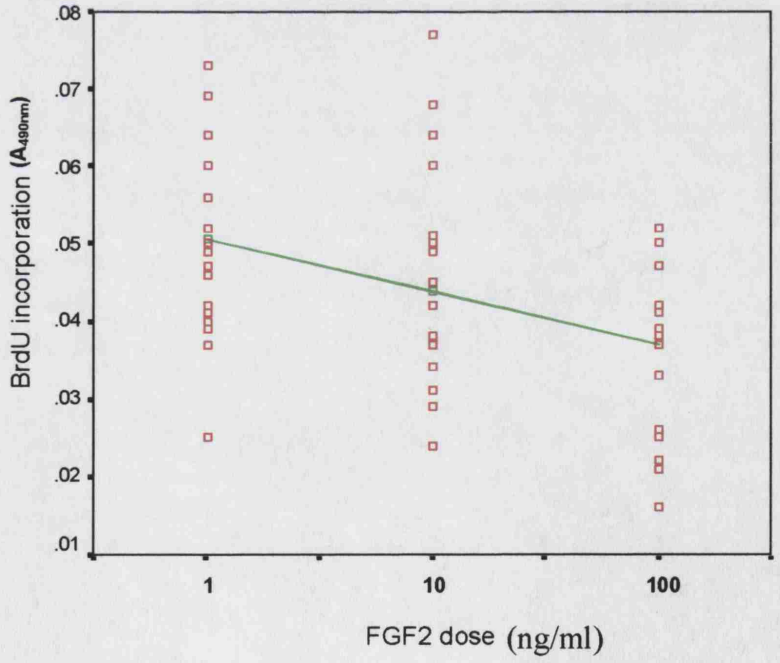
BrdU incorporation (A_{490nm})
.08
.07
.06
.05
.04
.03
.02
.01
1
10
100
FGF2 dose (ng/ml)

8.3 Discussion

8.3.1 TRCSFB-2 cell characterisation

This study confirmed that confluent TRCSFB-2 cells had a cuboidal shaped morphology characteristic of CPe cells as reported by Kitazawa et al. (2001), and expressed TTR at the protein level. The characterization of the TRCSFB-2 cells was extended by looking at the expression of genes associated with the CPe phenotype, namely the tight junction associated protein *ZO-1*, *TTR*, *FoxJ1*, *E2F5* and *p73* that appear to be important for the correct function of the CPe. The expression of E2F5 protein was interesting because its compartmentalisation changed dynamically with the state of growth of the culture: in confluent cells E2F5 tended to be cytoplasmic, while in actively growing cells E2F5 was largely nuclear. This suggested that E2F5 protein nuclear translocation was associated with exponential growth as described in myoblasts (Gill and Hamel, 2000) and supported by work in HaCat cells, where cell differentiation is associated with the downregulation of E2F5 transcripts (Marks et al., 2000). However, it should be noted that the relationship between the subcellular location of E2F5 and the proliferative state of cells is still controversial; for example expression of E2F5 protein and its nuclear location has also been associated with the quiescent, differentiated state of cells such as in murine differentiated epidermal keratinocytes (Lavia and Jansen-Durr, 1999; Apostolova et al., 2002; Dagnino et al., 1997). Furthermore, in-vivo, the relationship between E2F5 expression and sub-localization, and CPe cell proliferation was not observed (Chap. 5). Thus, if the relationship between E2F5 sub-localisation and cell proliferation was confirmed in TRCSFB-2 cells, this would either mean that they are inherently different to their in-vivo counterpart, or that the environment of the cells (the substrate they are grown on) is critical in determining their behaviour and the coupling of E2F5 with the cell-cycle.

The profile of expression of the different FGFR transcripts by the TRCSFB-2 cells was also studied, and was found to mirror that reported by Reid S. (2003) for the mouse 12.5 dpc CPe. In both, the FGFR1IIIc isoform was the one expressed at the highest level. In contrast, expression of FGFR RNA in TRCSFB-2 differed from the FGFR protein profile observed in 18.5 dpc as in this latter the levels of FGFR1 protein were very low and FGFR4 undetectable.

The TRCSFB-2 cells expressed the tight junction protein ZO-1 and formed tight confluent monolayers as measured by transepithelial electrical resistance

(TEER), which matched that published by Terasaki (2001). However, the integrity of the monolayer seemed to fail after 1-2 hours of the assay, and after about 6 hours, the monolayer appeared to become water tight again. This transient failure of the monolayer may have been because the cells need to condition their medium. Alternatively, the mitogenic serum that was added in the medium may have upset the integrity of the confluent monolayer as described by Hakvoort (1988) who reported that for the primary adult porcine epithelial cells grown on Transwell filters, growing the cells in serum free medium improved the morphological polarity of CPe cells and their barrier forming cell:cell interactions. However, the TRCSFB-2 did not respond in the same way to this treatment: the minimum concentration of serum that could be used was 0.1% FCS, as below this concentration they died. In some instances, after 22 hours a pH of about ΔpH: 0.5 was measured in TRCSFB-2 cultures between the top and bottom chambers, suggesting evidence of a pH gradient that is required for the secretion of fluid (Hakvoort et al., 1998b; Speake et al., 2001). Using porcine cells Hakvoort (1988b) reported that over 4 to 5 days the pH in the basolateral chamber significantly decreases as a function of time. This is paralleled by an increase of the pH in the apical chamber, which correlates with secretion of fluid. Unfortunately, since the TRCSFB-2 cells could not be grown for more than 72 hours at 37°C without starting to die, it was not possible to study secretion using this assay. Thus, although TRCSFB-2 cells may be useful for studying short term transport activity, such as amino acid transport as studied by Terasaki (2001), which usually requires a few minutes of incubation, the use of these cells for studying fluid secretion, that requires much longer times of incubation (usually a few days), was prevented by the fact that the cells do not suvive long enough at 37 °C. Therefore, primary CPe cells rather than TRCSFB-2 cells may have to be used in the future to study fluid secretion with this assay.

8.3.2 Effect of FGF2 on genes whose knockout cause hydrocephalus

FGF2 was found to significantly inhibit the mRNA expression of E2F5 and FoxJ1 in a dose dependent manner. In contrast *p73* and *TTR* were not affected. This latter gene has not been associated with hydrocephalus but rather with the differentiation of the CPe cells; the fact that its expression was not affected by FGF2 showed that FGF2 was not affecting the CPe identity of the TRCSFB-2 cells. The effect of 10 ng/ml

FGF2 on E2F5 protein expression was studied by Western blot analysis that showed a decrease in E2F5 protein levels consistent with the decrease in transcript expression.

The effect of FGF2 on the mRNA expression of the FGFRs in TRCSFB-2 cells was also investigated (not shown) and no change in their level was observed. This experiment, however, was not repeated to reach statistical significance, and small changes might have been overlooked.

At this point, one can only speculate on how FGF2 transduces the inhibition of E2F5 and FoxJ1 expression, and how this affects the cells. It should be noted that the knockout mice for these two genes cause the animals to suffer from non-obstructive hydrocephalus consecutive to a dysfunctional CPe. Thus it may be that FGF2, by reducing the expression of E2F5 and FoxJ1 mRNA, increases fluid secretion by the cells. Unfortunately, this idea could not be investigated farther since it was not possible to study fluid secretion using the TRCSFB-2 cells in the Transwell secretion assay. However, if this were the case it would contradict the finding by Hakvoort (1988) who found that FGF2 as well as TGFβ1 inhibit the fluid secretion by porcine CPe cells grown as a monolayer on Transwell filters. In the light of this finding, it is interesting to note that recently TGFβ signalling was found to be in part mediated by a complex containing smad 3, E2F4/5, DP1 and p107 proteins (Chen et al., 2002). This observation suggests that if FGF signal transduction also requires E2F5 protein and can modulate E2F5 expression as shown by my results; this raises the possibility that FGF and TGFβ pathways may cross-talk via the use of E2F5. Of course, it cannot be presently ruled out that the downregulation of FoxJ1 and E2F5 transcripts by FGF2 treatment may not be related to CSF secretion but as a consequence for example of the mitogenic effect of FGF2 on the TRCSFB-2 cells.

8.3.3 Effect of FGF2 on cell proliferation and other TRCSFB-2 function

The effect of FGF2 was first studied using the Alamar blue assay, a metabolica assay. Only one dose of FGF2 (50 ng/ml) was tested, and did not increase cell proliferation in a significant way. This assay really reflects the number of cells present in culture. This can be affected by differences in cell death as well as cell proliferation. A more specific assay was therefore used to investigate the effect of FGF2 on TRCSFB-2 cell cycle. The BrdU-based ELISA assay, that measures the total number of cells synthesising DNA over a certain time, was used to test the effect of different

concentrations of FGF2 on cell proliferation. This showed that the most active dose of FGF2 was the lowest dose (1 ng/ml), the other doses of FGF2 (10 ng/ml and 100 ng/ml) caused a reduction in DNA synthesis in a dose-dependent manner. These results were therefore consistent with the fact that cell proliferation was not detectable in the Alamar blue assay using 50 ng/ml FGF2. In addition, these findings paralleled results obtained in cultured neuroepithelial cells where low doses of FGF2 increased survival and proliferation, and high concentrations induced the cells to differentiate (Murphy et al., 1990).

It is interesting that the dose-dependent decrease in cell proliferation from 1 ng/ml to 100 ng/ml FGF2 mirrors the decrease in E2F5 mRNA expression. The relationship, however, is not absolute since E2F5 expression is highest in the absence of FGF2, whereas cell proliferation is highest with 1ng/ml FGF2. It would be interesting to study the effect of 1 ng/ml FGF2 on the expression and intra-cellular localization of E2F5. If expression of E2F5 was to mirror the cell proliferation response, this dose would be expected to increase E2F5 expression. Of course, the pathways may not be linked and be independent of one another. For instance, FGF2 may be inhibiting the expression of E2F5 as part of an inhibitory feedback loop.

8.3.4 Summary

The characterisation of the rat adult choroid plexus epithelial cell line (TRCSFB-2) was extended by showing that the TRCSFB-2 cells expressed selected gene markers associated with a CPe phenotype namely, *TTR*, *E2F5*, *FoxJ1*, and *p73*. The cells also displayed an FGFR transcript profile that was similar to that described for the in-vivo CPe at each stages of development. Confluent cells had a cuboidal morphology, expressed the tight junction protein ZO-1, and were capable of forming a TEER similar to that published for this cell line. Using a Transwell assay, it was not possible to show that the cells were capable of fluid secretion since they did not survive long enough at 37°C for a detectable amount of fluid to be secreted. Consequently, it was not possible to test the effect of FGF2 on fluid secretion directly. Instead, the effect of FGF2 on the mRNA expression of genes whose knockouts cause hydrocephalus was studied. FGF2 was observed to downregulate E2F5 and FoxJ1 mRNA in a dose dependent manner while p73 was not significantly affected (it should be noted that the expression of the different isoforms was not studied; changes in isoform expression would have been overlooked). Interestingly, FGF2 at lower doses increased TRCSFB-

2 cell proliferation while at higher doses it gradually decreased cell proliferation. Hence, the effect of FGF2 on the cell cycle may be related to its effect on E2F5 expression, although more work needs to be done to follow on this idea. If this relationship was confirmed, it would mean that either TRCSFB-2 cells do not behave as CPe cells do in-vivo, where E2F5 expression appeared independent of the cell-cycle (see Chap. 5), or that the environment of the cells (the substrate they are grown on) is critical in determining ther behaviour and coupling E2F5 with the cell-cycle.

Chapter 9 Mouse model with Apert/Pfeiffer syndrome-like phenotypes

9.1 Introduction

FGFR activating mutations can induce raised intra-cranial pressure and hydrocephalus as discussed in Chap 1.8. FGFRs as well as FGF2 are expressed in the CPe (Reid and Ferretti, 2003), and FGF2 affects various aspects of CPe cell behaviour in the culture systems I have studied (Chaps 7-8), and when injected in-vivo (Pearce et al., 1996; Hakvoort and Johanson, 2000). Therefore, I decided to study the CP development and the size of the ventricles in an animal model of craniosynostosis. Very few animal models with activating point mutations in the *FGFR* gene, that cause a craniosynostosis syndrome, have been generated (see Chap. 1.7.1). In this study, I used a mouse model with Apert/Pfeiffer like phenotypes that was obtained from (Hajihosseini et al., 2001) and generated by the heterozygotic abrogation of *FGFR2* exon 9 (IIIc) as described in Chap. 1.7.1. In this heterozygotic knockout *FgfR2*IIIc$^{+/\Delta}$ mouse, there is a splice-switch from the IIIc to the IIIb isoform, so that cells that would normally express the IIIc isoform will instead express both isoforms. Therefore, the craniosynostosis phenotype in this mouse model is not due to an activating point mutation as most frequently observed in patients with syndromic craniosynostosis, but more likely due to a change in ligand specificity. The aim of this chapter was to investigate whether these Apert/Pfeiffer mice had a hydrocephalic phenotype and whether the development of the choroid plexus (CP) was affected by the gain of function-like mutation of the *FGFR2* gene. The cerebral development of these mice was also studied since FGF signalling has been shown to be important for normal neurogenesis (Vaccarino et al., 1999a; Vaccarino et al., 1999a; Ohmiya et al., 2001), and Apert patients have often been reported to suffer from mental retardation coincident with an intrinsic neurological disorder (Renier et al., 1996; Cohen, Jr. and Kreiborg, 1990b; de Leon et al., 1987).

In this study I have 1) characterised the choroid plexus of the *FgfR2*IIIc$^{+/\Delta}$ mice by histological analysis; 2) studied whether there is dilation of the brain ventricles in the *FgfR2*IIIc$^{+/\Delta}$ mice; 3) used a histological and stereological analysis to establish whether the development of the brain is affected in the *FgfR2*IIIc$^{+/\Delta}$ mice.

9.2 Results

9.2.1 Histological analysis of Apert/Pfeiffer choroid plexus

The choroid plexuses (CPs) (lateral, third and fourth ventricle) of *FgfR2*IIIc$^{+/\Delta}$ mice observed did not present any visible histological defects at developmental stages ranging from 18.5 dpc to P6 in brain sections stained by haematoxylin and eosin staining. The normal organisation of the villi and epithelium was maintained, and the CPe expressed TTR protein as shown in the P3 CP (Fig. 9.1A-B). Cell proliferation (Fig. 9.1C-D), either studied by p-H3 (not shown) or PCNA immunohistochemistry (Fig. 9.2), was very rarely observed in the CPs of either *FgfR2*IIIc$^{+/\Delta}$ or wild type mice, but detected in the sub-ventricular zone of both mice.

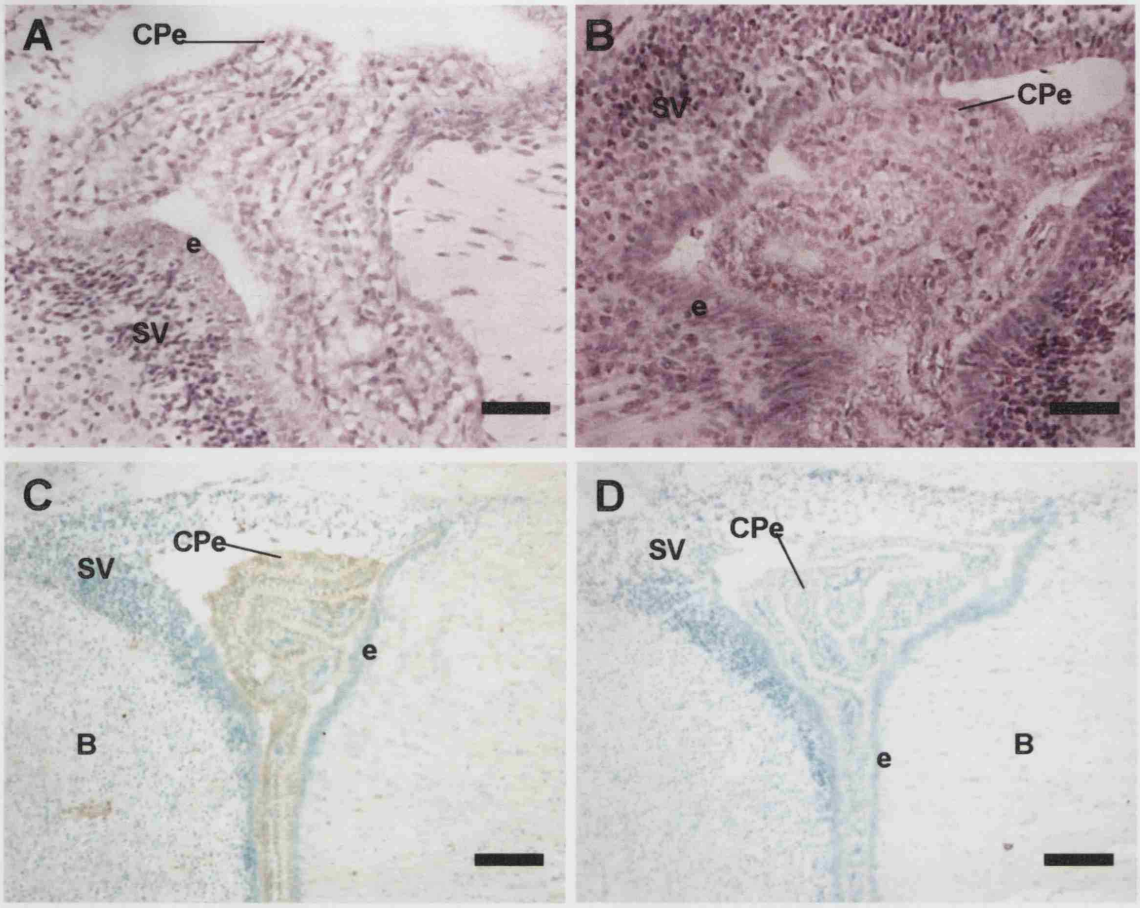

Figure 9. 1 Characterization of the *FgfR2*IIIc$^{+/\Delta}$ mouse choroid plexus at P3 (coronal view)

A: Haematoxylin and eosin (HAE) staining of WT lateral CP. **B**: HAE staining of a *FgfR2*IIIc$^{+/\Delta}$ lateral CP; no gross morphological anomalies are noticeable. **C**: TTR staining of the *FgfR2*IIIc$^{+/\Delta}$ lateral CP. **D**: TTR control staining where the primary antibody was omitted. Scale bars are 50 μm in A-B, and 100 μm in C-D. **CPe** = choroid plexus epithelium, **SV** = sub-ventricular zone, **e** = ependyma, **B** = brain tissue.

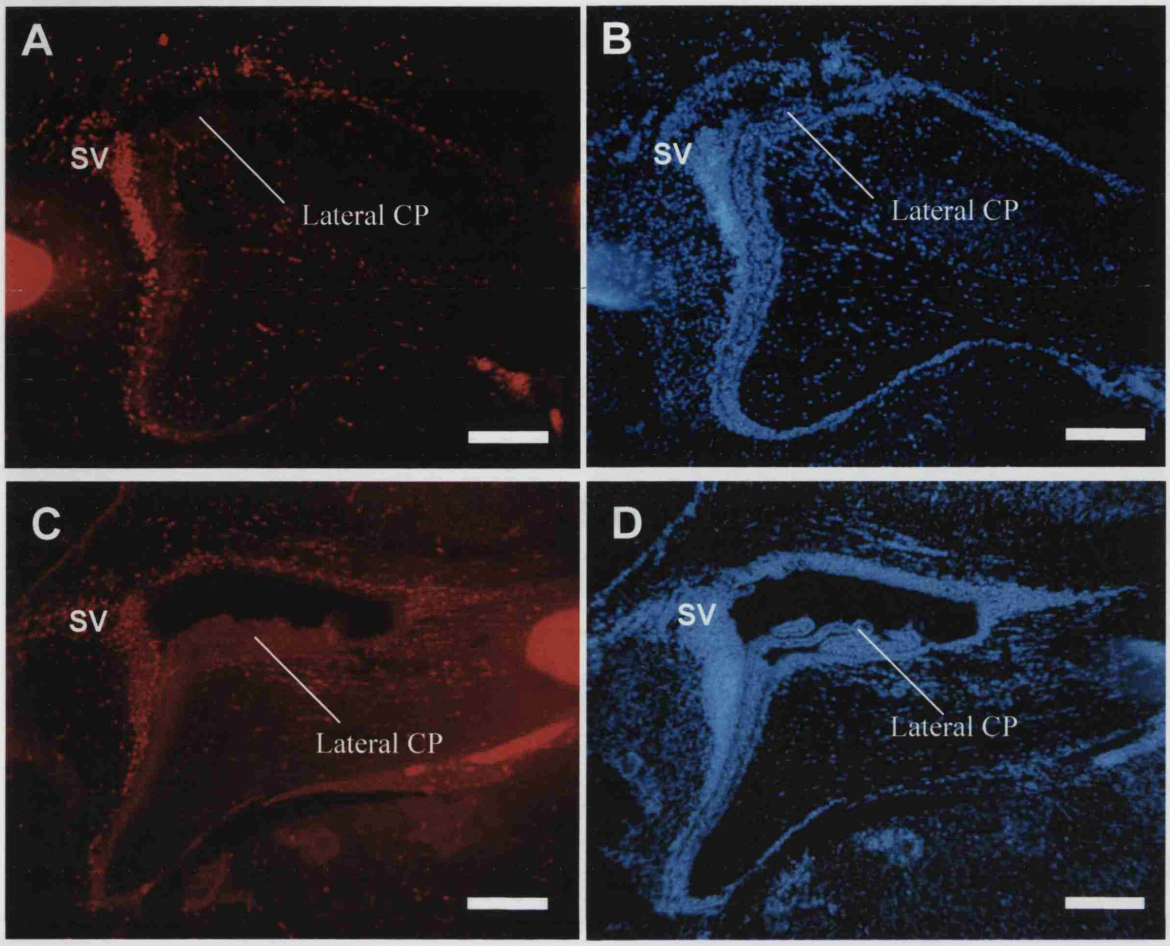

Figure 9. 2 Cell proliferation in the *FgfR2*IIIc$^{+/\Delta}$ mouse choroid plexus at post-natal day 3 (coronal view)

A: Wild-type (WT) lateral CP stained for PCNA (red), positive staining is observed in the neuroepithelium but not in the CPe. **B**: Same field of view as in A stained with Hoechst nuclear stain (blue). **C**: *FgfR2*IIIc$^{+/\Delta}$ lateral CP; staining is observed in the sub-ventricular zone, but not in the CPe. **D**: Same field of view as (C) stained with Hoechst nuclear stain. In all scale bars are 50 μm. **CPe** = choroid plexus epithelium, **SV** = sub-ventricular zone.

9.2.2 Ventricle size

In order to test whether the *FgfR2*IIIc$^{+/\Delta}$ mice had enlarged ventricles before they died within 9 days after birth (Hajihosseini et al., 2001), the three dimensional volume of the ventricles in mutant and wild-type (WT) mice at 18.5 dpc and P2, was measured using a stereological approach based on the Cavalieri principle (Chap. 3.17.2): every four sections (50 μm thick) were selected by systematic random uniform sampling method; the area associated with one point (a/p) of the "point grid system" on which the Cavalieri principle formula is based was 139 μm^2. It was found that in both 18.5 dpc and P2 mice, the volume of the ventricles was in fact smaller in *FgfR2*IIIc$^{+/\Delta}$ mice compared to WT mice. The statistical analysis of the results is given in Table 9.1 and summarized graphically in Figs. 9.3-9.4. The average ventricle volume was 4.7x10$^{\wedge-3}$ mm^3 in WT P2 mice and 3.7x10$^{\wedge-3}$ mm^3 in *FgfR2*IIIc$^{+/\Delta}$ mice. However, the difference was not significant as assessed by independent Student's t-test (p: 0.35). The coefficient of error (CE) for the individual estimates was generally under 0.1 (the highest CE being 0.15), which showed that the precision of the estimator counting probe was satisfactory (Table 9.1A). As described in Chap. 3.16.2 the overall coefficient of variance (**CV^2**) of the study is equal to the sum of the biological coefficient of variance (**BCV^2**) and the coefficient of variance of the estimates as expressed by the mean CE^2 (**CE^2**) (summarized by the equation: **CV^2 = BCV^2 + CE^2**). To give an example in WT P2 mice, the CV^2 was 0.11, the BCV^2 was 0.099, and the CE^2 was 0.009 (see Table 1.9B). The coefficient of variance of the estimates (CE^2) was satisfactory since smaller than 50% of the overall variance. The biological coefficient of variance (BCV^2) due to different animal samples was the main contributor to the overall coefficient of variance (CV^2). Hence, the number of animals needed to be increased in order to decrease the BCV^2 and reduce the variance. It could however, be shown that the *FgfR2*IIIc$^{+/\Delta}$ P2 mice did not have enlarged ventricles (see Table 9.1 and Fig. 9.3).

In 18.5dpc mice, the volume of the ventricular system was measured in three *FgfR2*IIIc$^{+/\Delta}$ mice but only one WT mouse was available to me. In the WT mouse, the ventricular volume was 5.9x10$^{\wedge-3}$ mm^3, and in *FgfR2*IIIc$^{+/\Delta}$ mice the average volume was 4.43x10$^{\wedge-3}$ mm^3 (Fig. 9.3)

A.

phenotype	animal	10^{-3} mm^3	CE
WT	1	4	0.05
	2	5.3	0.03
	3	6.6	0.15
	4	3.03	0.15
FgfR2IIIc$^{+/\Delta}$	1	3.6	0.06
	2	3.8	0.04
	3	4.5	0.15
	4	3	0.02

B.

	WT	FgfR2IIIc$^{+/\Delta}$
volume	4.732	3.725
SD	1.554	0.62
CE^2	0.009	0.0045
CV^2	0.108	0.0275
BCV^2	0.0997	0.023

Table 9. 1 Stereological estimates and statistics of the ventricular volume in wild type (WT) and *FgfR2*IIIc$^{+/\Delta}$ in post-natal day 2 mice

A: This table shows the individual estimates of ventricular volume (10^{-3} mm^3) for four WT and *FgfR2*IIIc$^{+/\Delta}$ mice. The coefficient of error (CE) of the individual estimates for each animal is given. The mean CE for WT mice is 0.095, and for *FgfR2*IIIc$^{+/\Delta}$ mice is 0.067. **B**: This table shows the average ventricular volume, standard deviation of average estimates (SD), the average variance of the estimator (CE^2), the total variance of the study (CV^2), and the biological variance of the study (BCV^2) for WT and *FgfR2*IIIc$^{+/\Delta}$ mice.

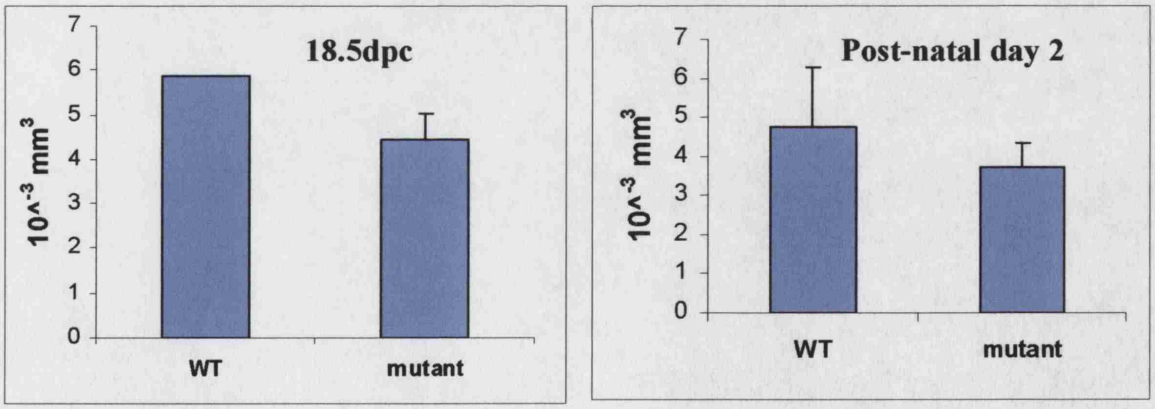

Figure 9. 3 Ventricle volume in wild type (WT) and *FgfR2*IIIc$^{+/\Delta}$ mice

Bar charts showing the mean ventricle volume of in WT and *FgfR2*IIIc$^{+/\Delta}$ mice at 18.5dpc and P2; the error bars represent the standard deviation of the mean. Note that only one 18.5dpc WT mouse was studied.

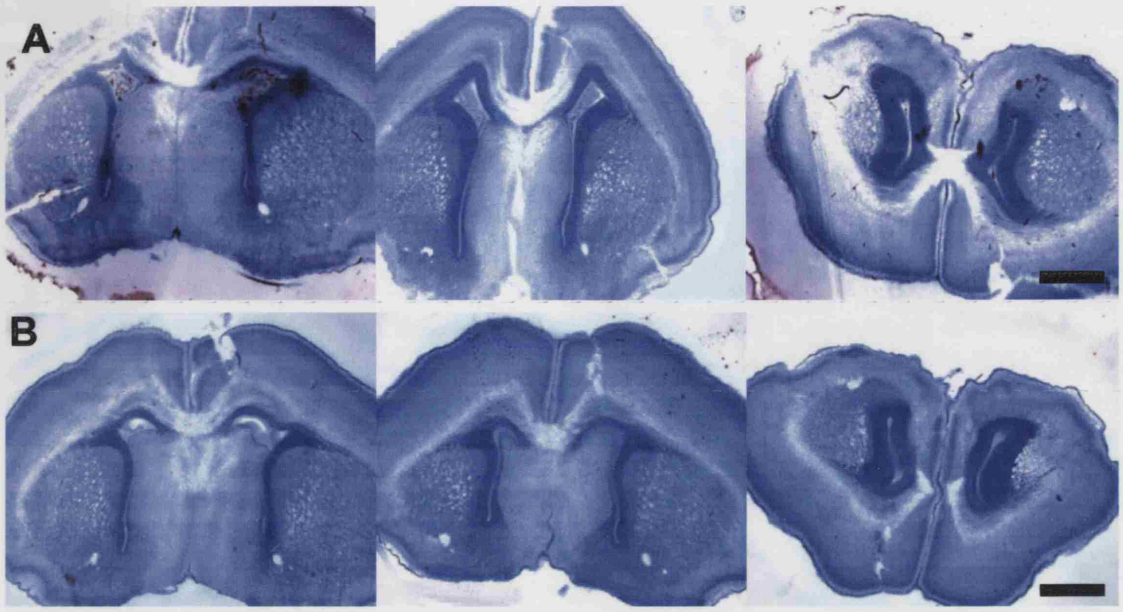

Figure 9. 4 Example of lateral ventricles from *FgfR2*IIIc$^{+/\Delta}$ and wild type (WT) 18.5dpc mice stained by haematoxylin and eosin

Representative coronal sections (eight sections apart from one another) of the lateral brain ventricles of 18.5dpc WT (A) and *FgfR2*IIIc$^{+/\Delta}$ mice (B). **A**: WT mouse sections. **B**: *FgfR2*IIIc$^{+/\Delta}$ mouse showing no apparent ventricular enlargement. Scale bars in A-B are 500μm.

9.2.3 Apert/Pfeiffer mouse cortex characterisation

9.2.3.1 Cortical neuron number and density in post-natal mice

To further characterise the brain structure in *FgfR2*IIIc$^{+/\Delta}$ mice, immunocytochemical staining of paraffin wax sections for the neuron specific marker NeuN was carried out in one WT and one mutant P2 mice, and in two WT and two mutant P3 mice. At these stages, a higher density of neurons seemed present in the cortex of mutant mice, especially in layer II/III (Fig. 9.5). This may have been at least in part due to embedding artifact, since shrinkage and tissue deformation is a common problem of paraffin wax embedding. In order to establish whether there was a significant change in the number of cortical neurons, a stereological analysis was used to quantify the density of neurons, revealed by NeuN, in the whole cortex of WT and *FgfR2*IIIc$^{+/\Delta}$ mice (see Chap. 3.17.1). It was unfortunately only possible to carry out this quantification in one *FgfR2*IIIc$^{+/\Delta}$ and one WT at P3, because in the initial experiments there was improper penetration of the neuN antibody into thick vibratome sections. The basis of the method was to estimate the total number of cortical neurons stained for NeuN, and the total volume of the cortex (all layers) using the Cavalieri principle. The ratio of the values gives the density of neurons per volume of cortex (mm^3). For each WT and *FgfR2*IIIc$^{+/\Delta}$ mice that were sectioned into 50 μm sections, every 10th was evaluated using a systematic random uniform (SRU) procedure; this resulted in 7 SRU sampled sections. The method of sampling neuron counting fields in each section is shown in Fig. 9.6, and the method of counting neurons in each selected counting field by optical deconvolution is shown in Fig. 9.7 (See Chap. 3.16.1 for details of calculation method). The details of the counting procedure are shown in Table 9.2. Using this approach, the neuron density in the WT cortex of a P3 mouse was 3.76x10$^{\wedge 5}$ neurons/mm^3, while in the FgfR2IIIc$^{+/\Delta}$ mouse the density was 5.90x10$^{\wedge 5}$ neurons/mm^3. This initial stereological quantification confirmed the observation from paraffin wax sections that the neuron density in *FgfR2*IIIc$^{+/\Delta}$ mice was higher than in WT mice.

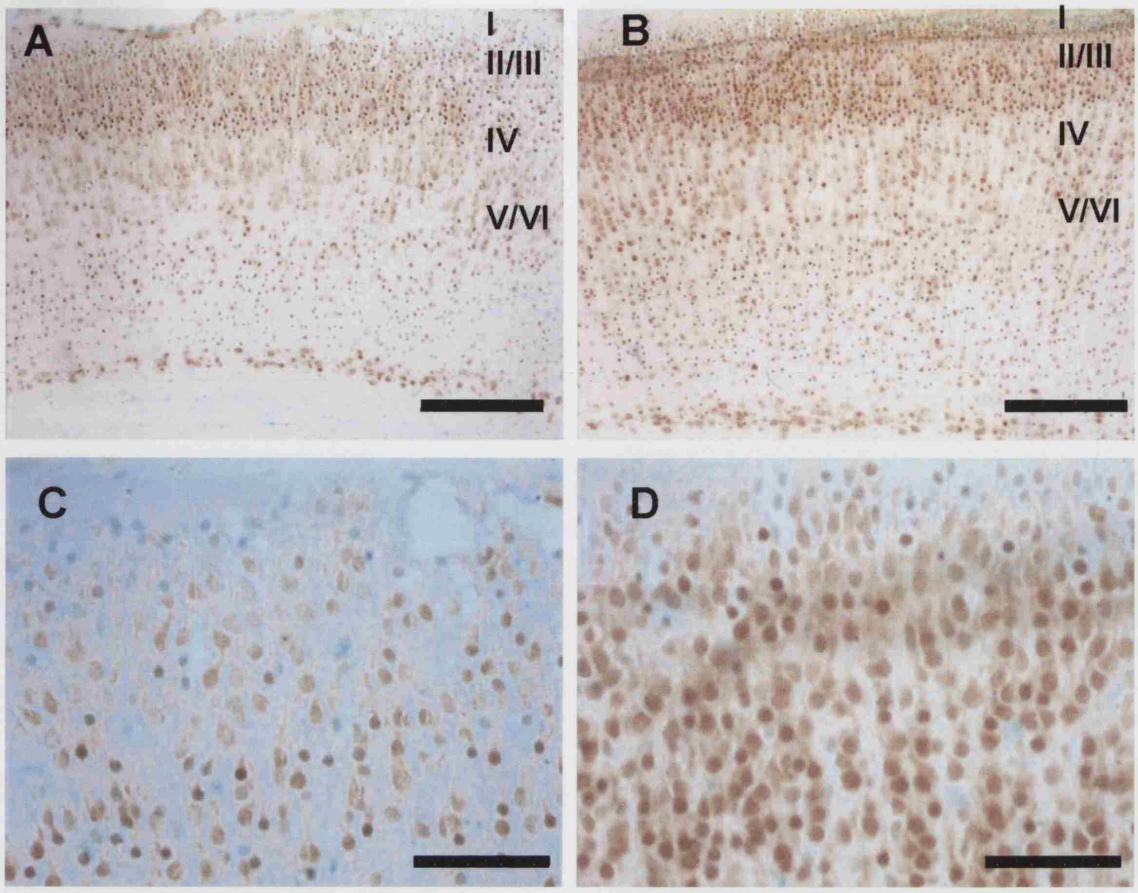

Figure 9. 5 Coronal sections of wild-type (WT) and *FgfR2*IIIc$^{+/\Delta}$ post-natal day 3 mice cortex stained for the neuronal marker NeuN

A: WT mouse cortex. **B**: *FgfR2*IIIc$^{+/\Delta}$ mouse cortex. **C**: High magnification of the cortical layers II/III of the WT mouse cortex shown in (A) in. **D**: High magnification of the cortical layers II/III of the *FgfR2*IIIc$^{+/\Delta}$ mouse cortex shown in (B) in. Scale bar are 100 μm in A-B, and 50 μm in C-D.

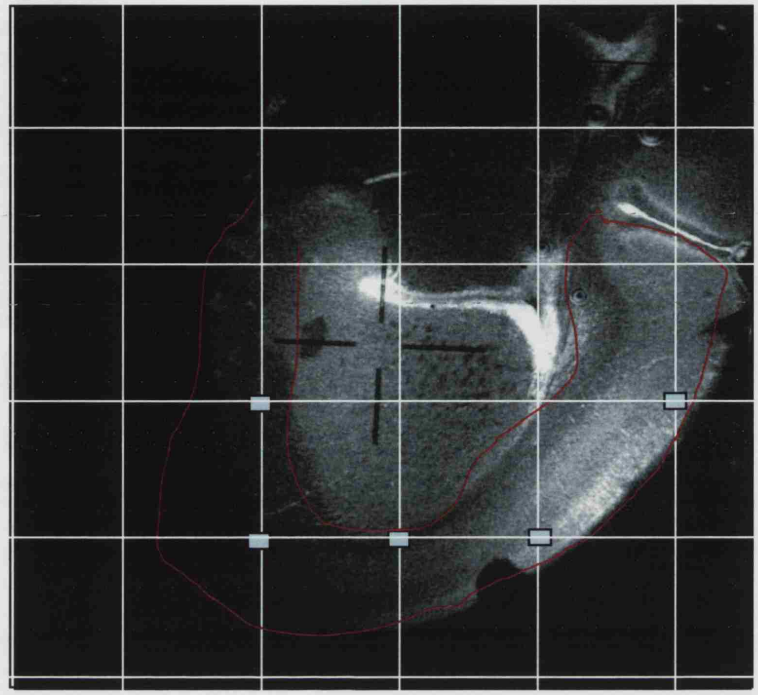

Figure 9. 6 Example of the method for sampling neuron counting fields in one selected brain coronal section

The figure shows an example of a sampling grid for the systematic random uniform sampling (SRUS) of neuron counting fields in the cortex of one brain hemisphere (delineated in red) taken at a low power magnification (x2.5). The picture is apposed randomly on the sampling grid and each intersection of a grid cross with the cortex is shown by a blue square, which corresponds to a counting field. The focusing cross (Black- shown in the middle) is brought unto the counting field and the magnification changed to a high power magnification using a x63 oil immersion lens for optical sectioning and all the neurons that come into focus through the thickness of the section are then counted (see Fig. 9.6). The cumulative number of all the neurons counted this way in the sampled counting fields of one SRU selected section is equal to Q^{-}.

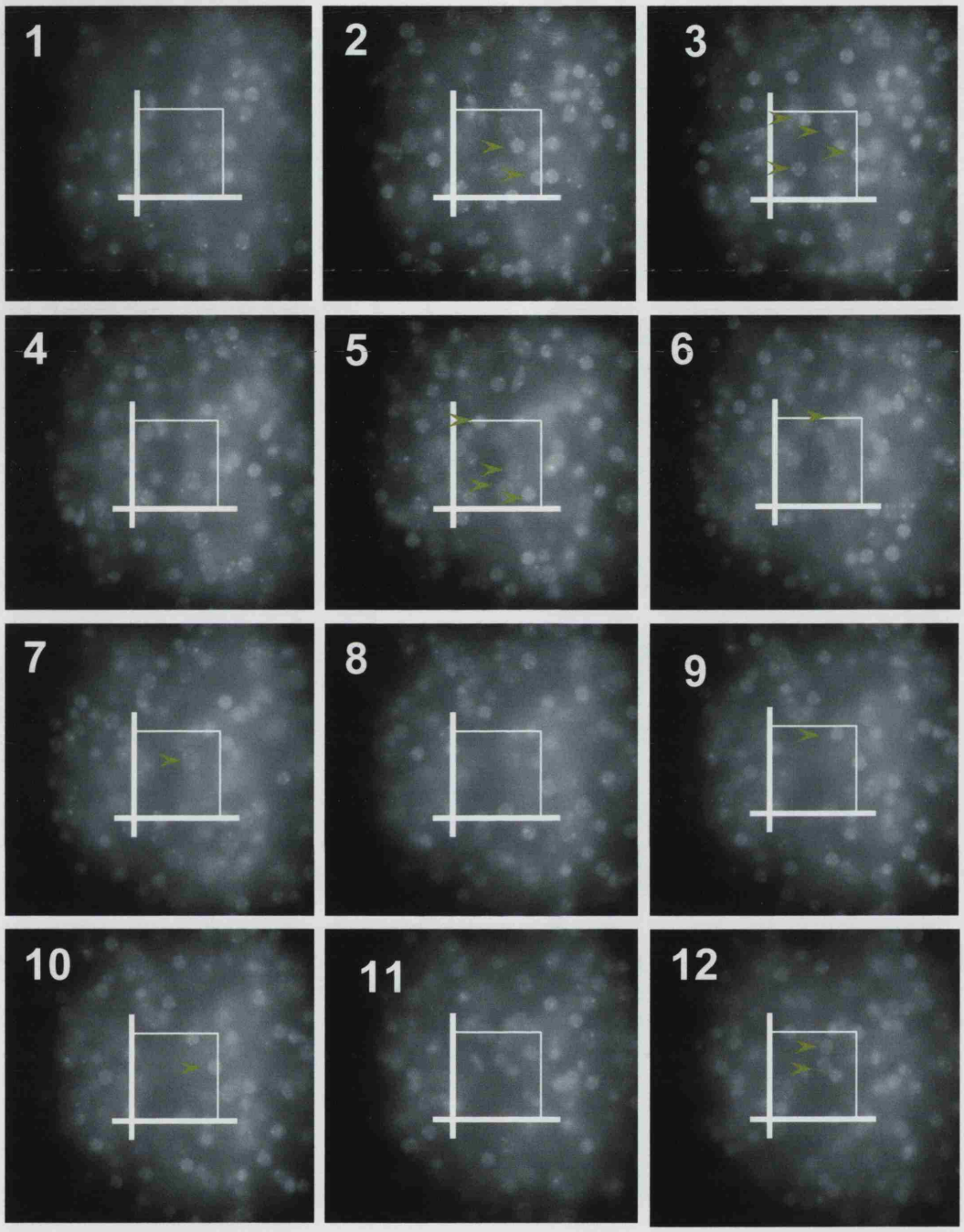

Figure 9. 7 Example of an optical disector in a sampled neuron counting field

An optical disector is composed of a series of optical sections (picture 1-12) taken every 3 μm through a vibratome section of 50 μm (in the z-direction); the first and last 6 μm are left out (safety guards), hence the height (h) of the disector is 38μm. The area of the dissector frame is *a(frame)* = 0.028x0.029 mm^2), and is used to count the cells which come into focus following disector counting rules (Chap.3.16.1.2). The green arrowheads point to the neurons that come into focus and are counted. The volume (Vdis) of the dissector probe (*a(frame)* x h) is $3.08x10^{\wedge-5}$ mm^3 (0.028x0.029x0.038)

FgfR2IIIc$^{+/\Delta}$	Q^-	$Q^-.Q^-$	$Q^-.Q^-_{+1}$	$Q^-.Q^-_{+2}$	FgfR2IIIc$^{+/\Delta}$	P_i	$P_i.P_i$	$P_i.P_{i+1}$	$P_i.P_{i+2}$
1	53	2809	3816	5830	1	16	256	256	384
2	72	5184	7920	4752	2	16	256	384	416
3	110	12100	7260	5610	3	24	576	624	600
4	66	4356	3366	1716	4	26	676	650	702
5	51	2601	1326	3009	5	25	625	675	575
6	26	676	1534		6	27	729	621	
7	59	3481			7	23	529		
ΣQ^-	**437**	**31207**	**25222**	**20917**	ΣP_i	**157**	**3647**	**3210**	**2677**
Nv_{mutant}= 437/(24x 3.08x10^-5) = 5.90x10^5 neurons/mm³ CE = 0.002					$Vref_{mutant}$ = (0.43)² x 157x 0.50 = 14.5 mm³ CE = 0.001				
N_{mutant} = 5.90x10^5 x 14.5 = 8.55x10^6 neurons									
WT	Q^-	$Q^-.Q^-$	$Q^-.Q^-_{+1}$	$Q^-.Q^-_{+2}$	WT	P_i	$P_i.P_i$	$P_i.P_{i+1}$	$P_i.P_{i+2}$
1	72	5184	2736	4608	1	12	36	48	78
2	38	1444	2432	1520	2	16	64	104	112
3	64	4096	2560	2112	3	26	169	182	195
4	40	1600	1320	800	4	28	196	210	210
5	33	1089	660	660	5	30	225	225	210
6	20	400	400		6	30	225	210	
7	20	400			7	28	196		
ΣQ^-	**287**	**14213**	**9708**	**9040**	ΣP_i	**170**	**1111**	**979**	**805**
Nv_{WT} = 287/(23x 3.08x10^-5) = 3.76x10^5 neurons/mm³ CE = 0.004					$Vref_{WT}$ = (0.43)² x 170 x 0.50 = 15.8 mm³ CE = 0.001				
N_{WT} = 3.76x10^5 x 15.8 =5.90x10^6 neurons									

Table 9. 2 Neuron cortical numbers and reference volume for wild-type (WT) and *FgfR2*IIIc$^{+/\Delta}$ mice obtained by stereological counting method

The left part of the table (grey) shows the sum of the neurons counted (**Σ Q⁻**) in each selected vibratome section (1-7) from which is calculated the average number of neurons per mm³ (Nv), as well as the CE (Chap. 3.17.4 and 3.17.5). Effectively Nv gives the average density of neurons in the cortex based on the neuron counts in each optical disector (Q^-). The volume of the disector probe (Vdis = *a(frame)*x h) was 3.08x10^-5 mm³ (0.028x0.029x0.038); The number of disectors (n) in each selected vibratome sections was 23 for WT and 24 for the mutant mouse. It follows that $Nv_{FgfR2IIIc^{+/\Delta}}$ = 5.90x10^5 neurons/mm³ (CE: 0.002), and Nv_{Wt} = 3.76x10^5 neurons/mm³ (CE: 0.004). The right part of the table (light blue) shows the sum of points (**Σ Pi**) from a point grid system that falls within the reference volume (Vref) from which the volume of Vref was calculated using the Cavalieri principle, as well as the CE (Chap 3.17.3); the area per point (a/p) was (0.43)² mm³, and the spacing between each sampled section was 0.50 mm, so that the $Vref_{Mutant}$ = 14.5 mm³ (CE: 0.001) and the $Vref_{Wt}$ = 15.8 mm³ (CE: 0.001). The bottom part of each table (in yellow) for the mutant and WT mice shows the total neuron number (N = Nv * Vref). It follows tha $N_{FgfR2IIIc^{+/\Delta}}$ = 8.55x10^6 neurons and N_{WT} = 5.90x10^6 neurons.

9.2.3.2 Cell proliferation in the cortex of post-natal mice

Since the density of neurons appeared higher in the cortex of mutant mice, it was investigated whether cell proliferation was increased in the sub-ventricular zone and cortex of *FgfR2*IIIc$^{+/\Delta}$ compared to WT P2 to P4 mice by looking at the expression of the mitotic marker p-H3 and the S-phase marker PCNA. Cortical neurons are born before birth. Hence, it was no surprise that very little or no cell proliferation was observed in both FgfR2IIIc$^{+/\Delta}$ and WT mice (Fig. 9.8A-B). No striking differences in neuroepithelial cells around the ventricles was observed between *FgfR2*IIIc$^{+/\Delta}$ and WT mice at these ages. Since in the cerebellum neuroblast proliferation is still occurring at birth, cell proliferation was also investigated in the cerebellum of P2 to P4. An initial observation in a set of WT and *FgfR2*IIIc$^{+/\Delta}$ P3 mice suggested that cell proliferation in certain areas of the cerebellum was higher in the *FgfR2*IIIc$^{+/\Delta}$ than WT mice (Fig. 9.8C-D). However, further studies where selected serial sections at fixed interval were systematically analysed showed that these regional differences were sectioning artefacts and that there was no significant differences in cell proliferation. This analysis was carried out in one WT and mutant mice at P2, and two WT and mutant mice at P3. The number of p-H3 positive cells was not quantified as there was no obvious difference, but the possibility that there are small differences between WT and mutant cannot be ruled out.

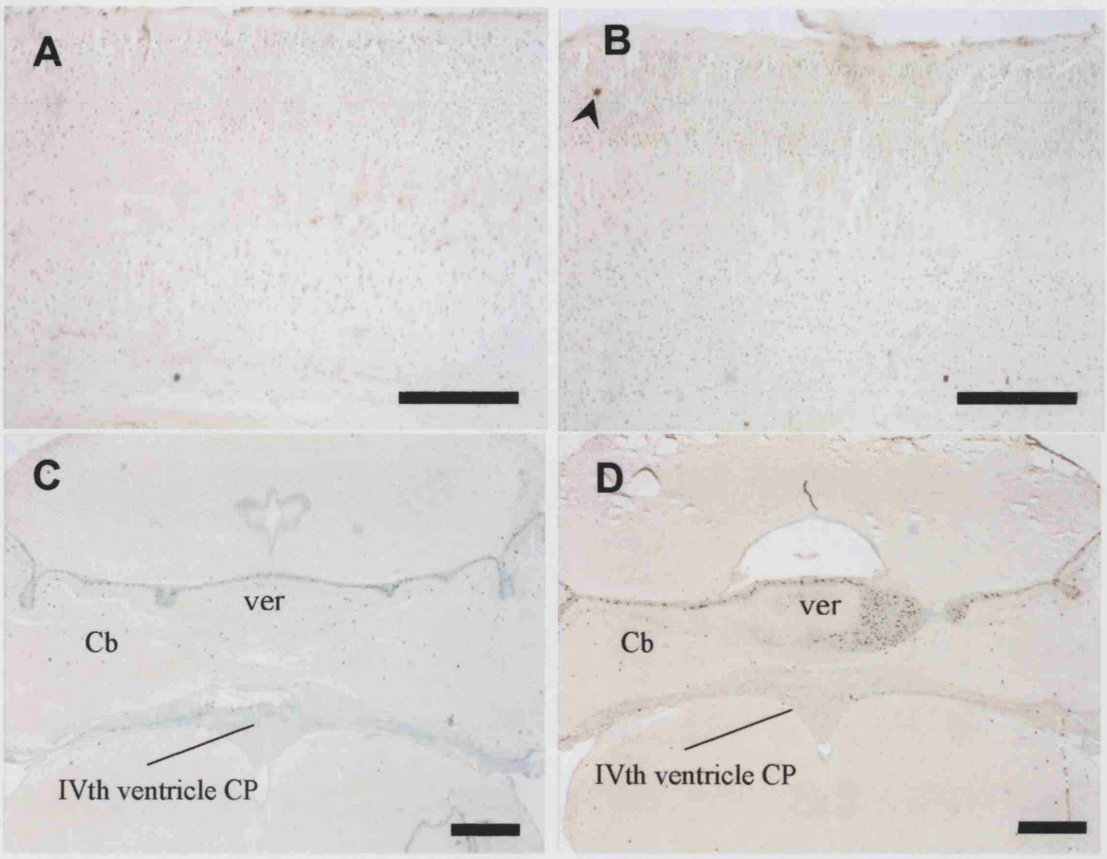

Figure 9. 8 Cell proliferation in the cortex and cerebellum of mutant and wild type (WT) post-natal day 3 mice

A: WT cortex, negative for p-H3; **B**: *FgfR2*IIIc$^{+/\Delta}$ cortex, with one positive p-H3 labelled cell (arrowhead). **C**: WT cerebellum (Cb) and IVth ventricle CP; a few p-H3 positive cells are observed in the cerebellum. **D**: *FgfR2*IIIc$^{+/\Delta}$ cerebellum (Cb) and IVth ventricle CP, an area of intense cell proliferation localised in the vermis (Ver) of the cerebellum is observed. Scale bars are 100 μm in A-B, and 400 μm in C-D.

9.3 Discussion

9.3.1 CP differentiation

The ectopic expression of FGFR2IIIb at sites also expressing FGFR2IIIc in the *FgfR2*IIIc$^{+/\Delta}$ mouse with Apert/Pfeiffer-like syndromes did not appear to affect the development of the choroid plexus (CP). A normal CP histology was observed in *FgfR2*IIIc$^{+/\Delta}$ and WT mice, and both expressed TTR protein. In addition, cell proliferation was not increased in the CPs; in fact it was pretty much absent in both WT and *FgfR2*IIIc$^{+/\Delta}$ mice. Although no CP abnormalities were observed at the histological level, an ultrastructural analysis by electron microscopy may reveal more subtle developmental abnormalities. For example, in the E2F5 k/o mouse the hydrocephalus was caused by a dysfunctional CPe that oversecreted fluid into the ventricles, and water laden electron-lucent CPe cells were only demonstrable by electron-microscopy (Lindeman et al., 1998). It is also probable that the CPs were unaffected because they normally express both the IIIb and IIIc isoforms (Reid and Ferretti, 2003). Indeed, in 8 to 10 week human embryos the CPe has been reported to strongly express both the FGFR2IIIb and IIIc isoforms (Chan and Thorogood, 1999). It would however be informative to confirm which isoforms are expressed in the post-natal mouse CPe.

Unfortunately, there was not sufficient tissue available to study the expression of *E2F5*, *p73* and *FoxJ1* genes that have been associated with a hydrocephalic phenotype in knockout-mice. Changes in their expression may reveal subtle developmental defects of the CPs in the *FgfR2*IIIc$^{+/\Delta}$ mice.

The *FgfR2*IIIc$^{+/\Delta}$ mice did not exhibit any significant signs of ventricular enlargement, symptomatic of a hydrocephalic phenotype, as assessed by stereological analysis at P2 and embryonic day 18.5 dpc. Hydrocephalus occurs relatively frequently especially in Apert as well as Pfeiffer syndromic patients (Cinalli et al., 1998b; Murovic et al., 1993b). However, hydrocephalus is usually progressive particularly in Apert syndrome and may not be present at birth. In the *E2F5* k/o mutant mouse, a hydrocephalic phenotype was only apparent two to three weeks after birth (Lindeman et al., 1998). Thus, it may be that the enlargement of the ventricles would also occur in the mice with Apert/Pfeiffer syndrome-like phenotypes if they did not die after P9 due to visceral organ abnormalities (Hajihosseini et al., 2001).

It should also be noted that although *FgfR2*IIIc$^{+/\Delta}$ mice exhibited Apert/Pfeiffer-syndrome-like phenotypes, the molecular aetiology differed from that underlying the major types of craniosynostosis syndromes, which are due to activating point mutations in the FGF receptors. It thus cannot be excluded that the development and function of the CP would be more conspicuously affected, or affected in a different way, in a mouse model bearing an activating point mutation in one of the FgfRs, or in human CP from syndromic patients.

9.3.2 Neuron number and density

The density of cortical neurons appeared higher in the mutant mice in 10μm paraffin wax sections stained for NeuN. However, wax embedding is known to induce shrinkage and cause deformation of tissue, even though the histology is good (Dorph-Petersen et al., 2000). Furthermore, in these studies the brains were embedded without dissecting them from the skull. Thus the premature fusion of the coronal sutures in mutant mice might have constricted the brain giving the impression of higher cell density. This did not seem to be the case as when brains from P2 mice were dissected out their skulls and cut with a vibratome into thick 50 μm sections to avoid tissue shrinkage and deformation, and neurons counted using a stereological analysis, the neuron numbers was much higher in the mutant than the WT.

This result is consistent with the finding by other authors who reported that FGF2 regulates neuronal density (Dono et al., 1998; Ortega et al., 1998) and number (Vaccarino et al., 1999a) in the cerebral cortex. For instance, the ectopic administration of FGF2 in the 15.5dpc rat increased by 87% the number of neurons in the cortex (Vaccarino et al., 1999a), while in the *Fgf2* knockout mice the number of cortical neurons was 50% lower than in wild-type mice (Vaccarino et al., 1999a). Accordingly, Raballo et al. (2000) hypothesised that FGF2 induces neural progenitor cells to undergo additional mitosis. In fact, the authors showed that this may affect ~50% of the cortical progenitor cell pool as early as 10.5 dpc. It was not surprising that no differences in cell proliferation in the cortex and neuroepithelium between *FgfR2IIIc*$^{+/\Delta}$ and WT post-natal day 2 to 3 mice was observed, since at this post-natal stage cortical neurogenesis is essentially completed. However, also in the cerebellum where neurons mature later and neuroblasts continue proliferating post-natally (Fujita et al., 2002), no marked differences were observed between mutant and WT mice,

although a comprehensive stereological analysis may reveal small differences in cell proliferation.

It will be most informative to study cell proliferation at the early stages of brain development, when FGFR2 protein is most strongly expressed throughout the CNS, and neural progenitor cells are actively dividing. By 15.5 dpc, FGFR2 protein expression is much less strongly expressed (Reid and Ferretti, 2003). Indeed this finding is supported by a study in the mouse showing FGFR2 mRNA expression throughout the brain and most strongly in the midbrain and hindbrain of 9.5 dpc to 16 dpc (Peters et al., 1992). FGFR2IIIc is expressed in the mouse cortical cells at 10 dpc, 12 dpc and 14 dpc (Qian et al., 1997). In the chick, it appears that FGFR2IIIb is more diffusely expressed throughout the neuroepithelium within the dorsal and ventral regions of the developing brain, whereas FGFR2IIIc expression appears more restricted to the ventricular zone of the basal forebrain and other more ventral structures (Orr-Urtreger et al., 1993; Ford-Perriss et al., 2001). This raises the possibility that the additional ectopic expression of the IIIb isoform in the *FgfR2*IIIc$^{+/\Delta}$ mice may make the neural progenitor cells more responsive to a broader set of FGF ligands and thus upset the differentiation/proliferation balance. In the adult, FGFR2 is primarily expressed in glial cells (Asai et al., 1993). Interestingly, when FGF2 is injected at 20.5dpc in the rat, it selectively increases the glial cell population (Vaccarino et al., 1999a). It would be also relevant to study whether the glial cell population is affected in the *FgfR2*IIIc$^{+/\Delta}$ mice.

Other authors reported that FGF2 infusion increased both cell number and cell density of the upper layers (II/III) and the lower layer (IV-VI) of the cerebral cortex (Ohmiya et al., 2001). It was also suggested that when *Fgf2* was knocked out the neuronal defects observed in the cerebral cortex were mostly due to the fact that a fraction of neuronal precursors failed to colonize their normal target layers II and III during cerebral cortex development (Dono et al., 1998). Interestingly, this was also the layer where the neuronal density appeared higher in the cortex of *FgfR2*IIIc$^{+/\Delta}$ mice. Therefore it cannot be excluded that the aberrant expression of the *FgfR2*IIIb isoform increases the number of neuronal cells by increasing the migration of neuronal precursors to the cortex rather than by proliferation.

As mentioned earlier on, this *FgfR2*IIIc$^{+/\Delta}$ mouse model for syndromic craniosynostosis does not carry the type of mutations described in syndromic patients. Therefore, it would be interesting to see whether the neuron number and density also

appear increased in the human cortex of syndromic patients or in mouse models bearing point mutations corresponding to known craniosynostosis syndromes

9.3.3 Summary

A mouse model for syndromic craniosynostosis (*FgfR2*IIIc$^{+/\Delta}$) with defects reminiscent of Apert and Pfeiffer syndromes was studied.

The CPs of these *FgfR2*IIIc$^{+/\Delta}$ mice did not show any histological abnormalities or increased cell proliferation. It was unfortunately not possible to investigate the expression of the genes associated with hydrocephalus *E2F5*, *FoxJ1* and *p73*, since the antibodies did not work on the sections used in this study. The mice at P2 did not show any signs of enlarged ventricles. However, the hydrocephalus may develop over a longer period of time, which would not be detectable since the mice die 10 days after birth. An analysis at the ultra-structural level may reveal more subtle anomalies such as those observed in the E2F5 knockout mouse which exhibits water-laden electron-lucent CPe cells.

The brain of these *FgfR2*IIIc$^{+/\Delta}$ animals appeared normal except that on closer inspection the neuronal cell density appeared higher than in WT animals. An initial stereological quantification approach, based on one specimen, confirmed this observation. The study would need to be repeated to confirm this result and carry out statistical analysis. Cell proliferation appeared normal in the cortex and cerebellum of the *FgfR2*IIIc$^{+/\Delta}$ mice at P3. However, if cell proliferation was affected it would likely be during early development (10 dpc to 14 dpc) when neurogenesis is actively taking place. The observation that these mutant mice may suffer neurological abnormalities is interesting with regard to the fact that many patients with Apert syndrome have been reported to suffer from mental retardation that is independent of raised ICP.

Since this *FgfR2*IIIc$^{+/\Delta}$ mouse model did not reflect the true molecular aetiology underlying the main cases of syndromic craniosynostosis, future studies should also concentrate on looking at whether CPe development and function is affected in syndromic patients and in mutant mice bearing an activating point mutation in an *FgfR* equivalent to a known clinical case of syndromic craniosynostosis.

Chapter 10 Final discussion

This thesis studied the effect of FGF signalling on the function and development of the CPe in order to understand whether the high incidence of increased intra-cranial pressure and hydrocephalus encountered in patients with syndromic craniosynostosis could be explained by an oversecretion of CSF fluid. I used different strategies to study the effect of FGF-signalling on CPe cell function and development, and more specifically whether it affected fluid secretion and/or cell proliferation. I firstly studied the normal development of the CPe in mouse and human, where I showed that expression of *FGF2* (Chap. 4), as well as that of *E2F5*, *FoxJ1*, and *p73* whose knockout cause hydrocephalus. I used these genes as markers to confirm the phenotype of CPe cells grown in culture (Chap. 5). The effect of FGF2 on CPe cell function was then studied using an embryonic cell culture vesicle model (Chap. 6-7) and a rat adult cell line (TRCSFB-2) (Chap. 8). In addition, this latter model was used to assess the effect of FGF2 on E2F5, FoxJ1 and p73 mRNA expression (Chap. 8). Finally, I also investigated whether a mouse model for syndromic craniosynostosis with Apert/Pfeiffer-like phenotypes suffered from hydrocephalus and CP abnormalities (Chap. 9).

10.1 FGF signalling and choroid plexus epithelial cell proliferation

In the CPe vesicle model, I found that FGF2 increased the size of the vesicles by increasing cell migration and/or cell:cell adhesion so that the CPe cells formed bigger aggregates, which then hollowed out into proportionally bigger vesicles (Chap. 7). FGF2 did not increase cell proliferation, which was anyway quite rare or absent in CPe cell cultures grown on Matrigel. This was reminiscent of the in-vivo situation where I found that the normal expression of FGF2 in the mouse and human embryonic CPe bore no relationship to cell proliferation. In fact, cell proliferation was absent in most of the CPe during development, except at the root of the CPs where cell proliferation was intense. At all ages investigated, FGF2 was expressed strongly throughout the embryonic human and mouse CPe with no specific pattern (Chap. 4). In addition, according to Reid (2003) and Chan CTJ (2001) FGFRs did not appear to

be expressed in any pattern that may suggest a relationship between FGF signalling and proliferation of CPe cells.

In contrast, in TRCSFB-2 cells grown as a monolayer on collagen I, cell proliferation was high even in absence of FGF2, and only the lowest dose of FGF2 tested (1 ng/ml) strongly increased cell proliferation. Higher doses of FGF2 had a proportionally smaller effect on cell proliferation similar to that described for neuroprogenitor cells (Murphy et al., 1990; Qian et al., 1997), with the exception that no obvious change in cell phenotype was obverved (Chap. 8). This is consistent with previous work showing that primary embryonic mouse CPe cells grown on laminin as a monolayer exhibit a relatively high rate of cell proliferation, which is increased by FGF2 (10 ng/ml) (Reid S, Phd thesis 2001). This discrepancy in cell proliferation between the CPe cells grown on three-dimensional Matrigel, even not contact inhibited, and CPe cells grown as a monolayer was most likely due to differences in the environment of the cells such as: 1) positive and/or negative factors within the Matrigel regulating cell proliferation; 2) the three dimensional (3-D) structure of the Matrigel matrix which induces a change of behaviour and even morphology, since single cells appear bipolar rather than fibroblastic-like as in on monolayer culture.

The idea that the discrepancy in cell proliferation between the vesicle cell model and CPe cell cultures grown as a monolayer on collagen I or laminin was either due to growth inhibiting factors present in the Matrigel or/and to mechanochemical signalling differences based on different interactions between integrins and their matrix ligand is supported by work by Stadler and Dziadek (1996). These authors reported that mouse embryonic cells grown in 100% Matrigel exhibit significantly less proliferation than cells grown in 33% Matrigel diluted with collagen I, but they were unable to penetrate the matrix and form vesicles. It was hypothesised by the authors that the higher rate of cell proliferation in 33% Matrigel/67% collagen I must have been due to a dilution of growth inhibitors, such as TGFβ1 and TGFβ2, (Lyons et al., 1990; Massague et al., 1990; Daniel and Robinson, 1992) or of protein components of the extracellular matrix within the Matrigel. Addition of the extracellular matrix proteins nidogen and/or laminin allowed formation of CPe vesicles, but cell proliferation was not assessed in these vesicles (Stadler and Dziadek, 1996).

Overall, these experiments did not convincingly explain why the proliferation index was lower in Matrigel cultures compared to monolayer cultures. It is possible

that the absence of CPe cell proliferation in Matrigel was directly caused by the three-dimensional structure of the matrix, which modified the behaviour of the CPe cells. This idea is corroborated by studies which suggest that cells grown in culture in a 3-D matrix are able to recognize the 3-D structure of their environment compared to a 2-D environment, which is accompanied by a change in function and morphology of the cells (Sato et al., 2004; Song et al., 2001). For instance, the profile of gene expression of vascular smooth muscle cells plated onto 3-D collagen matrix is different from that of cells grown on a 2-D matrix. Most significantly, cell proliferation is lower for cells grown in 3-D collagen I matrix and they express more strongly the cyclin-dependent kinase inhibitor 1 (p21), suggesting that p21 may be responsible for the lower cell proliferation (Li et al., 2003). It is therefore possible that a similar change in gene expression profile applies for CPe cells grown on Matrigel compared to laminin or collagen I. Until further experiments are conducted, it would thus appear that the lack of CPe cell proliferation in Matrigel was in part a consequence of the 3-D structure of the matrix and in part due to negative and/or positive factors contained within the Matrigel that influenced the proliferative state of the cells and their response to FGF2.

Although cell proliferation of CPe cells grown on Matrigel was not affected by the doses of FGF2 (10-100 ng/ml) tested, it is nonetheless possible that lower doses of FGF2 would have increased cell proliferation of the embryonic CPe cells. This idea is supported by ventricular infusion experiments where 1 ng FGF2 in the Marmoset caused CPe hyperproliferation (Pearce et al., 1996), whereas in the rat higher concentrations of FGF2 (250-1000 ng) did not conspicuously enlarge the CPs (Johanson et al., 2001). The knockout mouse with Apert/Pfeiffer syndrome-like phenotypes also did not show any increased signs of CPe cell proliferation and concomitant enlargement. Although it is possible that FGFR signalling was increased above the threshold that triggers cell proliferation, it is also possible that since the genetic aetiology underlying the phenotype was not due to an activating point mutation in one of the *FgfR* gene members but to the heterozygous splice switching from the *FgfR2*IIIc to IIIb isoform: 1) the change of FGFR profile did not significantly increase FGFR signalling and thus affect CPe cell proliferation; 2) the CPe was not affected since FGFR2 IIIb and IIIc isoforms are both already normally expressed.

10.2 FGF-signalling and choroid plexus epithelial cell fluid secretion

Using ouabain and acetazolamide which inhibit two enzymatic pathways critical for the secretion of fluid as reported in the literature (Davson and Segal, 1970), I showed that it was possible to collapse and inhibit growth of CPe vesicles. This indicates that the CPe cells actively secreted fluid (Chap. 6). Using this model, I found that FGF2 appeared to have an inhibitory effect on secretion, as also noticed by Reid (PhD thesis, 2001) who found that a 100 ng/ml FGF2 transiently inhibited vesicle growth (Chap. 7). This was supported by published data that shows that PKC, a second messenger in one of the FGF2 signalling pathways, inhibits the activity of the Na^+/K^+ ATPase (Cheng et al., 1997), and the inward rectifying Cl^- channel similar to CIC-2 in the rat choroid plexus. Furthermore, in rat astrocytes PKC inhibits the transcription of aquaporin 4 (Zelenina et al., 2002; Nakahama et al., 1999). My observation on the inhibitory effect of FGF2 on CPe cell secretion also supported the finding by Hackvoort A (2000) and Johanson CE (1999) who found that FGF2 inhibited fluid secretion. Unfortunately, it was not possible to use the Transwell assay based on the TRCSFB-2 cell line to test the effect of FGF2 on fluid secretion, since the cells did not survive long enough at 37°C to detect fluid secretion with the assay used. However, using these same cells I showed that FGF2 inhibited the transcription of both *E2F5* and *FoxJ1* whereas neither *p73* nor *TTR* were affected (Chap. 8). According to the data from the hydrocephalic knockout mice for *E2F5* and *FoxJ1*, the decrease in expression levels of E2F5 and FoxJ1 should translate in an increase in fluid secretion. This observation contradicted the observation in the vesicle model where FGF2 had a slight inhibitory effect on fluid secretion. It may be possible that FGF2 initially inhibited fluid secretion, but it then directly or indirectly inhibited the expression of E2F5 and FoxJ1 as part of a homeostatic mechanism to increase fluid secretion. This explanation would agree with the observation that the inhibition by FGF2 was transient, especially at higher doses as found by Reid (Phd thesis, 2001). An alternative explanation is that the downregulation of these two genes is independent of fluid secretion, since *FoxJ1* has been associated with ciliogenesis (Chen et al., 1998), and *E2F5* with the cell cycle (Vaishnav et al., 1998; Gaubatz et al., 2000).

The knockout mouse with Apert-Pfeiffer syndrome-like phenotypes did not exhibit any signs of ventricular dilation as quantified by stereological analysis. Moreover the histology of the CPs appeared normal (Chap. 9). However, this does not mean that the CP epithelial cells at the ultrastructural level were not abnormal as reported for the *E2F5* k/o mouse which had water laden, electron lucent cells. In fact these animals developed signs of hydrocephalus by the second week after birth, which would be reminiscent of the hydrocephalus and raised ICP in syndromic craniosysnostosis, which is also found to develop over time after birth (Lindeman et al., 1998). The density of cortical neurons appeared increased in these mice compared to WT (Chap. 9). This is an interesting observation since patients with Apert and Pfeiffer syndromes often suffer from mental retardation that is independent of raised ICP (Sarimski, 1997; Cohen, Jr. and Kreiborg, 1990a). Further work will have to be carried out to confirm the increase in cortical neuron number, and it will also be important to study whether there is increased cell proliferation/delayed differentiation during neurogenesis.

10.3 Summary

My data thus showed that FGF2 could modulate cell migration and/or cell:cell adhesion but did not affect cell proliferation of embryonic CPe cells grown on Matrigel, which was also supported by the observation that in-vivo the pattern of expression of FGF2 did not directly correlate with CPe cell proliferation. However, experiments using the rat adult cell line showed that low doses of FGF2 (1ng/ml) strongly affected cell proliferation and this was supported by ventricular infusion experiments of FGF2 (Pearce et al., 1996; Johanson et al., 1999). Since FGF2 has different affinities for the different FGFR isoforms (Ornitz et al., 1996), it may be that at an FGF2 concentration just above the normal in-vivo concentration, the combination of FGFR isoforms activated triggers cell proliferation; above this concentration, FGF2 would bind to a greater number or all FGFR isoforms triggering a different (e.g. anti-mitogenic) or stronger (e.g. cell adhesion) cellular response. If this model was correct, it would be informative to test other FGFs with broader or more restricted FGFR specificity such as FGF1 and FGF7 respectively, which are both expressed either by the CP (FGF7) (Finch et al., 1995b) or in its vicinity (FGF1) (Nurcombe et al., 1993), in order to see whether they have different effects on the

function of the adult and embryonic CPe cells, and to compare their dose-response curves with that of FGF2.

At high doses, FGF2 did not affect CPe cell proliferation, and inhibited CSF secretion. This is consistent with the phenotype in human syndromic craniosynostosis caused by FGFR hyperactivation as well as the Apert/Pfeiffer mouse model I studied, where CPs are not enlarged due to increased cell proliferation and appear normal at the macroscopical level (not shown for human). It could thus be expected on the basis of in-vitro and in-vivo work that the hyper-activation of FGFRs would inhibit fluid secretion; see Chap. 7 and (Hakvoort and Johanson, 2000; Johanson et al., 1999). If this was the case, syndromic patients might exhibit an increased number of dark cells at the ultrastructural level, to reflect a decreased secretory activity (Sturrock, 1979), and it will therefore be important to carry out a careful analysis at the ultrastructural level. It is possible, however, that the FGF-signalling pathway is modulated to buffer the hyper-activation of one FGFR member so that normal function and development of CPe cells would be largely preserved.

The fact that the FGFRs along with FGF2 are expressed by the CPe cells from the time the CP first forms, suggests that FGF signalling must have an important role in the function and development of the CPe cells. One could hypothesize for instance that FGF2 has an autocrine regulation on the CPe cells and could function: 1) either as a survival cue as reported in a variety of differentiated/quiescent cells (Spector et al., 2002; Blottner and Baumgarten, 1992; Pittman et al., 1993; Haimovitz-Friedman et al., 1994); 2) a component of a homeostatic system that allows cell proliferation when the CPe is disrupted, as in quiescent smooth muscle cells of the arterial media (Fox and Shanley, 1996) or renal tubular epithelial cells, where bFGF is thought to be involved in autocrine regulation to promote recovery from injury (Anderson and Ray, 1998); 3) as a modulator of CSF secretion, as suggested by the fact that FGF2 appears to inhibit fluid secretion (Chap. 7) (Hakvoort and Johanson, 2000). Overall, my results brought evidence that FGF-signalling can modulate the function of CPe cells and may also be important for development. However, the precise role of FGF signalling and the different FGFR members for the development and function of CPe cells remains to be understood.

Appendix I

AI. 1 Openlab automation for time lapse-microscopy using three channels: bright field or/and two fluorescent channels

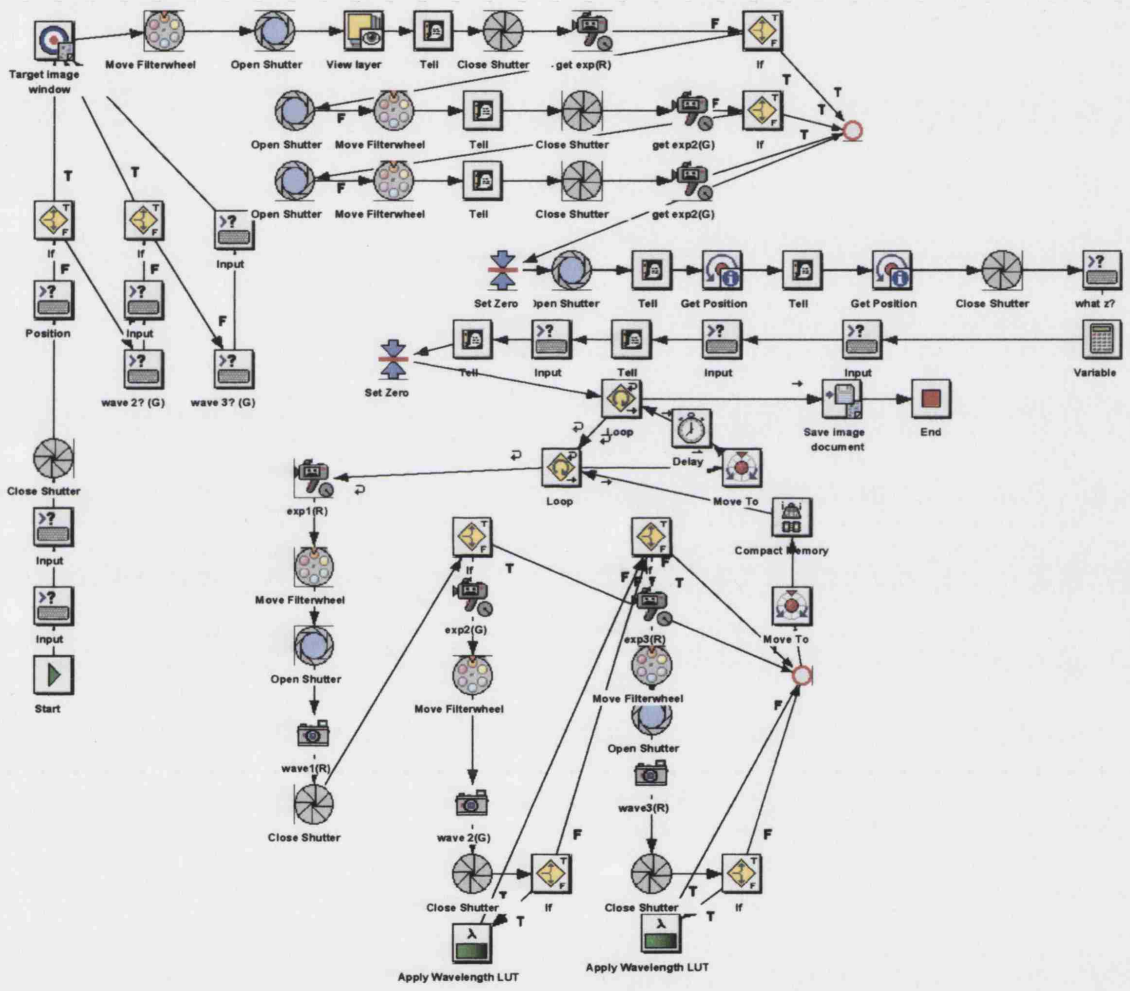

Refer to the Openlab automation manual (Improvision, UK) for a detailed description of the above automator tasks that make up the programme.

AI. 2 **Table of incubation times for embedding mouse embryos of different ages in paraffin wax**

Preparation of paraffin embedded embryos

Process	Solution	Crown-rump length of embryo (mm)			
		<2	3-5 (E9.5 – E 11.5)	6-15 (E12.5-E16.5)	>15 (-E17.5)
Fixation	4% formaldehyde	2-24h	2-24h	2-24h	2-24h
Storage after Fixation	70% ethanol	variable	variable	variable	variable
Dehydration and Clearing	80% Ethanol	1 min	3-5 min	30 min	2 hours
	90% Ethanol	1 min	3-5 min	30 min	2hours
	100% Ethanol I	1 min	3-5 min	30 min	2hours
	100% Ethanol II	1 min	3-5 min	30 min	2hours
	(1:1) 100% Ethanol: Histoclear	1 min	3-5 min	30 min	2hours
	Histoclear (60°C)	1 min	3-5min	30 min	2hours
Embedding	Paraplast I	1 min	3-5 min	30 min	2hours
	Paraplast II	1 min	3-5 min	30 min	2hours
	Paraplast III	1 min	3-5 min	30 min	2hours

Appendix II

AII. 1 Effect of Ara-C on early CPe vesicle formation

A

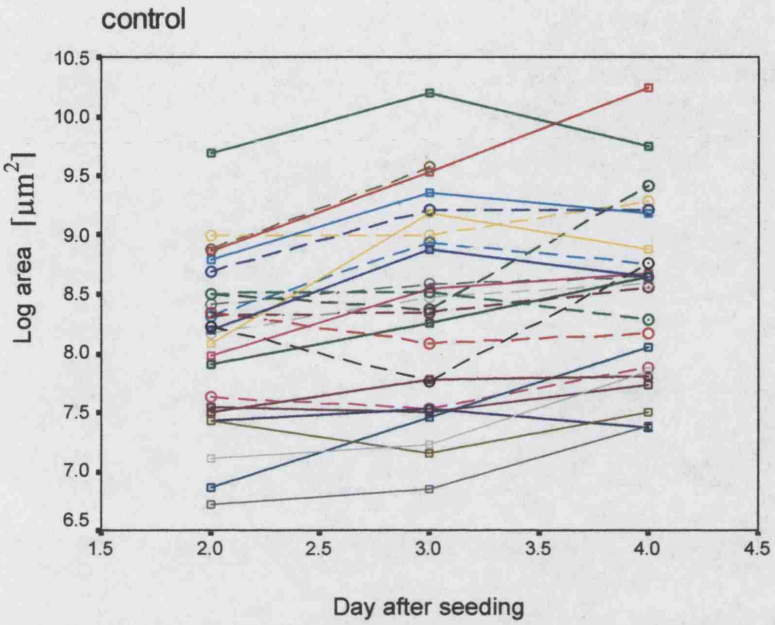

B

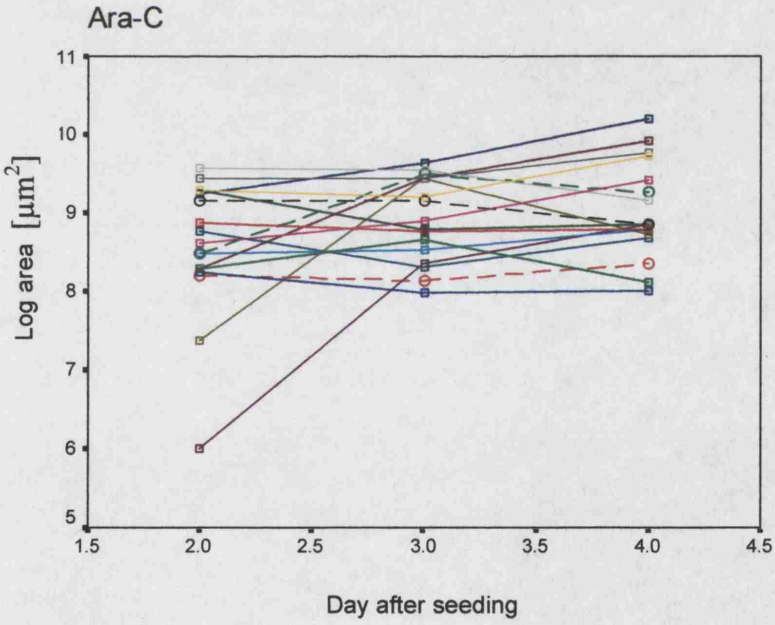

Graphs showing the growth of individual aggregates and vesicles over four days since seeding the CPe cells in the absence (**A**-Control) or presence of 50µM Ara-C added one day after plating (**B**-Ara-C). The log area of aggregates was measured at two, three and four days after seeding the CPe cells, and each coloured line represents an individual aggregagte/vesicle.

AII. 2 Independent Student's t-test of the effect of Ara-C on early vesicle growth

	t-test for Equality				
				95% Confidence Interval of the Difference	
Day	Significance	Mean Difference	SE	Lower	Upper
2	.036	-2286.81	1057.015	-4418.489	-155.140
3	.212	-1973.85	1557.430	-5114.709	1167.005
4	.143	-2802.97	1879.194	-6595.341	989.393

Table showing the results from Independent Student's t-test comparing the **significance** in the **mean difference** in size of control and Ara-C treated vesicles at 2, 3 and 4 days since plating the CPe cells. The Ara-C was added one day after plating the CPe cells. The **upper** and **lower** boundaries of the **95% confidence interval** are given for each test, with the standard error (**SE**).

AII. 3 Multi-level model for the effect of Ara-C on vesicle growth

Area = $\beta 0$ **(constant)** + $\beta 1$ **(treatment)** + $\beta 2$ **(day)** + $\beta 3$ int**(day*treatment)**

Where, $\begin{cases} \text{level 1: variation of vesicle area on each day of growth} \\ \text{level 2: variation between vesicle growth curves} \end{cases}$

The model takes into account the effect of Ara-C **treatment**, of the **days** in culture, and of the interaction between these two parameters int**(day*treatment)**, which allows to compute the average difference in growth between Ara-C treated and control vesicles for every day in culture, are included in the model. A β_n coefficient is given for each explanatory variable. The multi-level model assesses the general variation in the size of vesicles at each day (level 1) and the variation between individual vesicle growth curves (level 2).

AII. 4 Effect of Ara-C on mature CPe vesicle growth

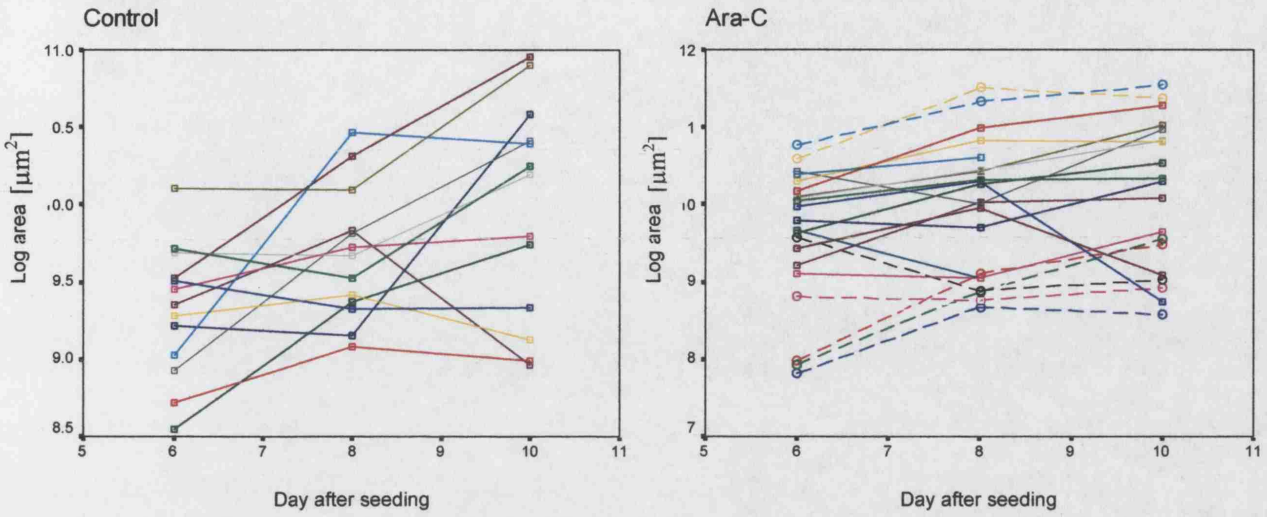

Graphs showing the growth of individual vesicles over four days in the absence (**Control**) or presence of 50µM Ara-C (**Ara-C**) added five days after plating. The log area of aggregates was measured at six, eight and ten days after seeding the CPe cells, and each coloured line represents an individual vesicle.

AII. 5 Independent Student's t-test of effect of Ara-C on mature vesicle growth

	t-test for Equality				
				95% Confidence Interval of the Difference	
Day	Significance	Mean Difference	SE	Lower	Upper
6	.255	-4482.733	3876.316	-12336.9	3371.428
8	.352	-7002.700	7431.016	-22059.4	8053.968
10	.221	-10298.42	8253.194	-27070.9	6474.093

Table showing the results from Independent Student's t-test comparing the **significance** in the **mean difference** in size of control and Ara-C treated vesicles at 6, 8 and 10 days since first plating the CPe cells. The Ara-C was added to vesicles grown for five days after plating the CPe cells. The **upper** and **lower** boundaries of the **95% confidence interval** are given for each test, with the standard error (**SE**)

Appendix III

AIII. 1 Scatter plots of the effect of FGF2 on the size of CPe aggregates

A

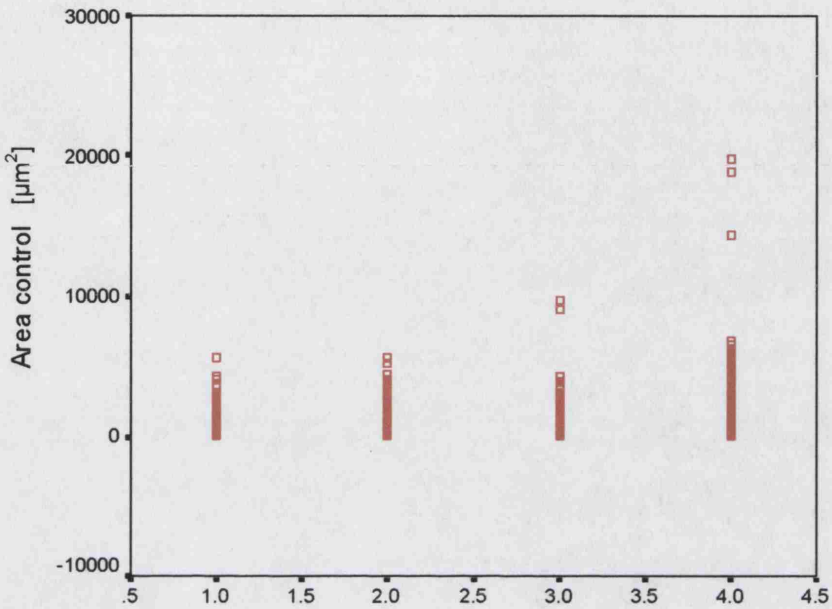

B

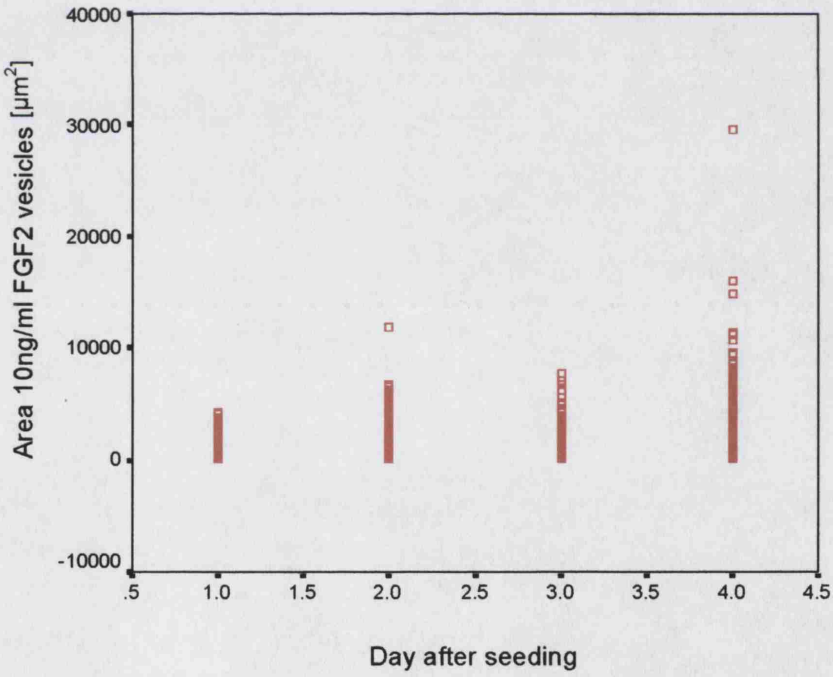

Graphs showing focal mid-plane area (Area) of vesicles and aggregates at one, two, three, and four days after seeding CPe cells. **A**: non-treated control vesicles and aggregates, **B**: vesicles and aggregates treated with 10ng/ml FGF2.

AIII. 2 Statistical data for the size of aggregates and vesicles in ± FGF2 treated early vesicle cultures

Day	Treatment	Mean	N	SD	SE	Min	Max	Med
1	Control	573.06	764	633.162	22.907	44	5600	341
	10FGF2	580.33	689	596.227	22.714	28	4266	383
2	Control	725.70	838	728.172	25.154	31	5676	489
	10FGF2	1233.98	531	1270.478	55.134	68	11928	780
3	Control	883.33	288	1069.893	63.044	42	9799	588
	10FGF2	1802.01	113	1604.535	150.942	108	7742	1301
4	Control	1312.07	727	1613.777	59.852	37	19832	830
	10FGF2	2850.47	318	3000.122	168.239	126	29567	1798

The table summarises the mean area for each culture treatment on each measurement day. **Mean:** mean area (μm^2), **N:** number of aggregates and vesicles counted, **SD:** standard deviation, **SE:** standard error of the mean **Min:** minimum area (μm^2), **Max:** maximum area (μm^2), **Med:** median area (μm^2).

AIII. 3 Independent Student's t-test of the size of aggregates and vesicles between ± FGF2 treated early vesicle cultures

Day	significance	Mean	SE	95% confidence interval	
				Lower	Upper
1	8.22 e-1	7.27	32.360	-56.204	70.750
2	2.22 e-20	508.28	54.076	402.204	614.364
3	9.32 e-11	918.68	138.021	647.339	1190.019
4	1.51 e-25	1538.40	143.385	1257.044	1819.757

Independent student t-tests (FGF2-control) were performed to determine statistical significance between the size of aggregates and vesicles in untreated (controls) and FGF2 treated cultures at the different days of measurement. Following the rows downwards are the different time points (Day), following the columns from left to right the following are given: the significance of the test (or p-value), the Mean difference (Mean) and the Standard Error of the mean difference (SE), as well the 95% confidence intervals of the mean difference (lower and upper).

AIII. 4 Statistics for the number of aggregates and vesicles in ± FGF2 treated early vesicle cultures

Day	Treatment	Mean	N	SD	SE	Min	Max	Med
1	Control	310.00	3	33.511	19.348	277	344	309
	10FGF2	289.33	3	38.070	21.980	250	326	292
2	Control	188.50	4	29.011	14.506	152	223	189.50
	10FGF2	103.50	4	31.859	15.930	58	127	114.50
4	Control	163.75	4	30.270	15.135	122	194	169.50
	10FGF2	72.25	4	21.156	10.578	47	93	74.50

The table summarises the mean number of aggregates and vesicles counted on one, two and four days after seeding CPe cells. **Mean:** is the mean number of aggregates and vesicles, **N:** the number of cultures counted, **SD:** standard deviation of the mean, **SE:** standard error of the mean, **Min:** minimum number counted per culture, **Max:** maximum number per culture, **Med:** median number counted per culture.

AIII. 5 Independent Student's t-test for the number of aggregates and vesicles between ± FGF2 treated early vesicle cultures

Day	significance	Mean	SE	95% confidence interval	
				Lower	Upper
1	0.519	20.67	29.282	-60.634	101.967
2	0.008	85.00	21.545	32.282	137.718
4	0.003	91.50	18.465	46.318	136.682

The table shows the results from Independent Student's t-test (control-FGF2) that were performed comparing the number of aggregates and vesicles between control and FGF2 treated early vesicle cultures. Following the rows downwards are the time points of the measurements (**Day**). Following the columns from left to right are given: the **significance** of the test (or p-value), the mean difference between control and FGF2 (**Mean**), the standard error of the difference (**SE**), and the 95% confidence interval (**upper** and **lower** bounds).

AIII. 6 Scatter plot of the size of choroid plexus epithelial aggregates cultured with +/- 100ng/ml FGF2

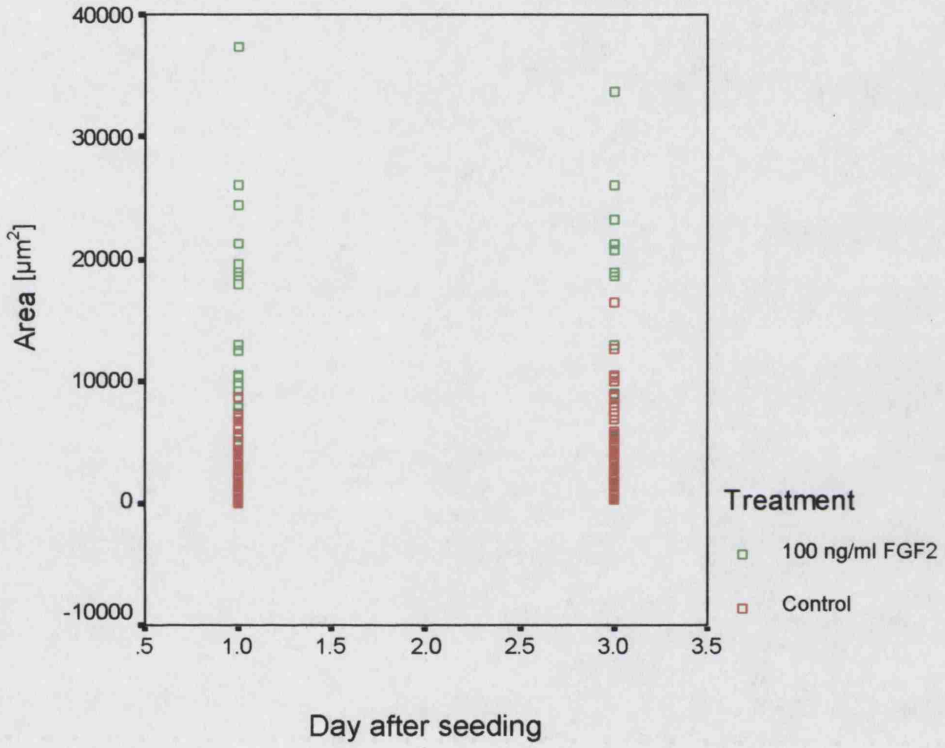

Graph showing the superimposed values for the focal mid-plane area (Area) of non-treated control and 100ng/ml FGF2-treated vesicles and aggregates at one and four days after seeding the CPe cells.

AIII. 7 Statistics table of the mean area of aggregates in ±100ng/ml FGF2 treated early vesicle cultures

Day	Treatment	Mean	N	SD	SE	Min	Max	Med
1	control	1137.90	290	1375.804	80.790	28	8743	652.5
	100FGF2	10749.61	41	13570.655	2119.380	375	78075	6200
3	control	2922.17	94	3252.675	335.488	256	16520	1488
	100FGF2	15724.00	17	9804.947	2378.050	1824	33776	13040

Table summarizes the mean number of aggregates counted on one, and three days after seeding CPe cells. **Mean:** is the mean area of aggregates, **N:** the number of cultures counted, **SD:** standard deviation of the mean, **SE:** standard error of the mean, **Min:** minimum area, **Max:** maximum area, **Med:** median area.

AIII. 8 Statistics table for the mean number of aggregates in ±100ng/ml FGF2 treated early vesicle cultures

Day	Treatment	Mean	N	SD	SE	Min	Max	Med
1	control	143.5	4	27.197	13.598	104.00	166.00	152.00
	100FGF2	18.00	3	6.928	4.000	10.00	22.00	22.00
3	control	92.00	2	19.800	14.000	78.00	106.00	92.00
	100FGF2	18.66	3	7.572	4.371	10.00	24.00	22.00

The table summarises the mean number of aggregates counted on one, and three days after seeding CPe cells. **Mean:** is the mean number of aggregates and vesicles, **N:** the number of cultures counted, **SD:** standard deviation of the mean, **SE:** standard error of the mean, **Min:** minimum number counted per culture, **Max:** maximum number per culture, **Med:** median number counted per culture.

AIII. 9 Growth curves of recovering vesicles +/- FGF2 after treatment with acetazolamide/ouabain

A

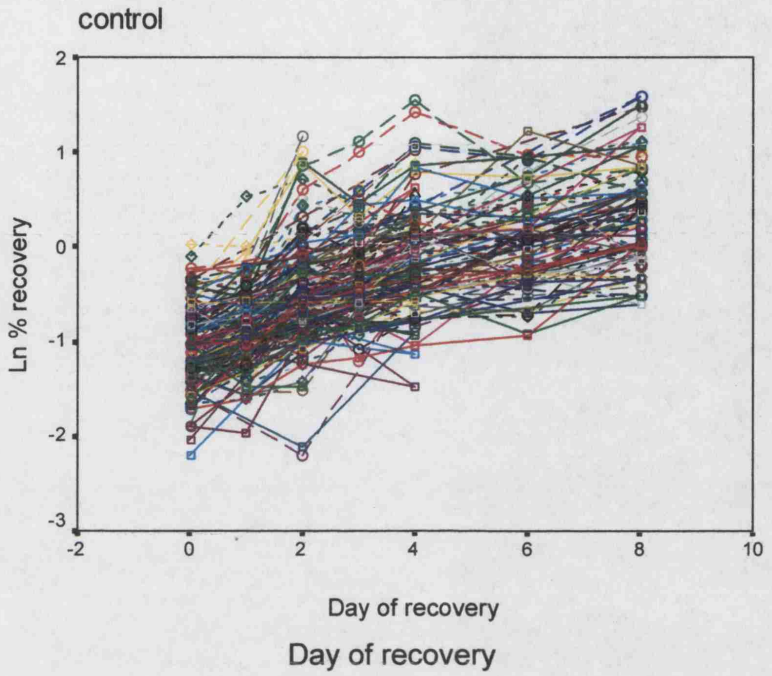

B

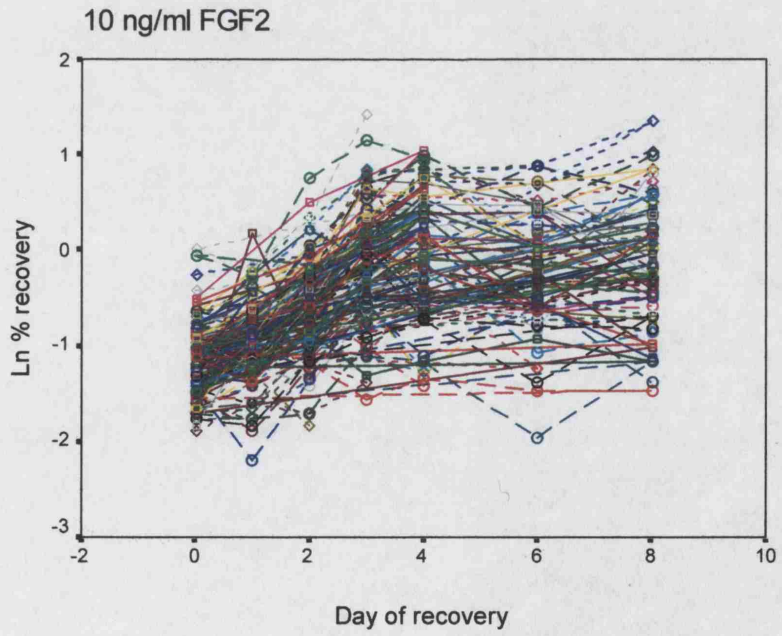

Recovery curves for individual vesicles in natural log (Ln) % recovery units measured over eight days. **A**: Control vesicles, **B**: 10 ng/ml FGF2 treated vesicles. Each coloured line represents the recovery of a single vesicle.

AIII. 10 Correlation between the % of original size after vesicle collapsing and the % recovery in size after eight days

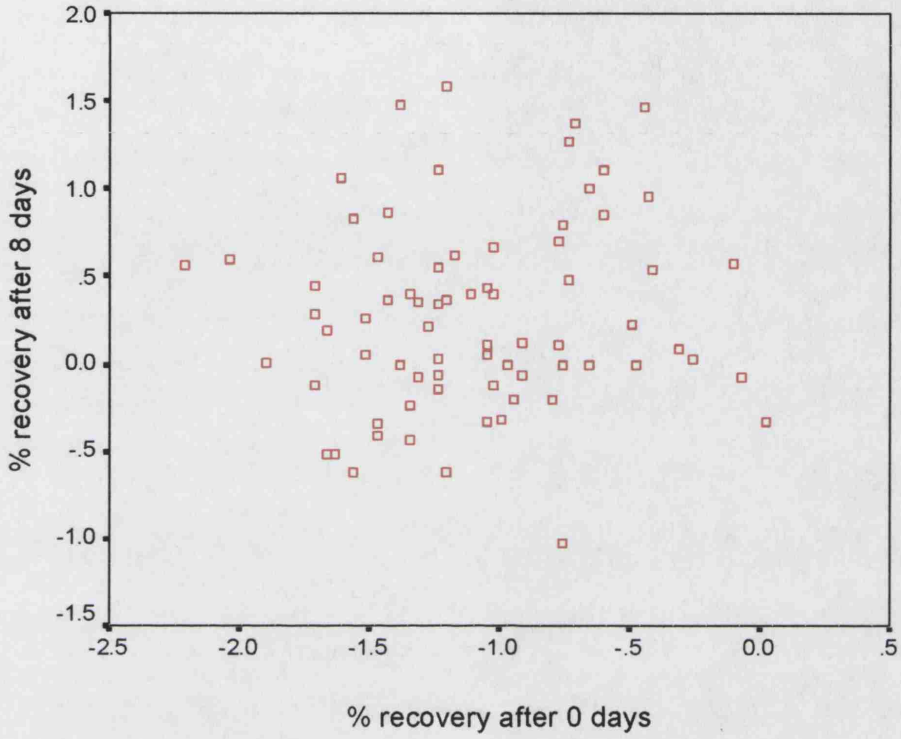

Graph showing the relationship between % of original size of vesicles after they have just been collapsed by ouabain/acetazolamide treatment and the % recovery in size of the same vesicles after eight days recovery from the treatment. The Spearman's Rho correlation coefficient between the two variables is R: 0.095 and is non-significant (p: 0.419). The graph tells us that the rate of recovery of the collapsed vesicles is independent of the initial size of the vesicles or the extent to which the vesicles had collapsed.

AIII. 11 **Multi-level modelling vesicle recovery growth curves +/- FGF2**

A

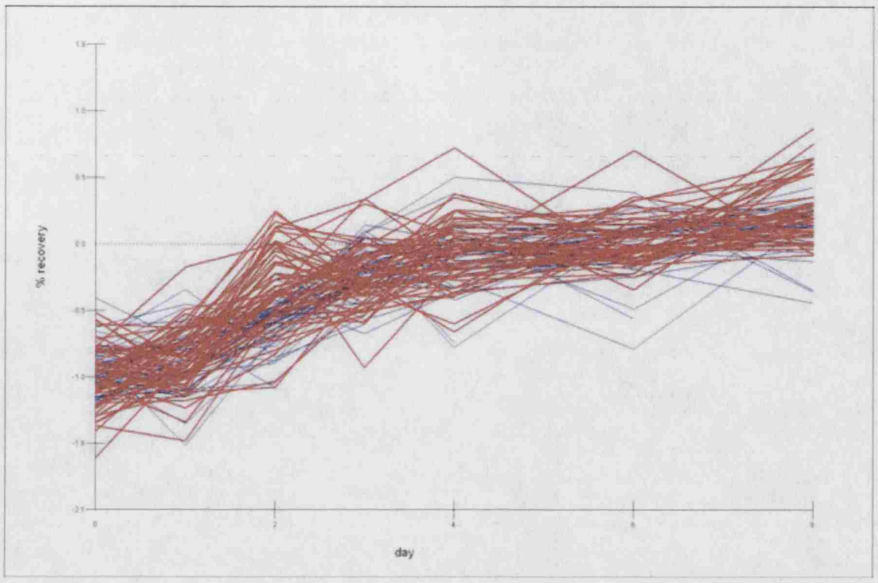

B

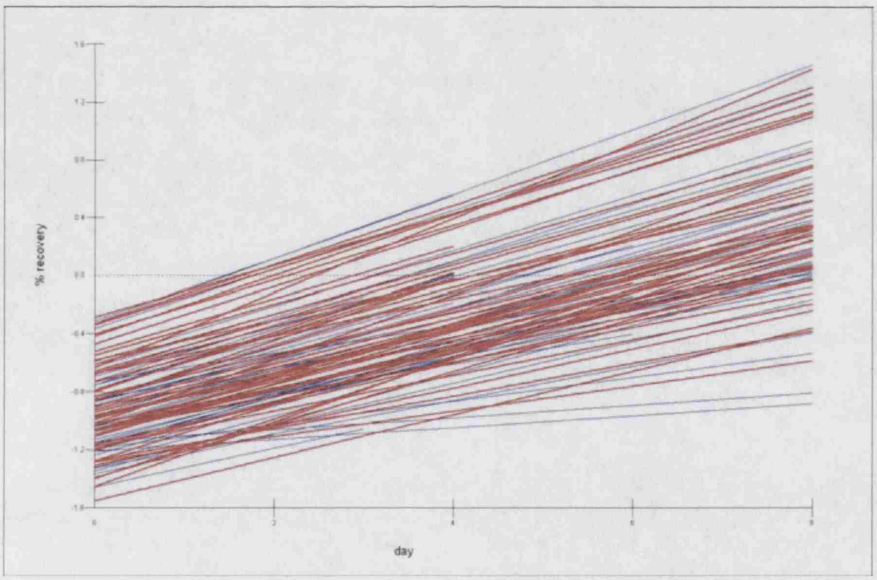

Graphical representation of the predicted levels of variation from the multi-level model describing the recovery of vesicles after ouabain/acetazolamide treatment. **A**: level 1 variation at each day of recovery, **B**: level 2 variation between each fitted growth lines, which has a normal distribution. Level 3 is not shown.

Appendix IV

AIV. 1 Testing primers for FGFR isoforms on mRNA extract from 11.5dpc whole mouse

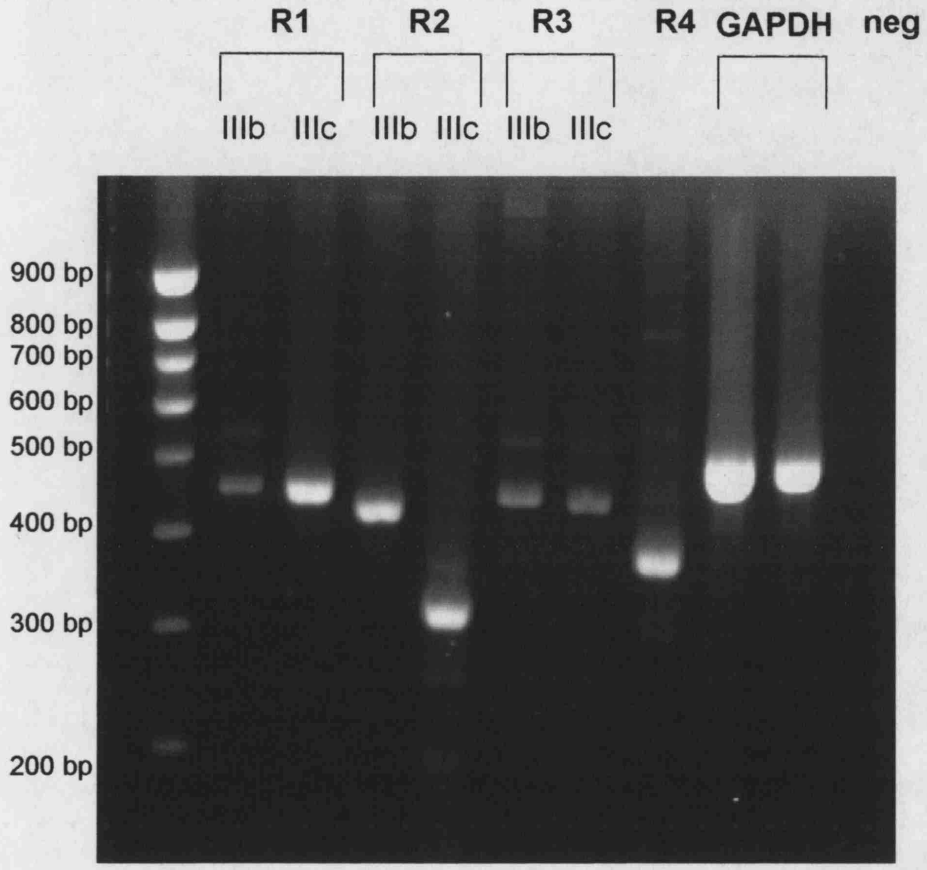

RT-PCR products of FGFR1 (**R1**) IIIb (466bp) and IIIc (453bp), FGFR2 (R2) IIIb (422bp) and IIIc (310bp), FGFR3 (R3) IIIb (471bp) and IIIc (428bp), FGFR4 (R4) (397bp), and GAPDH (491bp); neg: RT-PCR ran with water instead of cDNA.

AIV. 2 Effect of FGF2 on E2F5 mRNA expression

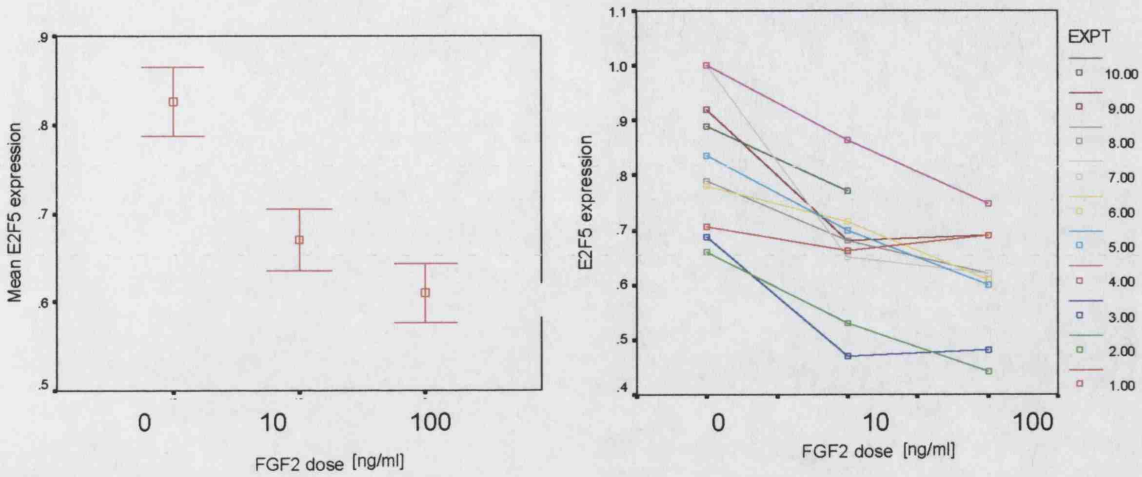

Right graph: bar chart summarizing all densitometric values for each dose of FGF2, ***Left graph***: Graph representing the RT-PCR bands for the different doses of FGF2 as linked variables for each experimental run (listed 1-10)

AIV. 3 Effect of FGF2 on FoxJ1 mRNA expression

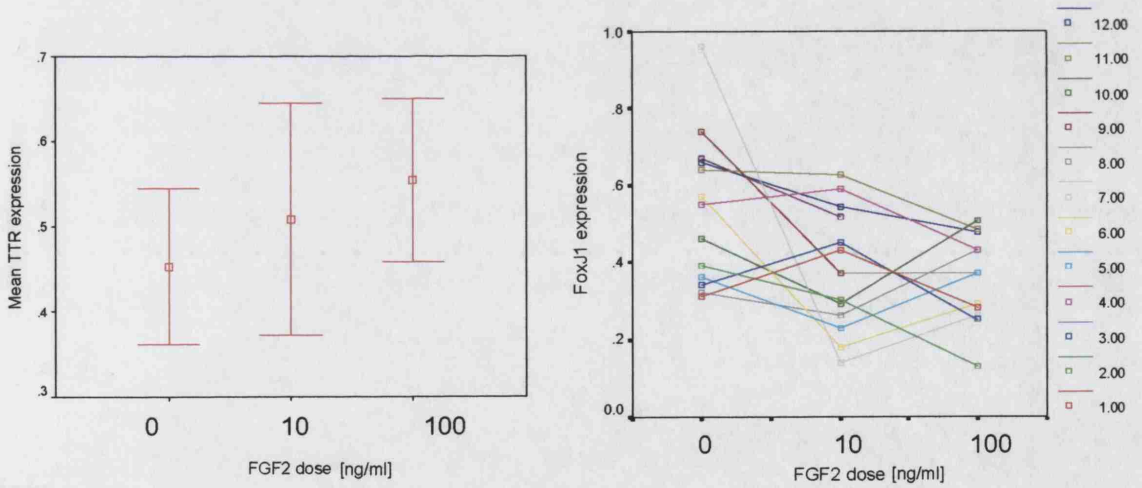

Right graph: bar chart summarizing all densitometric values for each dose of FGF2, ***Left graph***: Graph representing the RT-PCR bands for the different doses of FGF2 as linked variables for each experimental run (listed 1-12).

AIV. 4 Effect of FGF2 on P73 mRNA expression

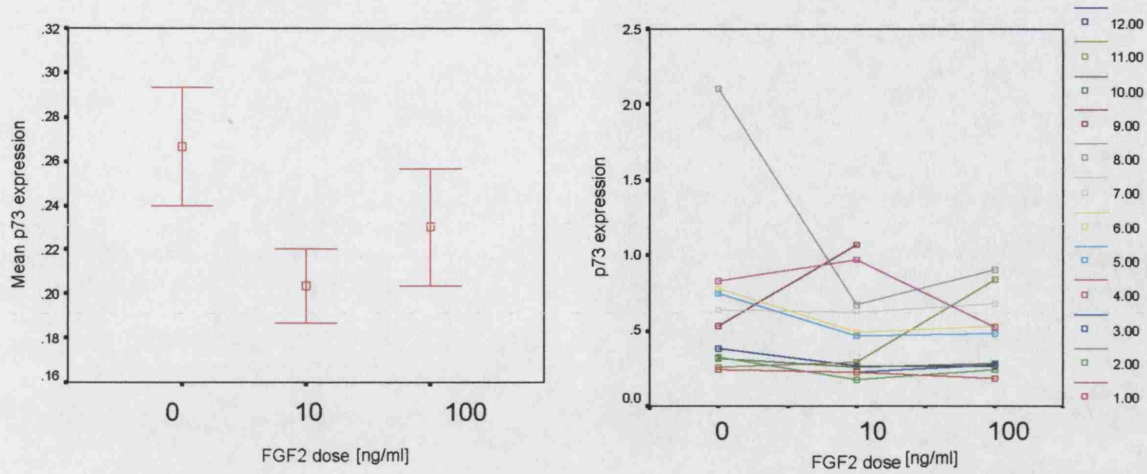

Right graph: bar chart summarizing all densitometric values for each dose of FGF2, ***Left graph***: Graph representing the RT-PCR bands for the different doses of FGF2 as linked variables for each experimental run (listed 1-12).

AIV. 5 Effect of FGF2 on TTR mRNA expression

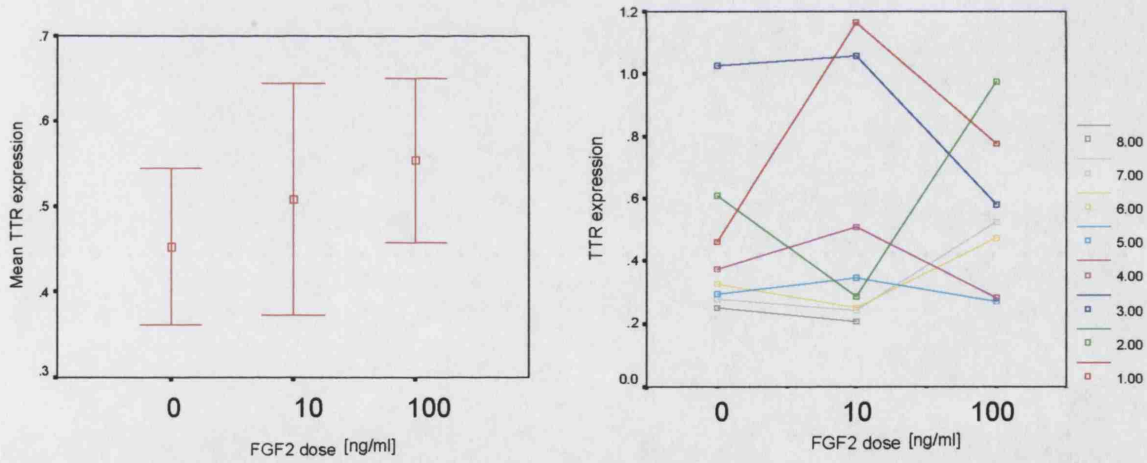

Right graph: bar chart summarizing all densitometric values for each dose of FGF2, ***Left graph***: Graph representing the RT-PCR bands for the different doses of FGF2 as linked variables for each experimental run (listed 1-8).

AIV. 6 Multi-level model for the effect of FGF2 on the mRNA expression of selected genes: E2F5, FoxJ1, P73, and TTR

Gene expression = β_0 x **constant** + β_1 x (**FGF2 dose**)

With { Level 1: variation between treatment dose levels
Level 2: variation between experiment levels

A level 2 analysis was used. The fixed part of the model incorporated the effect of increasing doses of FGF2 (**FGF2 dose**) on the mRNA expression levels of the genes studied (**Gene expression**). The basic model was the following. **Gene expression** refers to the normalised band intensity of any given gene relative to GAPDH. It is the β_1 term that gives the trend in change (positive or negative) for the dose effect on the expression of a given gene and is given with a standard error of the mean (SE). The random part of the model looked at the variation at two levels between treatment doses and between experiments.

AIV. 7 Effect of FGF2 on TRCSFB-2 cell proliferation assessed by Alamar blue analysis

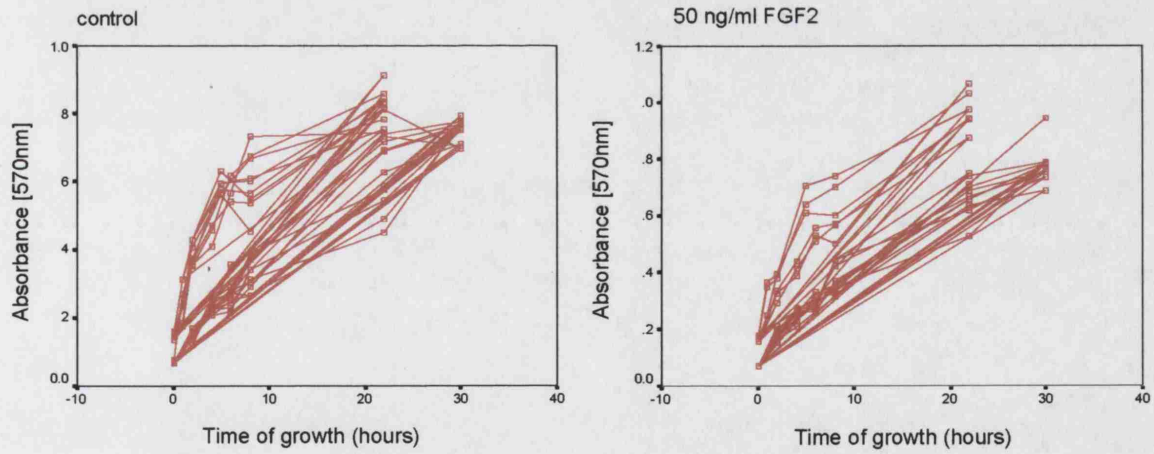

Graphs showing the **absorbance** (at 570nm wavelength) from the oxidation of the Alamar blue at the different time points (0h, 2h, 4h, 8h, 16h, 22h, 30h) for TRCSFB-2 cells grown in absence (control) or in presence of 50 ng/ml FGF2. Each set of wells dispensed with a multi-well pipette are represented as linked variables.

AIV. 8 Graphical prediction from the multi-level model for the effect of FGF2 on TRCSFB-2 cell proliferation assessed by Alamar blue

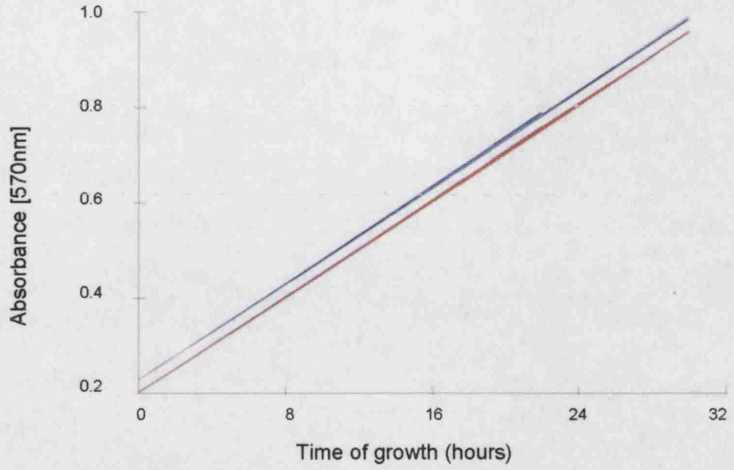

Graph summarising the average increase in cell proliferation as assessed by Alamar blue over two experimental runs in FGF2-treated (red) and non-treated (blue) cultures. The variation due to the experimental runs is negligible since the growth line superimpose.

Reference List

Ago,H., Kitagawa,Y., Fujishima,A., Matsuura,Y., and Katsube,Y. (1991). Crystal structure of basic fibroblast growth factor at 1.6 A resolution. J. Biochem. (Tokyo) *110*, 360-363.

Aleshire,S.L., Bradley,C.A., Richardson,L.D., and Parl,F.F. (1983). Localization of human prealbumin in choroid plexus epithelium. J. Histochem. Cytochem. *31*, 608-612.

Ali,J., Mansukhani,A., and Basilico,C. (1995). Fibroblast growth factor receptors 1 and 2 are differentially regulated in murine embryonal carcinoma cells and in response to fibroblast growth factor-4. J. Cell Physiol *165*, 438-448.

Anderson,J., Burns,H.D., Enriquez-Harris,P., Wilkie,A.O., and Heath,J.K. (1998). Apert syndrome mutations in fibroblast growth factor receptor 2 exhibit increased affinity for FGF ligand. Hum. Mol. Genet *7*, 1475-1483.

Anderson,R.J. and Ray,C.J. (1998). Potential autocrine and paracrine mechanisms of recovery from mechanical injury of renal tubular epithelial cells. Am. J. Physiol *274*, F463-F472.

Apostolova,M.D., Ivanova,I.A., Dagnino,C., D'Souza,S.J., and Dagnino,L. (2002). Active nuclear import and export pathways regulate E2F-5 subcellular localization. J. Biol. Chem. *277*, 34471-34479.

Arman,E., Haffner-Krausz,R., Chen,Y., Heath,J.K., and Lonai,P. (1998). Targeted disruption of fibroblast growth factor (FGF) receptor 2 suggests a role for FGF signaling in pregastrulation mammalian development. Proc Natl Acad Sci U S A *95*, 5082-5087.

Arnaud,E., Touriol,C., Boutonnet,C., Gensac,M.C., Vagner,S., Prats,H., and Prats,A.C. (1999). A new 34-kilodalton isoform of human fibroblast growth factor 2 is cap dependently synthesized by using a non-AUG start codon and behaves as a survival factor. Mol. Cell Biol. *19*, 505-514.

Asai,T., Wanaka,A., Kato,H., Masana,Y., Seo,M., and Tohyama,M. (1993). Differential expression of two members of FGF receptor gene family, FGFR-1 and FGFR-2 mRNA, in the adult rat central nervous system. Brain Res. Mol. Brain Res. *17*, 174-178.

Aviezer,D., Hecht,D., Safran,M., Eisinger,M., David,G., and Yayon,A. (1994). Perlecan, basal lamina proteoglycan, promotes basic fibroblast growth factor-receptor binding, mitogenesis, and angiogenesis. Cell *79*, 1005-1013.

Besser,D., Presta,M., and Nagamine,Y. (1995). Elucidation of a signaling pathway induced by FGF-2 leading to uPA gene expression in NIH 3T3 fibroblasts. Cell Growth Differ. *6*, 1009-1017.

Birge,W.J. (1962). Induced choroid plexus development in the chick metencephalon. J. Comp. Neurol *118*, 89-95.

Bitgood,M.J. and McMahon,A.P. (1995). Hedgehog and Bmp genes are coexpressed at many diverse sites of cell-cell interaction in the mouse embryo. Dev. Biol. *172*, 126-138.

Blatt,E.N., Yan,X.H., Wuerffel,M.K., Hamilos,D.L., and Brody,S.L. (1999). Forkhead transcription factor HFH-4 expression is temporally related to ciliogenesis. Am. J Respir. Cell Mol. Biol *21*, 168-176.

Blottner,D. and Baumgarten,H.G. (1992). Basic fibroblast growth factor prevents neuronal death and atrophy of retrogradely labeled preganglionic neurons in vivo. Exp. Neurol. *118*, 35-46.

Boncinelli,E., Gulisano,M., and Broccoli,V. (1993). Emx and Otx homeobox genes in the developing mouse brain. J. Neurobiol. *24*, 1356-1366.

Brewer,M. and Scott,T. (1983). Concise encyclopedia of biochemistry. (Berlin: New York : de Gruyter).

Brightman,M.W. (1968). The intracerebral movement of proteins injected into blood and cerebrospinal fluid of mice. Prog. Brain Res. *29*, 19-40.

Brody,S.L., Yan,X.H., Wuerffel,M.K., Song,S.K., and Shapiro,S.D. (2000). Ciliogenesis and left-right axis defects in forkhead factor HFH-4-null mice. Am. J Respir. Cell Mol. Biol *23*, 45-51.

Burgess,W.H. and Maciag,T. (1989). The heparin-binding (fibroblast) growth factor family of proteins. Annual Review of Biochemistry *58*, 575.

Burke,D., Wilkes,D., Blundell,T.L., and Malcolm,S. (1998). Fibroblast growth factor receptors: lessons from the genes. Trends Biochem. Sci. *23*, 59-62.

Caron,E. (2003). Cellular functions of the Rap1 GTP-binding protein: a pattern emerges. J. Cell Sci *116*, 435-440.

Catala,M. (1998). Embryonic and fetal development of structures associated with the cerebro-spinal fluid in man and other species. Part I: The ventricular system, meninges and choroid plexuses. Arch. Anat. Cytol. Pathol. *46*, 153-169.

Cavallaro,T., Martone,R.L., Stylianopoulou,F., and Herbert,J. (1993). Differential expression of the insulin-like growth factor II and transthyretin genes in the developing rat choroid plexus. J. Neuropathol. Exp. Neurol. *52*, 153-162.

Chan,C.T. and Thorogood,P. (1999). Pleiotropic features of syndromic craniosynostoses correlate with differential expression of fibroblast growth factor receptors 1 and 2 during human craniofacial development. Pediatr. Res. *45*, 46-53.

Chen,C.R., Kang,Y., Siegel,P.M., and Massague,J. (2002). E2F4/5 and p107 as Smad cofactors linking the TGFbeta receptor to c-myc repression. Cell *110*, 19-32.

Chen,J., Knowles,H.J., Hebert,J.L., and Hackett,B.P. (1998). Mutation of the mouse hepatocyte nuclear factor/forkhead homologue 4 gene results in an absence of cilia and random left-right asymmetry. J Clin. Invest *102*, 1077-1082.

Chen,L., Adar,R., Yang,X., Monsonego,E.O., Li,C., Hauschka,P.V., Yayon,A., and Deng,C.X. (1999). Gly369Cys mutation in mouse FGFR3 causes achondroplasia by affecting both chondrogenesis and osteogenesis. J. Clin. Invest *104*, 1517-1525.

Chen,L., Li,C., Qiao,W., Xu,X., and Deng,C. (2001). A Ser(365)-->Cys mutation of fibroblast growth factor receptor 3 in mouse downregulates Ihh/PTHrP signals and causes severe achondroplasia. Hum. Mol. Genet. *10*, 457-465.

Chen,L., Li,D., Li,C., Engel,A., and Deng,C.X. (2003). A Ser250Trp substitution in mouse fibroblast growth factor receptor 2 (Fgfr2) results in craniosynostosis. Bone *33*, 169-178.

Cheng,X.J., Hoog,J.O., Nairn,A.C., Greengard,P., and Aperia,A. (1997). Regulation of rat Na(+)-K(+)-ATPase activity by PKC is modulated by state of phosphorylation of Ser-943 by PKA. Am. J. Physiol *273*, C1981-C1986.

Chodobski,A. and Szmydynger-Chodobska,J. (2001). Choroid plexus: target for polypeptides and site of their synthesis. Microsc. Res. Tech. *52*, 65-82.

Cinalli,G., Sainte-Rose,C., Kollar,E.M., Zerah,M., Brunelle,F., Chumas,P., Arnaud,E., Marchac,D., Pierre-Kahn,A., and Renier,D. (1998a). Hydrocephalus and craniosynostosis. J. Neurosurg. *88*, 209-214.

Cinalli,G., Sainte-Rose,C., Kollar,E.M., Zerah,M., Brunelle,F., Chumas,P., Arnaud,E., Marchac,D., Pierre-Kahn,A., and Renier,D. (1998b). Hydrocephalus and craniosynostosis. J. Neurosurg. *88*, 209-214.

Cohen,M.M., Jr. (1988). Craniosynostosis update 1987. Am. J. Med. Genet. Suppl *4*, 99-148.

Cohen,M.M., Jr. and Kreiborg,S. (1990b). The central nervous system in the Apert syndrome. Am. J. Med. Genet. *35*, 36-45.

Cohen,M.M., Jr. and Kreiborg,S. (1990a). The central nervous system in the Apert syndrome. Am. J. Med. Genet. *35*, 36-45.

Cohen,M.M., Jr. and Kreiborg,S. (1993). Skeletal abnormalities in the Apert syndrome. Am. J. Med. Genet. *47*, 624-632.

Collmann,H., Sorensen,N., Krauss,J., and Muhling,J. (1988). Hydrocephalus in craniosynostosis. Childs Nerv. Syst. *4*, 279-285.

Couly,G.F., Coltey,P.M., and Le Douarin,N.M. (1993). The triple origin of skull in higher vertebrates: a study in quail-chick chimeras. Development *117*, 409-429.

Coumoul,X. and Deng,C.X. (2003). Roles of FGF receptors in mammalian development and congenital diseases. Birth Defects Res. Part C. Embryo. Today *69*, 286-304.

Counillon,L. and Pouyssgur,J. (2000). The expanding family of eucaryotic Na+/H+ exchangers. The Journal of Biological Chemistry *275*, 1-4.

Crossman,A.R. and Neary,D. (1995). Neuroanatomy-An illustrated colour text. (London: Churchill Livingstone).

Cserr,H.F. (1971). Physiology of the choroid plexus. Physiol Rev. *51*, 273-311.

Cserr,H.F. and Bundgaard,M. (1984). Blood-brain interfaces in vertebrates: a comparative approach. Am. J. Physiol *246*, R277-R288.

Cuevas,P., Carceller,F., Reimers,D., Fu,X., and Gimenez-Gallego,G. (1994). Immunohistochemical localization of basic fibroblast growth factor in choroid plexus of the rat. Neurol. Res. *16*, 310-312.

D'Souza,S.J., Pajak,A., Balazsi,K., and Dagnino,L. (2001). Ca2+ and BMP-6 signaling regulate E2F during epidermal keratinocyte differentiation. J. Biol. Chem. *276*, 23531-23538.

Dagnino,L., Fry,C.J., Bartley,S.M., Farnham,P., Gallie,B.L., and Phillips,R.A. Expression patterns of the E2F family of transcription factors during mouse nervous system development.

Dagnino,L., Fry,C.J., Bartley,S.M., Farnham,P., Gallie,B.L., and Phillips,R.A. (1997). Expression patterns of the E2F family of transcription factors during mouse nervous system development. Mechanisms of Development *66*, 13-25.

Daniel,C.W. and Robinson,S.D. (1992). Regulation of mammary growth and function by TGF-beta. Mol. Reprod. Dev. *32*, 145-151.

David,D.J. and Simpson,D.A. (1982). Surgical indications in single suture craniosynostosis. Neurosurgery *11*, 466.

Davis,J.C. (1978). Morphogenesis by dissociated immature rat testicular cells in primary culture. J. Embryol. Exp. Morphol. *44*, 297-302.

Davson,H. (1955). A comparative study of the aqueous humour and cerebrospinal fluid in the rabbit. J. Physiol *129*, 111-133.

Davson,H. and Segal,M.B. (1996). physiology of the CSF and blood-brain barriers. (Boca Raton: CRC Press).

Davson,H., Welch K, and Segal,M.B. (1987). The physiology and pathophysiology of the cerebrospinal fluid. (Edinburgh: Churchill Livingstone).

Davson,H. and Segal,M.B. (1970). The effects of some inhibitors and accelerators of sodium transport on the turnover of 22Na in the cerebrospinal fluid and the brain. J. Physiol *209*, 131-153.

de Leon,G.A., de Leon,G., Grover,W.D., Zaeri,N., and Alburger,P.D. (1987). Agenesis of the corpus callosum and limbic malformation in Apert syndrome (type I acrocephalosyndactyly). Arch. Neurol. *44*, 979-982.

De Moerlooze,L. and Dickson,C. (1997). Skeletal disorders associated with fibroblast growth factor receptor mutations. Curr. Opin. Genet Dev *7*, 378-385.

Debiais,F., Lemonnier,J., Hay,E., Delannoy,P., Caverzasio,J., and Marie,P.J. (2001). Fibroblast growth factor-2 (FGF-2) increases N-cadherin expression through protein kinase C and Src-kinase pathways in human calvaria osteoblasts. J. Cell Biochem. *81*, 68-81.

Delrieu,I. (2000). The high molecular weight isoforms of basic fibroblast growth factor (FGF-2): an insight into an intracrine mechanism. FEBS Lett. *468*, 6-10.

Deng,C.X., Wynshaw-Boris,A., Shen,M.M., Daugherty,C., Ornitz,D.M., and Leder,P. (1994). Murine FGFR-1 is required for early postimplantation growth and axial organization. Genes Dev. *8*, 3045-3057.

Desmond,M.E. and Jacobson,A.G. (1977). Embryonic brain enlargement requires cerebrospinal fluid pressure. Dev. Biol. *57*, 188-198.

Dewulf,N., Verschueren,K., Lonnoy,O., Moren,A., Grimsby,S., Vande,S.K., Miyazono,K., Huylebroeck,D., and ten Dijke,P. (1995). Distinct spatial and temporal expression patterns of two type I receptors for bone morphogenetic proteins during mouse embryogenesis. Endocrinology *136*, 2652-2663.

Dickson,P.W., Aldred,A.R., Marley,P.D., Bannister,D., and Schreiber,G. (1986). Rat choroid plexus specializes in the synthesis and the secretion of transthyretin (prealbumin). Regulation of transthyretin synthesis in choroid plexus is independent from that in liver. J. Biol. Chem. *261*, 3475-3478.

Dono,R., Texido,G., Dussel,R., Ehmke,H., and Zeller,R. (1998). Impaired cerebral cortex development and blood pressure regulation in FGF-2-deficient mice. EMBO J. *17*, 4213-4225.

Dorph-Petersen,K.A., Gundersen,H.J., and Jensen,E.B. (2000). Non-uniform systematic sampling in stereology. J. Microsc. *200 (Pt 2)*, 148-157.

Dziegielewska,K.M., Ek,J., Habgood,M.D., and Saunders,N.R. (2001). Development of the choroid plexus. Microsc. Res. Tech. *52*, 5-20.

Dziegielewska,K.M., Evans,C.A., Malinowska,D.H., Mollgard,K., Reynolds,J.M., Reynolds,M.L., and Saunders,N.R. (1979). Studies of the development of brain barrier systems to lipid insoluble molecules in fetal sheep. J. Physiol *292*, 207-231.

El Ghouzzi,V., Le Merrer,M., Perrin-Schmitt,F., Lajeunie,E., Benit,P., Renier,D., Bourgeois,P., Bolcato-Bellemin,A.L., Munnich,A., and Bonaventure,J. (1997). Mutations of the TWIST gene in the Saethre-Chotzen syndrome. Nat. Genet. *15*, 42-46.

El Hariry,I., Pignatelli,M., and Lemoine,N.R. (2001). FGF-1 and FGF-2 regulate the expression of E-cadherin and catenins in pancreatic adenocarcinoma. Int. J. Cancer *94*, 652-661.

El,G., V, Lajeunie,E., Le Merrer,M., Cormier-Daire,V., Renier,D., Munnich,A., and Bonaventure,J. (1999). Mutations within or upstream of the basic helix-loop-helix domain of the TWIST gene are specific to Saethre-Chotzen syndrome. Eur. J. Hum. Genet. *7*, 27-33.

Engelhardt,B., Wolburg-Buchholz,K., and Wolburg,H. (2001). Involvement of the choroid plexus in central nervous system inflammation. Microsc. Res. Tech. *52*, 112-129.

Epstein,M.H., Feldman,A.M., and Brusilow,S.W. (1977). Cerebrospinal fluid production: stimulation by cholera toxin. Science *196*, 1012-1013.

Ernst,S.A., Palacios,J.R., and Siegel,G.J. (1986). Immunocytochemical localization of Na+,K+-ATPase catalytic polypeptide in mouse choroid plexus. J. Histochem. Cytochem. *34*, 189-195.

Feller,S.M. (2001). Crk family adaptors-signalling complex formation and biological roles. Oncogene *20*, 6348-6371.

Ferguson,I.A. and Johnson,E.M., Jr. (1991). Fibroblast growth factor receptor-bearing neurons in the CNS: identification by receptor-mediated retrograde transport. J. Comp Neurol. *313*, 693-706.

Finch,P.W., Cunha,G.R., Rubin,J.S., Wong,J., and Ron,D. (1995b). Pattern of keratinocyte growth factor and keratinocyte growth factor receptor expression during mouse fetal development suggests a role in mediating morphogenetic mesenchymal-epithelial interactions. Dev. Dyn. *203*, 223-240.

Finch,P.W., Cunha,G.R., Rubin,J.S., Wong,J., and Ron,D. (1995a). Pattern of keratinocyte growth factor and keratinocyte growth factor receptor expression during mouse fetal development suggests a role in mediating morphogenetic mesenchymal-epithelial interactions. Dev. Dyn. *203*, 223-240.

Fisone,G., Snyder,G.L., Fryckstedt,J., Caplan,M.J., Aperia,A., and Greengard,P. (1995). Na+,K(+)-ATPase in the choroid plexus. Regulation by serotonin/protein kinase C pathway. J. Biol. Chem. *270*, 2427-2430.

Flamme,I., Frohlich,T., von Reutern,M., Kappel,A., Damert,A., and Risau,W. (1997). HRF, a putative basic helix-loop-helix-PAS-domain transcription factor is closely related to hypoxia-inducible factor-1 alpha and developmentally expressed in blood vessels. Mech. Dev. *63*, 51-60.

Flanders,K.C., Ludecke,G., Engels,S., Cissel,D.S., Roberts,A.B., Kondaiah,P., Lafyatis,R., Sporn,M.B., and Unsicker,K. (1991). Localization and actions of transforming growth factor-beta s in the embryonic nervous system. Development *113*, 183-191.

Florkiewicz,R.Z., Anchin,J., and Baird,A. (1998). The inhibition of fibroblast growth factor-2 export by cardenolides implies a novel function for the catalytic subunit of Na+,K+-ATPase. J. Biol. Chem. *273*, 544-551.

Florkiewicz,R.Z., Majack,R.A., Buechler,R.D., and Florkiewicz,E. (1995). Quantitative export of FGF-2 occurs through an alternative, energy-dependent, non-ER/Golgi pathway. J. Cell Physiol *162*, 388-399.

Fok,H., Jones,B.M., Gault,D.G., Andar,U., and Hayward,R. (1992). Relationship between intracranial pressure and intracranial volume in craniosynostosis. Br. J. Plast. Surg. *45*, 394-397.

Ford-Perriss,M., Abud,H., and Murphy,M. (2001). Fibroblast growth factors in the developing central nervous system. Clin. Exp. Pharmacol. Physiol *28*, 493-503.

Ford-Perriss,M., Guimond,S.E., Greferath,U., Kita,M., Grobe,K., Habuchi,H., Kimata,K., Esko,J.D., Murphy,M., and Turnbull,J.E. (2002). Variant heparan sulfates synthesized in developing mouse brain differentially regulate FGF signaling. Glycobiology *12*, 721-727.

Fox,J.C. and Shanley,J.R. (1996). Antisense inhibition of basic fibroblast growth factor induces apoptosis in vascular smooth muscle cells. J. Biol. Chem. *271*, 12578-12584.

Franz,T. (1994). Extra-toes (Xt) homozygous mutant mice demonstrate a role for the Gli-3 gene in the development of the forebrain. Acta Anat. (Basel) *150*, 38-44.

Fujita,N., Furukawa,Y., Itabashi,N., Okada,K., Saito,T., and Ishibashi,S. (2002). Differences in E2F subunit expression in quiescent and proliferating vascular smooth muscle cells. Am. J. Physiol Heart Circ. Physiol *283*, H204-H212.

Furuta,Y., Piston,D.W., and Hogan,B.L. (1997). Bone morphogenetic proteins (BMPs) as regulators of dorsal forebrain development. Development *124*, 2203-2212.

Fuxe,K., Tinner,B., Zoli,M., Pettersson,R.F., Baird,A., Biagini,G., Chadi,G., and Agnati,L.F. (1996). Computer-assisted mapping of basic fibroblast growth factor immunoreactive nerve cell populations in the rat brain. J. Chem. Neuroanat. *11*, 13-35.

Gao,B. and Meier,P.J. (2001). Organic anion transport across the choroid plexus. Microsc. Res. Tech. *52*, 60-64.

Garner,C. and Brown,P.D. (1992). Two types of chloride channel in the apical membrane of rat choroid plexus epithelial cells. Brain Res. *591*, 137-145.

Gaubatz,S., Lindeman,G.J., Ishida,S., Jakoi,L., Nevins,J.R., Livingston,D.M., and Rempel,R.E. (2000). E2F4 and E2F5 play an essential role in pocket protein-mediated G1 control. Mol. Cell *6*, 729-735.

Gaudenz,K., Roessler,E., Vainikka,S., Alitalo,K., and Muenke,M. (1998). Analysis of patients with craniosynostosis syndromes for a pro246Arg mutation of FGFR4. Mol. Genet. Metab *64*, 76-79.

Gault,D.T., Renier,D., Marchac,D., and Jones,B.M. (1992). Intracranial pressure and intracranial volume in children with craniosynostosis. Plast. Reconstr. Surg. *90*, 377-381.

German,T. and Barash,I. (2002). Characterization of an epithelial cell line from bovine mammary gland. In Vitro Cell Dev. Biol. Anim *38*, 282-292.

Gill,R.M. and Hamel,P.A. (2000). Subcellular compartmentalization of E2F family members is required for maintenance of the postmitotic state in terminally differentiated muscle. J. Cell Biol. *148*, 1187-1201.

Gjerris,A. (1990). Studies on cerebrospinal fluid in affective disorders. Pharmacol. Toxicol. *66 Suppl 3*, 133-138.

Gomez-Pinilla,F., Lee,J.W., and Cotman,C.W. (1994). Distribution of basic fibroblast growth factor in the developing rat brain. Neuroscience *61*, 911-923.

Gonzalez,A.M., Berry,M., Maher,P.A., Logan,A., and Baird,A. (1995). A comprehensive analysis of the distribution of FGF-2 and FGFR1 in the rat brain. Brain Res. *701*, 201-226.

Gonzalez,A.M., Buscaglia,M., Ong,M., and Baird,A. (1990b). Distribution of basic fibroblast growth factor in the 18-day rat fetus: localization in the basement membranes of diverse tissues. J. Cell Biol. *110*, 753-765.

Gonzalez,A.M., Buscaglia,M., Ong,M., and Baird,A. (1990a). Distribution of basic fibroblast growth factor in the 18-day rat fetus: localization in the basement membranes of diverse tissues. J. Cell Biol. *110*, 753-765.

Gonzalez,A.M., Hill,D.J., Logan,A., Maher,P.A., and Baird,A. (1996). Distribution of fibroblast growth factor (FGF)-2 and FGF receptor-1 messenger RNA expression and protein presence in the mid-trimester human fetus. Pediatr. Res. *39*, 375-385.

Gonzalez-Martinez,L.M., Avila,J., Marti,E., Lecuona,E., and Martin-Vasallo,P. (1994). Expression of the beta-subunit isoforms of the Na,K-ATPase in rat embryo tissues, inner ear and choroid plexus. Biol. Cell *81*, 215-222.

Gorlin,R.J., Cohen,M.M., Jr., and Levin,L.S. (1990). Syndromes of the head and neck. (Oxford: Oxford University Press).

Gosain,A.K., McCarthy,J.G., Glatt,P., Staffenberg,D., and Hoffmann,R.G. (1995). A study of intracranial volume in Apert syndrome. Plast. Reconstr. Surg. *95*, 284-295.

Graeff,R.W., Wang,G., and McCray,P.B., Jr. (1999). KGF and FGF-10 stimulate liquid secretion in human fetal lung. Pediatr. Res. *46*, 523-529.

Green,P.J., Walsh,F.S., and Doherty,P. (1996). Promiscuity of fibroblast growth factor receptors. Bioessays *18*, 639-646.

Greitz,D., Greitz,T., and Hindmarsh,T. (1997). A new view on the CSF-circulation with the potential for pharmacological treatment of childhood hydrocephalus. Acta Paediatr. *86*, 125-132.

Grove,E.A., Tole,S., Limon,J., Yip,L., and Ragsdale,C.W. (1998). The hem of the embryonic cerebral cortex is defined by the expression of multiple Wnt genes and is compromised in Gli3-deficient mice. Development *125*, 2315-2325.

Gualandris,A. and Presta,M. (1995). Transcriptional and posttranscriptional regulation of urokinase-type plasminogen activator expression in endothelial cells by basic fibroblast growth factor. J. Cell Physiol *162*, 400-409.

Guimond,S., Maccarana,M., Olwin,B.B., Lindahl,U., and Rapraeger,A.C. (1993). Activating and inhibitory heparin sequences for FGF-2 (basic FGF). Distinct requirements for FGF-1, FGF-2, and FGF-4. J. Biol. Chem. *268*, 23906-23914.

Guimond,S.E. and Turnbull,J.E. (1999). Fibroblast growth factor receptor signalling is dictated by specific heparan sulphate saccharides. Curr. Biol. *9*, 1343-1346.

Gundersen,H.J. (1986). Stereology of arbitrary particles. A review of unbiased number and size estimators and the presentation of some new ones, in memory of William R. Thompson. J. Microsc. *143 (Pt 1)*, 3-45.

Gundersen,H.J., Bendtsen,T.F., Korbo,L., Marcussen,N., Moller,A., Nielsen,K., Nyengaard,J.R., Pakkenberg,B., Sorensen,F.B., Vesterby,A., and . (1988). Some new, simple and efficient stereological methods and their use in pathological research and diagnosis. APMIS *96*, 379-394.

Habgood,M.D., Sedgwick,J.E., Dziegielewska,K.M., and Saunders,N.R. (1992). A developmentally regulated blood-cerebrospinal fluid transfer mechanism for albumin in immature rats. J. Physiol *456*, 181-192.

Hackett,B.P., Brody,S.L., Liang,M., Zeitz,I.D., Bruns,L.A., and Gitlin,J.D. (1995). Primary structure of hepatocyte nuclear factor/forkhead homologue 4 and characterization of gene expression in the developing respiratory and reproductive epithelium. Proc. Natl. Acad. Sci. U. S. A *92*, 4249-4253.

Haimovitz-Friedman,A., Balaban,N., McLoughlin,M., Ehleiter,D., Michaeli,J., Vlodavsky,I., and Fuks,Z. (1994). Protein kinase C mediates basic fibroblast growth factor protection of endothelial cells against radiation-induced apoptosis. Cancer Res. *54*, 2591-2597.

Hajihosseini,M.K., Wilson,S., De Moerlooze,L., and Dickson,C. (2001). A splicing switch and gain-of-function mutation in FgfR2-IIIc hemizygotes causes Apert/Pfeiffer-syndrome-like phenotypes. Proc. Natl. Acad. Sci. U. S. A *98*, 3855-3860.

Hakvoort,A., Haselbach,M., and Galla,H.J. (1998a). Active transport properties of porcine choroid plexus cells in culture. Brain Res. *795*, 247-256.

Hakvoort,A., Haselbach,M., Wegener,J., Hoheisel,D., and Galla,H.J. (1998b). The polarity of choroid plexus epithelial cells in vitro is improved in serum-free medium. J. Neurochem. *71*, 1141-1150.

Hakvoort,A. and Johanson,C.E. (2000). Growth factor modulation of CSF formation by isolated choroid plexus: FGF-2 vs. TGF-beta1. Eur. J. Pediatr. Surg. *10 Suppl 1*, 44-46.

Harbour,J.W., Luo,R.X., Dei,S.A., Postigo,A.A., and Dean,D.C. (1999). Cdk phosphorylation triggers sequential intramolecular interactions that progressively block Rb functions as cells move through G1. Cell *98*, 859-869.

Haselbach,M., Wegener,J., Decker,S., Engelbertz,C., and Galla,H.J. (2001). Porcine Choroid plexus epithelial cells in culture: regulation of barrier properties and transport processes. Microsc. Res. Tech. *52*, 137-152.

Hayward,R., Harkness,W., Kendall,B., and Jones,B. (1992). Magnetic resonance imaging in the assessment of craniosynostosis. Scand. J. Plast. Reconstr. Surg. Hand Surg. *26*, 293-299.

Howard,T.D., Paznekas,W.A., Green,E.D., Chiang,L.C., Ma,N., Ortiz de Luna,R.I., Garcia,D.C., Gonzalez-Ramos,M., Kline,A.D., and Jabs,E.W. (1997). Mutations in TWIST, a basic helix-loop-helix transcription factor, in Saethre-Chotzen syndrome. Nat. Genet. *15*, 36-41.

Hromas,R. and Costa,R. (1995). The hepatocyte nuclear factor-3/forkhead transcription regulatory family in development, inflammation, and neoplasia. Crit Rev. Oncol. Hematol. *20*, 129-140.

Humbert,P.O., Rogers,C., Ganiatsas,S., Landsberg,R.L., Trimarchi,J.M., Dandapani,S., Brugnara,C., Erdman,S., Schrenzel,M., Bronson,R.T., and Lees,J.A. (2000). E2F4 is essential for normal erythrocyte maturation and neonatal viability. Mol. Cell *6*, 281-291.

Hyde-Dunn,J. and Jones,G.E. (1997). Visualization of cell replication using antibody to proliferating cell nuclear antigen. Methods Mol. Biol. *75*, 341-347.

Imamura,T., Engleka,K., Zhan,X., Tokita,Y., Forough,R., Roeder,D., Jackson,A., Maier,J.A., Hla,T., and Maciag,T. (1990). Recovery of mitogenic activity of a growth factor mutant with a nuclear translocation sequence. Science *249*, 1567-1570.

Ino,H. and Chiba,T. (2000). Expression of proliferating cell nuclear antigen (PCNA) in the adult and developing mouse nervous system. Brain Res. Mol. Brain Res. *78*, 163-174.

Iwata,T., Li,C.L., Deng,C.X., and Francomano,C.A. (2001). Highly activated Fgfr3 with the K644M mutation causes prolonged survival in severe dwarf mice. Hum. Mol. Genet. *10*, 1255-1264.

Jabs,E.W., Muller,U., Li,X., Ma,L., Luo,W., Haworth,I.S., Klisak,I., Sparkes,R., Warman,M.L., Mulliken,J.B., and . (1993). A mutation in the homeodomain of the human MSX2 gene in a family affected with autosomal dominant craniosynostosis. Cell *75*, 443-450.

Jacobsen,M., Jacobsen,G.K., Clausen,P.P., Saunders,N.R., and Mollgard,K. (1982). Intracellular plasma proteins in human fetal choroid plexus during development. II. The distribution of prealbumin, albumin, alpha-fetoprotein, transferrin, IgG, IgA, IgM, and alpha 1-antitrypsin. Brain Res. *255*, 251-262.

Johanson,C.E., Gonzalez,A.M., and Stopa,E.G. (2001). Water-imbalance-induced expression of FGF-2 in fluid-regulatory centers: choroid plexus and neurohypophysis. Eur. J. Pediatr. Surg. *11 Suppl 1*, S37-S38.

Johanson,C.E., Szmydynger-Chodobska,J., Chodobski,A., Baird,A., McMillan,P., and Stopa,E.G. (1999). Altered formation and bulk absorption of cerebrospinal fluid in FGF-2-induced hydrocephalus. Am. J. Physiol *277*, R263-R271.

Kaelin,W.G., Jr. (1999). The p53 gene family. Oncogene *18*, 7701-7705.

Kajita,H., Omori,K., and Matsuda,H. (2000). The chloride channel ClC-2 contributes to the inwardly rectifying Cl- conductance in cultured porcine choroid plexus epithelial cells. J. Physiol *523 Pt 2*, 313-324.

Kanda,Y., Goodman,D.S., Canfield,R.E., and Morgan,F.J. (1974). The amino acid sequence of human plasma prealbumin. J. Biol. Chem. *249*, 6796-6805.

Kannan,K. and Givol,D. (2000). FGF receptor mutations: dimerization syndromes, cell growth suppression, and animal models. IUBMB. Life *49*, 197-205.

Kappers,J.A. (1958). Structural and functional changes in the telencephalic choroid plexus during human ontogenesis. (London: Churchill), pp. 3-25.

Kato,M., Soprano,D.R., Makover,A., Kato,K., Herbert,J., and Goodman,D.S. (1986). Localization of immunoreactive transthyretin (prealbumin) and of transthyretin mRNA in fetal and adult rat brain. Differentiation *31*, 228-235.

Keep,R.F. and Xiang,J. (1995). Choroid plexus potassium cotransport: modulation by osmotic stress and external potassium. J. Neurochem. *64*, 2747-2754.

Kiefer,P., Acland,P., Pappin,D., Peters,G., and Dickson,C. (1994). Competition between nuclear localization and secretory signals determines the subcellular fate of a single CUG-initiated form of FGF3. EMBO J. *13*, 4126-4136.

Kim,I., Moon,S., Yu,K., Kim,U., and Koh,G.Y. (2001). A novel fibroblast growth factor receptor-5 preferentially expressed in the pancreas(1). Biochim. Biophys. Acta *1518*, 152-156.

Kitazawa,T., Hosoya,K., Watanabe,M., Takashima,T., Ohtsuki,S., Takanaga,H., Ueda,M., Yanai,N., Obinata,M., and Terasaki,T. (2001). Characterization of the amino acid transport of new immortalized choroid plexus epithelial cell lines: a novel in vitro system for investigating transport functions at the blood-cerebrospinal fluid barrier. Pharm. Res. *18*, 16-22.

Klagsbrun,M. and Baird,A. (1991). A dual receptor system is required for basic fibroblast growth factor activity. Cell *67*, 229-231.

Klarr,S.A., Ulanski,L.J., Stummer,W., Xiang,J., Betz,A.L., and Keep,R.F. (1997). The effects of hypo- and hyperkalemia on choroid plexus potassium transport. Brain Res. *758*, 39-44.

Klint,P. and Claesson-Welsh,L. (1999). Signal transduction by fibroblast growth factor receptors. Front Biosci. *4*, D165-D177.

Kopelman,M., Cogan,U., Mokady,S., and Shinitzky,M. (1976). The interaction between retinol-binding proteins and prealbumins studied by fluorescence polarization. Biochim. Biophys. Acta *439*, 449-460.

Kotera,T. and Brown,P.D. (1994). Evidence for two types of potassium current in rat choroid plexus epithelial cells. Pflugers Arch. *427*, 317-324.

Kuchler-Bopp,S., Ittel,M.E., Dietrich,J.B., Reeber,A., Zaepfel,M., and Delaunoy,J.P. (1998). The presence of transthyretin in rat ependymal cells is due to endocytosis and not synthesis. Brain Res. *793*, 219-230.

Kurashima,K., Szabo,E.Z., Lukacs,G., Orlowski,J., and Grinstein,S. (1998). Endosomal recycling of the Na+/H+ exchanger NHE3 isoform is regulated by the phosphatidylinositol 3-kinase pathway. J. Biol. Chem. *273*, 20828-20836.

Lagunowich,L.A., Schneider,J.C., Chasen,S., and Grunwald,G.B. (1992). Immunohistochemical and biochemical analysis of N-cadherin expression during CNS development. J. Neurosci. Res. *32*, 202-208.

Lajeunie,E., Bonaventure,J., El,G., V, Catala,M., and Renier,D. (2000). Monozygotic twins with Crouzon syndrome: concordance for craniosynostosis and discordance for thumb duplication. Am. J Med. Genet *91*, 159-160.

Lajeunie,E., Catala,M., and Renier,D. (1999). Craniosynostosis: from a clinical description to an understanding of bone formation of the skull. Childs Nerv. Syst. *15*, 676-680.

Lavia,P. and Jansen-Durr,P. (1999). E2F target genes and cell-cycle checkpoint control. Bioessays *21*, 221-230.

Lemmon,M.A. and Schlessinger,J. (1994). Regulation of signal transduction and signal diversity by receptor oligomerization. Trends Biochem. Sci. *19*, 459-463.

Levine,S.A., Nath,S.K., Yun,C.H., Yip,J.W., Montrose,M., Donowitz,M., and Tse,C.M. (1995). Separate C-terminal domains of the epithelial specific brush border Na+/H+ exchanger isoform NHE3 are involved in stimulation and inhibition by protein kinases/growth factors. J. Biol. Chem. *270*, 13716-13725.

Li,C., Chen,L., Iwata,T., Kitagawa,M., Fu,X.Y., and Deng,C.X. (1999). A Lys644Glu substitution in fibroblast growth factor receptor 3 (FGFR3) causes dwarfism in mice by activation of STATs and ink4 cell cycle inhibitors. Hum. Mol. Genet. *8*, 35-44.

Li,S., Lao,J., Chen,B.P., Li,Y.S., Zhao,Y., Chu,J., Chen,K.D., Tsou,T.C., Peck,K., and Chien,S. (2003). Genomic analysis of smooth muscle cells in 3-dimensional collagen matrix. FASEB J. *17*, 97-99.

Lim,L., Zhou,H., and Costa,R.H. (1997). The winged helix transcription factor HFH-4 is expressed during choroid plexus epithelial development in the mouse embryo. Proc. Natl. Acad. Sci. U. S. A *94*, 3094-3099.

Lim,Y.P., Low,B.C., Lim,J., Wong,E.S., and Guy,G.R. (1999). Association of atypical protein kinase C isotypes with the docker protein FRS2 in fibroblast growth factor signaling. J. Biol. Chem. *274*, 19025-19034.

Lindeman,G.J., Dagnino,L., Gaubatz,S., Xu,Y., Bronson,R.T., Warren,H.B., and Livingston,D.M. (1998). A specific, nonproliferative role for E2F-5 in choroid plexus function revealed by gene targeting. Genes Dev. *12*, 1092-1098.

Lindeman,G.J., Gaubatz,S., Livingston,D.M., and Ginsberg,D. (1997). The subcellular localization of E2F-4 is cell-cycle dependent. Proc. Natl. Acad. Sci. U. S. A *94*, 5095-5100.

Lindsey,A.E., Schneider,K., Simmons,D.M., Baron,R., Lee,B.S., and Kopito,R.R. (1990). Functional expression and subcellular localization of an anion exchanger cloned from choroid plexus. Proc. Natl. Acad. Sci. U. S. A *87*, 5278-5282.

Ling,E.A., Kaur,C., and Lu,J. (1998). Origin, nature, and some functional considerations of intraventricular macrophages, with special reference to the epiplexus cells. Microsc. Res. Tech. *41*, 43-56.

Lundar,T. and Nornes,H. (1991). Steady-state lumbar infusion tests in the management of children with craniosynostosis. Childs Nerv. Syst. *7*, 31-33.

Lyons,R.M., Gentry,L.E., Purchio,A.F., and Moses,H.L. (1990). Mechanism of activation of latent recombinant transforming growth factor beta 1 by plasmin. J. Cell Biol. *110*, 1361-1367.

MacKenzie,A., Ferguson,M.W., and Sharpe,P.T. (1991). Hox-7 expression during murine craniofacial development. Development *113*, 601-611.

Maddala,R., Reddy,V.N., Epstein,D.L., and Rao,V. (2003). Growth factor induced activation of Rho and Rac GTPases and actin cytoskeletal reorganization in human lens epithelial cells. Mol. Vis. *9*, 329-336.

Makover,A., Soprano,D.R., Wyatt,M.L., and Goodman,D.S. (1989). An in situ-hybridization study of the localization of retinol-binding protein and transthyretin messenger RNAs during fetal development in the rat. Differentiation *40*, 17-25.

Maren,T.H. (1962). The binding of inhibitors to carbonic anhydrase in vivo: drugs as markers for enzyme. Biochem. Pharmacol. *9*, 39-48.

Maren,T.H. (1977). Ion secretion into cerebrospinal fluid. Exp. Eye Res. *25 Suppl*, 157-159.

Marks,P.A., Richon,V.M., and Rifkind,R.A. (2000). Histone deacetylase inhibitors: inducers of differentiation or apoptosis of transformed cells. J. Natl. Cancer Inst. *92*, 1210-1216.

Marrs,J.A., Napolitano,E.W., Murphy-Erdosh,C., Mays,R.W., Reichardt,L.F., and Nelson,W.J. (1993). Distinguishing roles of the membrane-cytoskeleton and cadherin mediated cell-cell adhesion in generating different Na+,K(+)-ATPase distributions in polarized epithelia. J. Cell Biol. *123*, 149-164.

Massague,J., Cheifetz,S., Boyd,F.T., and Andres,J.L. (1990). TGF-beta receptors and TGF-beta binding proteoglycans: recent progress in identifying their functional properties. Ann. N. Y. Acad Sci *593*, 59-72.

Massip,A., Mulnard,J., Vanderzwalmen,P., Hanzen,C., and Ectors,F. (1982). The behaviour of cow blastocyst in vitro: cinematographic and morphometric analysis. J. Anat. *134 (Pt 2)*, 399-405.

Masuzawa,T., Ohta,T., and Sato,F. (1985). [Enzyme cytochemistry of ventricular choroid plexus. Ultrastructural localization of Na+, K+-adenosinetriphosphatase by immunocytochemical technique]. Neurol. Med. Chir (Tokyo) *25*, 881-885.

McCarthy,J.G., Glasberg,S.B., Cutting,C.B., Epstein,F.J., Grayson,B.H., Ruff,G., Thorne,C.H., Wisoff,J., and Zide,B.M. (1995). Twenty-year experience with early surgery for craniosynostosis: I. Isolated craniofacial synostosis--results and unsolved problems. Plast. Reconstr. Surg. *96*, 272-283.

McKelvie,P.A., Rosen,K.M., Kinney,H.C., and Villa-Komaroff,L. (1992). Insulin-like growth factor II expression in the developing human brain. J. Neuropathol. Exp. Neurol. *51*, 464-471.

Mignatti,P., Morimoto,T., and Rifkin,D.B. (1992). Basic fibroblast growth factor, a protein devoid of secretory signal sequence, is released by cells via a pathway independent of the endoplasmic reticulum-Golgi complex. J. Cell Physiol *151*, 81-93.

Miller,F.D., Pozniak,C.D., and Walsh,G.S. (2000). Neuronal life and death: an essential role for the p53 family. Cell Death. Differ. *7*, 880-888.

Mittnacht,S. (1998). Control of pRB phosphorylation. Curr. Opin. Genet. Dev. *8*, 21-27.

Mollgard,K., Jacobsen,M., Jacobsen,G.K., Clausen,P.P., and Saunders,N.R. (1979). Immunohistochemical evidence for an intracellular localization of plasma proteins in human foetal choroid plexus and brain. Neurosci. Lett. *14*, 85-90.

Mollgard,K. and Saunders,N.R. (1986). The development of the human blood-brain and blood-CSF barriers. Neuropathol. Appl. Neurobiol. *12*, 337-358.

Monsonego-Ornan,E., Adar,R., Feferman,T., Segev,O., and Yayon,A. (2000). The transmembrane mutation G380R in fibroblast growth factor receptor 3 uncouples ligand-mediated receptor activation from down-regulation. Mol. Cell Biol. *20*, 516-522.

Muenke,M. (1995). Finding genes involved in human developmental disorders. Curr. Opin. Genet. Dev. *5*, 354-361.

Muenke,M., Schell,U., Hehr,A., Robin,N.H., Losken,H.W., Schinzel,A., Pulleyn,L.J., Rutland,P., Reardon,W., Malcolm,S., and . (1994). A common mutation in the fibroblast growth factor receptor 1 gene in Pfeiffer syndrome. Nat. Genet. *8*, 269-274.

Muir,D., Varon,S., and Manthorpe,M. (1990). An enzyme-linked immunosorbent assay for bromodeoxyuridine incorporation using fixed microcultures. Anal. Biochem. *185*, 377-382.

Murakami,T., Yasuda,Y., Mita,S., Maeda,S., Shimada,K., Fujimoto,T., and Araki,S. (1987). Prealbumin gene expression during mouse development studied by in situ hybridization. Cell Differ. *22*, 1-9.

Murovic,J.A., Posnick,J.C., Drake,J.M., Humphreys,R.P., Hoffman,H.J., and Hendricks,E.B. (1993b). Hydrocephalus in Apert syndrome: a retrospective review. Pediatr. Neurosurg. *19*, 151-155.

Murovic,J.A., Posnick,J.C., Drake,J.M., Humphreys,R.P., Hoffman,H.J., and Hendricks,E.B. (1993a). Hydrocephalus in Apert syndrome: a retrospective review. Pediatr. Neurosurg. *19*, 151-155.

Murphy,M., Drago,J., and Bartlett,P.F. (1990). Fibroblast growth factor stimulates the proliferation and differentiation of neural precursor cells in vitro. J. Neurosci. Res. *25*, 463-475.

Murphy,M., Reid,K., Ford,M., Furness,J.B., and Bartlett,P.F. (1994). FGF2 regulates proliferation of neural crest cells, with subsequent neuronal differentiation regulated by LIF or related factors. Development *120*, 3519-3528.

Nakahama,K., Nagano,M., Fujioka,A., Shinoda,K., and Sasaki,H. (1999). Effect of TPA on aquaporin 4 mRNA expression in cultured rat astrocytes. Glia *25*, 240-246.

Napolitano,E.W., Venstrom,K., Wheeler,E.F., and Reichardt,L.F. (1991). Molecular cloning and characterization of B-cadherin, a novel chick cadherin. J. Cell Biol. *113*, 893-905.

Naski,M.C., Wang,Q., Xu,J., and Ornitz,D.M. (1996). Graded activation of fibroblast growth factor receptor 3 by mutations causing achondroplasia and thanatophoric dysplasia. Nat. Genet. *13*, 233-237.

Neelamegham,S., Munn,L.L., and Zygourakis,K. (1997). A model for the kinetics of homotypic cellular aggregation under static conditions. Biophys. J. *72*, 51-64.

Netsky,M.G. and Shuangshoti,S. (1970). Studies on the choroid plexus. Neurosci. Res. (N. Y.) *3*, 131-173.

Netsky,M.G. and Shuangshoti,S. (1975). The choroid plexus in health and disease. (Bristol: Wright).

Nguyen,D.H., Beuerman,R.W., Thompson,H.W., and DiLoreto,D.A. (1997). Growth factor and neurotrophic factor mRNA in human lacrimal gland. Cornea *16*, 192-199.

Nicholson,C. (1999). Signals that go with the flow. Trends Neurosci. *22*, 143-145.

Nicholson-Flynn,K., Hitchcock-DeGregori,S.E., and Levitt,P. (1996). Restricted expression of the actin-regulatory protein, tropomyosin, defines distinct boundaries,

evaginating neuroepithelium, and choroid plexus forerunners during early CNS development. J. Neurosci. *16*, 6853-6863.

Nilsson,C., Lindvall-Axelsson,M., and Owman,C. (1992). Neuroendocrine regulatory mechanisms in the choroid plexus-cerebrospinal fluid system. Brain Res. Brain Res. Rev. *17*, 109-138.

Nogradi,A., Kelly,C., and Carter,N.D. (1993). Localization of acetazolamide-resistant carbonic anhydrase III in human and rat choroid plexus by immunocytochemistry and in situ hybridisation. Neurosci. Lett. *151*, 162-165.

Nurcombe,V., Ford,M.D., Wildschut,J.A., and Bartlett,P.F. (1993). Developmental regulation of neural response to FGF-1 and FGF-2 by heparan sulfate proteoglycan. Science *260*, 103-106.

O'Rahilly,R. and Muller,F. (1990). Ventricular system and choroid plexuses of the human brain during the embryonic period proper. Am. J. Anat. *189*, 285-302.

Ohmiya,M., Fukumitsu,H., Nitta,A., Nomoto,H., Furukawa,Y., and Furukawa,S. (2001). Administration of FGF-2 to embryonic mouse brain induces hydrocephalic brain morphology and aberrant differentiation of neurons in the postnatal cerebral cortex. J. Neurosci. Res. *65*, 228-235.

Ong,S.H., Lim,Y.P., Low,B.C., and Guy,G.R. (1997). SHP2 associates directly with tyrosine phosphorylated p90 (SNT) protein in FGF-stimulated cells. Biochem. Biophys. Res. Commun. *238*, 261-266.

Oosterwegel,M., van de,W.M., Timmerman,J., Kruisbeek,A., Destree,O., Meijlink,F., and Clevers,H. (1993). Differential expression of the HMG box factors TCF-1 and LEF-1 during murine embryogenesis. Development *118*, 439-448.

Ornitz,D.M. (2000). FGFs, heparan sulfate and FGFRs: complex interactions essential for development. Bioessays *22*, 108-112.

Ornitz,D.M. and Itoh,N. (2001). Fibroblast growth factors. Genome Biol. *2*, REVIEWS3005.

Ornitz,D.M., Xu,J., Colvin,J.S., McEwen,D.G., MacArthur,C.A., Coulier,F., Gao,G., and Goldfarb,M. (1996). Receptor specificity of the fibroblast growth factor family. J. Biol. Chem. *271*, 15292-15297.

Orr-Urtreger,A., Bedford,M.T., Burakova,T., Arman,E., Zimmer,Y., Yayon,A., Givol,D., and Lonai,P. (1993). Developmental localization of the splicing alternatives of fibroblast growth factor receptor-2 (FGFR2). Dev. Biol. *158*, 475-486.

Ortega,S., Ittmann,M., Tsang,S.H., Ehrlich,M., and Basilico,C. (1998). Neuronal defects and delayed wound healing in mice lacking fibroblast growth factor 2. Proc. Natl. Acad. Sci. U. S. A *95*, 5672-5677.

Ozawa,K., Uruno,T., Miyakawa,K., Seo,M., and Imamura,T. (1996). Expression of the fibroblast growth factor family and their receptor family genes during mouse brain development. Brain Res. Mol. Brain Res. *41*, 279-288.

Palha,J.A., Hays,M.T., Morreale,d.E., Episkopou,V., Gottesman,M.E., and Saraiva,M.J. (1997). Transthyretin is not essential for thyroxine to reach the brain and other tissues in transthyretin-null mice. Am. J. Physiol *272*, E485-E493.

Pawson,T. (1995). Protein modules and signalling networks. Nature *373*, 573-580.

Pearce,R.K., Collins,P., Jenner,P., Emmett,C., and Marsden,C.D. (1996). Intraventricular infusion of basic fibroblast growth factor (bFGF) in the MPTP-treated common marmoset. Synapse *23*, 192-200.

Pelton,R.W., Dickinson,M.E., Moses,H.L., and Hogan,B.L. (1990). In situ hybridization analysis of TGF beta 3 RNA expression during mouse development: comparative studies with TGF beta 1 and beta 2. Development *110*, 609-620.

Peters,A. (1976). The fine structure of the nervous system; the neurons and supporting cells. (Philadelphia: Ws Saunder).

Peters,K., Ornitz,D., Werner,S., and Williams,L. (1993). Unique expression pattern of the FGF receptor 3 gene during mouse organogenesis. Dev. Biol. *155*, 423-430.

Peters,K.G., Werner,S., Chen,G., and Williams,L.T. (1992). Two FGF receptor genes are differentially expressed in epithelial and mesenchymal tissues during limb formation and organogenesis in the mouse. Development *114*, 233-243.

Pittman,R.N., Wang,S., DiBenedetto,A.J., and Mills,J.C. (1993). A system for characterizing cellular and molecular events in programmed neuronal cell death. J. Neurosci. *13*, 3669-3680.

Plotnikov,A.N., Eliseenkova,A.V., Ibrahimi,O.A., Shriver,Z., Sasisekharan,R., Lemmon,M.A., and Mohammadi,M. (2001). Crystal structure of fibroblast growth factor 9 reveals regions implicated in dimerization and autoinhibition. J. Biol. Chem. *276*, 4322-4329.

Plotnikov,A.N., Schlessinger,J., Hubbard,S.R., and Mohammadi,M. (1999). Structural basis for FGF receptor dimerization and activation. Cell *98*, 641-650.

Posnick,J.C., Lin,K.Y., Jhawar,B.J., and Armstrong,D. (1994). Apert syndrome: quantitative assessment by CT scan of presenting deformity and surgical results after first-stage reconstruction. Plast. Reconstr. Surg. *93*, 489-497.

Powers,C.J., McLeskey,S.W., and Wellstein,A. (2000). Fibroblast growth factors, their receptors and signaling. Endocr. Relat Cancer *7*, 165-197.

Profit,S. and Unteregger,G. (2001). Quantitative measurement of cell proliferation using the BrdU ELISA: a comparison between colorimetric anc chemiluminescent detection. Biochemica *4*, 33-35.

Przylepa,K.A., Paznekas,W., Zhang,M., Golabi,M., Bias,W., Bamshad,M.J., Carey,J.C., Hall,B.D., Stevenson,R., Orlow,S., Cohen,M.M., Jr., and Jabs,E.W. (1996). Fibroblast growth factor receptor 2 mutations in Beare-Stevenson cutis gyrata syndrome. Nat. Genet. *13*, 492-494.

Qian,X., Davis,A.A., Goderie,S.K., and Temple,S. (1997). FGF2 concentration regulates the generation of neurons and glia from multipotent cortical stem cells. Neuron *18*, 81-93.

Raballo,R., Rhee,J., Lyn-Cook,R., Leckman,J.F., Schwartz,M.L., and Vaccarino,F.M. (2000). Basic fibroblast growth factor (Fgf2) is necessary for cell proliferation and neurogenesis in the developing cerebral cortex. J. Neurosci. *20*, 5012-5023.

Reardon,W. and Winter,R.M. (1995). The molecular pathology of syndromic craniosynostosis. Mol. Med. Today *1*, 432-437.

Redies,C., Engelhart,K., and Takeichi,M. (1993). Differential expression of N- and R-cadherin in functional neuronal systems and other structures of the developing chicken brain. J. Comp Neurol. *333*, 398-416.

Reid S. Fibroblast growth factor signalling in the development and function of the choroid plexus. 1. 2001. University College London.
Ref Type: Thesis/Dissertation

Reid,S. and Ferretti,P. (2003). Differential expression of fibroblast growth factor receptors in the developing murine choroid plexus. Brain Res. Dev. Brain Res. *141*, 15-24.

Renier,D., Arnaud,E., Cinalli,G., Marchac,D., Brunet,L., Sebag,G., Sainte-Rose,C., and Zerah,M. (1996). [Mental prognosis of Apert syndrome]. Arch. Pediatr. *3*, 752-760.

Renier,D., Sainte-Rose,C., Marchac,D., and Hirsch,J.F. (1982). Intracranial pressure in craniostenosis. J. Neurosurg. *57*, 370-377.

Reuss,B. and Bohlen und,H.O. (2003). Fibroblast growth factors and their receptors in the central nervous system. Cell Tissue Res. *313*, 139-157.

Rose,C.S., Patel,P., Reardon,W., Malcolm,S., and Winter,R.M. (1997). The TWIST gene, although not disrupted in Saethre-Chotzen patients with apparently balanced translocations of 7p21, is mutated in familial and sporadic cases. Hum. Mol. Genet. *6*, 1369-1373.

Rousseau,F., Bonaventure,J., Legeai-Mallet,L., Pelet,A., Rozet,J.M., Maroteaux,P., Le Merrer,M., and Munnich,A. (1994). Mutations in the gene encoding fibroblast growth factor receptor-3 in achondroplasia. Nature *371*, 252-254.

Roussel,G., Delaunoy,J.P., Nussbaum,J.L., and Mandel,P. (1979). Demonstration of a specific localization of carbonic anhydrase C in the glial cells of rat CNS by an immunohistochemical method. Brain Res. *160*, 47-55.

Ruberte,E., Friederich,V., Chambon,P., and Morriss-Kay,G. (1993). Retinoic acid receptors and cellular retinoid binding proteins. III. Their differential transcript distribution during mouse nervous system development. Development *118*, 267-282.

Russell,J.M. (2000). Sodium-potassium-chloride cotransport. Physiol Rev. *80*, 211-276.

Saito,Y. and Wright,E.M. (1987). Regulation of intracellular chloride in bullfrog choroid plexus. Brain Res. *417*, 267-272.

Sarimski,K. (1997). Cognitive functioning of young children with Apert's syndrome. Genet. Couns. *8*, 317-322.

Sato,M., Sato,T., Kojima,N., Imai,K., Higashi,N., Wang,D.R., and Senoo,H. (2004). 3-D structure of extracellular matrix regulates gene expression in cultured hepatic stellate cells to induce process elongation. Comp Hepatol. *3 Suppl 1*, S4.

Saunders,N.R., Habgood,M.D., and Dziegielewska,K.M. (1999a). Barrier mechanisms in the brain, I. Adult brain. Clin. Exp. Pharmacol. Physiol *26*, 11-19.

Saunders,N.R., Habgood,M.D., and Dziegielewska,K.M. (1999b). Barrier mechanisms in the brain, II. Immature brain. Clin. Exp. Pharmacol. Physiol *26*, 85-91.

Schatteman,G.C., Morrison-Graham,K., van Koppen,A., Weston,J.A., and Bowen-Pope,D.F. (1992). Regulation and role of PDGF receptor alpha-subunit expression during embryogenesis. Development *115*, 123-131.

Schell,U., Hehr,A., Feldman,G.J., Robin,N.H., Zackai,E.H., Die-Smulders,C., Viskochil,D.H., Stewart,J.M., Wolff,G., Ohashi,H., and . (1995). Mutations in FGFR1 and FGFR2 cause familial and sporadic Pfeiffer syndrome. Hum. Mol. Genet. *4*, 323-328.

Schreiber,G., Richardson,S.J., and Prapunpoj,P. (2001). Structure and expression of the transthyretin gene in the choroid plexus: a model for the study of the mechanism of evolution. Microsc. Res. Tech. *52*, 21-30.

Segal,M.B. (2000). The choroid plexuses and the barriers between the blood and the cerebrospinal fluid. Cell Mol. Neurobiol. *20*, 183-196.

Segal,M.B. (2001). Transport of nutrients across the choroid plexus. Microsc. Res. Tech. *52*, 38-48.

Sepp,N.T., Li,L.J., Lee,K.H., Brown,E.J., Caughman,S.W., Lawley,T.J., and Swerlick,R.A. (1994). Basic fibroblast growth factor increases expression of the alpha v beta 3 integrin complex on human microvascular endothelial cells. J. Invest Dermatol. *103*, 295-299.

Shiang,R., Thompson,L.M., Zhu,Y.Z., Church,D.M., Fielder,T.J., Bocian,M., Winokur,S.T., and Wasmuth,J.J. (1994). Mutations in the transmembrane domain of FGFR3 cause the most common genetic form of dwarfism, achondroplasia. Cell *78*, 335-342.

Shuangshoti,S. and Netsky,M.G. (1966). Histogenesis of choroid plexus in man. Am. J. Anat. *118*, 283-316.

Song,J., Rolfe,B.E., Hayward,I.P., Campbell,G.R., and Campbell,J.H. (2001). Reorganization of structural proteins in vascular smooth muscle cells grown in collagen gel and basement membrane matrices (Matrigel): a comparison with their in situ counterparts. J. Struct. Biol. *133*, 43-54.

Southwell,B.R., Duan,W., Tu,G.F., and Schreiber,G. (1991). Ontogenesis of transthyretin gene expression in chicken choroid plexus and liver. Comp Biochem. Physiol B *100*, 329-338.

Speake,T., Whitwell,C., Kajita,H., Majid,A., and Brown,P.D. (2001). Mechanisms of CSF secretion by the choroid plexus. Microsc. Res. Tech. *52*, 49-59.

Spector,J.A., Greenwald,J.A., Warren,S.M., Bouletreau,P.J., Detch,R.C., Fagenholz,P.J., Crisera,F.E., and Longaker,M.T. (2002). Dura mater biology: autocrine and paracrine effects of fibroblast growth factor 2. Plast. Reconstr. Surg. *109*, 645-654.

Spivak-Kroizman,T., Lemmon,M.A., Dikic,I., Ladbury,J.E., Pinchasi,D., Huang,J., Jaye,M., Crumley,G., Schlessinger,J., and Lax,I. (1994). Heparin-induced oligomerization of FGF molecules is responsible for FGF receptor dimerization, activation, and cell proliferation. Cell *79*, 1015-1024.

Spraul,C.W., Kaven,C., Lang,G.K., and Lang,G.E. (2004). Effect of growth factors on bovine retinal pigment epithelial cell migration and proliferation. Ophthalmic Res. *36*, 166-171.

Stadler,E. and Dziadek,M. (1996). Extracellular matrix penetration by epithelial cells is influenced by quantitative changes in basement membrane components and growth factors. Exp. Cell Res. *229*, 360-369.

Stevenson,B.R., Siliciano,J.D., Mooseker,M.S., and Goodenough,D.A. (1986). Identification of ZO-1: a high molecular weight polypeptide associated with the tight junction (zonula occludens) in a variety of epithelia. J. Cell Biol. *103*, 755-766.

Strano,S., Rossi,M., Fontemaggi,G., Munarriz,E., Soddu,S., Sacchi,A., and Blandino,G. (2001). From p63 to p53 across p73. FEBS Lett. *490*, 163-170.

Strazielle,N. and Ghersi-Egea,J.F. (2000). Choroid plexus in the central nervous system: biology and physiopathology. J. Neuropathol. Exp. Neurol. *59*, 561-574.

Sturrock,R.R. (1979). A morphological study of the development of the mouse choroid plexus. J. Anat. *129*, 777-793.

Sullivan,K.A. and Feldman,E.L. (1994). Immunohistochemical localization of insulin-like growth factor-II (IGF-II) and IGF-binding protein-2 during development in the rat brain. Endocrinology *135*, 540-547.

Sunde,M., Richardson,S.J., Chang,L., Pettersson,T.M., Schreiber,G., and Blake,C.C. (1996). The crystal structure of transthyretin from chicken. Eur. J. Biochem. *236*, 491-499.

Szebenyi,G. and Fallon,J.F. (1999). Fibroblast growth factors as multifunctional signaling factors. Int. Rev. Cytol. *185*, 45-106.

Takakura,N., Yoshida,H., Ogura,Y., Kataoka,H., Nishikawa,S., and Nishikawa,S. (1997). PDGFR alpha expression during mouse embryogenesis: immunolocalization

analyzed by whole-mount immunohistostaining using the monoclonal anti-mouse PDGFR alpha antibody APA5. J. Histochem. Cytochem. *45*, 883-893.

Tanner,G.A., Maxwell,M.R., and McAteer,J.A. (1992). Fluid transport in a cultured cell model of kidney epithelial cyst enlargement. J. Am. Soc. Nephrol. *2*, 1208-1218.

Taylor,W.J., Hayward,R.D., Lasjaunias,P., Britto,J.A., Thompson,D.N., Jones,B.M., and Evans,R.D. (2001). Enigma of raised intracranial pressure in patients with complex craniosynostosis: the role of abnormal intracranial venous drainage. J. Neurosurg. *94*, 377-385.

Tennyson,V.M. and pappas,G.D. (1968). The fine structure of the choroid plexus adult and developmental stages. Prog. Brain Res. *29*, 63-85.

Terasaki,T. and Hosoya,K. (2001). Conditionally immortalized cell lines as a new in vitro model for the study of barrier functions. Biol. Pharm. Bull. *24*, 111-118.

Thomas,T., Power,B., Hudson,P., Schreiber,G., and Dziadek,M. (1988). The expression of transthyretin mRNA in the developing rat brain. Dev. Biol. *128*, 415-427.

Thomas,T., Schreiber,G., and Jaworowski,A. (1989). Developmental patterns of gene expression of secreted proteins in brain and choroid plexus. Dev. Biol. *134*, 38-47.

Thomas,T., Stadler,E., and Dziadek,M. (1992). Effects of the extracellular matrix on fetal choroid plexus epithelial cells: changes in morphology and multicellular organization do not affect gene expression. Exp. Cell Res. *203*, 198-213.

Thompson,D.N., Jones,B.M., Harkness,W., Gonsalez,S., and Hayward,R.D. (1997). Consequences of cranial vault expansion surgery for craniosynostosis. Pediatr. Neurosurg. *26*, 296-303.

Thompson,D.N., Malcolm,G.P., Jones,B.M., Harkness,W.J., and Hayward,R.D. (1995). Intracranial pressure in single-suture craniosynostosis. Pediatr. Neurosurg. *22*, 235-240.

Tichelaar,J.W., Wert,S.E., Costa,R.H., Kimura,S., and Whitsett,J.A. (1999). HNF-3/forkhead homologue-4 (HFH-4) is expressed in ciliated epithelial cells in the developing mouse lung. J Histochem. Cytochem. *47*, 823-832.

Unsicker,K., Flanders,K.C., Cissel,D.S., Lafyatis,R., and Sporn,M.B. (1991). Transforming growth factor beta isoforms in the adult rat central and peripheral nervous system. Neuroscience *44*, 613-625.

Vaananen,H.K., Carter,N.D., and Dodgson,S.J. (1991). Immunocytochemical localization of mitochondrial carbonic anhydrase in rat tissues. J. Histochem. Cytochem. *39*, 451-459.

Vaccarino,F.M., Schwartz,M.L., Raballo,R., Nilsen,J., Rhee,J., Zhou,M., Doetschman,T., Coffin,J.D., Wyland,J.J., and Hung,Y.T. (1999a). Changes in cerebral cortex size are governed by fibroblast growth factor during embryogenesis. Nat. Neurosci. *2*, 246-253.

Vaccarino,F.M., Schwartz,M.L., Raballo,R., Rhee,J., and Lyn-Cook,R. (1999b). Fibroblast growth factor signaling regulates growth and morphogenesis at multiple steps during brain development. Curr. Top. Dev. Biol. *46*, 179-200.

Vainikka,S., Partanen,J., Bellosta,P., Coulier,F., Birnbaum,D., Basilico,C., Jaye,M., and Alitalo,K. (1992). Fibroblast growth factor receptor-4 shows novel features in genomic structure, ligand binding and signal transduction. EMBO J. *11*, 4273-4280.

Vaishnav,Y.N., Vaishnav,M.Y., and Pant,V. (1998). The molecular and functional characterization of E2F-5 transcription factor. Biochem. Biophys. Res. Commun. *242*, 586-592.

Venero,J.L., Vizuete,M.L., Machado,A., and Cano,J. (2001). Aquaporins in the central nervous system. Prog. Neurobiol. *63*, 321-336.

Voetmann,E. (1949). On the structure and surface area of the human choroid plexus; a quantitative anatomical study. Acta Anat. *8*, 1.

Walshe,J. and Mason,I. (2000). Expression of FGFR1, FGFR2 and FGFR3 during early neural development in the chick embryo. Mech. Dev. *90*, 103-110.

Wang,Y., Spatz,M.K., Kannan,K., Hayk,H., Avivi,A., Gorivodsky,M., Pines,M., Yayon,A., Lonai,P., and Givol,D. (1999). A mouse model for achondroplasia produced by targeting fibroblast growth factor receptor 3. Proc. Natl. Acad. Sci. U. S. A *96*, 4455-4460.

Watts,A.G., Sanchez-Watts,G., Emanuel,J.R., and Levenson,R. (1991). Cell-specific expression of mRNAs encoding Na+,K(+)-ATPase alpha- and beta-subunit isoforms within the rat central nervous system. Proc. Natl. Acad. Sci. U. S. A *88*, 7425-7429.

Webster,M.K. and Donoghue,D.J. (1997). FGFR activation in skeletal disorders: too much of a good thing. Trends Genet *13*, 178-182.

Weigel,D., Jurgens,G., Kuttner,F., Seifert,E., and Jackle,H. (1989). The homeotic gene fork head encodes a nuclear protein and is expressed in the terminal regions of the Drosophila embryo. Cell *57*, 645-658.

Wilkie,A.O. (1997). Craniosynostosis: genes and mechanisms. Hum. Mol. Genet. *6*, 1647-1656.

Wilkie,A.O., Slaney,S.F., Oldridge,M., Poole,M.D., Ashworth,G.J., Hockley,A.D., Hayward,R.D., David,D.J., Pulleyn,L.J., Rutland,P., and . (1995). Apert syndrome results from localized mutations of FGFR2 and is allelic with Crouzon syndrome. Nat. Genet. *9*, 165-172.

Wilting,J. and Christ,B. (1989). An experimental and ultrastructural study on the development of the avian choroid plexus. Cell Tissue Res. *255*, 487-494.

Wislocki,G.B. and Ladman,A.J. (1958). The fine structure of the mammalian choroid plexus. In Ciba Foudation on Cerebrospinal Fluid, G.E.W.Wolstenhome and C.M.O'Connor, eds. (Boston: Little Brown & Co), pp. 55-79.

Woods,A.L., Hall,P.A., Shepherd,N.A., Hanby,A.M., Waseem,N.H., Lane,D.P., and Levison,D.A. (1991). The assessment of proliferating cell nuclear antigen (PCNA) immunostaining in primary gastrointestinal lymphomas and its relationship to histological grade, S+G2+M phase fraction (flow cytometric analysis) and prognosis. Histopathology *19*, 21-27.

Wright,E.M. (1978). Transport processes in the formation of the cerebrospinal fluid. Rev. Physiol Biochem. Pharmacol. *83*, 3-34.

Xiao,Z.S., Thomas,R., Hinson,T.K., and Quarles,L.D. (1998). Genomic structure and isoform expression of the mouse, rat and human Cbfa1/Osf2 transcription factor. Gene *214*, 187-197.

Yamaguchi,T.P., Harpal,K., Henkemeyer,M., and Rossant,J. (1994). fgfr-1 is required for embryonic growth and mesodermal patterning during mouse gastrulation. Genes Dev. *8*, 3032-3044.

Yamaguchi,T.P. and Rossant,J. (1995). Fibroblast growth factors in mammalian development. Curr. Opin. Genet Dev *5*, 485-491.

Yang,A. and McKeon,F. (2000). P63 and P73: P53 mimics, menaces and more. Nat. Rev. Mol. Cell Biol. *1*, 199-207.

Yang,A., Walker,N., Bronson,R., Kaghad,M., Oosterwegel,M., Bonnin,J., Vagner,C., Bonnet,H., Dikkes,P., Sharpe,A., McKeon,F., and Caput,D. (2000). p73-deficient mice have neurological, pheromonal and inflammatory defects but lack spontaneous tumours. Nature *404*, 99-103.

Yazaki,N., Hosoi,Y., Kawabata,K., Miyake,A., Minami,M., Satoh,M., Ohta,M., Kawasaki,T., and Itoh,N. (1994). Differential expression patterns of mRNAs for members of the fibroblast growth factor receptor family, FGFR-1-FGFR-4, in rat brain. J. Neurosci. Res. *37*, 445-452.

Yip,J.W. (1997). Regulation of the epithelial brush border Na+/H+ exchanger isoform 3 stably expressed in fibroblasts by fibroblast growth factor and phorbol esters is not through changes in phosphorylation of the exchanger. The Journal of Biological Chemistry *272*, 18473-18480.

Yoshida,M., Suda,Y., Matsuo,I., Miyamoto,N., Takeda,N., Kuratani,S., and Aizawa,S. (1997). Emx1 and Emx2 functions in development of dorsal telencephalon. Development *124*, 101-111.

Yu,K., Herr,A.B., Waksman,G., and Ornitz,D.M. (2000). Loss of fibroblast growth factor receptor 2 ligand-binding specificity in Apert syndrome. Proc. Natl. Acad. Sci. U. S. A *97*, 14536-14541.

Zelenina,M., Zelenin,S., Bondar,A.A., Brismar,H., and Aperia,A. (2002). Water permeability of aquaporin-4 is decreased by protein kinase C and dopamine. Am. J. Physiol Renal Physiol *283*, F309-F318.

Zeuthen,T. (1994). Cotransport of K+, Cl- and H2O by membrane proteins from choroid plexus epithelium of Necturus maculosus. J. Physiol *478 (Pt 2)*, 203-219.

Zeuthen,T. and Wright,E.M. (1981). Epithelial potassium transport: tracer and electrophysiological studies in choroid plexus. J. Membr. Biol. *60*, 105-128.

Zhan,X., Plourde,C., Hu,X., Friesel,R., and Maciag,T. (1994). Association of fibroblast growth factor receptor-1 with c-Src correlates with association between c-Src and cortactin. J. Biol. Chem. *269*, 20221-20224.

Zhao,Y., Sheng,H.Z., Amini,R., Grinberg,A., Lee,E., Huang,S., Taira,M., and Westphal,H. (1999). Control of hippocampal morphogenesis and neuronal differentiation by the LIM homeobox gene Lhx5. Science *284*, 1155-1158.

Zheng,W., Blaner,W.S., and Zhao,Q. (1999). Inhibition by lead of production and secretion of transthyretin in the choroid plexus: its relation to thyroxine transport at blood-CSF barrier. Toxicol. Appl. Pharmacol. *155*, 24-31.

Zheng,W., Lu,Y.M., Lu,G.Y., Zhao,Q., Cheung,O., and Blaner,W.S. (2001). Transthyretin, thyroxine, and retinol-binding protein in human cerebrospinal fluid: effect of lead exposure. Toxicol. Sci. *61*, 107-114.

Zheng,X. and Chen,X. (2001). Aquaporin 3, a glycerol and water transporter, is regulated by p73 of the p53 family. FEBS Lett. *489*, 4-7.

Zhou,L., Graeff,R.W., McCray,P.B., Jr., Simonet,W.S., and Whitsett,J.A. (1996). Keratinocyte growth factor stimulates CFTR-independent fluid secretion in the fetal lung in vitro. Am. J. Physiol *271*, L987-L994.

Zhou,Y.X., Xu,X., Chen,L., Li,C., Brodie,S.G., and Deng,C.X. (2000). A Pro250Arg substitution in mouse Fgfr1 causes increased expression of Cbfa1 and premature fusion of calvarial sutures. Hum. Mol. Genet. *9*, 2001-2008.

Zlokovic,B.V., Mackic,J.B., Wang,L., McComb,J.G., and McDonough,A. (1993). Differential expression of Na,K-ATPase alpha and beta subunit isoforms at the blood-brain barrier and the choroid plexus. J. Biol. Chem. *268*, 8019-8025.